LBL-34553
UC-403

Lawrence Berkeley Laboratory
UNIVERSITY OF CALIFORNIA

EARTH SCIENCES DIVISION

Iterative Electromagnetic Born Inversion Applied to Earth Conductivity Imaging

D.L. Alumbaugh
(Ph.D. Thesis)

August 1993

Prepared for the U.S. Department of Energy under Contract Number DE-AC03-76SF00098

DISCLAIMER

LBL-34553

Iterative Electromagnetic Born Inversion Applied to Earth Conductivity Imaging

David Lee Alumbaugh

(Ph.D. Thesis)

Engineering Geoscience
University of California

and

Earth Sciences Division
Lawrence Berkeley Laboratory
University of California
Berkeley, California 94720

August 1993

This work was supported by the Director, Office of Energy Research, Office of Basic Energy Sciences, Engineering and Geosciences Division, of the U.S. Department of Energy under Contract No. DE-AC03-76SF00098.

Abstract

Iterative Electromagnetic Born Inversion Applied to Earth Conductivity Imaging

by

David L. Alumbaugh

Doctor of Philosophy in Material Science and Mineral Engineering

University of California at Berkeley

Professor H. F. Morrison, Chair

This thesis investigates the use of a fast imaging technique to deduce the spatial conductivity distribution in the earth from low frequency (< 1 MHz), crosswell electromagnetic (EM) measurements. The theory embodied in this work is the extension of previous strategies and is based on the Born series approximation to solve both the forward and inverse problem. Nonlinear integral equations are employed to derive the series expansion which accounts for the scattered magnetic fields that are generated by inhomogeneities embedded in either a homogenous or a layered earth. A sinusoidally oscillating, vertically oriented magnetic dipole is employed as a source, and it is assumed that the scattering bodies are azimuthally symmetric about the source dipole axis. The use of this model geometry reduces the 3-D vector problem to a more manageable 2-D scalar form.

Two different strategies for approximate forward modeling are analyzed and compared to a full nonlinear integral equation solution. This analysis is accomplished in terms of the dimensionless *anomalous induction number* which is defined as $\Delta\sigma\omega\mu S$, where $\Delta\sigma$ is the conductivity contrast between the background and the body, ω is the frequency of operation, μ is the magnetic permeability of free space and S is the cross sectional area of the scattering body. The first order Born approximation, which represents the first term in the Born series, is found to be valid for $\Delta\sigma\omega\mu S \leq 0.02$, while the Born series is demonstrated to yield accurate results up to $\Delta\sigma\omega\mu S \approx 2.0$.

To examine how measurements with different source-receiver combinations and operating frequencies are combined to probe the medium under investigation, the first

order Born approximation is applied to linearize the integral equations. From these simplified equations, sensitivity functions are derived which define the ability of the crosswell magnetic field measurements to detect small local changes in conductivity. Plots of the spatial variation in sensitivity indicate that vertical resolution is a function of the spatial sampling density in the vertical direction, while the horizontal resolution depends on the vertical separation between the source and receiver. Additional improvement in the horizontal resolution can be provided by making additional measurements with both the source and receiver in the same hole.

Further sensitivity analysis is completed in terms of a dimensionless *background induction number* that is defined by $\sigma\omega\mu l^2$ where σ is the background conductivity and l is the source-receiver separation. Analysis of the crosswell sensitivity in terms of this parameter facilitates experimental system design for a given borehole separation and background conductivity, as well as the determination of the operating frequency which falls within an optimal range of $\sigma\omega\mu l^2$.

For $\sigma\omega\mu l^2 < 10$, the scattered fields are very small compared to the primary field, making measurements of the inhomogenous response very difficult in the presence of noise. In addition, a given source-receiver pair is sensitive to a large volume of strata outside of the interwell zone rather than just the region immediately between the probes. The latter property requires that a larger region be considered in the interpretation phase and that the proper 2-D or 3-D model geometry is employed. As the induction number is increased the nature of the sensitivity functions change. For $\sigma\omega\mu l^2 > 50$ a given source-receiver pair is sensitive only to a "ray-path" shaped zone immediately between the two probes and the scattered fields are on the same order of magnitude as the primary fields. Unfortunately the attenuation at these large induction numbers prevents accurate measurement of the fields for large vertical probe separation due to the dynamic range limitations of the measurement system.

The validity of using a 2-D cylindrical model to simulate a generally inhomogenous earth is investigated by comparing the 2-D Born series solution to other 1-D, 2-D and 3-D modeling algorithms. For $\sigma\omega\mu l^2 < 50$ the size of the region outside of the wells that is included in the model has a significant effect on the properties of the calculated EM fields with the different model geometries producing significantly different results. At larger induction numbers ($\sigma\omega\mu l^2 > 50$) a given source-receiver pair senses only the medium directly between the probes and the resulting fields are fairly independent of whether a 1-D, 2-D or 3-D model is employed. Unfortunately at these large induction numbers the Born series does not readily converge.

To image the subsurface conductivity structure between two wells, the 2-D

cylindrical Born series approximation is incorporated into an iterative Born inversion scheme. The inversion problem is stabilized by using bounding constraints and regularization method which results in a smoothest model that fits the data to the desired noise level. Resolution of this imaging scheme is defined by employing two small conductive anomalies that are located adjacent to each other. At low background induction numbers ($\sigma\omega\mu l^2 < 10$) the resolution is poor due to small signal strength. For $\sigma\omega\mu l^2 > 50$ the resolution is excellent, however the Born series approximation tends to fail. In between these two extremes lies a range of $\sigma\omega\mu l^2$ in which both the resolution and modeling accuracy are very good.

The applicability of cross well EM for imaging and monitoring changes caused by subsurface processes is demonstrated using 1-D layered models as well as 2-D and 3-D models that simulate an injected plume of conductive fluid. Here also the extension of the model outside of the interwell region is very important at low induction numbers. When $\sigma\omega\mu l^2 < 50$, image artifacts that mimick structure can appear if the proper geometry is not employed. These effects are found to be minimal for $\sigma\omega\mu l^2 > 50$ as long as the Born series approximation yields accurate forward modeling results.

The validity of the cross well EM method is tested by applying the imaging scheme to two sets of field data. Images of the data collected at the Devine, Texas test site show excellent correlation with the well logs. Unfortunately there is a drift error present in the data that limits the accuracy of the results. A more complete set of data collected at the Richmond field station in Richmond, California demonstrates that cross well EM can be successfully employed to monitor the position of an injected mass of salt water. Both the data and the resulting images clearly indicate the plume migrates toward the north-northwest. The plausibility of these conclusions is verified by applying the imaging code to synthetic data generated by a 3-D sheet model.

Table of Contents

List of commonly used symbols

$\mathbf{A}_h, \mathbf{A}_v$	Matrices representing a discretization of the first derivative in the horizontal and vertical directions
$d_i, \mathbf{D}$	Data in discreet and vector form
$D_i(\lambda)$	Downgoing component of the wavefield in the i'th layer
$\mathbf{E}$	Electric field in Volts/m (a vector)
$E_\phi, E_\phi^p, E_\phi^s$	Total, primary and scattered electric field in the $\hat{\phi}$ direction (Volts/m)
EM	electromagnetic
f	Frequency
G	2-D electric field Green's function
g	3-D electric field Green's function
G_{Hr}, G_{Hz}	2-D radial and vertical magnetic field Green's functions
g_{Hr}, g_{Hz}	3-D radial and vertical magnetic field Green's functions
$\mathbf{H}, \mathbf{H}^p, \mathbf{H}^s$	Total, primary and scattered magnetic fields in Amps/m (vectors)
H_r^p, H_z^p	Primary magnetic field in the radial and vertical directions (Amps/m)
H_r^s, H_z^s	Scattered magnetic field in the radial and vertical directions (Amps/m)
$\mathbf{H}_0, \mathbf{H}_1$	Struve functions of the first kind of orders 0 and 1
i	$\sqrt{-1}$
$\mathbf{J}_s$	Source current density in Amps /m^2(a vector)
J_ϕ	Source current flowing in a magnetic dipole (Amps/m^2)
$J_0(\lambda r)$	Zero'th order Bessel's function of the first kind
$J_1(\lambda r)$	First order Bessel's function of the first kind
k_0	Background wavenumber = $\sqrt{-i\omega\sigma_0\mu}$
K_{Hr}, K_{Hz}	Born kernel for the radial and vertical scattered magnetic fields
$k_{ij}, \mathbf{K}$	Sensitivity in discreet and matrix form
K_i	γ_i / σ_i for the i'th layer
M	Number of data points
N	Number of cells in model or number of unknowns
O(r),O	Object function - $\frac{(\sigma(\mathbf{r}) - \sigma_0)}{\sigma_0}$
$\mathbf{O}'$	Object function in matrix form
R	Distance between two points
r=(r,z)	Location of point of interest in cylindrical coordinates
$\hat{r}, \hat{\phi}, \hat{z}$ (r,ϕ,z)	Cylindrical coordinate system
r_c, z_c	Location of a single cell anomaly

$\mathbf{r}_{rx} = (r_{rx}, z_{rx})$	Receiver location in cylindrical coordinates
$\mathbf{r}_{tx} = (0, z_{tx})$	Source position in cylindrical coordinates
r^i_{TE}	Reflection coefficient at the i'th layer boundary
S	Cross-sectional area of a inhomogenous body
$U_i(\lambda)$	Upgoing component of the wavefield in the i'th layer
VMD	Vertical magnetic dipole
$\hat{\mathbf{x}}, \hat{\mathbf{y}}, \hat{\mathbf{z}}$ (x,y,z)	Cartesian coordinate system
x_c, y_c, z_c	Location of the center of a 3-D sheet
$\tilde{\mathbf{Z}}$	Impedance matrix
Z_i	Input impedance at the i 'th layer interface
δ	Delta function
Δ	Length of the side of a cell
$\Delta\sigma$	$\sigma(\mathbf{r}) - \sigma_0$
γ	$\sqrt{\lambda^2 + k_0^2}$
λ	Hankel transform wavenumber
λ_h, λ_v	Lagrangian multipliers controlling smoothness in the horizontal and vertical directions
μ	Magnetic permeability
ν	Function defined on page 67.
π	Pi
σ	Electrical conductivity
σ_0	Background electrical conductivity
σ_a	Anomalous conductivity
σ_c	Conductivity of a single cell anomaly
ω	Radial frequency = $2\pi f$
∇	Gradient operator (a vector)

Preface

"That's what learning is. You suddenly understand something you've understood all your life, but in a new way."

Doris Lessing

Acknowledgments

I would like to express my sincere appreciation and gratitude to Professor Frank Morrison who served as my research advisor throughout most of my stay at Berkeley. Trough his guidance and friendship I not only gained valuable scientific wisdom and insight, but also examples of how to properly balance science with other pursuits. I feel lucky to have worked under him. My gratitude also goes out to Proffesor Alex Becker, my part time research advisor who taught me the intricacies of proper data collection and analysis. Finally I would like to thank the third member on my committee, Proffesor Thomas Budinger, for his constructive criticism on how to extend my work outward from the geophysical community to the general scientific community.

Several other people deserve thanks for their input to this work. Ki Ha Lee provided much of the guidance in the early stages and was always available for follow-up discussions. Mike Wilt not only provided financial support but also encouragement when things were not going so well. Carlos-Torres Verdin and Greg Newman both provided enlightening answers to the many questions that were asked of them, and Jamie Rector provided thought provoking comments on the similarities and differences between seismic and EM measurements. Finally I need to thank Marylla Deszsz-Pan, Hung Wen (Ocean) Tseng, Jim Doherty and Don Lippert for their help in collecting the data at the Richmond Field Station.

Not to be outshined by the names above, I would like to express my love and gratitude to my family. To my parents, Bob and Elaine, your emotional and financial support got me to where I am today. To my brother Jim, your companionship as a room-mate and a friend made relocating to, and the stay in Berkeley much easier than I initially imagined. Finally my heart goes out to my loving wife Jennifer. I am very lucky to have found someone as supportive and wonderful as you to spend my life with.

I am appreciative of my friends that I have made in EG, MSME and LBL with whom I have been able to share many good times and many insightful discussions. The "U.C. Mining Association" basketball game always provided good laughs and muscle soreness, and promoted the idea of Engineering Geoscience as a place where "science interferes with fun." I would also like to thank and express my friendship to the other members of my ex-band " A Different Kitchen". Those five years of creating, gigging, recording and general mayhem were the best of times, and I wouldn't trade them for anything.

Finally I must thank the financial support which I received throughout the years without which this work would of never got off the ground. I am indebted to Chevron

and the department of MSME for fellowships that I received at various times. Also a large amount of funding was supplied by an industrial research consortium that includes MOBIL, SCHLUMBERGER, SHELL, NORANDA, EXXON, NITETSU MINING CORPORATION, BRITISH PETROLEUM, TEXACO and AMOCO.

This work was partially supported by the Director, Office of Energy Research, Office of Basic Energy Sciences, Engineering and Geosciences Division, of the U.S. Department of Energy under contract no. DE-AC03-76SF0098.

Chapter 1
Introduction

The cross-well electromagnetic (EM) method is a rapidly evolving geophysical technique that has recently experienced increased attention due to improvements in field instrumentation, computing power and methods of interpretation. The principal goal of this method is to obtain high resolution images of the subsurface electrical conductivity distribution from which vital information on geological structure, rock porosity, fluid saturation and fracture orientation can be deduced. In the oil patch this type of knowledge is extremely useful in determining reservoir heterogeneity and the amount of oil in situ. In environmental and engineering studies it can be used to estimate water quality, to monitor the subsurface position of contaminants and to characterize aquifer properties.

One of the most promising areas for using cross well EM is the monitoring of processes which alter the physical properties of the subsurface. In enhanced oil recovery (EOR) projects, techniques such as steam injection, in situ combustion,water flooding and carbon dioxide injection are routinely employed to either mobilize hydrocarbons in heavy oil deposits and/or recover additional oil from depleted reservoirs (van Poolen and Associates Inc.,1980). Steam injection is also rapidly developing as an economically sound method of cleaning up hazardous waste and petroleum spills (Adenekan and Patzek, 1993). Unfortunately, due to reservoir complexity the injected fluid often does not migrate in the predicted direction. Thus by using cross-hole geophysics to more accurately define the reservoir conditions that exist between the wells we may be able to save both time and money.

In this chapter we will review the electrical properties of rocks and how these properties can be altered by the injection of fluids. Next, geophysical techniques will be discussed which have been succesful in monitoring reservoir processes. Finally, I will summarize the research results are presented in each chapter of this thesis.

1.1 Electrical properties of reservoir rocks

It is well known that the electrical conductivity (and its reciprocal, the resistivity) of rocks is dependent on a wide variety of factors. As shown in Figure 1.1, the conductivty of naturally ocurring earth materials varies over several orders of magnitude. In sedimentary rocks the electric current flow is through the ionic pore fluid rather than through the rock matrix. Thus the conductivity is primarily dependent on the rock porosity, the fluid conductivity, the rock saturation, and to a lesser degree the formation

temperature and pressure, the pore geometry and the wettability of the grains. An additional property that severly affects the bulk conductivity of sedimentary rocks is the percentage of clay minerals present in the rock matrix. This effect will be discussed more fully below.

For an isotropic, fully saturated medium free of clay, Archie (1942) found an empirical relationship between the bulk conductivity of the rock (σ_b) ,the porosity of the rock (ϕ) and the conductivity of the pore fluid(σ_f). This relationship has come to be known as Archie's Law and is given by

$$\sigma_b = \sigma_f \phi^n. \qquad (1.1)$$

Here n is a constant dependent on the rock matrix which in most cases takes on values between 1.8 and 2.2.

The dependence of the rock conductivity on the fluid properties is immediately evident from this equation. Keller (1988) shows that the conductivity of water can vary over several orders of magnitude depending on its salinty (Figure 1.2). Fresh waters tend to be resistive while saline brines are very conductive. Oils on the other hand are resistive. Thus a 'clean' sand of constant porosity can exhibit conductivities which range over several orders of magnitude depending on the type of fluid that is present in its pores. The introduction of gas into the medium further complicates matters with equation 1.1 becoming also dependent on the percentage of fluid saturation.

If clays are present in the rock matrix, the relationship between the bulk rock conductivity and porosity becomes even more complicated (Waxman and Smits, 1968). This complexity arises from the presence of absorbed cations that are present on the surface of the clay particles. These cations diffuse into the pore fluid adjacent to the clay surface adding to the number of ions already present in solution and thus allowing the rock to carry a larger electric current (Ward and Fraser, 1967). This process accounts for the relatively high conductivty values of clays and shales as shown in Figure 1.1. In addition because clay minerals tend to exhibit a flat 'platy' shape when compared to the spherical grains found in clean sandstones, the geometry of the pores will also affect the bulk conductivity.

Though the affects of the rock temperature are not as significant as those described above, Figure 1.3 demonstrates that increasing the temperature will result in more conductive fluid due to increased ion mobility. Therefore if the rock is fully saturated, higher temperatures will result in greater bulk rock conductivities. However, higher temperatures can also evaporate the pore fluid which decreases the saturation. Thus raising the temperature can in some cases increase the resitivity of the rock.

The dependence of the bulk rock conductivity on the electrical properties of the pore fluid as described above is very useful for monitoring EOR processes. For example, the most commonly employed EOR process in heavy oil reservoirs involves the injection of hot water and steam into the pay zone. Increasing the temperature in this manner makes the oil less viscous thereby allowing for easier extraction. The process not only increases the temperature in the reservoir and surounding rocks, but as the fluid is pumped further into the formation it displaces resistive oil there by increasing the percentage of water saturation. If the injected water is saline it will increase the salinity of the formation. However if it is fresh, the water will tend to 'flush out' any saline pore fluid and thus decrease the salinity within the injection zone.

Mansure and Meldau (1990) have hypothesized a model for such a flood (Figure 1.4) and determined that the processes described above can cause changes in the bulk rock conductivity of an order or magnitude or greater. Figure 1.5 shows the ratio of the final-to-initial formation resitivities due to changes in salinity, temperature and water saturation. Thus if we are able to monitor the spatial variation of resitivity within the reservoir as a function of time, we will be able to deduce the progress of the steam front in the subsurface. Examples of geophysical methods used to monitor this and other types of reservoir processes will be discussed in the next section.

1.2 Geophysical methods for reservoir process monitoring

Because the process we are interested in monitoring involves either the injection or withdrawal of fluids and/or gases in a reservoir at depth, monitoring wells are often installed to track its progress. Unfortunately measurements of pressure, temperature and conductivity made within these wells are single point measurements which reflect properties of the reservoir only in the immediate vicinity of the hole. However, geophysiscs can be employed to fill in the gaps between wells.

Surface geopysical techniques can provide high resolution imaging of changes within the reservoir if the injection zone is near the surface. Of the methods available, 3-D seismic monitoring has been extremely successful in detecting changes in both seismic velocities and amplitude attenuation (Greaves and Fulp, 1987, Robertson, 1989). Surface electromagnetic methods have showed some success in detecting conductivity changes at depth (Bartel, 1982, Bartel and Ranganayaki, 1989) and self-potential anomallies have been measured on the surface which can be correlated with oil field stimulation effects (Dorfman, et al., 1977). However, due to the small volume of rock affected by these processes and the depth at which they occur, surface methods often do not produce optimum resolution.

If one borehole is available, the surface geophysical methods described above can be improved upon by employing surface-to-borehole techniques. Vertical seismic profiling (VSP) is routinely employed to achieve better resolution of reservoir properties than can be deduced from the surface (Hardage, 1985). Surface to borehole resistivity measurements have been exteremely succesful for environmental monitoring of contaminant injections (Bevc and Morrison, 1991, Schenkel, 1991) and to determine the direction of groundwater flow (Sill and Sjostrom, 1990). However, attempts to use the same processes to monitor EOR in an oilfield have shown very limited sucess (Bevc, et al. 1989). Numerical modeling has shown that surface to borehole EM can detect changes caused by EOR processes as far as 100m away from the instrument well (Spies and Greaves, 1991) and these types of mesurements have been made both in an oil field environment (Wilt and Ranganayaki, 1990) as well as in a shallow injection experiment(Hanson, et al. 1991). Methods for interpreting surface to borehole EM data are under development.

If multiple bore-holes are available, then conductivity well logging before, during and after the injection process has been completed can yield useful estimates of the spatial variation in conductivity and of the changes that have occured within the reservoir. Ranganayaki, et al. (1992) show how the conductivity increases over time within a steam injection zone by running resitivity logs in several oil field wells before and during an EOR experiment. Newmark and Wilt (1992) found similar results in the simulated steam clean-up of a gasoline spill. Unfortunately to adequately sample the spatial changes in conductivity in this manner requires a large number of wells which can be extremely costly.

To estimate the reservoir properties at depth between wells, cross-well geophysics can be employed. Seimic tomography has been very succesful in monitoring EOR produced changes with respect to time. Excellent examples of the seismic mapping of steam injection and in-situ combustion processes can be found in Bregman, et al. (1989), Justice, et al. (1989) and Paulsson, et al. (1992). Cross-well resistivity tomography has shown promise in monitoring both oil and environmental related steam injections (Beasley and Tripp,1991, Shima and Imamura, 1991, Ramirez, et al, 1992) and Daily and Ramirez (1992) have found it useful for tracking the flow of ground water through the unsaturated zone.

High frequency EM (f>1MHz) has also been useful in monitoring changes in reservoir properties between boreholes. Davis, et al (1979) reported on the changes in measured electromagnetic fields caused by an in situ coal gassification project. Daily (1984) and Laine (1987) describe variations in tomographic images of attenuation caused

by an oil shale retort and steam flood, respectively. The benefit of working at these frequencies is that the EM fields obey the wave equation thus allowing techniques developed for seismic interpretation to be applied. Unfortunately, due to the extremely high attenuation rate of these fields in conductive media the boreholes must be fairly close together . Thus the high frequncy method is unusable in conductive areas where the wells are tens to hundreds of meters apart.

Because of the diffusive nature of lower frequency EM fields in conductive media where displacement currents are negligible, the audio frequency range has until recently largely been ignored. However, the work of Zhou (1989) showed that a low frequency analog to diffraction tomography is useful in determining the orientation of fractures in a fracture zone. Wilt, et al. (1991) have demonstrated that single frequency measurements can be made in oil wells separated by 100m, while Wilt and Schenkel (1992) and Hanson, et al. (1991) have shown that these type of cross well measurements are useful in monitoring environmental injection processes. In this thesis methods will be developed to both model the audio frequency EM response to conductivity changes caused by these processes, and to interpret data collected in cross-well EM surveys.

1.3 Scope of this research

Although the word itself has appeared in the literature only within the last two decades, Worthington (1984) states that *tomography* has routinely been employed in geophysics since seismic surveys were first used to define the location of salt domes in the 1920's. The basic idea behind tomography is to obtain a two dimesional image of a selected plane or 'slice' through a solid object. In some cases the process can be extended to three dimensions to obtain a volume image of the object. In geophysics this imaging process usually implies making measurements of the seismic or electromagnetic fields at multiple positions that are produced by sources at various other locations. Tomographic reconstruction tecniques are then applied to these data to produce images of earth properties such as seismic velocity and/or attenuation, electrical conductivity, dielectric constant, ect., from which subsurface geology can be inferred.

Following the work of Wu and Toksoz (1987), Zhou (1989) developed a technique similar to seismic diffraction tomography to interpret crosswell electromagnetic data. The problem is simplified by applying either the weak scattering Born or Rytov approximations to the integral equations governing electromagnetic wave propogation. To be consistant with Wu and Toksoz, Zhou formulated the problem in the *wave-number* domain rather than in the space domain. Unfortunately this is where the similarity

between seismic and electromagnetic tomography ends. Due to the diffusive nature of the EM fields in the frequency range that we are interested, the concept of geophysical ray tomography is invalid and thus raytracing, algebraic reconstruction, and filtered backprojection image reconstruction tecniques are invalid. Zhou dubbed this method *electromagnetic diffusion tomography.*

In this thesis I build on the theoretical work found in Chapter 3 of Zhou and apply a cross-well EM imaging technique to data collected in an injection experiment. However, unlike Zhou I have developed the formulation in the space domain rather than the wave-number domain. The reason for this is three fold. First , the wavenumber domain formulation requires large numbers of evenly spaced source and receiver points which at this time is unfeasible. Second, the space domain formulation allows for easier forward modeling thus allowing us to iteratively find better estimates of the conductivity. Lastly, the space domain formulation allows for more complicated starting models than the wave-number domain formulation. These concepts will be discussed more fully in the proceeding chapters.

In Chapter 2, I will develop the integral equation formulation for calculating the scattered electromagnetic fields resulting from inhomogeneities imbedded in an otherwise homogenous medium that are excited by a magnetic dipole source . To simplify the problem it is assumed that the scattering bodies are symmetric about the source dipole axis in an azimuthal direction. Next a perturbation method known as the Born approximation is applied (Morse and Feschbach, 1953) and a *sensitivity function* is derived. This function describes the sensitivity of a given source-receiver pair to points within the medium. The spatial variation of the sensitivity will be analized for both different source and receiver combinations as well as different operating frequencies. In addition it will be employed to compare the simple cylindrically symmetric 2-D geometry to more realistic model geometries.

In Chapter 3, the Born approximation of the integral equations are investigated as a quick, numercial forward modelling scheme. The limitations of this approach are discussed as well as the benefit in computational time savings. Next, a more accurate iterative Born approximation is developed. Again its limitations are discussed and weighed against the savings in computing time. This solution is compared to both simpler one dimensional models to determine its accuracy and against more complicated two and three dimensional models to determine the usefulness of the cylindrically symmetric geometry.

In Chapter 4 an imaging scheme is developed which applies the Born approximation to obtain an initial estimate of the conductivity distribution, and then applies the iterative

Born series to obtain more accurate estimates of the conductivity. The resolution of the method as a function of frequency will be discussed and the effects of noise determined. EOR injection processes will be simulated with forward models and the resulting conductivity images analized for accuracy. The theory for a more complicated, one dimensional layered background model will be incorporated into the imaging scheme and then applied to field data collected by Wilt, et al. (1991). Finally as in the preceeding chapters we will use the 2D cylindrically symmetric imaging scheme on synthetic data generated with 3D models to determine the limitations of the simplified cylindrical geometry.

Chapter 5 will describe a field experiment in which cross well EM data were collected to monitor the injection of electrically conductive salt water into an aquifer at depth. Estimates of the data quality will be derived and possible sources of error determined. The 2D imaging scheme will then be applied to the data and the resulting images interpreted. Finally, simple forward 3D models will be employed to determine if the images correspond to the observations.

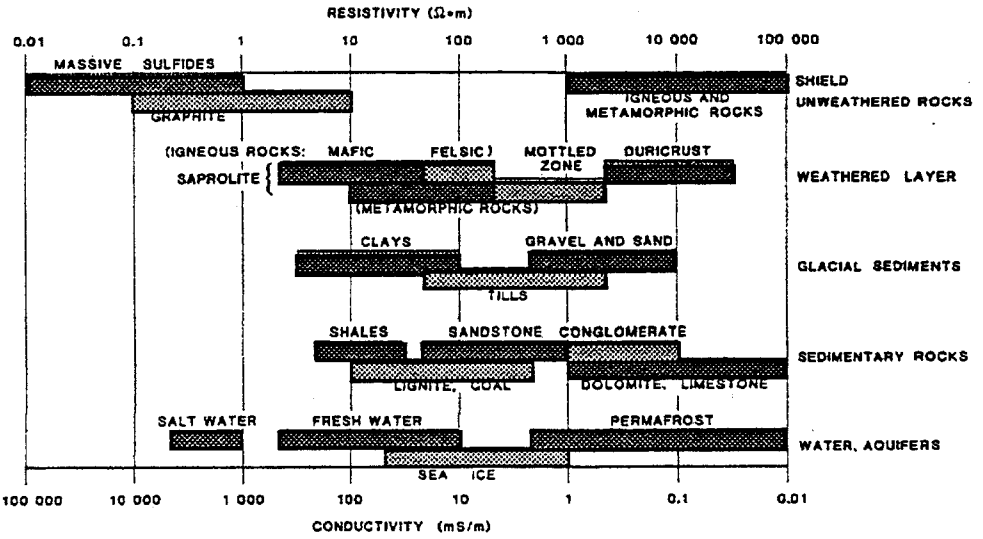

Figure 1.1 Typical ranges of conductivities of earth materials (Palacky,1988).

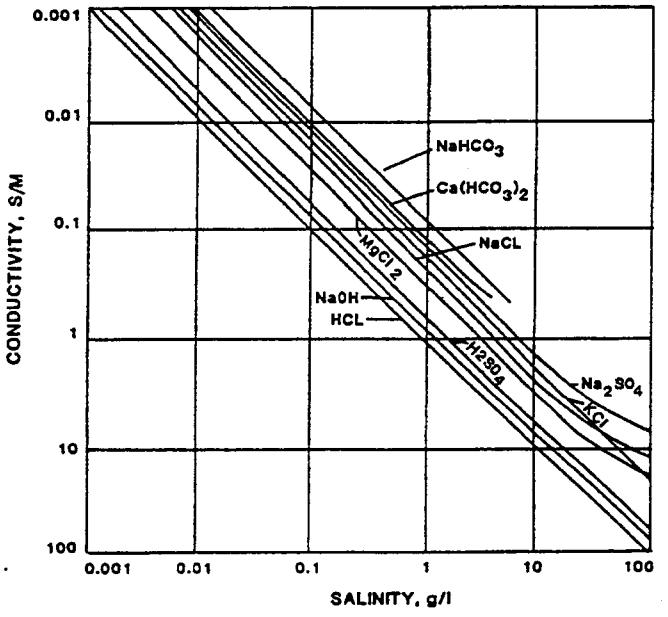

Figure 1.2 Conductivity of solutions of various salts as a function of concentration. Temperature of 20 °C (Keller,1998).

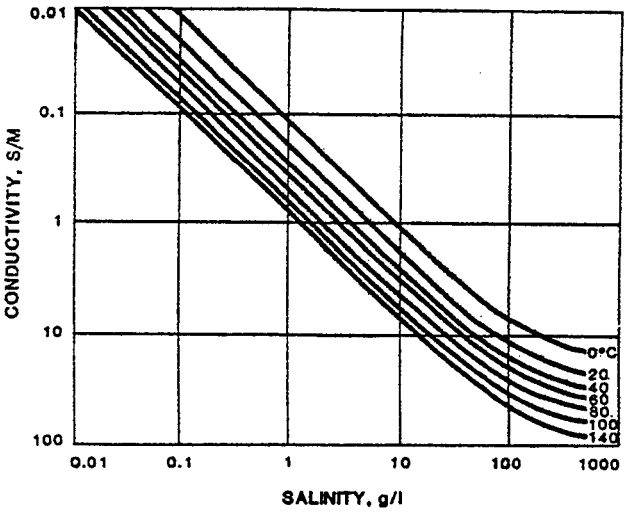

Figure 1.3 - Conductivity of a solution of NaCl as a function of temperature and concentration (Keller,1988).

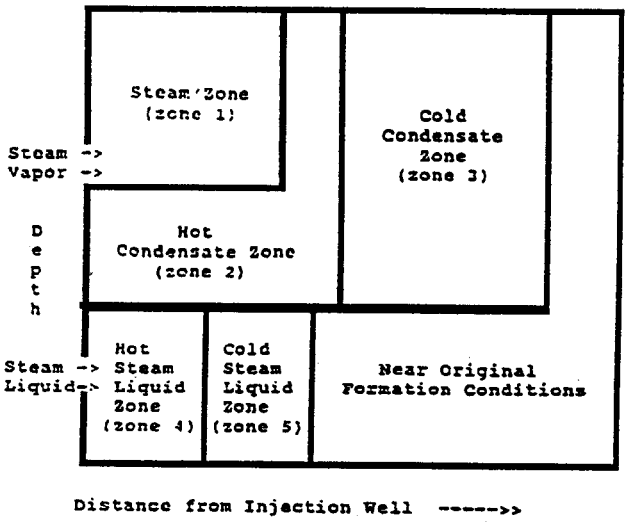

Figure 1.4 - Fluid zones of an idealized heavy-oil steamflood-vertical section (Mansure and Meldau, 1990).

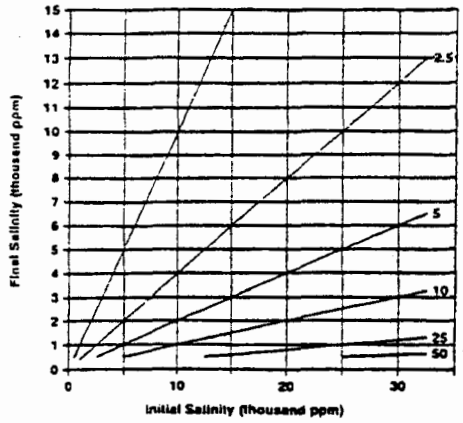

a)

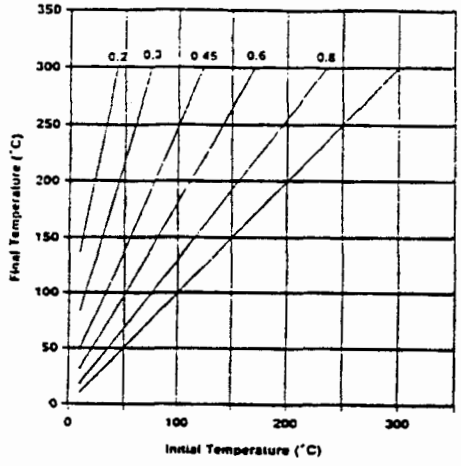

b)

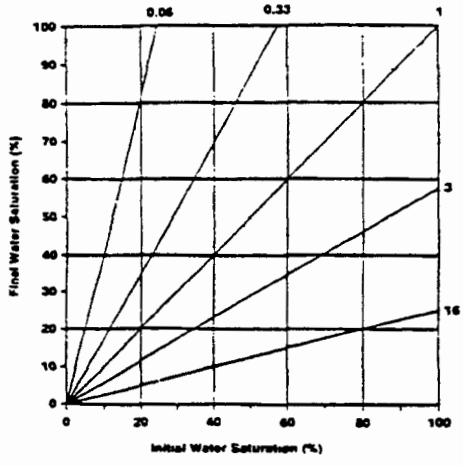

c)

Figure 1.5 - (a) Ratio of formation resistivity after a salinity change to initial resistivity. The saturation and temperature have been held constant. (b) Ratio of formation resistivity after a temperature change to initial resistivity. The saturation and salinity have been held constant. (c) Ratio of formation resistivity after a saturation change to initial resistivity. The temperature and salinity have been held constant (Mansure and Meldau,1990).

Chapter 2
Two Dimensional Formulation for a Magnetic Dipole Source in a Conductive Whole Space

The numerical formulation for the transverse electric (TE) electromagnetic response that is induced in a two dimensional (2-D) earth by an oscillating magnetic field is fairly trivial. Hohmann (1971) used an integral equation solution to investigate the use of a line source of alternating current on the surface of the earth for mineral exploration. Chang and Anderson (1984), Pai and Huang (1988) and Chew, et al (1991) developed solutions for a medium which is cylindrically symmetric about the transmitter borehole (Figure 2.1) to model the effects of drilling mud invasion in thin beds. The former uses a finite element method, while the last two employ a Haskill matrix - mode matching scheme. Unfortunately, these three solutions were designed with borehole induction logging in mind rather than cross well measurements. Recently Zhou (1989) and Sasaki, et al (1992) have developed forward modeling schemes to calculate the crosswell electromagnetic (EM) response of two dimensional, cylindrically symmetric conductors in an otherwise homogenous medium. The former uses an integral equation approach while the latter uses a finite element method.

In this chapter the mathematical theory is developed for low frequency ($f < 1MHz$) electromagnetic scattering by two dimensional conductors that are cylindrically symmetric about the source dipole. This formulation, which provides the starting point for the imaging scheme given in Chapter 4, is very similar to that of Zhou (1989) except that it is developed in the space domain rather than the wave-number domain. To simplify the theory the Born approximation is applied. From these approximate equations *sensitivity functions* are derived which yield valuable information about how a given source-receiver pair senses the medium between and around the probes. These sensitivity functions are then analyzed for different source-receiver configurations to determine both how they vary with respect to the *background induction number*, and how they vary spatially. In addition the limitations of the cylindrical geometry are explored by comparing the 2-D cylindrical sensitivity functions to the those that result from employing a two and one-half dimensional (2 1/2-D) model. The space-domain conclusions will then be compared to the wave number domain analysis of Zhou(1989) and Zhou, et al. (1993).

2.1 Mathematical formulation of the two-dimensional integral equation

As shown in Figure 2.1, the region of interest is imbedded in an otherwise homogenous background medium of electrical conductivity σ_0. A magnetic dipole source which is harmonic in time is located at r=0, z=z_{tx} on the axis of symmetry. If the anomalous conductivity , $\sigma(r,z)$, is distributed symmetrically about this axis then electric currents induced by the source can exist only in the azimuthal ($\hat{\phi}$) direction. These currents in turn produce magnetic fields in the $\hat{r}$ and $\hat{z}$ directions which can be measured either within the transmitter borehole as is commonly done in electromagnetic well logging, or in a second borehole some distance away as is done for crosswell EM measurements.

Because we are operating in a conductive medium at frequencies below a megahertz, displacement currents can be ignored (Ward and Hohman, p136). Using this quasi-static approximation, Maxwell's equations for the electric and magnetic fields in the frequency domain are given by

$$\nabla \times \mathbf{H} = \sigma \mathbf{E} + \mathbf{J}_s \qquad (2.1a)$$

and

$$\nabla \times \mathbf{E} = -i\omega\mu\mathbf{H} \qquad (2.1b)$$

where **E** and **H** are the total electric and magnetic fields respectively, $\mathbf{J}_s$ is the source current density, σ is the conductivity, ω is the operating frequency in radians, μ is the magnetic permeability which is assumed to be that of free space, and $i = \sqrt{-1}$.

Because the electric field has only one component in the azimuthal or $\hat{\phi}$ direction, a scalar differential equation can be derived for E_ϕ in cylindrical coordinates by taking the curl of equation 2.1b and combining it with equation 2.1a. The resulting expression has the form

$$\nabla^2 E_\phi - \frac{1}{r^2} E_\phi - i\omega\mu\sigma E_\phi = i\omega\mu J_\phi \qquad (2.2)$$

where now J_ϕ represents the external source current flowing within the magnetic dipole. The object function O(**r**) is now defined as

$$O(\mathbf{r}) = \frac{(\sigma(\mathbf{r}) - \sigma_0)}{\sigma_0} \qquad (2.3)$$

and the background wave number, k_0 to be

$$k_0 = \sqrt{-i\omega\sigma_0\mu}. \qquad (2.4)$$

Substituting these two expressions into equation 2.2 and rearranging yields

$$\nabla^2 E_\phi - \frac{1}{r^2} E_\phi + k_0^2 E_\phi = i\omega\mu J_\phi + k_0^2 O(\mathbf{r}) E_\phi . \qquad (2.5)$$

The total electric field in the inhomogenous medium (E_ϕ) is now decomposed into two parts. The first part, E_ϕ^p, is the field resulting from a magnetic dipole source operating in a homogenous background of conductivity σ_o. This background or *primary* electric field satisfies the scalar wave equation

$$\nabla^2 E_\phi^p - \frac{1}{r^2} E_\phi^p + k_0^2 E_\phi^p = i\omega\mu J_\phi \qquad (2.6)$$

and is given by the analytical expression (Ward and Hohmann, 1988)

$$E_\phi^p = -\frac{i\omega\mu}{4\pi}\left[\frac{r}{R^3}(1+ik_0R)e^{-ik_0R}\right] \qquad (2.7)$$

where $R = \sqrt{r^2 + (z - z_{tx})}$ and r and z define the point of interest. The second part, E_ϕ^s is the *scattered* or *secondary* electric field resulting from anomalous currents which are induced in any conductivity inhomogeneities that are present in the region. The total electric field is simply the summation of these two separate parts, i.e..

$$E_\phi = E_\phi^p + E_\phi^s . \qquad (2.8)$$

Substituting this expression into equation 2.5 , rearranging terms and removing the primary field contribution yields a wave equation for the secondary electric fields,

$$\nabla^2 E_\phi^s - \frac{1}{r^2} E_\phi^s + k_0^2 E_\phi^s = k_0^2 O(\mathbf{r}) E_\phi \qquad (2.9)$$

where the term on the right represents the source induced or scattered currents within the inhomogeneities. This is the Helmholtz equation for the secondary fields written in cylindrical coordinates which can be solved using the Green's function formulation (Sena and Tokoz, 1990):

$$E_\phi(\mathbf{r}_{rx}, \mathbf{r}_{tx}) = E_\phi^p(\mathbf{r}_{rx}, \mathbf{r}_{tx}) - \sigma_0 \iint_{rz} O(\mathbf{r}) E_\phi(\mathbf{r}, \mathbf{r}_{tx}) G(\mathbf{r}_{rx}, \mathbf{r}) dr dz . \qquad (2.10)$$

In this expression the receiver lies at the point $\mathbf{r}_{rx} = (r_{rx}, z_{rx})$, the source dipole at $\mathbf{r}_{tx} = (0, z_{tx})$ and the integration is over the entire region containing anomalous conductors. The Green's function, G, represents the electric field at $\mathbf{r}_{rx}$ induced by a circular loop of

current that is symmetric about the source dipole axis , passes through **r**, and satisfies the equation

$$\nabla^2 G - \frac{1}{r^2} G + k_0^2 G = i\omega\mu\delta(\mathbf{r} - \mathbf{r}'). \tag{2.11}$$

Ward and Hohmann (1988) show it to have the form of a first order Hankel transform,

$$G(\mathbf{r}_{rx}, \mathbf{r}) = -i\omega\mu \frac{r}{2} \int_0^\infty e^{-\gamma|z_{tx}-z|} \frac{\lambda J_1(\lambda r)}{\gamma} J_1(\lambda r_{tx}) d\lambda \tag{2.12}$$

where $\gamma^2 = \lambda^2 + k_0^2$ and $J_1(\lambda r)$ is the first order Bessels function of the first kind.

In the borehole environment, it is the magnetic fields (**H**) that we are interested in measuring rather than the electric fields . Thus an expression for the magnetic field equivalent to equation 2.10 must be developed. This is accomplished by taking the curl of the vector form of 2.10, i.e., $\nabla \times E_\phi(\mathbf{r}_{rx}, \mathbf{r}_{tx})\hat{\phi}$ with respect to the observation point $\mathbf{r}_{rx}$. This operation results in an integral equation for magnetic fields which is given by,

$$\mathbf{H}(\mathbf{r}_{rx}, \mathbf{r}_{tx}) = \mathbf{H}^p(\mathbf{r}_{rx}, \mathbf{r}_{tx}) - \sigma_0 \iint_{rz} O(\mathbf{r}) E_\phi(\mathbf{r}, \mathbf{r}_{tx}) \mathbf{G}_H(\mathbf{r}_{rx}, \mathbf{r}) dr dz. \tag{2.13}$$

In equation 2.13, $\mathbf{H}^p(\mathbf{r}_{rx}, \mathbf{r}_{tx})$ is the primary magnetic field generated by a magnetic dipole source in a homogenous medium of conductivity σ_0 which is given by

$$\mathbf{H}^p(\mathbf{r}_{rx}, \mathbf{r}_{tx}) = \frac{1}{4\pi R^3} e^{-ik_0 R} \left[\left(\frac{z_{rx}^2}{R^2} \hat{\mathbf{z}} + \frac{r_{rx} z_{rx}}{R^2} \hat{\mathbf{r}} \right) \left(-k_0^2 R^2 + 3ik_0 R + 3 \right) + \right. \tag{2.14}$$

$$\left. \left(k_0^2 R^2 - ik_0 R - 1 \right) \hat{\mathbf{z}} \right]$$

(Ward and Hohmann, 1988) and $\mathbf{G}_H(\mathbf{r}_{rx}, \mathbf{r})$ is the is the Green's function which relates the induced current loop at a point **r** to the magnetic fields at the receiver location. Equation 2.13 can be simplified by subtracting the primary field and decomposing the remaining vector equation into two scalar equations for the secondary horizontal and vertical magnetic fields. This results in the expressions

$$H_r^s(\mathbf{r}_{rx}, \mathbf{r}_{tx}) = -\sigma_0 \iint_{rz} O(\mathbf{r}) E_\phi(\mathbf{r}, \mathbf{r}_{tx}) G_{Hr}(\mathbf{r}_{rx}, \mathbf{r}) dr dz \tag{2.15}$$

and

$$H_z^s(\mathbf{r}_{rx}, \mathbf{r}_{tx}) = -\sigma_0 \iint_{rz} O(\mathbf{r}) E_\phi(\mathbf{r}, \mathbf{r}_{tx}) G_{Hz}(\mathbf{r}_{rx}, \mathbf{r}) dr dz \tag{2.16}$$

where the Green's functions are given by

$$G_{Hr}(\mathbf{r}_{rx},\mathbf{r}) = \frac{r}{2}\int_0^\infty e^{-\gamma|z_{rx}-z|}\lambda\, J_1(\lambda r) J_1(\lambda r_{rx}) d\lambda \qquad (2.17)$$

and

$$G_{Hz}(\mathbf{r}_{rx},\mathbf{r}) = \frac{r}{2}\int_0^\infty e^{-\gamma|z_{rx}-z|}\frac{\lambda^2}{\gamma} J_1(\lambda r) J_0(\lambda r_{rx}) d\lambda \qquad (2.18)$$

and $J_0(\lambda r_{rx})$ and $J_1(\lambda r)$ are the zero-th and first order Bessel's functions of the first kinds, respectively.

2.2 The Born approximation solution

The relationship between $\mathbf{H}^s$ and the object function $O(\mathbf{r})$ is nonlinear because E_ϕ is also dependent on $O(\mathbf{r})$. Thus both the forward modeling and the estimation of the conductivity structure through inversion are nonlinear processes that require large amounts of computer time and memory so that only the simplest problems can be examined. Even a simple analysis of the field behavior nontrivial.

These solutions however, can be simplified by assuming that the medium contains only weak scatterers. When this is true, $O(\mathbf{r})$ is small and linearized versions of 2.15 and 2.16 are obtained through the use of the Born approximation, $E_\phi \approx E_\phi^P$, which simply assumes that the field in the scatterer is equal to the primary field (Kong,1975):

$$H_r^s(\mathbf{r}_{rx},\mathbf{r}_{tx}) = -\sigma_0 \iint_{rz} O(\mathbf{r}) E_\phi^P(\mathbf{r},\mathbf{r}_{tx}) G_{Hr}(\mathbf{r}_{rx},\mathbf{r}) dr dz \qquad (2.19)$$

and

$$H_z^s(\mathbf{r}_{rx},\mathbf{r}_{tx}) = -\sigma_0 \iint_{rz} O(\mathbf{r}) E_\phi^P(\mathbf{r},\mathbf{r}_{tx}) G_{Hz}(\mathbf{r}_{rx},\mathbf{r}) dr dz. \qquad (2.20)$$

The linearity between the object function and the magnetic fields implies that the scattering currents within the inhomogeneities are small and that coupling between individual scattering currents can be neglected. Because this represents the first term in the Born series, I will refer to it at times as the *first order* Born approximation. The limits of this approximation will be discussed more fully in chapters 3 and 4.

2.2.1 The Born Kernel

Equations 2.19 and 2.20 relate small perturbations in the magnetic field, H_z^s and H_r^s, to small perturbations in the model, $\sigma_0 O(\mathbf{r}) = \Delta\sigma$, through the functions

$$K_{Hz} = E_\phi^p(\mathbf{r}, \mathbf{r}_{tx}) G_{Hz}(\mathbf{r}_{rx}, \mathbf{r}) \qquad (2.21a)$$

and

$$K_{Hr} = E_\phi^p(\mathbf{r}, \mathbf{r}_{tx}) G_{Hr}(\mathbf{r}_{rx}, \mathbf{r}) \qquad (2.21a)$$

which are dependent only on the background conductivity, σ_0, and the relative positions of the source, the receiver, and the location and dimensions of the region of interest. Thus the terms on the right hand side of equations 2.19 and 2.20 can be thought of as the *Frechet' derivatives* for a homogenous whole space model (Hohmann and Raiche, 1988) with the functions given in 2.21 representing the Frechet' kernels or *sensitivity functions*. Use of the Frechet' derivative in linear inverse theory dates back to the work of Backus and Gilbert (1968), and since that time these functions have been used quite extensively for EM inversion and sensitivity analysis (e.g. Parker,1977, Chave, 1985, E. Gomez-Trevino, 1987 and Spies and Habashy, 1992).

Closer examination of equations 2.19 through 2.21 indicates that if the background conductivity, σ_0, is grouped with the Frechet' kernels in 2.21 rather than the object function ,i.e.,

$$K_H = \sigma_0 E_\phi^p(\mathbf{r}, \mathbf{r}_{tx}) G_H(\mathbf{r}_{rx}, \mathbf{r}) \qquad (2.22)$$

the relationship between the perturbed fields and the integrated kernel is dimensionless. This allows us to present a sensitivity analysis for the cylindrical crosswell problem as a function of background induction number ($\omega\mu\sigma_0 * R^2$) where R is source-receiver separation, rather than as a function of specific models. Thus we can determine the corresponding sensitivity for any combination of frequency, conductivity and borehole separation. Because the function given in 2.22 is derived using the Born approximation, it will be referred to here after as the *Born Kernel.*

2.3 Sensitivity analysis as a function of the background induction number

The first sensitivity analysis has been done for the general crosswell model shown in Figure 2.2a. The transmitter and receiver are located at a depth z=0 in two separate boreholes located a distance $R=r_{rx}$ apart. Because the value of the Born kernel is dependent not only on the source and receiver locations but also on the point of interest within the medium, it has been calculated at five different positions located on a line extending radially outward from the source toward the receiver.

Figure 2.3a shows the amplitude of the H_z^s Born kernel as a function of the background induction number, and the real and imaginary components of the kernel at two of the points has been plotted on the same scale in Figure 2.3b. Because the scattered fields at the receiver are proportional to these sensitivity functions, the primary magnetic field (H_z^p) has also been plotted in Figure 2.3a which allows us to compare the relative behavior of the primary and secondary fields. The abscissa of these graphs starts at an induction number of 0.01 because below this point the total field is almost equal to that of the free space value (Spies, 1992). The largest induction number used is 1000 as above this value the fields are difficult to measure because of attenuation (Deszcz-Pan,1993).

At this point an explanation is required to define how the kernel values on the ordinate have been normalized so that both axis are dimensionless. All values have first been divided by the free space magnetic field for the given source-receiver separation. This removes a $1/R^3$ component from the kernel values and fully normalizes the primary field such that at low frequencies it is unity. However a there still exists a $1/m^2$ in the Born kernel because the integration in **r** and **z** has not been completed. To remedy this matter the kernel values have arbitrarily been multiplied by the square of the source-receiver separation. The primary field has also been multiplied by this value so that it scales appropriately when compared to the kernel.

Several important characteristics about the cylindrically symmetric geometry and its application to cross borehole studies can be derived from a Figures 2.3a and 2.3b. The linear increase in sensitivity amplitude with increasing induction numbers below 1.0 indicates that we are in the near field. In this region the primary field dominates the secondary field which suggests that the response of small conductors will be unmeasurable. However the primary field is dominated by the real component while the scattered field is dominated by the imaginary. Thus even in this low induction number region anomalous conductors may be detected by measuring the quadrature alone .

At an induction number of approximately 10, the kernel amplitude is maximum which indicates that this is the point at which the secondary fields will be most easily detected. In addition Figure 2.3b shows that the phase changes quite rapidly as the induction number is increased. Replotting the kernel as a function of source-receiver separation divided by skin depth (Figure 2.3c) shows that this region occurs when the receiver is approximately 2 to 6 skin depths away from the source. This figure can be used when designing a survey to maximize the measured response.

At higher induction numbers the sensitivity falls off very rapidly implying a severe decrease in secondary field magnitude. However, the fact that the primary field

amplitude decreases at even a quicker rate implies that this fall off is not due to a lack of sensitivity to the region but rather is the product of severe attenuation.

A characteristic that is immediately apparent from these figures is the relative size of the kernel to the primary field. If the scatterer consists of a small cell of low contrast with respect to the background, the secondary fields will be at best two to three orders of magnitude less than the background field. However if the body is given some size and/or a higher conductivity contrast then the scattered field is approximately equal to the kernel multiplied by area-object function product. Thus the difference between the primary and secondary fields becomes one order of magnitude or even less which is easily measurable.

Some interesting properties of the secondary fields which are dependent on the scatterer location can be deduced from Figure 2.3. The most noticeable of these is that the sensitivity is much greater for points near the receiver than for points near the source. Spies and Habashy (1992) show that for two and one-half dimensional (2 1/2-D) and three dimensional (3-D) geology the sensitivity is reciprocal, or symmetric about a line drawn between the source and receiver, i.e. regions near the source and receiver have identical values. The disparity between these 2 1/2-D and 3-D cases and the 2-D cylindrical case is a function of the geometry that has been imposed on the problem. For the cylindrical case, a point near the transmitter forms a small ring of current about the axis of symmetry , while near the receiver the point forms a large ring of current. Thus unlike the 2 1/2-D and 3-D cases, the geometry produces sensitivities which are not reciprocal between the source and receiver.

Another interesting phenomenon dependent on the location of the scattering body is the decreasing frequency at which the kernel peaks with increasing distance to the point of interest. This again is a function of the geometry imposed on the problem. The Green's function can be though of as a circular loop of wire which is exited by a dipole source at its center. West and Macnae (1991) give the induction number of such a loop to be $\omega L / R$ where L is the inductance of the loop and R the resistance. For such a loop L is given by Romo and Whinnery (1953) to be

$$L \cong l\mu\left[\ln\left(\frac{8l}{a}\right)-2\right] \tag{2.23}$$

where l is the radius of the loop and a is the radius of the wire. For a wire of given resistance per unit length R_0, R is given simply as $R = 2\pi l R_0$. Thus, $\omega L/R$ is proportional to $\omega \ln l$ and thus as the radius of the loop l is increased, the frequency ω must decrease to keep the response at its peak.

A third and very important characteristic that can be deduced from these sensitivity diagrams is that at low induction numbers (<1), the response from zones outside of the wells (for example the point at 1.25R) can produce secondary fields that are larger than those generated from region between the wells. This reemphasizes the benefit of operating in the range of 2 to 6 skin depths between wells. Unfortunately this also demonstrates a problem with making crosswell measurements in steel cased wells as suggested by Uchida, et al. (1991), and Newman (1992a) who determined that crosswell EM signals can be detected through casing as long as frequencies below 1kHz are employed. This problem of being sensitive to regions outside the wells will be discussed in more detail later.

To demonstrate that the behavior of the sensitivity function is relatively independent of the source - receiver geometry, the Born kernel has been calculated for the geometry shown in Figure 2.2b. In this case the receiver is a distance $R=\sqrt{2}rx$ to the left and below the source, and thus both horizontal and vertical components of the magnetic field will exist. Again the points of interest are located on a straight line between the source and receiver at the same intervals of 0.05*R, 0.50*R, 0.95*R, 1.05*R and 1.25*R as before. Figures 2.4a and 2.4b show that the behavior of the Born kernel for both the vertical and horizontal components is in general the same as when the source and receiver are at the same depth (Figure 2.3)with the sensitivity peaking when the transmitter and receiver are approximately 2 to 6 skin depths apart.

One noticeable difference between the vertical and horizontal components of the kernel is in their relative sensitivities to the region outside the wells at induction numbers less than 1. The vertical component (Figure 2.4a) shows a relatively large sensitivity response when compared to the horizontal component (Figure 2.4b). This suggests that if we are going to make low frequency measurements through steel well casing as suggested by Uchida, et al.(1991), it may be beneficial to use the horizontal component of the field rather than the vertical.

In addition to the crosswell models, the Born kernel has been calculated for the in-hole case (Figure 2.2c). In addition to being useful for well log analysis and design (Barber,1992), the sensitivity plots (Figure 2.5) can be employed to examine the relative merits of using the *back scattered* response for improving image quality in crosswell tomography experiments (Zhou,1989). Although the sensitivity amplitude is much different compared to those for the crosswell models, the curves show the same general characteristics as noticed before with the response peaking at an induction number of approximately 10 and the frequency at which the kernel peaks decreasing as the radial distance to the scatterer increases. Notice that at low induction numbers, the sensitivity

peaks between 0.25*R and 1*R away from the borehole while at higher induction numbers the peak occurs closer to the borehole. This agrees well with induction log theory where lower frequencies are employed to sense further out into the medium.

In general these Born kernel plots are very useful to determine how the sensing ability of a given source-receiver configuration changes with respect to induction number (or frequency). Though the magnitude of the Born kernel is not constant for different source-receiver configurations, the general behavior of the fields is. A general rule of thumb has been proposed which states that the peak response of an inhomogenous region for a crosswell experiment will occur when the transmitter is 2 to 6 skin depths away from the receiver, and that for in-hole measurements the maximum sensitivity will never extend radially beyond the transmitter-receiver separation. Unfortunately these curves yield only limited information about the spatial characteristics of the Born kernel. Thus in the next section I will analyze the spatial variation of the Born kernel for constant induction numbers.

2.4 Spatial sensitivity analysis

Spies and Habashy (1992) showed how the Frechet' derivative can be employed in a spatial sensitivity analysis of the low frequency crosswell EM problem. The illustrations they present for a 3-D geometry are very useful for defining the region of the earth that a given source-receiver pair is sensitive to in a frequency range where the concept of *ray paths* is inappropriate. Although the sensitivity function they define is nonlinear in the anomalous conductivity σ, it is essentially the 3-D Born kernel multiplied by a localized Nonlinear Operator (Habashy, et al., 1992) and normalized by the background conductivity σ_o. In the first part of this section I will analyze the spatial sensitivity of the vertical magnetic field at three distinct frequencies (and induction numbers) for the cylindrically symmetric crosswell geometry. The second part will consist of a comparison between these results and the 2 1/2-D sensitivity formulated by Spies and Habashy (1992). In the third part we will look at the sensitivity functions for the horizontal field and then in the fourth part examine these functions for the back scattered or in hole vertical magnetic fields.

2.4.1 Spatial sensitivity of the vertical magnetic field for a 2-D cylindrical geometry

The crosswell model employed in this spatial sensitivity analysis is shown in Figure 2.6. In order to analyze the importance of vertical *coverage* or *offset* on target delectability and resolution, the spatial sensitivity distribution has been calculated for a single source and three different receiver locations representing *aspect ratios* (z_{rx}/r_{rx}), or

apertures of 0:1 , 1:1 and 2:1 . Three frequencies (1kHz, 10kHz and 100kHz) have been employed to illustrate the varying sensing capabilities of different frequencies. The low frequency of 1kHz was chosen because below this point Figures 2.2 and 2.3 show the amplitude of the sensitivities, and thus the secondary fields to be several orders of magnitude less than that of the primary. The high frequency of 100kHz was chosen as above this point the field source field falls off very quickly with distance due to attenuation and the fields become difficult to measure. Although the model is defined for a specific background conductivity and source-receiver separation, the dimensionless relationship between the integrated Born kernel and the measured fields implies that the results will be identical for constant induction numbers $\omega\mu\sigma^*R^2$ and source-receiver configuration.

For the sake of comparison the sensitivity values have all have been normalized in the same manner as given in Spies and Habashy(1992). The Born kernel is calculated at a constant interval of r and z, normalized by the total sensitivity which has been integrated over the region of interest, and then multiplied for display purposes by an appropriate constant which in this case was $1.5x10^4$. The absolute values of the sensitivity are then converted to decibels and then the results plotted as positive and negative values of the real and imaginary components. Choosing an appropriate scaling factor allows us to plot the results over 3 orders of magnitude from 1 to 60 dB with the white space representing values 83dB or more below the integrated value. In addition, the small white 'lines' between areas of shading represent regions where that particular component of the sensitivity is undergoing a reversal of sign (i.e. a 180° phase shift). The position of these lines is independent of the scaling factor used. In all the results the arrow on the left represents the dipole source location and the arrow on the right the receiver location. Due to plotting considerations the sensitivity values at 1kHz were calculated at 10m intervals while at 10kHz and 100kHz the interval was 5m.

Figure 2.7 shows the sensitivities calculated at 1kHz for aspect ratios of 0:1, 1:1, and 2:1 which correspond to a induction numbers of 0.8, 1.6 and 3.9, respectively. Comparing these induction numbers to those plotted on the abscissa in Figures 2.3 and 2.4 show that this frequency lies on the low side of the Born kernel, that is we are operating in the near field. The most noticeable characteristics of Figure 2.7 that are also illustrated in Figures 2.3 and 2.4 are 1) the kernel is maximum near the receiver and 2) it is very sensitive to a large area outside of the interwell region. The size of the region that the various source-receiver combinations are sensitive to and the smoothly varying nature of the kernel suggest that imaging at this frequency will recover smooth, large scale features and provide good estimates of the average background conductivity. However

the images at these low induction numbers will not have very good resolution. In addition, the sensitivity to the zone outside the wells implies that bodies in this region will produce anomalies that could be mistaken to originate from bodies located between the wells. Notice also that the sensitivities in the interwell region near the receiver have opposite signs compared to the region just outside the wells. Thus the effect of horizontal features near the receiver (for example layers) will be diminished (Spies and Habashy,1992).

Some general conclusions can be made from Figure 2.7 about the horizontal and vertical resolution with respect to different array aspect ratios. For an aspect of 0:1 and induction number of 0.8 (Figure 2.7a), the imaginary component dominates the response. For a point of interest centered between the source and receiver, small changes (for example 10% of the separation) in both its horizontal and vertical position due not cause substantial changes in the sensitivity of this component. Though the real component is very sensitive at the central location do to a reversal in sign, the response from outside the interwell region will dominate any response originating between the wells. This demonstrates the low resolution of the 0:1 aspect ratio array for this induction number.

Increasing the aspect ratio to 1:1 (Figure 2.7b) offers definite improvements to the resolution. Small changes in both the vertical and horizontal position of a point centrally located between the source and receiver cause measurable changes in both the real and imaginary sensitivities do to sign reversals in this region. Also the relative magnitude of the imaginary sensitivity compared to that of the real component has been reduced with the larger induction number. Increasing the aspect ratio to 2:1 improves matters further. Small changes in the scatterer location between the source and receiver result in different sensitivity for both components which suggests an increase of resolution. In addition the increase of the induction number to 3.94 has produced real and imaginary components of almost the same amplitude which agrees well with the curves shown in Figure 2.3b. However, any increases in resolution due to larger aspect ratios must be weighed against the large sensitivity to zones outside the interwell region.

Figure 2.8 shows the normalized Born kernel for a frequency of 10kHz (and induction numbers for the different aspect ratios of 8, 16 and 39) plotted on a scale which is twice that of Figure 2.7. The reduction in the area outside the wells being sensed is immediately noticeable when compared to Figure 2.7. Also, though the kernel still peaks near the receiver small maxima now appear near the transmitter.

Further comparison of these plots to Figure 2.7 indicates that a substantial improvement in resolution has occurred with the increase in frequency and induction number. For the 0:1 aspect ratio (Figure 2.8a), the area of constant sensitivity in the

central region between the source and receiver has narrowed in the vertical direction indicating an in increase in the vertical resolution. However there is still a definite lack of resolution in the horizontal direction except near the source and receiver. Increasing the aperture to 1:1 (Figure 2.8b) increases both the vertical and horizontal resolution significantly. Notice that a focused zone of sensitivity stretching almost directly between the source and receiver has developed in the real component, and that excellent vertical resolution exists in the imaginary component due to a sign reversal in the central region. Increasing the aspect ration to 2:1 improves the horizontal resolution even further due to the almost vertical alignment of the sensitivity variations. Thus small horizontal position changes will cause fairly large changes in the measured fields.

Increasing the frequency to 100kHz such that the induction numbers for the three different aspect ratios are 80,160 and 390 once again reduces the area being sensed and thus improves the resolution. Figure 2.9 shows that the contribution from outside the wells has been reduced to almost nothing indicating that at these higher induction numbers we are primarily sensing the area directly between the transmitter and receiver. A very defined maximum sensitivity 'path' has developed between the source and receiver which is suggestive of a ray path and implies the use of ray theory and ray tracing to interpret the results. In addition a symmetry between the regions near the source and receiver is beginning to develop which will be discussed in more detail in the next subsection.

Once again the increase in aperture causes an increase in horizontal resolution with very poor resolution at an aspect ratio of 0:1 and very good resolution at an aspect ratio 2:1. Also due to the formation of the previously mentioned 'ray path', there is considerable vertical resolution improvement for the 0:1 aspect ratio compared to those at lower frequencies and induction numbers.

Several conclusions can be made about the results presented above, the first being that single frequency (monochromatic) crosswell data should be collected at as high a frequency as possible to maximize resolution while minimizing the contribution of the zone outside the interwell region. This agrees well with Zhou's (1989) results who found that higher frequency data resulted in higher resolution images. However, the benefits of multiple frequency data should not be overlooked. Different frequencies sense the medium differently thus supplying additional information which can be used to better constrain the interpretation. This agrees well with the use of wave number domain *coverage diagrams* introduced by Zhou (1989) and Zhou, et al (1993). These diagrams show how the wave number spectrum of anomalous bodies are sampled by an EM array of multiple sources and receivers. Low frequencies are shown to sample low wave

number components of the target shape and higher frequencies sample larger components. Thus with multiple frequencies we sample a larger portion of the target's wave number spectrum and thus better reconstruction of a conductivity image should result. Finally, the real and imaginary components sense the medium differently at different frequencies with the imaginary component dominating at low induction numbers. This suggests that the imaginary component alone can be used to image the medium through steel casing when using low frequencies as suggested by Uchida, et al. (1991).

2.4.2 Comparison of the sensitivity for 2-D cylindrical and 2 1/2-D geometries

Although the cylindrical geometry shown in Figure 2.1 crudely simulates current flow in the earth resulting from a VMD source, it is not very realistic as the earth does not often exhibit this type of symmetry about the dipole axis. In addition the cylindrical formulation accounts only for TE current flow and thus does not account for current crossing conductivity boundaries. A different geometry that can better approximate EM scattering in the inhomogenous region between two wells is the 2 1/2-D geometry. As shown in Figure 2.10, this geometry employs a VMD source but extends the earth infinitely in the 'y' direction.

The sensitivity functions for the 2 1/2-D problem can be derived from the linear versions of the 3-D sensitivity functions given in Spies and Habashy (1992) which have the form

$$K_{Hz}(\mathbf{r}_{rx},\mathbf{r},\mathbf{r}_{tx}) = \frac{i\omega\mu}{(4\pi)^2}\left[(x-x_{tx})(x-x_{rx})+(y-y_{tx})(y-y_{rx})\right]S^{Rx}S^{Tx} \qquad (2.24)$$

for the vertical component sensitivity and

$$K_{Hx}(\mathbf{r}_{rx},\mathbf{r},\mathbf{r}_{tx}) = \frac{-i\omega\mu}{(4\pi)^2}\left[(x-x_{tx})(z-z_{rx})\right]S^{Rx}S^{Tx} \qquad (2.25)$$

for the radial or x component. In these expressions $\mathbf{r}_{rx}$, $\mathbf{r}$, and $\mathbf{r}_{tx}$ represent the distance from the origin to the receiver location , to the point at which the sensitivity is calculated, and to the source location, respectively and S^{Rx} and S^{Tx} are given by

$$S^{Rx} = \frac{e^{ik_0|\mathbf{r}-\mathbf{r}_{rx}|}}{|\mathbf{r}-\mathbf{r}_{rx}|^3}\left(1-ik_0|\mathbf{r}-\mathbf{r}_{rx}|\right) \qquad (2.26)$$

and

$$S^{Tx} = \frac{e^{ik_0|\mathbf{r}-\mathbf{r}_{tx}|}}{|\mathbf{r}-\mathbf{r}_{tx}|^3}\left(1 - ik_0|\mathbf{r}-\mathbf{r}_{tx}|\right). \qquad (2.27)$$

It is easy to show that expressions 2.24 and 2.25 are simply the magnetic fields at the receiver produced by an electric dipole source at the point of interest, multiplied by the electric field at that same point resulting from an oscillating magnetic dipole at the source location. That is, the expressions given in 2.24 and 2.25 are simply the 3-D Born kernel divided by the background conductivity σ_0. To calculate the 2 1/2-D sensitivity requires integrating these functions along the y axis from minus to positive infinity. The 2 1/2-D sensitivity functions then become

$$K_{Hz}(\bar{\mathbf{r}}_{rx}, \bar{\mathbf{r}}, \bar{\mathbf{r}}_{tx}) = \int_{y=-\infty}^{\infty} \frac{i\omega\mu}{(4\pi)^2}\left[(x - x_{tx})(x - x_{rx}) + (y - y_{tx})(y - y_{rx})\right] S^{Rx} S^{Tx} dy \qquad (2.28)$$

and

$$K_{Hx}(\bar{\mathbf{r}}_{rx}, \bar{\mathbf{r}}, \bar{\mathbf{r}}_{tx}) = \int_{y=-\infty}^{\infty} \frac{-i\omega\mu}{(4\pi)^2}\left[(x - x_{tx})(z - z_{rx})\right] S^{Rx} S^{Tx} dy \qquad (2.29)$$

where S^{Rx} and S^{Tx} are defined as above. Note, though these functions are not multiplied by σ_0, normalizing them by the total integrated sensitivity removes the dependence of this factor and thus these results can be compared to the Born kernel's in section 2.4.1.

To compare the relative merits and drawbacks of the two different geometries I have calculated the 2 1/2-D sensitivity functions at the same three frequencies employed in the last subsection for the 0:1 and 1:1 aspect ratio models shown in Figure 2.6. Figure 2.11 shows the 2 1/2-D sensitivities at 1kHz which should be compared to the cylindrical case in given Figures 2.7a and 2.7b. Though there are many differences in the two sets of plots, the general characteristics are the same. For both cases the imaginary component dominates the response and is less sensitive to regions outside the well compared to the real component, which is very sensitive to some distance outside this region.

The most noticeable difference between the kernels for the two different geometries is that the 2 1/2-D sensitivities have sidelobes outside the interwell region near the transmitter as well as near the receiver. Thus one possible advantage of the cylindrical symmetry is that forward modeling requires smaller meshes due to the fact that the region on the negative side of the source doesn't have to be accounted for. A second interesting comparison that was discussed earlier is the reciprocity of the 2 1/2-D geometry with respect to the source and receiver position.

There are other, more subtle differences between the two geometries at this frequency. The vertical resolution for the 0:1 aspect ratio may be better for the 2 1/2-D model due to the fact that a narrow band of high sensitivity extends all the way across from the source to receiver. However, because the regions near the source and receiver for the cylindrical geometry are not reciprocal, it may provide better horizontal resolution. This is especially evident in the real component which shows a sign reversal in the interwell region for both the 0:1 and 1:1 aspect ratios which is not present in the 2 1/2-D sensitivity functions. However, as was mentioned in the last subsection any increased resolution in the real component for these low induction numbers is negated by the fact that it is sensitive to a large region outside the wells, and that the primary field dominates the in-phase response.

The 2 1/2-D sensitivity functions for 10kHz are plotted in Figure 2.12. Again there is a general similarity between the cylindrical symmetry (Figures 2.8a and 2.8b) and the 2 1/2-D geometry, especially in the region near the receiver. In fact these two sets of sensitivities show many more similarities when compared to the 1kHz results. This suggests that as we go to higher frequencies, the geometry of the problem becomes less important and a greater proportion of the response comes from the region immediately between the source and receiver. In addition, these results imply that the response of 2 1/2-D and cylindrically symmetric objects will be nearly identical in the region near the receiver .

However, some noticeable differences still exist between the sensitivities for the two geometries. The vertical resolution for the 0:1 aspect ratio is somewhat better for the 2 1/2-D case as it shows a narrower region of maximum sensitivity, especially in the imaginary component. The cylindrical symmetry again shows slightly better horizontal resolution due to the non-reciprocal nature of points near the transmitter and receiver. The cylindrically symmetric sensitivities also show a sign reversal in the interwell region, in this case in the imaginary component for the 1:1 aspect ratio (Figure 2.8b), which may tend to produce better resolution both horizontally and vertically. In general however, the differences between the two geometries are less significant at this frequency compared to 1kHz.

The 2 1/2-D sensitivity functions at 100kHz (Figure 2.13) show remarkable similarity to the cylindrical equivalents (Figure 2.9) for both the 0:1 and 1:1 aspect ratios. This similarity is especially evident in the real components which show almost no differences except immediately adjacent to the source. Noticeable differences do exist in the imaginary components, however even these have been reduced compared to those existing at lower frequencies. These results verify that at higher frequencies and for low

conductivity contrasts, the scattering currents sensed by a crosswell EM array are the same whether the body is extended in the $\hat{y}$ direction or symmetric about the transmitter axis. Thus at this point it is hypothesized that at high frequencies 2 1/2-D data are interpretable assuming a cylindrically symmetric geometry. This independence of geometry also may explain why ray theory solutions like those proposed by Nekut (1992) and Stolarchyk (1992) work well at higher frequencies but not at lower. This concept will be investigated more thoroughly in the next chapter.

2.4.3 Horizontal magnetic field sensitivity analysis

Using wave number domain analysis Zhou (1993) showed that if we assume a cylindrical geometry and we have complete, continuous data in both boreholes with large aspect ratios, then use of both the horizontal and vertical magnetic fields is redundant. Thus his work focused on using the vertical magnetic fields to image the conductivity structure. In practice however, data are collected at discreet points over a smaller vertical distance than we would hope for (e.g.. Wilt, et al. 1991). Because of this, the horizontal magnetic field sensitivity plots have been examined to determine the benefits, if any, of measuring this component of the field. The model used in the sensitivity analysis is the same as Figure 2.6 with the H_z (vertical) receivers replaced with H_r (horizontal) field receivers.

Figure 2.14 shows the horizontal field sensitivity plotted for the three different aspect ratios at 1kHz, and thus induction numbers of 0.8, 1.6 and 3.9. The most notable difference between these figures and those of the vertical field sensitivities (Figure 2.7) that was also evident in Figure 2.4 is that the horizontal component of the field is less sensitive to regions outside the wells. The simplest way to explain this is by analyzing the sidelobes that develop near the receiver. For the vertical field sensitivity, the sidelobes are oriented horizontally about the receiver as demonstrated in Figure 2.7. This tends to draw the sensitivity to the right of the receiver out into the region beyond the wells. However for the horizontal field sensitivity the side lobes are oriented vertically and thus more of the high sensitivity region lies between the wells. A second phenomenon is that the two components tend to compliment each other at these induction numbers. Regions of little or no vertical field sensitivity tend to coincide with regions of maximum horizontal field sensitivity and vice versa.

Other benefits of measuring the horizontal field are determined by comparing the horizontal and vertical field sensitivities for each of the different aspect ratios separately. The most notable difference occurs for an aspect ratio of 0:1. When the source and receiver are in this configuration they are null coupled and thus the horizontal component

(Figure 2.14a) is very sensitive to vertical changes in the conductivity. The figure also indicates that the horizontal component is sensitive to radial changes in position when the scatterer is not directly in line with the source and receiver. This suggests that for limited angle data, i.e. data collected using aspect ratios from 0:1 up to 1:1, we might get slightly better resolution by employing the horizontal component then from the vertical component. In addition, the fact that the source and receiver are null coupled means that the primary field will be absent for this configuration. Thus the only field measured will be the secondary fields of scatterers we wish to detect.

As the aspect ratio increases to 1:1 and 2:1 the differences between the horizontal field sensitivity and vertical field sensitivity decrease. The sign reversals apparent in the vertical component for these larger aspect ratios (Figures 2.7b and 2.7c) do not appear in the horizontal component. This suggests that the gain in vertical resolution achieved by measuring the horizontal component at the 0:1 aspect ratio may be lost at greater aspect ratios. However as can be seen from figures 2.14b and 2.14c the sensitivity to the horizontal position of a scatterer increases with increasing aspect ratio which is consistent with what we found in sections 2.4.1 and 2.4.2.

Figure 2.15 shows the horizontal field sensitivities at 10kHz (corresponding to induction numbers of 8, 16 and 39). Comparing these to the vertical field sensitivities (Figure 2.8) indicates that many of the same comparisons exist that were found between the 1kHz horizontal and vertical sensitivities. The horizontal component tends to be less sensitive to the region outside the wells, especially at larger aspect ratios. Again, because of the null coupling at an aspect ratio of 0:1, the horizontal component (Figure 2.15a) is much more sensitive to vertical and horizontal changes in position compared to the vertical component (Figure 2.8a). However, notice that at these induction numbers the horizontal and vertical components no longer complement each other at larger aspect ratios. Instead we find that the zones of maximum horizontal and vertical field sensitivity tend to occupy the same region. This suggests that one of the two components becomes redundant at higher frequency and supports Zhou's conclusion on this matter.

This redundancy becomes more apparent at 100kHz. Except for the 0:1 aperture, there is very little difference between the horizontal field sensitivities (Figure 2.16) and the vertical field sensitivities (Figure 2.9). The maximum kernel values occupy the same regions except immediately adjacent to the receiver, and in both cases there is very little sensitivity to the region outside the wells. In addition, the regions of maximum sensitivity form patterns that resemble ray paths. Once again, because the horizontal component (Figure 2.16a) is significantly different for the 0:1 aspect ratio compared to the vertical component (Figure 2.9a) , measuring both the horizontal and vertical

components may be useful at this frequency for limited angle data. However, the above results show that measuring both magnetic field components at large aspect ratios may only be useful at lower frequencies.

2.4.4 Spatial sensitivity analysis of the vertical magnetic field for in-hole geometries

Zhou (1989) showed that improvements in image resolution can result from using in hole or back scattered data. Thus I have chosen to briefly examine the sensitivity functions for the source and receiver in the same borehole. As previously mentioned, this analysis has previously been used for well logging analysis and tool design (e.g.. Barber,1992) however here we are more concerned in its use to supplement crosswell data.

The model used for this analysis is given in Figure 2.17. Two VMD's , a source and a receiver, are separated vertically by 100m in a whole space of conductivity 0.01S/m. The same three frequencies of 1kHz, 10kHz and 100kHz have been used as previously. Again the dimensions of the problem can be normalized to the induction number of the background medium, which ultimately allows this analysis to be related to any scale by keeping this number constant. The induction numbers corresponding to the above frequencies are 0.8, 8.0 and 80, respectively.

The vertical field sensitivities for all three frequencies have been plotted on the same scale in Figure 2.18. Immediately it is evident that with increasing frequency, less of the region is sensed by this source-receiver configuration. As predicted by figure 2.5a, as the frequency is increased upward from 1kHz, the region of maximum sensitivity moves closer to the well.

The benefit of using the in hole data with the cross well data for imaging is very evident from the spatial sensitivity plots. As a point is moved horizontally away from the well out into the medium, the sensitivity changes quite dramatically, especially at higher induction numbers. This added horizontal sensitivity explains why Zhou (1989) improved his crosswell images by incorporating the in-hole component with the crosshole fields.

Another noteworthy phenomenon apparent in these plots is that the region of maximum sensitivity is controlled primarily by the source-receiver separation. In fact except for the low induction number case, that region doesn't extend out much past .5 to .75 times the source receiver separation. This rapid fall off of the sensitivity functions with radial distance explains why Zhou (1989) was able to image object edges near the borehole in his single hole inversions, but couldn't recover edges far away from the borehole.

2.5 Summary

To summarize this chapter, the Born kernel which results from applying the Born approximation to the integral equations governing EM propagation is a very useful tool for studying how well various source-receiver configurations and frequencies can be used to sense the conductivity structure in the region between two boreholes. At low frequencies both field components arise from a zone that is largely outside the region of interest between the source and receiver. However the horizontal component is less sensitive than the vertical to this unwanted region suggesting that it should be employed if measurements through casing are to be made as suggested by Uchida, et al(1991) and Newman (1992a). As the frequency is raised, the sensed region becomes more focused between the boreholes and the difference between the vertical and horizontal components response is reduced. In addition, it has been shown that at higher frequencies, the geometry of the target body is less important with a 2 1/2-D geometry producing almost the same sensitivity coverage as a 2-D cylindrical geometry, especially near the receiver. This topic will be investigated more thoroughly in the next chapter.

Because the sensitivity functions are very useful in determining how well an array resolves a target body, comparisons can be made with the conclusions of Zhou(1989) who analyzed the problem with coverage diagrams in the wave number domain. The analysis in both domains indicates that there is greater resolution at higher frequencies, and that higher aspect ratios lead to better horizontal resolution. In addition it has been determined that the in-hole component of the vertical magnetic field offers additional horizontal resolution. However, although the both components of the magnetic field seem to be redundant for higher induction numbers and aspect ratios of 1:1 and greater, the space domain sensitivity analysis indicates that the horizontal component may be very useful in supplementing the vertical component at lower frequencies and when only small aperture data is available. These characteristics will be examined again in Chapter 4.

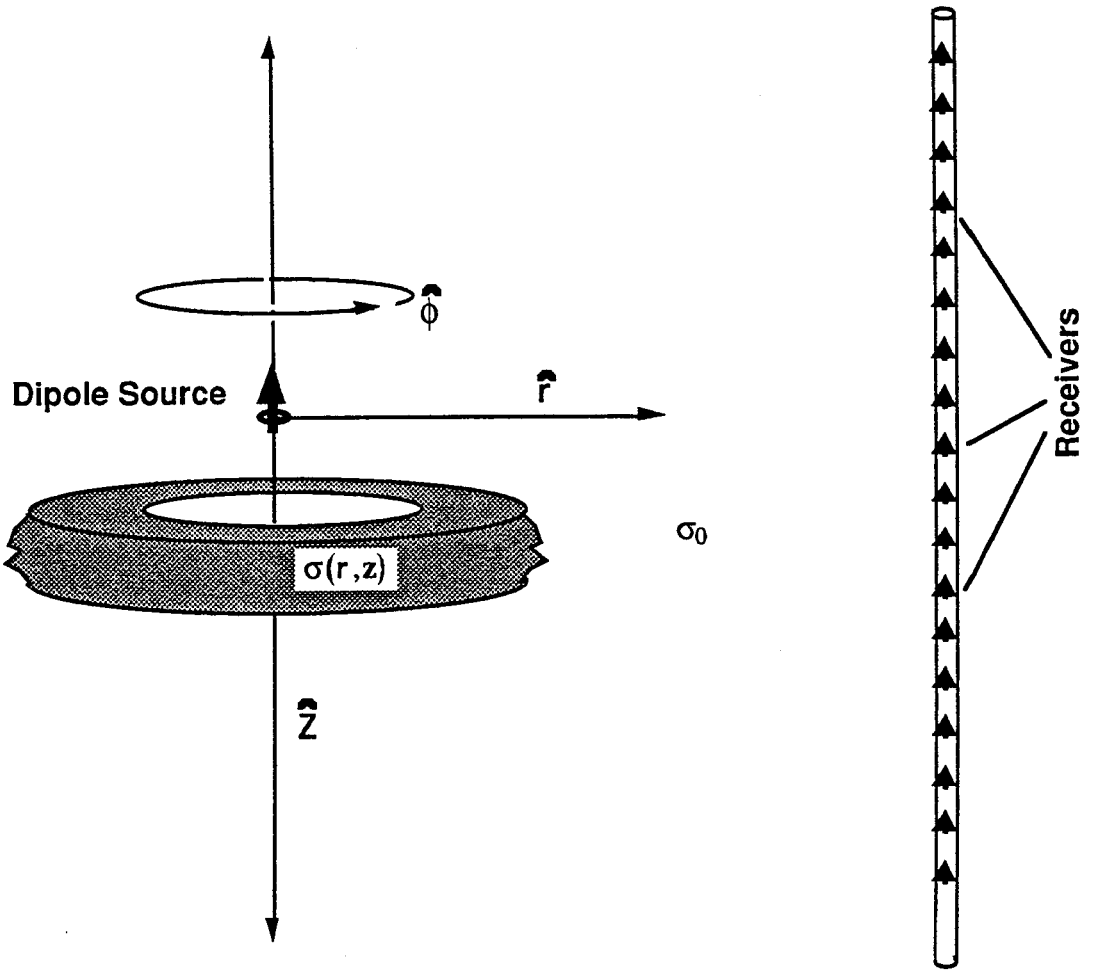

Figure 2.1 - Cylindrical two dimensional (2-D) geometry for the crosswell problem. The inhomogenous body is cylindrically symmetric about the magnetic dipole axis.

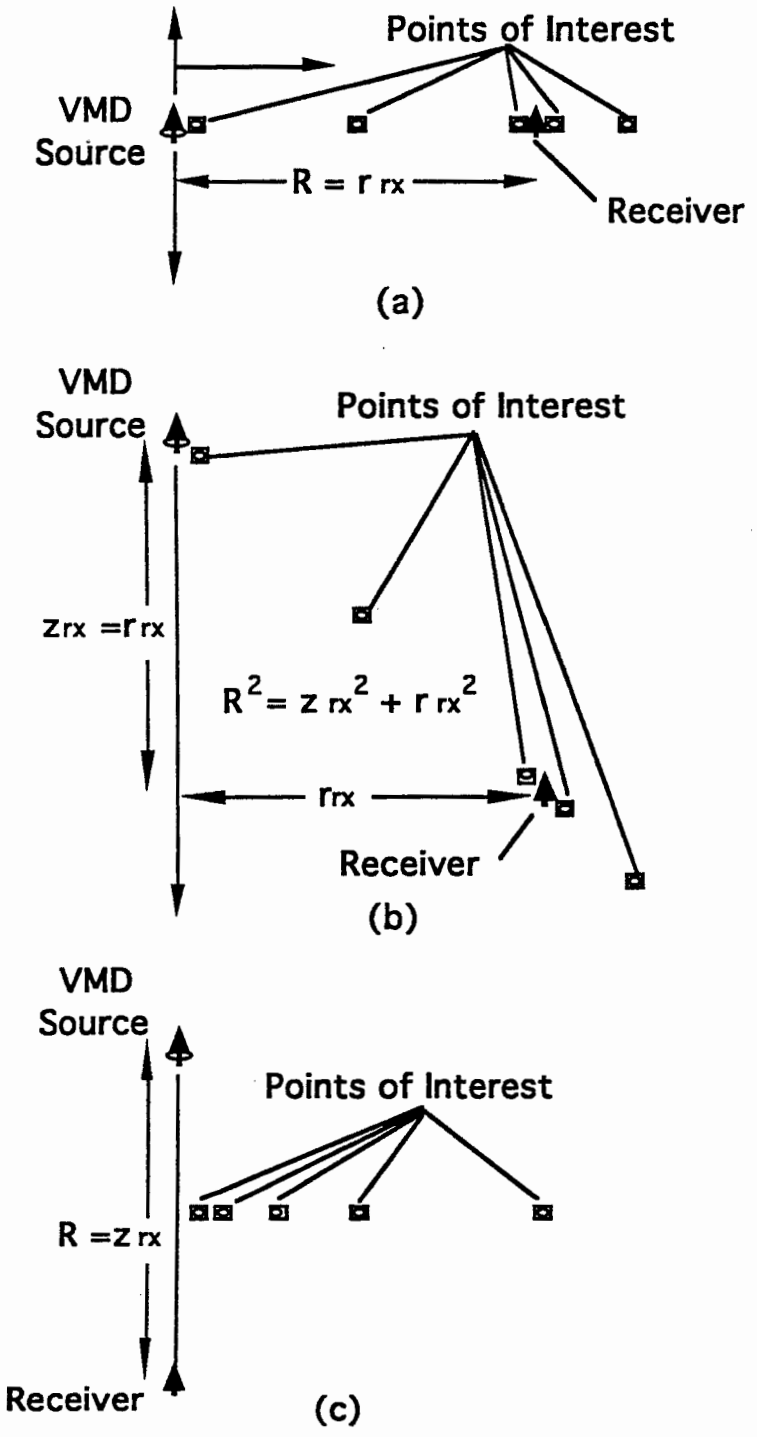

Figure 2.2 - Models used to demonstrate the properties of the Born kernel. (a) Crosswell model with source and receiver at the same depth. (b) Crosswell model with receiver the same distance below and to the side of the source. (c) In hole with receiver directly below source.

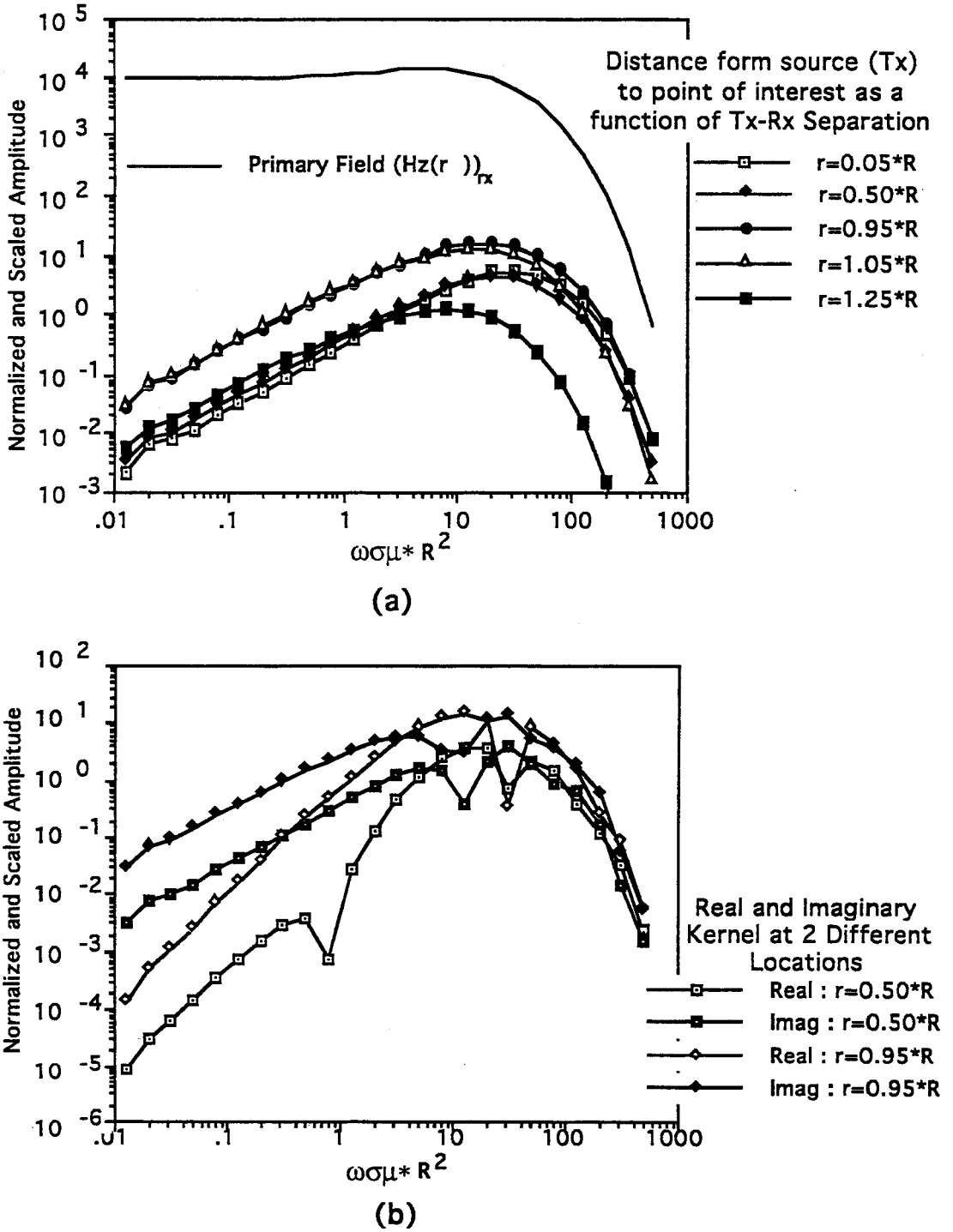

Figure 2.3 - (a) The Born kernel at different points of interest and the primary magnetic field plotted as a function of background induction number for the model in Figure 2.2a. (b) The absolute values of the real and imaginary components of the Born kernel for two of the points shown in FIgure 2.2a. (c) See following page.

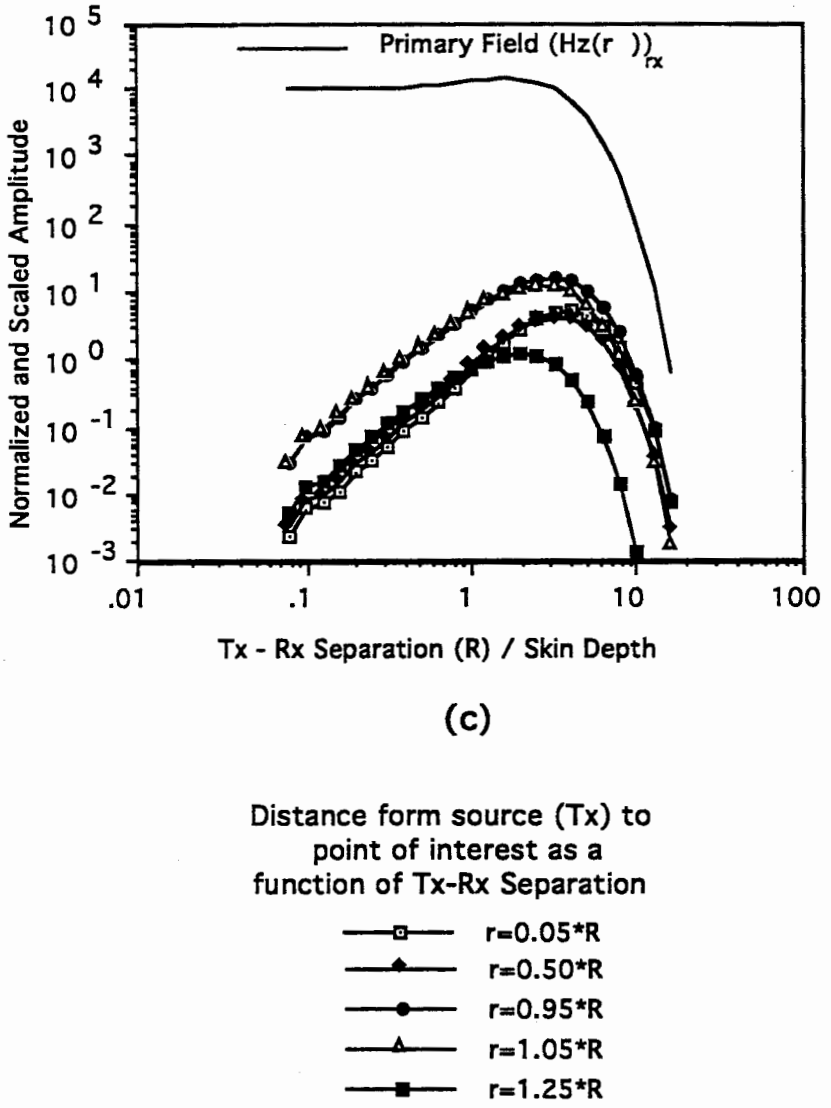

Figure 2.3 - (Continued from previous page.) (c) The Born kernel at different points of interest and primary magnetic field plotted as a function of source-receiver separation normalized by skin depth for the model in figure2.2a.

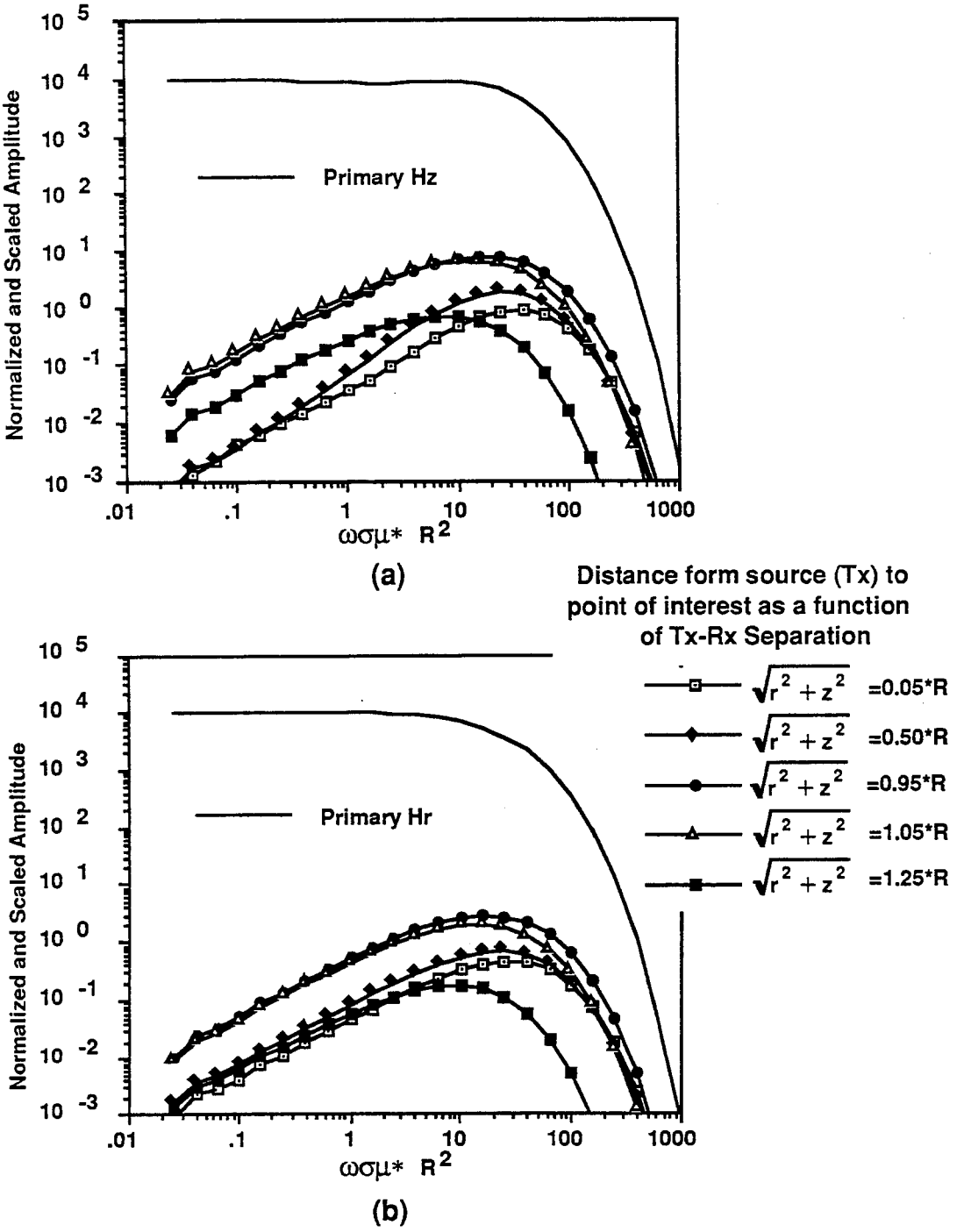

Figure 2.4 - (a) The vertical components of the Born kernel at different points of interest and the primary magnetic field plotted as a function of the background induction number for the model in Figure 2b. (b) The horizontal components of the Born kernel at different points of interest and the primary magnetic field plotted as a function of the background induction number for the model in Figure 2b.

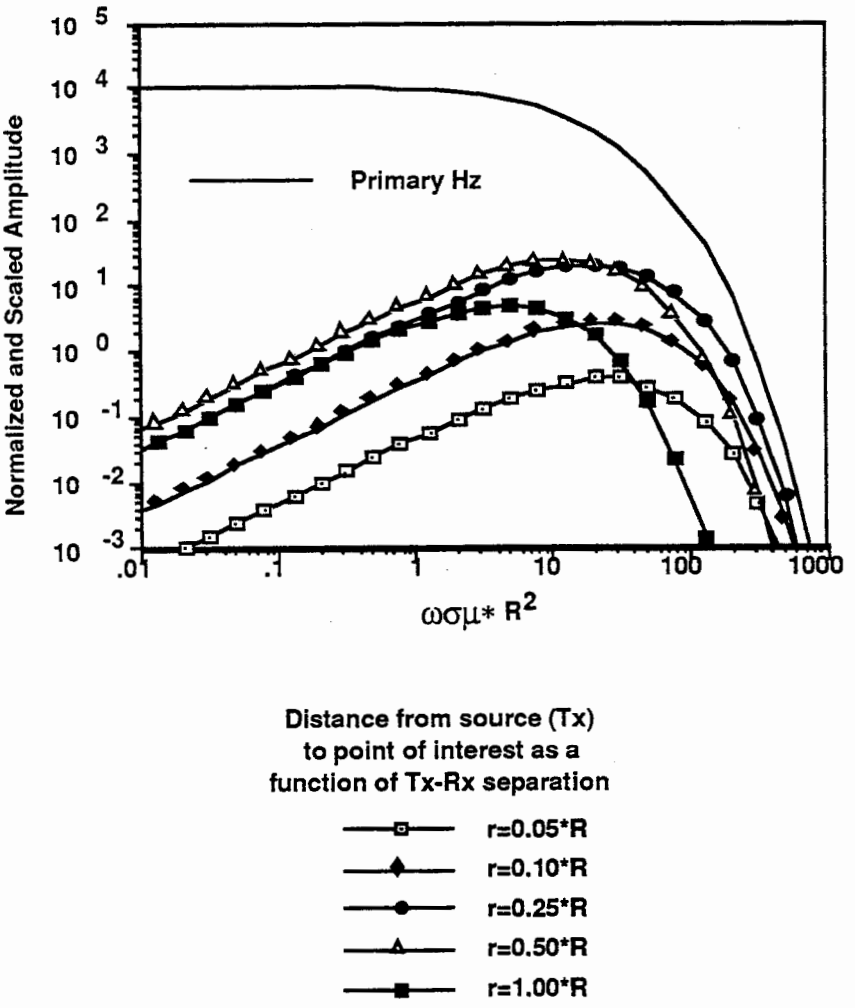

Figure 2.5 - The vertical components of the Born kernel at different points of interest and the primary magnetic field plotted as a function of the background induction number for the model in Figure 2c.

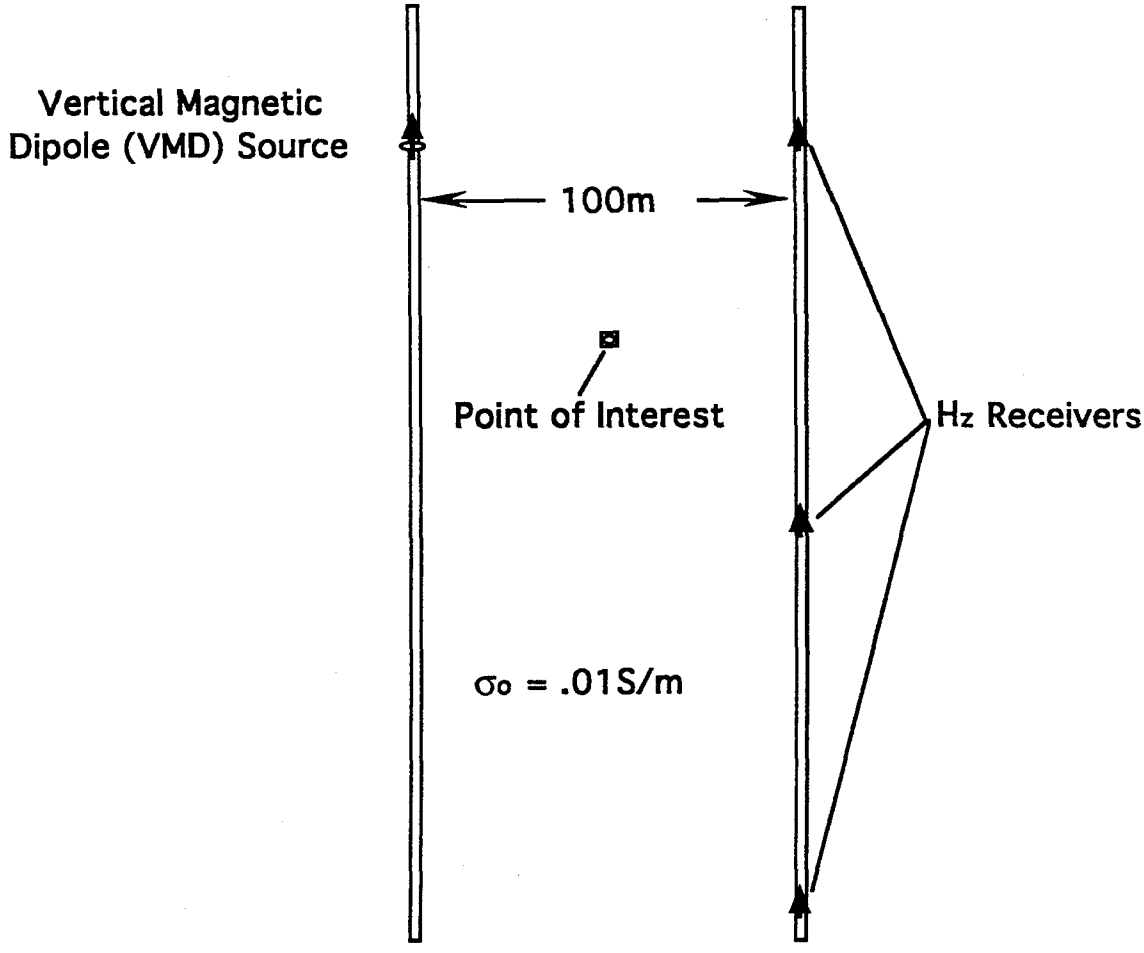

Figure 2.6 - Model used for the the Born kernel crosswell sensitivity analysis. Two wells are located 100m apart in a 0.01S/m whole space with a VMD source located in one borehole, and a vertical magnetic receiver in the other. The spatial sensitivties are calculated for three different receiver locations. The upper receiver position represents an aspect ratio or aperture (zrx/rrx) of 0:1, the middle an aspect ratio of 1:1 and the bottom an aspect ratio of 2:1.

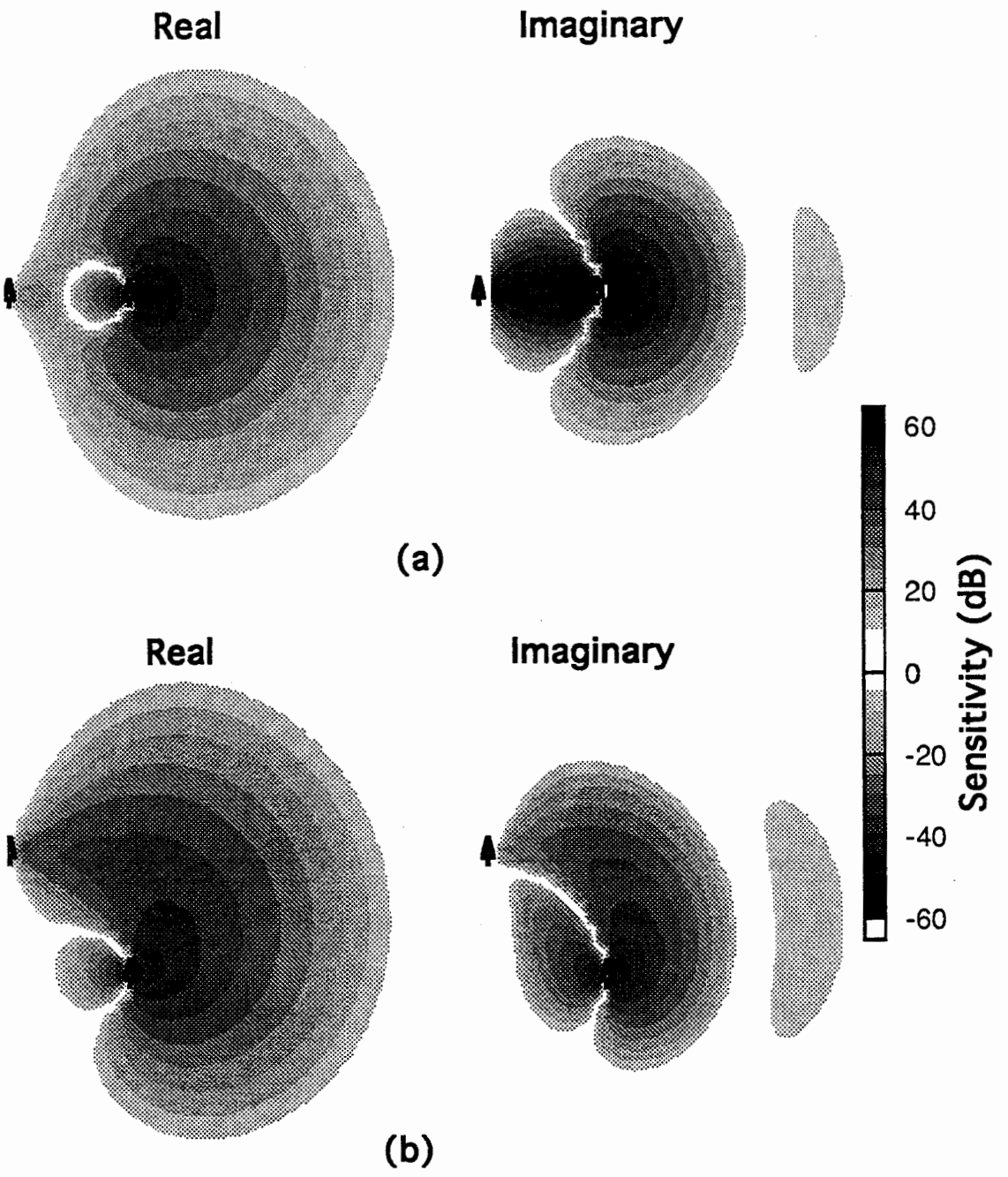

Figure 2.7 - 1kHz Born kernel sensitivities calculated at 10m intervals for the model shown in Figure 2.6. (a) Aspect ratio = 0:1, induction number =0.8. (b) Aspect ratio =1:1, induction number = 1.6. (c) See following page.

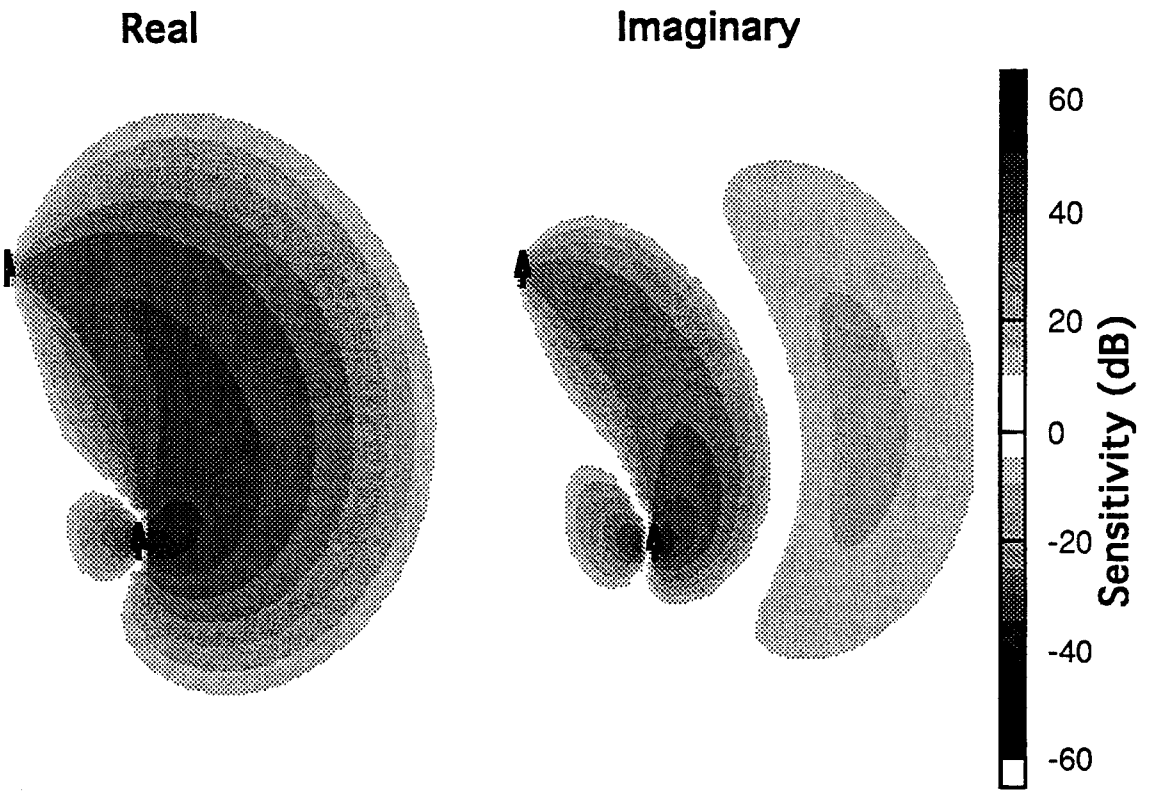

(c)

Figure 2.7 - (Continued from preceeding page). (c) Aspect ratio=2:1, induction number=3.9.

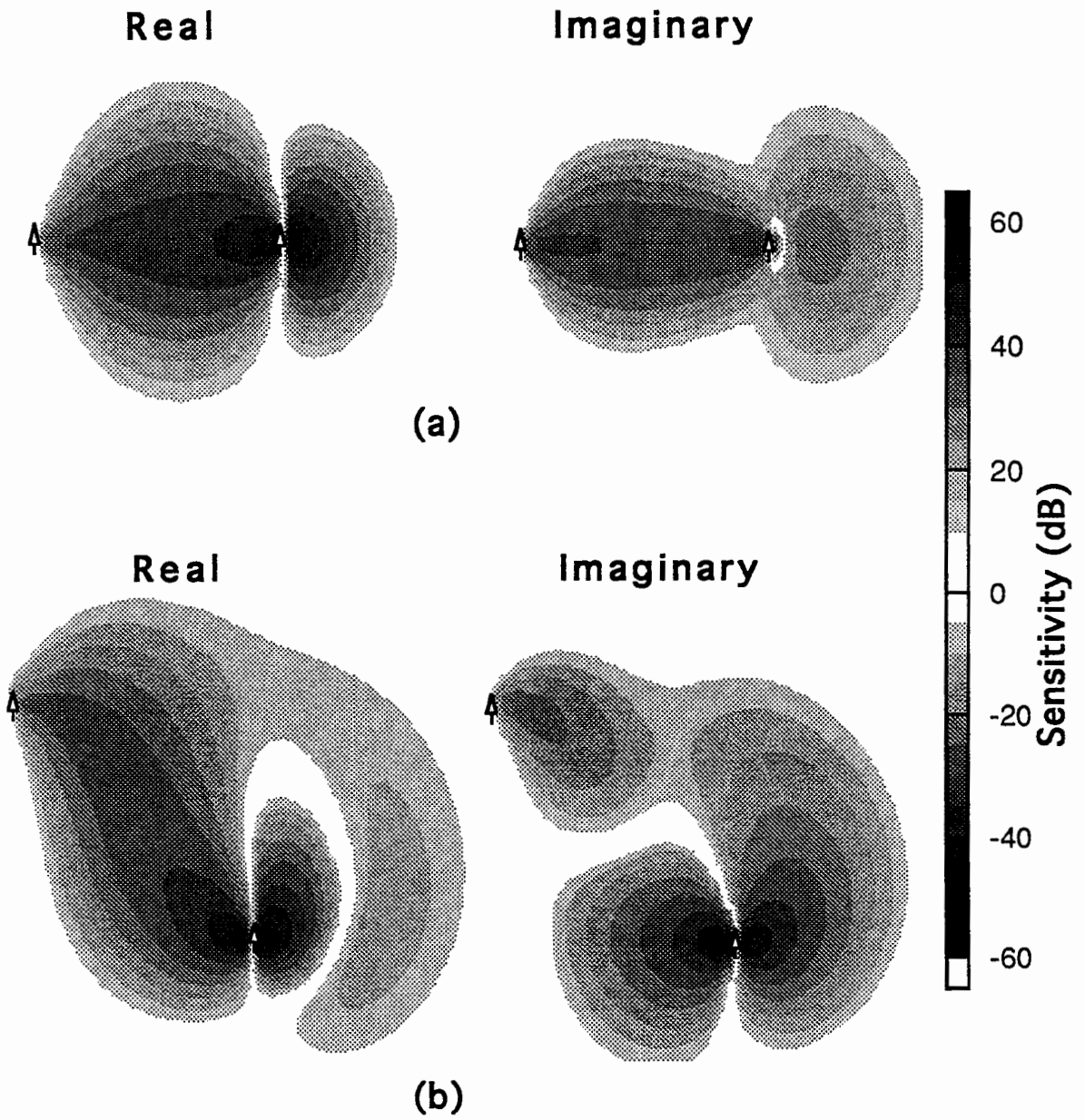

Figure 2.8 - 10kHz Born kernel sensitivities calculated at 5m intervals for the model shown in Figure 2.6. (a) Aspect ratio = 0:1, induction number =8.0. (b) Aspect ratio =1:1, induction number = 16. (c) See following page.

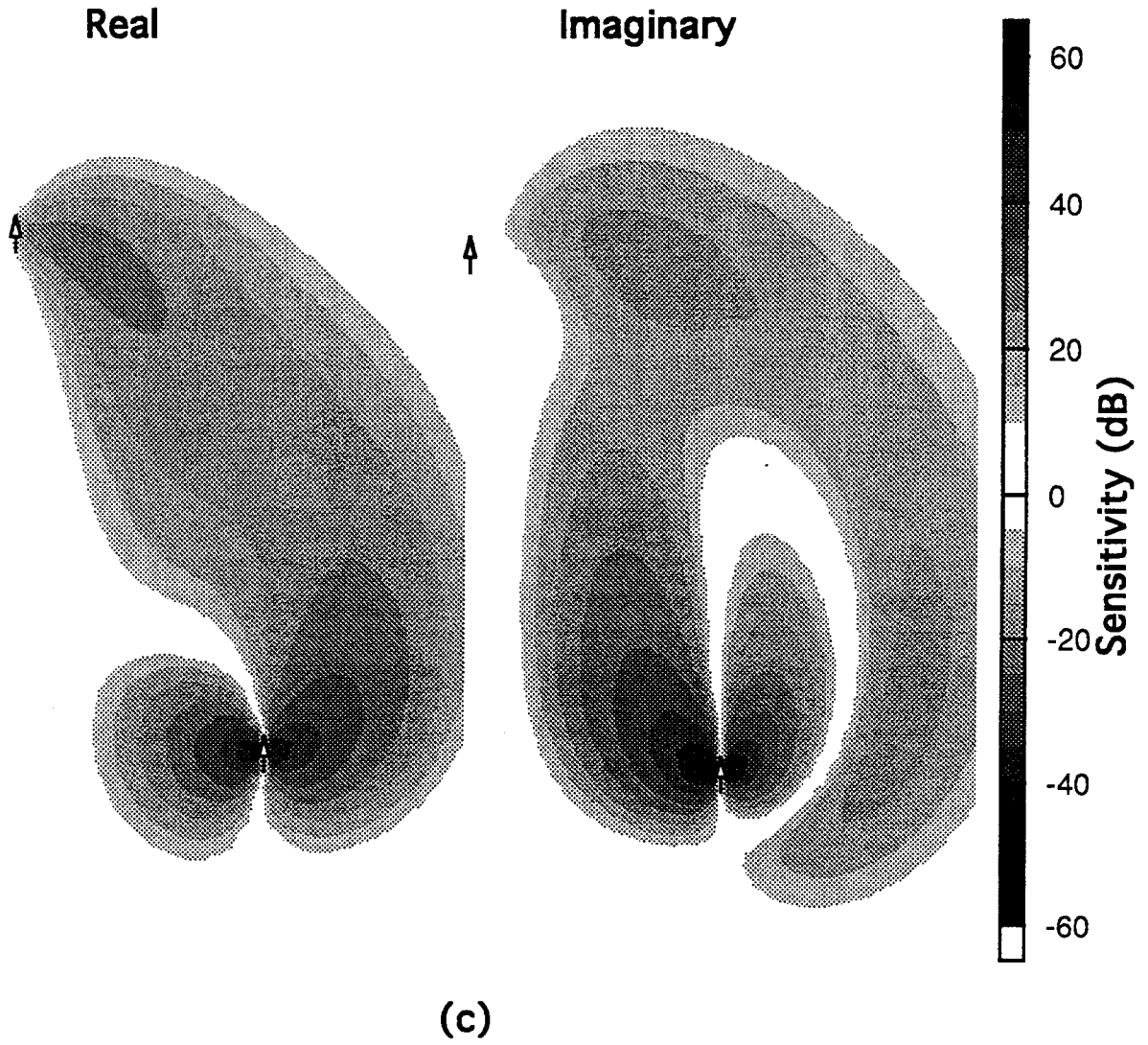

Figure 2.8 -(Continued from preceeding page.) (c) Aspect ratio = 2:1, induction number=39.

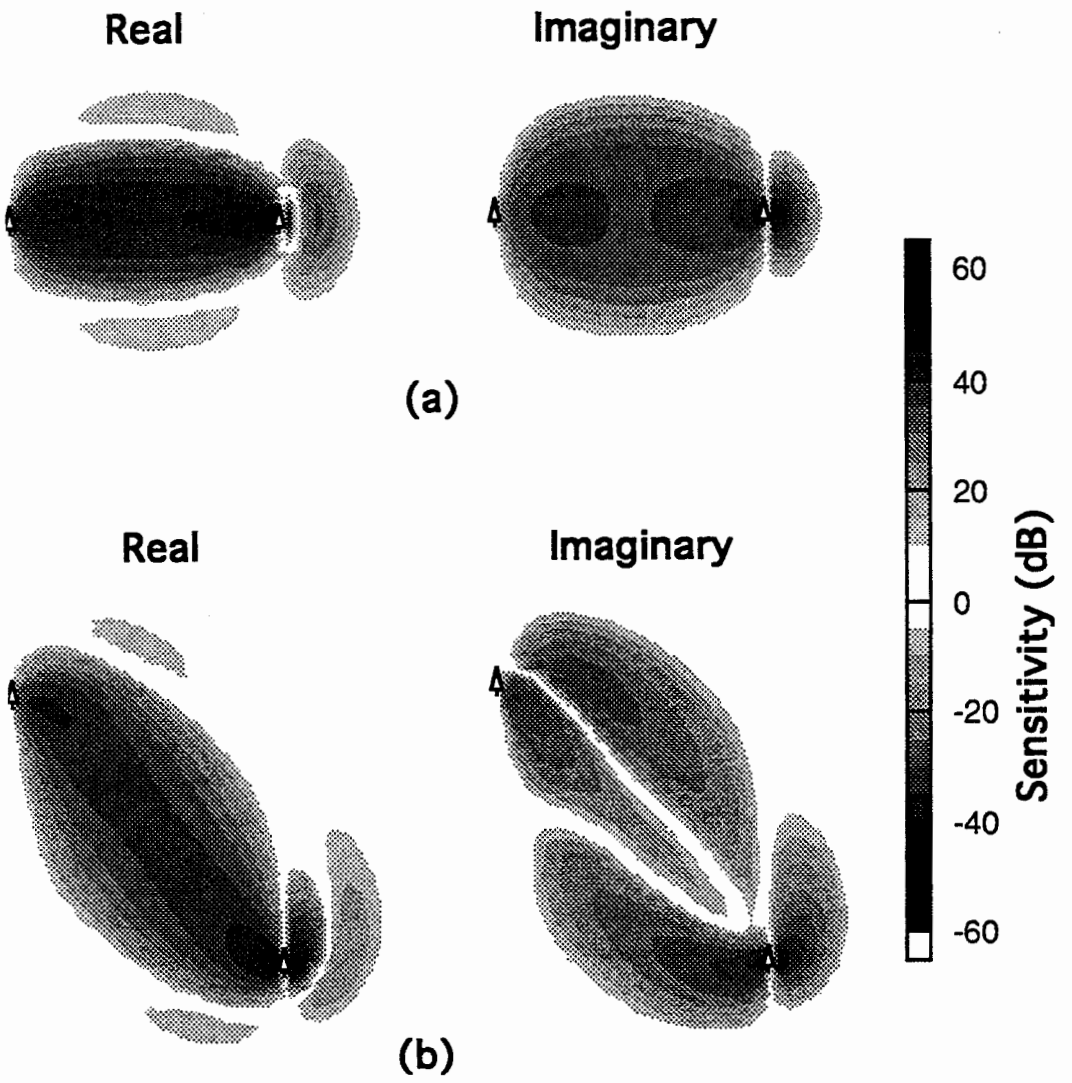

Figure 2.9 - 100kHz Born kernel sensitivities calculated at 5m intervals for the model shown in Figure 2.6. (a) Aspect ratio = 0:1, induction number =80. (b) Aspect ratio =1:1, induction number = 160. (c) See following page.

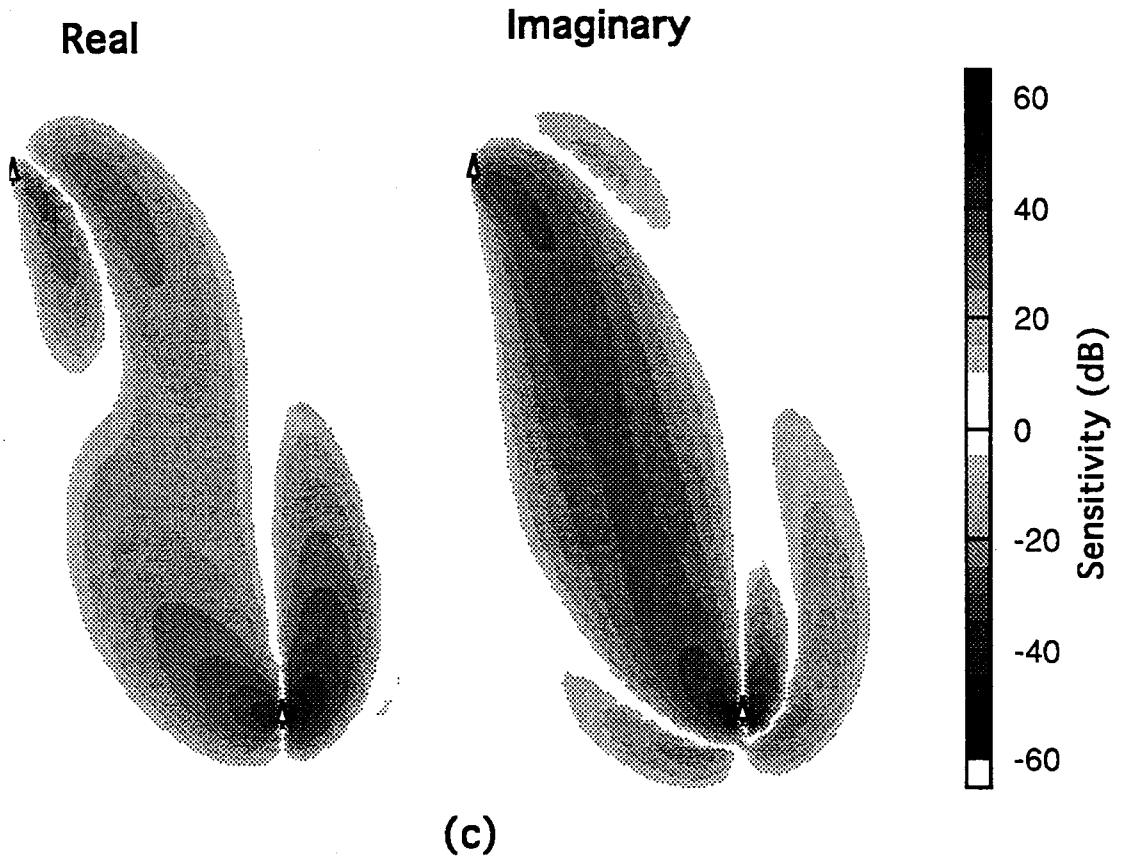

Figure 2.9 - (Continued from preceeding page) (c) Aspect ratio=2:1, induction number=390.

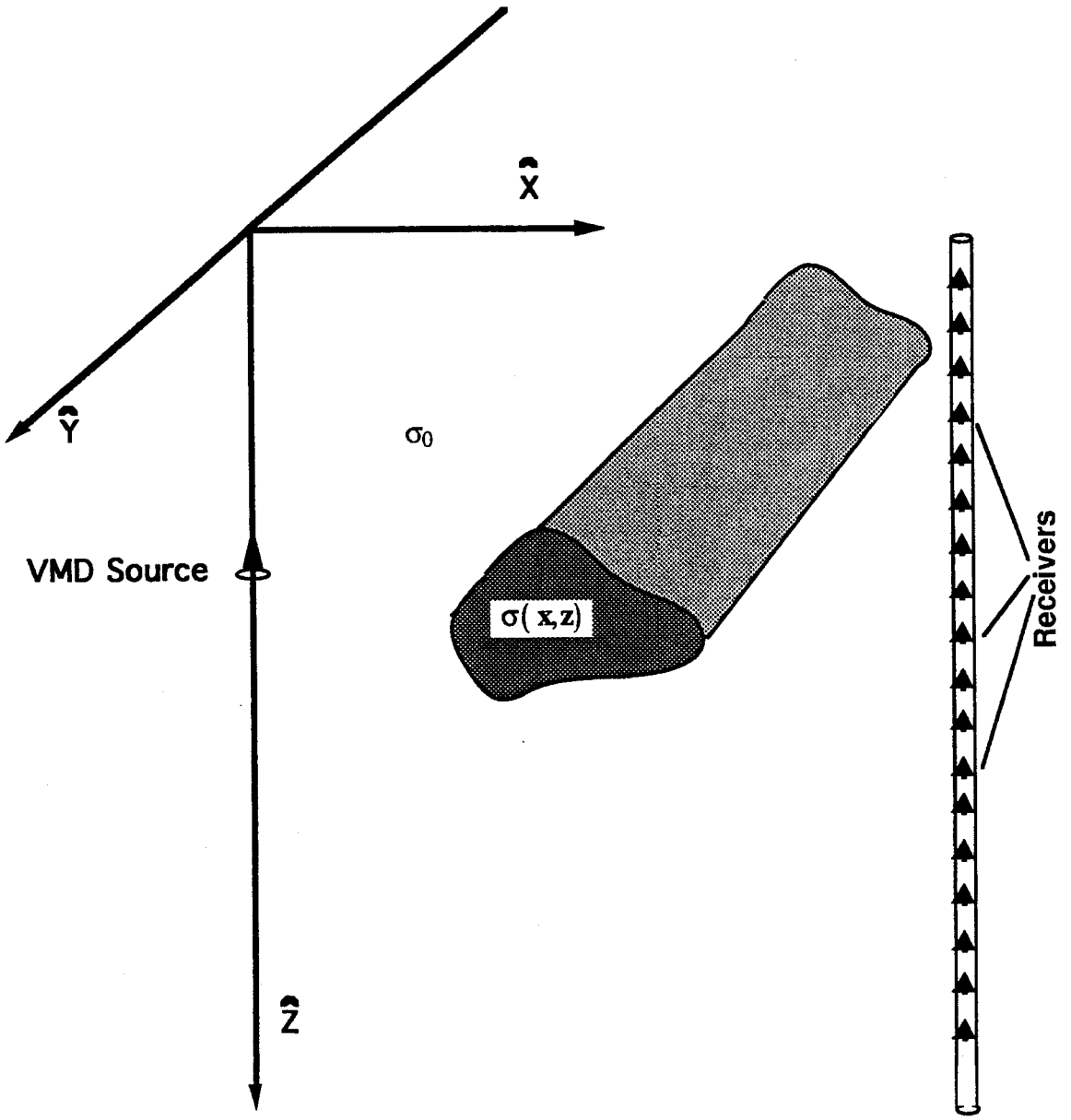

Figure 2.10 - 2 1/2-D geometry for the crosswell problem. The inhomogenous body is infinate in the y direction and is is excited by a 3-D vertical magnetic dipole.

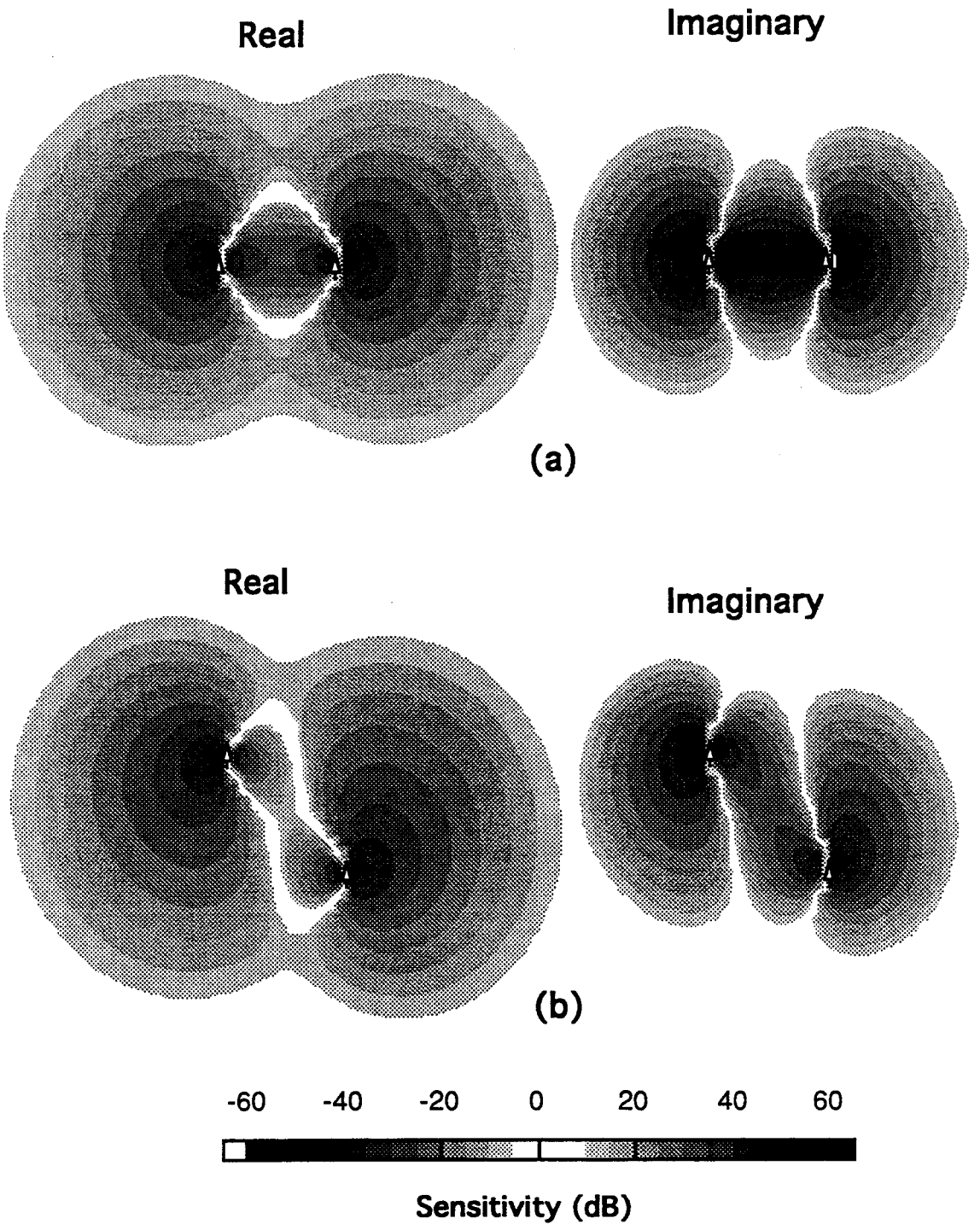

Figure 2.11 - 1kHz Born kernel sensitivities calculated at 10m intervals for the 2 1/2-D equivalent of the model shown in Figure 2.6. (a) Aspect ratio = 0:1, induction number =0.8. (b) Aspect ratio =1:1, induction number = 1.6.

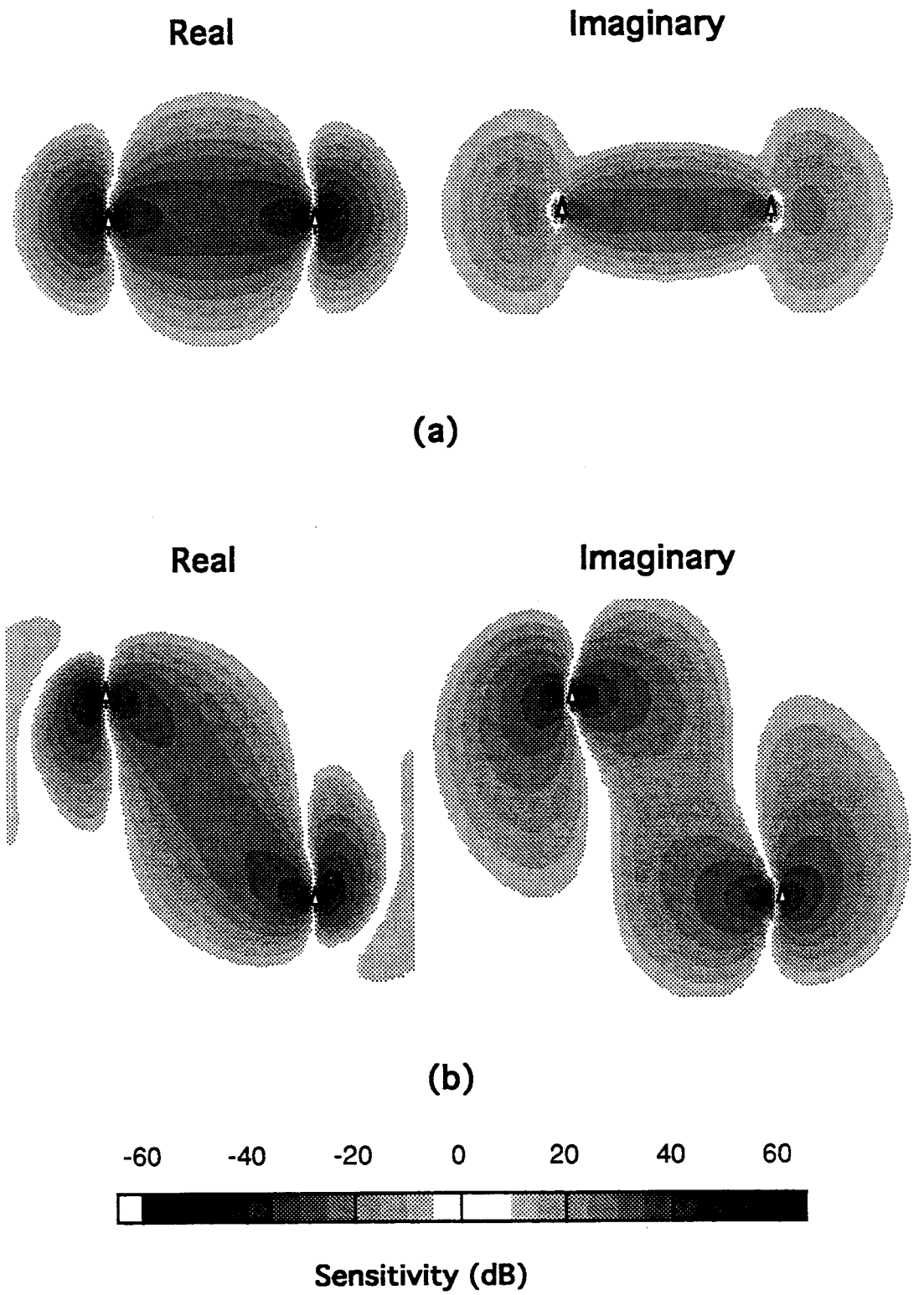

Figure 2.12 - 10kHz Born kernel sensitivities calculated at 5m intervals for the 2 1/2-D equivalent of the model shown in Figure 2.6. (a) Aspect ratio = 0:1, induction number =8. (b) Aspect ratio =1:1, induction number = 16.

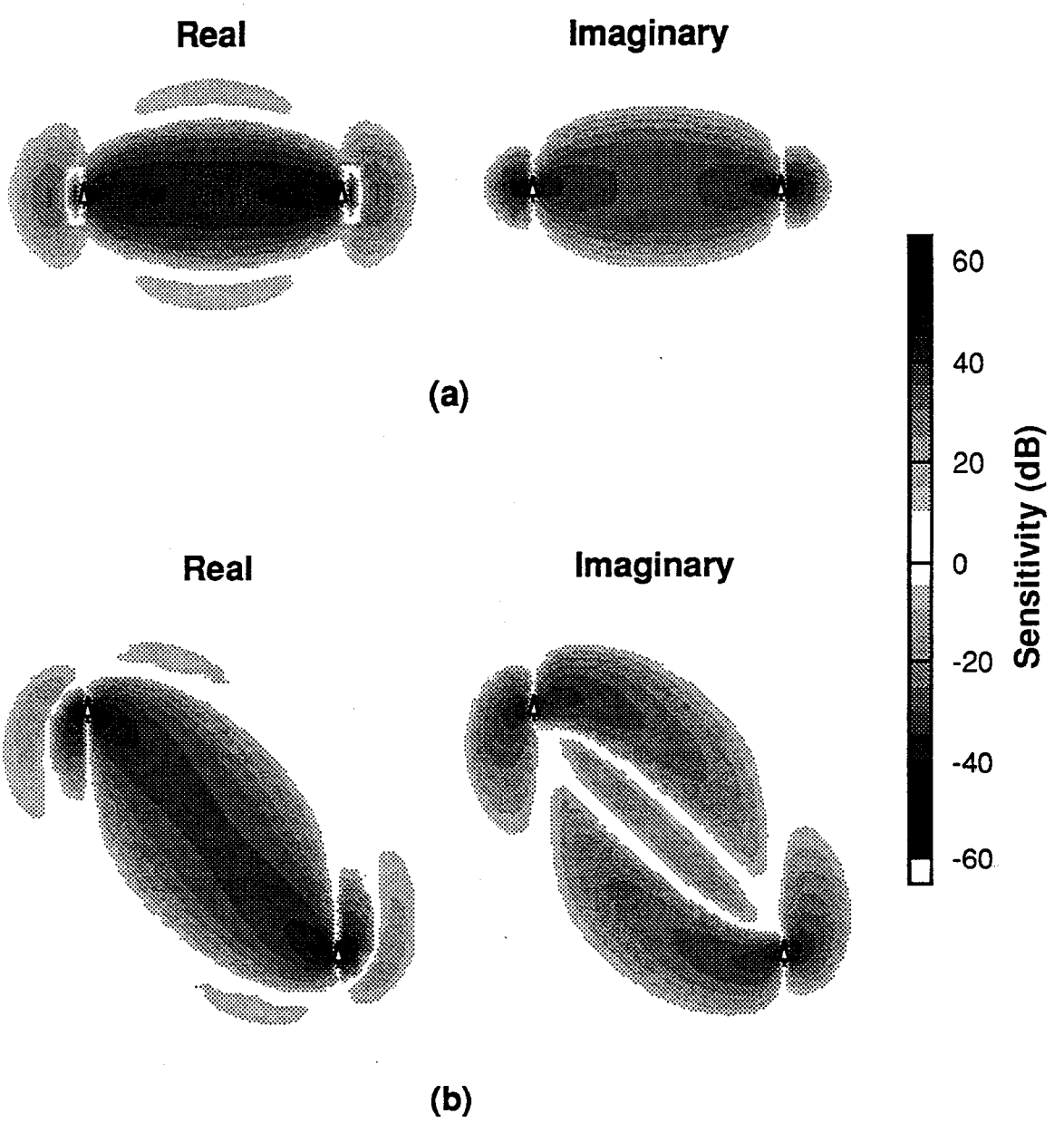

Figure 2.13 - 100kHz Born kernel sensitivities calculated at 5m intervals for the 2 1/2-D equivalent of the model shown in Figure 2.6. (a) Aspect ratio = 0:1, induction number =80. (b) Aspect ratio =1:1, induction number = 160.

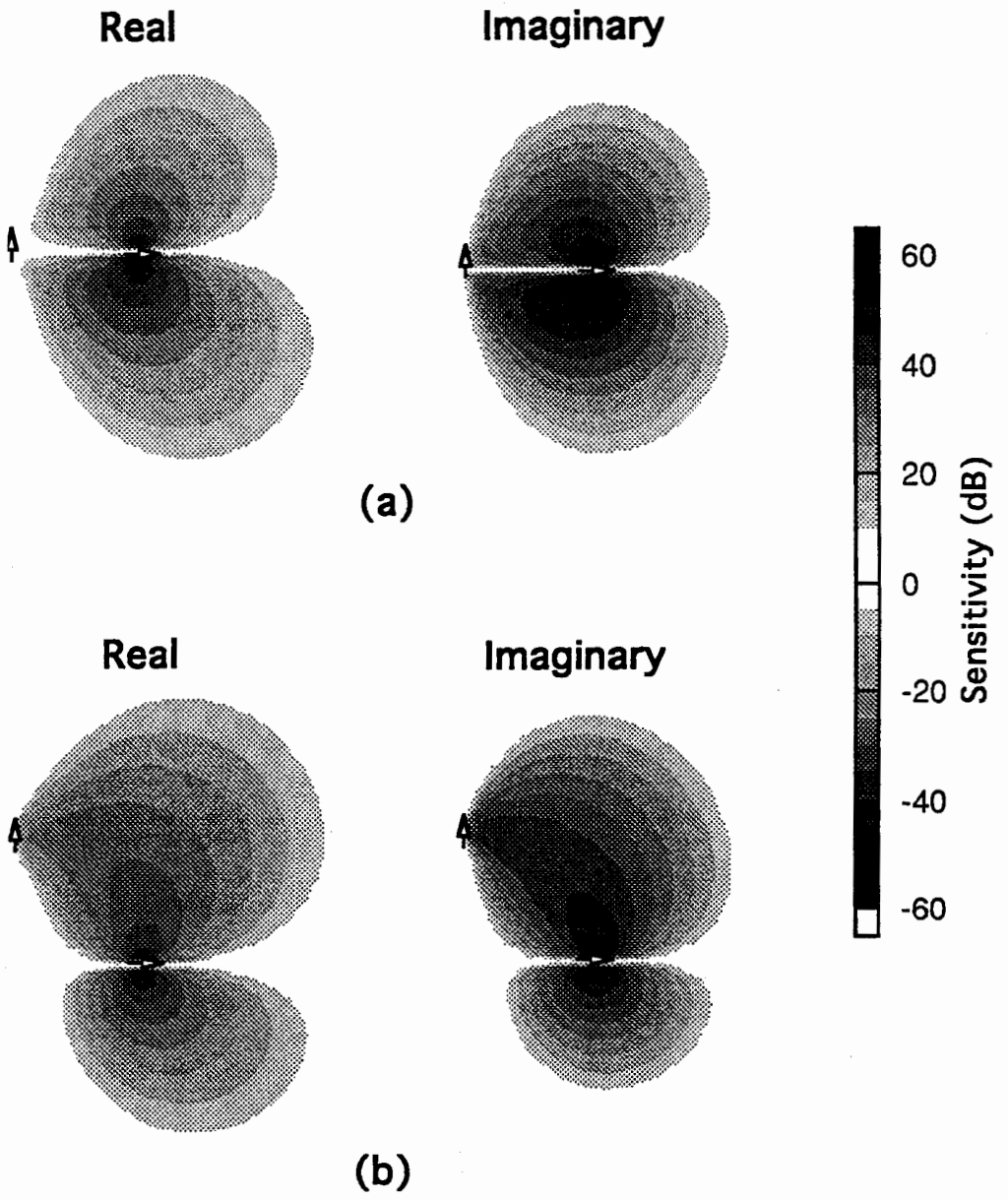

Figure 2.14 - 1kHz Born kernel sensitivities for the horizontal field calculated at 10m intervals for the model shown in Figure 2.6. (a) Aspect ratio = 0:1, induction number =0.8. (b) Aspect ratio =1:1, induction number = 1.6. (c) See following page.

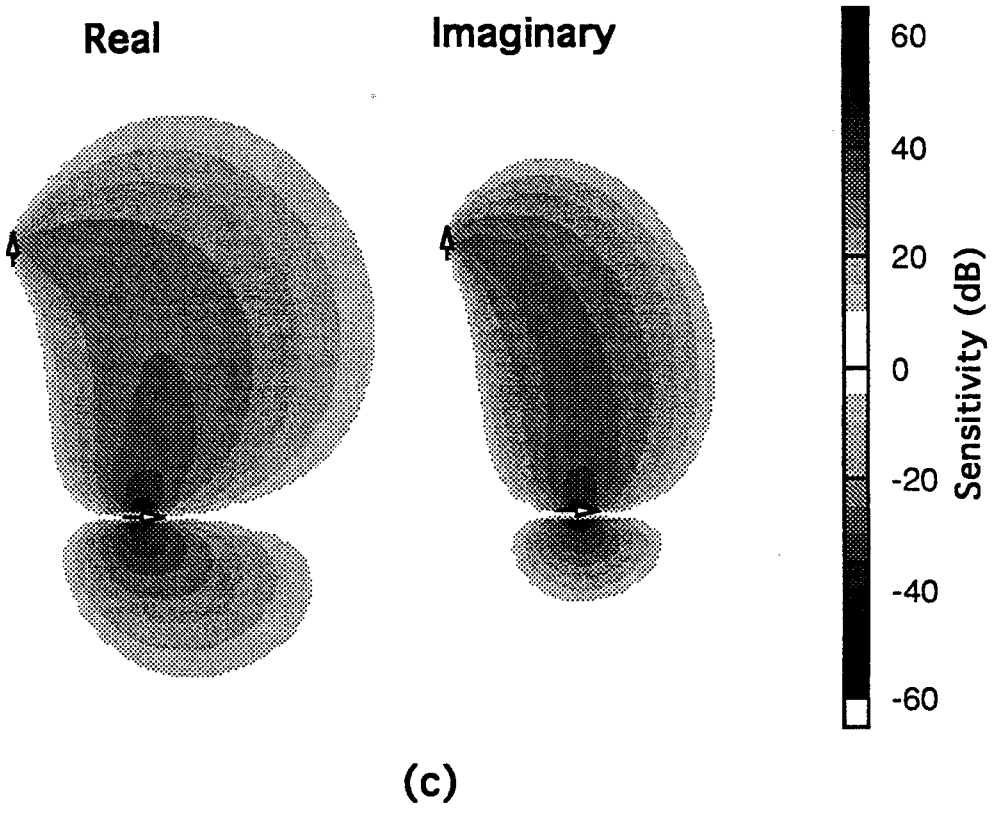

Figure 2.14 - (Continued from preceeding page) (c) Aspect ratio=2:1, induction number=3.9.

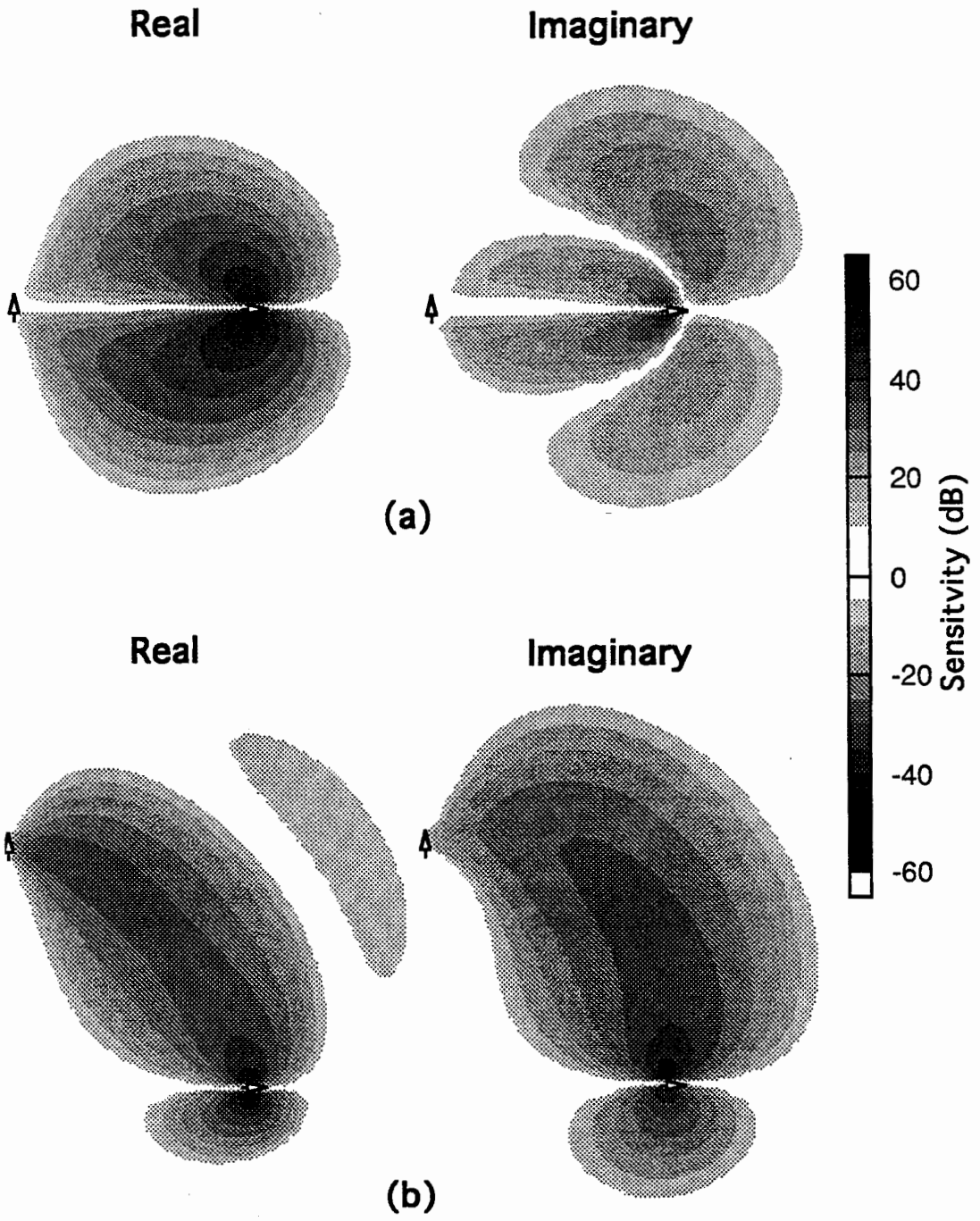

Figure 2.15 - 10kHz Born kernel sensitivities for the horizontal field calculated at 5m intervals for the model shown in Figure 2.6. (a) Aspect ratio = 0:1, induction number =8.0. (b) Aspect ratio =1:1, induction number = 16. (c) See following page.

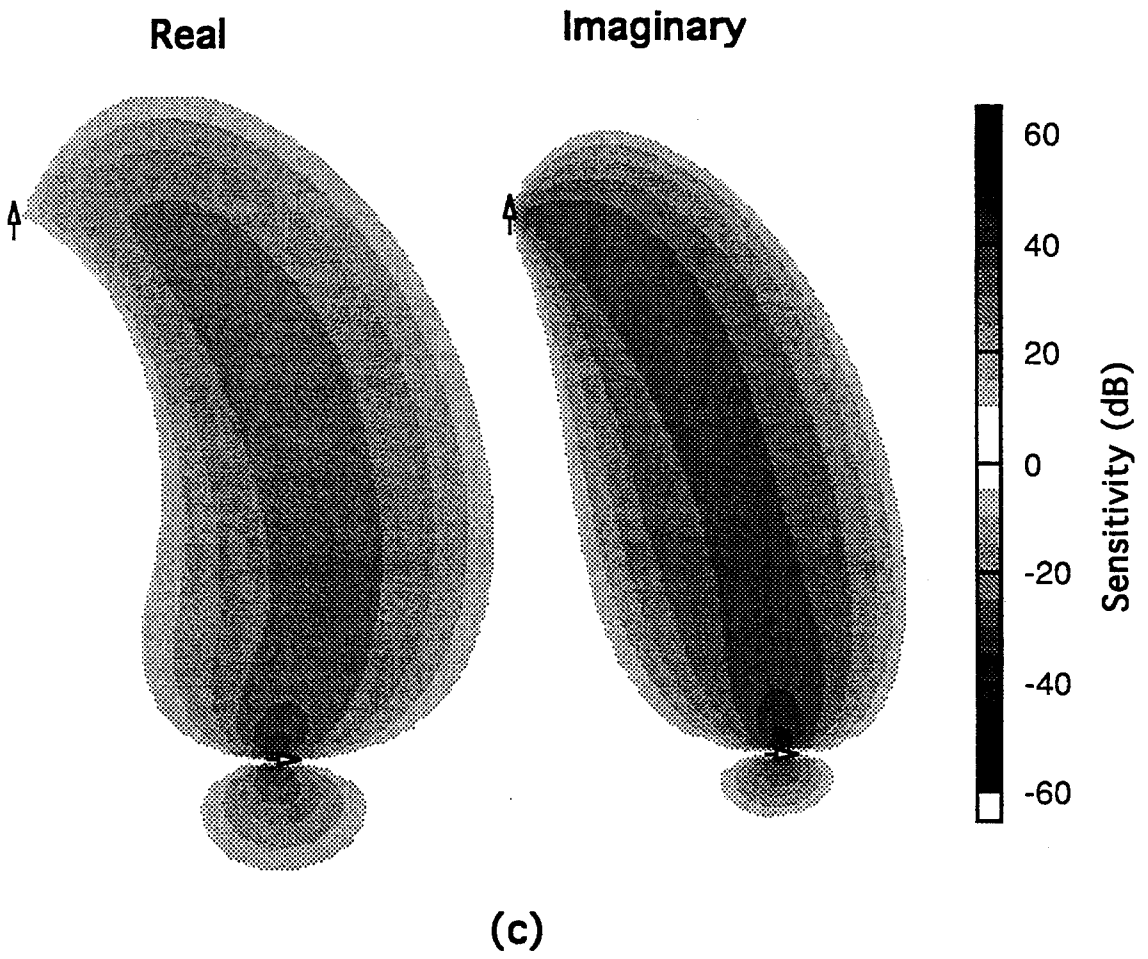

Figure 2.15 - (Continued from preceeding page). (c) Aspect ratio=2:1, induction number=39.

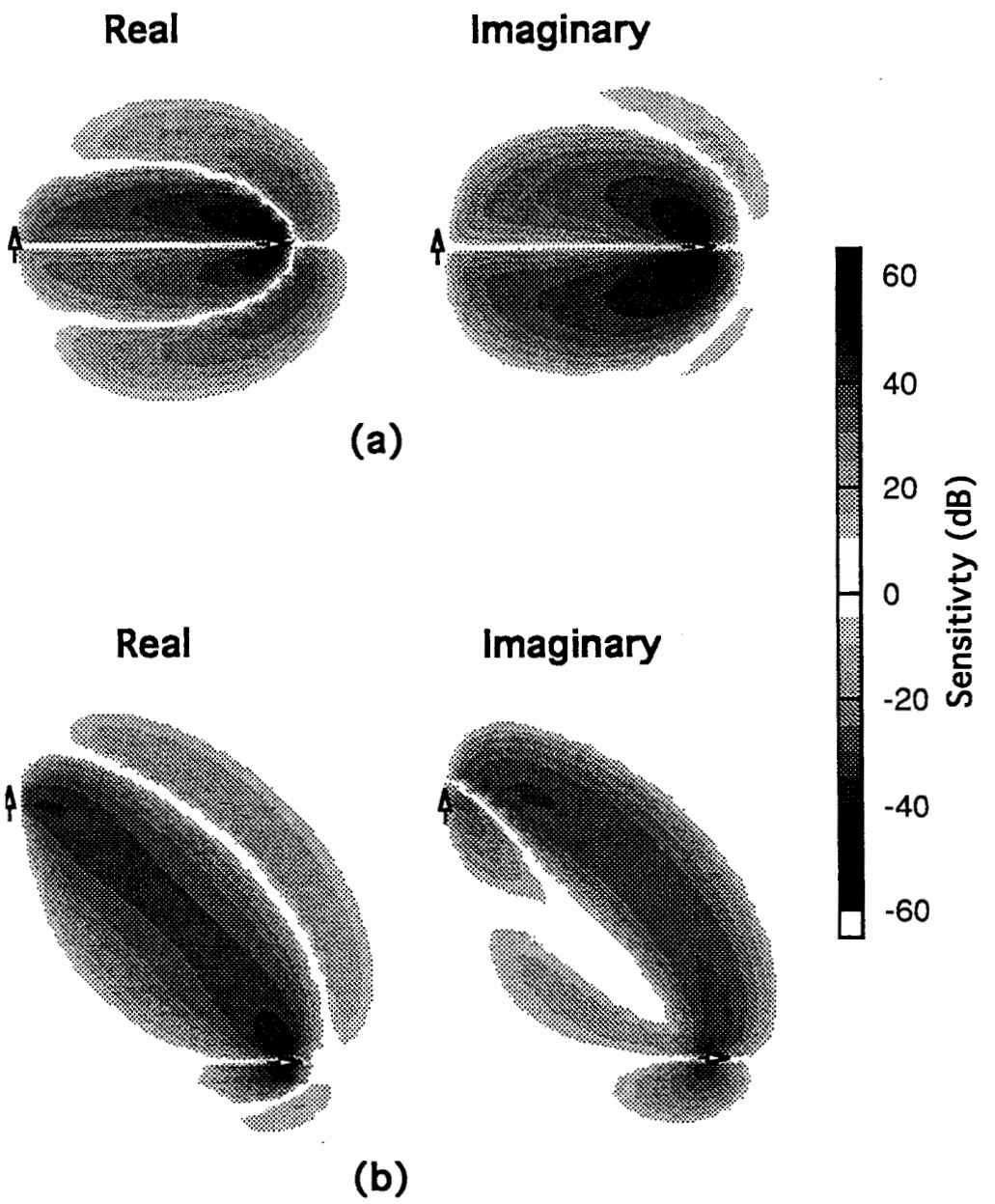

Figure 2.16 - 100kHz Born kernel sensitivities for the horizontal field calculated at 5m intervals for the model shown in Figure 2.6. (a) Aspect ratio = 0:1, induction number =80. (b) Aspect ratio =1:1, induction number = 160. (c) See following page.

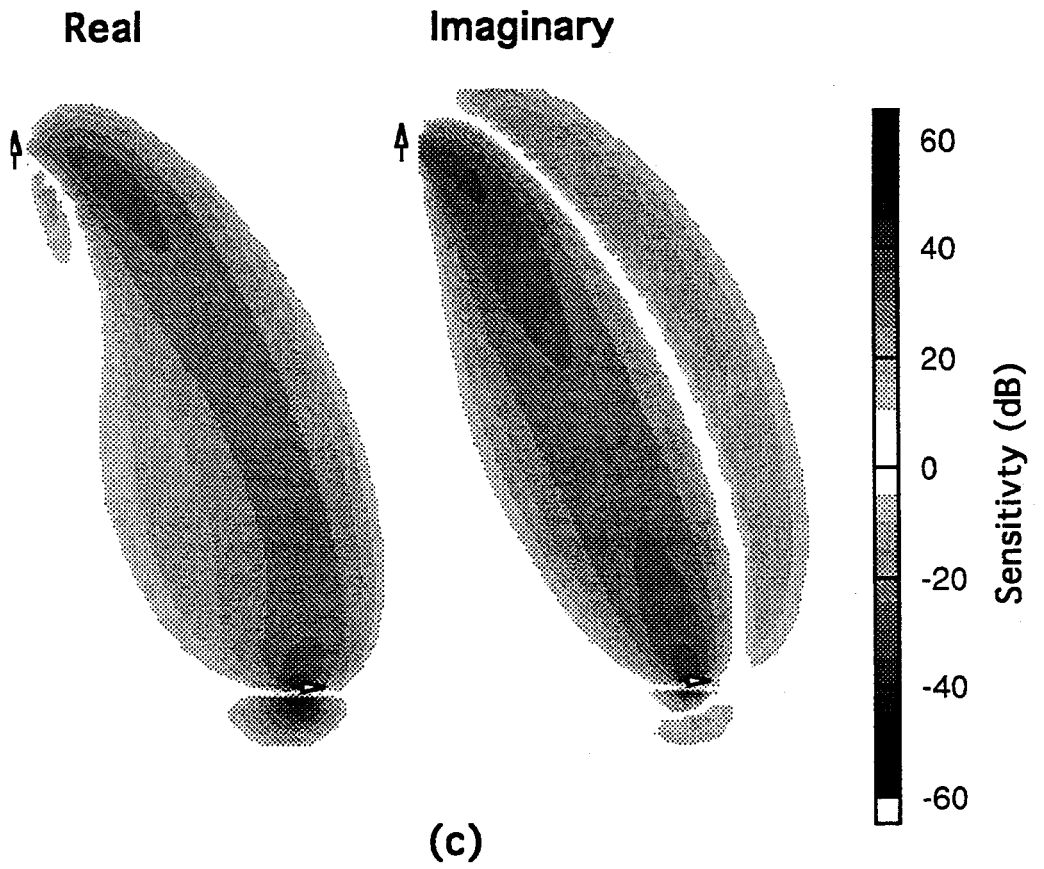

Figure 2.16 - (Continued from preceeding page). (c) Aspect ratio=2:1 , induction number=390.

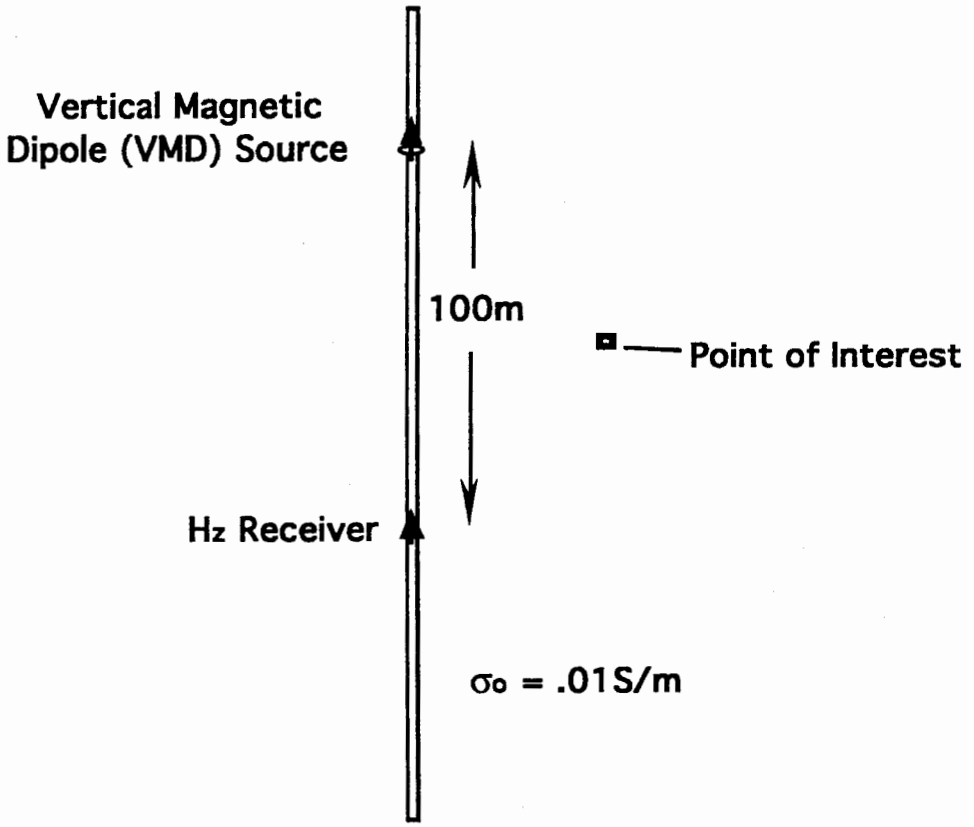

Figure 2.17 - Model used for the the Born kernel in-hole sensitivity analysis. A VMD source is located in 100m above the vertical magnetic receiver in the same borehole. The background conductivity is 0.01S/m.

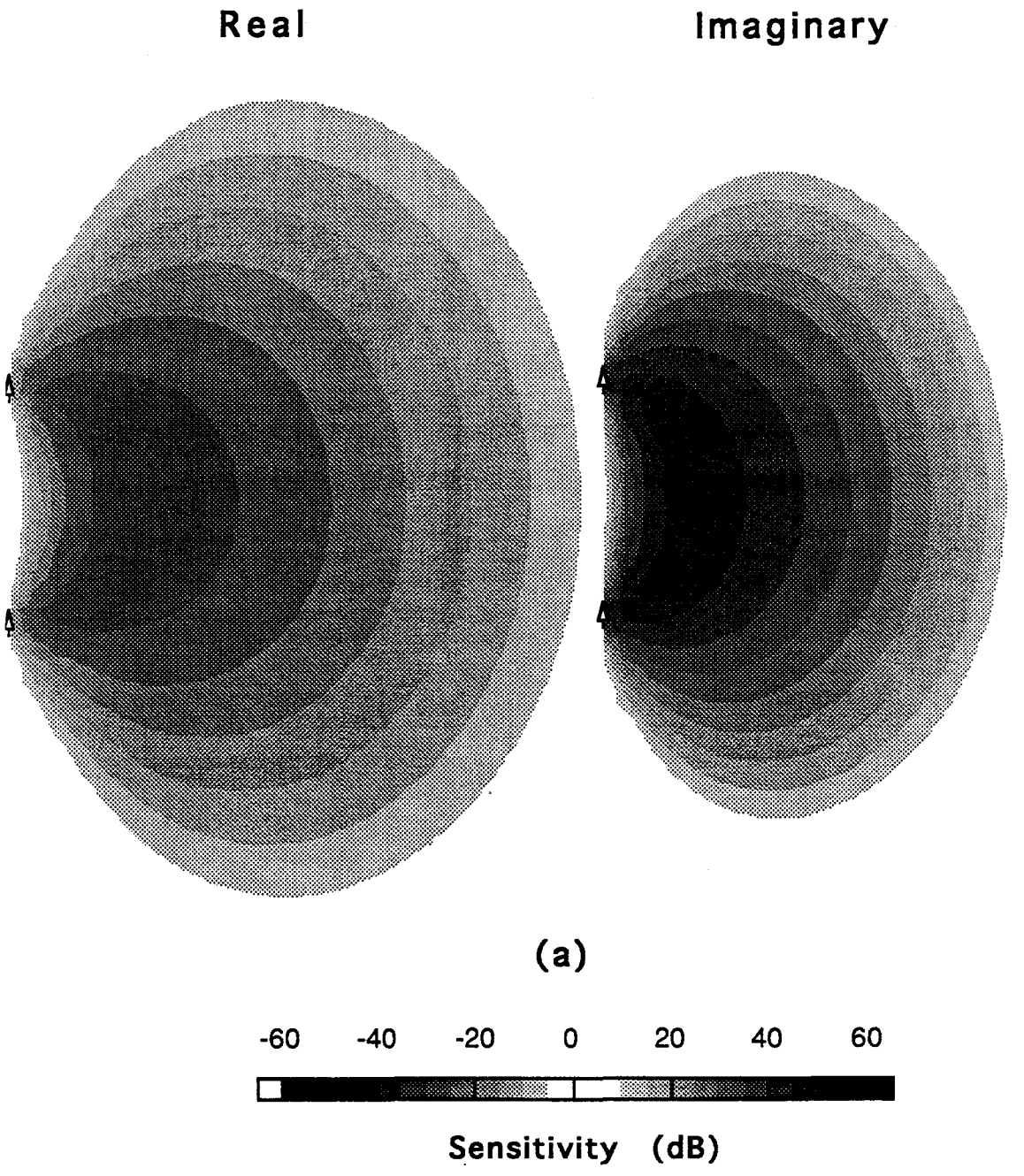

Figure 2.18 - Born kernel sensitivities for the vertical field calculated at 5m intervals for the model shown in Figure 2.17. (a) Frequency 1kHz, induction number = 0.8. (b) See following page. (c) See following page.

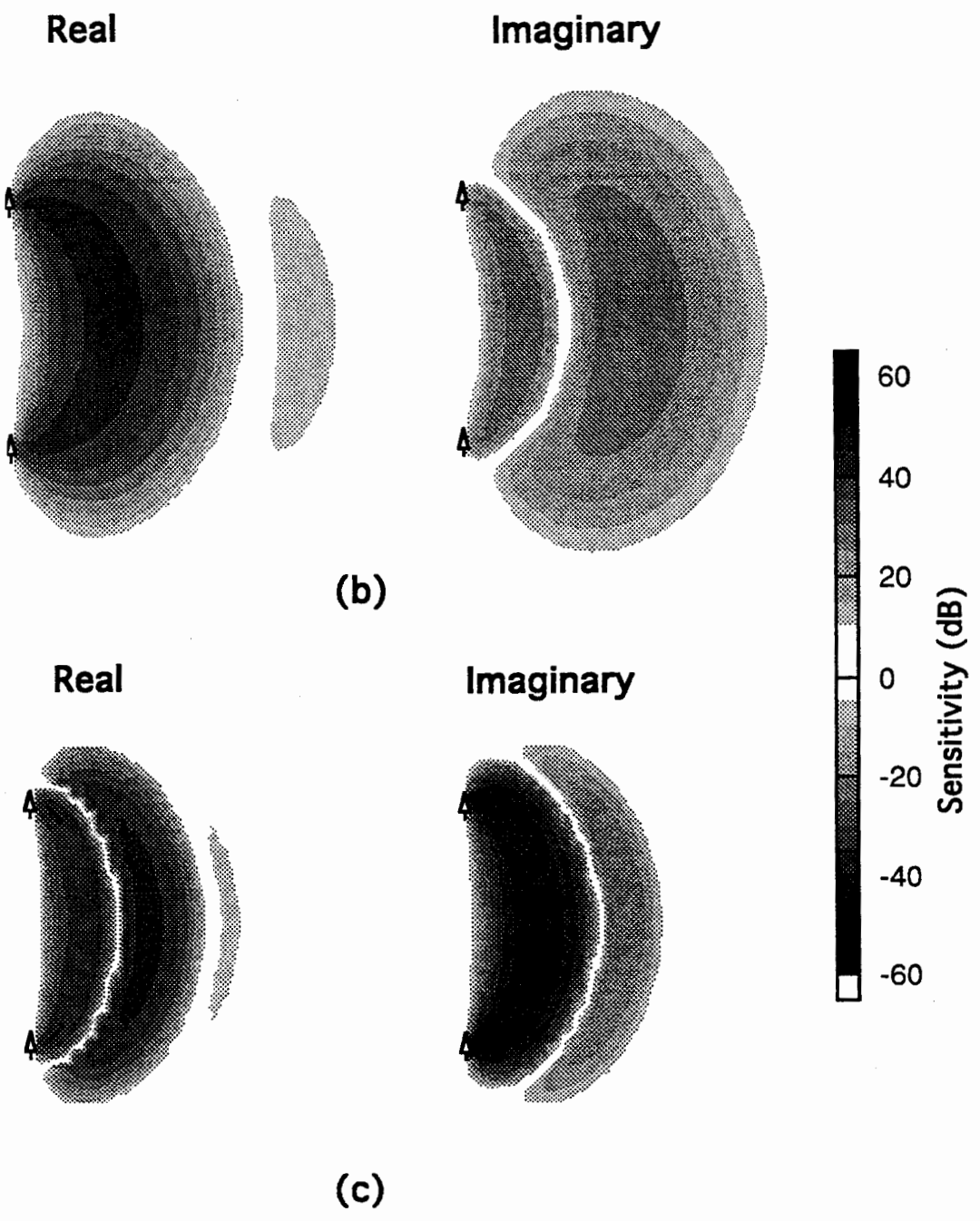

Figure 2.18 - (Continued from preceeding page.) (b) Frequency 10kHz, induction number = 8.0. (c) Frequency 100kHz, induction number =80.

Chapter 3
Forward Modeling with the First-Order Born and Born Series Approximations

As mentioned in Chapter 2, electromagnetic modeling in two dimensions is a fairly simple process. For the cylindrically symmetric medium which is considered here an integral equation solution similar to that developed by Zhou (1989) is employed. However it will be shown that the forward problem involves the integration of Green's functions which involve the Hankel Transform. Because the Hankel transform can be associated with numerical instability under certain geometries, a stable Simpson's integration method will be developed to evaluate these integrals under these conditions.

Even with the added stability of the Green's function calculations, the full integral equation formulation requires the inversion of a N X N full matrix where N is the number of cells in the model. Thus the computer simulation of large, complicated models is a time consuming and memory intensive process which limits the applicability of this method. To speed up this forward modeling process which will eventually be incorporated into the imaging scheme developed in Chapter 4, two approximate schemes will be analyzed.

The first of these is the first order Born approximation that was introduced in the last chapter. The use of this approximation in a numerical forward modeling scheme will be demonstrated and the results compared to those calculated with the full forward modeling scheme. In this comparison, benefits in computational time savings will be contrasted against the limitations in accuracy.

A Born series solution which utilizes higher order terms in the Born series will also be developed. This approximation provides for better accuracy than the first order Born formulation yet again does not require the inversion of a matrix. To ascertain its accuracy, this solution will be tested not only against the full integral equation solution but also against 1-D layered models. Comparisons will also be made against 2 1/2-D and 3-D solutions to determine the usefulness and limitations of the cylindrically symmetric model.

3.1 Mathematical formulation of the two-dimensional forward modeling scheme

Although the integral equation modeling scheme employed in this work was originally developed by Zhou (1989), the formulation is included here for completeness. In the forward problem the object function ($O(\mathbf{r})$) is given and it is the total electric field within the medium ($E_\phi(\mathbf{r},r_\alpha)$ in equation 2.10) that is unknown. In order to generate a set of linear equations appropriate for modeling, the region of interest is first discretized

into N cells. If $E_\phi(\mathbf{r},\mathbf{r}_{tx})$ and $O(\mathbf{r})$ are assumed to be constant across each one of these cells, then a discrete form of equation 2.10 can be written as

$$E_{\phi_j} = E^p_{\phi_j} - \sigma_0 \sum_{i=1}^{N} O_i E_{\phi_i} \int_{i-th\ cell} G(\mathbf{r}_i,\mathbf{r}_j)\,dr_i dz_i \qquad (3.1)$$

where the field point is the *j-th* cell and the integrals are evaluated over the *i-th* cell. Because there are N such equations for N unknowns, expression (3.1) can be written for j =1, 2, 3, . . . , N in a matrix equation format (Hohmann, 1988)

$$\tilde{\mathbf{Z}}\mathbf{E} = \mathbf{E}_p \qquad (3.2)$$

where $\mathbf{E}$ and $\mathbf{E}_p$ are N x 1 element vectors of the unknown total and the known primary fields respectively and the elements of the *impedance matrix* $\tilde{\mathbf{Z}}$ are given by

$$z_{ij} = \delta_{ij} - \sigma_0 O_i \int_{i-th\ cell} G(\mathbf{r}_i,\mathbf{r}_j)\,dr_i dz_i \qquad (3.3)$$

with

$$\delta_{ij} = \begin{cases} 1 \text{ for } i = j \\ 0 \text{ for } i \neq j \end{cases}. \qquad (3.4)$$

After solving for $\mathbf{E}$ in equation 3.2 through inversion of the matrix $\tilde{\mathbf{Z}}$, the secondary magnetic fields can be calculated using the discrete forms of equations 2.15 and 2.16 which are given by

$$H^s_r(\mathbf{r}_{rx},\mathbf{r}_{tx}) = -\sigma_0 \sum_{j=1}^{N} O_j E_{\phi_j} \int_{j-th\ cell} G_{Hr}(\mathbf{r}_{rx},\mathbf{r}_j)\,dr_j dz_j \qquad (3.5)$$

for the radial field and

$$H^s_z(\mathbf{r}_{rx},\mathbf{r}_{tx}) = -\sigma_0 \sum_{j=1}^{N} O_j E_{\phi_j} \int_{j-th\ cell} G_{Hz}(\mathbf{r}_{rx},\mathbf{r}_j)\,dr_j dz_j \qquad (3.6)$$

for the vertical field.

3.1.1 Integration of the Green's functions

Recall from equation 2.12 that the electric field Green's function is given by a first order Hankel transform. Thus for a square cell of side Δ the integration is given by

$$\int_{i-th\ cell} G(\mathbf{r}_i,\mathbf{r}_j)d\mathrm{r}_i dz_i = -\frac{i\omega\mu}{2}\int_0^{\infty}\left[\int_{z_i-\Delta/2}^{z_i+\Delta/2} e^{-\gamma|z_j-z_i|}dz_i\right]\left[\int_{r_i-\Delta/2}^{r_i+\Delta/2}\frac{\mathrm{r}_i\lambda\ J_1(\lambda \mathrm{r}_i)}{\gamma}d\mathrm{r}_i\right]J_1(\lambda \mathrm{r}_j)d\lambda. \qquad (3.7)$$

When $z_i = z_j$ then the expression is singular and special care must be given to the integration. Luke (1962) shows that 3.7 can be integrated through the singularity to yield

$$\int_{i-th\ cell} G(\mathbf{r}_i,\mathbf{r}_j)d\mathrm{r}_i dz_i = -\frac{i\omega\mu\pi}{2}\int_0^{\infty}\left[1-e^{-\gamma\Delta/2}\right]V(\lambda,\mathrm{r}_1,\mathrm{r}_2)\frac{J_1(\lambda \mathrm{r}_j)}{\gamma^2}d\lambda \qquad (3.8)$$

where

$$V(\lambda,\mathrm{r}_1,\mathrm{r}_2) = \mathrm{r}_2\left[\ J_1(\lambda \mathrm{r}_2)\mathbf{H}_0(\lambda \mathrm{r}_2) - \mathbf{H}_1(\lambda \mathrm{r}_2)\ J_0(\lambda \mathrm{r}_2)\right] - \mathrm{r}_1\left[\ J_1(\lambda \mathrm{r}_1)\mathbf{H}_0(\lambda \mathrm{r}_1) - \mathbf{H}_1(\lambda \mathrm{r}_1)\ J_0(\lambda \mathrm{r}_1)\right], \qquad (3.9)$$

$\mathbf{H}_0$ and $\mathbf{H}_1$ are the Struve functions of the first kind of orders 0 and 1 respectively, $J_0(\lambda r_n)$ and $J_1(\lambda r)$ are the zero-th and first order Bessel's functions of the first kinds, respectively, $\mathrm{r}_2 = \mathrm{r}_i + \Delta/2$, and $\mathrm{r}_1 = \mathrm{r}_i - \Delta/2$. For the non-singular cell, the integration results in the expression

$$\int_{i-th\ cell} G(\mathbf{r}_i,\mathbf{r}_j)d\mathrm{r}_i dz_i = -\frac{i\omega\mu\pi}{4}\mathrm{sign}(z_2-z_j)\int_0^{\infty}\left[e^{-\gamma|z_j-z_2|}-e^{-\gamma|z_j-z_1|}\right]V(\lambda,\mathrm{r}_1,\mathrm{r}_2)\frac{J_1(\lambda \mathrm{r}_j)}{\gamma^2}d\lambda \qquad (3.10)$$

where $z_2 = z_i + \Delta/2$, $z_1 = z_i - \Delta/2$, and the other quantities are defined the same as in equation 3.8.

The expressions for the magnetic fields involve similar integration of the Green's functions given in 2.17 and 2.18. For the horizontal magnetic field it has the form

$$\int_{i-th\ cell} G_{Hr}(\mathbf{r}_i,\mathbf{r}_{rx})d\mathrm{r}_i dz_i = \frac{\pi}{2}\int_0^{\infty}\left[1-e^{-\gamma\Delta/2}\right]V(\lambda,\mathrm{r}_1,\mathrm{r}_2)\frac{J_1(\lambda \mathrm{r}_{rx})}{\gamma}d\lambda \qquad (3.11)$$

for the singular cell and

$$\int_{i-th\ cell} G_{Hr}(\mathbf{r}_i,\mathbf{r}_{rx})d\mathrm{r}_i dz_i = \frac{\pi}{4}\mathrm{sign}(z_2-z_{rx})\int_0^{\infty}\left[e^{-\gamma|z_{rx}-z_2|}-e^{-\gamma|z_{rx}-z_1|}\right]V(\lambda,\mathrm{r}_1,\mathrm{r}_2)\frac{J_1(\lambda \mathrm{r}_{rx})}{\gamma}d\lambda \qquad (3.12)$$

for the non-singular cell. For the vertical field the integration results in the expressions

$$\int_{i-th\ cell} G_{Hz}(\mathbf{r}_i,\mathbf{r}_{rx})dr_i dz_i = \frac{\pi}{2}\int_0^{\infty}[1-e^{-\gamma\Delta/2}]V(\lambda,r_1,r_2)\ J_0(\lambda r_{rx})\frac{\lambda}{\gamma^2}d\lambda \qquad (3.13)$$

for the singular cell and

$$\int_{i-th\ cell} G_{Hz}(\mathbf{r}_i,\mathbf{r}_{rx})dr_i dz_i = \frac{\pi}{4}\text{sign}(z_2-z_{rx})\int_0^{\infty}\left[e^{-\gamma|z_{rx}-z_2|}-e^{-\gamma|z_{rx}-z_1|}\right]V(\lambda,r_1,r_2)\ J_0(\lambda r_{rx})\frac{\lambda}{\gamma^2}d\lambda \qquad (3.14)$$

for the non-singular cell.

3.1.2 Numerical instability of the Fast Hankel transform

Inspection of the integrals given in equations 3.9 to 3.14 reveal that they have the form of Hankel transforms of zero and first order. To evaluate these numerically, a lagged convolution routine for fast Hankel transforms developed by Anderson (1982) can be employed in most instances. Unfortunately, Ryu, et al. (1970) showed that when a loop of current and the field point are located in the same horizontal plane, the numerical integration of expressions similar to (2.12) become extremely unstable. To determine if this instability exists when the loop of current is integrated over a cell of area Δ^2, expression 3.8 has been plotted at three different field points, $\mathbf{r}_j$ as a function of current cell location $\mathbf{r}_i$. The current cell dimensions are 5m by 5m, the background conductivity is 0.01S/m, and the operating frequency is 5 kHz. Figure 3.1 shows that although the imaginary component is fairly stable, the real component tends to oscillate when the distance from the source to the current cell is large. Thus the fast Hankel transform can't be used to calculate the Green's function for the singular cell.

3.1.3 Calculation of the Green's function using Simpson integration

Because of the previously mentioned numerical instabilities, Zhou (1989) computes the Green's functions integrals using a Simpson integration method. Magnetic dipoles of unit moment are summed in a plane radially outward from the source to a radius $\mathbf{r}'$. The summation of the electromagnetic fields produced by each individual dipole is the same as the field resulting from a current loop of radius $\mathbf{r}'$ which is symmetric about the source axis. This summation of dipoles is repeated at discreet intervals of $\mathbf{r}'$ across a cross-sectional area to determine the fields resulting from a volume of current flowing in a 'doughnut' shaped cell. Although results calculated with this method have been shown to be accurate with comparisons to scale model data, it is a very time consuming process for all but the simplest models. To improve upon this approach a method has been

developed that employs the 3-D Green's function for an electric dipole which is analytically integrated over a 3-D volume element. These elements are then summed in a circle about the source dipole axis to yield a value for the cylindrical Green's function. The result is just as accurate as that for Zhou's method while the computation is orders of magnitude faster.

In the full 3-D problem, Hohmann (1988) shows that the integral equation formulation for EM problems involves calculating a Green's function which is a tensor rather than a scalar. Matters are further complicated by the fact that each component of this tensor contains both an inductive or vector component which results from current sources, and a scalar component resulting from charge sources. Fortunately it has been determined that because the cylindrical problem exhibits pure TE propagation in which there are only induced current elements, there are no charge sources generated at boundaries and thus the scalar component can be ignored.

The inductive component of the 3-D electric field Green's function at a point $\mathbf{r}_j$ due to a current source at $\mathbf{r}_k$ is given by Hohmann (1975) to be

$$g(\mathbf{r}_k,\mathbf{r}_j) = -i\omega\mu\frac{e^{-ik_o|\mathbf{r}_j-\mathbf{r}_k|}}{4\pi|\mathbf{r}_j-\mathbf{r}_k|}. \qquad (3.15)$$

Becasue the integration of this function over a volume is independent of the volume shape, a cubic cell of side Δ can be replaced with a sphere of volume Δ^3 which makes the integration analytic. When the field point, $\mathbf{r}_j$, is inside the sphere the singularity can be integrated through to obtain

$$\int_{k-th\ cell} g(\mathbf{r}_k,\mathbf{r}_j)dV_k = -\frac{i\omega\mu}{k_o^{\,2}}\left[(ik_oa+1)e^{-ik_oa}-1\right] \qquad (3.16)$$

where a is the radius of the sphere. Similarly when $\mathbf{r}_j$ is outside the sphere,

$$\int_{k-th\ cell} g(\mathbf{r}_k,\mathbf{r}_j)dV_k = -\frac{i\omega\mu e^{-ik_o|\mathbf{r}_j-\mathbf{r}_k|}}{k_o^{\,3}|\mathbf{r}_j-\mathbf{r}_k|}\left[\sin(k_oa)-k_oa\cos(k_oa)\right]. \qquad (3.17)$$

Simpson integration of these 3-D functions to replace a cylindrical cell of current is illustrated in Figure 3.2. The 'doughnut' is divided up into a number of segments of volume Δ^3 and the radius of an equivalent spherical volume is determined. The

contribution of the 'starting cell' in Figure 3.2 is computed first. The summation of cells then proceeds in both a clockwise and counter clockwise direction with the contributions from both $\hat{\mathbf{x}}$ and $\hat{\mathbf{y}}$ components of the secondary currents calculated. This process is continued until the angle ϕ_k is approximately 180° and a volume less than 2-D^3 remains at the point furthest away from the field point. The volume of this 'left over' cell is calculated, the radius of the equivalent volume sphere is determined and its contribution added to the sum. The resulting equation has the form

$$\int_{i-th\ cell} G\ dr_i dz_i = g(\mathbf{r}_i,\mathbf{r}_j)_{Start\ cell} + \sum_{k=1}^{(N-1)/2}\Big[\cos(\phi_k)g(\mathbf{r}_k,\mathbf{r}_j)+\sin(\phi_k)g(\mathbf{r}_k,\mathbf{r}_j) \qquad (3.18)$$
$$+\cos(-\phi_k)g(\mathbf{r}_k,\mathbf{r}_j)+\sin(-\phi_k)g(\mathbf{r}_k,\mathbf{r}_j)\Big] - g(\mathbf{r}_k,\mathbf{r}_j)_{Left\ Over}$$

where $g(\mathbf{r}_i,\mathbf{r}_j)_{Start\ cell}$ is calculated using equation 3.16 if it is singular and 3.17 otherwise, $g(\mathbf{r}_k,\mathbf{r}_j)$ and $g(\mathbf{r}_k,\mathbf{r}_j)_{Left\ Over}$ are calculated using equation 3.17, and N is the total number of whole cells with volume Δ^3 . The magnetic field Green's functions are calculated in the same manner with the expressions having the form

$$\int_{k-th\ cell} g_{Hr}(\mathbf{r}_k,\mathbf{r}_{rx})dV_k = -\frac{z_k e^{-ik_o|\mathbf{r}_{rx}-\mathbf{r}_k|}}{k_o{}^2|\mathbf{r}_{rx}-\mathbf{r}_k|^2}\left[1+\frac{1}{k_o|\mathbf{r}_{rx}-\mathbf{r}_k|}\right]\left[\sin(k_o a)-k_o a\cos(k_o a)\right] \qquad (3.19)$$

for the radial field and

$$\int_{k-th\ cell} g_{Hz}(\mathbf{r}_k,\mathbf{r}_{rx})dV_k = -\frac{x_k e^{-ik_o|\mathbf{r}_{rx}-\mathbf{r}_k|}}{k_o{}^2|\mathbf{r}_{rx}-\mathbf{r}_k|^2}\left[1+\frac{1}{k_o|\mathbf{r}_{rx}-\mathbf{r}_k|}\right]\left[\sin(k_o a)-k_o a\cos(k_o a)\right] \qquad (3.20)$$

for the vertical field.

This method of calculating the cylindrical Green's functions has been verified by comparing it to both the fast Hankel transform as well as Zhou's numerical summation of magnetic dipoles. A comparison of this method to the fast Hankel transform for the singular cell is shown in Figure 3.3. Notice that the 3-D Simpson integration method avoids the erroneous oscillations present in the fast Hankel transform results. For a non-singular cell the difference between the results produced by the two methods is almost negligible. Comparisons of this method to Zhou's method again show almost identical results for both singular and non-singular cells. In fact the only major difference between the different methods of calculating the Green's function for the non-singular cell is the computational time involved. The 3-D Simpson integration is 3 to 5 times quicker than the fast Hankel transform and at least 2 orders of magnitude faster than Zhou's method.

This fact alone allows significantly more difficult models to be calculated and thus for the remainder of this thesis this schema for the remainder of this thesis to calculate the Green's functions.

3.2 Forward modeling with the first order Born approximation

In his thesis, Zhou(1989) compared images of the conductivity distribution resulting from synthetic data that were calculated with the first order Born approximation to images of data generated with the full forward solution. For the low contrast models employed in that work, the two images were almost identical. In this section a forward modeling algorithm will be developed which employs the first order Born approximation as developed in the last chapter and these approximate results compared to those calculated with the full solution. This new work will thoroughly analyze the limits of the Born approximation as a forward modeling scheme and determine the point at which it fails.

The approximate magnetic fields are calculated using the linearized forms of equations 3.5 and 3.6. Once again, this is accomplished by replacing E_{ϕ_j}, which is dependent on O_j, with $E_{\phi_j}^{p}$ which depends only on the background conductivity. The resulting expressions have the form

$$H_r^s(\mathbf{r}_{rx},\mathbf{r}_{tx}) = -\sigma_0 \sum_{j=1}^{N} O_j E_{\phi_j}^{p} \int_{j-th\ cell} G_{Hr}(\mathbf{r}_{rx},\mathbf{r}_j)\,dr_j\,dz_j \qquad (3.21)$$

for the radial secondary field and

$$H_z^s(\mathbf{r}_{rx},\mathbf{r}_{tx}) = -\sigma_0 \sum_{j=1}^{N} O_j E_{\phi_j}^{p} \int_{j-th\ cell} G_{Hz}(\mathbf{r}_{rx},\mathbf{r}_j)\,dr_j\,dz_j \qquad (3.22)$$

for the vertical field where $E_{\phi_j}^{p}$ is calculated at the center of the j 'th cell using equation 2.7.

As mentioned in Chapter 2 the first order Born approximation is only valid when *weak* scattering occurs within the medium. Habashy, et al. (1992) show that the definition of *weak* is not only dependent on the conductivity contrast between the body and the background medium, but also the size of the scattering body and the operating frequency. Under these conditions it was also shown by Zhou (1989) that the error is on the order of the perturbation in the background wave number times the distance the wave travels in the anomalous material. Thus the usefulness in the Born approximation is dependent on the anomalous induction number, $\Delta\sigma\omega\mu S = 2O\,S/\delta^2$ where S is the cross-

sectional area of the inhomogeneities that are present in the medium and δ is the skin depth of the background medium.

To illustrate this concept the models shown in Figure 3.4 are employed. Four different bodies of square cross sectional area are located at different positions between two wells. The secondary vertical magnetic fields have been calculated using the full integral equation solution given in equations 3.1 through 3.6 and compared to the approximate Born solution given in expression 3.22. The mean phase and amplitude errors of the approximate fields and the standard deviation of these errors are listed in Table 3.1 as a function of the model and its anomalous induction number ($\Delta\sigma\omega\mu S$). The horizontal components of the scattered fields were also computed and the errors between the first order Born and full solutions determined. However because these errors were found to be of the same magnitude and to exhibit the same characteristics as the vertical field errors, they have not been included here.

The validity of the Born approximation in these results is clearly related to the magnitude of the scattering body's induction number. For a mean error of less than one percent, the induction number of the object must be less than approximately 0.02. It is also evident from the relatively small values of standard deviation that the magnitude of the error is fairly independent of the source and receiver position.

By multiplying the x axis of the Born kernel plots given in Figures 2.3 through 2.5 by the object function O(r) the kernel can be plotted as a function of anomalous body induction number rather than the background induction number. The kernel function that results from using the parameters of model 2 in Figure 3.4 is shown in Figure 3.5. Comparing this plot to the results in Table 3.4 indicates that the point at which the error reaches 1% occurs just below the peak of the kernel. Below this value the mean error decreases linearly with the kernel as the induction number is decreased, while above it the error increases with the induction number in a nonlinear manner. Thus it can be assumed that this is the point at which mutual interaction of the scattering currents must start being accounted for.

Though the error is dependent primarily on the size of $\Delta\sigma$, there is some reliance on the magnitude of the contrast between the body and the background (σ_a/σ_o), or in other words in terms of the object function $\Delta\sigma/\sigma_0$. To demonstrate this Model 2 in Figure 3.4 has again been employed with different background conductivities and object functions. Table 3.2 shows that although the errors for constant induction numbers are within the same order of magnitude, they are definitely larger when the contrast is greater. This coupled with the fact that the error is dependent on the position of the body with respect to the source well indicates that the value of $\Delta\sigma\omega\mu S$=0.02 should be used only as an

approximate rule of thumb when determining at which point the Born approximation becomes invalid.

Model	Freq (Hz)	$\Delta\sigma$ (S/m)	$\Delta\sigma\omega\mu S$	% Amplitude Error		Degrees Phase Error	
				Mean	Stand. Dev.	Mean	Stand. Dev.
1	$1x10^{2}$	0.01	$1.97x10^{-4}$	$3.2x10^{-3}$	$1.3x10^{-4}$	$-1.8x10^{-3}$	$7.4x10^{-5}$
1	$1x10^{3}$	0.01	$1.97x10^{-3}$	$3.1x10^{-2}$	$1.3x10^{-3}$	$-1.7x10^{-2}$	$7.4x10^{-4}$
1	$1x10^{4}$	0.01	$1.97x10^{-2}$	$3.2x10^{-1}$	$1.3x10^{-2}$	$-1.8x10^{-1}$	$7.4x10^{-3}$
1	$1x10^{5}$	0.01	$1.97x10^{-1}$	3.0	$1.3x10^{-1}$	-1.7	$7.4x10^{-2}$
1	$5x10^{5}$	0.01	$9.86x10^{-1}$	12.0	$6.4x10^{-1}$	-7.0	$4.1x10^{-1}$
2	$1x10^{2}$	0.01	$1.97x10^{-4}$	$1.0x10^{-2}$	$2.8x10^{-5}$	$-6.0x10^{-3}$	$1.6x10^{-5}$
2	$1x10^{3}$	0.01	$1.97x10^{-3}$	$9.9x10^{-2}$	$1.7x10^{-4}$	$-5.7x10^{-2}$	$9.7x10^{-5}$
2	$1x10^{4}$	0.01	$1.97x10^{-2}$	$9.0x10^{-1}$	$1.3x10^{-3}$	$-5.0x10^{-1}$	$7.9x10^{-4}$
2	$1x10^{5}$	0.01	$1.97x10^{-1}$	5.8	$1.6x10^{-2}$	-3.1	$1.5x10^{-2}$
2	$5x10^{5}$	0.01	$9.86x10^{-1}$	17.0	$1.3x10^{-1}$	-8.4	$1.8x10^{-1}$
2	$2x10^{3}$	0.05	$1.97x10^{-2}$	$9.9x10^{-1}$	$1.5x10^{-3}$	$-5.6x10^{-1}$	$8.5x10^{-4}$
3	$1x10^{2}$	0.01	$1.97x10^{-4}$	$1.2x10^{-2}$	$2.1x10^{-4}$	$-7.1x10^{-3}$	$1.2x10^{-4}$
3	$1x10^{3}$	0.01	$1.97x10^{-3}$	$1.2x10^{-1}$	$7.4x10^{-4}$	$-6.8x10^{-2}$	$4.1x10^{-4}$
3	$1x10^{4}$	0.01	$1.97x10^{-2}$	$9.3x10^{-1}$	$6.1x10^{-3}$	$-5.2x10^{-1}$	$3.6x10^{-3}$
3	$1x10^{5}$	0.01	$1.97x10^{-1}$	5.7	$9.1x10^{-2}$	$-3.0x10^{-1}$	$6.0x10^{-2}$
4	$2.5x10^{3}$	0.01	$1.97x10^{-2}$	$7.7x10^{-1}$	$4.3x10^{-3}$	$-4.4x10^{-1}$	$2.5x10^{-3}$
4	$2.5x10^{4}$	0.01	$1.97x10^{-1}$	5.8	$3.7x10^{-2}$	-3.2	$2.7x10^{-2}$
4	$2.5x10^{3}$	0.10	$1.97x10^{-1}$	7.7	$4.4x10^{-2}$	-4.4	$2.4x10^{-2}$

Table 3.1 - Error of first order Born approximation for the different models shown in Figure 3.4. 'Mean' refers to the calculated mean error for all source -receiver combinations and 'Stand. Dev. ' the standard deviation of the errors about the mean.

Freq (Hz)	σ_0 (S/m)	$\Delta\sigma$ (S/m)	$\Delta\sigma/\sigma_0$	$\Delta\sigma\omega\mu S$	% Amplitude Error		Degrees Phase Error	
					Mean	Stand. Dev.	Mean	Stand. Dev.
$1x10^{4}$	$1x10^{-3}$	0.01	10	$1.97x10^{-2}$	0.99	$1.7x10^{-3}$	-0.57	$9.7x10^{-4}$
$1x10^{5}$	$1x10^{-3}$	0.01	10	0.197	9.11	$1.3x10^{-2}$	-5.1	$7.9x10^{-3}$
$1x10^{4}$	$1x10^{-2}$	0.01	1.0	$1.97x10^{-2}$	0.90	$6.1x10^{-3}$	-0.50	$3.6x10^{-3}$
$1x10^{5}$	$1x10^{-2}$	0.01	1.0	0.197	5.8	$9.1x10^{-2}$	-3.1	$6.0x10^{-2}$
$1x10^{4}$	$1x10^{-1}$	0.1	1.0	0.197	5.9	$1.6x10^{-2}$	-3.1	$1.5x10^{-2}$
$1x10^{5}$	$1x10^{-1}$	0.01	0.1	0.197	2.89	$3.8x10^{-2}$	-1.34	$5.1x10^{-2}$

Table 3.2 - Error of first order Born approximation for different background conductivities and conductivity contrasts. The model employed is Model 2 in Figure 3.4. 'Mean' refers to the calculated mean error for all source -receiver combinations and 'Stand. Dev. ' the standard deviation of the errors about the mean.

To illustrate that these results hold for resistive bodies as well as conductors, i.e. bodies in which the conductivity is less than that of the background, Model 2 in Figure 3.4 has again been employed with the values listed Table 3.3. Comparing this to Tables 3.1 and 3.2 it is evident that the mean error is almost identical for conductive and restive bodies as long as the magnitudes of $\Delta\sigma$ and σ_0 are the same. However there is a definite difference in the response of equations 3.21 and 3.22 for conductors and resistors. As the anomalous body becomes more conductive relative to the background, $\Delta\sigma/\sigma_0$ goes to infinity and thus the Born approximation will at some point break down. However as the conductivity goes to zero, i.e. a perfect resistor, $\Delta\sigma/\sigma_0$ goes to -1 which doesn't necessarily cause the approximate solution to fail. This implies that the first order Born approximation will work better for calculating the response of resistors than for conductors. This also demonstrates why inductive methods are insensitive to resistive bodies which is a point that will be discussed more fully in the next chapter

					% Amplitude Error		Degrees Phase Error	
Freq (Hz)	σ_0 (S/m)	$\Delta\sigma$ (S/m)	$\Delta\sigma/\sigma_0$	$\Delta\sigma\omega\mu S$	Mean	Stand. Dev.	Mean	Stand. Dev.
$1x10^4$	1.0	-0.99	-0.99	-0.195	6.12	$1.6x10^{-2}$	3.25	$1.5x10^{-2}$
$1x10^4$	$1x10^{-2}$	-.0099	-0.99	$-1.95x10^{-2}$	0.91	$1.3x10^{-3}$	0.514	$7.8x10^{-4}$
$1x10^5$	$1x10^{-2}$	-.0099	-0.99	-0.195	5.98	$1.6x10^{-2}$	3.25	$1.5x10^{-2}$
$1x10^4$	$1x10^{-1}$	-.01	-0.1	$-1.97x10^{-2}$	0.59	$1.6x10^{-3}$	0.32	$1.5x10^{-3}$
$1x10^5$	$1x10^{-1}$	-0.01	-0.1	-0.197	2.97	$3.7x10^{-2}$	1.38	$3.3x10^{-3}$

Table 3.3 - Error of first order Born approximation for a resistive body of different conductivity in a background of various conductivities. The model employed is Model 2 in Figure 3.4. 'Mean' refers to the calculated mean error for all source -receiver combinations and 'Stand. Dev. ' the standard deviation of the errors about the mean.

3.3 The Born series approximation

Equations 3.1 through 3.4 demonstrate how a linear system of equations can be set up to solve for the internal electric fields (E_ϕ)within a scattering body. An alternative approach is to assume that E_ϕ can be expanded in a Born, or Neumann series of the form (Kong,1975)

$$E_\phi = \sum_{n=0}^{\infty} E_\phi^{(n)} . \qquad (3.23)$$

If this holds true than the electric field can be solved for iteratively. The schema for doing this is developed here.

The first term in the Born series is given by the first order Born approximation, i.e.,

$$E^{(1)}_{\phi_j} = E^{p}_{\phi_j} - \sigma_0 \sum_{i=1}^{I} O_i E^{p}_{\phi_i} \int_{i-th\ cell} G(\mathbf{r}_i, \mathbf{r}_j) d\mathbf{r}_i dz_i , \tag{3.24}$$

the second term by

$$E^{(2)}_{\phi_j} = E^{p}_{\phi_j} - \sigma_0 \sum_{i=1}^{I} O_i E^{(1)}_{\phi_i} \int_{i-th\ cell} G(\mathbf{r}_i, \mathbf{r}_j) d\mathbf{r}_i dz_i , \tag{3.25}$$

and so on with the N'th term having the form

$$E^{(N)}_{\phi_j} = E^{p}_{\phi_j} - \sigma_0 \sum_{i=1}^{I} O_i E^{(N-1)}_{\phi_i} \int_{i-th\ cell} G(\mathbf{r}_i, \mathbf{r}_j) d\mathbf{r}_i dz_i . \tag{3.26}$$

The process is repeated until convergence occurs at which time $E^{(n)}_{\phi_j}$ is substituted in equations 3.5 and 3.6 to calculate the magnetic fields at the receiver. The advantage of this method over the full forward solution is that no matrix inversion is required and thus very large models can be computed more efficiently. This advantage as well as the disadvantages of the method are discussed more fully below.

3.3.1 Theoretical limitations of the Born series approach

Although the Born series approach provides a more accurate alternative to the first order Born approximation, it will not work if the series expansion of the internal electric field does not converge. To determine if and under what conditions it diverges let's consider a body consisting of a single cell. In this case, N=1 for the summations given in equations 3.24 through 3.26. The first order term of the scattered field is given by

$$E^{s\,(1)}_{\phi_c} = -\sigma_0 O_c E^{p}_{\phi_c} \int_{c} G(\mathbf{r}_i, \mathbf{r}_j) d\mathbf{r}_c dz_c \tag{3.27}$$

where the c represents the position and dimensions of the single cell. The second order term is obtained by substituting this in 3.25:

$$E^{s\,(2)}_{\phi_c} = -\sigma_0 O_c \left[E^{p}_{\phi_c} + E^{s\,(1)}_{\phi_c} \right] \iint_{c} G(\mathbf{r}_i, \mathbf{r}_j) d\mathbf{r}_c dz_c = \tag{3.28}$$

$$-\sigma_0 O_c \left[E^{p}_{\phi_c} + -\sigma_0 O_c E^{p}_{\phi_c} \int_{c} G(\mathbf{r}_i, \mathbf{r}_j) d\mathbf{r}_c dz_c \right] \iint_{c} G(\mathbf{r}_i, \mathbf{r}_j) d\mathbf{r}_c dz_c .$$

Similarly the third order term is found to be

$$E_{\phi_c}^{s\,(3)} = -\sigma_0 O_c\left[E_{\phi_c}^{p} + E_{\phi_c}^{s\,(2)}\right]\iint_c G(\mathbf{r}_i,\mathbf{r}_j)dr_c dz_c = \tag{3.29}$$

$$= -\sigma_0 O_c E_{\phi_c}^{p}\left[1 - \sigma_0 O_c\int_c G(\mathbf{r}_i,\mathbf{r}_j)dr_c dz_c + \left(-\sigma_0 O_c\int_c G(\mathbf{r}_i,\mathbf{r}_j)dr_c dz_c\right)^2\right]\int_c G(\mathbf{r}_i,\mathbf{r}_j)dr_c dz_c$$

and so on. The function within the square brackets on the right hand side of equation 3.29 is now recognizable as a geometric series. Thus the N'th term in the series can be written as

$$E_{\phi_c}^{s\,(N)} = -\sigma_0 O_c\left[E_{\phi_c}^{p} + E_{\phi_c}^{s\,(N-1)}\right]\iint_c G(\mathbf{r}_i,\mathbf{r}_j)dr_c dz_c = \tag{3.30}$$

$$-\sigma_0 O_c E_{\phi_c}^{p}\int_c G(\mathbf{r}_i,\mathbf{r}_j)dr_c dz_c \sum_{n=0}^{N-1}\left(-\sigma_0 O_c\int_c G(\mathbf{r}_i,\mathbf{r}_j)dr_c dz_c\right)^n .$$

If N=∞, the infinite series will converge to

$$\frac{1}{1+\Delta\sigma_c\int_c G(\mathbf{r}_i,\mathbf{r}_j)dr_c dz_c} \tag{3.31}$$

if and only if (Swokowski,1979)

$$\left|-\Delta\sigma_c\int_c G(\mathbf{r}_i,\mathbf{r}_j)dr_c dz_c\right| < 1. \tag{3.32}$$

(Note: This the equivalent 2-D form of the 3-D non-linear operator developed by Habashy et al. (1993).) Thus if this value is greater than or equal to 1 then the series diverges and the Born series approximation can not be used to calculate the electromagnetic fields in the medium. In addition, because the integral of the Green's function given in equations 3.8 and 3.10 has an $\omega\mu$ term out front and the integration is over some area S, the limitations of this approximation are once again primarily dependent on the anomalous induction parameter ($\Delta\sigma\omega\mu S = 2O\,S/\delta^2$) of the body. Thus expression 3.32 gives us a method to determine when the series expansion is valid.

3.3.2 Comparison of the Born series method to the full integral equation solution

To demonstrate the use and limitations of the Born series approach the model shown in Figure 3.6 which consists of a body of tabular cross section centrally located between two wells is employed. (Notice that the model employed here is larger than those used to test the validity of the first order Born approximation in Section 3.2. As it will be demonstrated, this is due to the fact that the Born series is a more accurate approximation and thus can handle models with much larger anomalous induction numbers than can the first order Born approximation.) The operating frequency and the dimensions of the body have been fixed and the conductivity varied to yield five different anomalous induction numbers. The first model is a fairly low contrast model , while model 5 represents a case in which the Born series solution fails. Once again, because the mean amplitude and phase errors in the vertical and horizontal scattered magnetic fields exhibited the same characteristics, only results for the vertical component are presented here.

The mean error between the series and full solutions at each iteration are displayed for each of the five models in Figure 3.7. In addition to the magnetic field errors, the change in the internal electric fields between iterations has been plotted. The iterative process was terminated in each case when the amplitude of these electric fields changed less than 0.5% from one iteration to the next. The standard deviation of the error about the mean was also calculated but like for the first order Born approximation, it was 2 to 3 orders of magnitude below the mean. Thus in order to make the following figures easier to understand the standard deviations have not been included.

The results in Figure 3.7 show that for induction numbers less than or equal to one, the Born series scheme works extremely well. Initial tests with these small models have shown that when the Born series converges very quickly (under 5 iterations) this solution is at least three times faster than the full solution. This is due to the fact that the matrix inversion in the full solution requires $1/3N^3$ to N^3 calculations where N is the number of unknowns (Press, et al, 1986). However the Born series solution involves only IN^2 operations where I is the number of iterations. Thus when I is small, the Born series solution is much faster. This will be very important for the conductivity imaging process described in the next chapter.

It is evident from the slower series convergence of models 3 and 4 that the Born series solution is beginning to fail. Model 4 represents approximately the largest induction number (2.4) for which the Born series converges. Comparing this to the results listed in Tables 3.1 through 3.3 indicates that the this approximate solution is able to accurately calculate the electromagnetic fields for anomalous induction numbers two orders of magnitude greater than that of the first order Born approximation.

The Born series does not converge for model 5. Assuming that the body in Figure 3.6 can be thought of as a single cell allows us to estimate $\left|-\Delta\sigma_c \int_c G(\mathbf{r}_i,\mathbf{r}_j)dr_c dz_c\right|$ yielding a value of 1.33. Because this is larger than 1.0 , as determined by expression 3.32 the Born series fails to converge.

The above calculation verifies the mathematical cause for the divergence. To determine the physical significance of this, the electric fields have been calculated on a profile across the block shown in Figure 3.8 with the full integral equation solution . Figure 3.9 shows the total and scattered field amplitudes and the phase difference between the primary and total fields as a function of cell location. As the conductivity of the block is increased, the scattered field also increases while the total electric field becomes smaller. Comparing the results for models 4 and 5 indicates that the series diverges when the scattered electric field in the block becomes larger than the total field. Expression 3.30 can not converge when this happens because during the n'th iteration a value is present in the right hand side that is larger than for the n-1'th iteration and thus the magnitude of the left-hand side grows larger with each iteration. Incidentally this coincides with the point at which the phase difference between the primary and secondary fields well exceeds 45 degrees.

As it was determined in Section 3.3.1, the magnitude of the Green's function in expression 3.31 is primarily a function of the size of the object as well as the operating frequency and therefore the convergence of the series is strongly dependent on the anomalous induction number of the body. To demonstrate this the size and conductivity of the block is held constant and the frequency varied to produce the error analysis shown Figure 3.10. Next the size of the block was varied while the frequency-conductivity product was held constant (Figure 3.11) and these results are shown in Figure 3.12. As predicted both these Figures show that as the induction number of the body becomes larger than 1, the Born series begins to diverge.

The rate at which series converges is also dependent on the position of the body, especially for induction numbers greater than 1. This is illustrated with the models shown in Figure 3.13. A block with $\Delta\sigma\omega\mu S$=1.6 is placed in three different positions and the errors between the full and Born seriessolutions calculated at each iteration. Figure 3.14 shows that as the body gets closer to the receiver well, the solution takes longer to converge. This agrees well with the sensitivity diagrams in the last chapter which showed that the most sensitive region is directly adjacent to the receiver borehole.

Although from equation 3.32 it is apparent that it is primarily the difference ($\Delta\sigma_c$) rather than the ratio (σ_{ac}/σ_0) between the anomalous and background conductivities that

dominates the behavior of the Born series, the magnitude of the conductivity ratio does have some influence on the convergence. To illustrate this the model shown in Figure 3.6 has again been employed. With $\Delta\sigma$ held constant at 0.99 S/m, background conductivities of 1.0, 0.1, 0.01 and 0.001 S/m have been employed which varies σ_a accordingly. The results in Figure 3.15 show that as the background conductivity is decreased and thus the contrast increased, the series takes longer to converge. (Notice that only the internal electric fields have been plotted here. This is because if the magnetic field errors are included, the illustrations become very congested and difficult to comprehend.) The reason for this becomes evident when the singular cell Green's function is calculated for the same background conductivities and operating frequency as given in the model. It is evident figure 3.16 that as the background conductivity increases and thus the ratio decreases, the amplitude of this integrated function also decreases and thus expression 3.32 becomes easier to satisfy.

Finally to prove that the series converges in approximately the same manner for bodies that are less conductive than the background, i.e. resistive bodies, as it does for conductive bodies, the model shown in Figure 3.17 has been employed. The target in the first example has a conductivity of 0.01S/m and is embedded in a background of 1.0S/m, while the second employs a target of conductivity 0.1S/m embedded in a 10.0S/m background. The results shown in 3.18 are very similar to those given in Figures 3.7, 3.10 and 3.12 with the convergence of the series being dependent on the magnitude of $\Delta\sigma$.

3.4 Comparison of the 2-D cylindrically symmetric model to other models

Though the two dimensional, cylindrically symmetric model is computationally efficient and useful in describing some situations, useful geological models often require either more complicated 2 1/2-D and/or 3-D geometries or sometimes simpler 1-D layered geometries. In Chapter 2 a spatial sensitivity analysis showed that cross well electromagnetic measurements are very sensitive to the geometry and to the length extent of an anomalous body in the direction perpendicular to the plane containing the wells. However, it was also determined that the sensitivity to this region is decreased as the background induction number is increased. To tie these ideas in with those developed in this chapter, the Born series solution developed for a 2-D cylindrically symmetric medium will be compared to 1-D, 2 1/2-D, and 3-D models.

3.4.1 Comparison to 1-D horizontally layered models

In theory, the cylindrically symmetric integral equation solution can be used to compute the response of horizontal layers by extending the radius of the slab (r) to infinity. However due to numerical errors and limits on computer memory there are limitations of how large and complex the model can be. In addition, because the Born series approximation can only can be used to model bodies of finite induction number, at some point with increasing slab radius, frequency, conductivity and/or layer thickness the series will become divergent.

To both demonstrate the limitations of the Born seriessolution as well as illustrate certain properties that were revealed in the sensitivity analysis of Chapter 2, the model shown in Figure 3.19 is employed. A 20m thick layer of conductivity σ_a is located in a whole space of conductivity σ_0. Two 120m deep wells are separated by 100m and both penetrate the layer. The vertical magnetic field calculations for the layered model were made, for source and receiver intervals of 10m, with a 1-D solution written by Lee (1988) which is based on a method originally published by Stoyer (1977). To simulate the layer with the cylindrically symmetric model, a 20m thick slab was extended out to a radius of L. Different frequencies, conductivities and slab radii (L) have been employed and the errors between the two solutions computed. The results of this analysis are listed in Table 3.4 for a conductive layer, and Table 3.5 for a resistive layer.

Several things are evident from these results. As expected, the Born series converges as long as the induction number of the radial slab is small. At higher frequencies and large contrasts, more iterations are needed. Raising the frequency and thus the background induction number while keeping L constant causes the mean amplitude and phase errors in the scattered field to decrease. This phenomenon was discussed in Chapter 2 and is caused by a decrease in sensitivity of the array to the region outside of the well with increasing induction number. In fact the mean error at 100 kHz is less than 10% in amplitude and 5° in phase without extending the layer beyond the receiver well at all.

The 1% amplitude error at lower frequencies indicates that the cylindrically symmetric solution is accurate and can be used to calculate the EM response of layered media. Unfortunately, these results also demonstrate that the cylindrical slabs equivalent to the layers inherently have large anomalous induction numbers ($\Delta\sigma\omega\mu S$). In addition, the inability of the amplitude error to converge to less than 3% at 100 kHz indicates the integral equation solution might be exhibiting some numerical instabilities which will be discussed in more detail below. Both conclusions suggest that in order to more accurately and effectively determine the effects of smaller inhomogeneities, the layer response

should somehow be removed from the model . A method for doing this which employs a layered background model will be developed in the next chapter.

Freq (Hz)	σ_a (S/m)	Cell Dim(m)	L (m)	N	% Amplitude Error		Degrees Phase Error	
					Mean	Stand. Dev.	Mean	Stand. Dev.
$2x10^3$	0.02	10X10	100	2	95	28	48	16
$2x10^3$	0.02	10X10	200	3	6.7	2.3	2.6	1.6
$2x10^3$	0.02	10X10	300	3	1.2	0.61	0.018	0.27
$2x10^3$	0.02	10X10	400	3	1.1	0.86	0.45	0.33
$2x10^3$	0.10	10X10	100	6	73	24	35	14.6
$2x10^3$	0.10	10X10	200	18	2.7	1.3	1.3	0.87
$2x10^3$	0.10	10X10	300	54	1.0	0.80	0.33	0.34
$1x10^4$	0.02	10X10	100	3	32.	15	15.	6.4
$1x10^4$	0.02	10X10	200	4	1.4	0.66	0.20	0.09
$1x10^4$	0.02	10X10	300	5	1.3	0.72	0.21	0.12
$1x10^5$	0.02	5X5	100	12	7.0	6.5	3.1	3.0
$1x10^5$	0.02	5X5	200	20	3.3	4.0	1.1	1.9

Table 3.4 - Error between the Born series approximation and the 1-D solution for a conductive layer. The model employed is given in Figure 3.19 with a background conductivity of 0.01s/m. 'N' is the number of iterations the series takes to converge, 'Mean' refers to the calculated mean error for all source -receiver combinations and 'Stand. Dev. ' the standard deviation of the errors about the mean.

Freq (Hz)	σ_a (S/m)	Cell Dim(m)	L (m)	N	% Amplitude Error		Degrees Phase Error	
					Mean	Stand. Dev.	Mean	Stand. Dev.
$2x10^3$	0.01	5X5	100	4	22	12	6.5	4.3
$2x10^3$	0.01	5X5	200	6	0.38	0.16	0.16	0.06
$1x10^4$	0.01	5X5	100	9	6.5	5.5	5.3	1.51
$1x10^4$	0.01	5X5	200	17	1.3	0.32	1.15	0.31

Table 3.5 - Error between the Born series approximation and the 1-D solution for a resistive layer. The model employed is given in Figure 3.19 with a background conductivity of 0.01s/m. 'N' is the number of iterations the series takes to converge, 'Mean' refers to the calculated mean error for all source -receiver combinations and 'Stand. Dev. ' the standard deviation of the errors about the mean.

As the standard deviations in Tables 3.4 and 3.5 indicate, the error is not consistent for any source - receiver combination but rather varies depending on their position. In the previous sections when the first order and Born series approximate solutions were compared to the full integral solution this was not the case. In those comparisons the models that were employed exhibited the same 2-D cylindrically symmetric geometry, they were discretized in the same manner and were calculated using the approximately the same theory. Because of this, the standard deviation of the errors about the mean were 2 to 3 orders smaller than the mean error itself. Here a 1-D modeling scheme that employs impedance matching at boundaries (Stoyer, 1977) is being compared to a 2-D integral equation solution and thus the errors exhibit a wider distribution.

To illustrate how the error is distributed for the first and fourth models listed in Table 3.4, the error between the full integral equation solution and the Born series approximation is shown in gray scale format as a function of source position on the x axis and receiver position on the y axis. The first model represents a poor fit and the resulting errors are shown in Figure 3.20. Notice that the maximum error occurs when the source is far away from the layer. This can be contrasted to a better fitting model in which the calculated mean error between the two solutions was 1%. Figure 3.21 shows that the maximum errors occur when both the source and receiver are within the layer. The same type of error distribution exists at other frequencies, and for different layer conductivities which suggests that the integral equation solution exhibits numerical problems when the both the source and receiver are located within the layer. These could be caused by discretization which is too coarse near the source and receiver. On the other hand, the 1-D solution is designed to calculate the total fields in the medium. Recalculating the mean error of the total vertical magnetic field for the best fitting conductive layer models as shown in Table 3.6 demonstrates that the results actually fit to under 1% amplitude and 0.5° phase. Thus it is unclear which method is numerically more stable, and in fact there may be inconstancies present in both computational methods which are causing the errors between the two solutions.

Freq (Hz)	σ_a (S/m)	Cell Dim(m)	L (m)	N	Scattered Field Error		Total Field Error	
					Amp (%)	Phase (Deg)	Amp (%)	Phase (Deg)
$2x10^3$	0.02	10X10	400	3	1.1	0.45	0.062	0.029
$2x10^3$	0.10	10X10	300	54	1.0	0.33	0.55	0.26
$1x10^4$	0.02	10X10	300	5	1.3	0.21	0.25	0.11
$1x10^5$	0.02	5X5	200	20	3.0	1.1	0.80	0.24

Table 3.6 - Scattered and total field error between the Born series approximation and the 1-D solution . The model employed is given in Figure 3.19 with a background conductivity of 0.01s/m. 'N' is the number of iterations the series takes to converge and the amplitude and phase errors are the mean error..

3.4.2 Comparison to 3-D sheet models

In general the earth is not cylindrically symmetric about the source dipole axis but rather exhibits a three dimensional geometry. An excellent description of 3-D modeling techniques can be found in Hohmann (1988). Unfortunately up until a few years ago these modeling programs required a super computer to calculate the response for all but the simplest models. However due to recent advances in computing power, many of these programs can now be run on desktop computers. We have found the integral equation solution developed by Newman and Hohman (1988) to be very useful, though it is time consuming for larger models and high frequencies. Druskin (1992) has developed a super fast finite difference scheme which unfortunately is not readily available. Because of the computational time required by the former and the lack of availability of the latter, a thin sheet algorithm originally written by Wiedelt (1981) and modified by Zhou (1989) for the cross hole geometry is employed to compare simple 3-D models to the cylindrically symmetric formulation.

To determine how well the cylindrical solution can approximate a simple 3-D body, the model shown in Figure 3.22 is used. The scattered vertical magnetic fields have been calculated for a 40m by 40m conductive sheet located between two boreholes as shown. In the first model the sheet is located symmetrically about the source borehole. For this case the 2-D and 3-D formulations should match very well. The sheet is then moved progressively further away from the source borehole. For the 2-D model this corresponds to the enlargement of a ring of conductive material. The calculations were made at three different frequencies; 1 kHz , 10 kHz and 100 kHz. The results of this test in terms of the mean amplitude and phase error, and their standard deviations are given in Table 3.7.

When the sheet is located symmetrically about the source borehole (x_c =0), the error between the two solutions is less than 5% in all cases. This once again verifies the validity of the Born series approximate solution. The fact that the error gets larger as the frequency is raised may be indicating that higher frequencies are slightly more sensitive to the shape of the body, or that one or both of the solutions is breaking down at higher frequencies.

	1 kHz				10 kHz				100 kHz			
	% Amp Error		Phase Error (Deg)		% Amp Error		Phase Error (Deg)		% Amp Error		Phase Error (Deg)	
x_c (m)	Mean	Stan Dev.	Mean	Stan Dev.	Mean	Stan Dev.	Mean	Stan Dev.	Mean	Stan Dev.	Mean	Stan Dev.
0.	2.2	0.48	0.5	0.10	3.0	0.56	0.2	0.04	3.3	0.73	1.6	0.31
10.	62	6.9	20	5.3	36	4.4	20	2.7	3.9	1.8	2.0	1.2
20.	58	11	20	5.8	37	6.6	21	3.8	10	3.5	5.5	1.6
50.	36	13	19	9.0	73	6.6	6.7	3.8	39	5.0	12	0.33
80.	81	57	54	49	72	25	7.5	6.1	35	12.3	10	1.5
100.	1920	1423	236	9.0	250	174	38	13	31	17.	3.2	0.80

Table 3.7 - Error between the 2-D Born series approximation and the 3-D thin sheet solution for the models shown in Figure 3.22. 'x_c' refers to the location of the center of the sheet away from the source borehole, 'Mean' refers to the calculated mean error for all source -receiver combinations and 'Stand. Dev. ' the standard deviation of the errors about the mean. The labels at the top refer to calculations made at 1,10 and 100 kHz.

As the sheet is moved off center to x_c =10m and 20m, the error between the two solutions at 1 and 10 kHz quickly increases. This is likely due to current channeling effects that dominate the 3-D response at low frequencies. At 100 kHz however, the solutions match fairly well. At this frequency with the sheet centered at x_c =10m the mean error is approximately the same as it was for the centered sheet, and for x_c =20m the average amplitude error is only 10%. As the body is moved even further out into the medium (x_c =50.0, 80.0 and 100.0 m) the mean error at the lower frequencies continues to increase, maximizing when the sheet is symmetric about the receiver. Though the error also increases at 100 kHz, the average amplitude error is never larger than 40% even when the body surrounds the receiver borehole.

The above results confirm the analysis completed in section 2.4.2 where it was determined in that section that as the frequency is raised, the sensitivity for a given source-receiver pair becomes less dependent on the model geometry that is imposed upon

the problem. At 100 kHz the array will be less sensitive than lower frequencies to the edges of the 3-D body that are located at $y = \pm 20$ m, and thus the error between the two solutions will also be less. This will be discussed more fully in the next subsection.

When the sheet is located close to the source borehole, the standard deviation of the errors about the mean tends to be 5 to 10 times less than mean error itself. Though not as good as the standard deviations observed Section 3.3, this is definitely better than those observed in the comparison with the 1-D solution. However, as the sheet is moved out away from the source borehole, the magnitude of the standard deviation increases with respect to the mean such that when the sheet is symmetric about the receiver, the average error and its variation are on the same order of magnitude.

Because of the relatively large standard deviations in the cases described above, the distribution of the error is plotted as a function of source and receiver location, the location of the sheet, and frequency, in the gray scale format developed in the last subsection. Figure 3.23 shows the error between the 3-D and cylindrical models for x_c =20.0m and a frequency of 1 kHz, and Figure 3.24 the same model with the frequency of 100 kHz. At the lower frequency (Figure 3.23), the best fit occurs when the source is far from the sheet and the receiver is near it. This contrasts sharply with Figure 3.24 which shows that at 100 kHz the maximum error occurs with the source and receiver in this same configuration and the minimum error between the two solutions occurs when both the source and receiver are fairly close to the sheet. These two figures can in turn be compared to the error plots for the sheet that is symmetric across the receiver borehole. For both the low frequency (Figure 3.25) and the higher frequency (Figure 3.26) the minimum error occurs when the receiver is close to the sheet.

The error plots presented in Figures 3.23 through 3.26 do show different characteristics depending on the location of the body. For the imaging process described in the next chapter, a least squares minimization technique is used to fit the data to the image. If the image fits the data very well, the errors should be randomly distributed. The appearance of patterns like those displayed in these figures might indicate the presence of structure in the earth that the model employed in the imaging routine can not account for. Thus the use of this error analysis will be discussed more thoroughly in the next chapter.

3.4.3 Comparison to 2 1/2-D sheet models

In Chapter 2 the cylindrically symmetric geometry was compared to the 2 1/2-D geometry by calculating the sensitivity functions for the two different geometries. To verify the conclusions of that comparison a 2 1/2-D body is approximated with an extended version of the thin sheet models shown in Figure 3.27. The three bodies are

20m across and extend 300m in the direction perpendicular to the cross well plane. Again three frequencies were employed and the error between the two solutions calculated (Table 3.8).

	1 kHz				10 kHz				100 kHz			
	% Amp Error		Phase Error (Deg)		% Amp Error		Phase Error (Deg)		% Amp Error		Phase Error (Deg)	
x_c (m)	Mean	Stan Dev.	Mean	Stan Dev.	Mean	Stan Dev.	Mean	Stan Dev.	Mean	Stan Dev.	Mean	Stan Dev.
10.0	87	2.5	20	5.2	76	2.0	33	3.7	42	3.2	20	1.9
50.0	56	11	20	8.5	29	5.7	16	3.6	5.5	2.0	1.9	0.38
90.0	158	127	115	103	40	29	19	13	10	5.1	2.8	1.5

Table 3.8 - Error between the 2-D Born series approximation and the 2 1/2-D approximation with the thin sheet solution for the models shown in Figure 3.27. 'x_c' refers to the location of the center of the sheet away from the source borehole, 'Mean' refers to the calculated mean error for all source -receiver combinations and 'Stand. Dev. ' the standard deviation of the errors about the mean. The labels at the top refer to calculations made AR 1,10 and 100 kHz.

These results compliment well the conclusions drawn in section 2.4.2. The mean error is greatest when the body is near the source. The sensitivity diagrams indicated that the worst correlation between the two geometries occurs at these locations. When the sheet is centrally located both the mean error, and in the 100 kHz case, the standard deviation about the mean, are minimized. As the sheet is moved close to the receiver well, the mean error and standard deviation increase. However, once again the higher frequencies result in a smaller mean error. These results validate the spatial sensitivity analysis accomplished in Chapter 2 and prove that at low frequencies, a given source - receiver pair is very sensitive to the geometry of a scattering body outside of the interwell region and that this phenomenon is diminished by operating at higher frequencies.

3.5 Summary

In this chapter the benefits and drawbacks of both the Born and Born series approximations have been demonstrated as have the limitations of the cylindrically symmetric model. The first order Born approximation is computationally very simple but limited to modeling anomalous bodies whose anomalous induction numbers are relatively small. The Born series approximation can be used to accurately calculate the response of scatterers with anomalous induction numbers two orders of magnitude greater than those

that can be treated with the first order approximation and it is considerably faster than the full integral equation solution.

General rules have been developed to determine when both of these approximations degenerate to an unacceptable level of accuracy. These rules are based on the anomalous induction number of the scattering body which is defined as $\Delta\sigma\omega\mu S = 2O\,S/\delta^2$ and is dimensionless. The first order Born approximation has been found to be accurate to 1% for $\Delta\sigma\omega\mu S \leq 0.02$ while the Born series approximation converges for all $\Delta\sigma\omega\mu S \leq 2.0$.

The cylindrically symmetric model has been demonstrated to be very useful for modeling cross well EM problems. The computation of the Hankel transforms that constitute the Green's function can be unstable. Fortunately a Simpson integration method for a 3-D Green's function seems to eliminate this problem. The cylindrical geometry works rather well in modeling 1-D layered media although numerical errors exist when the source and receiver are within the anomalous layer. A comparison between the cylindrically symmetric models and 2 1/2-D and 3-D models shows that at higher frequencies the measurements are less sensitive to the dimensions of the conductivity anomaly outside of the plane containing the two wells. The effects of these geometries on an imaging scheme employing the cylindrical geometry will be discussed more fully in Chapter 4.

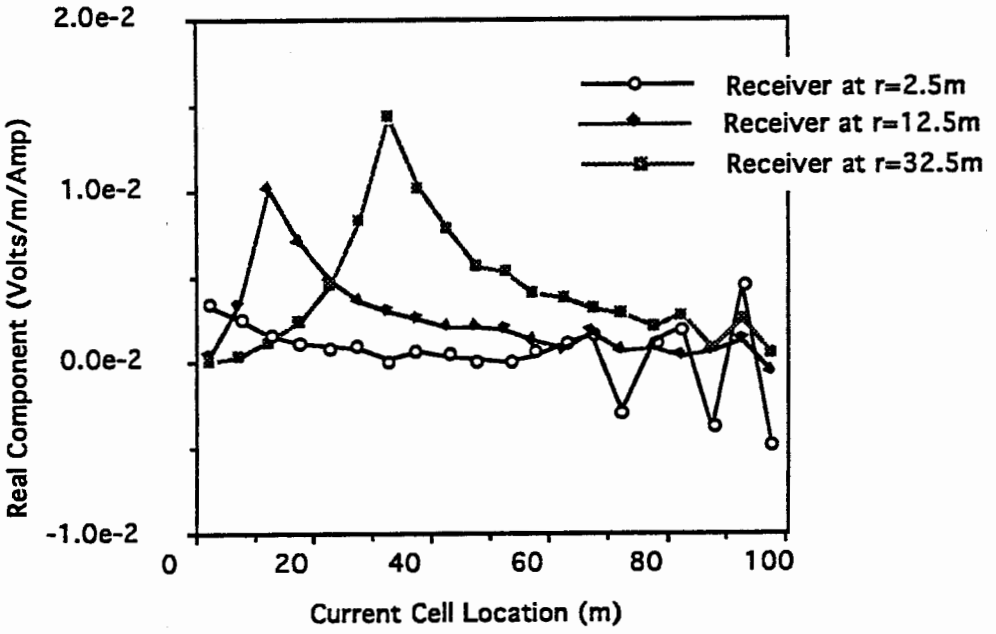

(a)

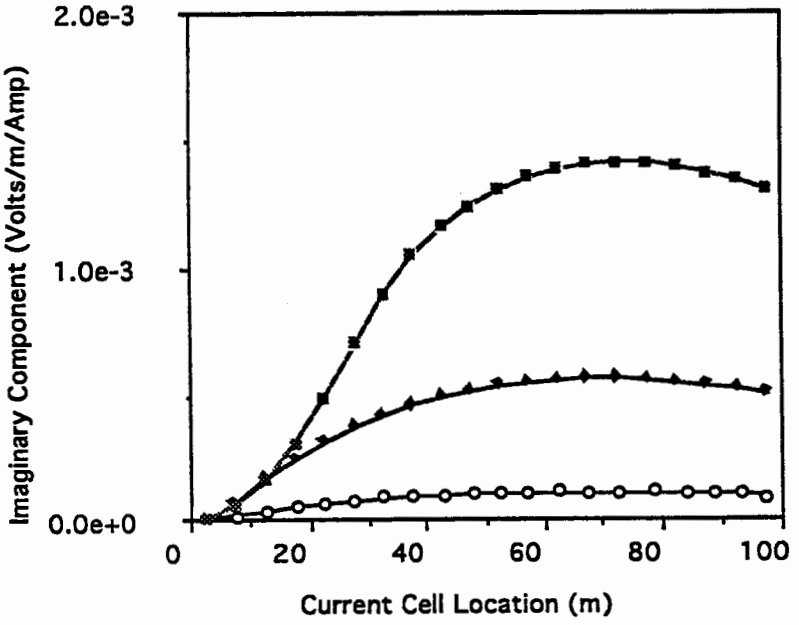

(b)

Figure 3.1 -The electric field Green's function (Expression 3.8) calculated numerically at three different field points as a function of the current cell location. The abscissa represents the radial distance from the origin to a 5m by 5m cell that contains of a unit amp of current flowing in the angular direction about the origin. (a) Real component. (b) Imaginary component.

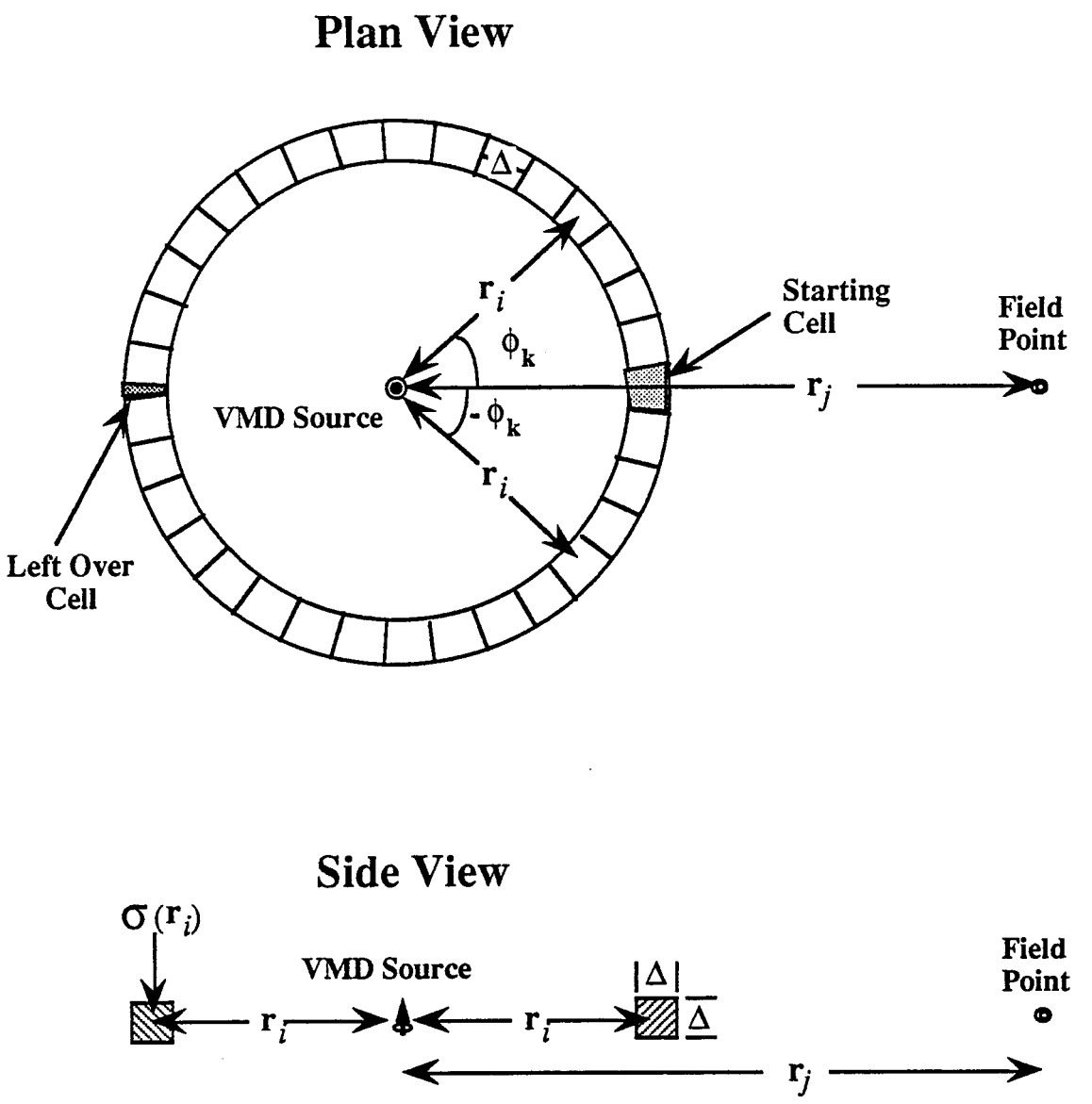

Figure 3.2 - Illustration of Simpson integration of 3D volume elements to produce a cylindrically symmetric Green's function that has been integrated over the cross sectional area of the cell.

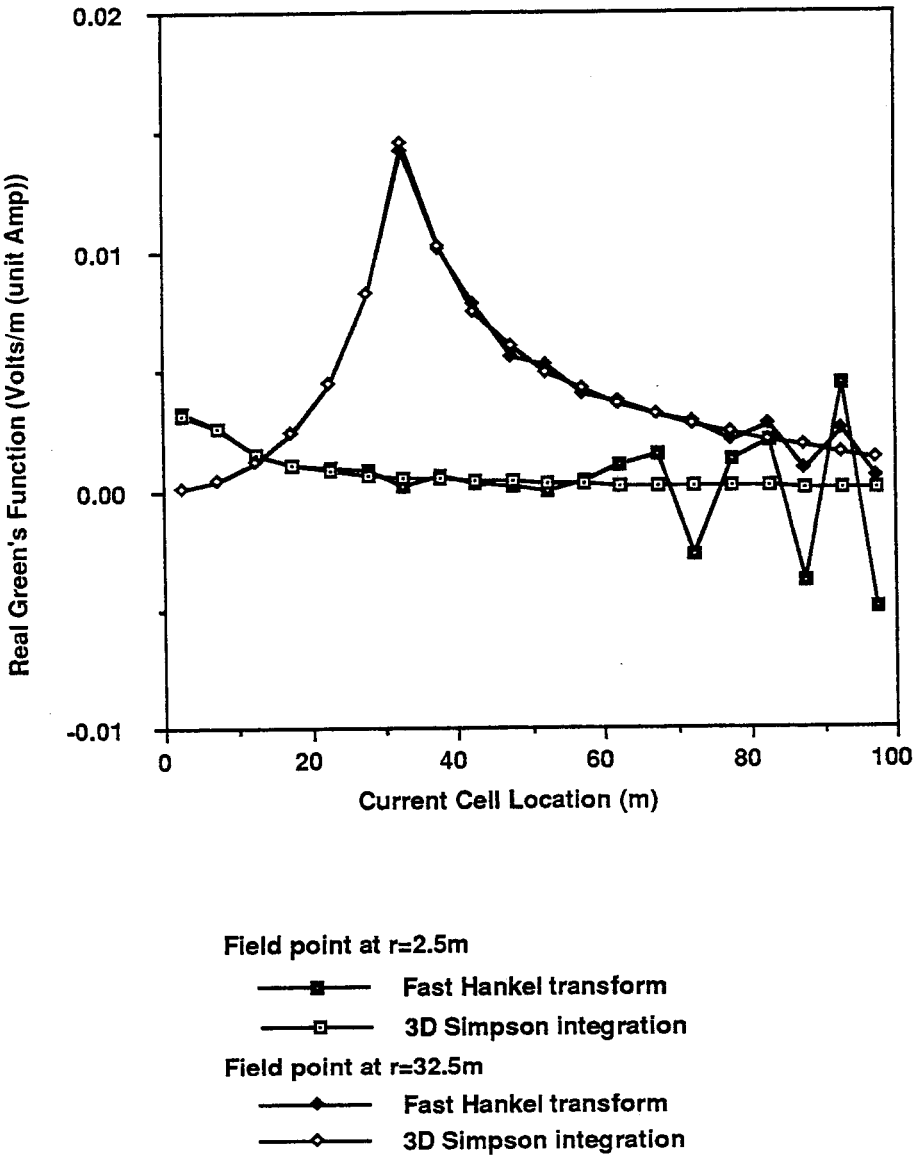

Figure 3.3 - Comparison of the 3D Simpson integration and the fast Hankel Transform method of calculating the cylindrical Green's function . Results have been calculated at two different field points as a function of the current cell location. The abscissa represents the radial distance from the origin to a 5m by 5m cell that contains one ampere of current flowing in the azimuthal direction about the origin. The current cell and the field point are both located at z=0 and thus the integration is over the singular cell.

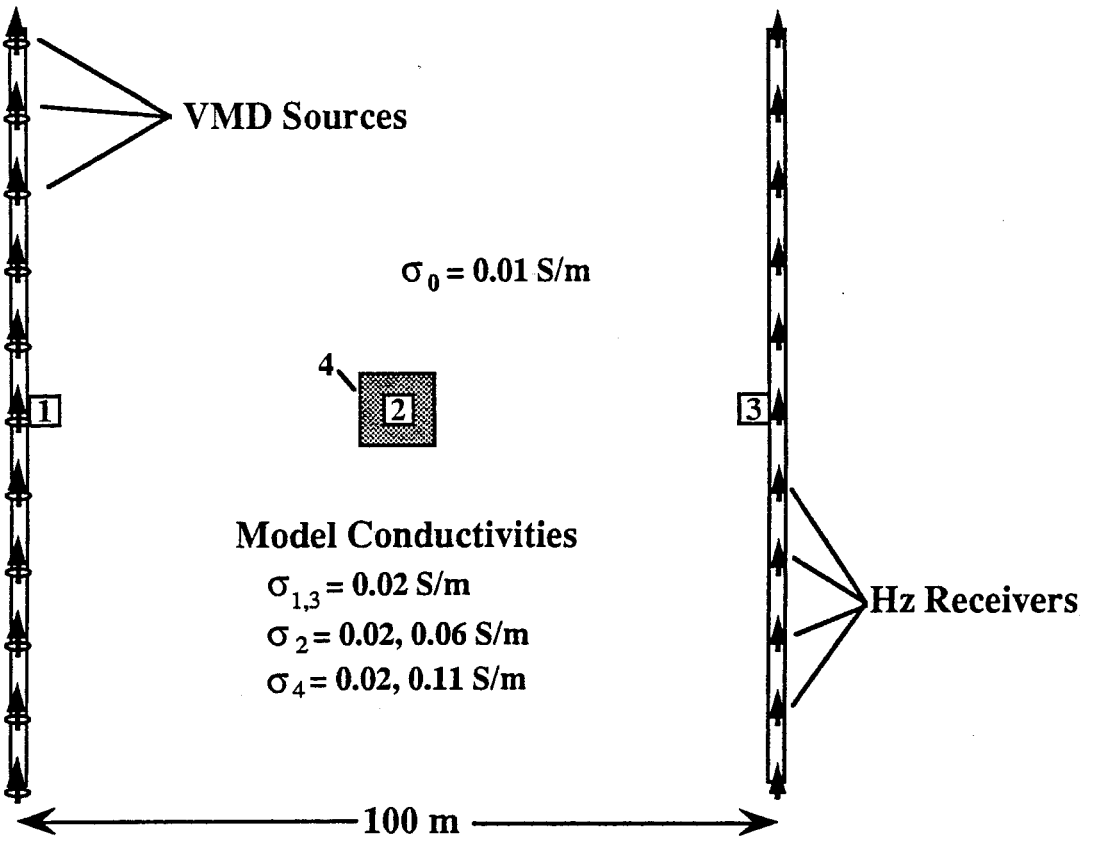

Figure 3.4 - Model used to analize the limits of the Born approximation as a forward modeling scheme. Two 100m deep wells are separated by 100m in a 0.01 S/m whole space. Sources and receivers are located at 10m intervals within the wells. Models 1,2 and 3 are 5m by 5m, and model 4 (the shaded square) is 10 m by 10 m. The models were discreetized into 1m by 1m cells and the secondary vertical magnetic fields calculated for each source-receiver pair.

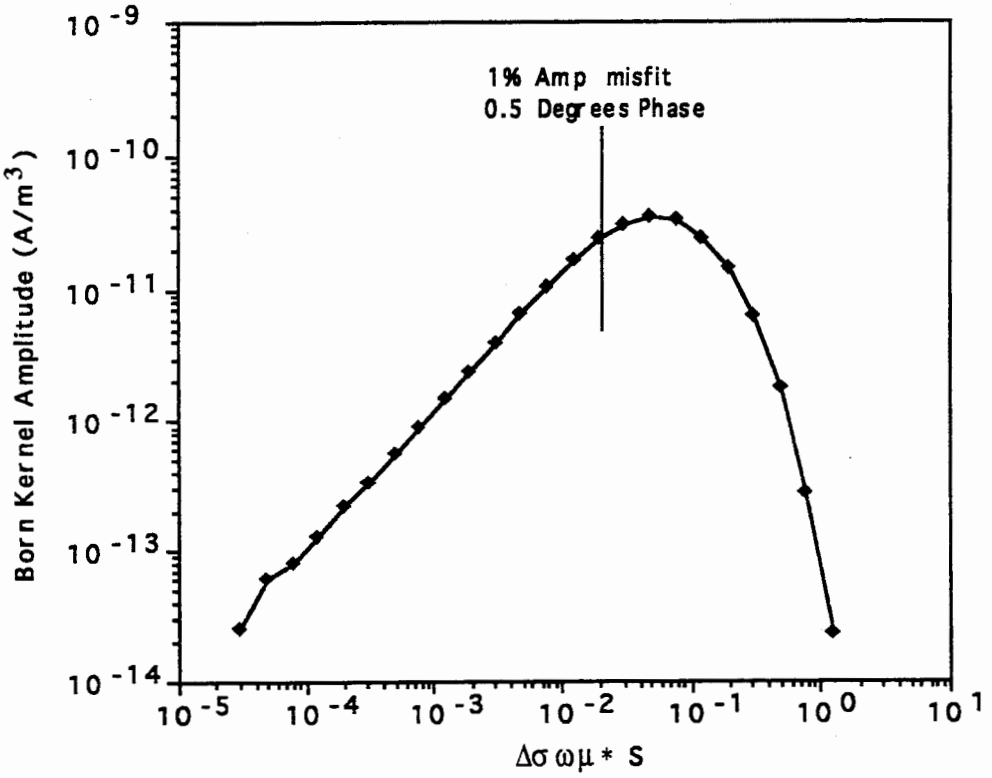

Figure 3.5 - The Born kernel for model 2 in Figure 3.4 plotted as a function of the anomalous induction number of the body. The line marks the point at which the error of the Born approximation for model 2 is 1% with the error increasing to the right.

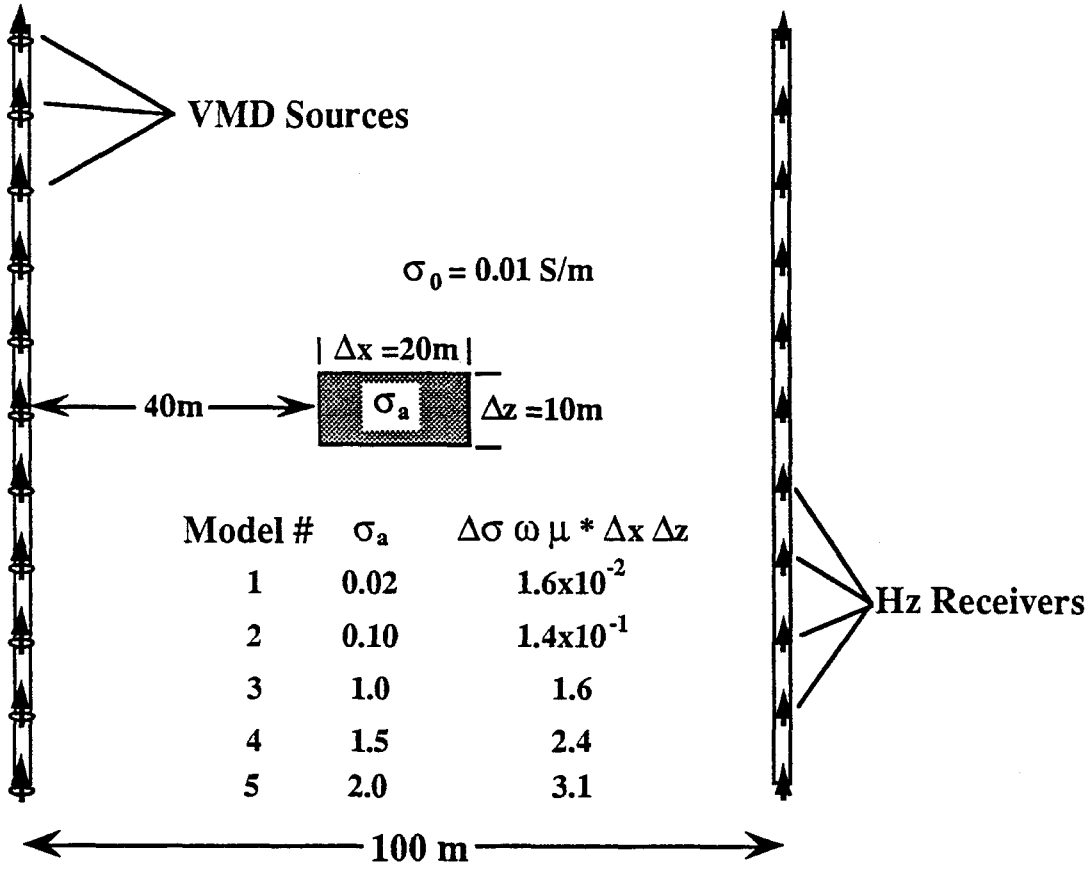

Model #	σ_a	$\Delta\sigma\ \omega\ \mu * \Delta x\ \Delta z$
1	0.02	1.6×10^{-2}
2	0.10	1.4×10^{-1}
3	1.0	1.6
4	1.5	2.4
5	2.0	3.1

Figure 3.6 - Model used to analize the limits of the Born series approximation as a forward modeling scheme. Two 100m deep wells are separated by 100m in a 0.01 S/m whole space. 11 sources and receivers are spaced at 10m intervals within the wells and the operating frequency is 1000 Hz. A conductive block of varying conductivity is situated in the center of the array. The body was discreetized into 50 2m by 2m cells and the secondary vertical magnetic fields calculated for each source-receiver pair.

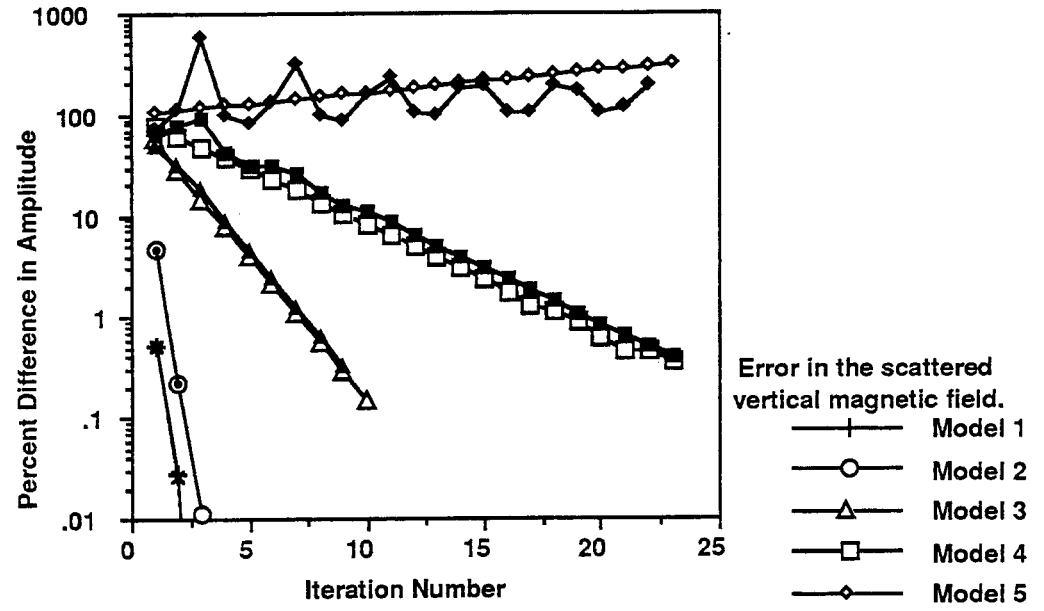

(a)

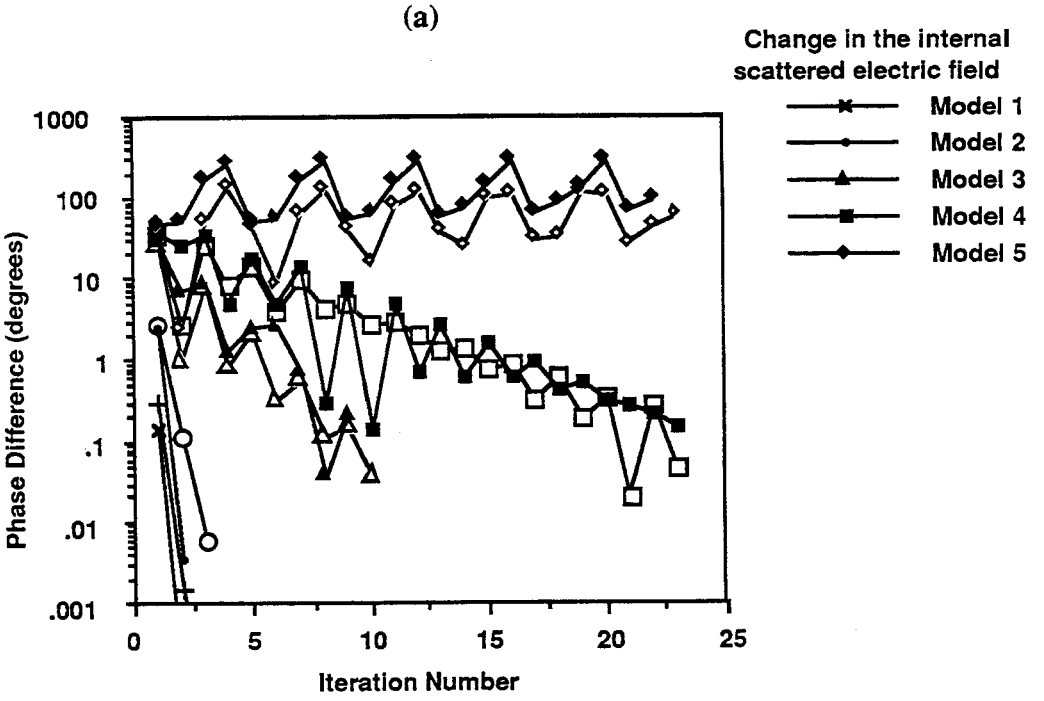

(b)

Figure 3.7 - Mean error in the scattered vertical magnetic field between the Born seriesand full solutions, and the mean change in the internal electric fields from one iteration to the next for the models shown in Figure 3.6 as a function of the iteration number. (a) Mean amplitude error and difference in percent. (b) Mean phase error and difference in degrees.

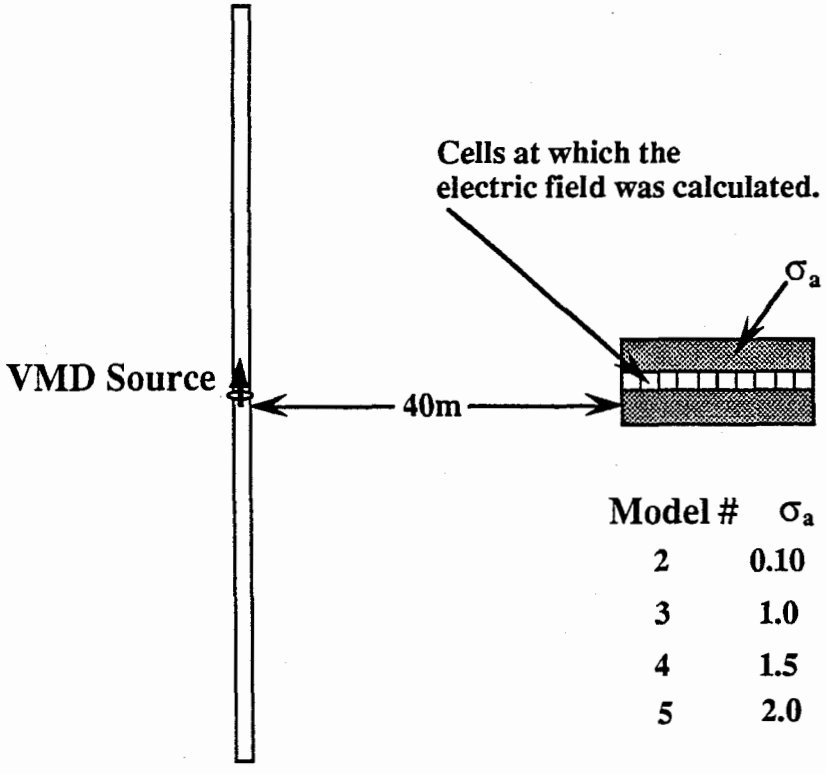

Figure 3.8 - Model used to analize the electric fields in the body at the limit of the Born series approximation. A conductive block of varying conductivity is situated in the center of the array and the electric field is calculated in10 cells across the blocks center . A vertical magnetic dipole source operating at 1000 Hz is located at the same depth as the body. 'Model #' refers to the models listed in Figure 3.6.

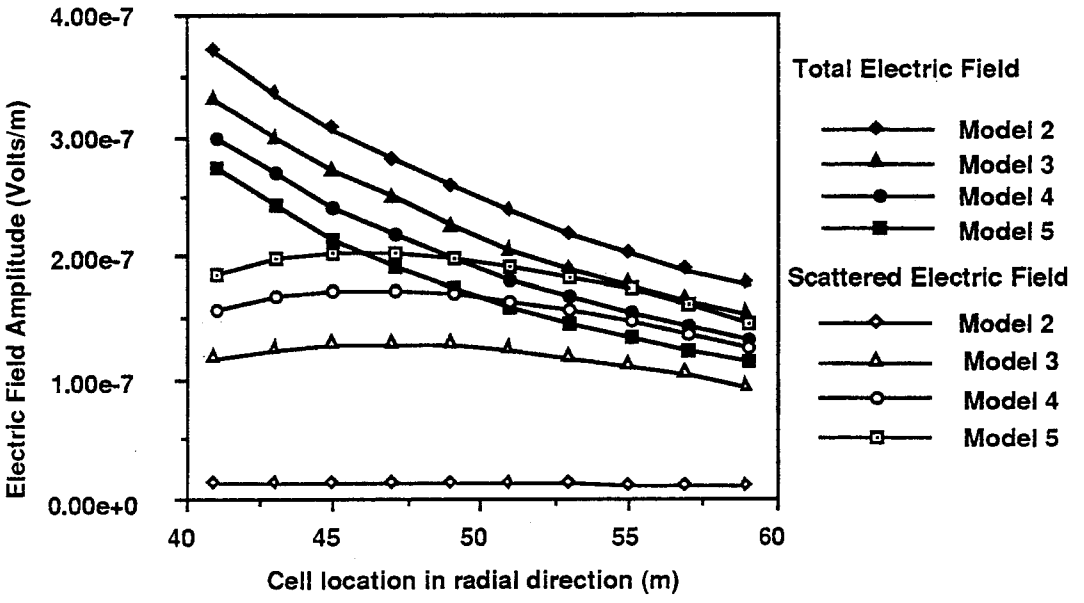

(a)

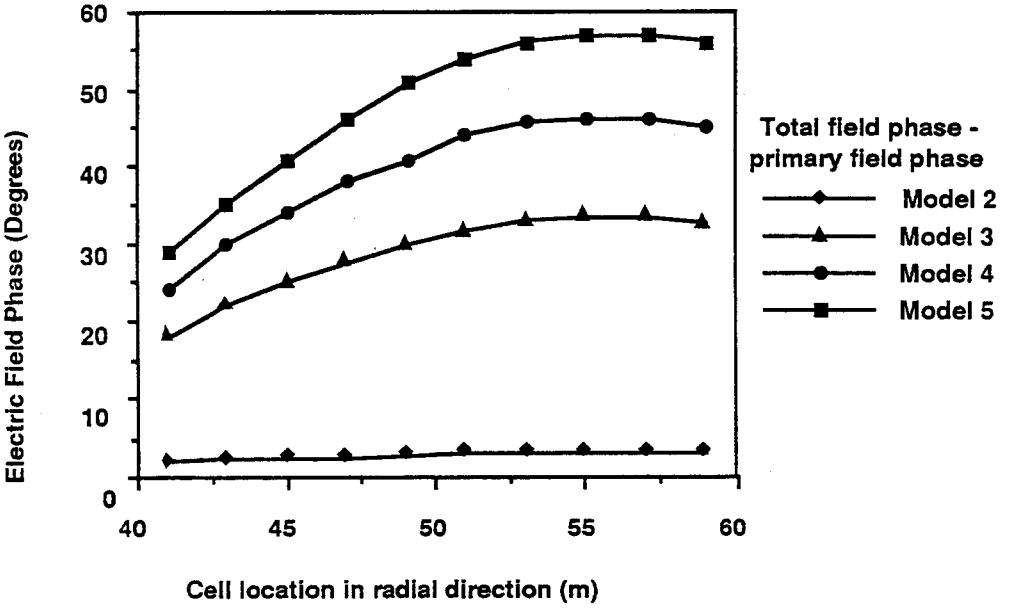

(b)

Figure 3.9 - The electric field behavior across the conductive block shown in Figure 3.8. The model numbers refer to the block conductivities listed in Figure 3.6. (a) The total and scattered electric field amplitude as a function of cell location. (b) The phase difference between the total and primary electric fields as a function of cell location.

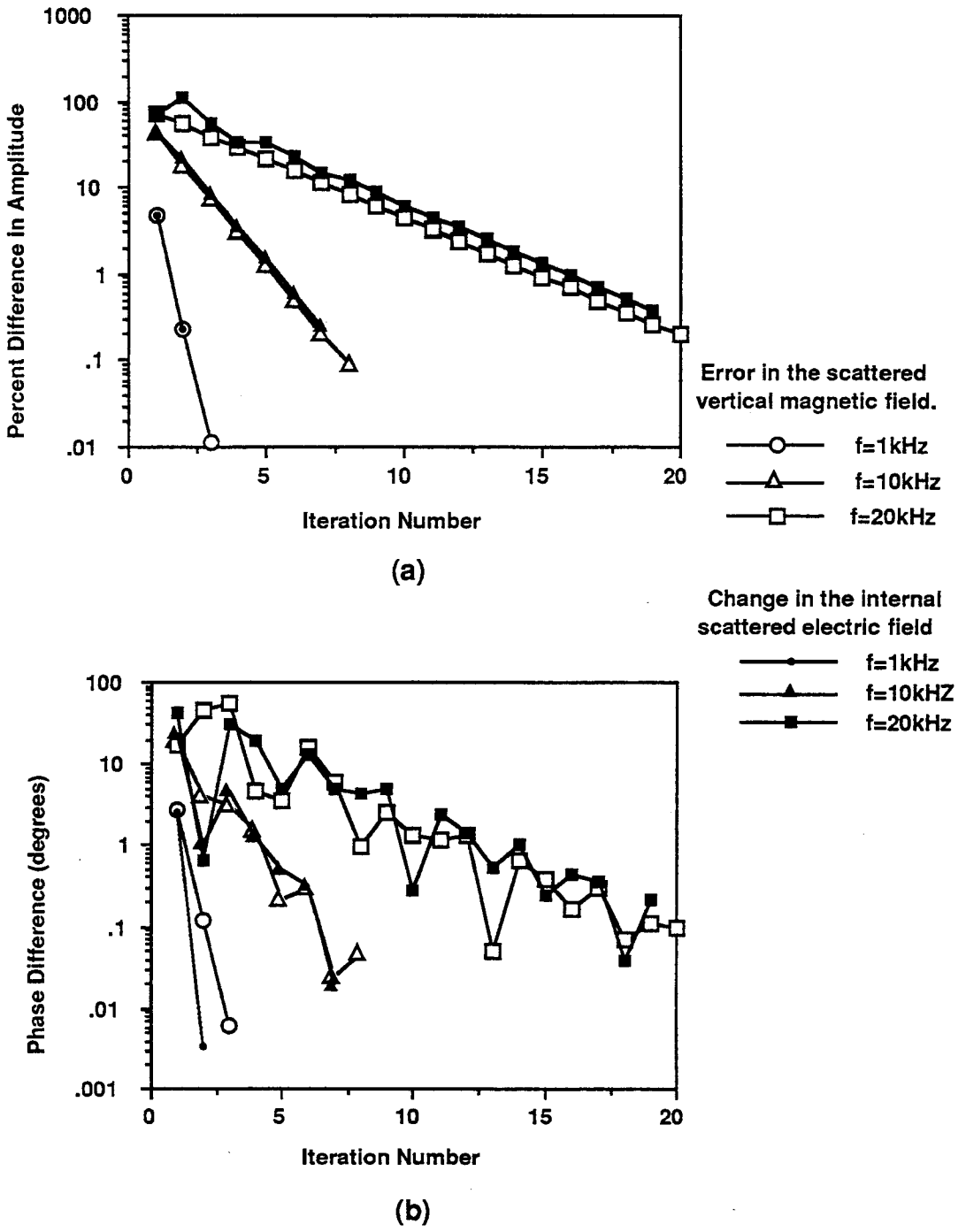

Figure 3.10 - Mean error in the scattered vertical magnetic field between the Born series and full solutions, and the mean change in the internal electric fields from one iteration to the next. Model 2 in Figure 3.6 has been employed with 3 different operating frequncies and the results plotted as a function of iteration number. (a) Mean amplitude error and difference in percent. (b) Mean phase error and difference in degrees.

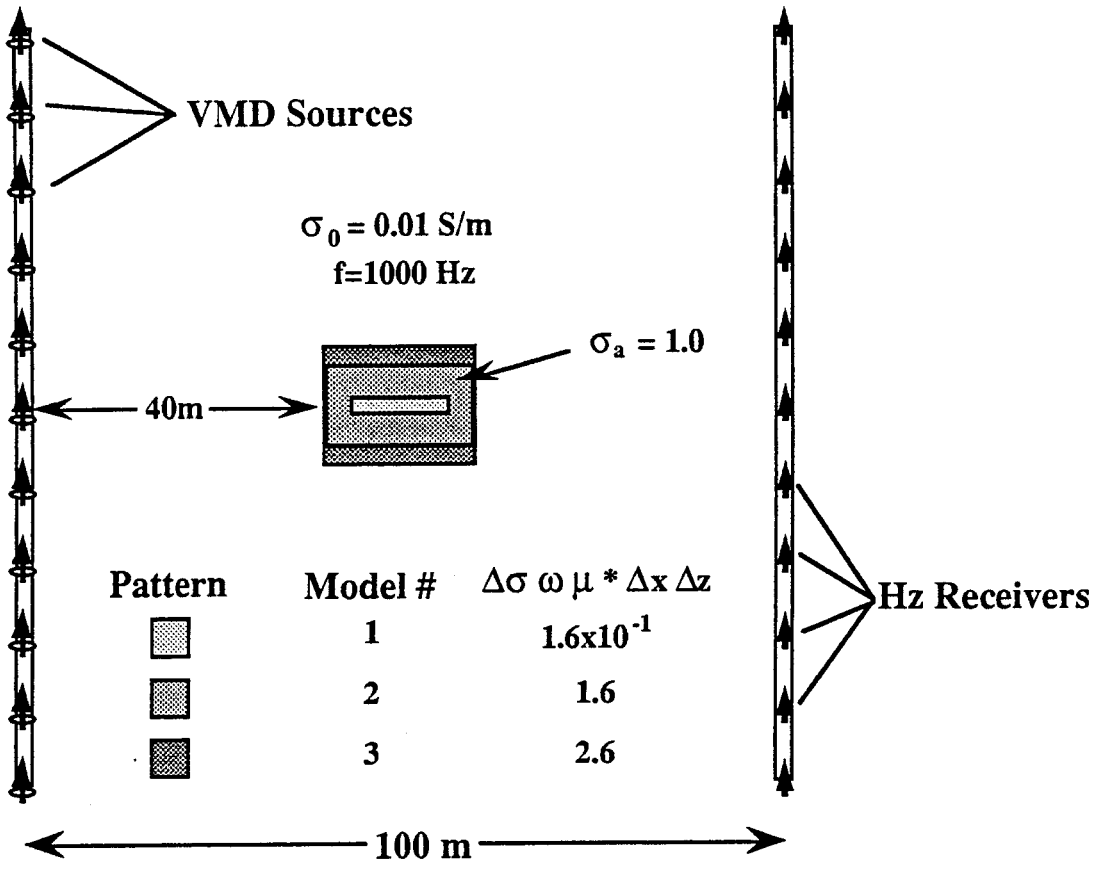

Figure 3.11 - Model used to analize the limits of the Born series approximation as a forward modeling scheme. Two 100m deep wells are separated by 100m in a 0.01 S/m whole space. 11 sources and receivers spaced at 10m intervals within the wells and the operating frequency is 1000 Hz. A conductive block of varying size is situated in the center of the array. The body was discreetized into 2m by 2m cells and the secondary vertical magnetic fields calculated for each source-receiver pair.

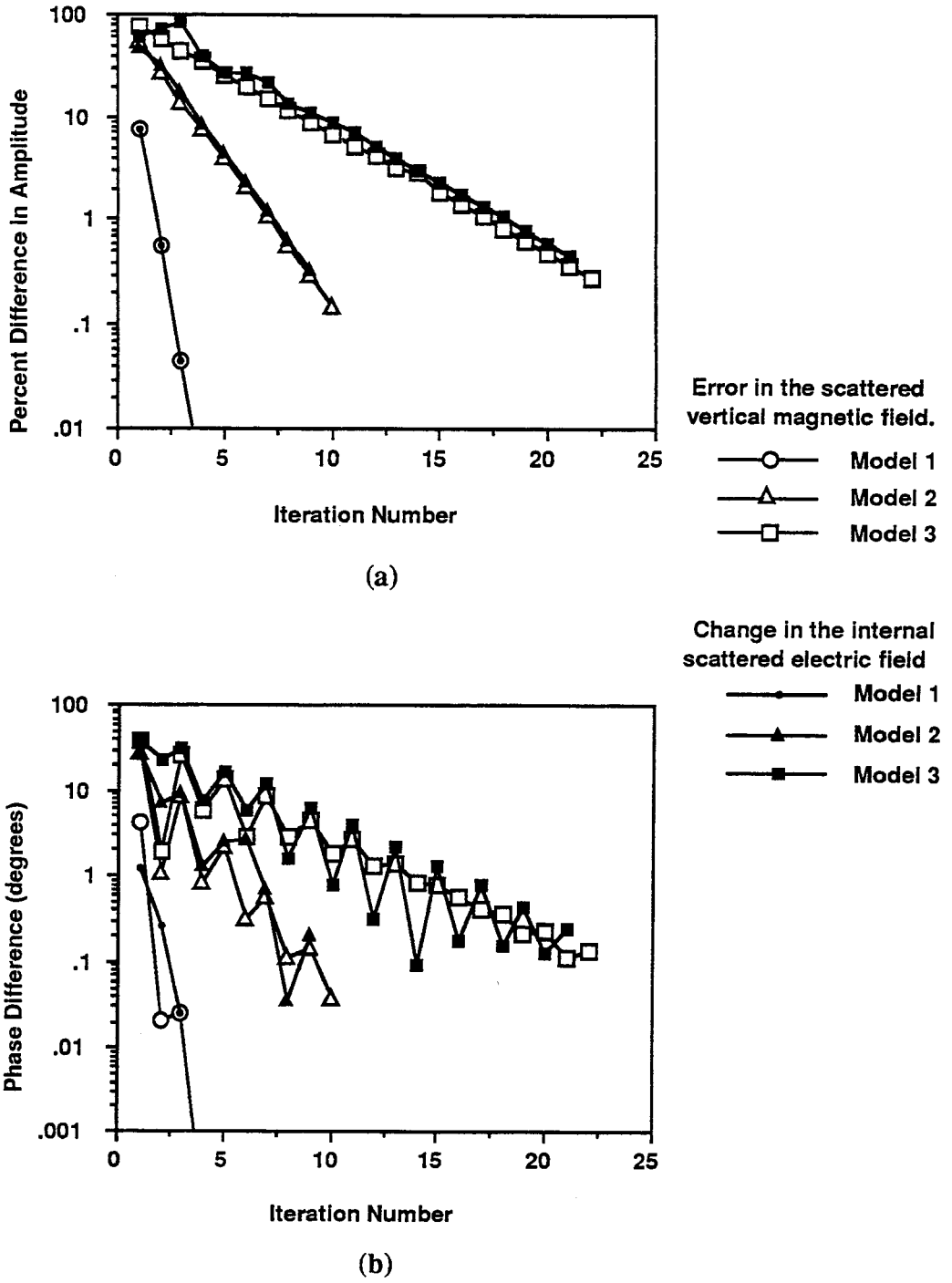

Figure 3.12 - Mean error in the scattered vertical magnetic field between the Born series and full solutions, and the mean change in the internal electric fields from one iteration to the next for the different models shown in Figure 3.11 as a function of the iteration number. (a) Mean amplitude error and difference in percent. (b) Mean phase error and difference in degrees.

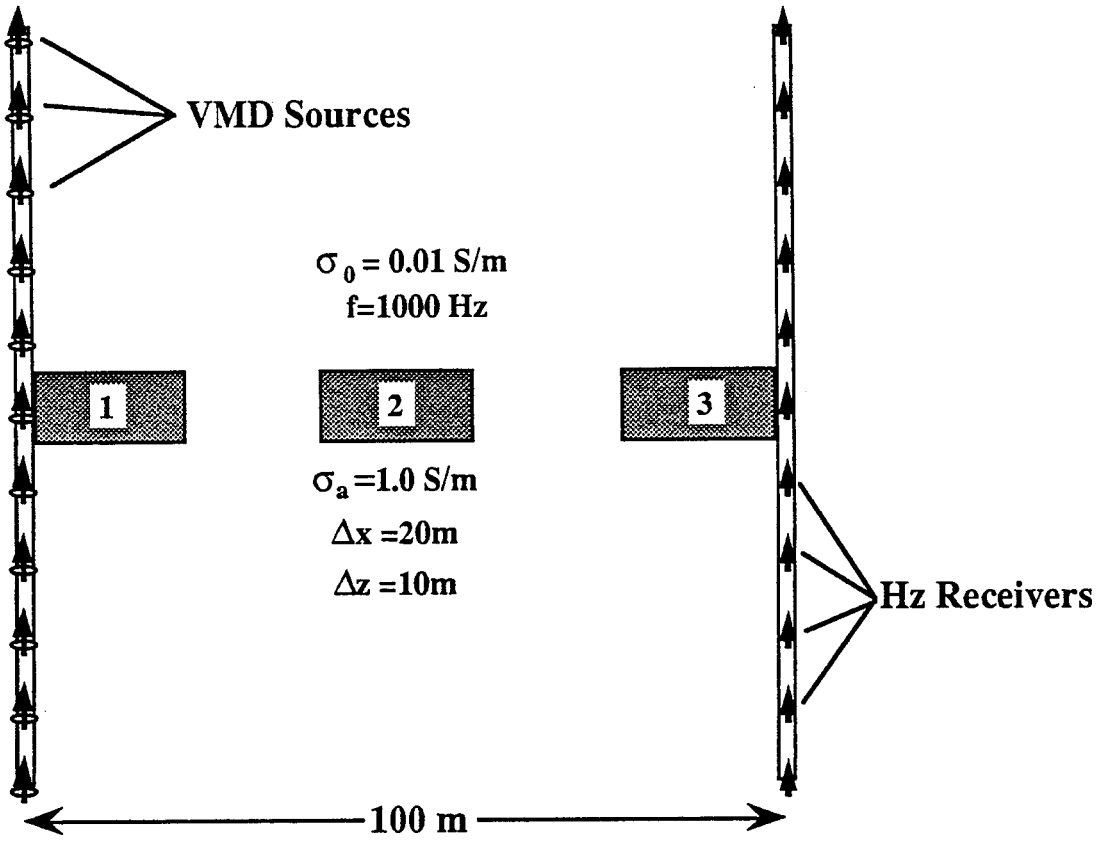

Figure 3.13 - Models used to analize the position dependence of the Born series approximation. Two 100m deep wells are separated by 100m in a 0.01 S/m whole space. A conductive block is located at three different positions from the source well. The two wells contain 11 sources and receivers spaced at 10m intervals and the operating frequency is 1000 Hz. Each body was discreetized into 50 2m by 2m cells and the secondary vertical magnetic fields calculated for each source-receiver pair.

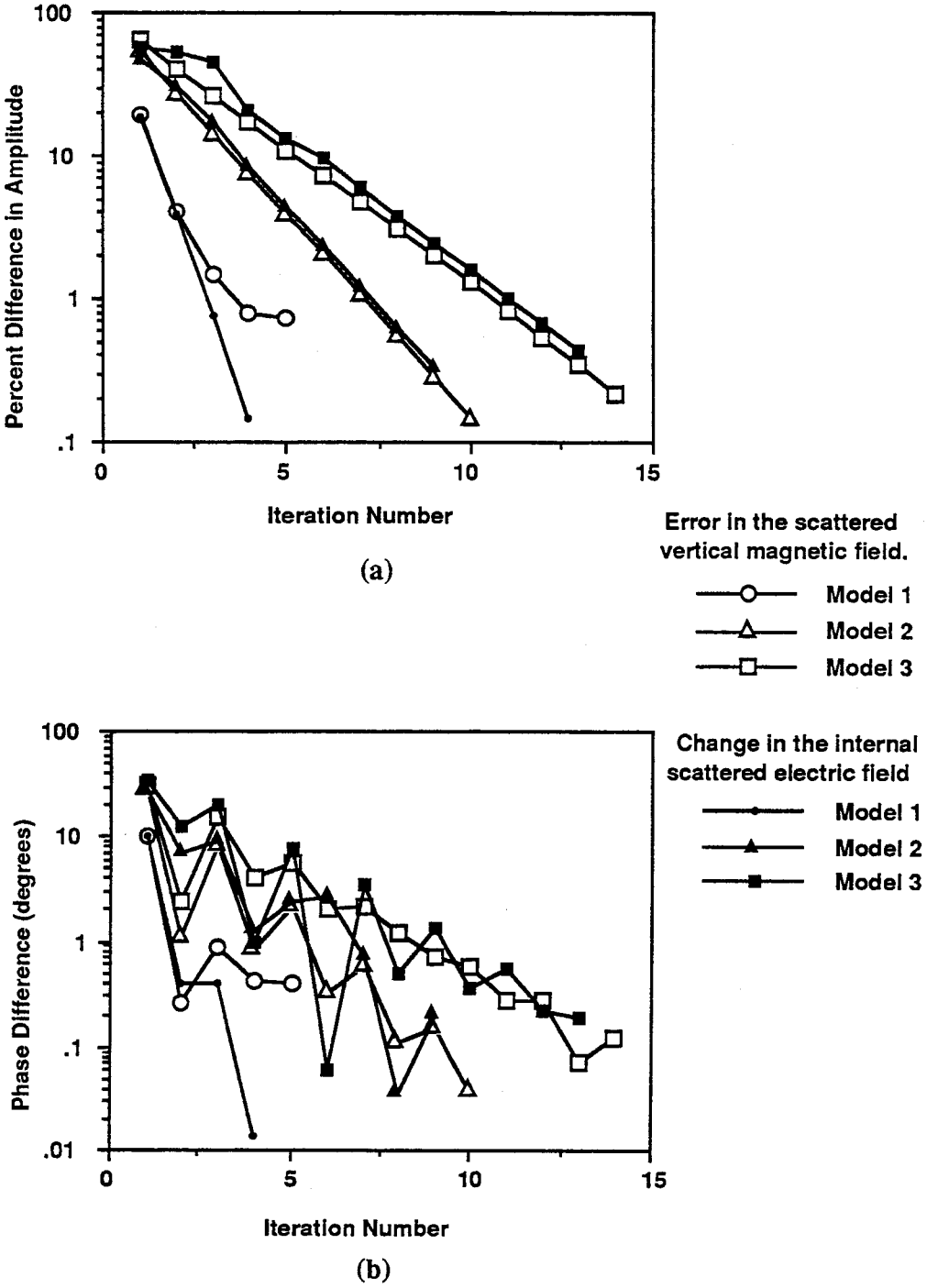

Figure 3.14 - Mean error in the scattered vertical magnetic field between the Born series and full solutions, and the mean change in the internal electric fields from one iteration to the next for the models shown in Figure 3.13 as a function of the iteration number. (a) Mean amplitude error and difference in percent. (b) Mean phase error and difference in degrees.

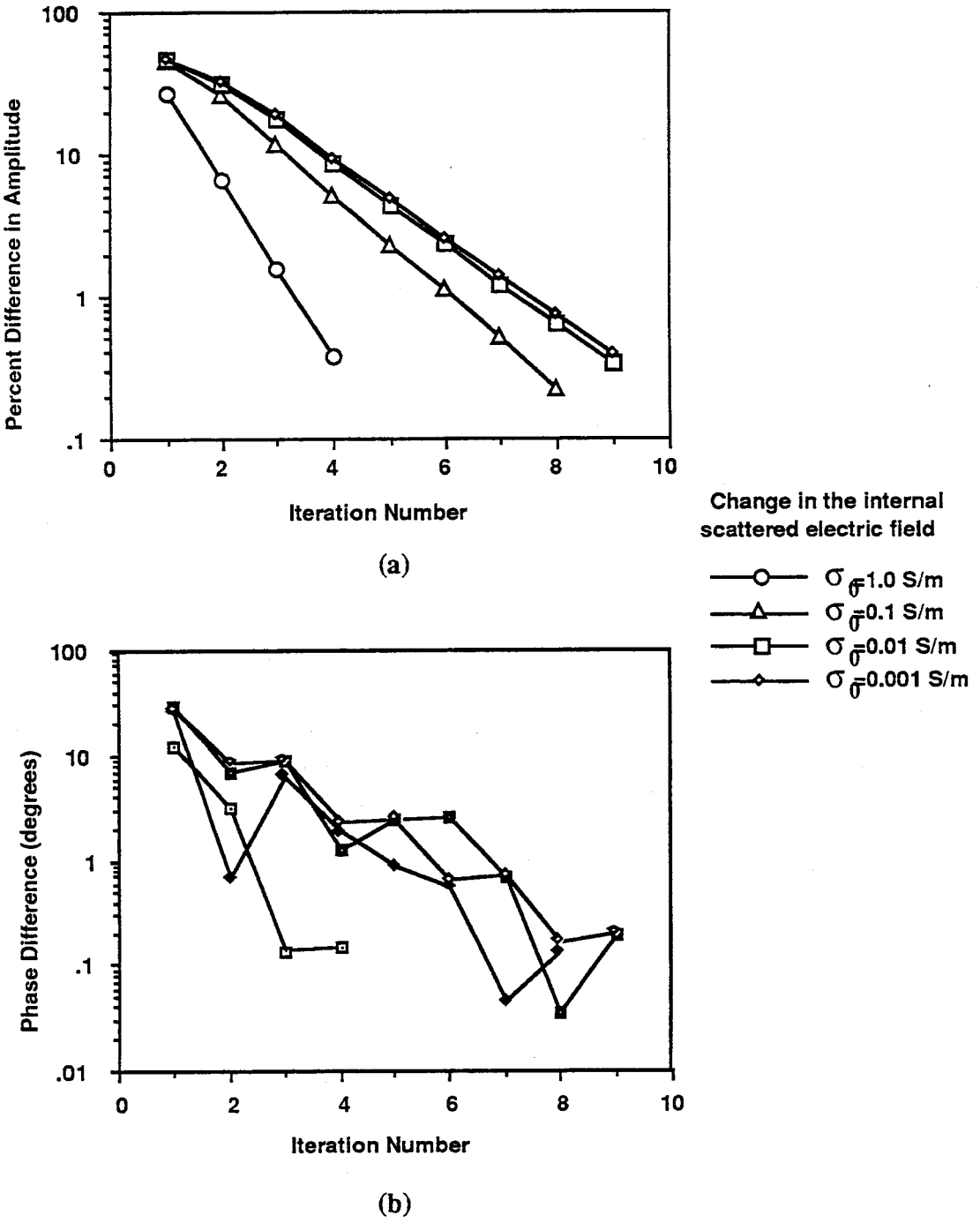

Figure 3.15 - The mean change in the internal electric fields from one iteration to the next for Model 2 shown in Figure 3.6 with differnt background conductivities as a function of the iteration number. (a) Mean amplitude difference in percent. (b) Mean phase difference in degrees.

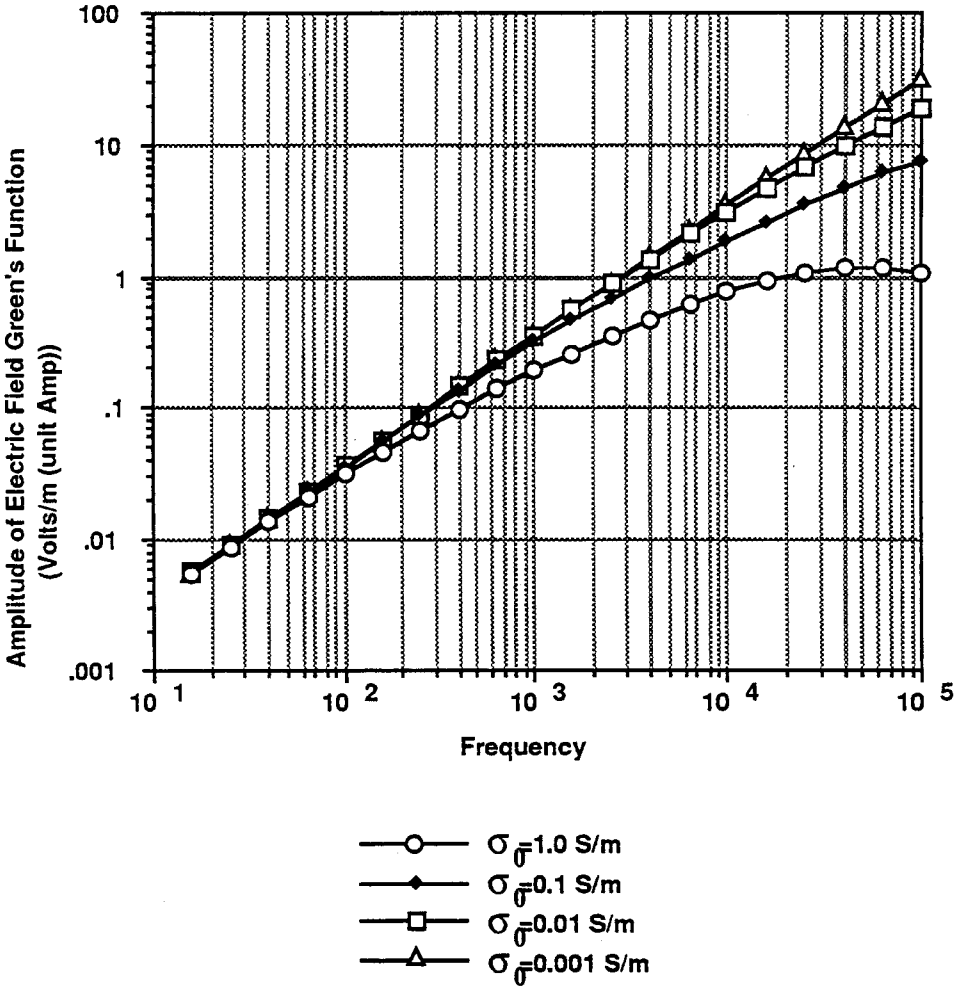

Figure 3.16 - The amplitude of the electric field Green's Function for a 5m by 5m singular cell located in a background of variable conductivity and centered 45m from the source borehole. THe amplitude has been plotted as a function of frequency.

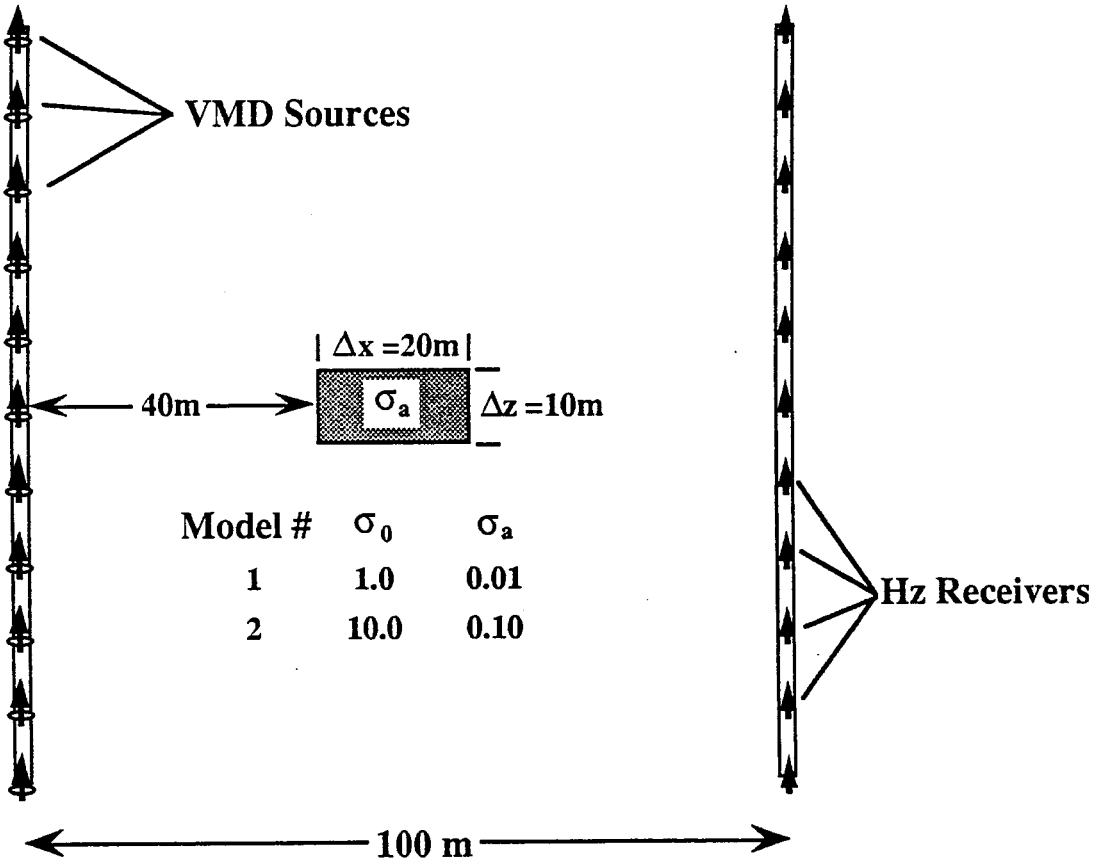

Figure 3.17 - Model used to analize the limits of the Born series approximation as a forward modeling scheme for resistive bodies. Two 100m deep wells are separated by 100m in a whole space of conductivity σ_0. 11 sources and receivers are spaced at 10m intervals within the wells and the operating frequency is 1000 Hz. A resistive block of varying conductivity is situated in the center of the array. The body was discreetized into 50 2m by 2m cells and the secondary vertical magnetic fields calculated for each source-receiver pair.

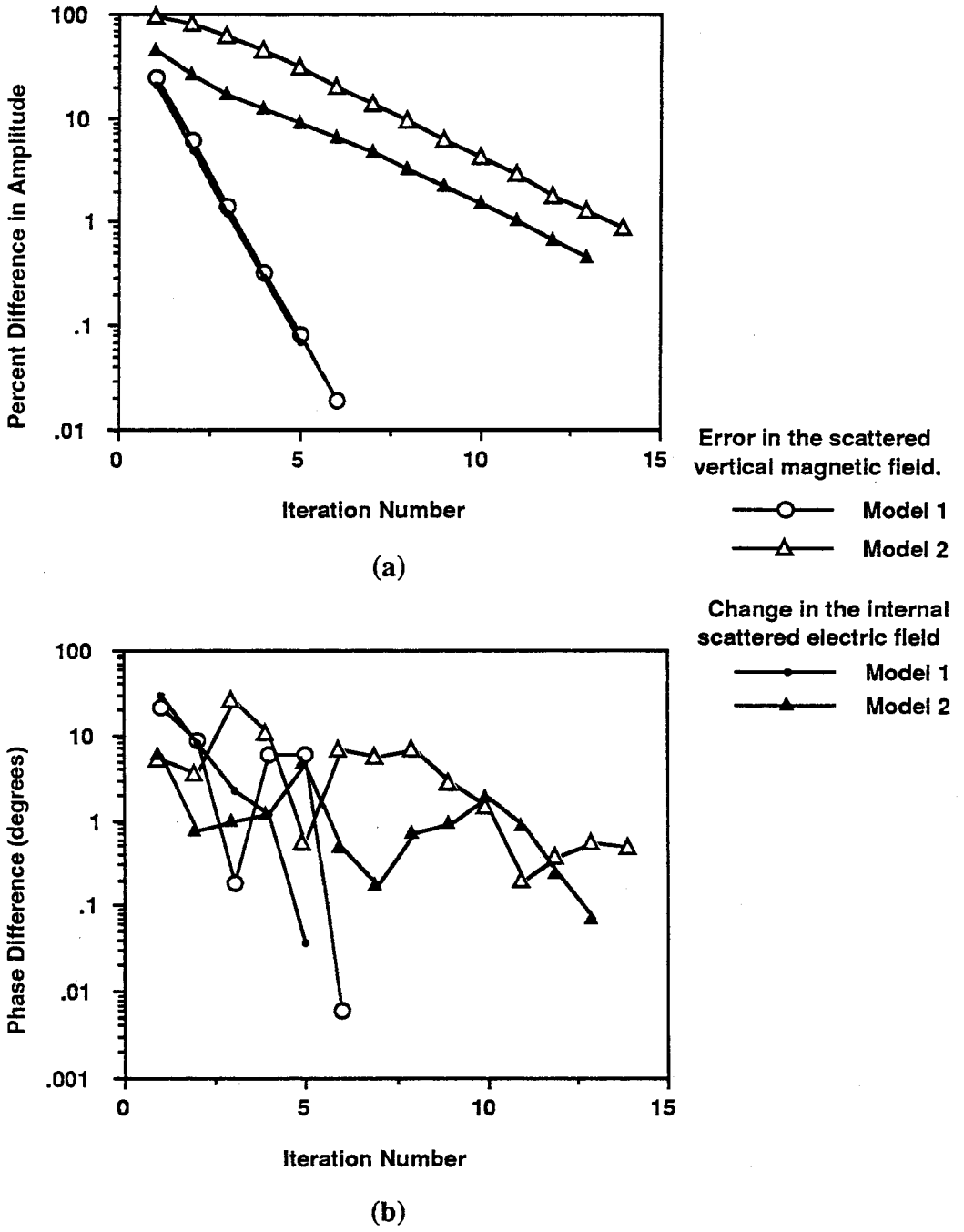

Figure 3.18 - Mean error in the scattered vertical magnetic field between the Born series and full solutions, and the mean change in the internal electric fields from one iteration to the next for the models shown in Figure 3.16 as a function of the iteration number. (a) Mean amplitude error and difference in percent. (b) Mean phase error and difference in degrees.

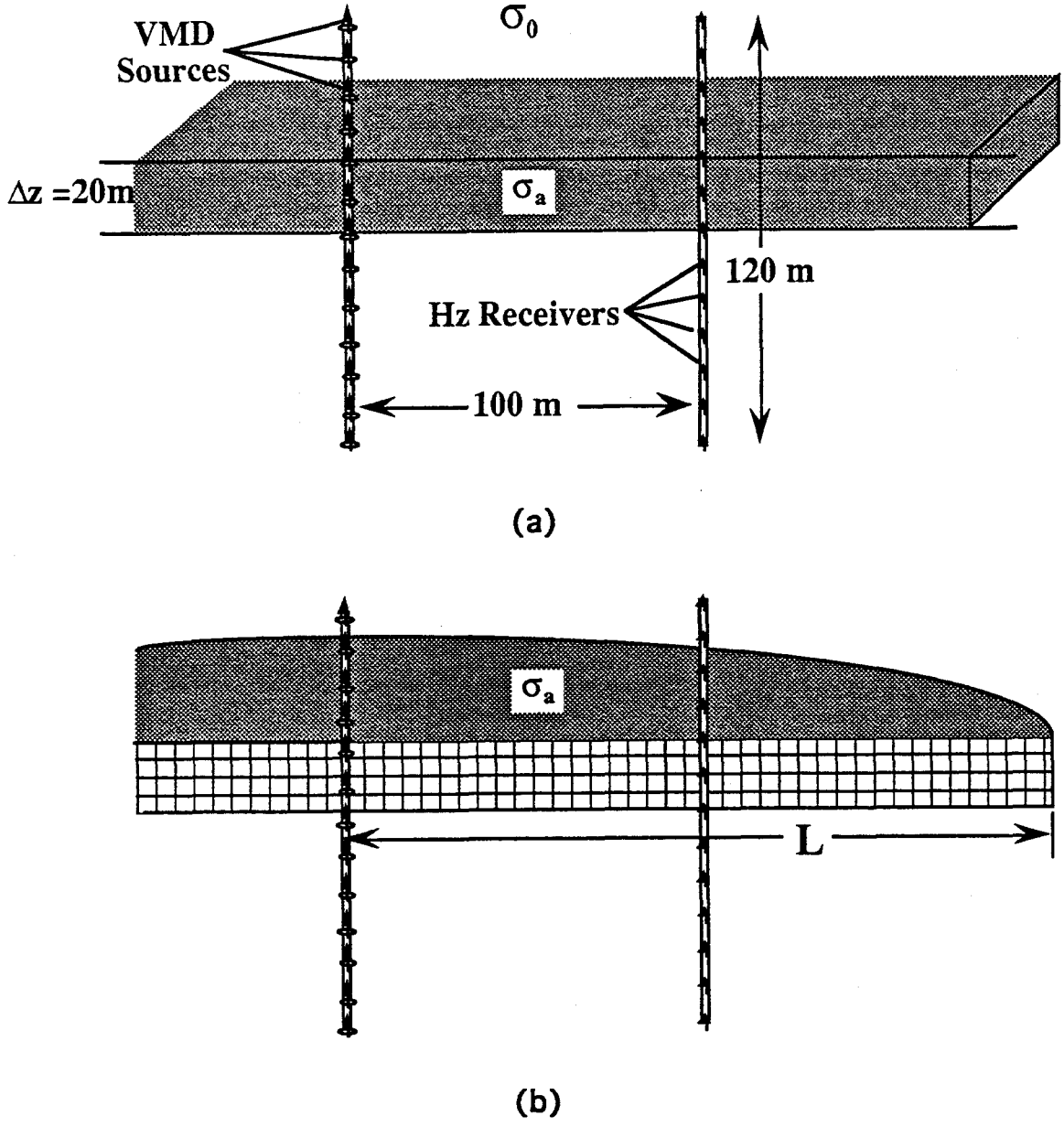

Figure 3.19 - Model used to compare the Born series solution for cylindrical geometry to a 1D layer. (a) The layered model. Two 100m deep wells are separated by 120m in a whole space of conductivity σ_0. For the conductive layer model, σ_0 =0.01S/m. For the resistive model σ_0=0.1S/m. A 20m thick layer of varying conductivity extends to infinity in the horizontal directions. The two wells contain 13 sources and receivers spaced at 10m intervals. (b) The cylindrically symmetric model. All dimensions are identical to the layered model except the slab extends horizontally outward from the source well to a radius of L.

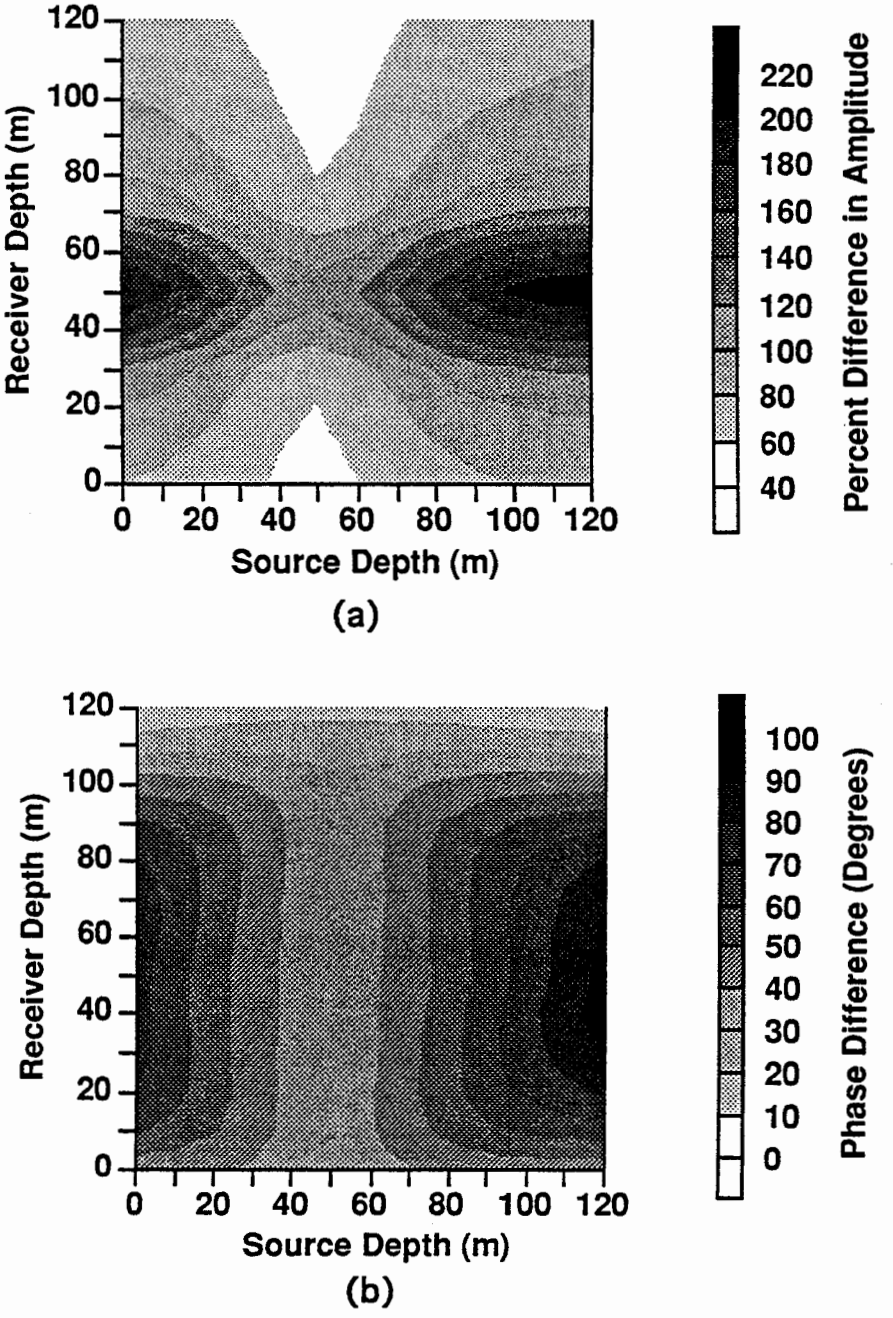

Figure 3.20 - Misfit error between the1D layered solution (Lee,1988) and 2D cylindrical integral equation solution employing the Born series approximation for the first model listed in Table 3.4. The errors have been plotted as a function of source and receiver location. (a) Amplitude error as a percentage of the 1D amplitude. (b) Phase difference between the two results.

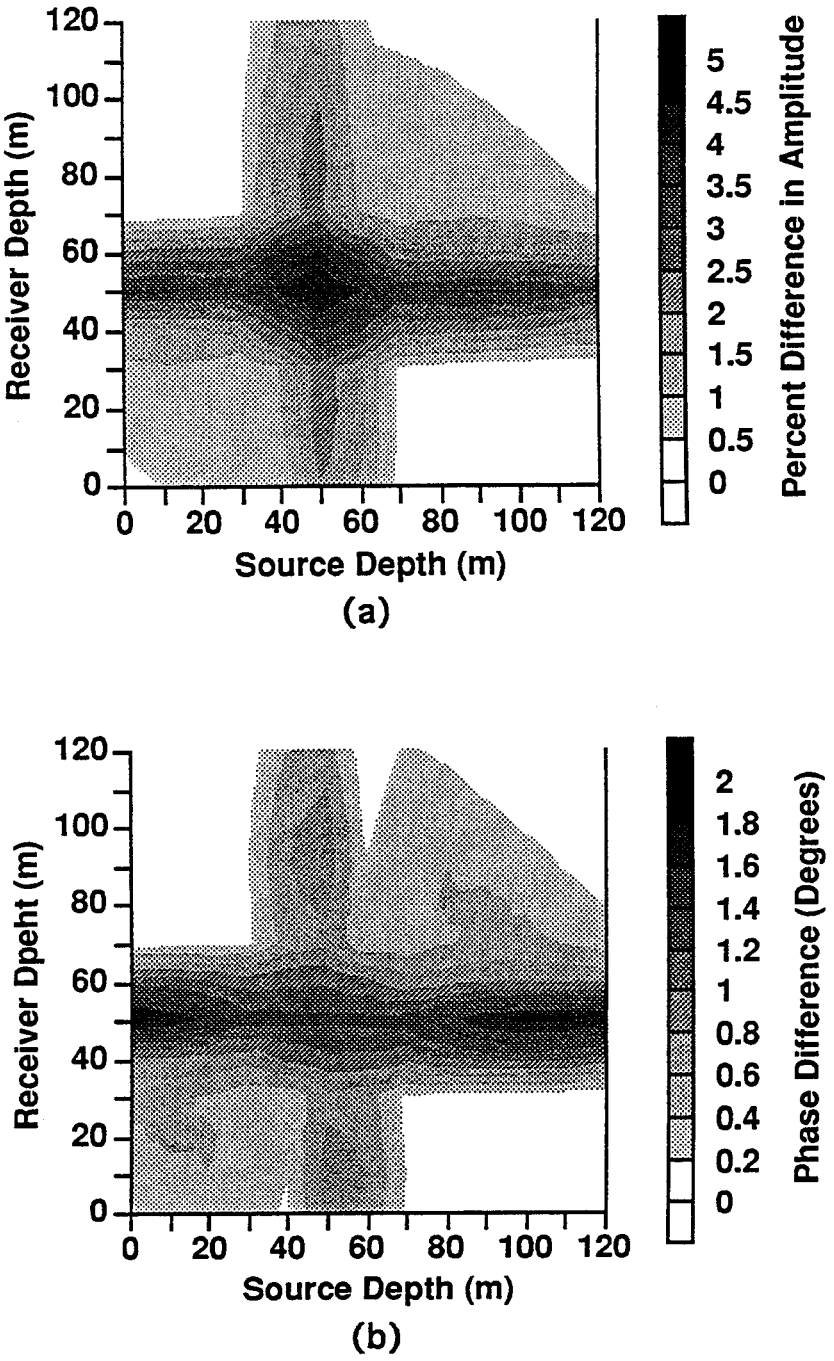

Figure 3.21 - Misfit error between the1D layered solution (Lee,1988) and 2D cylindrical integral equation solution employing the Born series approximation for the fourth model listed in Table 3.4. The errors have been plotted as a function of source and receiver location. (a) Amplitude error as a percentage of the 1D amplitude. (b) Phase difference between the two results.

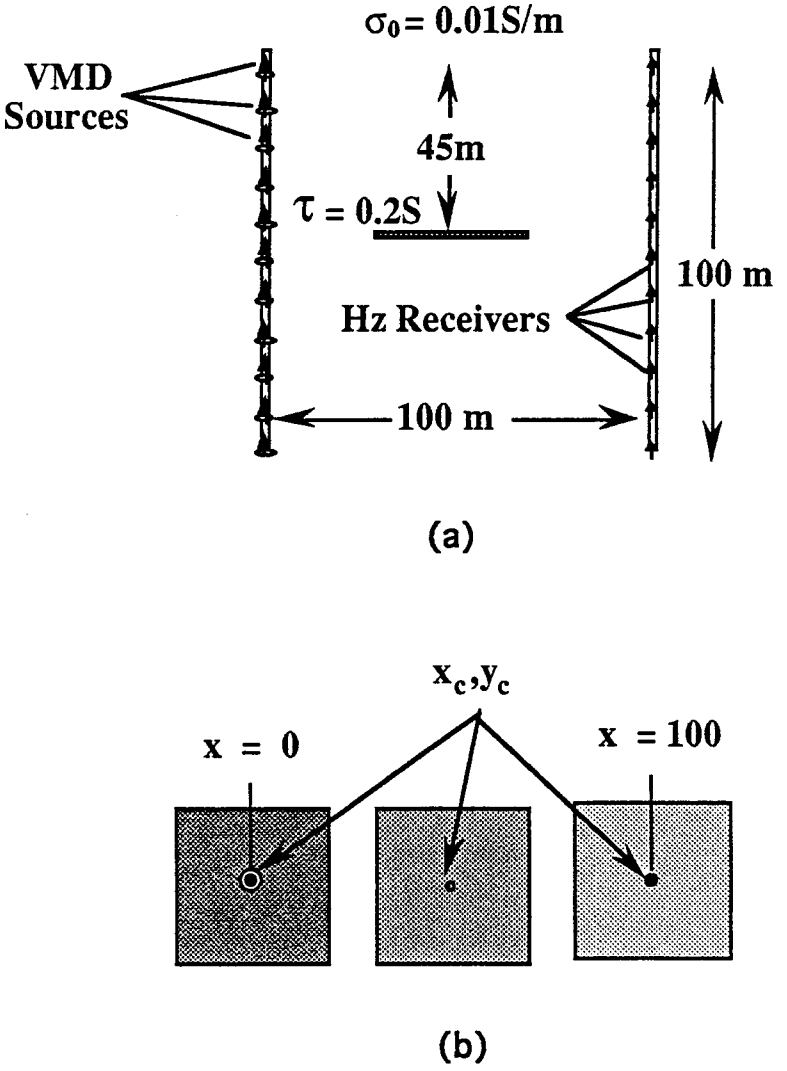

Figure 3.22 - Models used to compare the Born series olution with cylindrical geometry to a 3D thin sheet model. (a) Side view of the thin sheet model. (b) Plan view of the thin sheet model. Two 100m deep wells are separated by 100m in a whole space of conductivity 0.01S/m. A 40m by 40m thick of thin sheet of conductance 0.2S is located with its center at yc =0 and xc at 0m, 10m, 20m, 50m 80m and 100m. The two wells contain 11 sources and receivers spaced at 10m intervals. The sheet is discretized into 4m by 4m cells and the scattered vertical magnetic field calculated for each source-receiver pair. The three different sheets in b indicate models with xc =0m, xc =50m and xc =100m. (c) Continued on next page.

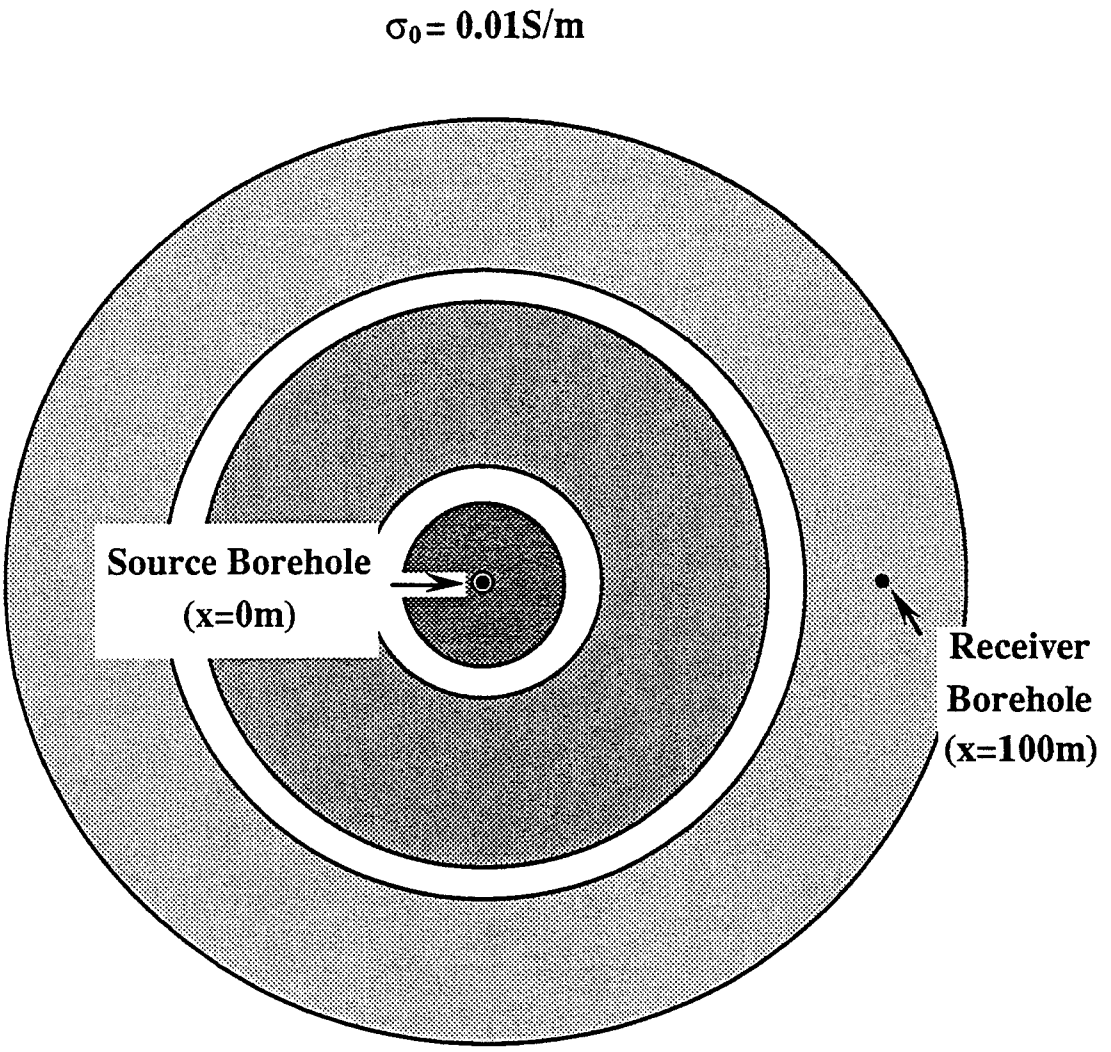

(c)

Figure 3.22 (Continued) (c) Plan view of the cylindrically symmetric models corresponding to the sheet models shown in b. The conductive rings are 0.5m thick in the and their conductivity is 0.4S/m. To simulate a thin sheet the rings have been discretized into a single layer of 0.5m by 0.5m cells.

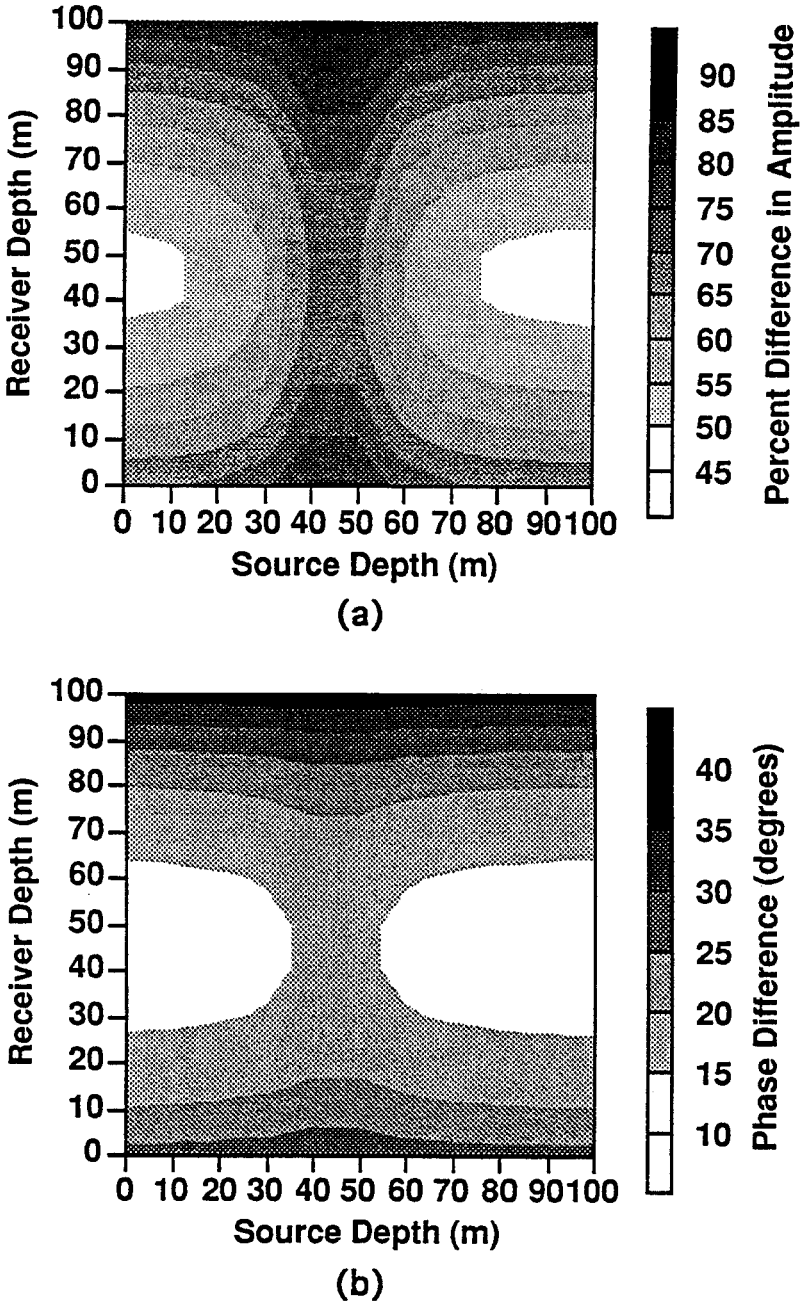

Figure 3.23 - Misfit error in the scattered vertical magnetic field between the 3D thin sheet solution (Zhou,1989) and the 2D integral equation solution employing the Born series approximation for the center of the sheet at xc =20m and a frequency of 1 kHz. The errors have been plotted as a function of source and receiver location. (a) Amplitude misfit in percentage of the thin sheet amplitude. (b)Phase difference.

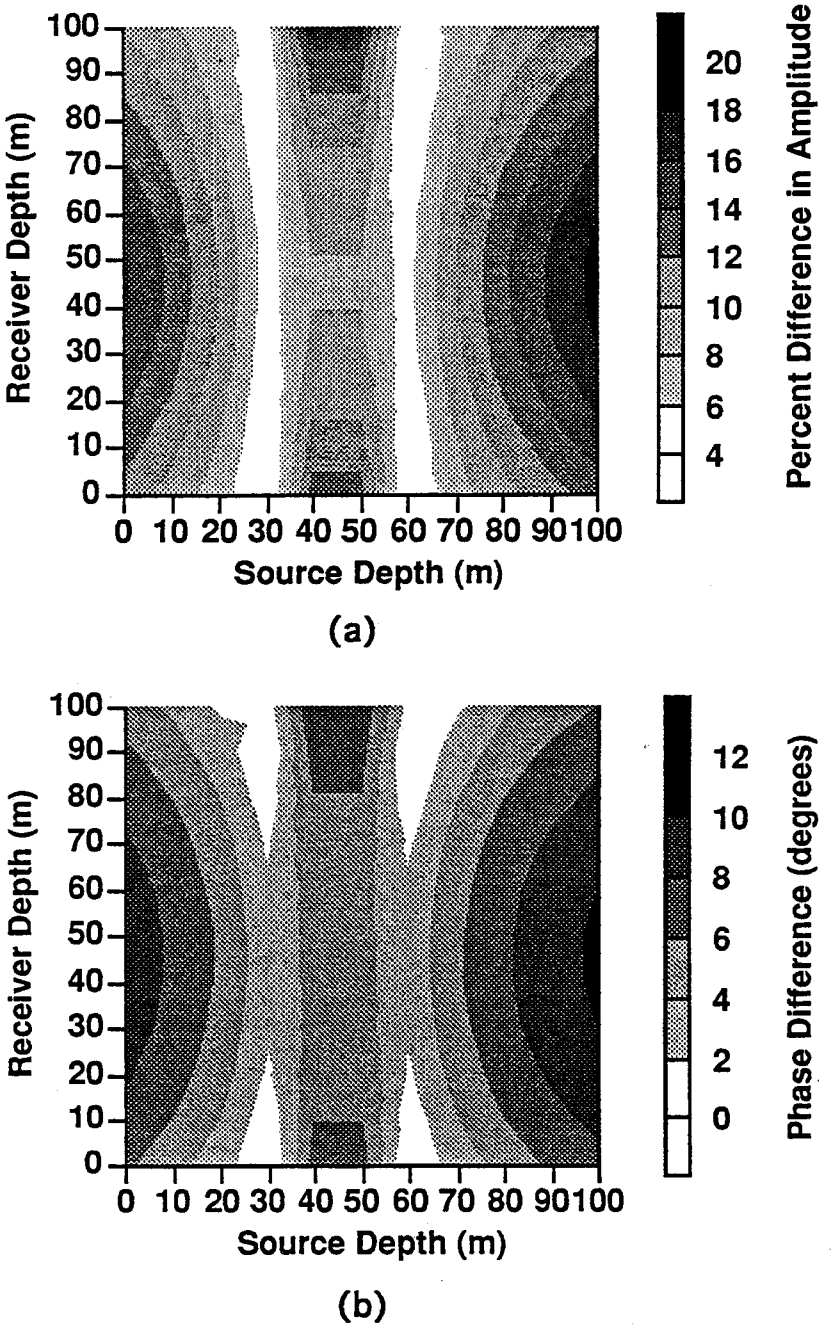

Figure 3.24 - Misfit error in the scattered vertical magnetic field between the 3D thin sheet solution (Zhou,1989) and the 2D integral equation solution employing the Born series approximation for the center of the sheet at xc =20m and a frequency of 100 kHz. The errors have been plotted as a function of source and receiver location. (a) Amplitude misfit in percentage of the thin sheet amplitude. (b)Phase difference.

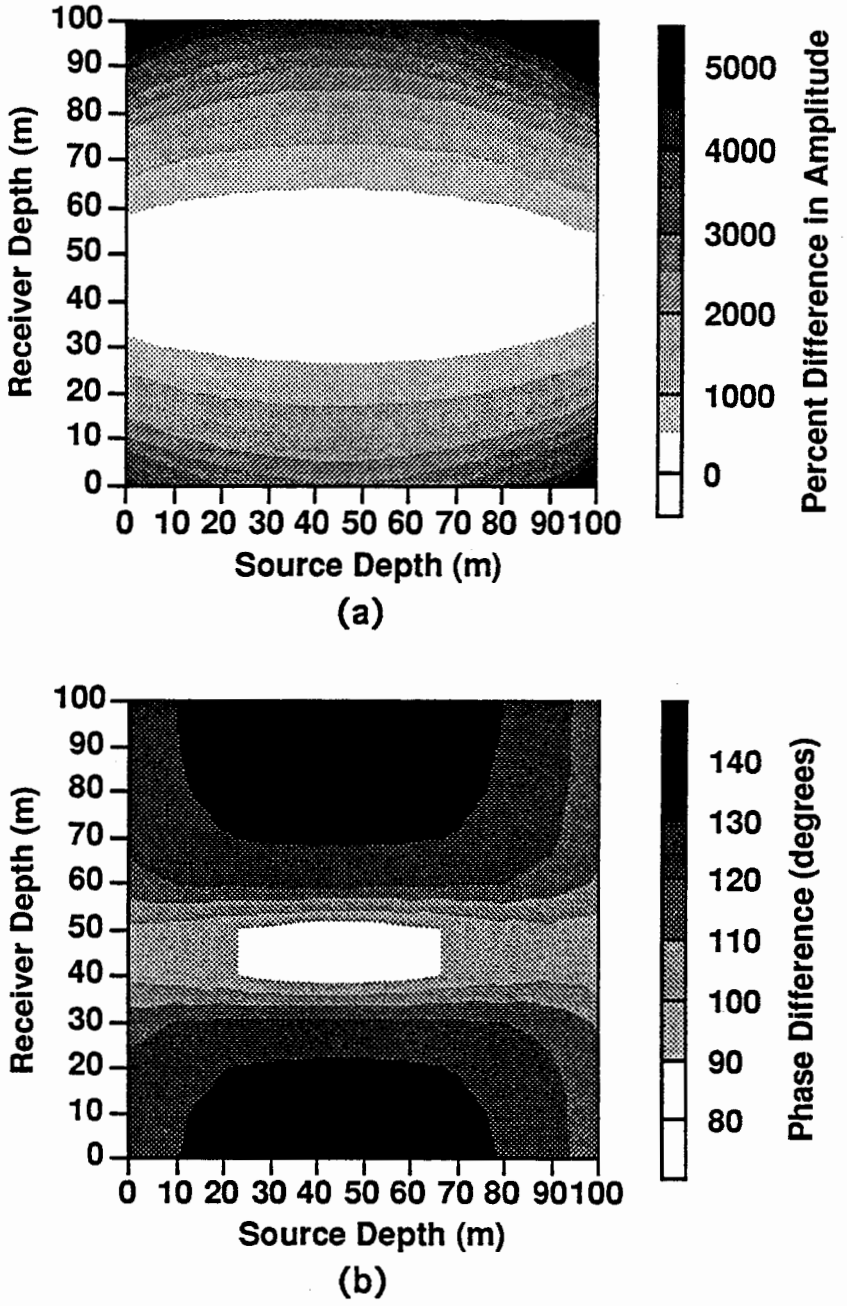

Figure 3.25 - Misfit error in the scattered vertical magnetic field between the 3D thin sheet solution (Zhou,1989) and the 2D integral equation solution employing the Born series approximation for the center of the sheet at xc =100m and a frequency of 1 kHz. The errors have been plotted as a function of source and receiver location. (a) Amplitude misfit in percentage of the thin sheet amplitude. (b)Phase difference.

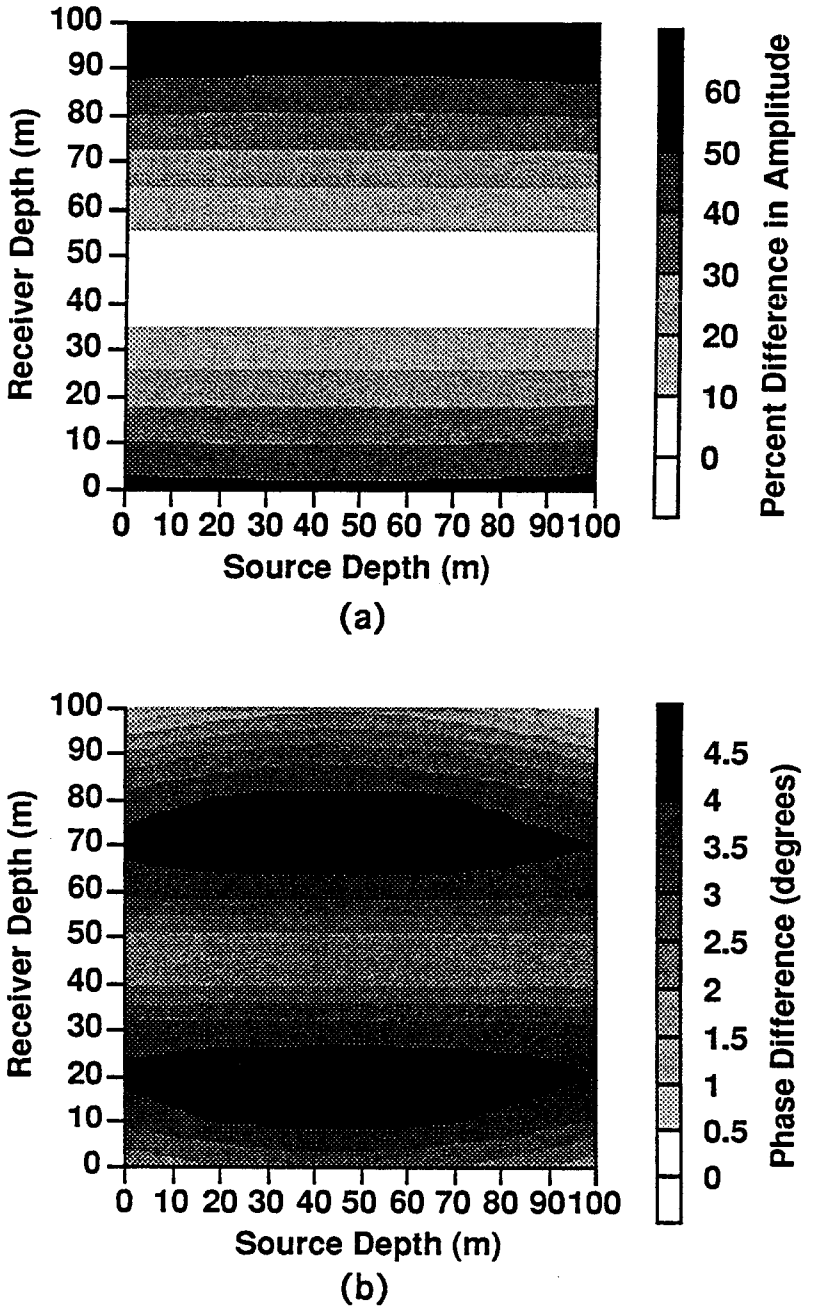

Figure 3.26 - Misfit error in the scattered vertical magnetic field between the 3D thin sheet solution (Zhou,1989) and the 2D integral equation solution employing the Born series approximation for the center of the sheet at xc =100m and a frequency of 100 kHz. The errors have been plotted as a function of source and receiver location. (a) Amplitude misfit in percentage of the thin sheet amplitude. (b)Phase difference.

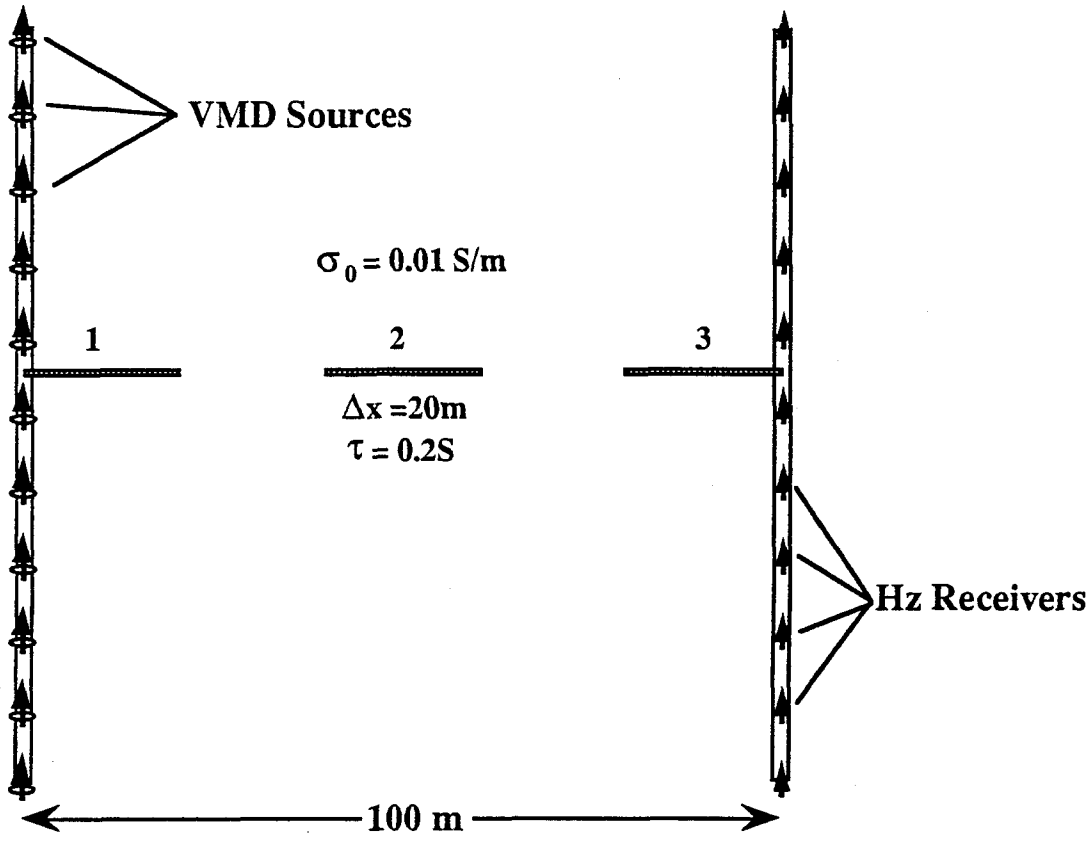

Figure 3.27 - Models used to compare the 2D cylindrical solution to the 2 1/2D solution. The thin sheets extend out of the page 150m in both directions. Two 100m deep wells are separated by 100m in a 0.01 S/m whole space. The two wells contain 11 sources and receivers spaced at 10m intervals. The sheets have been discretized into 3.3m by 6.6m cells and the scattered vertical magnetic fields calculated for each source-receiver pair. For the cylindrically symmetric models, rings of conductivity were discreetized into 0.5m by 0.5m cells.

Chapter 4
Electromagnetic Conductivity Imaging using an Iterative Born Approach

Electromagnetic imaging refers to the process of directly converting measured electromagnetic fields to a spatial distribution of electrical conductivity. Ideally this process takes place without the involvement of any a priori model. The results are then presented graphically to yield an image or picture of the distribution for visual interpretation by the eye.

Most of the previous research involved frequencies greater than 1 MHz because of the similarity between high frequency electromagnetic (HFEM) wave propagation in dielectrics and seismic propagation in acoustic media (e.g. Howard et al., 1983, Laine, 1987, Habashy and Mittra, 1987 and Sena and Toksoz, 1990). This similarity allows techniques which have previously been developed for seismic analysis to be applied to interpretation of the electrical structure of the earth. Unfortunately, because electrically conductive media are highly attenuating, good results can only be obtained when the background is extremely resistive or the boreholes are extremely close together. In many cases these requirements render HFEM methods impractical.

In order to propagate electromagnetic energy tens to hundreds of meters through conductive rocks, frequencies lower than 100 kHz must be employed. At these frequencies the EM fields act in a diffusive rather than a wave like manner. Zhou (1988) and Zhou et al. (1992) showed that a diffusion analog of seismic diffraction tomography (Devany, 1984, Wu and Toksoz, 1987) can be developed for these lower frequency fields by applying either the Born or the Rytov approximation. Although the resulting images recover the geometry of the heterogeneities remarkably well, it was demonstrated in previous chapters that for the Born approximation to be valid the scattering region (i.e. the induction number of the body) must be *electrically small* . Unfortunately in the earth this condition is often violated.

In order to account for greater conductivity perturbations, larger scattering bodies, and higher operating frequencies, an iterative Born inversion technique can be used. In this type of scheme the total electric fields in the medium are calculated at each iteration with some type of forward modeling. Chew and Chuang (1984) propose an *iterative distorted Born* approach to invert for a one dimensional profile using either a point or line source. In this approach the unperturbed field values in a background medium of anomalous electric conductivity and dielectric are used (Kong, 1975), i.e., the Green's functions used to calculate the primary field are altered. Habashy et al. (1986) apply this technique to a dipole source and a receiver in the same hole to recover the radially varying profile

parameters. Sena and Toksoz (1990) propose an iterative Born approach which doesn't alter the Green's function to simultaneously recover the conductivity and dielectric from cross well data in radially varying media. Unfortunately though all of these cases assume either a 1-D or 2-D cylindrical geometry, they all employ frequencies greater than 1 MHz.

The first published use of the an iterative Born inversion in the audio frequency range is given in Barthes and Vasseur (1978) who apply it as the first step in an iterative scheme to recover the conductance of a thin sheet imbedded in a layered half-space. More recently similar methods have been developed for the low frequency cross-well case. Newman (1992b) employs full 3-D modeling at each iteration to update the internal electric fields. Although the forward calculations are robust, the overall inversion process is extremely time and memory intensive. A much quicker method employing the second term in the Born series is developed by Alumbaugh and Morrison (1993). Unfortunately the simplicity of the 'second-order Born approximation' renders the routine only slightly more accurate than the first-order scheme of Zhou et al (1993). Torres-Verdin and Habashy (1993) propose a scheme that utilizes a 'non-linear localized operator' to approximate the electric fields in the medium. This routine not only proves to be time efficient but is also fairly robust at lower frequencies.

In this chapter an electromagnetic conductivity imaging scheme will be developed that employs the Born series approximation developed in Chapter 3 to calculate the electric fields at each iteration. The resolution of the method will be demonstrated as function of the frequency and the magnitude of the conductivity perturbation. Layered earth models and data will be examined and a 1-D layered background model is incorporated into the theory. An injection of conductive material at depth will be crudely simulated and the results imaged to determine the usefulness of cross well EM in monitoring the progress of such a process. This same model will be employed to determine the robustness of the imaging scheme by including various amounts of noise. Finally, in the last section the limits of the cylindrically symmetric model will be analyzed by imaging synthetic data calculated for a 3D sheet.

4.1 Formulation of the Iterative Born inversion scheme

The iterative imaging scheme developed in this thesis is essentially a two step process. The first step employs a least squares inversion technique to estimate the anomalous conductivity distribution, while the second step applies forward modeling to calculate the scattered electric fields within the anomalous zone. Because this forward modeling is accomplished using the Born series approximation that was analyzed in Chapter 3, the discussion here will focus on the least squares inversion process. A flow chart of the

imaging algorithm is given in figure 4.1, and periodic references will be made to it for clarification.

Before the imaging process is initiated, only the background conductivity is assumed to be known. Thus the initial image is constructed by employing the first order Born approximation. The discreet, approximate equations for the scattered magnetic fields are given by

$$H_{ri}^{s} = -\sigma_0 \sum_{j=1}^{N} O_j E_{\phi_{ij}}^{p} \int_{j-th\ cell} G_{Hrij} dr_j dz_j \tag{4.1}$$

for the radial or horizontal field and

$$H_{zi}^{s} = -\sigma_0 \sum_{j=1}^{N} O_j E_{\phi_{ij}}^{p} \int_{j-th\ cell} G_{Hrij} dr_j dz_j \tag{4.2}$$

for the vertical field where i designates the i'th source-receiver pair, j designates the j'th cell, and O_j is the object function to be solved for. All of the terms on the right hand side other than O_j are assumed to be known and can be grouped into what was referred to in Chapter 2 as the sensitivity function, i.e.

$$\mathbf{K_H} = \sigma_0 E_\phi^p(\mathbf{r}, \mathbf{r_{tx}}) \mathbf{G_H}(\mathbf{r_{rx}}, \mathbf{r}). \tag{4.3}$$

Integrating over the j'th cell and writing this in discreet form yields

$$k_{ij} = \sigma_0 E_{\phi_{ij}}^{p} \int_{j-th\ cell} G_{H_{ji}} dr_j dz_j . \tag{4.4}$$

Notice that this sensitivity equation can also be thought of as the *weighting* for the j'th pixel and i'th source-receiver combination. Using this formulation for k_{ij} we can write 4.1 and 4.2 as

$$d_i = \sum_{j=1}^{N} k_{ij} O_j \tag{4.5}$$

where now d_i is the measured scattered field data for i'th source-receiver pair. Rewriting this in matrix form yields

$$\mathbf{D} = \mathbf{KO'} \tag{4.6}$$

where **D** is an M element vector of the measurements, **K** is the N by M sensitivity or weighting matrix relating the geometry of the model to the transmitter-receiver positions, and **O'** is an N element solution vector. We can solve this set of linear equations for **O'** by a least squares method in which we minimize the squared error function defined as

$$s(\mathbf{O}') = \|\mathbf{K}\mathbf{O}' - \mathbf{D}\|^2 . \tag{4.7}$$

The scheme employed to do this is discussed more fully below.

Because the sensitivity matrix is initially calculated using the first order Born approximation, solving for $\mathbf{O}'$ using yields a first order image of the conductivity distribution. To improve on this solution, the scattered electric field generated by $\mathbf{O}'$ is calculated and included with the primary field in expression (4.4) to provide a better estimate of the total electric field. Thus the updated form of k_{ij} is given by

$$k_{ij} = \sigma_0 (E\phi^p_{ij} + E\phi^s_{ij}) \int_{j-th\ cell} G_{H_{ji}} dr_j dz_j \tag{4.8}$$

where $E\phi^s_{ij}$ are the secondary electric fields calculated using the Born series approximation given in Equations (3.24) through (3.26).

After the total electric fields have been determined for the region containing $\mathbf{O}'$, the magnetic fields generated by them are calculated for each source-receiver combination and the *mean residual error* is determined. This error is defined by the expression

$$\mathrm{Er(n)} = \frac{\sqrt{\sum_{i=1}^{n} (d_i - m_i)^2}}{n} \tag{4.9}$$

where d_i is the i'th data point, m_i is the magnetic field that is calculated from $\mathbf{O}'$for the i'th source-receiver pair, and n is the number of data points. If Er(n) is equal to or less than some predetermined noise level, then the scheme is terminated. However if the error is greater than the noise level, then the whole process (equations 4.5 through 4.9) repeated iteratively until Er(n) either approaches the estimated noise level or converges to a minimum.

4.4.1 The smoothest least squares inversion technique

Unfortunately, the inversion of electromagnetic data is generally non-unique. The problem is further complicated by the presence of noise in the data which can cause the inversion process to become unstable and oscillations appear in the solution. To solve for the conductivity structure ($\mathbf{O}'$) while reducing uncertainties and instabilities in the solution, the inversion needs to be *regularized* (Tikhonov and Arsenin,1977) which results in a smooth rather than oscillatory image of the object function. The method employed here minimizes the error function

$$s(\mathbf{O}') = \|\mathbf{K}\mathbf{O}' - \mathbf{D}\|^2 + \lambda_h \|\mathbf{A}_h \mathbf{O}'\|^2 + \lambda_v \|\mathbf{A}_v \mathbf{O}'\|^2 \qquad (4.10)$$

where $\mathbf{A}_h$ and $\mathbf{A}_v$ are matrices representing a discretization of the first derivative in the horizontal and vertical directions, respectively, and the λ's are the associated Lagrangian multipliers which control the degree of smoothness.

The greater the λ's are in equation (4.10) the smoother the resulting image will be. Unfortunately the choice of what value to use for λ is not an exact science. Too small a value for λ will result in an image that has good resolution but may contain oscillations. Because the earth is in general smoothly varying, a high resolution image containing sharp boundaries and rapidly varying conductivities may be an unreasonable representation of the structure. On the other hand if the value for λ is too large then the solution will be unreasonably smooth resulting in lower resolution than is provided by the data. An image which is too smooth will be evident from the relatively large magnitude of Er(n).

In order to balance these two extremes a *smoothest inversion* technique similar to that used by Constable, et al (1987), Park and Van (1991) and Sena and Toksoz (1990) is employed. In this type of inversion λ is relatively large for the first iteration which assures both a very smooth solution and a mean residual error (Er(n)) that is greater than the estimated noise level. At each successive iteration λ is decreased which provides for greater resolution and also a smaller Er(n). The process is continued until Er(n) either approaches the estimated noise level or reaches a minimum value. At this point the iterative scheme is terminated because if it were to continue, noise would be controlling the added resolution.

Imaging the data in this manner provides the choice of the smoothest model which best fits the data to the accuracy with which it was measured. However, unlike for the schemes discussed in the references above, here λ is not determined by s ($\mathbf{O}'$) or some eigenvalue criterion. Rather λ is decreased at each iteration by a constant amount which insures that the resolution is continually improving while the smoothest model is not overshot (Torres-Verdin, 1993, personnel communication).

The above regularization process greatly enhances the stability of the inversion. However the solution can be further stabilized by solving (4.10) subject to the constraints

$$L_i < O'_i < U_i \qquad i=1, 2, \ldots, N. \qquad (4.11)$$

where Li and Ui are the lower and upper bounds of the solution, respectively. These bounds help to enhance solution stability and resolution greatly (Stark, 1987), ensure a

reasonable solution, and for the cross well imaging case can easily be derived from borehole logs.

Because of the ease with which the quadratic programming technique (Gill et al. ,1981, Lawson and Hanson, 1974) handles linear bounding constraints, this method has been chosen as the least squares inversion scheme to solve for a best fitting solution. To get the least square error functional into quadratic form ,equation (4.10) must first be expanded which yields

$$s(\mathbf{O}') = \mathbf{O}'^T(\mathbf{K}^T\mathbf{K} + \lambda_h\mathbf{A}_h^T\mathbf{A}_h + \lambda_v\mathbf{A}_v^T\mathbf{A}_v)\mathbf{O}' - 2\mathbf{D}^T\mathbf{K}^T\mathbf{O}'^T + 2\mathbf{D}^T\mathbf{D} \qquad (4.12)$$

where $\mathbf{A}_h^T\mathbf{A}_h$ and $\mathbf{A}_v^T\mathbf{A}_v$ are the smoothing matrices which are more fully defined in Appendix A. Because the last term on the right hand side is not dependent on the object function, it can be moved to the left hand side such that

$$s(\mathbf{O}') - 2\mathbf{D}^T\mathbf{D} = \mathbf{O}'^T(\mathbf{K}^T\mathbf{K} + \lambda_h\mathbf{A}_h^T\mathbf{A}_h + \lambda_v\mathbf{A}_v^T\mathbf{A}_v)\mathbf{O}' - 2\mathbf{D}^T\mathbf{K}^T\mathbf{O}'^T. \qquad (4.13)$$

Solving for an $\mathbf{O}'$ that minimizes this expression subject to the linear bounding constraints given above constitutes the quadratic programming problem. The particular subroutine employed here is VE04A in the HARWELL mathematical program library (Hopper, 1979).

4.2 Image resolution of the Iterative Born imaging scheme

One of the most important properties of any imaging system is its *resolving power* or *resolution* , i.e., how well can it form distinct images of adjacent features in the medium that is being probed. For example in seismic imaging the resolution is defined by Raleigh quarter-wavelength criterion (Sherrif and Geldart, 1981). Two neighboring bodies will be imaged as separate objects as long as this criterion is met. Because no comparable measure has yet been formulated for the audio frequency EM method, Zhou et al. (1993) and Alumbaugh and Morrison (1993) employed models that consist of two single cells separated by some distance L. Though the models are fairly subjective and unrealistic, the resolution can be defined by how well the method images the two separate bodies with respect to their separation and the operating frequency.

This type of analysis will be incorporated in this section. However, in addition to defining the resolution in terms of frequency and separation, the difference between horizontal and vertical resolution will be examined as will the effect of the conductivity contrast. An improvement in resolution through a data weighting scheme will be

attempted, and the consequences of noise determined. The end result of this analysis will be a general description of the imaging characteristics for cross well EM with respect to this range of parameters, and in particular the iterative Born scheme developed here.

The general model configuration used in this section is shown in Figure 4.2. The 200 m deep wells are separated by 100 m in a 0.01 S/m whole space with 21 sources and 21 receivers spaced at 10 m intervals. This yields a vertical magnetic field measurement for a total of 441 source - receiver combinations. To save computing time, the imaging region was limited to one-half of the area between the wells and the anomalous conductivity distribution is located near the center of this zone. The frequencies employed are 1 kHz, 10 kHz and 100 kHz which correspond to the low induction number side of the Born kernel (Figure 2.3), the peak of the kernel, and the high induction number side of the kernel peak , respectively.

In most of the examples given below the scattering bodies are more conductive than the background medium. Thus except in the examples where it is explicitly noted, *positivity constraints* have been imposed upon the solution. These constraints imply that the solution must always be more conductive than the background. As mentioned in section 4.1 these types of constraints ensure both maximum resolution and stability in the imaging process.

In any experiment the measured data will always contain some type of noise. In the cross well experiments discussed below, the magnitude of the measured total field falls off with increasing source-receiver separation. Assuming that the noise is a function of the dynamic range of the system implies that the noise-to-signal ratio will be smallest when the source and receiver are at the same depth and the signal is strong, and it will become progressively greater as the source and receiver are moved further apart. To incorporate this phenomena into the analysis presented here, random Gaussian noise with a variance that is some percentage of the maximum total field amplitude at that frequency has been added to the synthetic data. In this section the variance of the noise is 0.001% of the maximum total field amplitude unless otherwise noted. Although this may seem to be an unreasonably small magnitude for the noise, it was needed due to the small amplitude of the scattered fields at 1 kHz for the models examined below.

In order to statistically compare one image to another, two different values will be calculated. The first is the mean residual error (Er(n) in Figure 4.1) which is described in Equation 4.9 above. This value describes how well the data fits the image and determines when the iterative Born inversion is terminated. To describe how well the image recovers the input model used to calculate the synthetic data, the *total model error* (TME) is also computed. This value is defined here to be the χ^2 error between the final image and the model over all the cells in the imaging region. After the χ^2 error is calculated it is

normalized by the integral over the perturbations from the background conductivity in the input model such that the final form is given by

$$TME = \frac{\sum_{i=1}^{N}\left(\sigma_i^{Im} - \sigma_i^{Mod}\right)^2}{\sum_{i=1}^{N}\left(\sigma_i^{Mod} - \sigma_0\right)^2} \tag{4.14}$$

where σ_i^{Im} is the image conductivity for the i'th cell, σ_i^{Mod} is the model conductivity for the i'th cell and N is the number of cells or pixels in the image. It must be pointed out that although this total model error may be a statistically sound description of the image, its definition of image quality does not always coincide with the visual definition, and thus it must be used with caution. Examples of where it could be considered to fail will be given below.

4.2.1 Image resolution versus frequency for low contrast models

In this section the horizontal and vertical resolution will be analyzed in terms of the operating frequency. Figure 4.3a shows the first model which will be referred to as the *low contrast-vertical resolution* model. Two 5m by 5m square bodies are located near the center of the interwell region and are separated by L=25m. The conductivity of the bodies is 0.02 S/m which is twice that of the background. Note, the polygonal shape of the two bodies in Figure 4.3a is a function of the software used to plot the images (DeltaGraph Professional for MacIntosh, 1991). Because the software automatically smoothes between adjacent points using a spline, single celled bodies are distorted into this polygonal shape. This distortion becomes less of a problem as more cells are added to the anomalous bodies.

Figures 4.3b through 4.3d yield valuable information about the vertical resolution of the method. At 1 kHz the two bodies are not separately defined and the conductivity is not recovered. This is due to the small magnitude of the scattered fields which in general are less than 0.1% of the total field. Because of these relatively insignificant values, the residual error between the calculated image results and the input data rapidly converges to the noise level. In contrast to this low frequency result, the images at 10 kHz and 100 kHz are quite sharp and precisely define the location of the two bodies. Though the difference is difficult to visually detect, the total model error indicates that the 100 kHz image is statistically better than the 10 kHz result. Thus at least for this low contrast example, the resolution increases with frequency.

In Figure 4.4 the horizontal resolution is examined for the low contrast case. Once again the lowest frequency exhibits poor resolution due to the small magnitude of the

scattered fields. For this example the 1 kHz secondary fields at maximum are no more than 0.2% of the total field. At 10 kHz the resolution is excellent with the position of the two cells recovered exactly. However notice that the TME is approximately twice that of the value for the low contrast-vertical example. This is a statistical affirmation that, because the measurements are made in vertical boreholes on each side of rather than all around the anomalous region, the horizontal resolution in worse than the vertical resolution. This same conclusion falls out of the wave number domain analysis by Zhou, et al. (1993) who show that the horizontal resolution is a function of the vertical coverage of the data.

At 100 kHz the imaging scheme develops problems in uniquely reconstructing the two cells (Figure 4.4d). Instead of resolving two separate bodies most of the conductivity is lumped into the center of the region with "ghosts" appearing on either side. To determine if this is a data sampling problem or an error in the algorithm, several variations of the model were calculated. Images were reconstructed using synthetic data with finer source and receiver sampling intervals to avoid aliasing, with the boreholes extended to provide greater vertical coverage, and with the cell size decreased in the imaging region to avoid numerical problems. Though none of these methods worked, a data weighting scheme discussed in subsection 4.2.3 did show some success. However as it will again be demonstrated below there does exist a loss of resolution at 100 kHz which may be the result of high frequency numerical instabilities.

4.2.2 Image resolution versus frequency for high contrast models

To examine the effects of higher conductivity contrasts on image resolution, the same model geometry shown in Figures 4.3 and 4.4 is employed. However the conductivity of the single cell anomalies is 0.1 S/m which corresponds to a contrast of 10 to 1 or a conductivity difference of 0.09 S/m. Figure 4.5 shows the results for the high contrast-vertical resolution model, and Figure 4.6 the high contrast-horizontal resolution model.

A comparison of the images shown in figures 4.5b and 4.6b to the equivalent images in the previous section (Figures 4.3b and 4.4b) indicates that the horizontal and vertical resolution at 1 kHz has improved both visually and statistically. This is primarily due to the fact that the scattered fields generated by the high contrast model at this frequency are an order of magnitude greater than those for the low contrast model. Thus a less smooth solution is required in order to fit the data to the desired noise level. This demonstrates that resolution is not only a function of the background conductivity, but also of the difference in conductivity between the background and the scatterer.

As demonstrated by Figure 4.5c the vertical resolution at 10 kHz remains approximately the same whether a low or high contrast model is employed. Visually the

same seems to be true for the horizontal resolution. Figure 4.6c distinctly shows the presence of two separate bodies of approximately the correct conductivity and position. However both the mean residual error and the total model error indicate that at least statistically this is a lower quality image. The large errors result from the body on the right hand side being misplaced one position to the left when compared to the model and illustrate the problem of using these statistical properties to define resolution. Unfortunately they do not take into account slight mispositioning errors or differences in amplitude.

At 100 kHz the images for both of the high contrast models (Figures 4.5d and 4.6d) are distorted in the horizontal direction. In addition, the relatively large mean residual errors indicate that the iterative Born scheme is finding it difficult to fit the data to the desired noise level. Because the anomalous induction numbers for these models as defined in Chapter 3 are near the break down point of the Born series approximation, this lack of horizontal resolution may be due to inaccurate forward modeling. Another possible source of instability is the inductive coupling between the two bodies which becomes larger as the conductivity and frequency increase. This mutual coupling may make it difficult for the imaging routine to distinguish the two separate bodies.

4.2.3 A data weighting scheme to improve horizontal resolution

As mentioned in section 4.2.1 several attempts were made to improve the horizontal resolution at 100 kHz for the low contrast - horizontal resolution model (Figure 4.4d). One possible source of error can be directly observed in the data amplitudes. From minimum to maximum source - receiver offsets these values change over five orders of magnitude. In Chapter 2 it was demonstrated that the horizontal resolution is controlled by the long offset data, i.e. when the source and receiver are separated by a large vertical distance. Thus because the data controlling the horizontal resolution are five orders of magnitude smaller than the near offset data, the inversion process is dominated by the larger values and thus has difficulty correctly recovering the horizontal position of the bodies. This effect is not as evident at lower frequencies because the fields do not fall off as quickly with increasing source-receiver separation.

The solution to this problem is to weight each source-receiver combination equally, that is, give each datum the same importance. Two simple methods of accomplishing this are to normalize the scattered fields by either the theoretical primary (background) field , or the measured total field. The advantage of using the total field is that it contains measurement noise. Thus normalizing by this value will not weight the noise present in the long offset data to the degree that the theoretical primary field does (Torres-Verdin,1993,personnel

communication).

The results of weighting the data at 100 kHz for the low contrast-horizontal resolution model (Figure 4.4a) are shown in Figure 4.7. In these examples no random noise was added to the data for reasons that will be evident shortly. Though the resolution is not of the quality that exists in the 10 kHz results (Figure 4.4c), these images certainly show improvement over the unweighted results given in Figure 4.4d. Applying the same weighting to the 100 kHz data in both of the high contrast models given in the last section improved the image quality somewhat. However there was not enough improvement to warrant showing the results here which again suggests the existence of some type of high frequency numerical instability.

A major concern when weighting the data in this manner is that the process also weights upward the noise that is in the long offset data. Thus when the noise is comparable to or larger than the signal, the weighting will have negative effects. This is illustrated in Figure 4.8 where 0.01% random noise has been added to the synthetic data. Without any normalization the noise has little effect on the resulting image (Figure 4.8a) . However Figures 4.8b and 4.8c show that by emphasizing the noise at large offsets serious image degradation results. As shown in Figure 4.9 the scheme can not converge to a reasonable solution as is illustrated by plotting the mean data error at each iteration.

To this point the image resolution of the iterative Born scheme has been demonstrated in terms of different operating frequencies and conductivity contrasts. Lower frequencies do not yield very good resolution simply because the scattered fields are very small. High frequencies offer the best results in some cases, but due to severe attenuation much of the data which contains the horizontal resolution information is unusable. In addition at high frequencies and conductivity contrasts the scheme exhibits some type of numerical instability which suggests that it is at its induction number limit. The best trade off between image resolution and numerical stability occurs for data collected in the induction number region near the peak of the Born kernel. In all of the examples given above, the 10 kHz images recovered both the conductivity and position of the dual scatterers extremely well. Therefore this frequency alone will be employed in the next section to determine the resolving power of the method with respect to the separation of the two scatterers.

4.2.4 Image resolution with respect to target separation

In this section the resolution will be analyzed with respect to the separation of the bodies. The same general geometries employed in the models above will be used with the operating frequency fixed at 10 kHz.

Figure 4.10 shows the first example which is for the low contrast-vertical resolution

model shown in Figure 4.3. It is clear from these images that the vertical resolution is excellent both visually and statistically for low contrast anomalies. Even when the two bodies are only one cell width apart, i.e. when the center-to-center separation 'L' is 10m, the image shows two separate maxima in the right locations separated by a lower conductivity region. Comparing these results to the high contrast examples (Figure 4.11) indicates that a greater conductivity contrast results in lower resolution. In these examples the imaging scheme is unable to properly determine the correct position of the anomalies when L=15m, and for L=10 m the conductivity is all lumped together at the center point between the two cells. Because of the cylindrical symmetry imposed upon the problem the two bodies can be thought of as rings or loops about the source axis. The loss in resolution for this high contrast model may be the result of increased mutual coupling between the two loops as they are brought closer together.

The horizontal resolution is also examined as a function of scatterer separation. As was demonstrated in Sections 4.2.1 and 4.2.2 the resolution is worse in this direction compared to that in the vertical. Figure 4.12 indicates that for the low contrast-horizontal resolution case the two separate bodies are not defined even for L=15 m while for L=10 the conductivity pattern is reconstructed as a single blob at the center of the imaging region. Although the horizontal resolution seems to improve visually with increasing conductivity contrast, statistically the results shown in Figure 4.13 are worse that those in Figure 4.12. Thus once again there is disagreement between the visual and statistical descriptions of image quality.

In this section the resolution as a function of target separation has been demonstrated. The vertical resolution has again been demonstrated to be better than the horizontal resolution for lower conductivity contrasts. In some cases larger conductivity contrasts seem to degrade image quality while in others the resolution seems to improve. Because all of the examples to this point have dealt with electrically conductive anomalies, a model containing both resistive and conductive bodies will be examined before moving on to more realistic models.

4.2.5 Resolution of adjacent conductors and resistors

A more difficult model to reconstruct is shown in Figure 4.14a. Two blocks of identical geometrical dimensions but of opposite conductivity contrast with respect to the background are separated by 10m in a 0.01S/m medium. Because of the size of the blocks, the scattered magnetic fields generated by them are almost an order of magnitude greater than those produced by the single cell anomalies presented in previous sections. Thus the random noise added to the synthetic data has been increased to 0.01% of the maximum total

the source and receiver are at the same depth. Because these sensitivity functions describe the weighting of points within the medium in relation to each other, those points at which the sensitivity is large will have more importance in the inversion process. Thus not only does the manner in which the data are weighted have to be considered with respect to resolution and noise, but the method in which the model cells are weighted must be understood in order to properly interpret the final image.

In Section 3.4 the benefit of plotting the error between the 1-D solution and the 2-D Born series approximation as a function of source and receiver depth was demonstrated. If geometrical patterns appear in these error plots then some type numerical problem exists in the 2-D cylindrical model. The major source of error in simulating 1-D media was determined to be edge effects caused by terminating the mesh too close to the receiver borehole rather than extending it horizontally outward. The same type of analysis is provided here to verify that none of these types of errors exist in the imaging process.

In Figure 4.17 the amplitude errors between the synthetic input data and the image results (Figure 4.16) calculated with the Born series approximation have been plotted. For both 1 kHz and 10 kHz the errors are randomly distributed as a function of source and receiver position. This verifies that the mesh extends far enough horizontally to eliminate any edge effects. This type of analysis will be applied in future sections to determine whether the data being reconstructed is of 2-D or 3-D origin.

In Figure 4.18 the resolution of a resistive layer is examined. Again the model consists of a single layer, however the conductivity in this case is ten times less than that of the background. To provide maximum stability and resolution in the solution for this particular model, negativity constraints have been imposed on the object function which requires the anomalous conductivity to be less than that of the background.

At 1 kHz (Figure 4.18b) the image is again very smooth and lacks spatial resolution of the layer boundaries. In fact it would be difficult to determine from this result that a layered structure exists. At 10 kHz the resolution is again much better (Figure 4.18c). However the similarity between the maxima within the layer and the sensitivity functions described in Chapter 2 still exist. A method to remedy this problem is demonstrated in the next subsection.

4.3.2 Imaging with the horizontal magnetic field

In section 2.4.3 it was determined from a cross-well sensitivity analysis that at frequencies on the low induction number side of the Born kernel, the horizontal field contains additional information that is not provided by the vertical field. To determine the benefits of measuring both the radial and vertical components, the horizontal magnetic

fields have been calculated for the model shown in Figure 4.16a. Images have been reconstructed using this component exclusively as well as both components simultaneously. Plots of the residual errors between the input data and the calculated image results have not been included here because they exhibit the same random nature as shown in Figure 4.17.

As Figure 4.19a shows there is a definite improvement in image quality at 1 kHz using the horizontal rather than the vertical fields. Comparing this image to that in Figure 4.16b demonstrates that the vertical boundaries of the layer are much better defined and the conductivity is more accurately recovered . These results agree well with the sensitivity analysis performed in Chapter 2 where a comparison between the horizontal and vertical fields indicated that the horizontal component is less sensitive to the region outside of the wells and more sensitive to the vertical position of a body. However the greater magnitude of the scattered horizontal fields when compared to the scattered vertical fields is at least partially responsible for this increase in resolution. Because of these larger magnitudes the radial component is less susceptible to measurement noise, and thus less smoothing is required for the inversion scheme to converge to the desired residual error. This difference in magnitude of the two different scattered field components becomes more apparent when both the horizontal and vertical fields are employed simultaneously. Figure 4.19b shows that only minor differences exists between it and Figure 4.19a suggesting that the radial component is dominating the inversion process.

Though the sensitivity analysis in Chapter 2 did show some differences between the horizontal (Figure 2.15) and vertical (Figure 2.8) components of the magnetic field at 10 kHz, they were not as large as those at 1 kHz. This becomes apparent when comparing the image reconstructed from the 10 kHz horizontal fields (Figure 4.19c) to that resulting from the inversion of the vertical fields (Figure 4.16c). Subtle differences, such as the different locations of the maxima within the conductive layer, do exist between the two images, but in general the two images have very similar characteristics. However as shown in Figure 4.19d imaging with both components simultaneously yields quite spectacular results. Rather than reconstructing a high conductivity zone with localized maxima, the scheme has reconstructed a layer in which the high conductivity region extends horizontally across the whole image. The only conductivity gradients that exists occur in the vertical direction. Thus it can be implied that by using both components each pixel between the two wells is being weighted equally. Unfortunately, because no horizontal component data have been collected in any of the crosswell experiments to date, the routine incorporation of this component will be left for now as a topic for future research.

4.3.3 Imaging of data collected at the Devine test site

Since 1989 researchers from Lawrence Berkeley Laboratory, Lawrence Livermore National Lab and U.C. Berkeley have jointly been involved in the development of a cross well EM system. The initial field test of this system was conducted in September of 1990 at British Petroleum's Devine test site near Devine, Texas (Wilt, et al., 1991). The purpose of the test was to prove system viability by collecting a set of cross well data that was repeatable to 1%. In this section the iterative Born imaging scheme will be applied to these data and the resulting images analyzed in terms of resolution and data quality.

The Devine site was chosen as a system testing ground primarily because of the simple 1-D layered geology that exists there as well as the general lack of cultural noise (Wilt et al. ,1991). The subsurface consists of flat lying, alternating layers of sand, shale and limestone which can be correlated from one well log to another. A conductivity log from a well surveyed in the experiment is given in Figure 4.20. The low conductivity zone that extends from approximately 600 to 630m depth consists of limestone, and it is this layer that was selected to be the target of the experiment.

The cross well EM survey was conducted at an operating frequency of 512 Hz between two PVC cased wells separated by 100m . While the receiver was held in a fixed position the source was slowly raised upward from a depth of 670m to 550m. Measurements were made at approximately 0.9m source intervals yielding a nearly continuous profile of data versus source depth. The receiver was then moved to a new position and the process repeated. This resulted in a data set consisting of 128 source locations for each of the 13 receiver depths shown in Figure 4.20.

An initial interpretation of the data was accomplished by fitting a layered earth model to the data in a least squares sense (Deszcz Pan ,1993). The resulting eight layer model for one of the receiver profiles is plotted with the conductivity well log in Figure 4.20. In addition the same least squares program was used to determine the best fitting whole space conductivity , which was found to be 0.35S/m (Deszcz Pan, personnel communication). Employing this value with an operating frequency of 512 Hz yields a background induction number of 14. Comparing this to Born kernel plotted in Figure 2.3 indicates that the system is operating near the peak in sensitivity which should provide for both image resolution and numerical stability. Thus this data set should provide an excellent test for the iterative Born inversion scheme presented here.

Due to computer limitations only half of the data (64 source by 13 receiver combinations) were employed in the imaging process. Because the measurements were made of the total vertical magnetic field, the scattered field data required by the iterative Born scheme were again calculated by subtracting the theoretical primary fields that would

exist in a whole space with a conductivity of 0.35S/m. Note that although these primary fields were calculated using the same analytic expression as employed in Section 4.3.1, here the background conductivity was unknown and thus an average or best fitting background conductivity had to be determined prior to applying the imaging scheme. The mesh was constructed from 800 5m by 5m cells extending vertically from 510m to 710m, and horizontally from 0 to 150m. A lower bounding constraint of 0.1 S/m was imposed upon the solution, and the noise was estimated from measurements of repeatability to be approximately 0.5% to 1% of the maximum field amplitude(Wilt, et al, 1991).

The results of the Devine data inversion after 4 and 6 iterations of the iterative Born scheme are plotted in Figure 4.21. Smoothed versions of the conductivity log (Figure 4.20) have been included next to each of the cross well images for comparison. Not only has the scheme defined the existence of the resistive zone between the more conductive layers, but the general trend is suggestive of a 1-D structure. Considering that the iterative Born imaging scheme is derived from theory which assumes small isolated scatterers rather than large slab like bodies, these results can be considered to be very good.

There do however exist serious deviations from the layered conductivity structure exhibited in the smoothed well log. The resistive zone is thicker near the receiver borehole while the conductive layers are imaged as maxima near the source well. To determine if these deviations from layered structure are due to poor quality data, limitations of the imaging scheme, or a combination of the two, synthetic results were calculated for the eight layer model shown in Figure 4.20 using the same source and receiver depths as the data. The imaging scheme was then applied to these synthetic data with 0.5% noise added.

The resulting images after 4 and 6 iterations have been plotted in Figure 4.22 along with the eight layer model. Comparison of these results to Figure 4.21 indicates that although the same general structure is recovered, the synthetic data images are more suggestive of a layered medium. The resistive zone exhibits a fairly constant thickness across the region between the boreholes and the conductivity maxima above and below this zone are not as prominent as in the image of the real data. Because the geology at the site is known to be 1-D, these results suggested that the noise in the field data may not be random but rather is correlated and have a magnitude greater than 1.0%.

To determine the characteristics of the noise present in the Devine data, both the ratio in total field amplitude and the phase difference between the field data and theoretical results have been calculated. Figure 4.23 shows the results plotted for each receiver position as a function of source depth. For the profiles with the receiver above 602m in depth, the amplitude ratio remains fairly constant at about 0.95 to 0.97. However for receiver depths greater than 617m this ratio is approximately 1.0. A similar change is apparent in Figure

4.23b with the mean phase difference decreasing with increasing receiver depth. Because the fields in a layered medium exhibit reciprocity with respect to source and receiver depth, and because the mean error between the real and synthetic data changes in a logical progression as a function of receiver depth, it is evident that a systematic drift occurred over time which was not accounted for.

To verify that this drift could cause the non-one dimensional distortions that are present in the images given in Figure 4.21, each receiver profile of the data was corrected with the mean amplitude and phase errors between the data and the layered model. After the corrections in Table 4.1 had been applied a second attempt was made to image the data. Though the "corrected" images in Figure 4.24 are not identical to the model images given in Figure 4.22, they are a significant improvement over the originals shown in Figure 4.23. Thus it can be concluded that a serious a drift error exists in the Devine data which needs to be removed in order to meet the initial data quality standards of 1%.

Receiver Depth (m)	Amplitude Correction	Phase Correction (Deg)
564	1.06	5.7
571	1.05	5.2
579	1.04	4.3
586	1.04	3.2
594	1.05	3.6
602	1.04	1.6
609	1.03	1.5
617	1.02	1.6
625	1.01	1.3
632	1.00	0.8
640	1.00	0.3
647	1.00	0.4
655	1.00	-0.6

Table 4.1 - Corrections applied to the Devine data set for each reciver profile.

To determine if the residual errors between the input data and the calculated results for the image could be used to detect this drift, the errors have been plotted as a function of source and receiver depth for both the original and corrected images in Figure 4.25. Notice that for the residuals of the uncorrected data (Figure 4.25a) a large error occurs when both the source and receiver are at approximately 610m depth, i.e., when the two are close to or inside of the resistive zone. This same error distribution does not exist in the corrected data errors (Figure 4.25b). Although certain receiver profiles have larger mean errors than others, the distribution is much more random suggesting that the cylindrical symmetry fits

the data. Thus to a certain degree the lack of data quality is indeed present in the residuals.

In this section we have analyzed the first cross well data set collected with the Lawrence Livermore Laboratory / Lawrence Berkeley Laboratory cross well EM system. A systematic drift has been found in the data which was not accounted for in the calibration phase. Not only does this drift produce distortions in the cross well images, but it is also evident in the plot of the residual errors. In the next section the theory will be developed to account for layered media, and an example of how this could employed in improving the quality of the Devine images will be given.

4.3.4 Theoretical formulation for a 1-D layered background model

To this point the imaging scheme has been formulated assuming that the region of interest is an isolated zone of anomalous conductivity lodged in an otherwise homogenous whole space of conductivity σ_0. This homogenous whole space serves as the background model for which the primary fields and Green's functions are calculated. However there are many instances where a different background model is appropriate. For instance, near the surface of the earth, the earth-air interface causes distortions of the electric field which are not accounted for by a whole space model. Another example which will be considered in the next chapter relates to monitoring reservoir processes in a layered media. In these cases the scattered fields resulting from the layers can dominate the response of the changes caused by the process. In addition the large magnitude of these fields coupled with the fact that the mesh has to be extended horizontally past the receiver well to account for layers causes the routine to need considerably more time to converge than if just the small volume affected by the process was being imaged. These types of problems can sometimes be overcome by incorporating a 1-D layered half space as the background model.

The theoretical formulation for a layered background has been used quite extensively in 3-D integral equation modeling to limit the mesh size and thus reduce the computational time involved (e.g. Wannemaker, et al., 1984, Newman and Hohman, 1988). To formulate the 1-D background model for the 2-D cylindrical geometry being considered here, the impedance concept originally introduced by Wait (1970) for plane waves and later modified for dipoles by Stoyer (1977) and loops by Wait and Hill (1980) will be employed. Because the derivation is fairly lengthy, it is given in Appendix B and only the results are presented here.

The geometry employed is shown in Figure 4.26. The source is either a vertical magnetic dipole, or a horizontal current loop of cross sectional area Δ^2, centered at z=-d, r=0 in layer 0. As before the $\hat{z}$ axis is oriented downwards, with the origin situated directly beneath the source at the base of this layer. N layers are located below the source

and M layers above with n and -m being semi infinite. Each layer is considered homogenous and isotropic with a conductivity of σ_i.

Because of the cylindrical symmetry imposed upon the model, the problem exhibits pure TE excitation which simplifies the theory considerably. The electric fields within the source layer resulting from a vertical magnetic dipole of unit moment can be expressed as the sum of the field that exists in a whole space of conductivity σ_0 and the fields that are reflected by the layer boundaries. The final expression has the form

$$E_\phi^L = E_\phi^P - \frac{i\omega\mu}{4\pi}\int_0^\infty \left[U_0(\lambda)e^{\gamma_0 z_R} + D_0(\lambda)e^{-\gamma_0 z_R}\right] \lambda J_1(\lambda r_R) d\lambda. \qquad (4.15)$$

where E_ϕ^P is the primary electric field given by expression 2.7 , $U_0(\lambda)$ and $D_0(\lambda)$ represent the reflected upgoing and downgoing components which are given by

$$D_0(\lambda) = \frac{\lambda}{\gamma_0} r_{TE}^{-1} e^{-2\gamma_0 h_0} \frac{e^{\gamma_0 d} + r_{TE}^1 e^{-\gamma_0 d}}{1 - r_{TE}^1 r_{TE}^{-1} e^{-2\gamma_0 h_0}} \qquad (4.16)$$

and

$$U_0(\lambda) = \frac{\lambda}{\gamma_0} r_{TE}^1 \frac{e^{-\gamma_0 d} + r_{TE}^{-1} e^{-\gamma_0 (d-2h_0)}}{1 - r_{TE}^1 r_{TE}^{-1} e^{-2\gamma_0 h_0}}, \qquad (4.17)$$

and $\gamma_0^2 = \lambda^2 + k_0^2$. If the source and receiver are located in the upper semi-infinite half space then downgoing component can not exist and thus $D_0(\lambda) = 0$. Similarly if the source layer is the semi-infinite basal half space then $U_0(\lambda) = 0$.

In equations 4.16 .and 4.17, r_{TE}^i represents the reflection coefficients at the i=-1 and i =1 interfaces which are given by

$$r_{TE}^i = \frac{K_0 - Z_i}{K_0 + Z_i} \qquad (4.18)$$

where K_i has the form

$$K_i = \frac{\gamma_i}{\sigma_i} \qquad (4.19)$$

and Z_i is the *input impedance* (Wait,1970) at the i 'th interface. This value is solved for recursively from the n'th layer upward, or the -m'th layer downward, to the interface of interest. For the region below the source layer Z_i is given by

$$Z_i = K_i \frac{Z_{i+1} + K_i \tanh(\gamma_i h_i)}{K_i + Z_{i+1} \tanh(\gamma_i h_i)} \tag{4.20}$$

while above the source layer the expression has the form

$$Z_i = K_i \frac{Z_{i-1} + K_i \tanh(\gamma_i h_i)}{K_i + Z_{i-1} \tanh(\gamma_i h_i)}. \tag{4.21}$$

Expressions 4.15 through 4.17 consider only points within the source layer. If the point lies within a different layer, then the primary field term in Equation 4.15 drops out and the electric field in the i 'th layer has the form

$$E_\phi^L = -\frac{i\omega\mu}{4\pi} \int_0^\infty \left[U_i(\lambda) e^{\gamma_i z_{rx}} + D_i(\lambda) e^{-\gamma_i z_{rx}} \right] \lambda J_1(\lambda r_{rx}) d\lambda. \tag{4.22}$$

For this scenario $U_i(\lambda)$ and $D_i(\lambda)$ must propagated either upward or downward from source layer to the layer of interest. For points below the source layer this is accomplished using

$$D_{i+1}(\lambda) = C_i^+ [D_i(\lambda) + \delta(i) \frac{\lambda}{\gamma_0} e^{-\gamma_0 d}] e^{(\gamma_{i+1} - \gamma_i) z_i} + C_i^- U_i(\lambda) e^{(\gamma_{i+1} + \gamma_i) z_i} \tag{4.23}$$

and

$$U_{i+1}(\lambda) = C_i^- [D_i(\lambda) + \delta(i) \frac{\lambda}{\gamma_0} e^{-\gamma_0 d}] e^{-(\gamma_i - \gamma_{i+1}) z_i} + C_i^+ U_i(\lambda) e^{(\gamma_i - \gamma_{i+1}) z_i} \tag{4.24}$$

where $\delta(i)$ is the Dirac delta function which equals unity for points within the source layer and zero otherwise, and the C 's are given by

$$C_i^\pm = \frac{1}{2} \left[\frac{\sigma_i}{\sigma_{i+1}} \pm \frac{\gamma_i}{\gamma_{i+1}} \right]. \tag{4.25}$$

For propagation to a layer above the source the expressions have the form

$$D_i(\lambda) = T_i^+ D_{i+1}(\lambda) e^{(\gamma_i - \gamma_{i+1}) z_i} + T_i^- [U_{i+1}(\lambda) + \delta(i+1) \frac{\lambda}{\gamma_0} e^{\gamma_0 d}] e^{(\gamma_i + \gamma_{i+1}) z_i} \tag{4.26}$$

and

$$U_i(\lambda) = T_i^- D_{i+1}(\lambda) e^{-(\gamma_i+\gamma_{i+1})z_i} + T_i^+ [U_{i+1}(\lambda) + \delta(i+1)\frac{\lambda}{\gamma_0} e^{\gamma_0 d}] e^{(\gamma_{i+1}-\gamma_i)z_i} \qquad (4.27)$$

where the T' s are given by

$$T_i^{\pm} = \frac{1}{2}\left[\frac{\sigma_{i+1}}{\sigma_i} \pm \frac{\gamma_{i+1}}{\gamma_i}\right]. \qquad (4.28)$$

The magnetic fields generated by the vertical magnetic dipole source can be derived by taking the curl of equations 4.15 through 4.27 with respect to the point of interest. Fortunately, the expressions for $U_i(\lambda)$ and $D_i(\lambda)$ remain the same as given above. The only differences in the formulations for the electric and magnetic fields appear in equations (4.15) and (4.22). Thus the expression for the vertical component of the magnetic field is given by

$$H_z^L = \delta(i) H_z^p + \frac{1}{4\pi}\int_0^{\infty} \left[U_i(\lambda) e^{\gamma_i z_m} + D_i(\lambda) e^{-\gamma_i z_m}\right] \lambda^2 J_0(\lambda r_m) d\lambda \qquad (4.29)$$

while the horizontal component is given as

$$H_r^L = \delta(i) H_r^p - \frac{1}{4\pi}\int_0^{\infty} \left[U_i(\lambda) e^{\gamma_i z_m} + D_i(\lambda) e^{-\gamma_i z_m}\right] \gamma_i \lambda J_1(\lambda r_m) d\lambda \qquad (4.30)$$

In these expressions H_z^p and H_r^p are the primary magnetic fields existing in a whole space of conductivity σ_0 and are given by equation (2.14), and $\delta(i)$ is the Dirac delta function for the source layer.

Similar expressions can be developed for the integrated forms of the Green's functions that were derived in Section 3.1. The electric field Green's function in a layered medium has the form

$$\int_{j^{th}\,cell} G^L = \delta(i)\int_j G(\mathbf{r}_j;\mathbf{r}_k)d\mathbf{r}_j dz_j - \frac{i\omega\mu\pi}{4}\mathrm{sign}(z_2 - z_k)\int_0^\infty \Big[U_i(\lambda)\big[e^{\gamma_i z_2} - e^{\gamma_i z_1}\big] + D_i(\lambda)\big[e^{-\gamma_i z_2} - e^{-\gamma_i z_1}\big]\Big] v(\lambda, r_1, r_2)\frac{J_1(\lambda r_k)}{\lambda\,\gamma_i}d\lambda \qquad (4.31)$$

where i designates the layer containing the point of interest, j indicates the source-cell across which the current is being integrated, k refers the cell containing the point of interest and $V(\lambda, r_1, r_2)$ is calculated using expression (3.9). The first integral on the right hand side of (4.31) represents the whole space term which is evaluated using expression (3.8) if $(z_1 + z_2)/2 = d$, i.e. if the cell is singular, and equation (3.10) otherwise. The expressions for $U_i(\lambda)$ and $D_i(\lambda)$ are almost identical to those given above except they must be evaluated at $d = z_1$ and $d = z_2$ and then differenced to account for the integration in $\hat{\mathbf{z}}$. For example, equation (4.16) becomes

$$D_0(\lambda) = \frac{\lambda}{\gamma_0} r_{TE}^{-1} e^{-2\gamma_0 h_0}\,\frac{e^{\gamma_0 z_2} - e^{\gamma_0 z_1} + r_{TE}^1\left(e^{-\gamma_0 z_2} - e^{-\gamma_0 z_1}\right)}{1 - r_{TE}^1 r_{TE}^{-1} e^{-2\gamma_0 h_0}} \qquad (4.32)$$

when the integration is completed. Because the change is trivial, the remaining integrated forms of $U_i(\lambda)$ and $D_i(\lambda)$ will not be written out explicitly here.

The expressions for the magnetic field Green's functions are given by expressions similar to equation (4.31). The vertical magnetic Green's function has the form

$$\int_{j^{th}\,cell} G_{Hz}^L = \delta(i)\int_j G_{Hz}(\mathbf{r}_j;\mathbf{r}_k)d\mathbf{r}_j dz_j - \frac{i\omega\mu\pi}{4}\mathrm{sign}(z_2 - z_k)\int_0^\infty \Big[U_i(\lambda)\big[e^{\gamma_i z_2} - e^{\gamma_i z_1}\big] + D_i(\lambda)\big[e^{-\gamma_i z_2} - e^{-\gamma_i z_1}\big]\Big] v(\lambda, r_1, r_2)\frac{J_1(\lambda r_k)}{\gamma_i}d\lambda \qquad (4.33)$$

where the first integral on the right hand side is calculated using either expressions (3.13) or (3.14) depending on the singularity of the cell over which the integration is taking place. Similarly, the horizontal magnetic field Green's function is given by

$$\int_{j^{th}\,cell} G_{Hr}^L = \delta(i)\int_j G_{Hr}(\mathbf{r}_j;\mathbf{r}_k)d\mathbf{r}_j dz_j - \frac{i\omega\mu\pi}{4}\mathrm{sign}(z_2 - z_k)\int_0^\infty \Big[U_i(\lambda)\big[e^{\gamma_i z_2} - e^{\gamma_i z_1}\big] + D_i(\lambda)\big[e^{-\gamma_i z_2} - e^{-\gamma_i z_1}\big]\Big] v(\lambda, r_1, r_2)\,\lambda\,J_1(\lambda r_k)d\lambda \qquad (4.34)$$

where now the first term on the right is calculated using either (3.11) or (3.12).

To demonstrate how a layered background model can be used to improve image resolution of the iterative Born technique, the synthetic data calculated for the eight layer Devine model (Figure 4.20) have again been employed. Figure 4.27a shows the image after 11 iterations with 0.5% amplitude noise added to the data. Notice that although the resolution of the layers in the upper part of the section is better than shown in Figure 4.22, the resistive layer does not extend across the region between the two wells and the zone from 630m to 670m suggests the existence of two dimensional structure.

The 2-D structure appearing in the lower part of the section is at least partly caused by the presence of a resistive layer in the model starting at 670m just below the bottom point of the survey region and extending downwards (Figure 4.20). Remember that the estimation of the scattered fields first involves finding the best fitting background conductivity that minimizes the sum of the scattered field amplitudes. The theoretical primary fields are then calculated for each source-receiver combination using this background conductivity and then subtracted off of the total field. Because of this procedure a layer immediately below the imaging region will generate secondary fields that are measurable when the source and receiver are in the lower part of the section. Thus because a lack of vertical source-receiver coverage exists in this region, the imaging scheme will experience problems determining if these anomalous fields are within or outside of the interwell zone.

To reduce these effects a three layer background model is employed. The first layer has a conductivity of 0.5 S/m and extends to 550m depth while the lower layer of conductivity 0.125 S/m starts at 670m and extends to infinity. The imaging region lies between these two layers and has a conductivity of 0.35 S/m. Because the scattered fields are calculated by subtracting the primary field generated by this model, the effects of the lower layer should be removed. Figure 4.27b shows that this is indeed the case as the zone between 630m and 670 m depth appears to be fairly homogenous and flat lying. In addition the resistive layer from 600m to 630m extends almost the entire distance between the two wells.

In this section the theory has been presented which allows a layered background model to be incorporated into the iterative Born imaging scheme. Though the primary motivation for this is to account for the earth-air interface in the experiment described in Chapter 5, the benefits of using this type of model have been demonstrated using a simulation of the Devine field experiment. In the next section models which simulate reservoir processes such as steam injection and contaminant disposal will be analyzed to determine how well we can monitor their progress using cross well EM imaging.

4.4 Imaging changes caused by reservoir processes

As mentioned in Chapter 1, one of the most promising applications of crosswell EM is the monitoring of changes in reservoir properties that are caused by some type of injection process. If these changes can be tracked with respect to time, then the position and progress of the steam, water or gas front can be determined. In Chapter 5 an experiment in which electrically conductive salt water is injected into an aquifer will be analyzed. In this section, the ground work for this analysis will be developed by examining how well the iterative Born scheme can image a body whose size and/or position is changing.

Because the theory for the iterative Born scheme assumes symmetry about the source borehole, this analysis will focus on examples in which the injection occurs at some depth within the transmitter well. The first set of examples assume that the injected plume expands symmetrically about the borehole such that the cylindrical geometry criterion is obeyed. Different amounts of noise will be added to the synthetic data, and the resulting images analyzed to determine the data accuracy that is required in order to accurately map the plume. In the second half of this section, problems associated with an asymmetrical plume will be addressed and a method to determine the validity of the 2-D geometry analyzed.

4.4.1 Imaging an expanding, symmetric body

When gas or fluid is injected into a reservoir at depth, it is sometimes assumed that the permeability of the injection zone is radially homogenous. In this scenario, the resulting plume spreads symmetrically about the injection zone, expanding horizontally at the same rate in all directions as the process continues. To analyze this ideal case and determine how well the iterative Born scheme can image such a process, the 2-D integral equation solution is employed to calculate the response of tabular bodies such as the one shown in Figure 4.28a. The simulated plume is ten times more conductive than the 0.01 S/m background which coincides with the conductivity contrast encountered in the experiment described in Chapter 5. The plume is 10m thick and results have been calculated for plume radii of 20, 30, 40 , 50 and 60 m. Again 21 source and receiver positions have been employed with a sampling interval of 10m. Initially a frequency of 10 kHz will be used due to the stability and resolution of the imaging scheme at the associated induction number.

Figure 4.28 shows the resulting images for different plume radii assuming that the measurements are accurate to 1% of the maximum total field. Resolution in both the vertical and horizontal directions is excellent, although the radial extent of the bodies is slightly distorted. In addition, the conductivity of the injection zone has been recovered almost exactly. Notice that for a radius of 60m the image is starting to develop conductivity

maxima similar to those observed in the 1-D layered images that were discussed in section 4.3.1.

Figure 4.29 shows the results when 5% random noise is added. Although the plume is still very prominent, the image resolution has degraded substantially. Both the radial and vertical boundaries of the plume are less well defined although the quality improves as the plume radius increases. The conductivity has not been recovered as accurately as above, and the maxima within the plume are now more prominent. Adding 10% random noise causes a further reduction in image quality (Figure 4.30). However, the fact that the general location and size of the plume can be recovered with this much added noise indicates that the imaging method is quite robust.

Because the cylindrically symmetric model has been employed to compute the input data, the residual errors between this input and the results calculated for the image should be randomly distributed with respect to the source and receiver depth. In Figure 4.31 the residual errors for two of the images in Figure 4.28 have been plotted. Because the input data contain 1% added random noise, the error distribution does not exhibit any type of pattern that would imply a non symmetrical geometry. Figure 4.32 shows the resulting residuals when 10% is added to the input. Comparing these plots to those given in Figure 4.31 indicates that the extra noise simply causes an amplitude shift in the errors while leaving the basic random distribution the same.

To illustrate that low frequency data can provide excellent resolution as long as they are accurate, the simulation above has been repeated at an operating frequency of 1 kHz with 0.1% added noise. The results given in Figure 4.33 reveal that the resolution is comparable to that at 10 kHz (Figure 4.28) although the convergence to the final solution is slower. This demonstrates the possibility of imaging the conductivity structure trough steel casing by making low frequency measurements as suggested by Uchida et al. (1991) and Newman (1992a). However it also indicates a need for measurement accuracy which probably has not yet been attained.

The analysis above demonstrates the use of the iterative Born imaging scheme to image a body that is expanding symmetrically in a radial direction over time. The trade off of resolution versus measurement noise has been discussed and it has been demonstrated that low frequency measurements can provide excellent resolution as long as the data is of high quality. Unfortunately aquifers and reservoirs tend to be extremely inhomogenous in terms of permeability and thus the injected matter rarely obeys the cylindrically geometry. This problem will be addressed in the next section where the ability of the 2-D imaging scheme to reconstruct 3-D data will be analyzed.

4.4.2 Imaging a 3-D body

To this point the imaging scheme has only been applied only to examples where the medium exhibits a cylindrical symmetry about the source well. In Chapter 3 the 2-D cylindrical solution was compared to a 3-D solution using models with identical cross-sectional areas. It was determined in this analysis that as the operating frequency and thus the background induction number is increased, the measurements become less sensitive to the third dimension of the body outside of the interwell plane. In this subsection the extent to which the iterative Born imaging scheme can be used to reconstruct a three dimensional inhomogeneity simulating an asymmetrical injection will be examined. These results will in turn be applied to analyze the experiment described in Chapter 5.

The model employed in this study consists of a 40m long by 40m wide conductive sheet located at 95m depth as shown in Figure 4.34a. The sheet is symmetrically positioned in the $\hat{y}$ direction in and out of the page, however its position can vary horizontally. In order to demonstrate some interesting properties that exist at high frequencies, the conductance of the sheet has been kept rather low (0.2S) so that the Born series approximation will not be violated. Because of the relatively small secondary fields generated by this body at 1 kHz, only 0.1% amplitude noise has been added to the synthetic data. As in section 4.2 the results are presented at 1 kHz , 10 kHz and 100 kHz, and positivity constraints have been imposed to stabilize the solution.

Figure 4.34 shows the first example in which the sheet is symmetric about the source borehole. Because of this symmetry the 3-D effects will be minimized. As expected from earlier results the image at 1 kHz (Figure 4.34b) is very smooth with poor definition. The resolution is much improved at 10 kHz and 100 kHz (Figures 4.34c and 4.34d, respectively). At both of these frequencies the horizontal extent of the sheet and its conductance are recovered almost exactly. The validity of fitting this particular 3-D sheet with a cylindrical model is demonstrated by plotting the residual amplitude errors between the input data and the calculated image results. Figure 4.35 indicates that a random error distribution exists at each frequency which suggests a 2-D geometry in the target.

It will be demonstrated below that moving the center of the sheet off of the source borehole axis results in a 3-D "bias" in the residual errors. Even though the smoothest inversion approach employed here results in a gradual decrease in the mean residual error with each iteration, the bias prevents this error from converging to the level of the added noise. Thus because of this lack of convergence, the imaging scheme does not know when to terminate. This illustrates a problem with decreasing the regularization parameter by a constant amount at each iteration. To avoid this dilemma in the analysis presented below, the program was terminated at the same iteration at which convergence was reached in the

symmetric example given above (Figure 4.35). This was done so that the same amount of smoothing is applied in each example.

The first asymmetric case is that in which the sheet is displaced 10% of the interwell separation towards the receiver (Figure 4.36). At 1 kHz the reconstructed image indicates that the body has been displaced horizontally. However notice that compared to Figure 4.34b there is a degradation in the vertical resolution and it is difficult to define the leading edge of the sheet. Although the vertical resolution is good at 10 kHz, the horizontal resolution has been degraded. Rather than extending the conductive region continuously out to 30m, the imaging routine has produced an artifact at r=60m. Finally, as predicted by the analysis in Chapter 3, the 100 kHz image resolves the position of the sheet extremely well with very little image distortion resulting from 3-D effects.

The residual errors for these images are plotted in Figure 4.37. Notice that the errors with the largest amplitude are concentrated at a source depth that is equal to that of the sheet. This effect is the previously mentioned 3-D bias and at 10 kHz it is so strong that it completely masks the random residual errors resulting from the added noise. As might be expected the bias is minimized at 100 kHz. Because these plots indicate when the scheme is having problems fitting the data, they are useful for determining how well the images represent the true subsurface structure.

Moving the sheet horizontally another 10% such that the center is displaced 20m off center causes further degradation in the lower frequency images. As demonstrated by Figure 4.38b 1 kHz data can barely resolve the sheet at all. At 10 kHz (Figure 4.38c) the artifact at r=60m has grown in magnitude such that it is as large as the main section near the injection hole. In addition the vertical resolution has been decreased. Again at 100 kHz the image recovers both the location and conductivity of the sheet very well. However plotting the residual errors (Figure 4.39) indicates strong 3D effects even at this highest frequency . This implies that even though the image is reconstructed remarkably well, the three dimensionality of the sheet is still being detected and can not be accounted for by the 2-D geometry.

When the sheet is placed at the center between the two wells (Figure 4.40), the imaging procedure fails almost completely at the two lowest frequencies. At 1 kHz a very diffuse region of slightly greater than background conductivity is recovered while at 10 kHz a delta function is reconstructed at the location of the previously described artifact. However, the 100 kHz image still correctly identifies both the position and conductivity of the body, even though the sheet is located relatively far away from the injection well. Notice that the residual errors plotted in Figure 4.41 do not indicate the presence of 3-D structure as clearly as those given in Figures 4.37 and 4.39 above. This indicates that a

thorough analysis of these plots may be required to avoid missing this type of problem.

The next example (Figure 4.42a) involves displacing the sheet 10% to the left of the source bore hole which demonstrates how the iterative Born scheme reacts when the plume moves away from the receiver. Again the 3-D nature of the data causes the scheme to completely fail at lower frequencies. Nothing is seen at 1 kHz while at 10 kHz two small artifacts are formed near the source borehole just above and below the sheet. And once again at 100 kHz the imaging process resolves the correct position and conductivity of the sheet (Figure 4.43d). As expected the residual errors indicate the presence of a large 3-D bias at all three frequencies (Figure 4.44).

As previously mentioned, the above results have incorporated positivity constraints to stabilize the inversion and provide better resolution. In many cases however, such as the experiment described in the next chapter, these constraints are unrealistic. To determine the degree of resolution that is possible when positivity is not imposed on the solution, three of the models given above are imaged with the constraints removed. Unfortunately, due to the instability of the scheme at higher frequencies, solution convergence was unattainable at 100 kHz. Thus the following images are reconstructed only for the 1 kHz and 10 kHz data. Because the residual amplitude errors have been found to display the same type of distribution as those presented above, they will not be plotted for these examples.

Figure 4.44 shows the images for the axially centered sheet shown in Figure 4.34a. Although the position of the sheet has been recovered, relaxing the positivity constraints has resulted in a serious loss of resolution, especially at 10 kHz. Where as the conductivity was reconstructed almost exactly in Figure 4.31c, the value recovered here is much less.

The images of the sheet when it is offset 10m toward the receiver well (Figure 4.36a) are shown in Figure 4.45, and the results for a -10m offset as shown Figure 4.42a are given in Figure 4.46. In both cases there is a loss of resolution compared to when positivity constraints are imposed. No definition is apparent at 1 kHz and at 10 kHz the shape of the sheet is severely distorted. In addition large 'side lobes' or regions of conductivity both greater than and less than the background have formed around the edges of the plume. The presence of these sidelobes will be employed in the analysis presented in the next chapter.

4.5 Summary

An imaging scheme has been developed which employs an iterative Born approach to reconstruct the conductivity structure from cross well EM data. The scheme assumes 2-D cylindrical symmetry and uses the Born series approximation developed in Chapter 3 as a

forward modeling scheme to calculate the electric fields existing in the region between the wells. This forward modeling allows the sensitivity matrix to be updated which results in more accurate images. To find a model which best fits the data in a least squares sense, a quadratic programming routine has been employed. The solution is stabilized through regularization and by applying a smoothest model inverse approach. Positivity constraints can also be used to further stabilize the solution and provide for better resolution.

A resolution analysis incorporating single cell scatterers has shown that the resolution in the cross well scenario is better in the vertical direction than in the horizontal. At higher frequencies the resolution tends to decrease with increasing conductivity contrast, while at lower frequencies the opposite is true. The former conclusion results from numerical instability of the iterative Born scheme while the latter conclusion is a function of the signal strength. The best trade off between resolution and stability seems to occur when the background induction number is somewhere between 10 and 50.

Images of synthetic data calculated for a layered model indicate that the horizontal component of the field may be very useful in the reconstruction process. At lower frequencies it was found to yield higher quality images that the vertical field. In addition it was demonstrated that a simultaneous inversion using both components can produce better results than either component by itself. An analysis of field data collected at Devine, Texas has shown that a systematic drift is present. Although the scheme is very robust in terms of random noise, it has been demonstrated to be very sensitive to this type of correlated noise.

Simple simulations of reservoir injections have indicated that cross well EM imaging can track changes in a reservoir over time. However it has also been determined that at frequencies on the low induction number side the Born kernel, any deviation in the medium from a 2-D cylindrically symmetric geometry can cause severe artifacts in the images. Fortunately the degree to which the medium is three dimensional can be estimated by plotting the residual errors between the input data and the numerical results calculated from the image. In the next chapter all of the tools that have been developed in this chapter will be applied to a salt water injection experiment at the Richmond Field Station test site in Richmond, California.

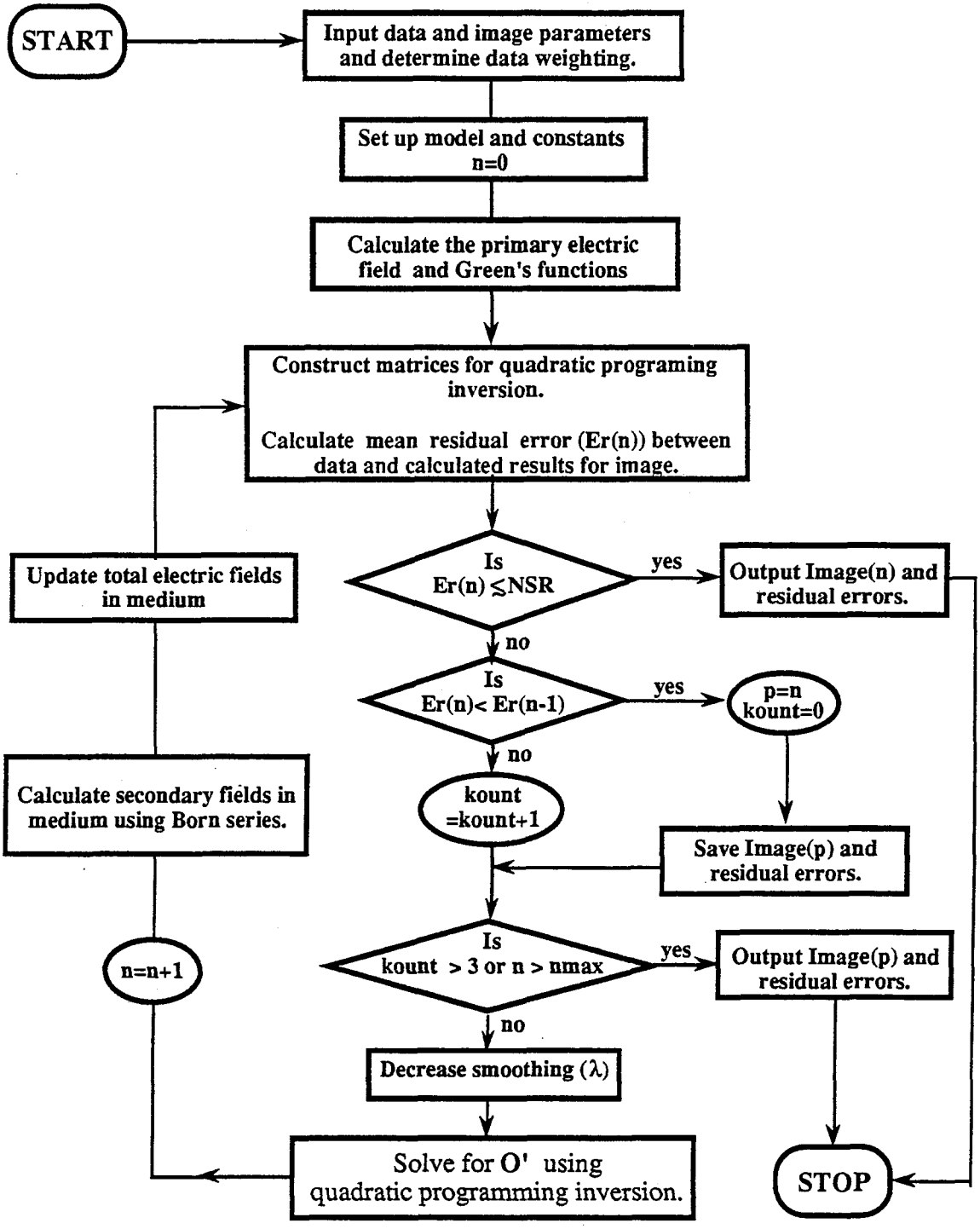

Figure 4.1 - Flow chart of the iterative Born imaging scheme. NSR refers to the estimated noise level, and nmax refers to the maximum number of iterations set by the user.

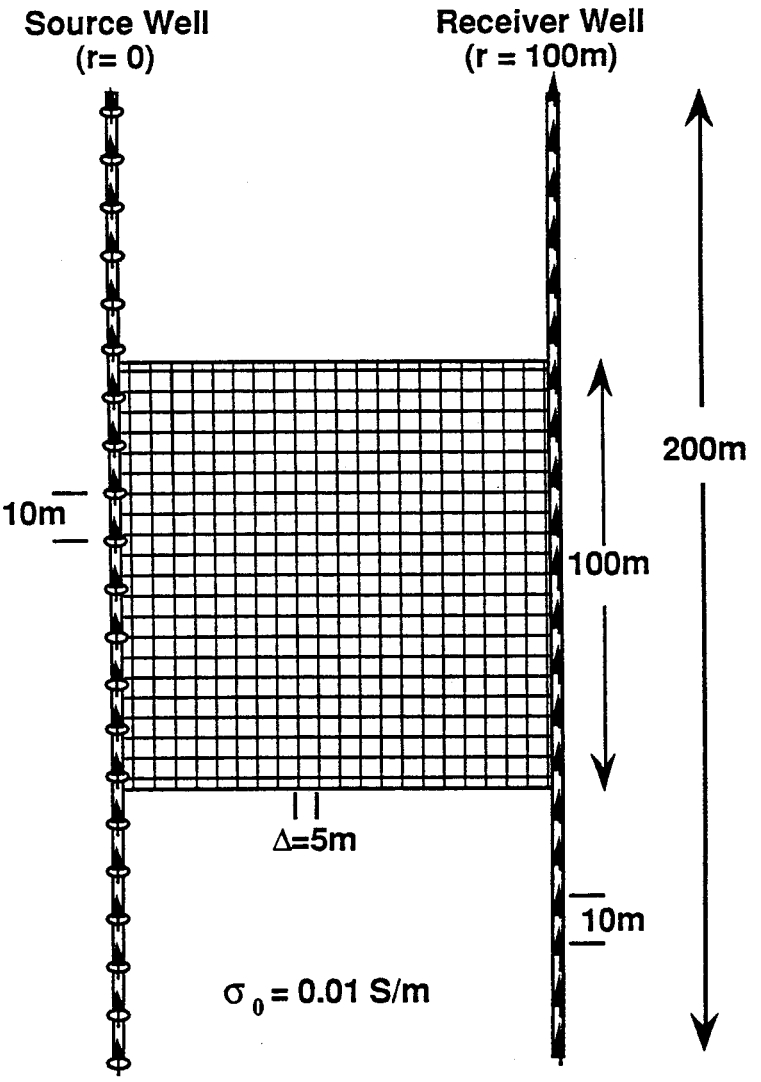

Figure 4.2 - Model and imaging configuration employed in section 4.2. Two 200 m deep wells are seperated by 100m in a 0.01 S/m whole space. 21 sources and 21 receivers are spaced at 10m intervals yielding 441 vertical magnetic field calculations at each frequency. The imaging area is 100m by 100m and has been divided into 400 5m by 5m square cells.

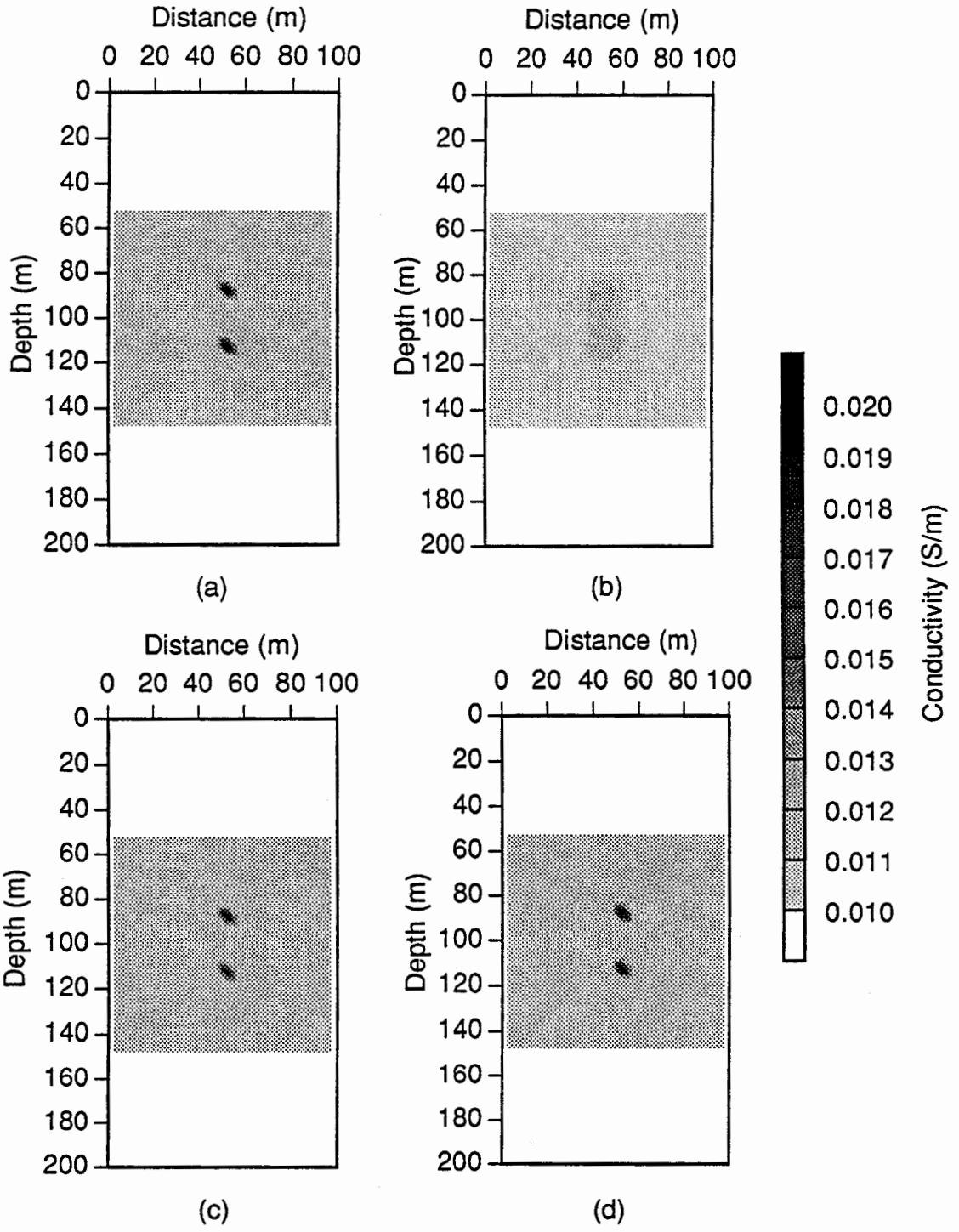

Figure 4.3 - Low contrast-vertical resolution model and images as a function of frequency. (a) Model with results calculated fot 21 source and receiver positions spaced at 10m intervals from 0 to 200m depth. The added noise is 0.001% of the maximum total field measured at each frequency. (b) 1 kHz image. Mean residual error after 23 iterations= 1.0e-5. Total model error=9.3e-1. (c) 10kHz image. Mean residual error after 25 iterations=1.0e-5. Total model error=1.4e-2. (d) 100kHz image. Mean residual error after 30 iterations=1.1e-5. Total model error= 5.3e-5.

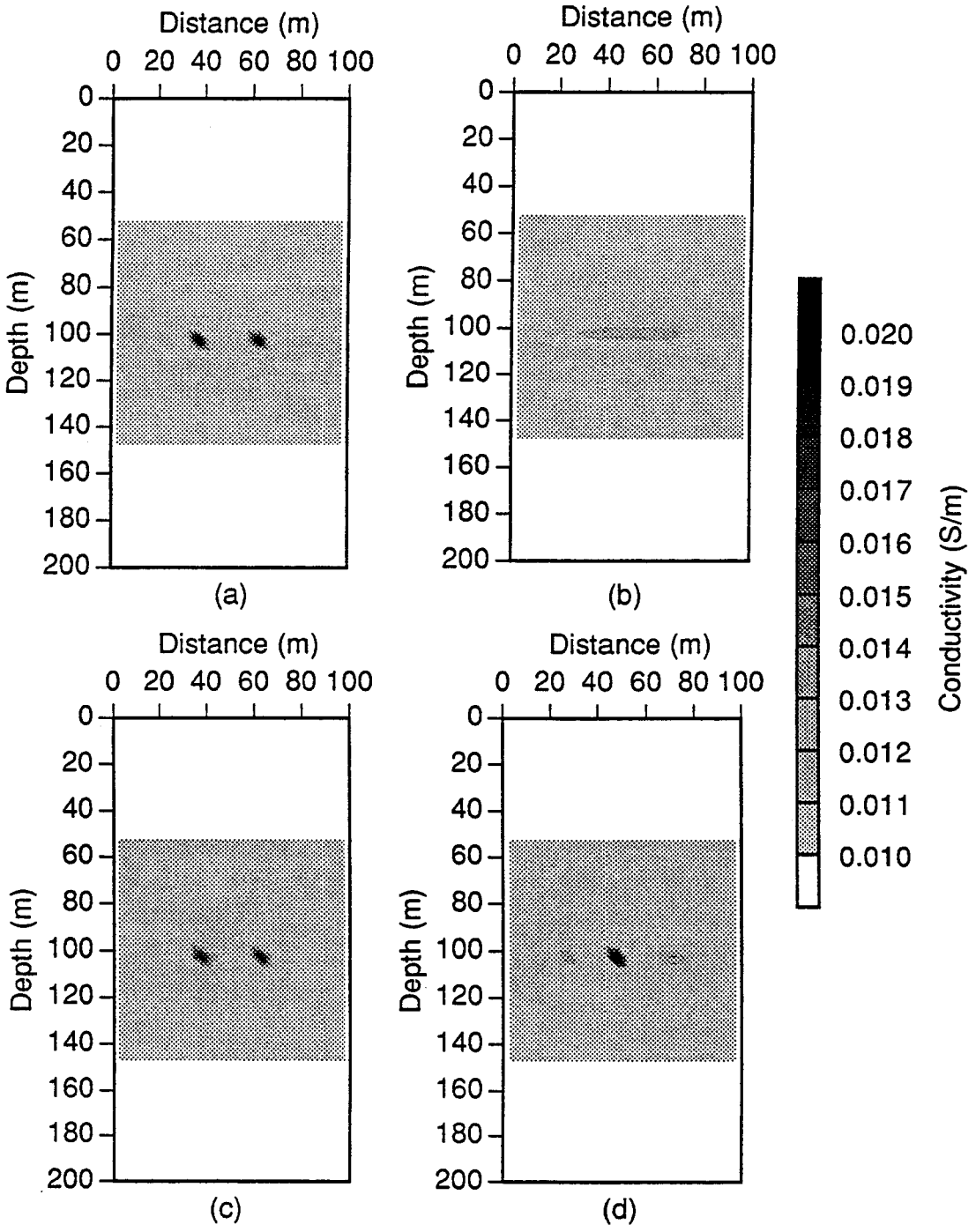

Figure 4.4 - Low contrast-horizontal resolution model and images as a function of frequency. (a) Model with results calculated for 21 source and receiver positions from 0 to 200m depth. The added noise is 0.001% of the maximum total field measured at each frequency. (b)1 kHz image. Mean residual error after 27 iterations =1.02e-5. Total model error=8.1e-1. (c) 10 kHz image. Mean residual error after 25 iterations =1.03e-4. Total model error = 2.2e-2. (d) 100 kHz image. Mean residual error after 20 iterations =2.90e-4. Total model error=1.9.

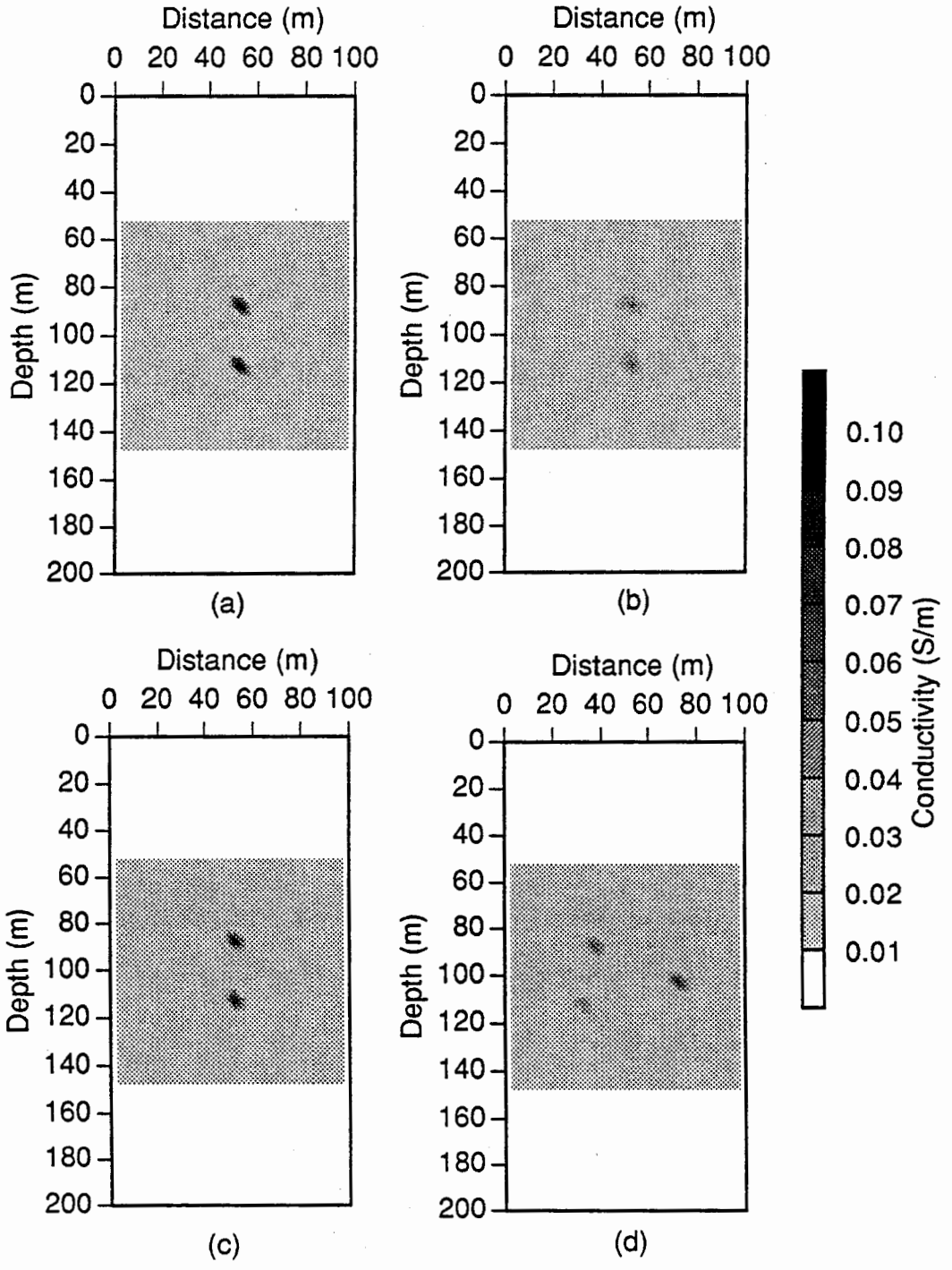

Figure 4.5 - High contrast-vertical resolution model and images as a function of frequency. (a) Model with results calculated at 21 source and receiver position from 0 to 200m depth. The added noise is 0.001% of the maximum total field measured at that frequency. (b) 1kHz image. Mean residual error after 28 iterations = 1.04e-5. Total model error= 3.4e-1. (c) 10 kHz image. Mean residual error after 30 iterations = 1.03e-5. Total model error=1.3e-2. (d) 100 kHz image. Mean residual error after 28 iterations = 4.6e-3. Total model error=3.4.

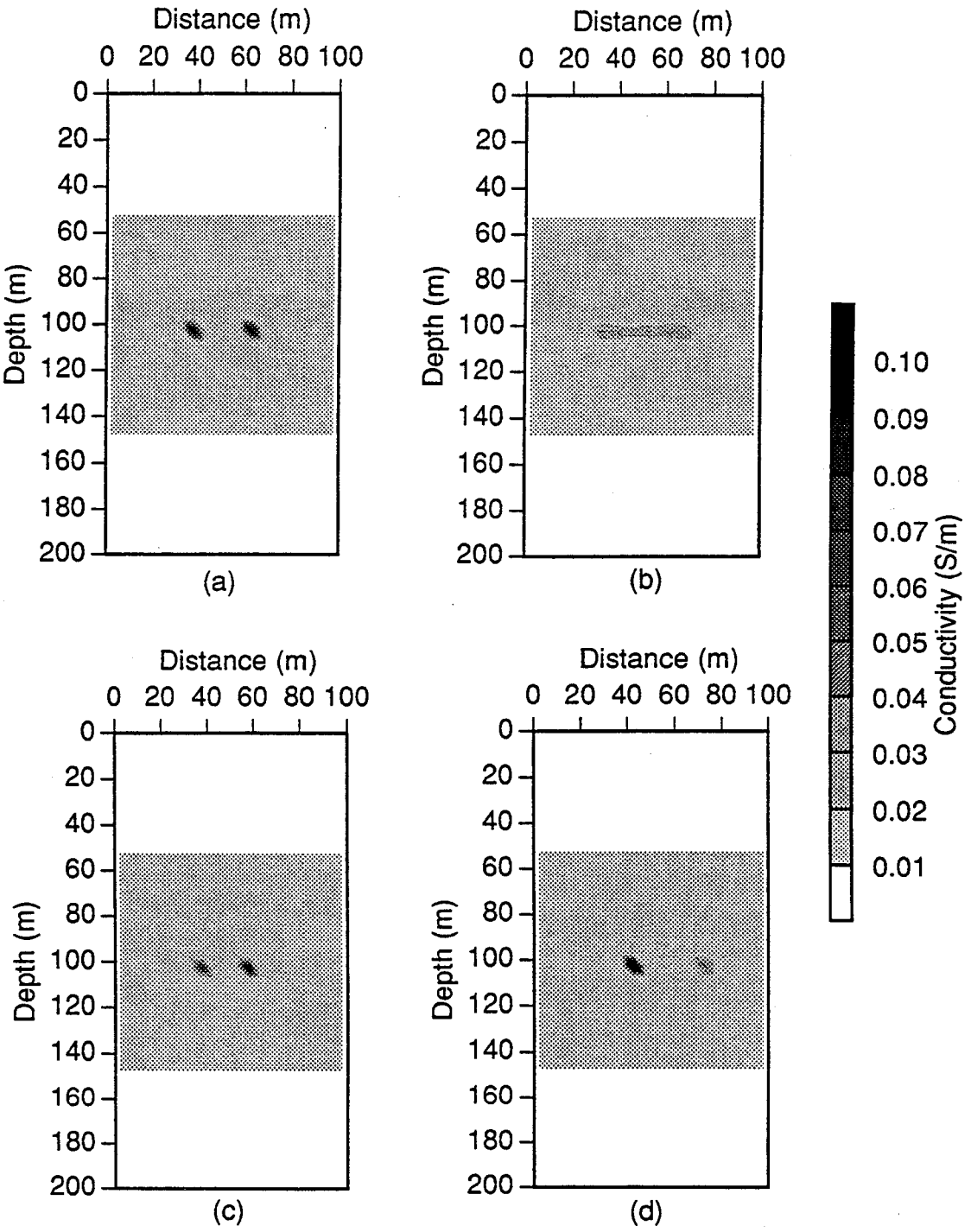

Figure 4.6 - High contrast-horizontal resolution model and images as a function of frequency. (a) Model with results calculated at 21 source and receiver positions at 10m intervals from 0 to 200m depth. The source borhole is at 0m and the added noise is 0.001% of the maximum total field measured at each frequency. (b)1 kHz image. Mean residual error after 26 iterations = 1.02e-5. Total model error= 6.4e-1. (c) 10 kHz image. Mean residual error after 23 iterations = 2.15e-4. Total model error = 1.07. (d) 100 kHz image. Mean residual error after 11 iterations=1.02 Total model error= 2.1.

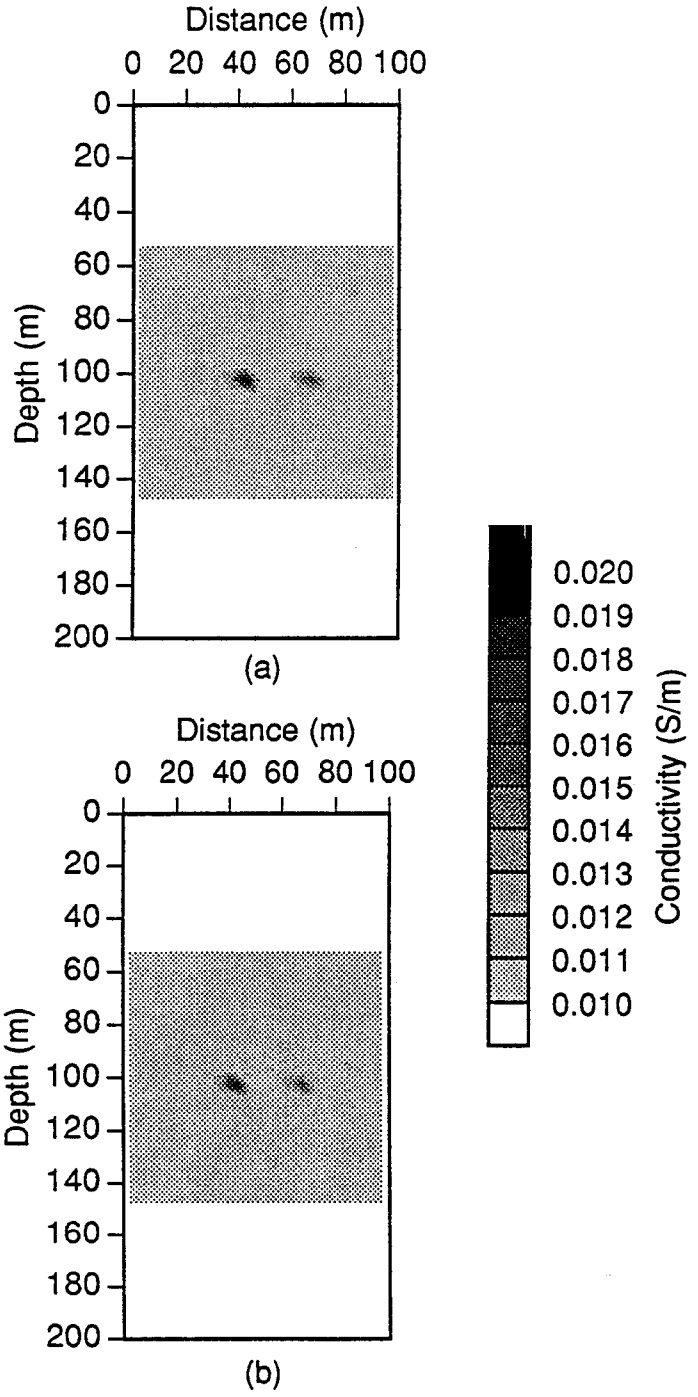

Figure 4.7 - 100 kHz images of the model shown in Figure 4.4a with no added noise. The inversion was terminated when the mean misfit approached 0.01% of the total field. (a) Image primary field weighting. Mean residual error after 15 iterations=9.0e-5. Total model error=9.9e-1. (b) Image for the total field weighting. Mean residual error after 15 iterations =9.0e-5. Total model error=1.0.

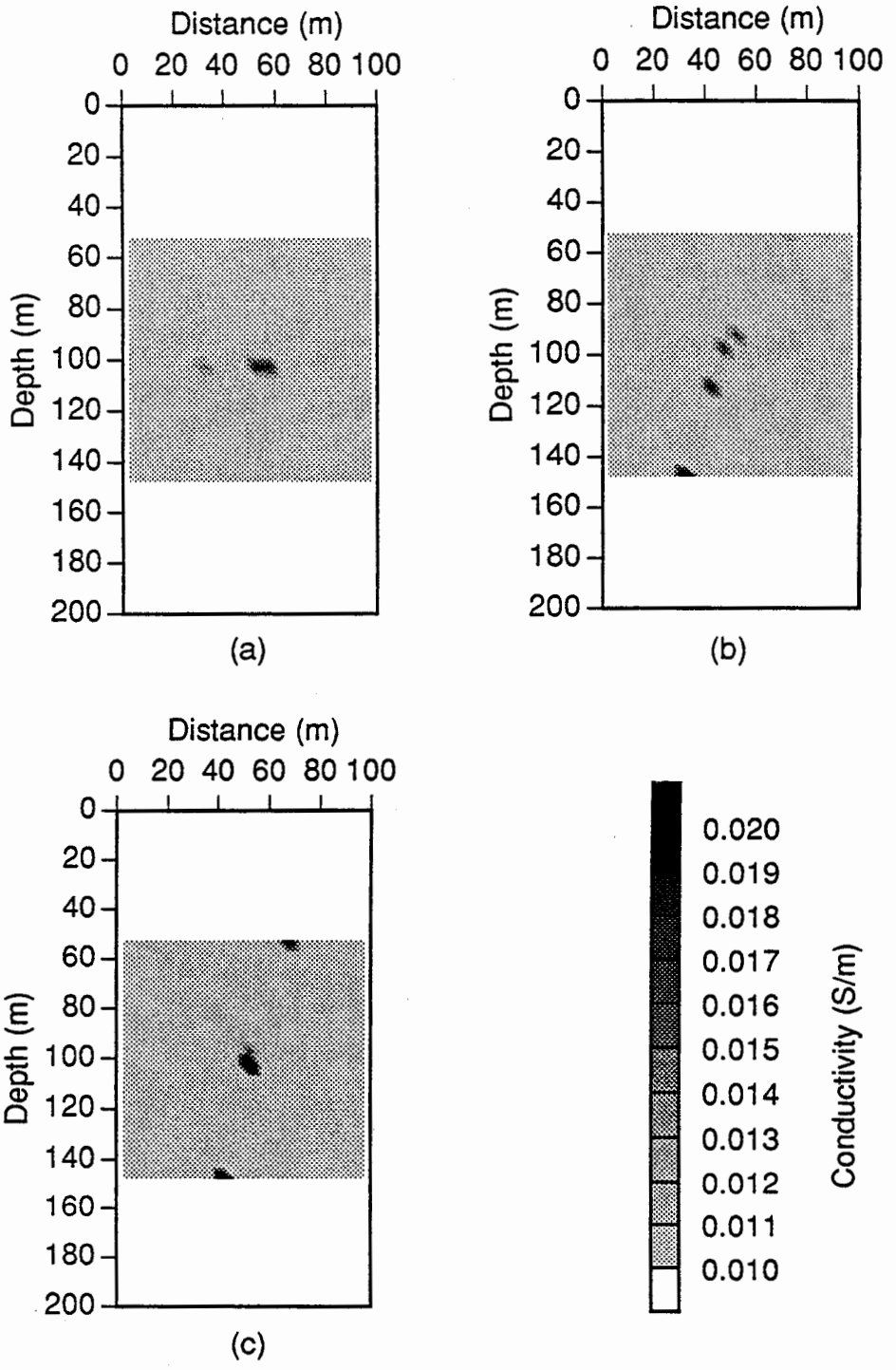

Figure 4.8 - 100 kHz images of the model shown in Figure 4.4a with 0.01%added random noise. The inversion was terminated when either the mean data error approached 0.01% of the total field or converged to a minimum. (a) Image with no weighting applied. Mean residual error after 25 iterations r=1.1e-5. Total model error=1.6. (b) Image for primary field weighting. Mean residual error after 25 iterations=4.0e-3. Total model error=2.7. (c) Image for the total field weighting. Mean residual error after 25 iterations =6.2e-3. Total model error=4.3.

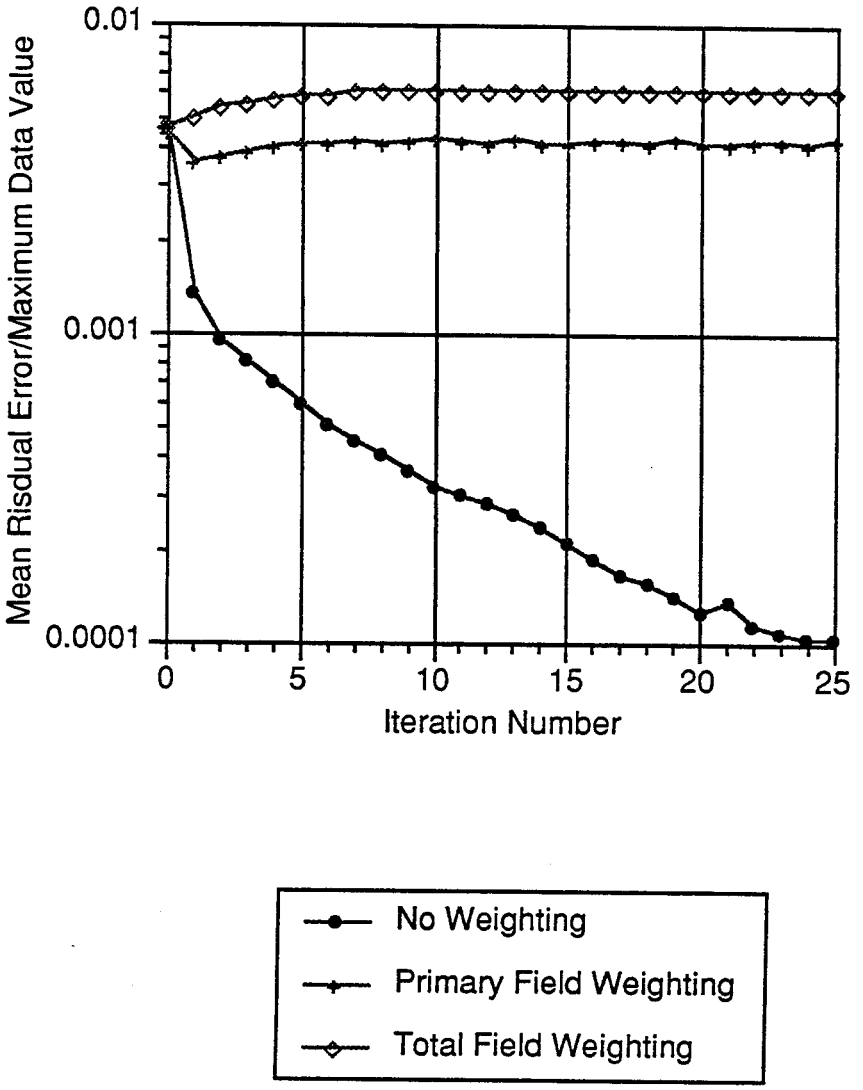

Figure 4.9- Convergence rate for the inversion results given in Figure 4.8

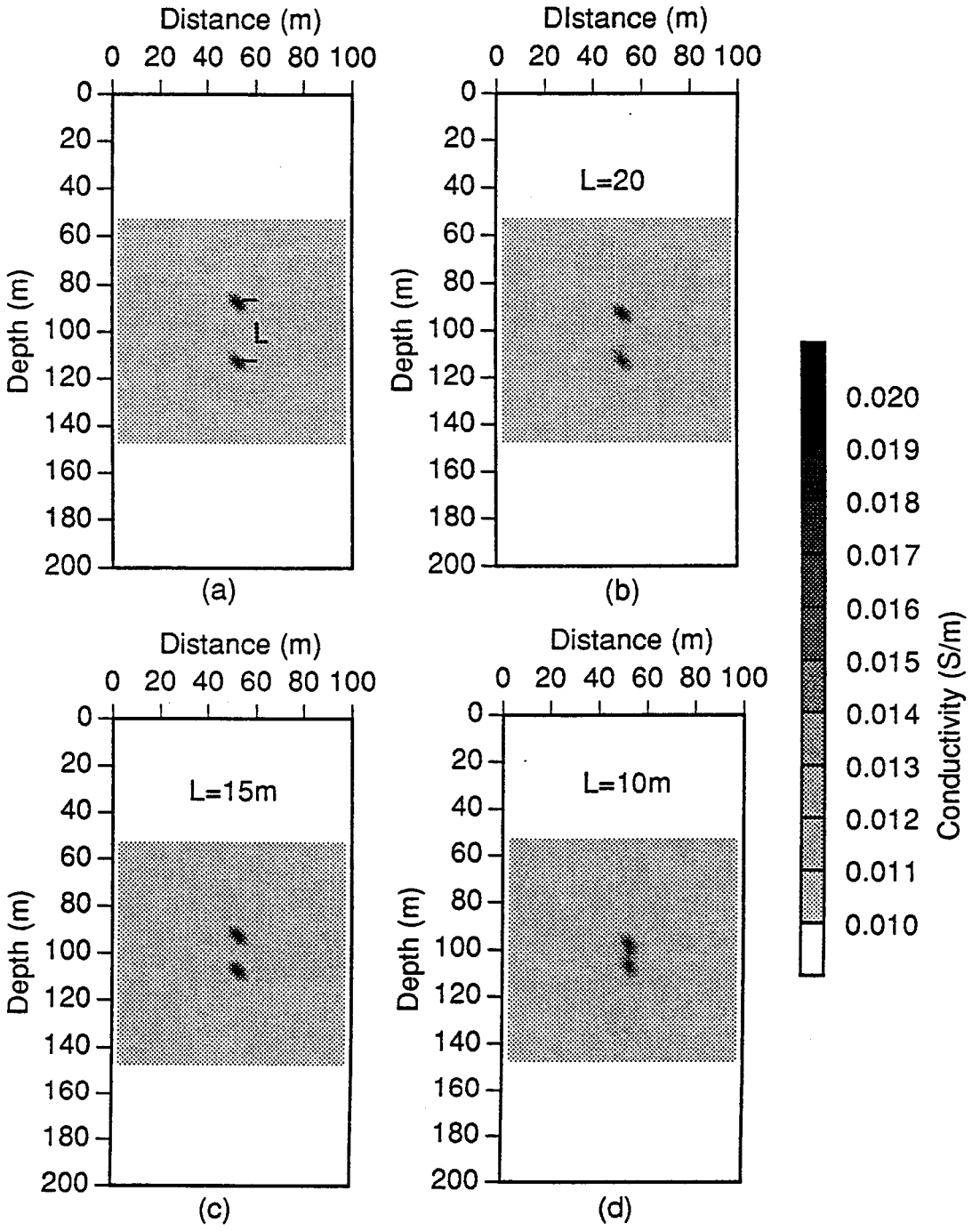

Figure 4.10 - Low contrast-vertical resolution model and images as a function 'L'. These results can be compared to those in Figure 4.3c in which L=25. (a) Model for L=25m with results calculated for 21 source and receiver positions from 0 to 200m depth. The added noise is 0.001% of the maximum total field. (b) Image for L=20m. Mean residual error after 26 iterations=1.0e-5. Total model error=3.7e-2 (c) Image for L=15m. Mean residual error after 27 iterations=9.9e-6. Total model error= 2.3e-3. (d) Image for L=10m. Mean residual error after 25 iterations=1.0e-5. Total model error=2.0e-1.

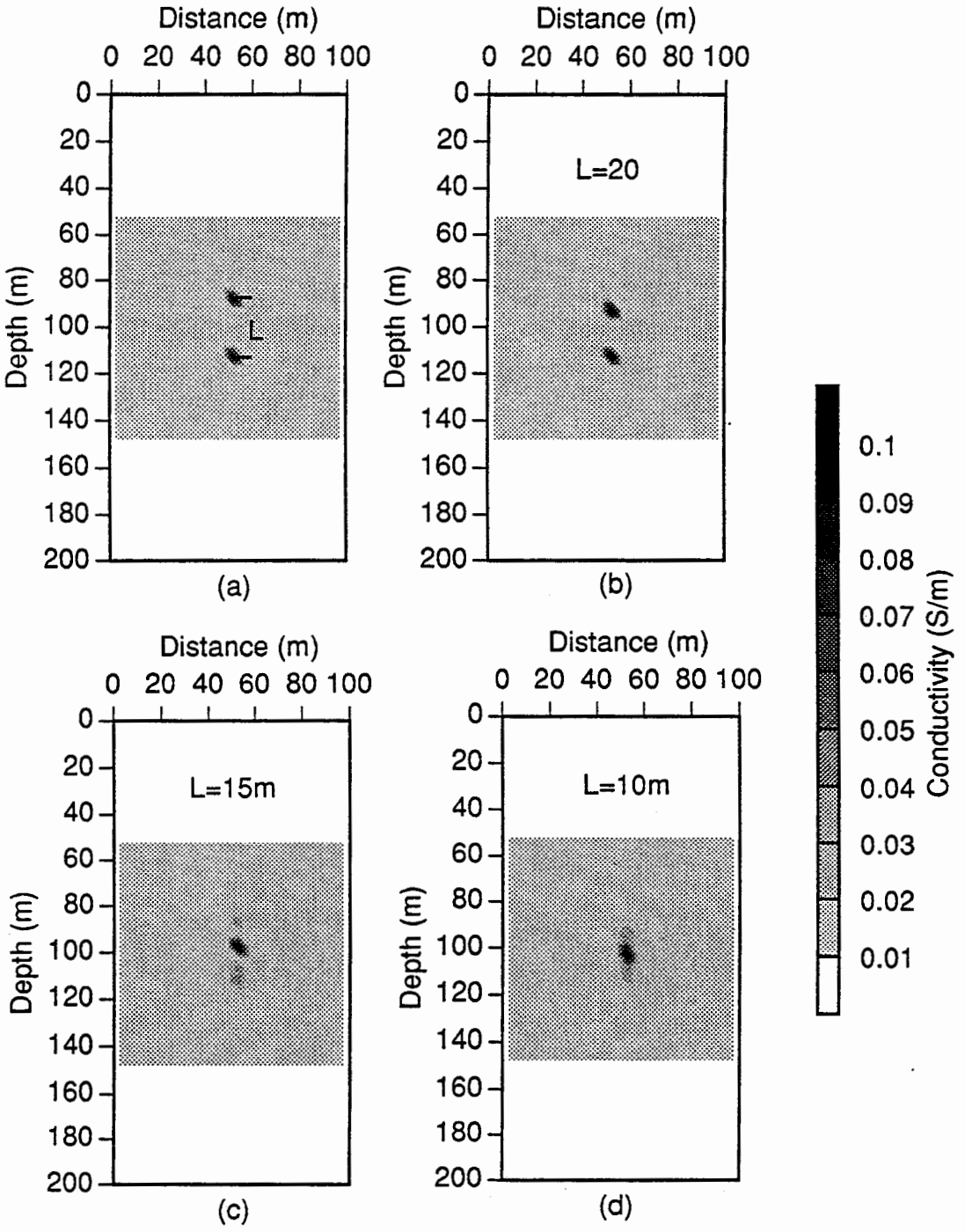

Figure 4.11 - High contrast-vertical resolution model and images as a function 'L'. These results can be compared to those in Figure 4.5c in which L=25. (a) Model for L=25m with results calculated for 21 source and receiver positions from 0 to 200m depth. The added noise is 0.001% of the maximum total field. (b) Image for L=20m. Mean data error after 31 iterations=1.4e-5. Total model error=2.3e-2. (c) Image for L=15m. Mean data error after 25 iterations =3.5e-5. Total model error=1.39. (d) Image for L=10m. Mean data error after 20 iterations =1.5e-5. Total model error=1.0.

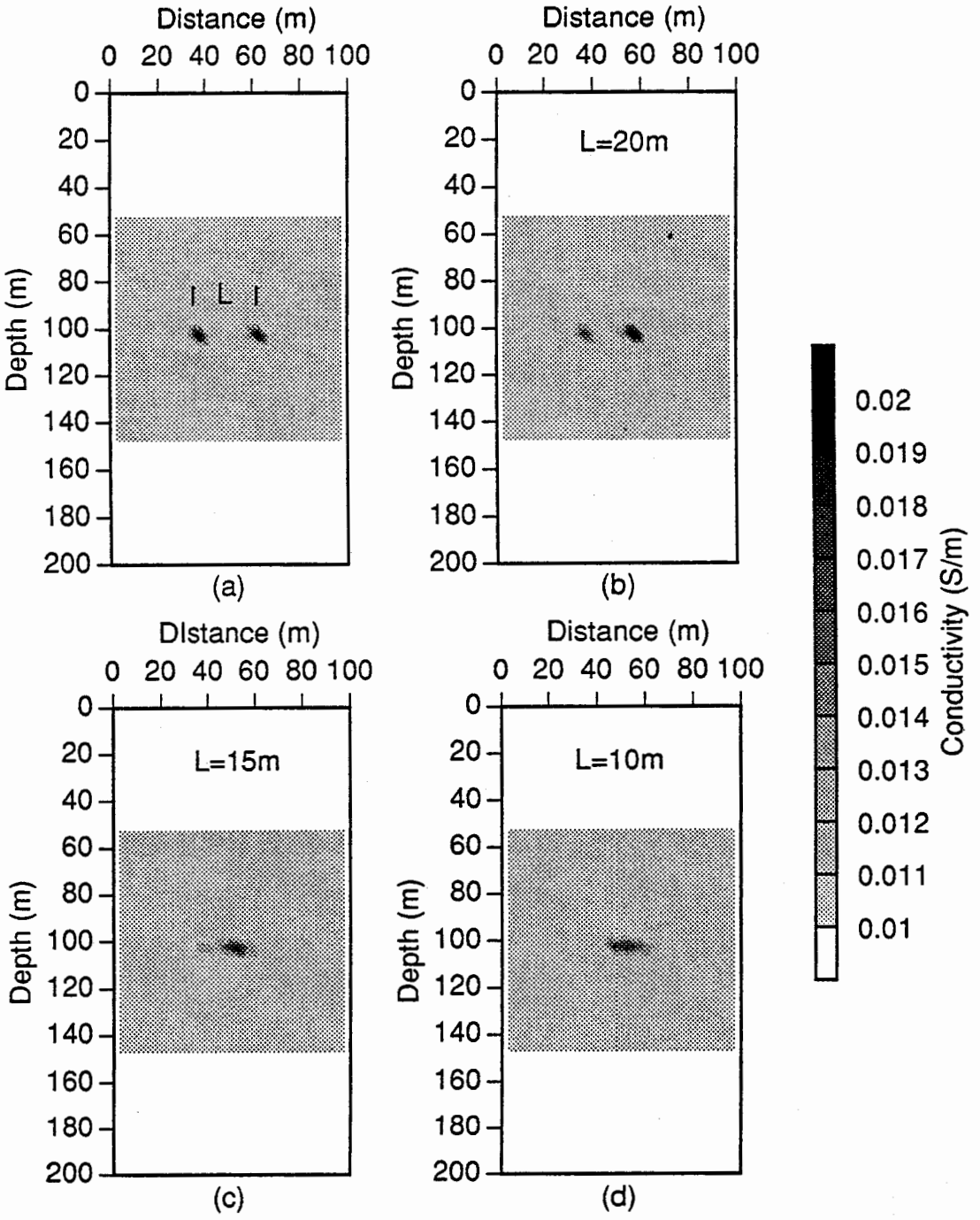

Figure 4.12 - Low contrast-horizontal resolution model and images as a function 'L'. These results can be compared to those in Figure 4.4c in which L=25. (a) Model for L=25 with results calculated for 21 source and receiver positions from 0 to 200m depth. The added noise is 0.001% of the maximum total field. (b) Image for L=20m. Mean residual error after 26 iterations=1.0e-5. Total model error=1.4e-1. (c) Image for L=15m. Mean residual error after 24 iterations=1.0e-5. Total model error=1.1. (d) Image for L=10m. Mean residual error after 23 iterations=1.0e-5. Total model error=8.0e-1.

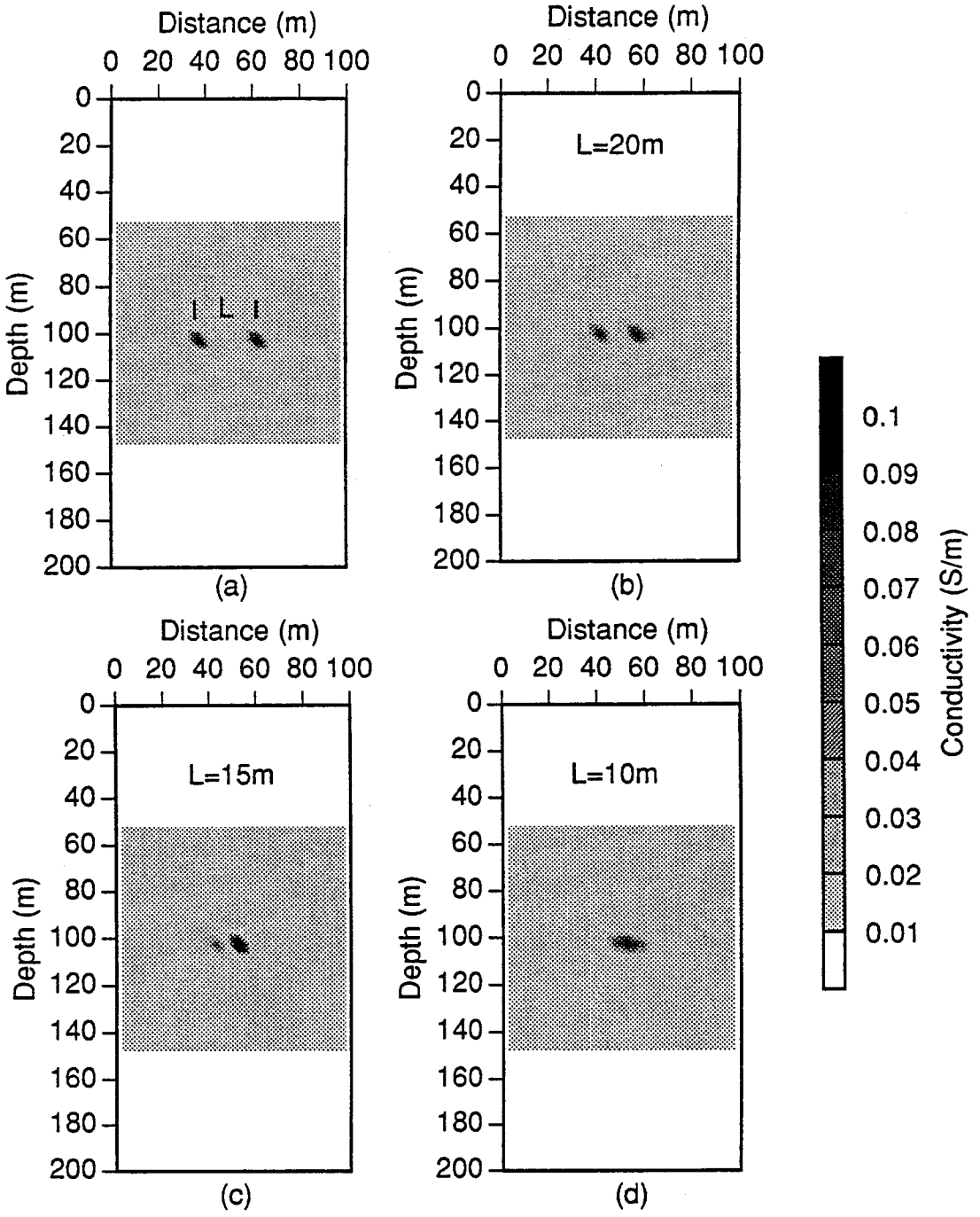

Figure 4.13 - High contrast-horizontal resolution model and images as a function 'L'. These results can be compared to those in Figure 4.6c in which L=25. (a) Model for L=25m with results calculated for 21 source and receiver positions from 0 to 200m depth. The added noise is 0.001% of the maximum total field. (b) Image for L=20m. Mean residual error after 27 iterations=1.8e-5. Total model error=8.4e-1. (c) Image for L=15m. Mean residual error after 22 iterations=1.4e-5. Total model error=1.23. (d) Image for L=10m. Mean residual error after 17 iterrations =1.2e-5. Total model error=6.1e-1.

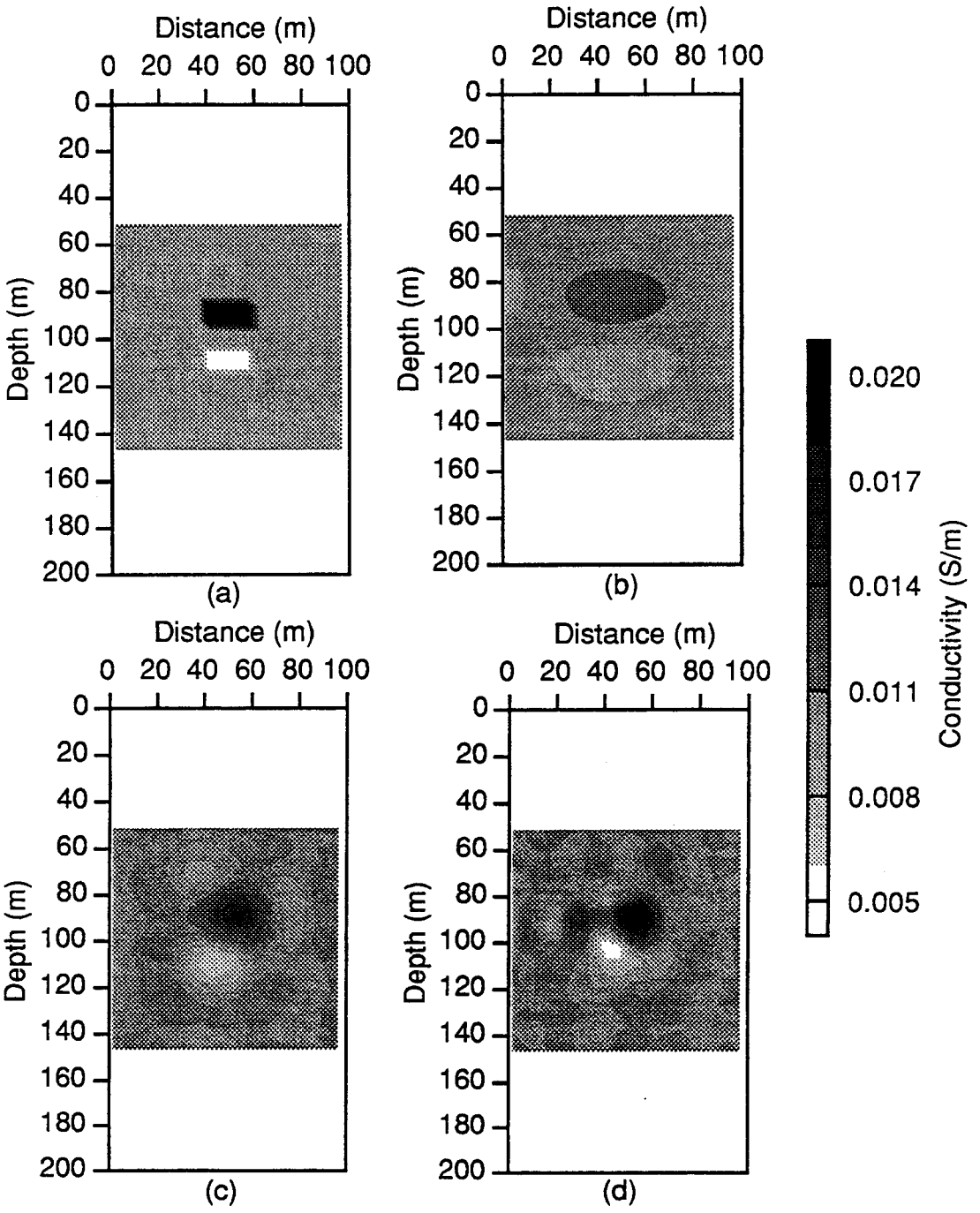

Figure 4.14- Model consisting of both a conductor and resistor in close proximity and images as a function of frequency. (a) Model with results calculated at 21 source and receiver positions at 10m intervals from 0 to 200m depth. The added noise is 0.01% of the maximum total field measured at each frequency. (b)1 kHz image. Mean residual error after 20 iterations =1.00e-4. Total model error=7.8e-1. (c) 10 kHz image. Mean residual error after 18 iterations=9.9e-5. Total model error = 5.8e-1. (d) 100 kHz image. Mean residual error after 16 iterations =1.66e-4. Total model error= 6.8e-1.

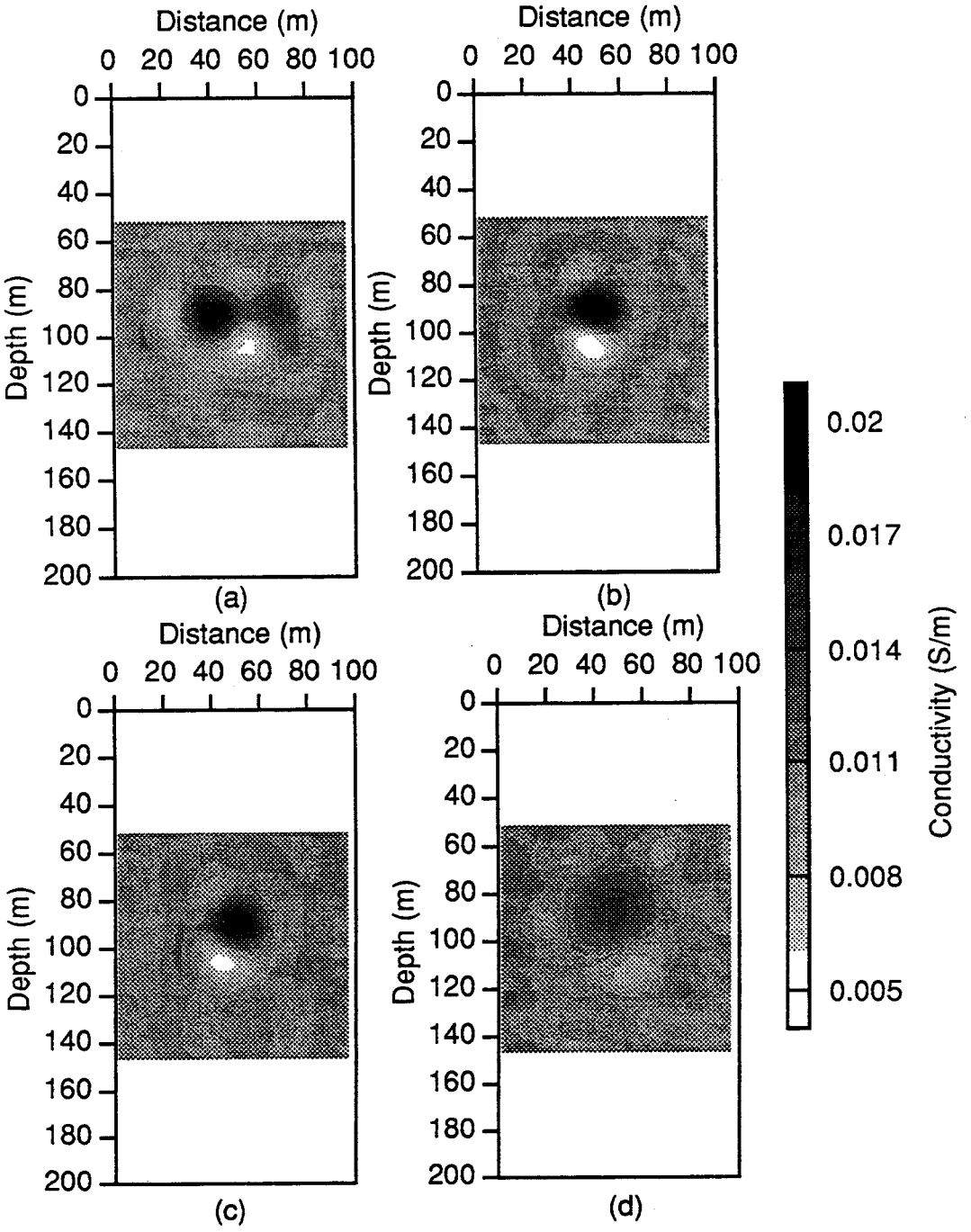

Figure 4.15 - Images of the conductor-resistor model shown in Figure 4.14a. The imaging scheme was terminated when the mean data error was a minimum for at least two of the frequencies. (a)Three frequency image with no weighting and 0.01% added noise. Total model error after 15 iterations =5.2e-1. (b) Three frequency image with weighting and no noise. Total model error after 15 iterations = 1.8e-1. (c) 100 kHz image with weighting and no noise. Total model misfit after 12 iterations = 2.2e-1. (d) Three frequency image with weighting and 0.01% noise. Total model error after 10 iterations = 4.3e-1.

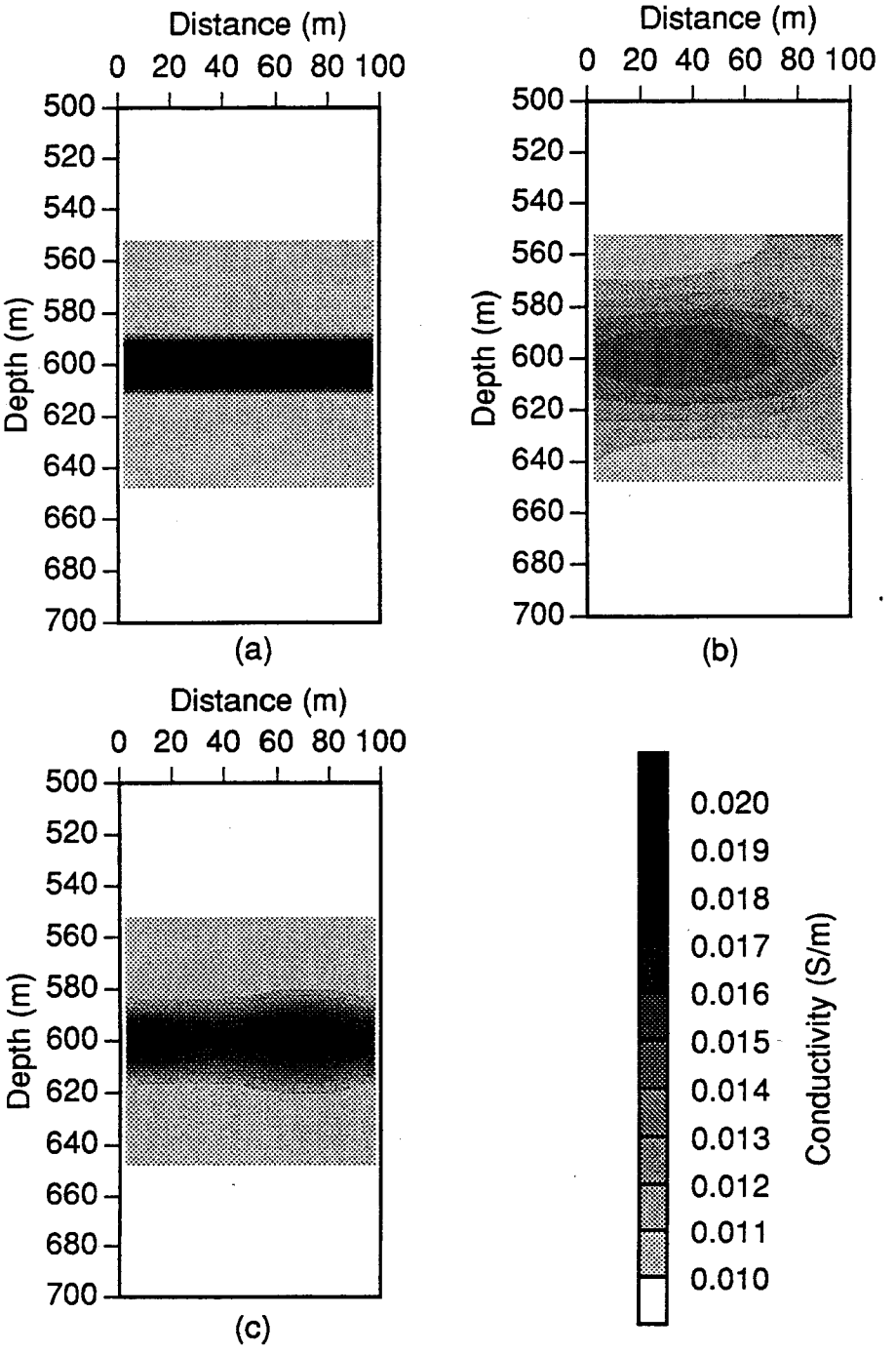

Figure 4.16 - Conductive layer model and images for two frequencies. (a) Model with results calculated for 21 source and receiver positions from 0 to 200m depth. The added noise is 1.0% of the maximum total field measured at each frequency. (b)1 kHz image. Mean residual error after 11 iterations=1.0e-2 (c) 10 kHz image. Mean residual error after 12 iterations=1.0e-1.

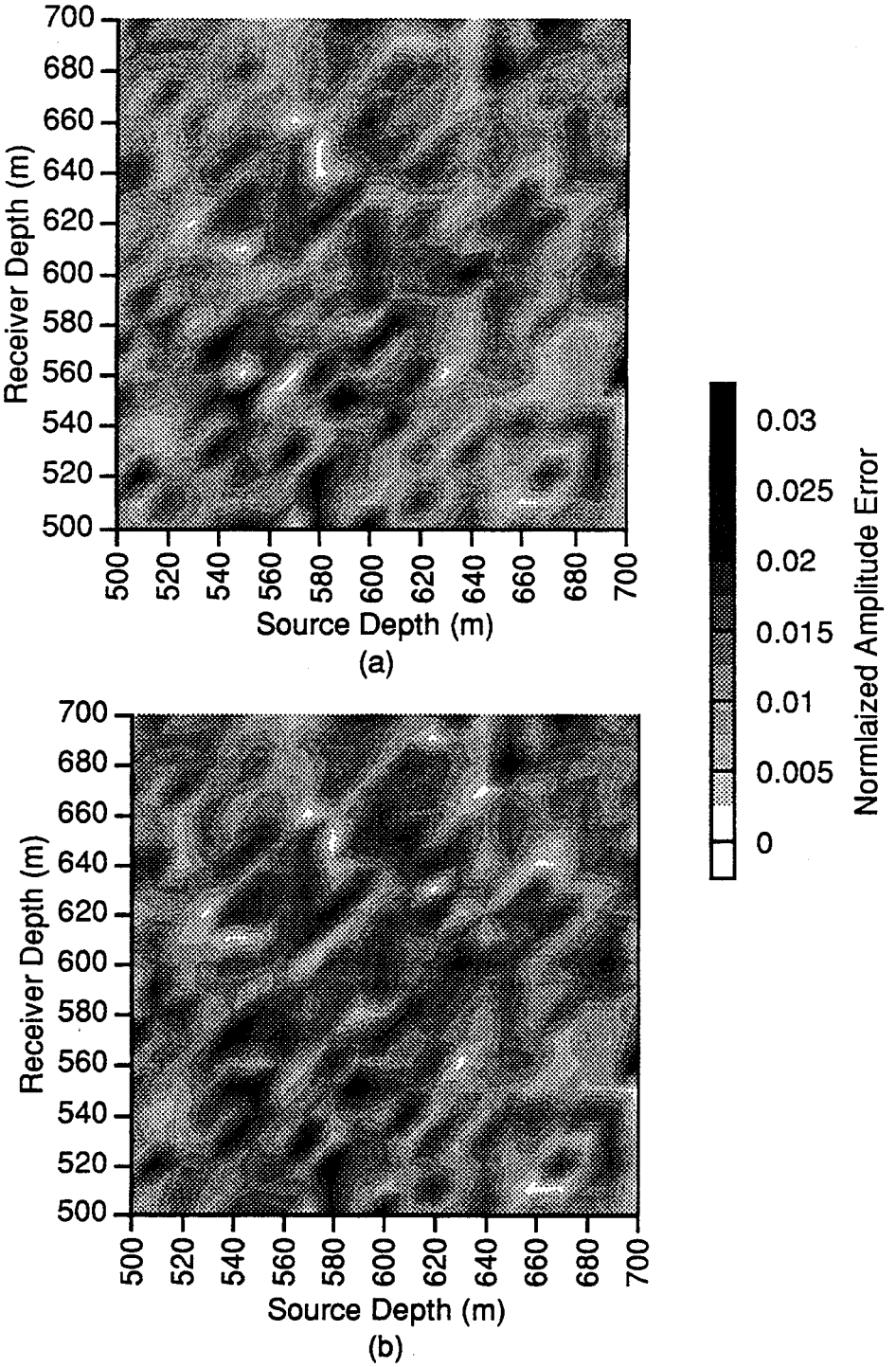

Figure 4.17 - Residual amplitude errors between the input data and the calculated results for the images as a function of source and receiver location. The errors have been normalized by the maximum value of the total field in the input data. (a) Residual errors for the 1kHz image in Figure 4.16b. (b)Residual errors for the 10kHz image in Figure 4.16c.

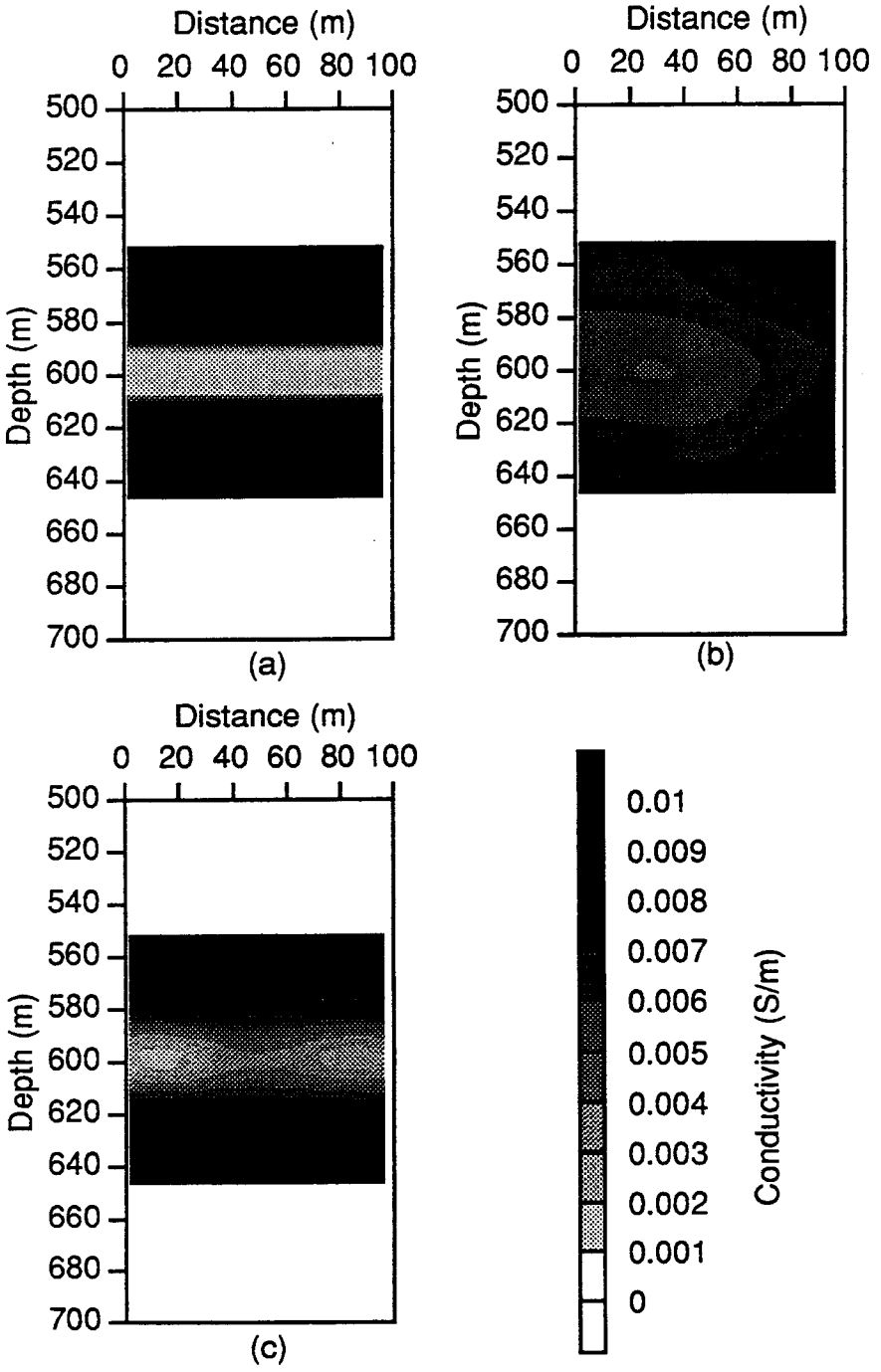

Figure 4.18 - Resistive layer model and images for two frequencies. (a) Model with results calculated for 21 source and receiver positions from 0 to 200m depth. The added noise is 1.0% of the maximum total field measured at each frequency. (b)1 kHz image. Mean residual error after 11 iterations =1.0e-2. (c) 10 kHz image. Mean residual error after 11 iterations=1.0e-2.

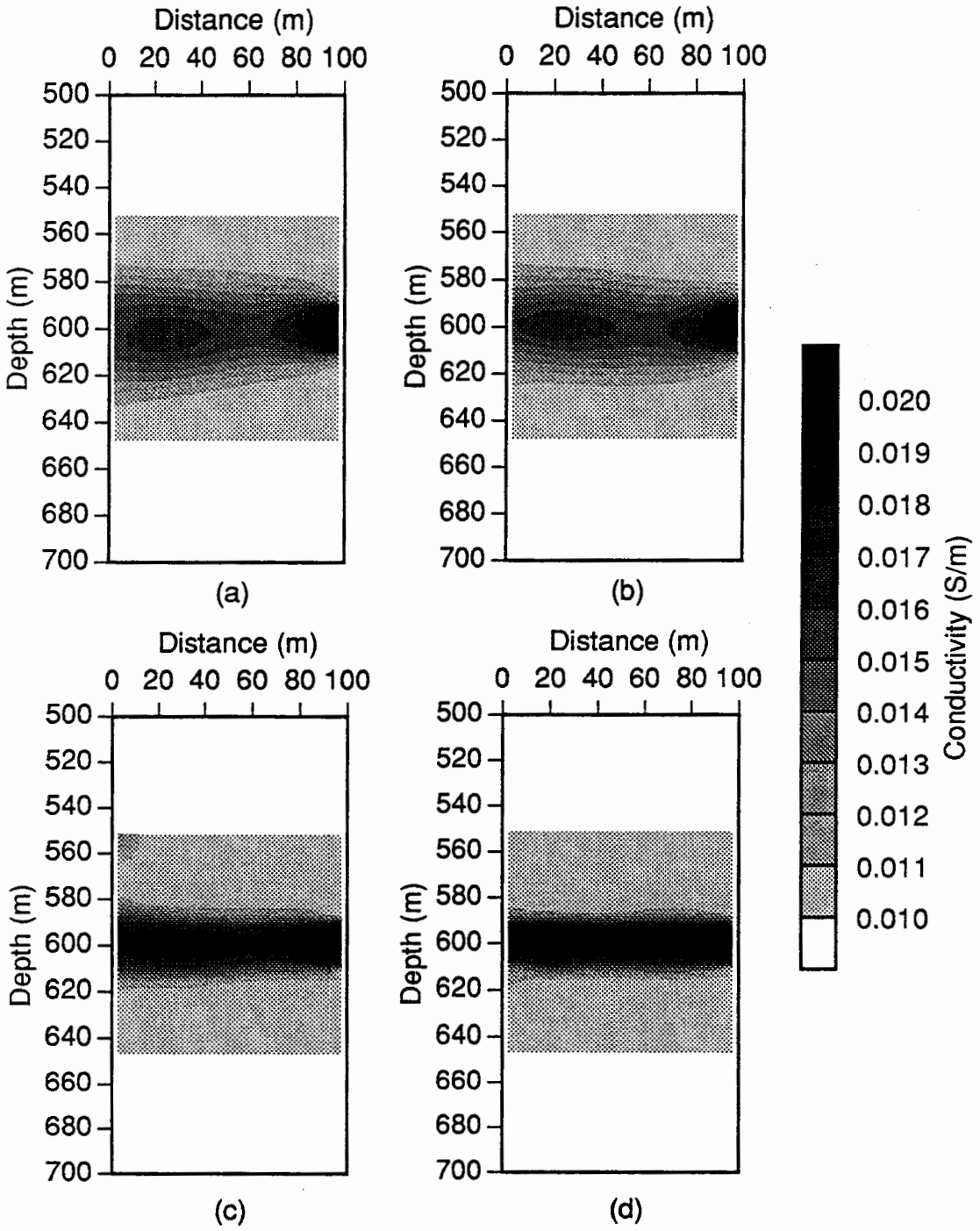

Figure 4.19 - Images of the model shown in Figure 4.16a reconstructed using the horizontal magnetic fields. (a) 1 kHz image using the horizontal magnetic fields. Mean residual error after 12 iterations =1.0e-2 (b) 1 kHz image using both the horizontal and vertical magnetic fields. Mean residual error after 12 iterations=1.0e-2. (c) 10 kHz image using the horizontal magnetic fields. Mean residual error after 13 iterations =1.0e-1. (d) 10 kHz image using both the horizontal and vertical magnetic fields. Mean residual error after 13 iterations =1.0e-1.

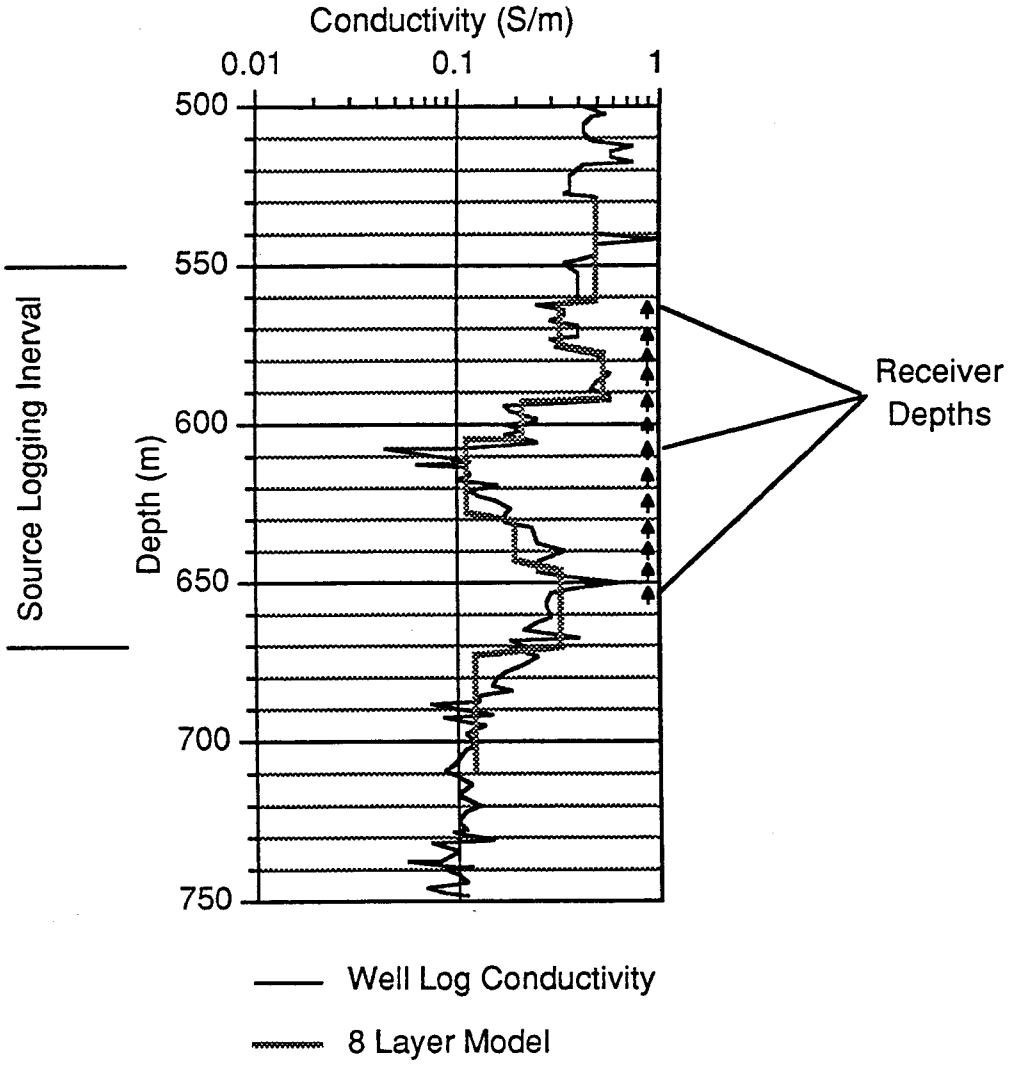

Figure 4.20 - Electrical conductivity log from a well used in the cross borehole EM experiment at the British Petroleum Devine test site near Devine, Texas. Included with the log is the best-fitting eight layer model. The "source logging interval" and "receiver depths" refer to the interval over which the source was moved and the discreet receiver locations employed in the cross well experiment, respectively.

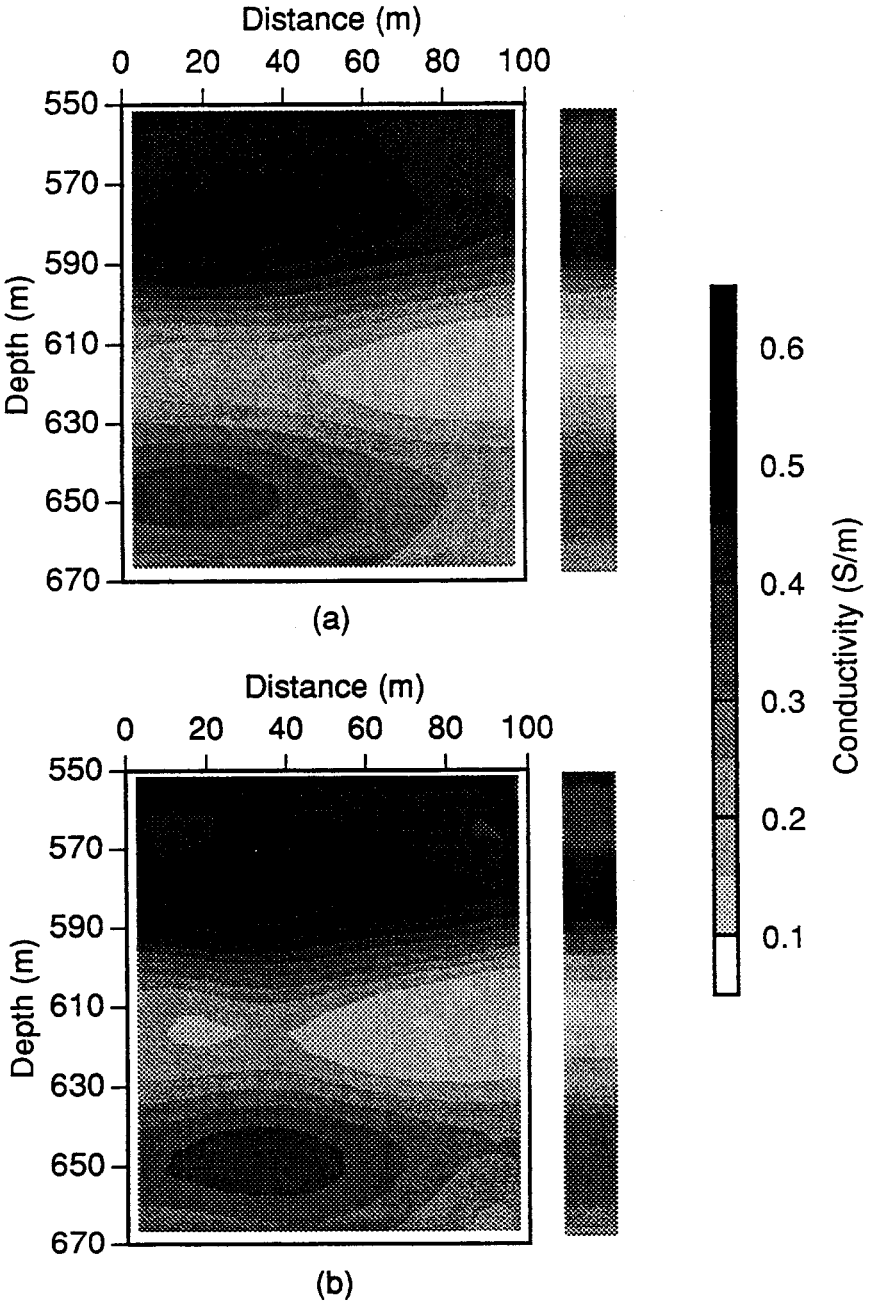

Figure 4.21 - Image of the Devine data after different number of iterations. 64 sources were employed from 548 to 672 m depth with the 13 receiver locations show in Figure 4.21. A smoothed version of the conductivity well log is plotted in gray scale format at the right of each image. (a) Image after 4 iterations. Mean residual error=0.96%. (b) Image after 6 iterations. Mean residual error= 0.65%.

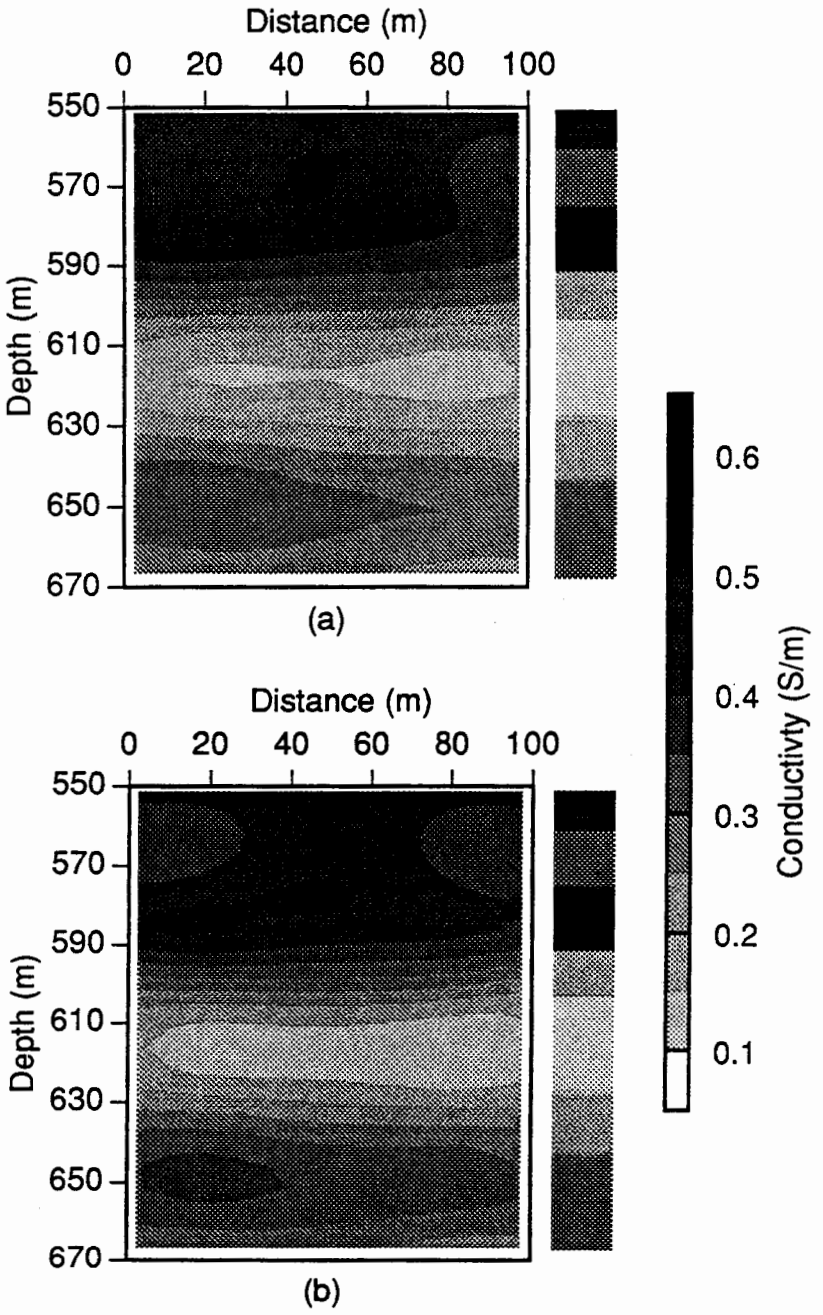

Figure 4.22 - Images of the synthetic data calculated for the 8 layer model given in Figure 4.21 with 0.5% random noise added. 64 sources were employed from 548 to 672 m depth with the 13 receiver locations shown in Figure 4.21. The model is plotted in gray scale format to the right of each image. (a) Image after 4 iterations. (b) Image after 6 iterations.

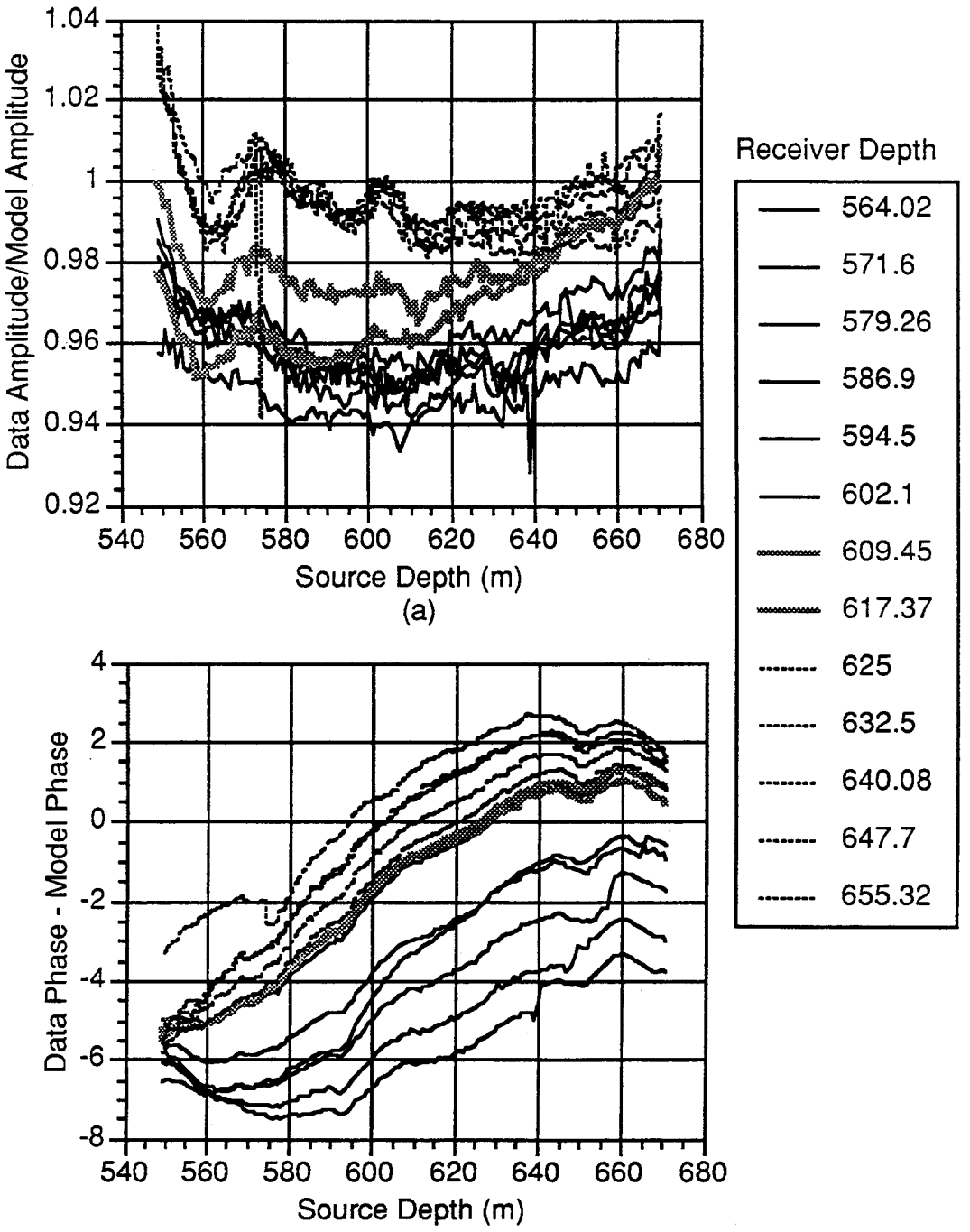

Figure 4.23 - Comparison of the Devine data to the theoretical fields calculated for the eight layered model shown in Figure 4.20. The results have been plotted in terms of the receiver depth. Receivers in the upper part of the section are represented as a thin black line, receivers in the 'drift zone' as a thick gray line, and receivers near the bottom as a dashed line. (a) Devine data amplitude normalized by the model amplitude. (b) Phase difference between the Devine data and the model results.

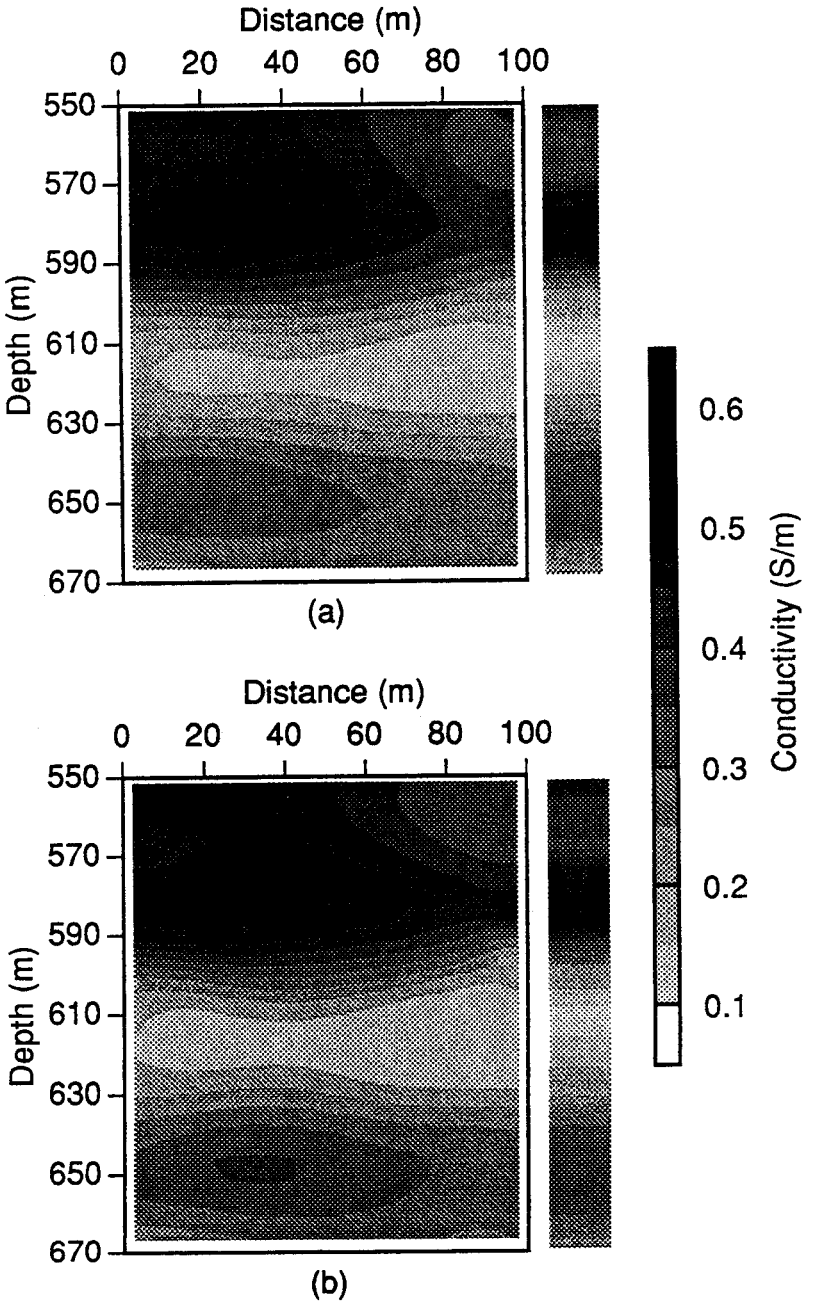

Figure 4.24 - Images of the corrected Devine data after a different number of iterations. 64 sources were employed from 548 to 672 m depth with the 13 receiver locations show in Figure 4.21. A smoothed version of the conductivity well log is plotted in gray scale format to the right of each image. (a) Image after 4 iterations. Mean residual error=0.87%. (b) Image after 6 iterations. Mean residual error= 0.57%.

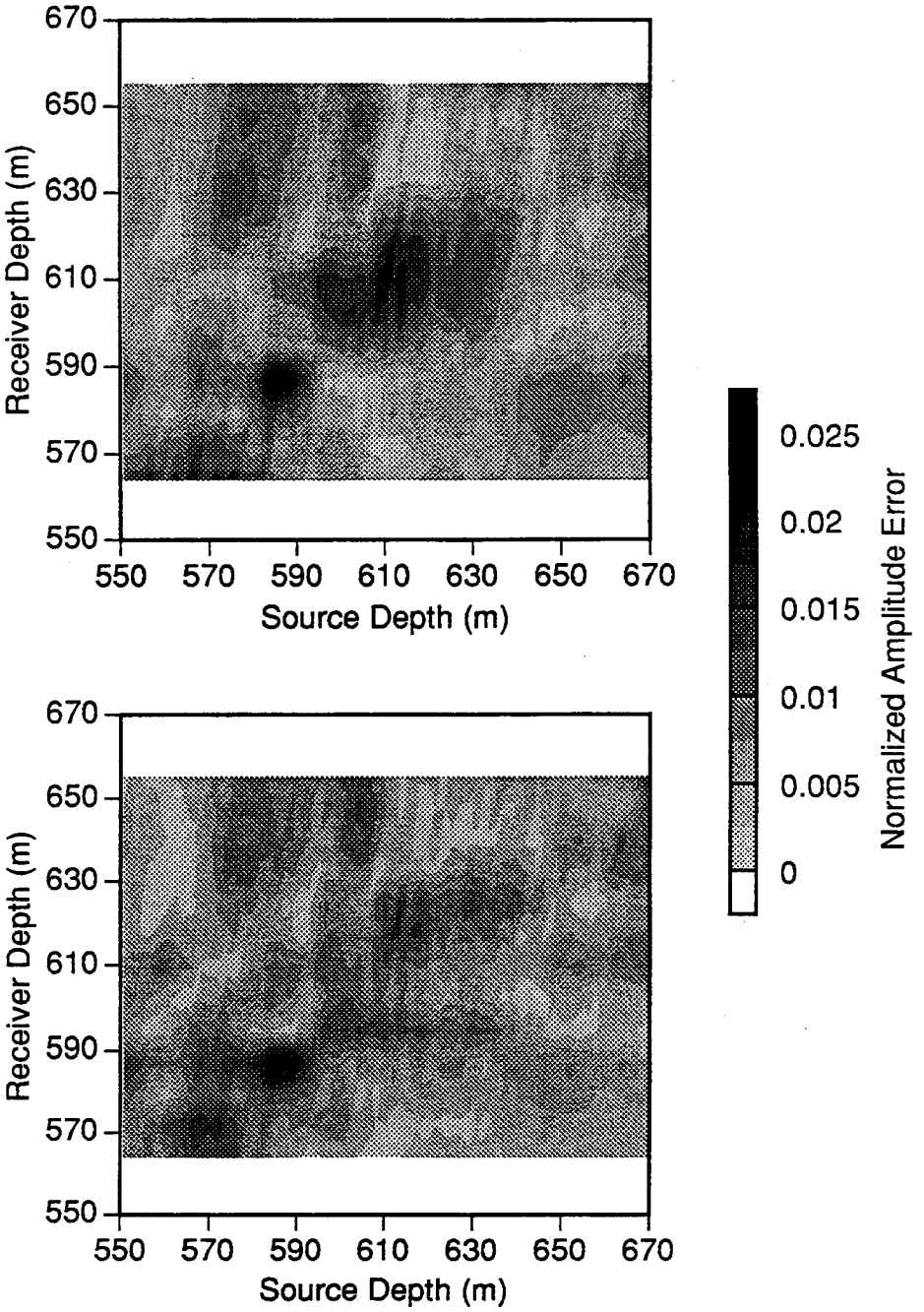

Figure 4.25 - Residual amplitude errors between the input data and the calculated results for the images as a function of source and receiver depth. the errors have been normalized by the maximmum value of the total field in the input data. (a) Residual errors for the image of the uncorrected Devine data in Figure 4.21b. (b) Residual errors for the image of the corrected Devine data in Figure 4.23b.

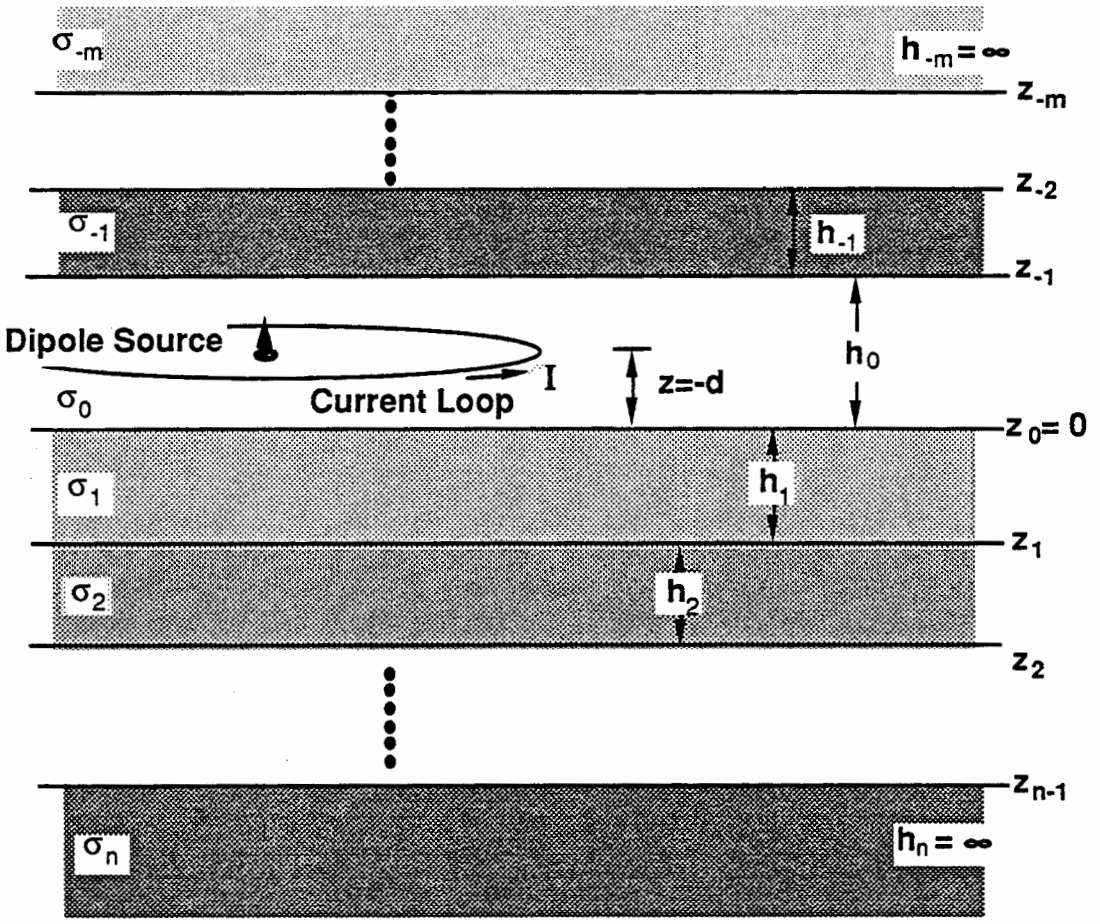

Figure 4.26 - Vertical magnetic dipole and a horizontal loop of current imbedded in a stratified medium. Both the dipole and loop are at a distance z=-d above the base of the source layer (z=0) and are centered radially at r=0.

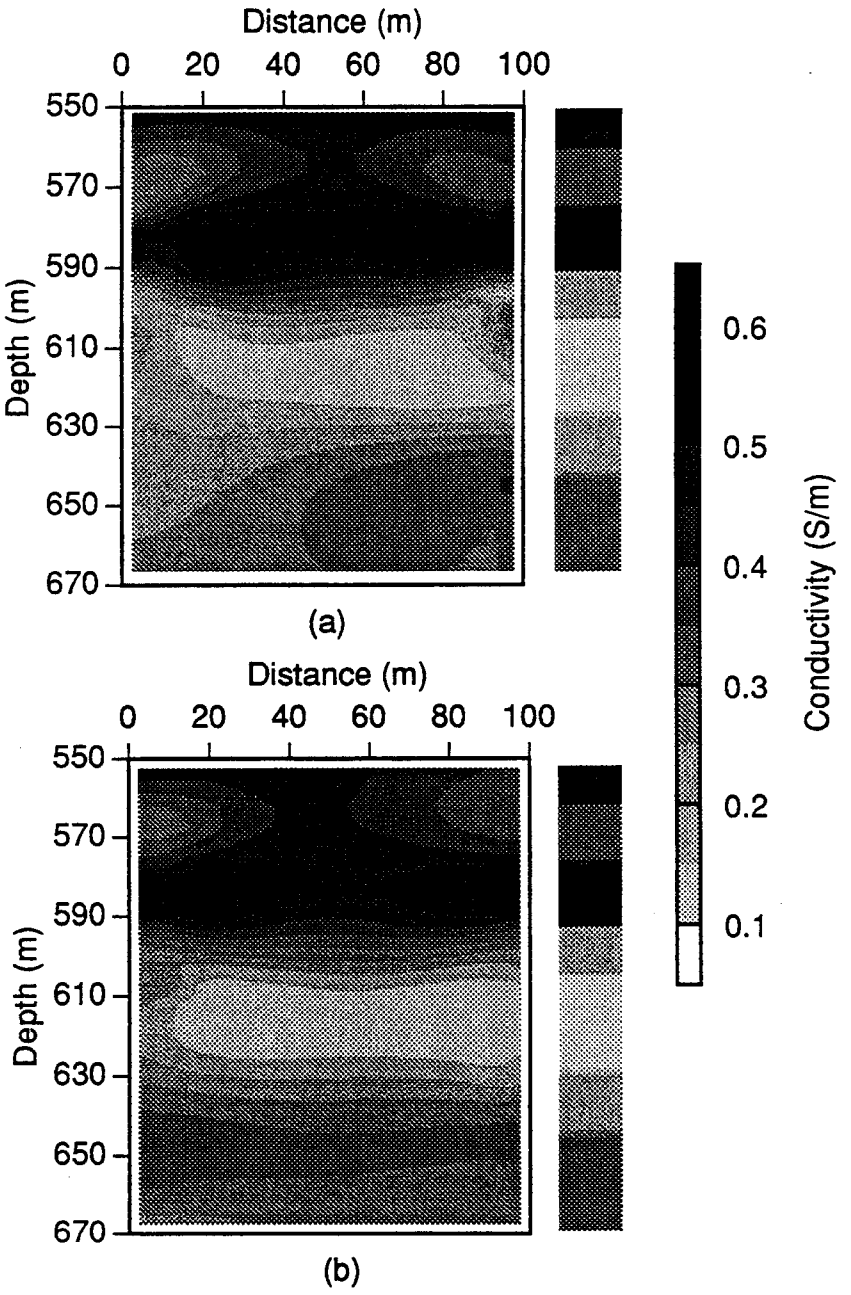

Figure 4.27 - Images of the synthetic data calculated for the 8 layer model given in Figure 4.20 using two different background models. 64 sources are evenly spaced from 550 to 670 m with 13 receivers spaced as shown in Figure 4.21 and 0.5% random noise have been added to the data. (a) Image using the whole space model with a conductivity of 0.33S/m. Mean residual error after 11 iterations=0.50%. (b) Image using 3 layered background model. Mean residual error after 10 iterations=0.50%. Layer 1 has a thickness of 550 m and a conductivity of 0.5S/m. Layer 2 has a thickness of 120m and a conductivity of 0.35 S/m. Layer 3 extends downward from 670m to infinity and has a conductivity of 0.125 S/m.

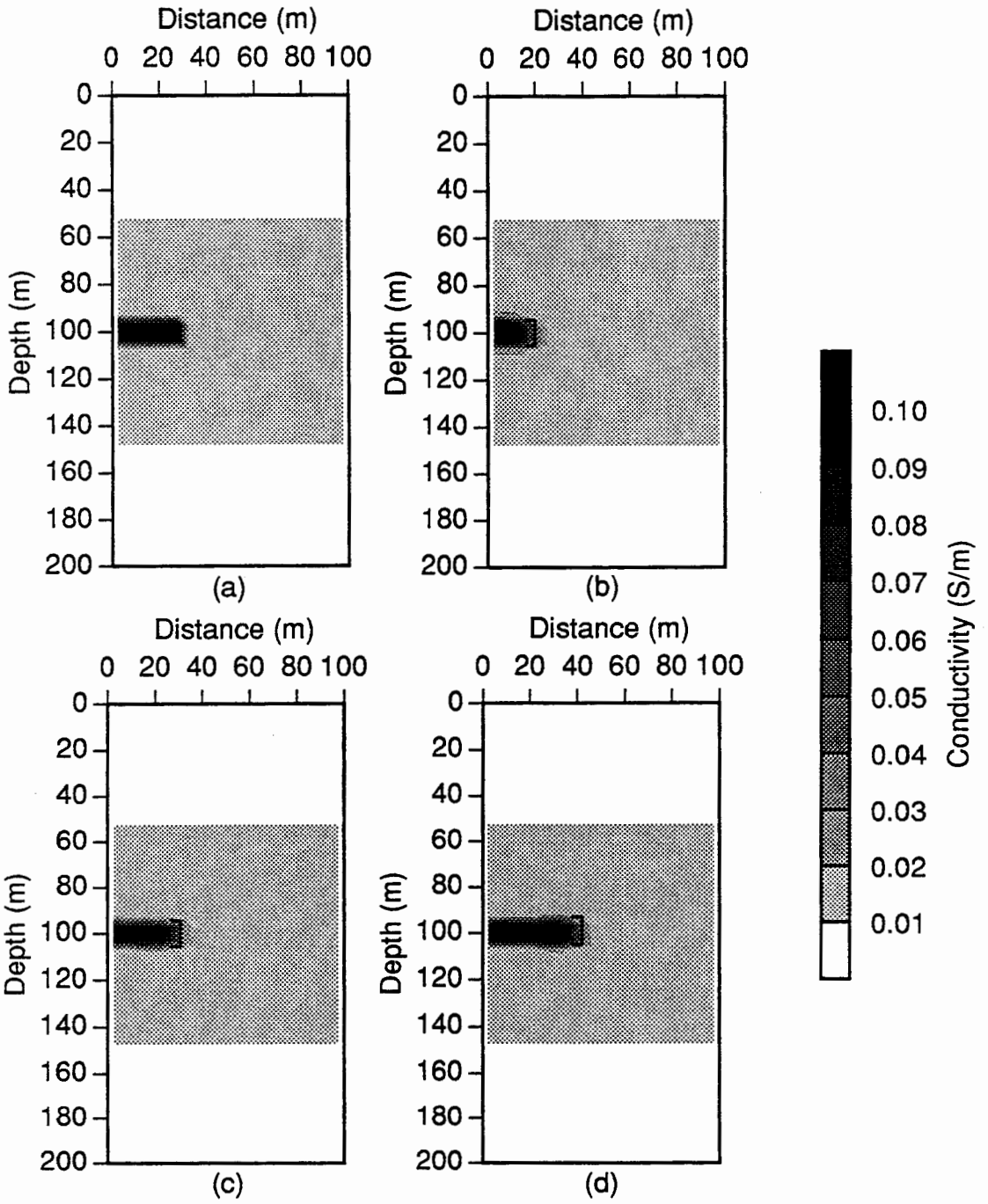

Figure 4.28 - Injected plume model and 10 kHz images for different plume radii (rp). The images were reconstructed using results calculated at 21 source and receiver positions spaced at 10m intervals from 0 to 200m depth. The added noise is 1.0% of the maximum total field and the bracket in each image indicates the radial extent and width of the body (a) Model for rp=30m. (b) Image for rp=20m. Mean residual error after 17 iterations = 1.0%. (c) Image for rp=30m. Mean residual error after 18 iterations = 1.0%. (d) Image for rp=40m. Mean residual error after 17 iterations = 1.0%. (Continued on next page)

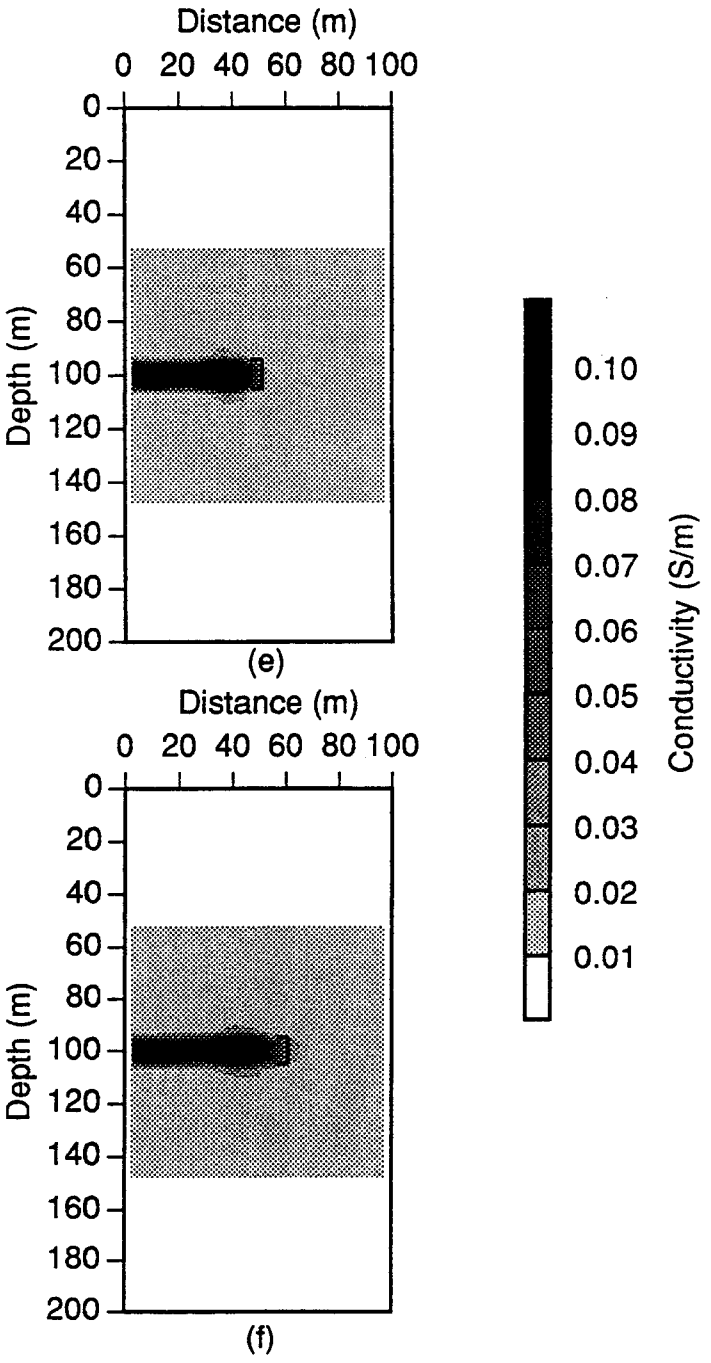

Figure 4.28 - (Continued from previous page) (e) Image for rp=50m. Mean residual error after 19 iterations = 1.0% (f) Image for rp=60m. Mean residual error after 19 iterations = 1.0%.

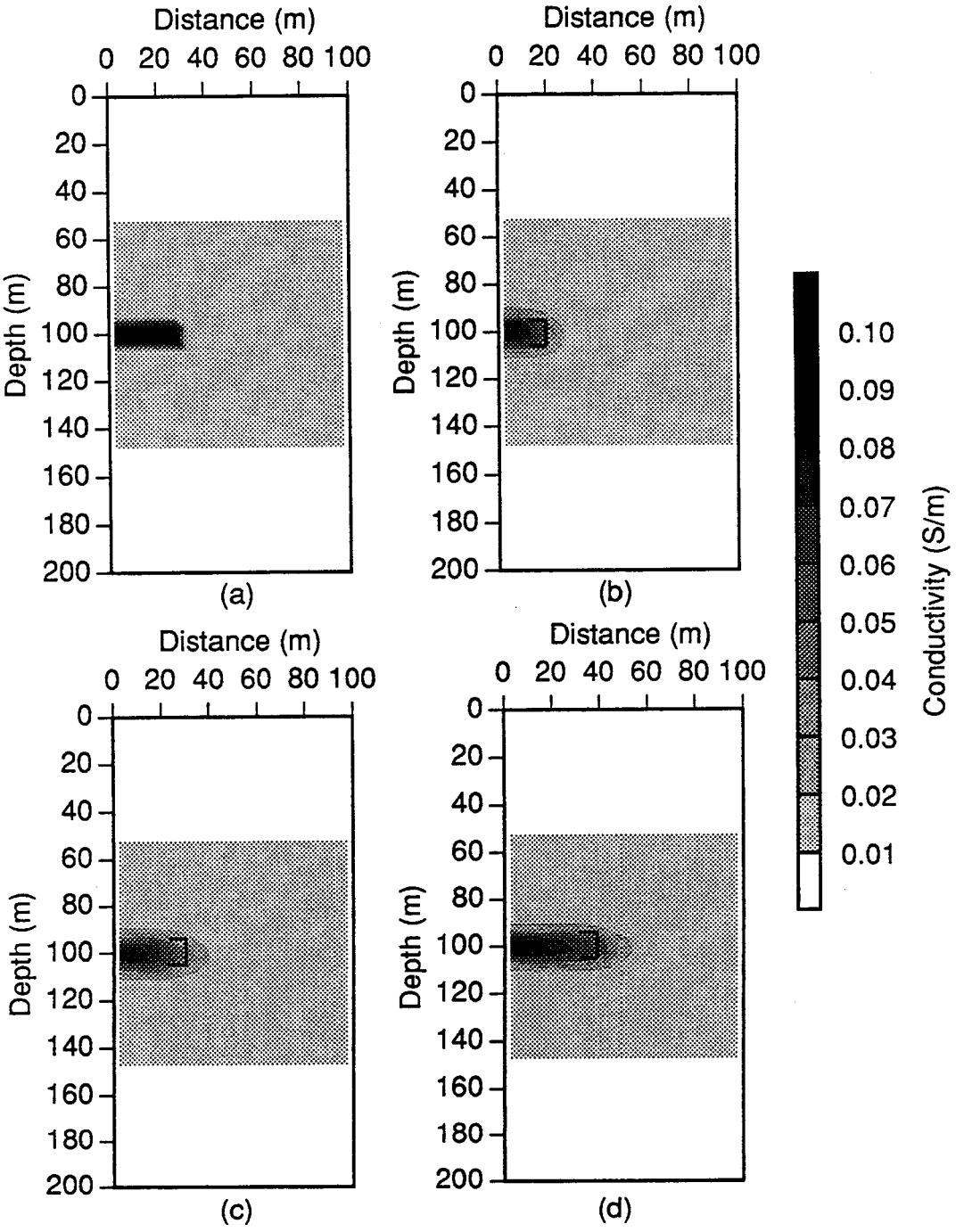

Figure 4.29 - Injected plume model and 10 kHz images for different plume radii (rp). The images were reconstructed using results calculated at 21 source and receiver positions spaced at 10m intervals from 0 to 200m depth. The added noise is 5.0% of the maximum total field and the bracket in each image indicates the radial extent and width of the body (a) Model for rp=30m. (b) Image for rp=20m. Mean residual error after 13 iterations = 5.0%. (c) Image for rp=30m. Mean residual error after 13 iterations = 5.0%. (d) Image for rp=40m. Mean residual error after 14 iterations = 5.0%. (Continued on next page)

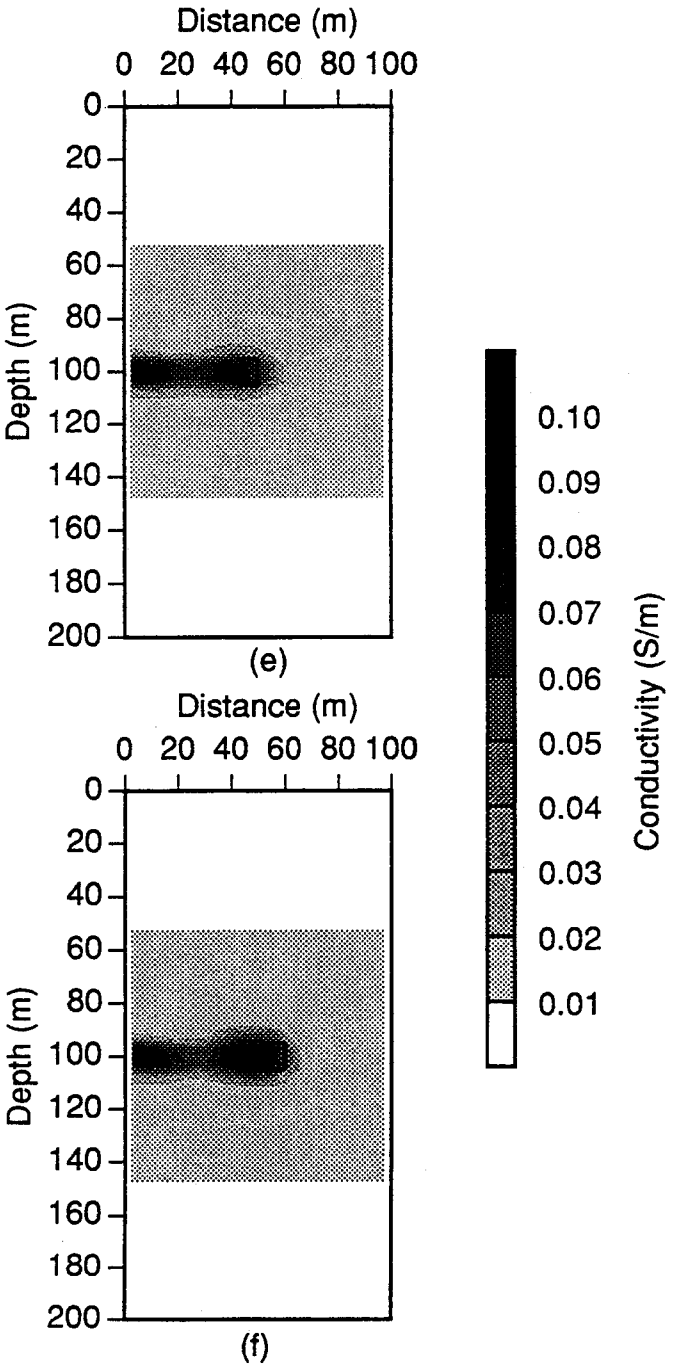

Figure 4.29 - (Continued from previous page) (e) Image for rp=50m. Mean residual error after 15 iterations = 5.0% (f) Image for rp=60m. Mean residual error after 15 iterations = 5.0%.

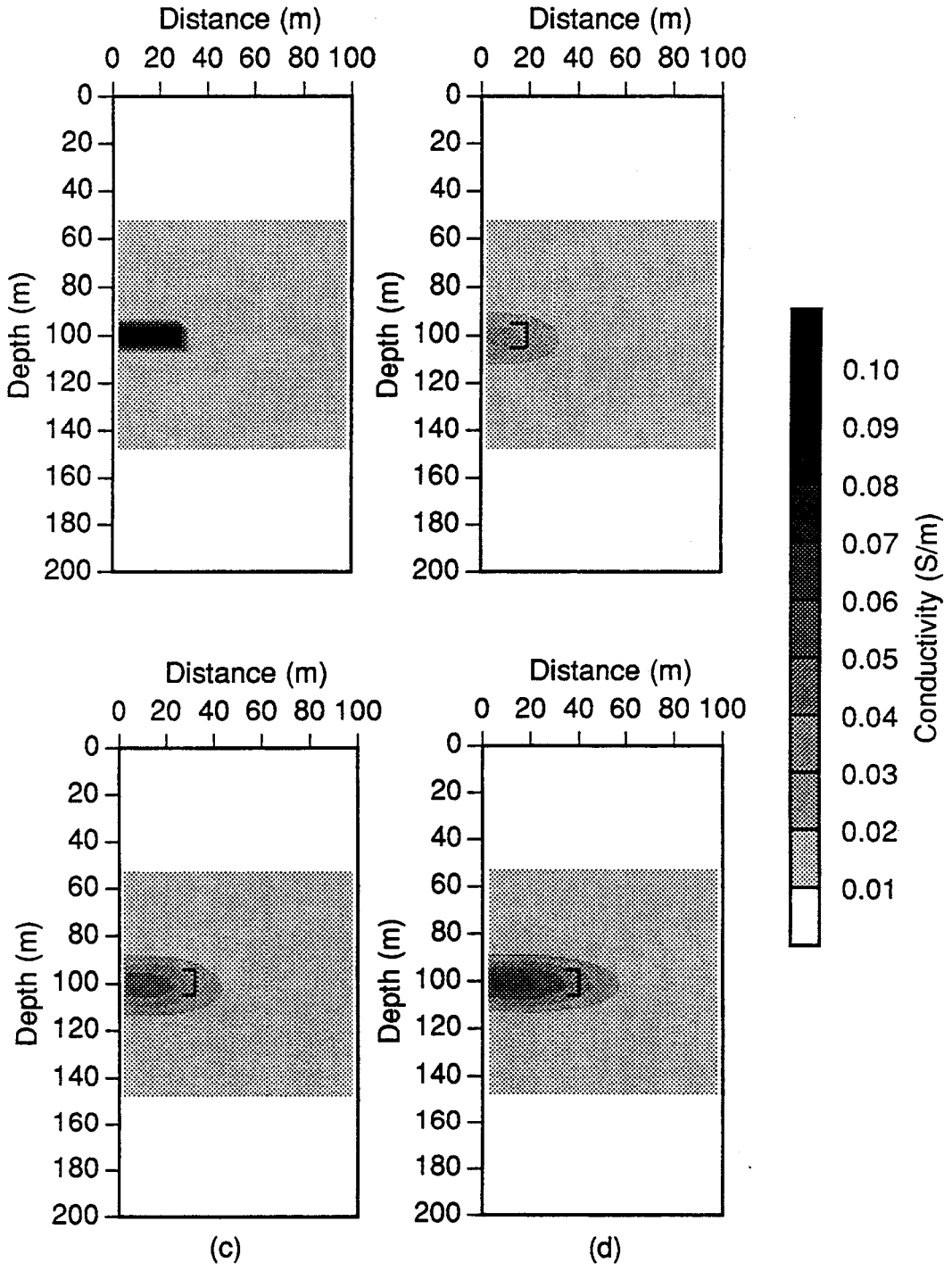

Figure 4.30 - Injected plume model and 10 kHz images for different plume radii (rp). The images were reconstructed using results calculated at 21 source and receiver positions spaced at 10m intervals from 0 to 200m depth. The added noise is 10.0% of the maximum total field and the bracket in each image indicates the radial extent and width of the body (a) Model for rp=30m. (b) Image for rp=20m. Mean residual error after 9 iterations = 10.1%. (c) Image for rp=30m. Mean residual error after 10 iterations = 10.1%. (d) Image for rp=40m. Mean residual error after 11 iterations = 10.1%. (Continued on next page)

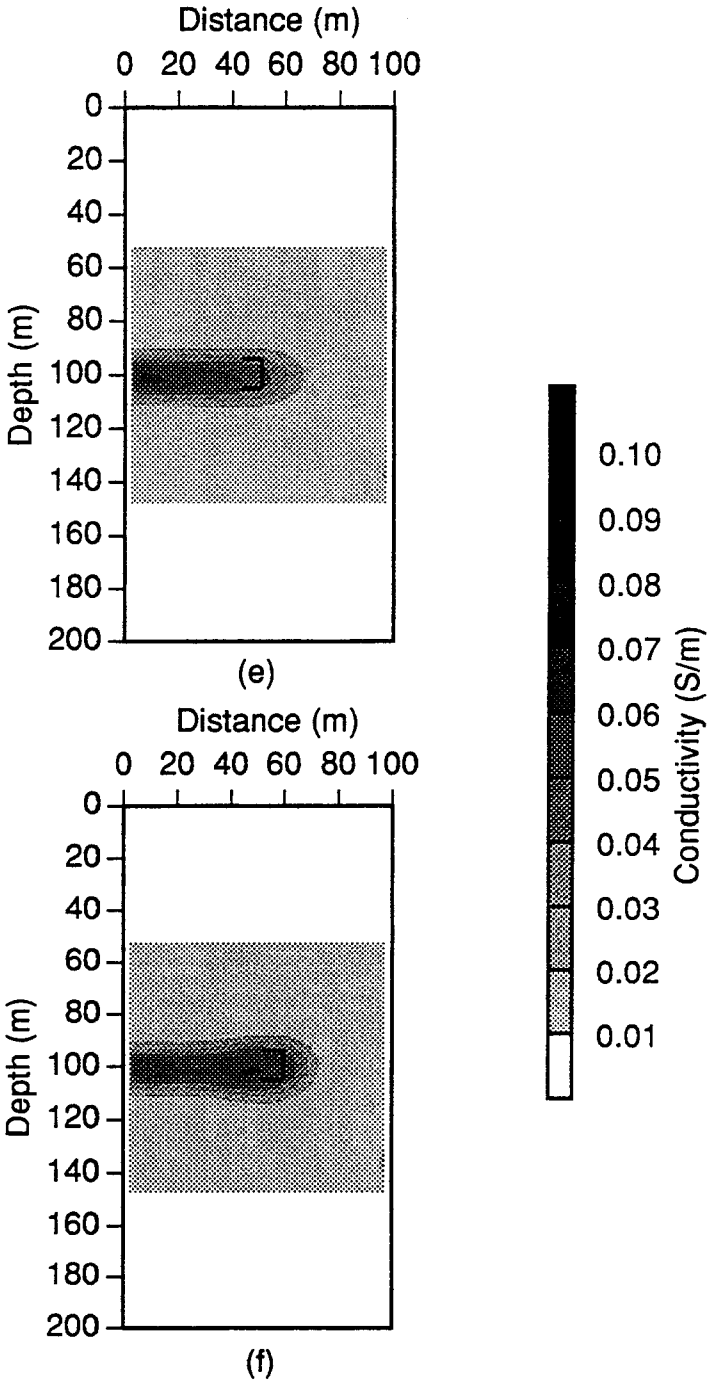

Figure 4.30- (Continued from previous page) (e) Image for rp=50m. Mean residual error after 12 iterations = 10.1% (f) Image for rp=60m. Mean residual error after 12 iterations = 10.1%.

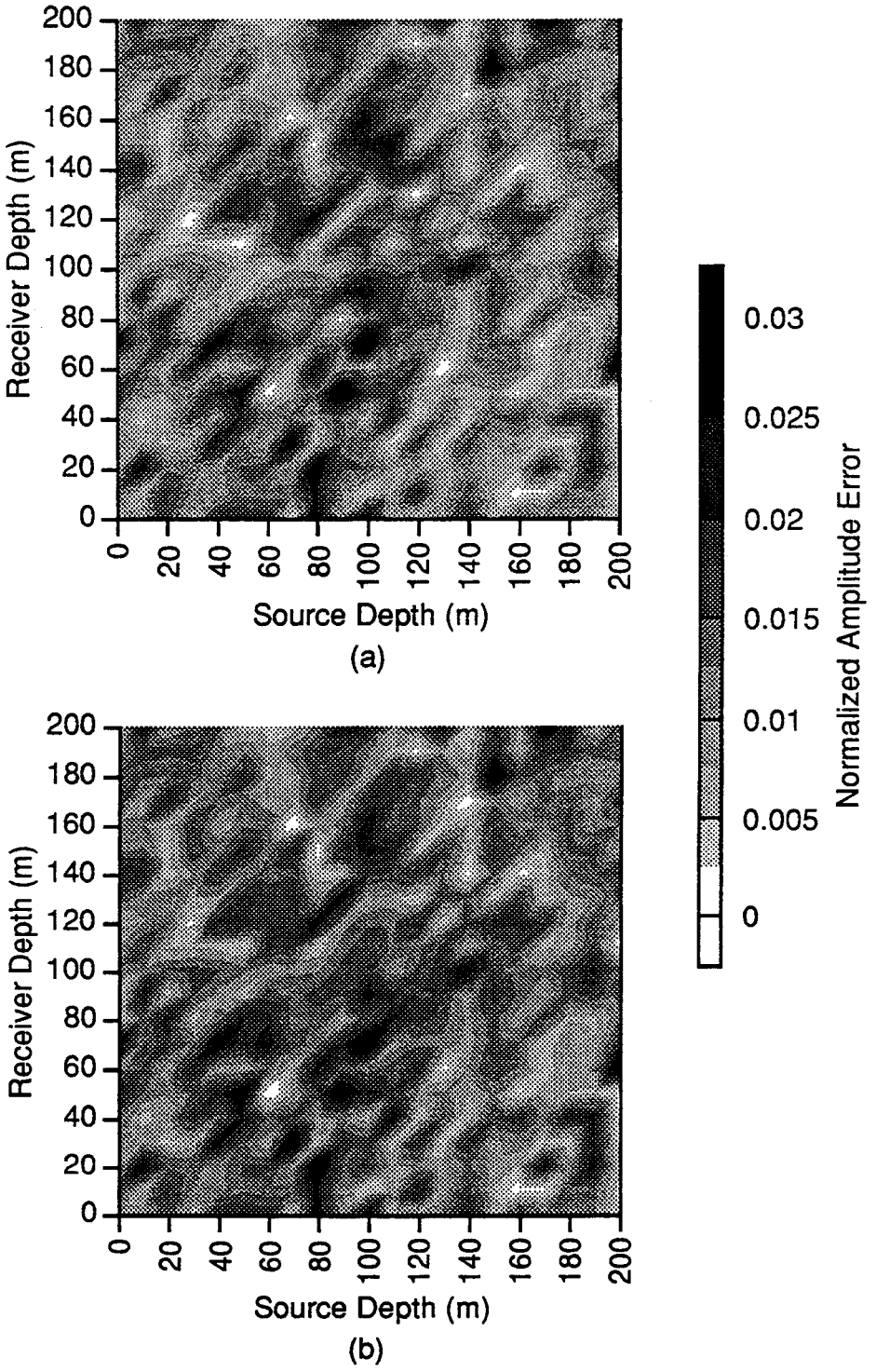

Figure 4.31 - Residual amplitude error between the input data and the calculated results for images given in Figure 4.28 as a function of source and receiver depth. The errors have been normalized by the maximum value of the total field in the data. (a) Residual errors for the image given in Figure 4.28b. (b) Residual errors for the image given in Figure 4.28e.

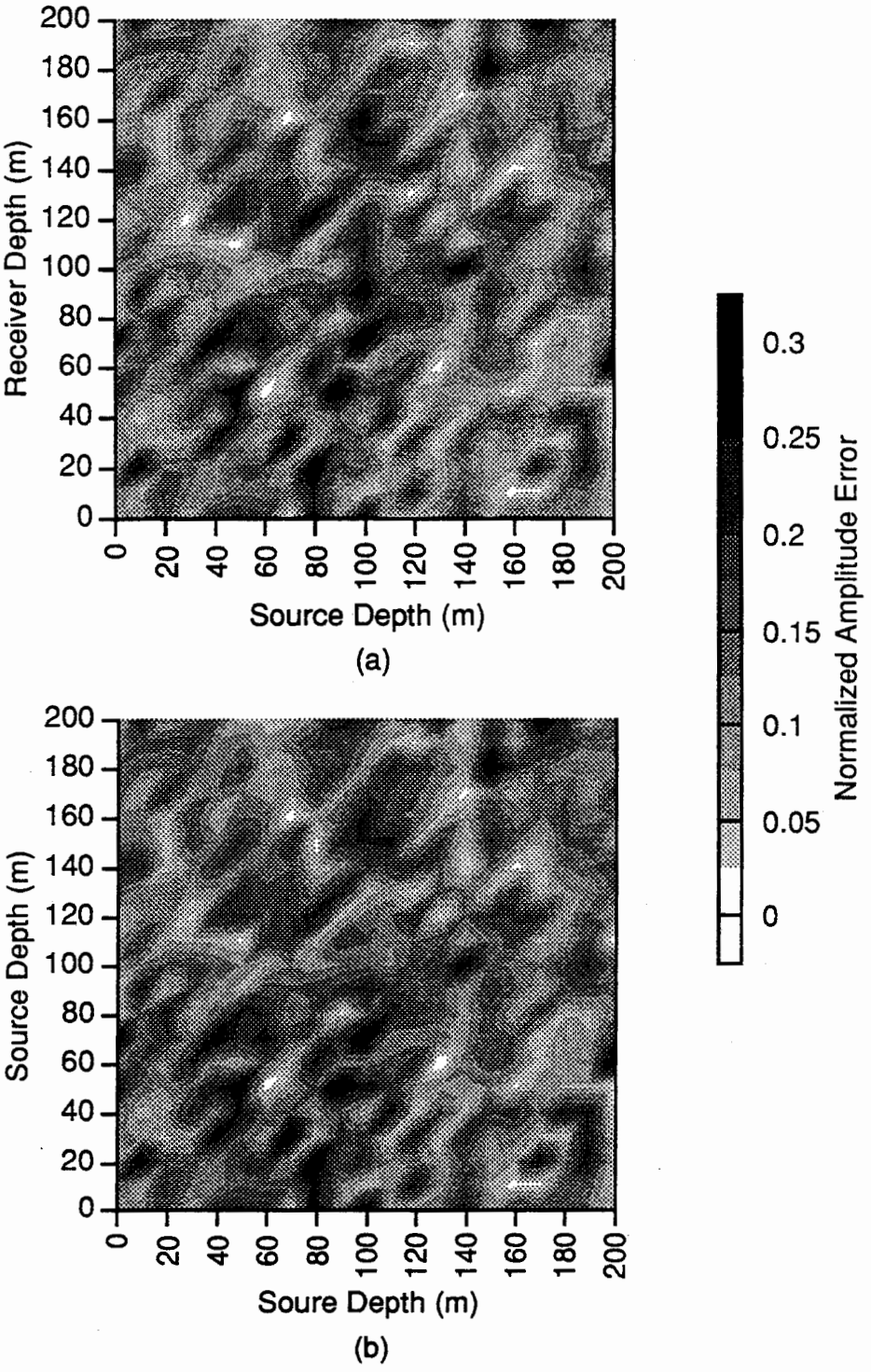

Figure 4.32 - Residual amplitude error between the input data and the calculated results for images given in Figure 4.30 as a function of source and receiver depth. The errors have been normalized by the maximum value of the total field in the data. (a) Residual errors for the image given in Figure 4.30b. (b) Residual errors for the image given in Figure 4.30e.

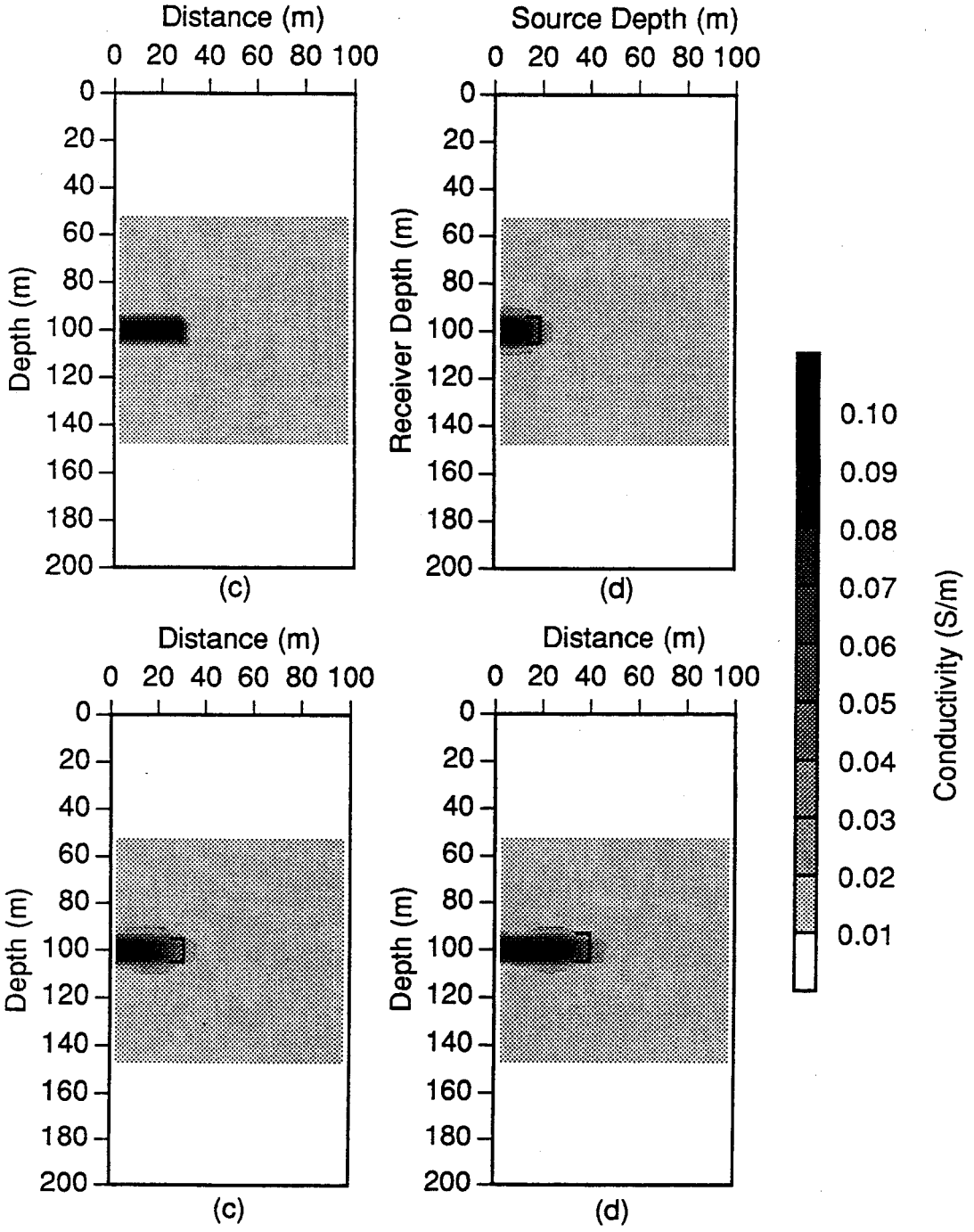

Figure 4.33 - Injected plume model and 1 kHz images for different plume radii (rp). The images were reconstructed using results calculated at 21 source and receiver positions spaced at 10m intervals from 0 to 200m depth. The added noise is 0.10% of the maximum total field and the bracket in each image indicates the radial extent and width of the body. (a) Model for rp=30m. (b) Image for rp=20m. Mean residual misfit after 24 iterations = 0.10%. (c) Image for rp=30m. Mean residual error after 25 iterations = 0.10%. (d) Image for rp=40m. Mean residual error after 26 iterations = 0.10%. (Continued on next page)

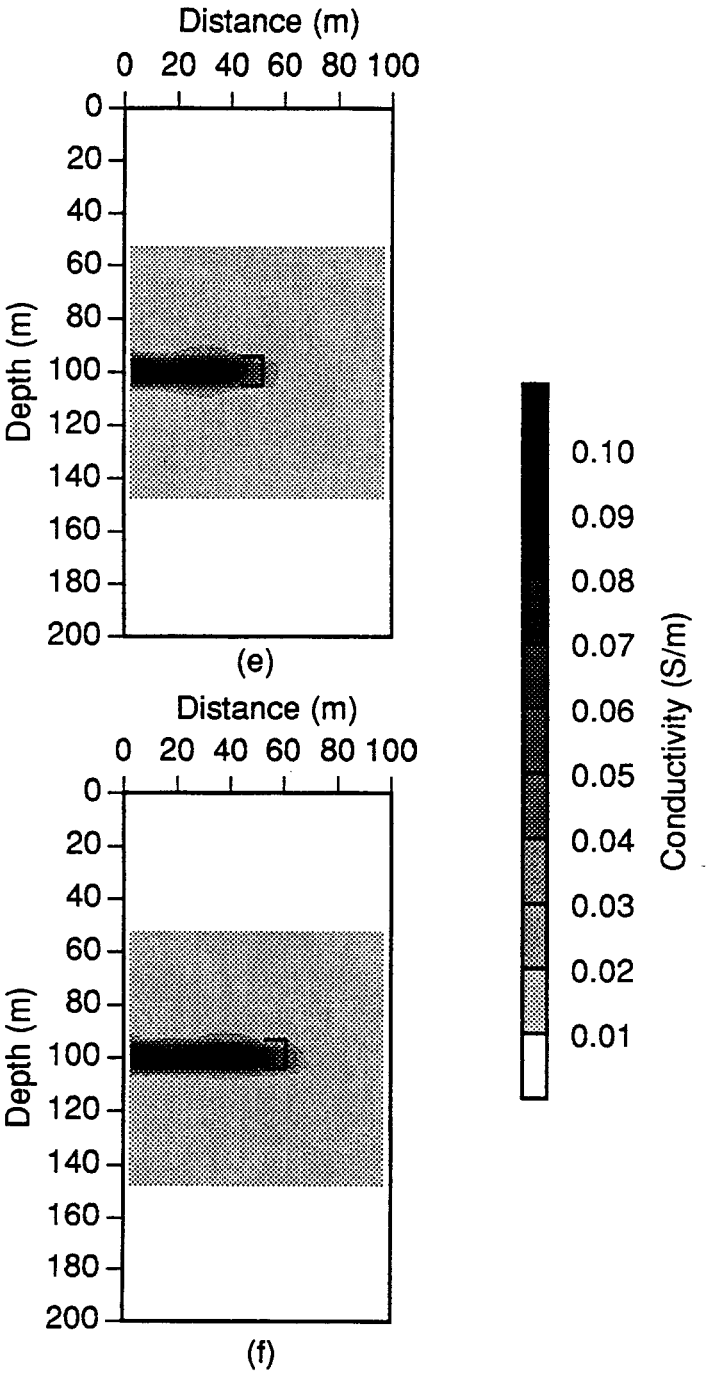

Figure 4.33- (Continued from previous page) (e) Image for rp=50m. Mean residual error after 12 iterations = 0.10%. (f) Image for rp=60m. Mean residual error after 12 iterations = 0.10%.

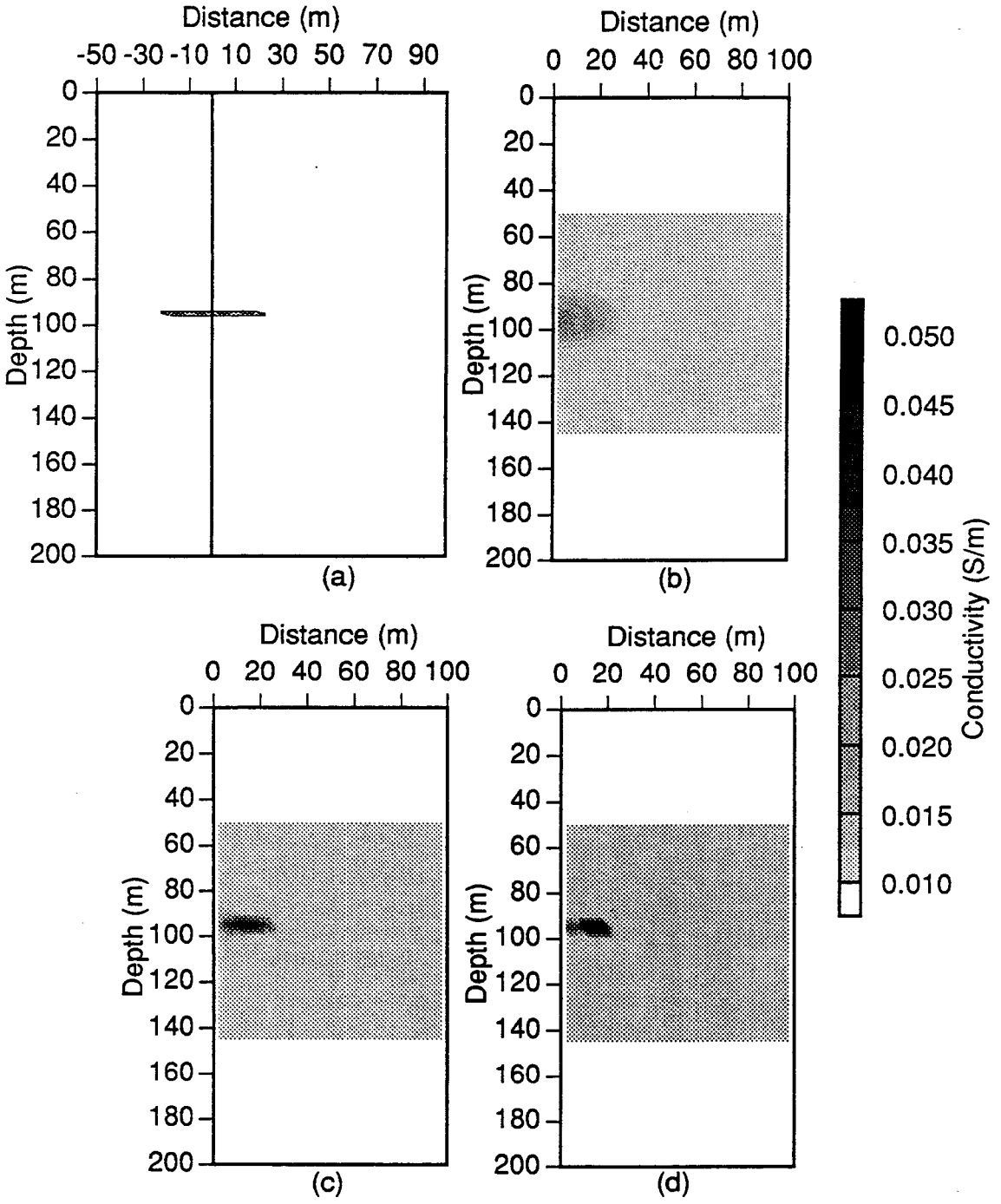

Figure 4.34- Centered 3D sheet model and images as a function of frequency. (a) 40m by 40m sheet model of conductance 0.2S which is centered both in the x and y directions about the source borehole. Results have been calculated for 21 source and receiver positions spaced at 10m intervals from 0 to 200m depth. The added noise is 0.1% of the maximum total field at each frequency. (b) 1 kHz image. Mean residual error after 11 iterations=0.10%. (c) 10 kHz image. Mean residual error after 19 iterations = 0.10%. (d) 100 kHz image. Mean residual error after 25 iterations = 0.12%.

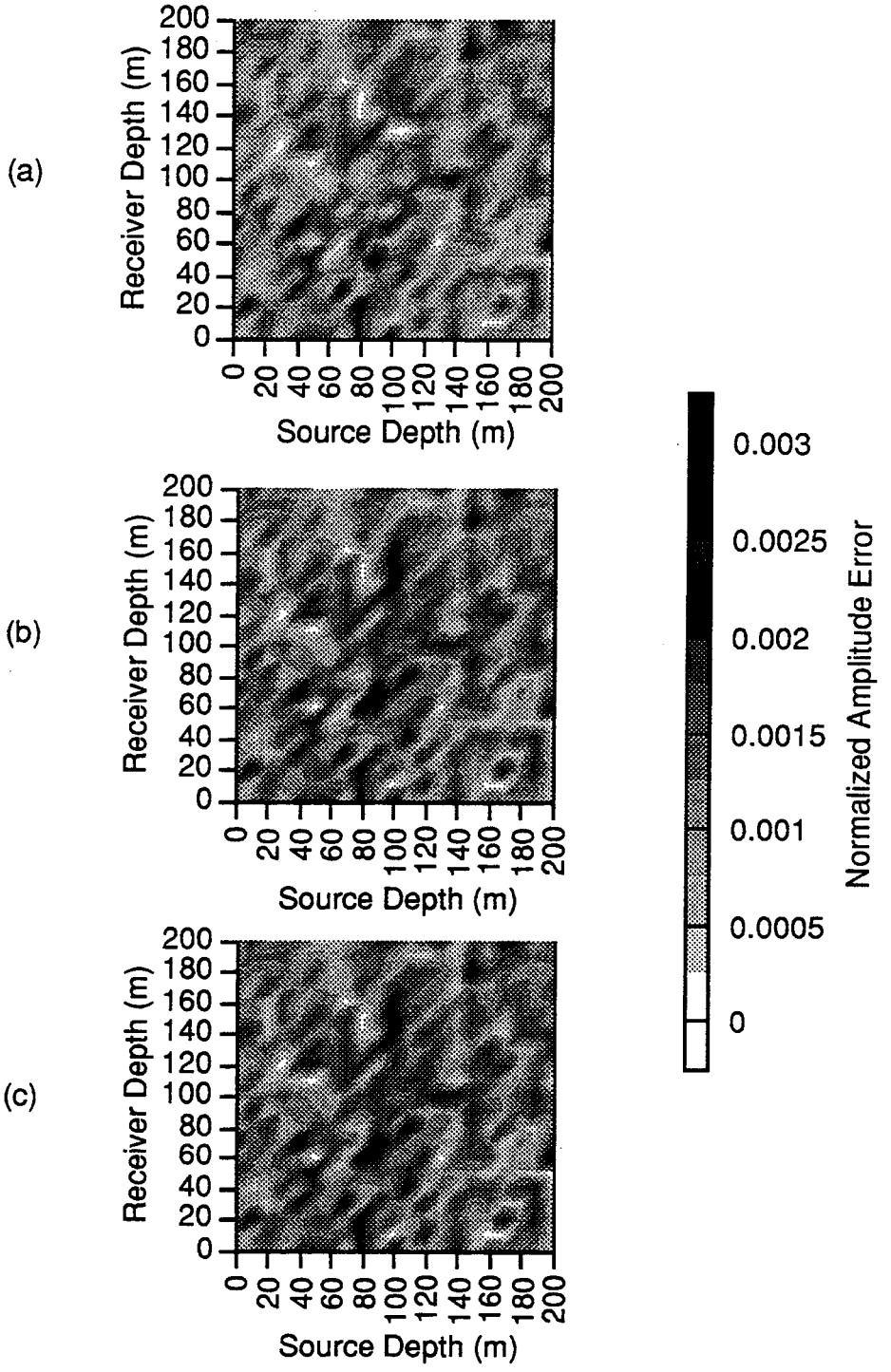

Figure 4.35 - Residual amplitude error between the input data and the calculated results for the images in Figure 4.34 plotted as a function of source and receiver depth. The errors has been normalized by the maximum value of the total field in the data. (a) Residual errors for the 1kHz image given in Figure 4.34b. (b) Residual errors for the 10 kHz image given in Figure 4.34c. (c) Residual errors for the 100 kHz image given in Figure 4.34d.

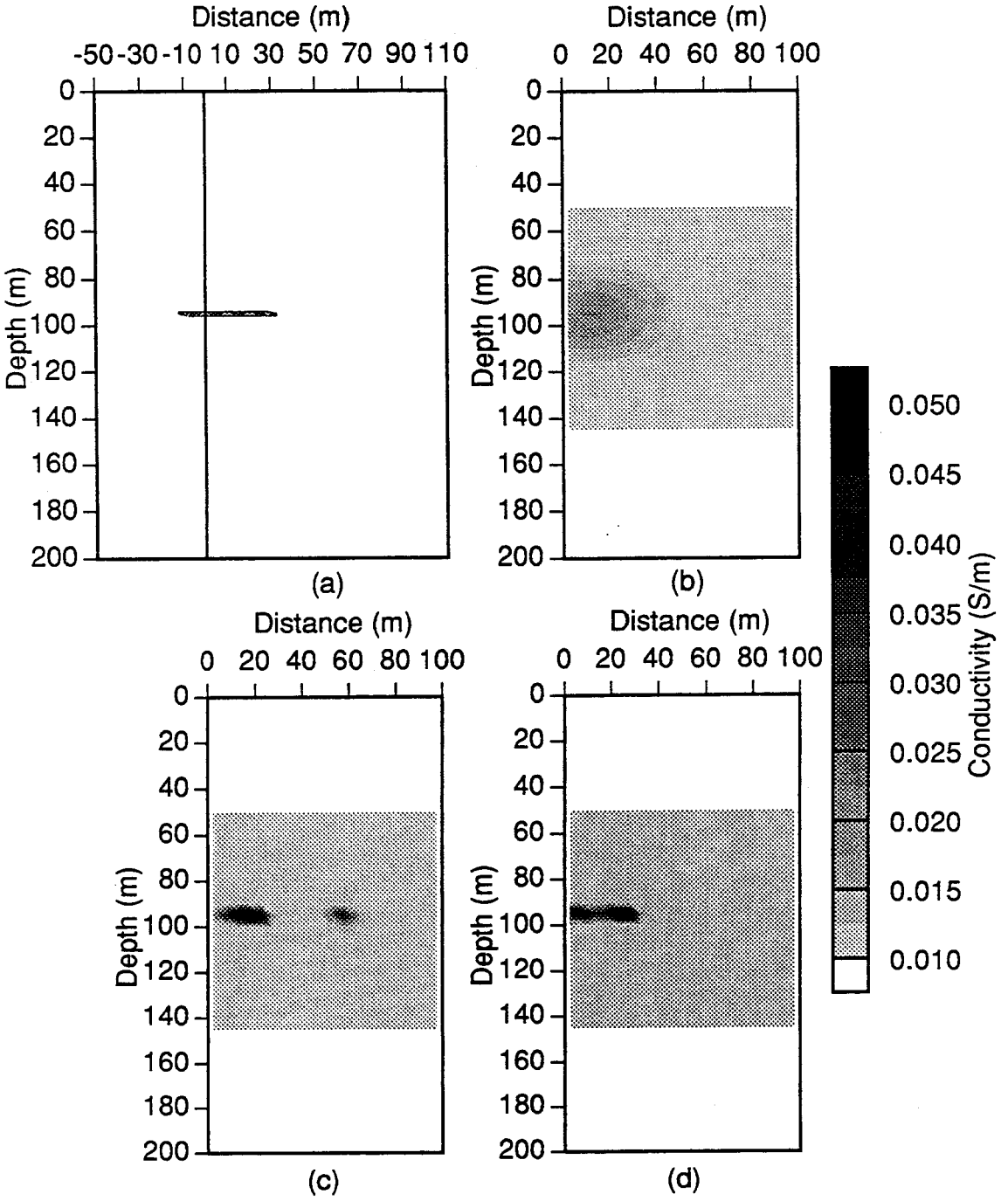

Figure 4.36- 3D model with the sheet offset from the source well by +10m and the resulting images as a function of frequency. (a) 40m by 40m sheet model of conductance 0.2S centered in the y direction (in and out of the page) about the source borehole. Results have been calculated for 21 source and receiver positions from 0 to 200m depth at 10m intervals. The added noise is 0.1% of the maximum total field at each frequency. (b) 1 kHz image. Mean residual error after 11 iterations=0.17%. (c) 10 kHz image. Mean residual error after 19 iterations = 0.49%. (d) 100 kHz image. Mean residual error after 25 iterations = 0.13%.

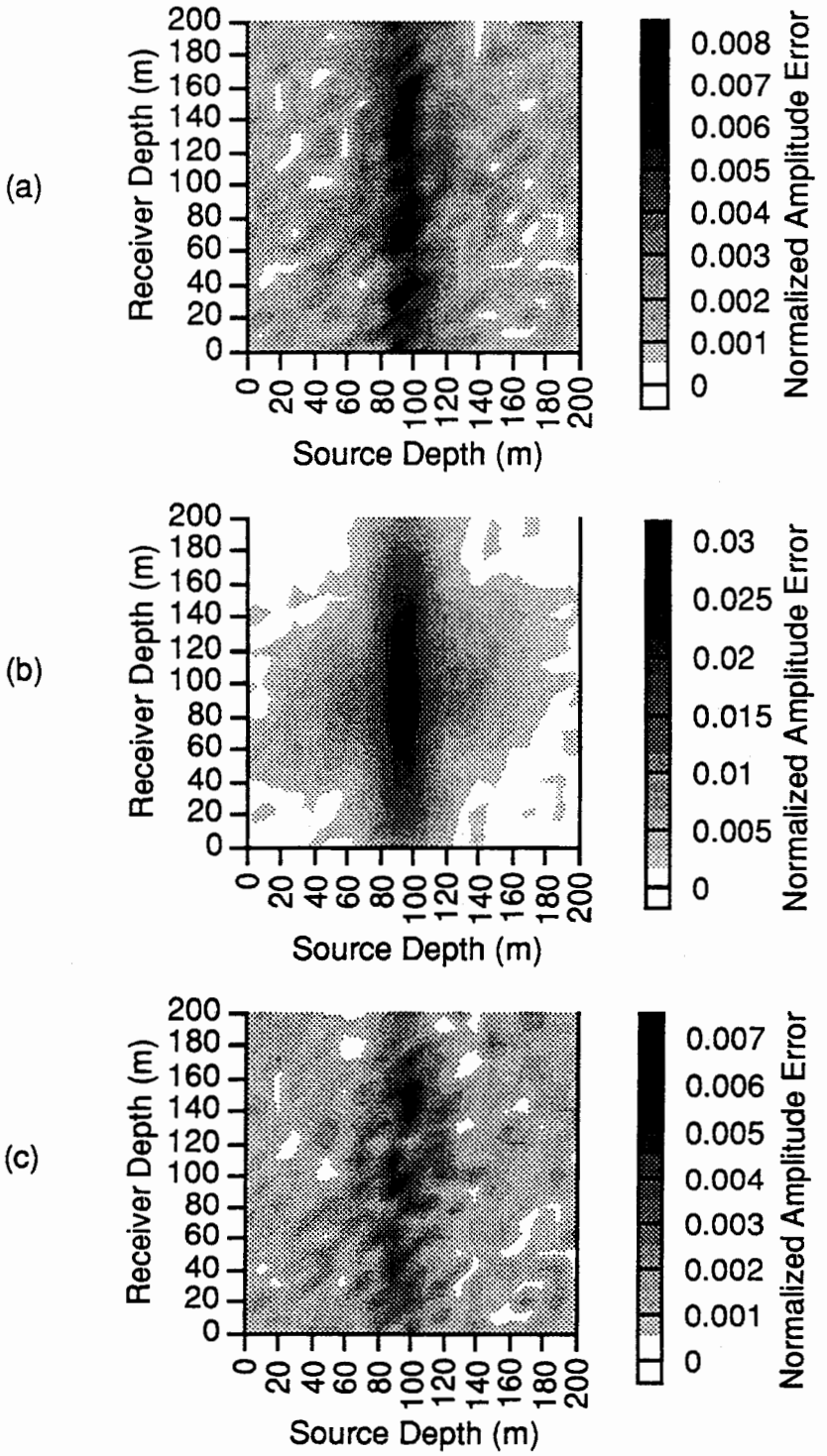

Figure 4.37 - Residual amplitude error between the input data and the calculated results for the images in Figure 4.36 plotted as a function of source and receiver depth. The errors has been normalized by the maximum value of the total field in the data. (a) Residual errors for the 1kHz image given in Figure 4.36b. (b) Residual errors for the 10 kHz image given in Figure 4.36c. (c) Residual errors for the 100 kHz image given in Figure 4.36d.

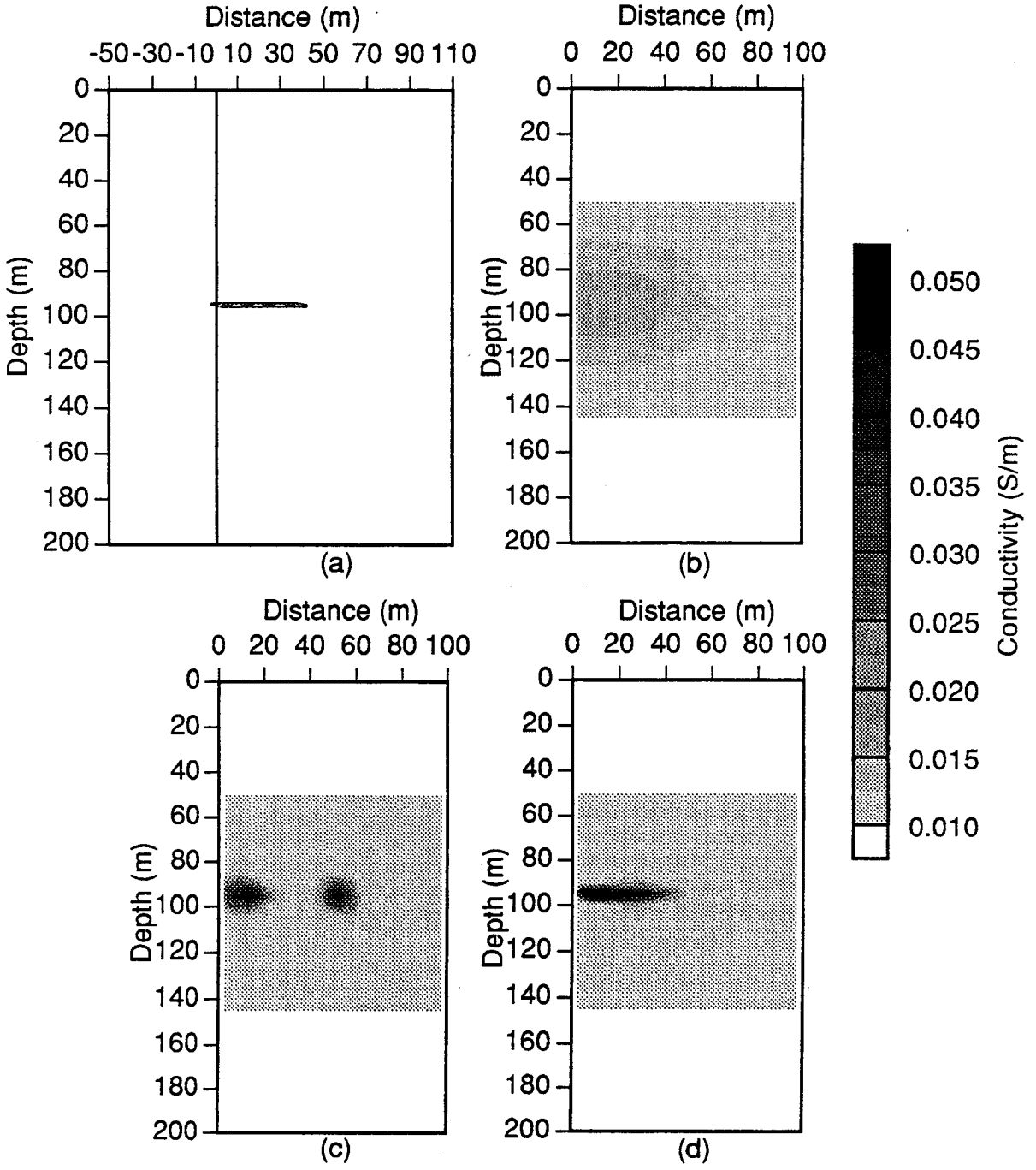

Figure 4.38- 3D model with the sheet offset from the source well by 20m and the resulting images as a function of frequency. (a) 40m by 40m sheet model of conductance 0.2S centered in the y direction (in and out of the page) about the source borehole. Results have been calculated for 21 source and receiver positions from 0 to 200m depth at 10m intervals. The added noise is 0.1% of the maximum total field at each frequency. (b) 1 kHz image. Mean residual error after 11 iterations=0.37%. (c) 10 kHz image. Mean residual error after 19 iterations = 1.1%. (d) 100 kHz image. Mean residual error after 25 iterations = 0.24%.

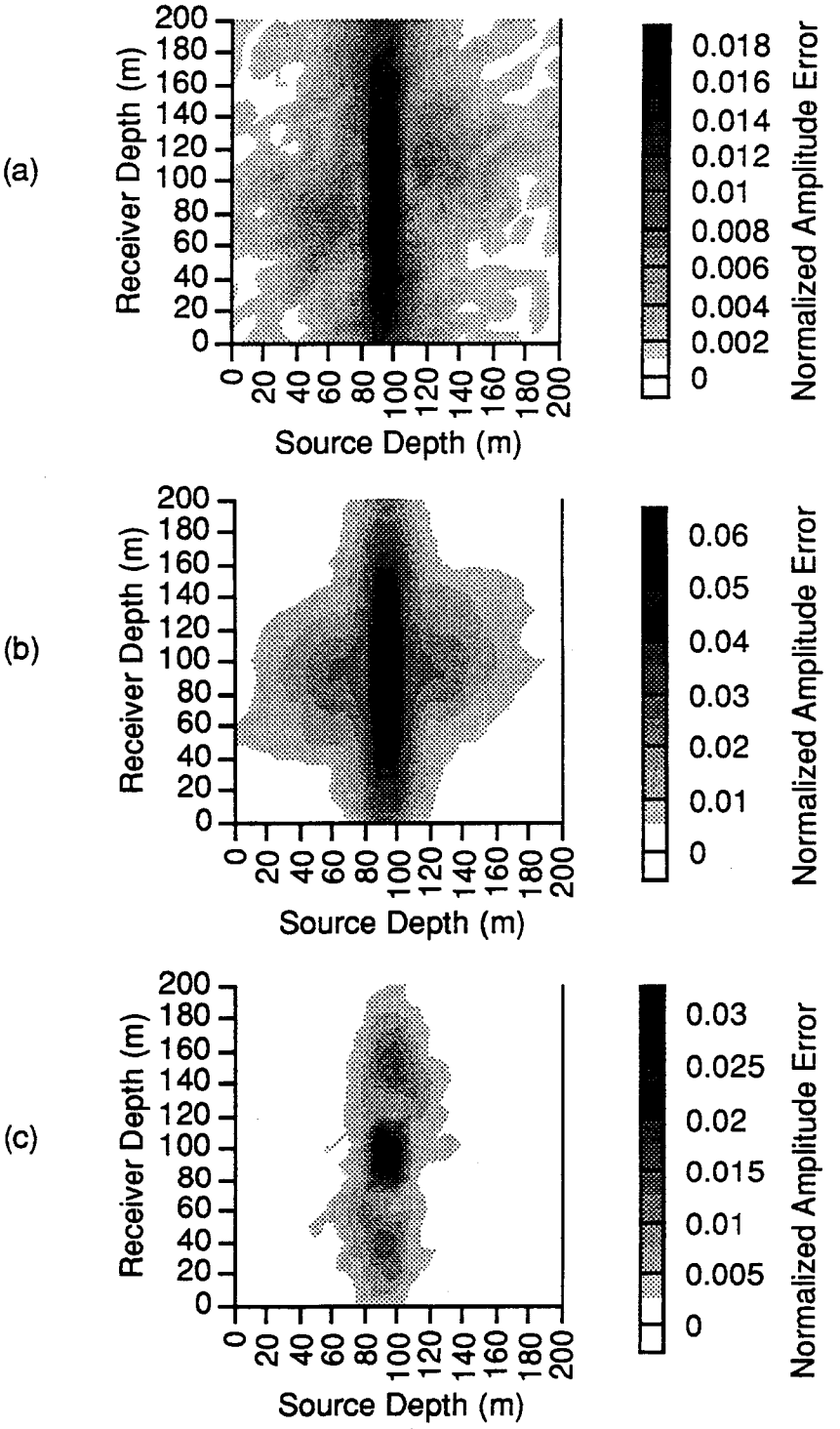

Figure 4.39 - Residual amplitude error between the input data and the calculated results for the images in Figure 4.38 plotted as a function of source and receiver depth. The errors has been normalized by the maximum value of the total field in the data. (a) Residual errors for the 1kHz image given in Figure 4.38b. (b) Residual errors for the 10 kHz image given in Figure 4.38c. (c) Residual errors for the 100 kHz image given in Figure 4.38d.

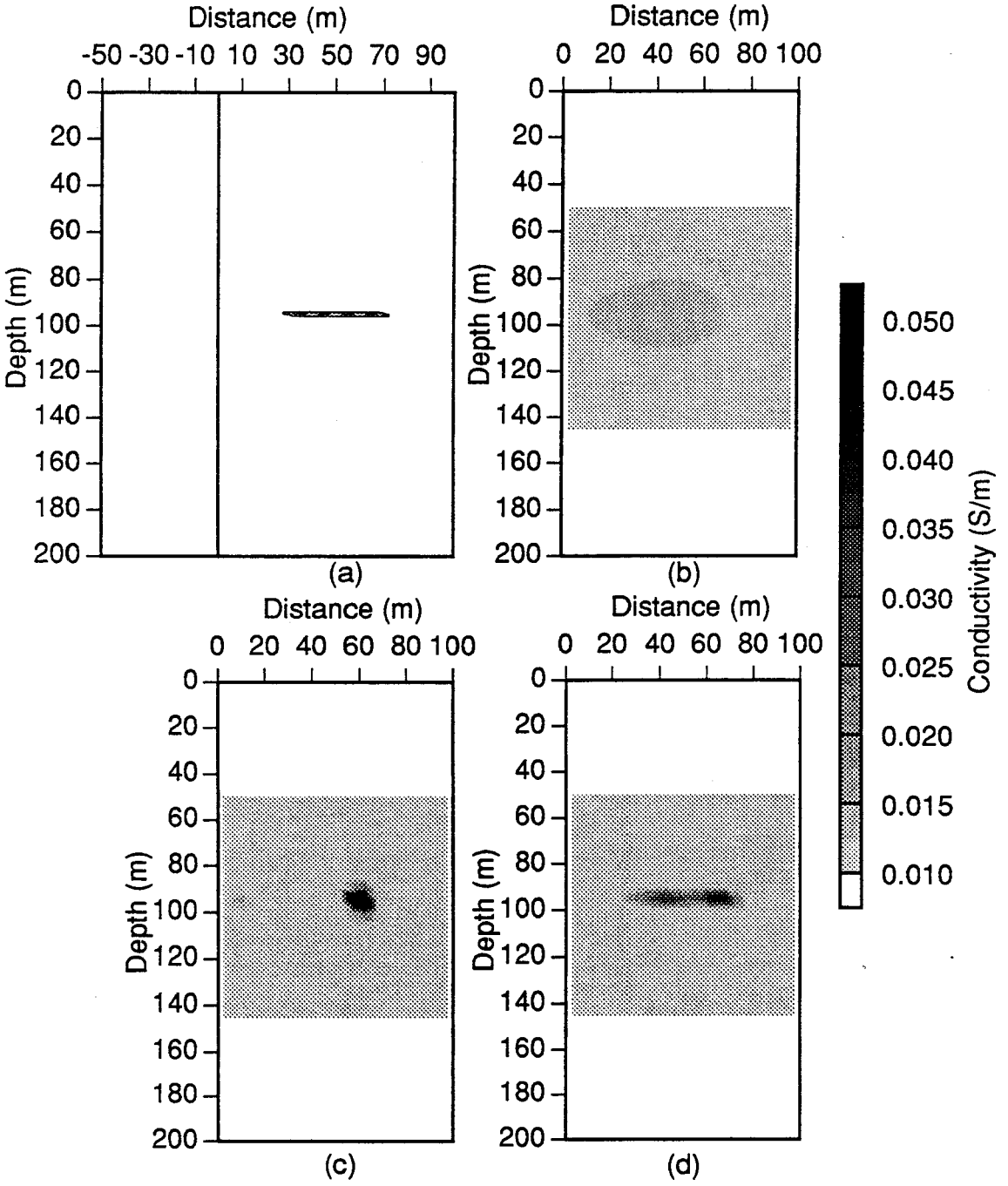

Figure 4.40- 3D model with the sheet offset from the source well by 50m and the resulting images as a function of frequency. (a) 40m by 40m sheet model of conductance 0.2S centered in the y direction (in and out of the page) about the source borehole. Results have been calculated for 21 source and receiver positions from 0 to 200m depth at 10m intervals. The added noise is 0.1% of the maximum total field at each frequency. (b) 1 kHz image. Mean residual error after 11 iterations=0.17%. (c) 10 kHz image. Mean residual error after 19 iterations = 0.27%. (d) 100 kHz image. Mean residual error after 25 iterations = 0.12%.

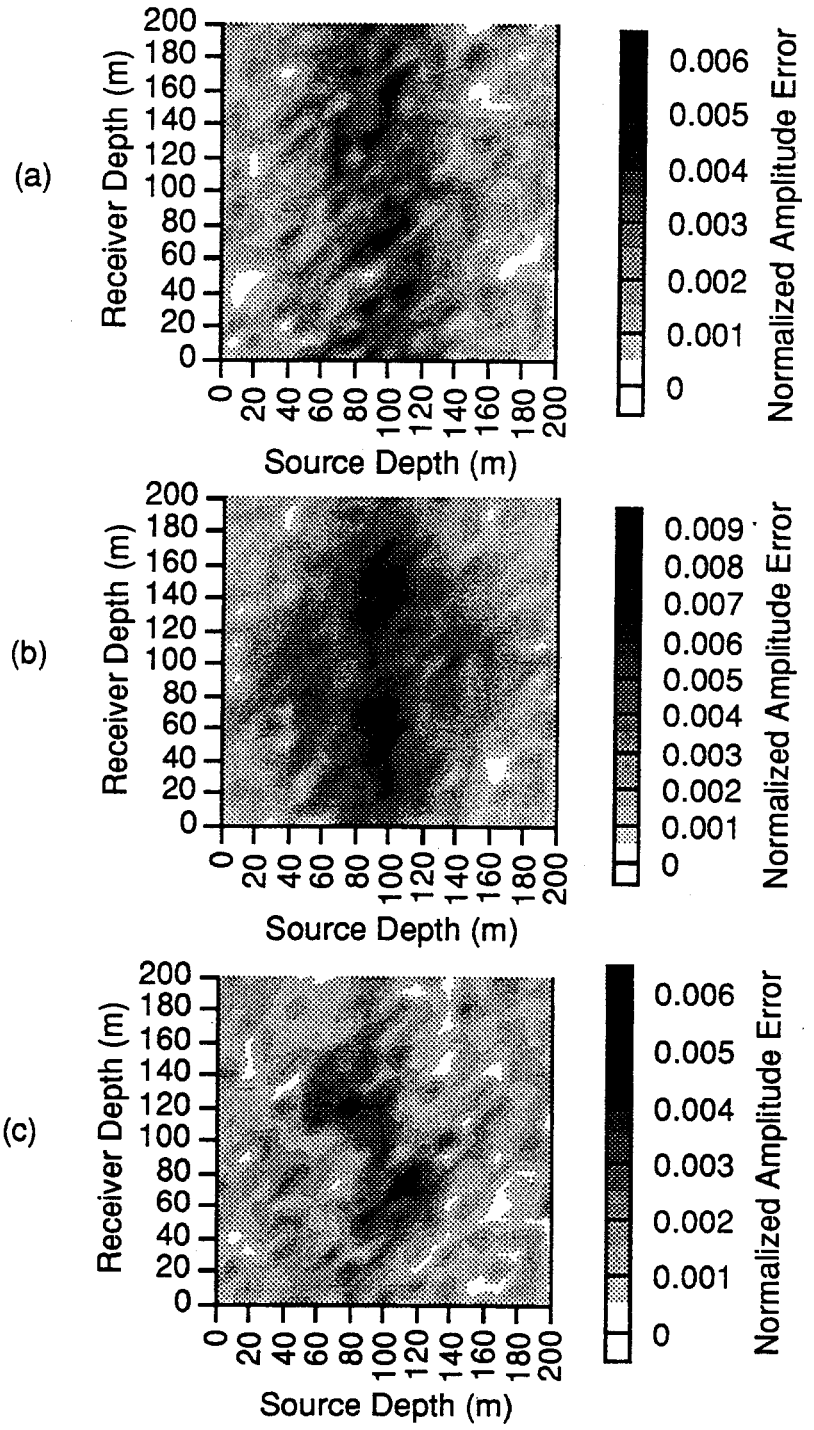

Figure 4.41 - Residual amplitude error between the input data and the calculated results for the images in Figure 4.40 plotted as a function of source and receiver location. The errors have been normalized by the maximum value in the data. (a) Residual errors for the 1kHz image given in Figure 4.40b. (b)Residual errors for the 10 kHz image given in Figure 4.40c. (c) Residual errors for the 100 kHz image given in Figure 4.40d.

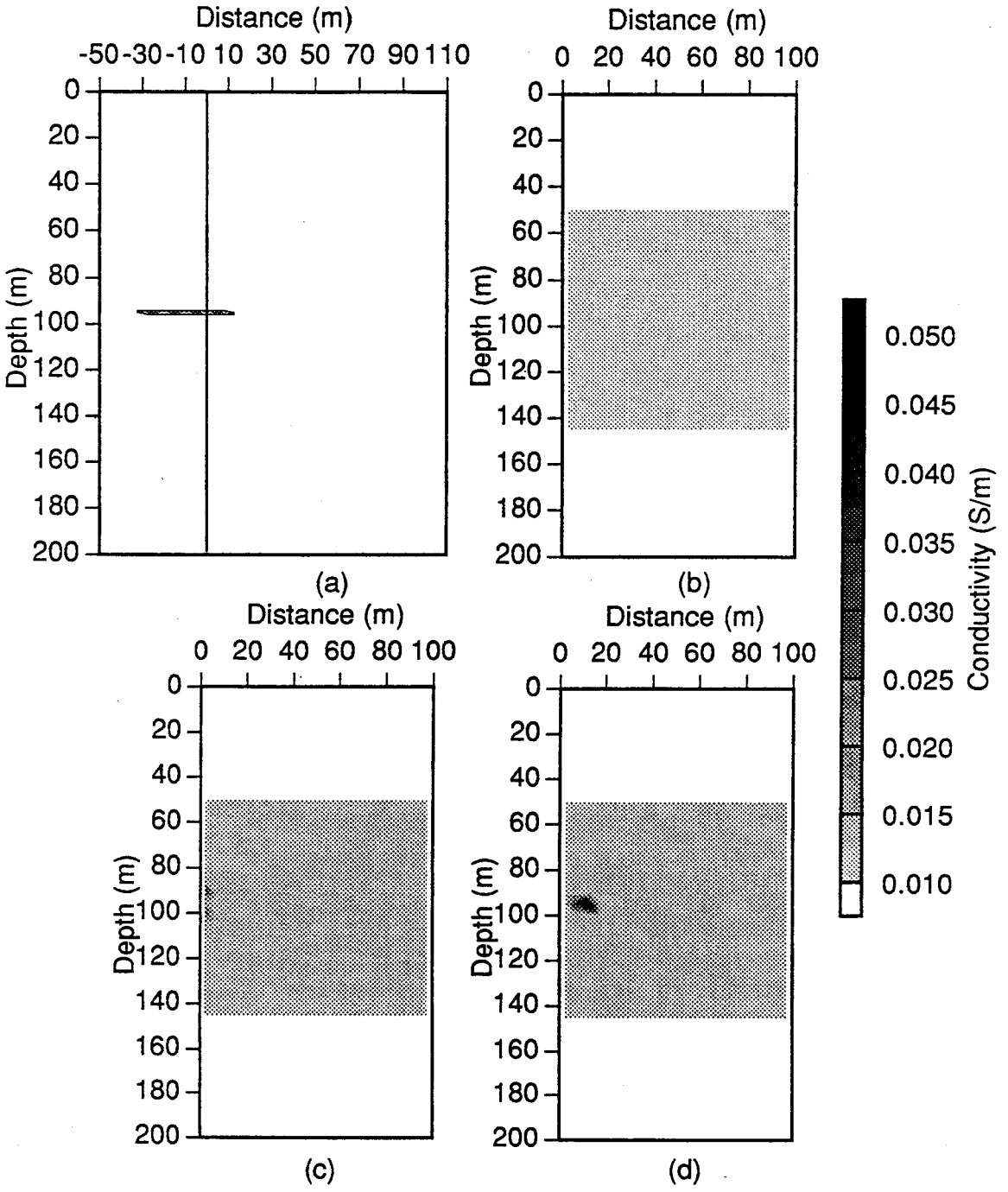

Figure 4.42- 3D model with the sheet offset from the source well by -10m and the resulting images as a function of frequency. (a) 40m by 40m sheet model of conductance 0.2S centered in the y direction (in and out of the page) about the source borehole. Results have been calculated for 21 source and receiver positions from 0 to 200m depth at 10m intervals. The added noise is 0.1% of the maximum total field at each frequency. (b) 1 kHz image. Mean residual error after 11 iterations=0.18%. (c) 10 kHz image. Mean residual error after 19 iterations = 0.29%. (d) 100 kHz image. Mean residual error after 25 iterations = 0.21%.

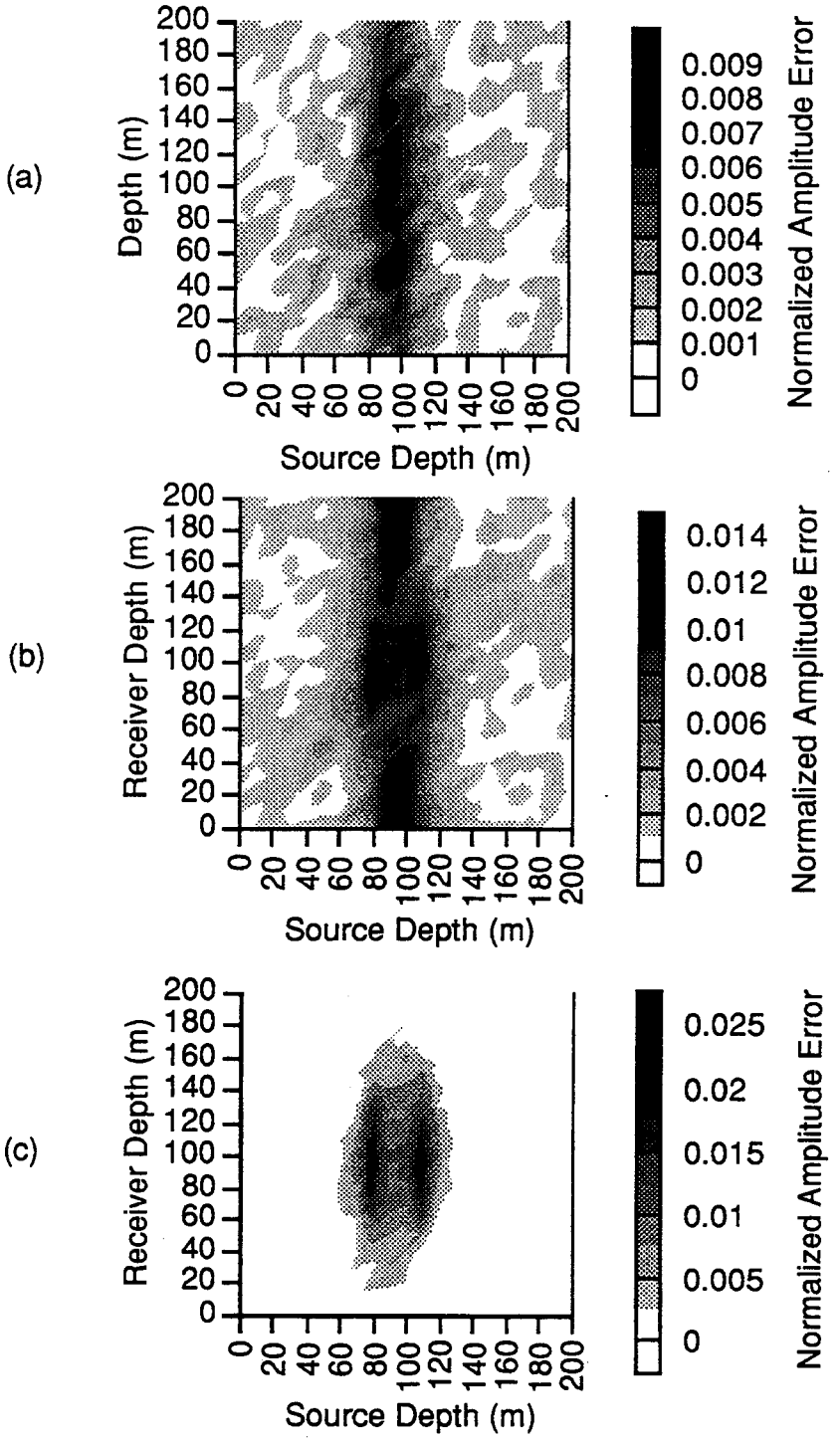

Figure 4.43 - Residual amplitude error between the input data and the calculated results for the images in Figure 4.42 plotted as a function of source and receiver location. The errors have been normalized by the maximum value in the data. (a) Residual errors for the 1kHz image given in Figure 4.42b. (b)Residual errors for the 10 kHz image given in Figure 4.42c. (c) Residual errors for the 100 kHz image given in Figure 4.42d.

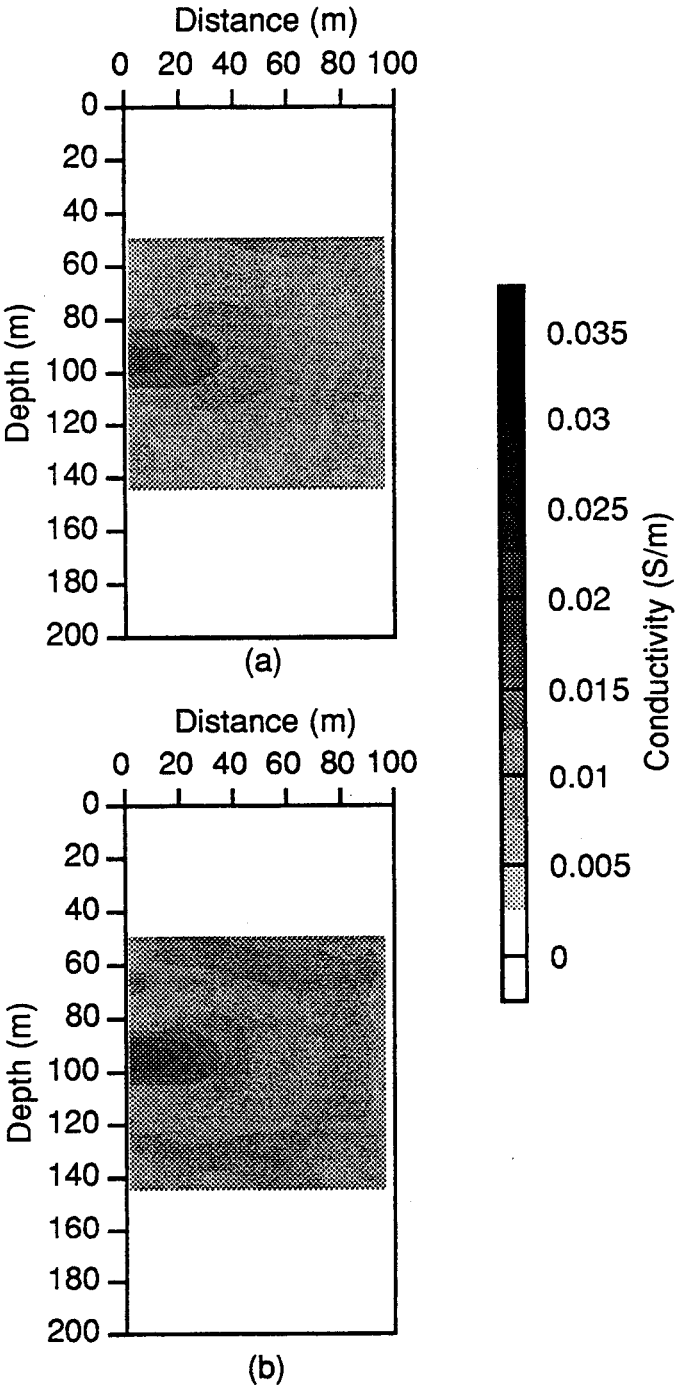

Figure 4.44- Images of the centered sheet model given in Figure 4.34a with no positivity constraints imposed. (a) 1 kHz image. Mean residual error after 8 iterations=0.10%. (b) 10 kHz image. Mean residual error after 15 iterations = 0.10%.

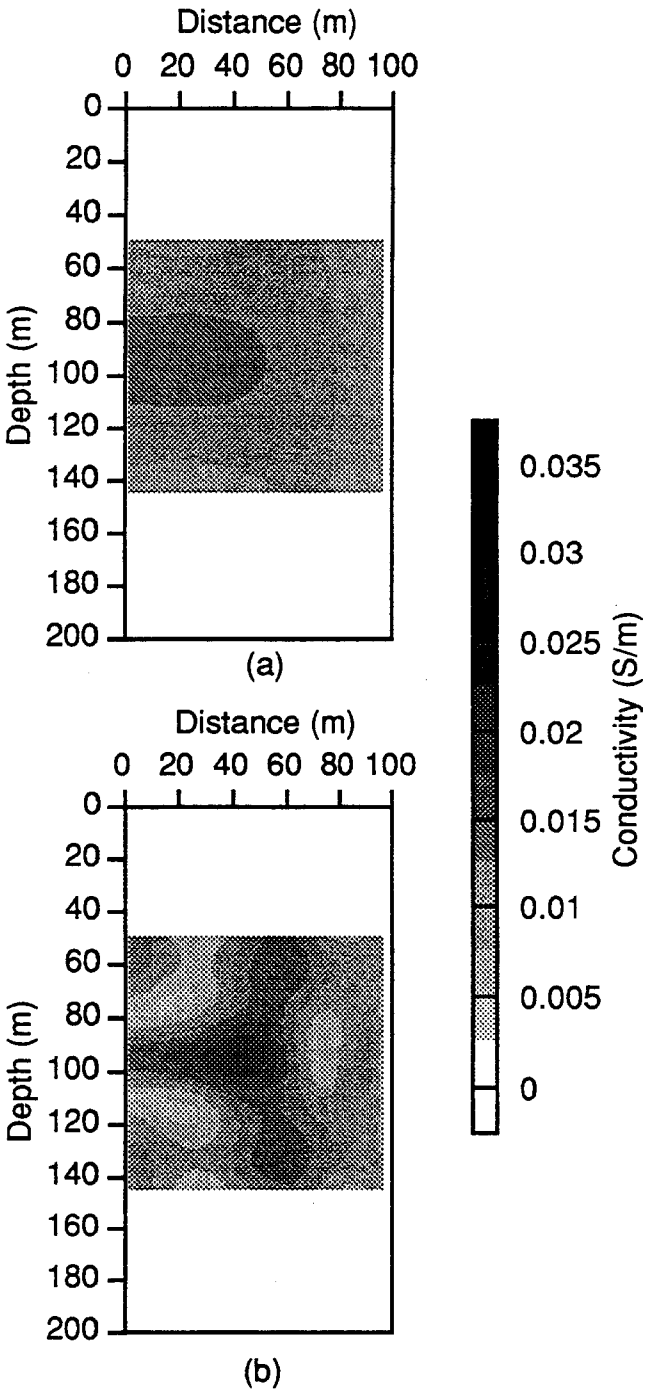

Figure 4.45- Images of the 10m offset model given in Figure 4.36a with no positivity constraints imposed. (a) 1 kHz image. Mean residual error after 8 iterations=0.19%. (b) 10 kHz image. Mean residual error after 15 iterations = 0.43%.

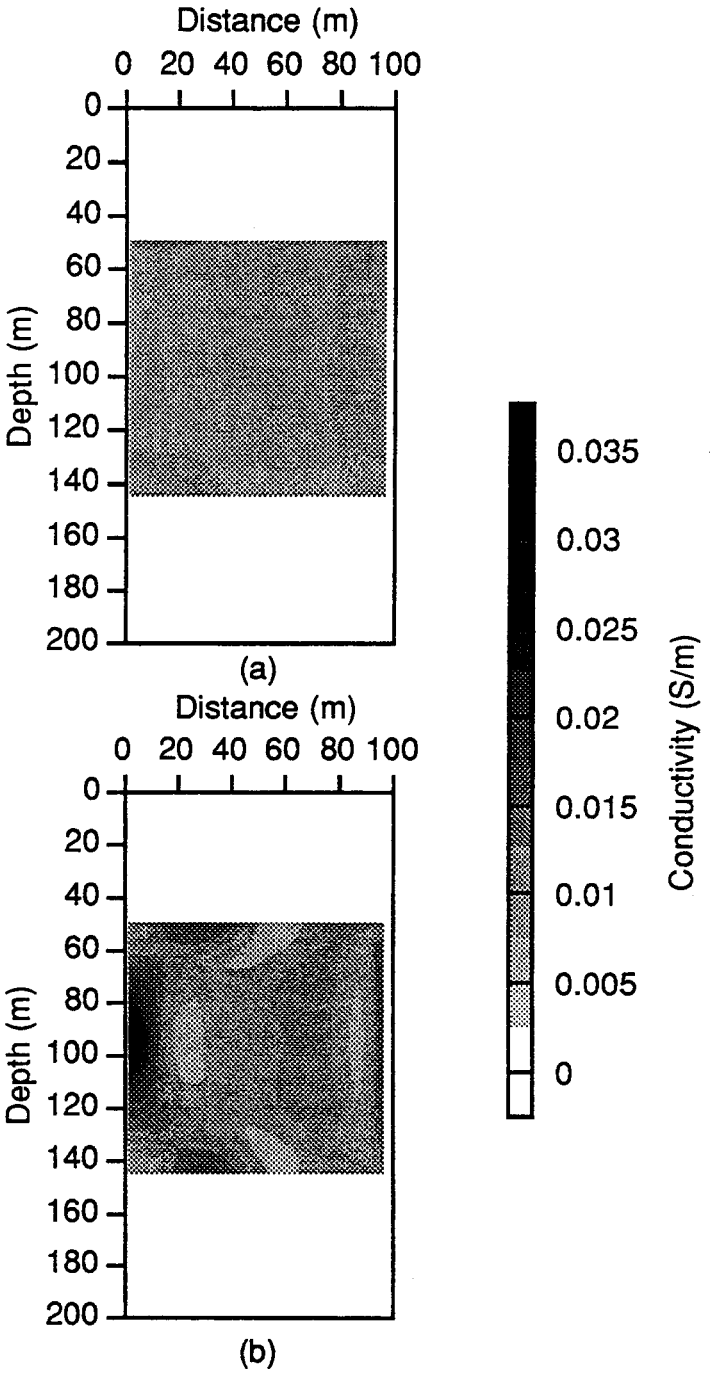

Figure 4.46- Images of the -10m offset sheet model given in Figure 4.42a with no positvity constraints imposed. (a) 1 kHz image. Mean residual error after 8 iterations=0.13%. (b) 10 kHz image. Mean residual error after 15 iterations = 0.39%.

Chapter 5
The Richmond Field Station Cross Well EM Experiment

Beginning in 1988, a series of salt water injection experiments were conducted at the University of California Richmond Field Station test site to evaluate the use of different geophysical methods for monitoring the injection process and for determining the geometry of the resulting plume. The first set of experiments involved surface-to-borehole resistivity measurements and were conducted in February of 1988 and 1989 (Bevc and Morrison , 1992). Approximately 25,000 gallons of 1.0 S/m salt water were pumped into a 3 m thick, 30 m deep, flat lying aquifer. Resistivity measurements were made both before and after injection with current electrodes above, in, and below the aquifer, and with potential electrodes spaced at 5m intervals along the surface in lines radiating outward from the injection well (INJ in Figure 5.1). These experiments were useful in determining the migration path of the salt water, but no inversion of the data was attempted to determine the geometry of the injected plume.

In the spring of 1991 cross borehole electromagnetic (EM) measurements were made by Lawrence Berkeley Laboratory and Lawrence Livermore Laboratory personnel to track a similar volume of injected salt water. About 36,000 gallons of water were employed in this experiment and cross-borehole EM data were collected both before and after the injection. The test employed two observation boreholes EMNE and EMSW (Figure 5.1) separated by 50m and approximately equidistant from the injection well (INJ). The EM data were collected at a frequency of 18,800 Hz using a tool spacing of 0.2 m from the surface to a depth of 85 m in the EMSW well. The receiver station spacing was 5 m starting at the surface and extending to a depth of 85 m.

The primary conclusion from this experiment was that the salt water slug provided an excellent target for cross borehole EM. The maximum difference between magnetic field measurements made before and after injection was more than ten percent in amplitude which was easily detectable with the cross well system. However attempts to interpret the data using both an imaging scheme developed by Zhou (1989) and by fitting the results with a simple 3-D "block" model in a layered host (Tripp, 1991 personal communication) were unsuccessful. These problems in interpretation were primarily caused by the complexity of the Richmond geology, i.e., the surrounding medium is neither a homogenous whole space or one-dimensionally layered, and the salt water body not a tabular block. Rather, the salt water plume appears to be an irregular three-dimensional zone of varying salt concentration that followed the existing high permeability network around the injection zone.

Although the 1991 experiment at the Richmond field station was a technical success and yielded a quality set of data, the geometry of the experiment does not conform to the cylindrical symmetry required for the iterative Born inversion scheme developed in the last chapter. Thus a second more involved cross well experiment was initiated in 1992, the design of which centered around providing this 2-D geometry by placing the source in the injection hole and the receivers in monitoring wells. In the following sections the geology of the Richmond Field station will be described and the experimental procedure will be outlined. Next a detailed description of the data is given which includes descriptions of the calibration process, a simple noise analysis, and general observations about what information the raw data yields. In the final section of this chapter the measurements will be interpreted by applying the imaging routine to both the field data and numerical models simulating the experiment.

5.1 Geology of the Richmond Field Station test site

The Richmond field station is located in a light industrial area which lies about six miles north of the University of California at Berkeley campus. The well field (Figure 5.1) is located in an open area approximately 400m north of San Francisco Bay. The upper 30-35 m of the site consists of unconsolidated alluvium, chiefly muds and silts interbedded with layers of sand and gravel of variable thickness. Below the unconsolidated sediments lies a basement of sandstone and shale, most likely from the Cenozoic Great Valley formation. A more complete description of the site geology including some well correlation is provided by Pouch (1987).

Figure 5.2 shows the EM induction logs for wells EMSW and EMNE together with stratigraphic logs derived from well cuttings. The logs were obtained in two wells that are 50.2 m apart and suggest that individual layers cannot be easily correlated over large distances at Richmond. Pouch (1987) found that a few of the layers, in particular some water-bearing sands and silts, could be traced across the field but that they varied considerably in thickness. He suggested that the sediments were deposited in a fluvial/deltaic environment with some of the individual sands deposited in channels.

The logs also show that the basement rock is variable. In four of the five wells that penetrated basement, the rock type was a very hard sandstone. In well EMNE, however, this basal unit is a softer, finer grained rock consisting predominantly of shale. This variation might represent a basement fault or possibly a stratified basal section with a steep dip.

Estimates of the conductivity distribution can also be made from these logs. The clays and silts, which constitute the majority of the overburden, range from 0.05 to 0.2 S/m,

while the coarser grained sand and gravel units tend to be more resistive (0.03 to 0.08 S/m). In the basement rocks the conductivity tends to drop substantially. The sandstones are often less than 0.01 S/m while the shales range between 0.015 and 0.025 S/m.

The variability in rock type, and hence the variability in conductivity that exists over short distances at Richmond illustrates the geologic complexity that made a simple interpretation of the 1991 data impossible. In order to get a better handle on the situation several new wells were drilled in early 1992, including a new injection well (INJ1) which allows the source to be placed within the injected plume. The hope was that by doing this, the geometry would crudely simulate the cylindrical symmetry used in the iterative Born inversion scheme, thus simplifying the interpretation. The description of this experiment, including measurements that were made in addition to the cross well EM, is given in the following section.

5.2 The 1992 Richmond Field Station experiment

The 1992 salt water injection experiment at Richmond proceeded in much the same manner as the previous experiments where cross hole EM data was collected both before and after the saline fluid was injected. The field system used in the experiment is described by Wilt et al. (1993) and is included in Appendix C.

The baseline cross hole EM data were measured in May, 1992 after an initial system set-up and debugging session. Four cross hole data sets were collected with the transmitter in the central well (INJ1) and the receiver tool deployed in each of the four EM observation holes. A frequency of 18.5 kHz was employed using a transmitter tool spacing of 0.5 m from the surface to a depth of 60 m. Receiver stations were separated by 5 m starting at 5 m depth and extending down to 55 m in each of the four observation holes. This yielded 111 source positions at 11 receiver depths for each cross well pair.

After the baseline EM data were collected a set of EM induction and water conductivity logs were made in each of 12 boreholes near the injection well (These can be found in appendix D). Just after these measurements were completed a volume of water was pumped into a 100,000 gallon holding pond and mixed with salt until the water conductivity reached 1 S/m. This fluid was then injected into a 3 m thick gravel aquifer through a perforated zone that extends from 26 m to 30 m depth in borehole INJ1. A rate of 10 gallons per minute was maintained for about 4 days yielding a total injected volume of approximately 50,000 gallons. This is 50 percent greater than that used in the 1991 experiment. Assuming a porosity of 30 percent, the injected water would sweep a cylindrical space 3 m high and 8 m in radius. Immediately following the termination of the injection process well INJ1 was flushed with fresh water to remove the conductive salt

water from the length of the borehole. A second set of cross hole EM, induction log and water conductivity data were then collected during a four week period in June following the injection .

After the post-injection measurements were made, fluid was pumped out of well INJ1 until the water conductivity was restored to the pre experiment background value. The total volume drawn out was 300,000 gallons which is about 6 times the amount injected. The pumping began on July 6 at a rate of 20 gallons per minute and lasted for 12 days. Water levels in the wells open to the aquifer were monitored during this period to better understand the hydrology of the site (Appendix E). After a two week period to allow the ground water level to recover to its original position, an attempt was made to repeat the baseline EM measurements in the EMNE well. Unfortunately, due to instrument problems the data quality was much poorer than in May and thus this data was not retained. In all, the experiment was conducted over a period of three months.

In Table 1 a summary is given of the cross well electromagnetic data collected in this experiment. The induction logging and borehole water conductivity data and results are listed in Appendix D and the water level draw-down data collected during the pumping out phase are given in Appendix E.

Source Well	Receiver Well	Pre Injection May 1992	Post Injection June 1992
INJ1	NW	yes	yes (2 sets)
INJ1	SW	yes	yes (2 sets)
INJ1	NE	yes	yes
INJ1	SE	yes	yes

Table 5.1 - Summary of the cross well EM data collected in the 1992 Richmond Field Station experiment. Each cross well data set consists of 18.5 kHz measurements made at 111 source positions for 11 receiver depths.

As described in Table 1, ten sets of cross-well data were collected with the transmitter in INJ1 and the receiver in each of the four surrounding EM wells. Four of these data sets were collected before injection and six after injection. The two extra sets were collected after injection in order to estimate the system noise. A full description of the data processing, estimates of the noise and qualitative descriptions of the data are given in the following sections.

5.2.1 System verification

As mentioned in the Section 5.2, considerable time was spent before the data collection to verify that the system was operating correctly. Three tests were employed for this purpose; 1) noise tests without the source connected, 2) repeatability tests, and 3) a reciprocity test. The noise test without the source operating was accomplished by shorting the transmitter cable at the cable head, capping it to waterproof it and lowering this shorted cable down the well. Once the ground loops had been eliminated from the system, the voltage measured by the receiver during this procedure did not exceed 30 μV, which corresponds to 3.7×10^{-9} A/m and is less by one order of magnitude than the smallest signal measured with the transmitter operating. In addition this signal did not vary by more than a few μV as the cable was lowered down the well.

During the system set up and ground loop elimination, profile repeatability measurements were done to check the system stability. These tests involved fixing the receiver at some point and then collecting data as the source was moved down the well. The measurements were then repeated either immediately after the source was returned to the surface, or overnight, and the errors between the two sets of measurements calculated. The final repeatability tests before the experiment began were done overnight from April 30 to May 1 and over the weekend from May 1 to May 4 with the transmitter in INJ1 and the receiver in EMNE at 5m depth. In both of these cases the amplitude and phase repeated to approximately 1% and 1°, respectively. Repeatability measurements like this were also made periodically during the experiment to verify that the system was operating properly.

The reciprocity measurements provided the final system check. This involved collecting two sets of cross hole measurements with the transmitter and receiver each at 15 m, 30 m and 45 m depth. This yields a total of nine source-receiver combinations. The first set of measurements were done with the transmitter in the INJ1 well and the receiver in EMNE. The two system elements were then physically interchanged for the second set of measurements such that the source was in EMNE and the receiver in INJ1. The reciprocity principle states that measurement at point A due to a source at point B should be identical if the points of the source and of the measurement are interchanged. Because this involves breaking down and moving the transmitter and receiver systems to opposite wells, errors at least twice that of the repeatability errors were expected.

Reciprocity results measured on May 1 are given in Table 5.2. Notice that except for the two points of maximum source - receiver separation, the results are very good. These results coupled with the repeatability measurements suggested that the ground loops had been eliminated and thus the system was stable enough for the experiment to proceed.

Depth of Tool in INJ1 (m)	Depth of Tool in EMNE (m)	% Amplitude Error	Degrees Phase Error
15	15	0.6	0.1
30	15	1.4	1.3
45	15	-7.8	-1.4
15	30	1.9	-0.1
30	30	0.1	0.1
45	30	-1.5	0.7
15	45	-.8	2.3
30	45	0.9	0.8
45	45	2.3	0.7

Table 5.2 - Reciprocity errors calculated for the test conducted on May 1, 1992 at the Richmond Field Station with the cross borehole EM system.

5.2.2 Data processing and system calibration

Because the receiver output is in Volts rather than units of magnetic field (A/m), the system must be calibrated before the data can be analyzed. This calibration process consists of determining an amplitude and phase constant, which when applied to the data convert the observed voltages to magnetic field intensity, **H**, per unit dipole moment. These two constants were determined after the post-injection measurements had been completed. Unfortunately both an amplitude and phase tare were noticed between the May and June measurements, and thus corrections had to be applied to tie the two data sets together.

Since the rocks at the Richmond Field station test site are fairly conductive, calibrating the system at the operating frequency without including the earth response is rather difficult. In addition, because the geology is relatively complex, determining the calibration constants by comparing the raw data to simple layered earth models may yield erroneous results. To minimize these problems a dual frequency method was employed to determine the amplitude calibration. The first frequency (100 Hz) is low enough so that the earth response is minimal at the transmitter-receiver separation employed (20 to 25 m). The second frequency is the operating frequency of 18.5 kHz at which the earth response is large.

The first step in the amplitude calibration is to determine the transfer function, or sensitivity of the receiver coil at each of the frequencies. This was accomplished by placing the receiver coil in a calibration solenoid and using a Hewlett Packard spectrum analyzer to determine the transfer function over a wide frequency band. The receiver sensitivity was found to be 640 V/(A/m) at 100 Hz and 722 V/(A/m) at 18.5 kHz. The phase shift of the

receiver coil at 18.5 kHz, which is used to determine the phase calibration constant, was also determined at this time.

The second step in the amplitude calibration is to determine the moment of the transmitter coil. This involved measuring the 100 Hz field that resulted from placing the transmitter at the top of INJ1 and the receiver in EMNW well. The voltage measured at the receiver was first converted to the equivalent magnetic field by applying the sensitivity constant determined above. Because the 100 Hz field 20 m away from the transmitter is not very sensitive to the conductivity distribution between the two wells, the magnetic field per unit dipole moment can be estimated using an analytic solution for the magnetic fields produced by a dipole source in a layered half-space. The program developed by Lee (1988) was again employed for this purpose.

The magnetic dipole moment is determined by dividing the measured field by this calculated field. In this case the moment/unit current (m_t) was found to be approximately 12.2 m^2 and was calculated using the formula

$$m_t = \frac{V_{R100}}{I_{100} H_{100} T_{100}} \qquad (5.1)$$

where V_{R100} and I_{100} are the voltage in the receiver coil and current in the transmitter during the 100 Hz measurements, H_{100} is the calculated 100 Hz magnetic field per unit moment at the receiver location, and T_{100} is the receiver coil transfer function at 100 Hz. The total amplitude calibration constant then takes the form

$$CAL = \frac{1.}{I_{18.5K}\ T_{18.5K}\ m_t} \qquad (5.2)$$

where $I_{18.5K}$ is the current in the transmitter during the data collection and $T_{18.5K}$ is the receiver coil transfer function at 18.5 kHz. This constant (CAL) is used to convert the amplitude of the observed voltage to the amplitude of the magnetic field per unit transmitter moment.

The above formula assumes that the transmitter moment per unit current is identical at 100 Hz and 18.5 kHz. To verify this, we measured the voltage generated in a small loop placed around the transmitter coil at the two frequencies. These measurements were made with the center of the transmitter coil 80 cm below the surface of the earth and 1 m below the loop of wire which was wound around the INJ1 casing. For a sinusoidal transmitter

current this voltage is equal to the mutual inductance between the loop and the transmitter multiplied by the transmitter current-frequency product, i.e.

$$V = M_{lt}\ I_t\ \omega \tag{5.3}$$

where M_{lt} is the mutual inductance, I_t is the current in the transmitter coil and ω is the angular frequency. Because the mutual inductance is dependent only on the geometrical relationship between the two coils, it is directly proportional to the transmitter moment. Thus if it is determined that the mutual inductance is constant at the two frequencies, then it can be implied that the moment per unit current is also constant. When this test was performed at Richmond it was found that the mutual inductance at the two frequencies varied only by 3.3% , thus verifying the constant moment / unit current assumption. However this value also indicates that the calibration is only good to 3% and that calibrating the data in this manner will introduce non-random error into the measurements.

Determining the phase calibration constant was relatively simple compared to that of the amplitude. The phase shift in each component of the system was first measured separately with the lock-in amplifier. The total phase calibration correction was then determined by summing all these individual phase shifts. This process was checked by referencing various combinations of the system components to a calibration coil of known phase shift placed immediately adjacent to the transmitter. The value obtained by summing the phase of the individual components was found to be within 1° of the value measured with the calibration coil.

As mentioned in the introduction of this section, a tare was noticed between the May and June data. To properly tie both sets of data together, the calibration constants were adjusted appropriately. We determined that the June data was of better quality compared to the May data as the error calculated between repeat measurements was less after the injection of the salt water. To verify this we kept the calibration constant for the June data the same for each of the wells. The calibration for the May data was then varied on a well to well basis such that for points with both the source and receiver at either the top or bottom of the well away from the injection zone, the average misfit between the May and June data was within approximately 2% amplitude and 1 degree phase. As shown in Table 3, the May phase calibration constants increase in the order that each data set was collected which seems to verify our hypothesis of system instability. The final check was to compare the resulting May calibration constants to those determined from a layered earth inversion routine developed by Deszcz-Pan (1992, personal communication) to ensure that they are correct. The final constants used to calibrate each set of data are given below.

Well	May Data			June Data		
	Start Date	Amp *	Phase **	Start Date	Amp *	Phase **
EMNW	5/5	1.23	60	6/5	1.30	58
EMNE	5/4	1.23	59	6/3	1.30	58
EMSW	5/11	1.25	63	6/2	1.30	58
EMSE	5/8	1.27	60	6/4	1.30	58

Table 5.3 - Calibration constants to convert the measured voltages to magnetic field. The units for the amplitude calibration are X 10^{-4} (Amps/m)/Volts and for the phase calibration are in degrees.

5.2.3 Error analysis and data quality

During the experiment, profiles for a given receiver position were repeated at the beginning of each day and whenever a new well was started to ensure that the system was operating properly. In general an average of 2% amplitude error and 1° phase difference were considered good stability bounds for the system. Due to time considerations however, greater amplitude errors were often considered acceptable if the phase was stable and vice versa. In addition it was noticed that the quality of the data decreases in a clockwise fashion from the EMNW well (best) to the EMSW well (worst). This is based not only on repeat error analysis but also on the secondary field calculations which are presented later. To determine the distribution of and the types of errors and noise present in the measurements, extra sets of post injection data were collected in the EMNW and EMSW wells 5 days and 2 weeks after the original data, respectively.

The overall mean error and standard deviation between the original and repeat measurements were the first statistics to be calculated. In order to compare the data for two wells which are located different distances away from INJ1 , the errors are presented in percent amplitude and degrees phase. Table 5.4 shows that both the mean error and standard deviation are greater for the EMSW repeat surveys compared to those done in the EMNW well. These larger errors may be due in part to the greater distances between INJ1 and EMSW, and the larger time separation between repeats. Histograms for the two sets of repeatability errors have also been plotted. As shown in Figures 5.3 and 5.4 the distribution is skewed about the mean rather than being equally distributed.

	E M N W		E M S W	
	% Amplitude	Degrees Phase	% Amplitude	Degrees Phase
Mean Error	2.26	-0.81	3.30	-1.09
Standard Deviation	1.40	0.92	2.18	1.31

Table 5.4 - Mean repeatability error between the two sets of post injection data collected between INJ1 and EMNW, and INJ1 and EMSW. The two sets of data involving EMNW were collected 5 days apart and the data involving EMSW two weeks apart.

To better understand the origin of the noise, two additional sets of statistical calculations were made. The first set involved calculating the mean error and the standard deviation with the transmitter and receiver at approximately the same level but at different depths below the surface. To get a mean error at each depth, the results for ten transmitter positions within ± 2.5m of the receiver depth were averaged. The differences were calculated in terms of magnetic field rather than relative (percent) amplitude so that errors present in both the real and imaginary components as well as amplitude and phase could be calculated and compared.

As shown in Figures 5.5 and 5.6, both the mean error and standard deviation show no correlation to the tool depth below the surface. This indicates first of all that the noise is not dependent on the length of cable down hole, i.e. the cable is not leaking. In addition, the errors do not seem to be caused by surface noise as the magnitude of this type of error would decay with increasing transmitter-receiver depth as the noise is attenuated by the earth.

The repeatability errors have also been calculated as a function of source-receiver separation to determine if the noise is truly random as suggested by the above results. Again the results were calculated for the real and imaginary components as well as amplitude and phase. Due to the geometry of the experiment, there are a larger number of data at smaller transmitter-receiver separations than at larger separations. This problem in itself may introduce some error to this analysis.

The results given in Figures 5.7 and 5.8 indicate that the noise is not constant with increasing source-receiver separation. Rather, from the closest separation to a source-receiver separation of 45m the error decreases at approximately the same rate as the magnetic source field. For source-receiver separations greater than 45 m the error stabilizes at about 1×10^{-8} A/m which suggests that this value represents the system noise floor.

These results coupled with those above strongly imply that some type of electrical leakage from the transmitter tool is occurring which is contaminating the results. Unfortunately the source of this leakage has not been located and thus this effect can not be decoupled from the data. Because of this the noise level is probably higher than the system noise floor, and thus here it is estimated to be approximately $5x10^{-8}$ A/m.

5.2.4 Data presentation and description

In order to present all the data measured in the cross well experiment simultaneously, they have been plotted in gray scale format as a function of source and receiver position. Notice that this is the same format employed to analyze the residual errors in Chapter 4. Presenting the data in this manner allows the continuity between profiles to be checked and also allows for the detection of any changes that occur due to the injection. Unfortunately because the receiver stations are spaced rather far apart (5 m), the interpolation between data points is greater in this direction than in that of the source. Because of this distortions can occur which are not properties of the data but rather are errors generated by the plotting routine.

Figures 5.9 and 5.10 show the EMNW data sets before and after injection, respectively. In both cases the data are smoothly varying both along each individual profile and in between the individual lines. In addition the amplitude is maximum along the diagonal which coincides with the source and receiver being at the same depth. Both of these properties tend to imply that the system is operating properly and thus the data is of good quality.

Although the magnitude of the changes is not spectacular, comparing the two sets of data indicates that the injection causes changes in both amplitude and phase when the source is at a depth of 30m, i.e. when the transmitter is in the plume. These changes become much more apparent if we calculate the secondary fields resulting from the introduction of the plume. This is a simple process which involves subtracting the fields measured before the injection from those measured after injection. Figure 5.11a shows the amplitude of the scattered fields measured in the EMNW well, and in Figure 5.11b the phase differences between the post and pre injection fields have been plotted. In both cases a fairly large anomaly is present at a source depth of 30m . The fact that this anomaly is several times larger than the noise estimates developed in the last section suggests that the EMNW data are of sufficient quality to be used in the iterative Born imaging scheme. It is easy to see that by calculating the scattered fields in this manner, the changes caused by the plume can be isolated which may lead to a more robust initial interpretation than would

result by using the total fields. In addition this shows the benefit of making measurements over time when trying to monitor injection processes.

The cross well data set collected in the EMNE well show similar characteristics when compared to those measured in EMNW. The pre and post injection measurements given in Figures 5.12 and 5.13, respectively, are smoothly varying which again implies fairly good data quality. However the magnitude of the fields measured in the EMNE well are about half those measured in EMNW. In addition the phase has been in general rotated by -30 degrees. These differences are caused not by very inhomogenous geology but rather by the interwell separation being 25m for the EMNE measurements compared to 20m for the EMNW data. The additional 5m results in a greater attenuation of the fields.

The scattered fields measured in the EMNE well that resulted from the injected body are plotted in Figure 5.14. These exhibit the same type of character as the fields measured in EMNW (Figure 5.11) except that once again the magnitude has been halved. Because the secondary fields plotted in these figures exhibit similar properties, a rough, initial interpretation can be made that the injected water seems to be heading at least partially in a northern direction.

As mentioned earlier, the data quality appeared to decrease in a clockwise fashion from the EMNW well to the EMSW well. This problem is not apparent in the pre and post injection data collected in the EMSW well. Figures 5.15 and 5.16 show that the EMSE data exhibit approximately the same character as those data collected in the EMNW well (Figures 5.9 and 5.10). This should be the case as both wells are located approximately 20m from the source bore hole. However the secondary fields in the two wells that result from the injection are very different. Notice that the scattered field amplitudes (Figure 5.17a) are much less in the EMSE data than those measured in the EMNW well (Figure 5.11a). In addition a second anomalous zone is apparent when both the source and receiver are at depth. The differenced phase data indicate even larger discrepancies. Whereas Figure 5.11b shows a phase anomaly for the EMNW data that displays a pattern similar to that displayed by the amplitude, the scattered phase measured in the EMSE well (Figure 5.17b) is much different, with the maximum occurring when the receiver furthest from the injection zone rather than at the same level.

The scattered field quality seems to be even worse for the data collected in the EMSW. Again the pre and post injection data as shown in Figures 5.18 and 5.19, respectively, seem to be of good quality. However the scattered fields plotted in Figure 5.20 indicate very little response to the injection process. In fact these results are fairly close to the repeatability noise level that was estimated in the last section.

The scattered fields measurements in each of the wells can be combined to produce an initial interpretation. The fact that the anomalies in the northern wells are much greater than those to the south indicates that the majority of the water is migrating to the North. This interpretation agrees fairly well with that of Bevc and Morrison (1992). Some migration may be occurring to the southeast, however the almost negligible anomaly observed in the southwest data indicates very little injection in this direction. In order to more accurately determine how far the plume is migrating in each direction, the iterative Born imaging scheme will be employed in the next section to image the conductive salt water body.

5.3 Interpretation of data

One of the prime considerations of the Richmond '92 experiment was to produce a data set in which the geology, to a first order, exhibits a geometry suitable for the 2-D inversion routine. However, because the Richmond geology consists of interbedded conductive shales and sands overlying a more resistive basement, the plume can't be interpreted as being injected into a homogenous half-space. There are two different methods of approaching the problem. The first is to image the entire conductivity structure between the two wells both before and after injection, and then compare the two images to determine what changes have occurred due to the injection. The second approach is to image only the scattered fields resulting from the injected body using a layered background model which approximately mimics the conductivity structure. Both of these methods are employed below to determine the position of the plume. In addition these images are compared to theoretical results using the sheet model in order to determine the accuracy of the process for this experiment.

5.3.1 Imaging the total field data

The first step in inverting the total field data before and after injection is to determine an average background conductivity. As was done for the Devine images, this value was determined by finding the conductivity that minimizes the sum of the residual errors between the data and the fields that would exist in a homogenous half space. The residual errors in turn are then the scattered fields to which the imaging process is applied. The background conductivities that were employed for each cross well pair are given in Table 5.5 along with the corresponding background induction number for that interwell separation.

As shown in Figure 2.3a the induction numbers listed in Table 5.5 indicate that the system is operating on the low induction number side of the Born kernel. In Chapter 4 it was demonstrated that at these low induction numbers, the iterative Born scheme

experiences problems converging to the estimated noise level. This is the result of a bias which is produced when trying to fit 3-D data to a 2-D cylindrically symmetric model. Thus because the conductivity distribution at Richmond exhibits a three dimensional behavior (Pouch,1986), we can expect that the solution will experience difficulty in converging to the noise levels that were estimated from the repeatability errors. Because of this, the results given in this section were obtained by arbitrarily terminating the scheme after 10 iterations. It will be seen that this provides adequate resolution of the injected plume while also exhibiting artifacts due to the three dimensional nature of the conductivity.

Cross Well Pair (See Figure 5.1)	Interwell Separation ,l (m)	Background Conductivity, σ_0 (S/m)	Induction Number ($\sigma_0 \omega \mu l^2$)
INJ1 - EMNW	20.0	0.051	3.0
INJ1 - EMNE	25.0	0.054	4.9
INJ1 - EMSE	19.6	0.057	3.2
INJ1 - EMSW	25.0	0.064	5.8

Table 5.5 - Background conductivities employed to image the Richmond field station cross well data. The corresponding background induction numbers have also been included.

It was also demonstrated in Chapter 3 that at the lower induction numbers, a given source-receiver pair is fairly sensitive to the region outside of the wells. To avoid edge effects, the mesh was extended horizontally to a distance twice that of the interwell separation, and also from the surface to a depth of 80m. A cell size of 2m by 2m was employed which yields a mesh of 800 to 1000 cells depending on the interwell separation. To account for the earth-air interface, the layered background model (Section 4.3.4) was employed to calculate the fields and Green's functions for a uniform half space. Because of the computer time and memory involved in these computations, only 56 source positions were incorporated at 1m intervals with the 11 receiver locations. This yields a total of 616 data points.

Figure 5.21 shows the images obtained by inverting the pre- and post-injection data collected in the EMNW well. For comparison these have been plotted with the conductivity logs measured in each of the wells (The well logs are plotted graphically in appendix D). Notice that the images do recover the general structure of conductive sediments overlying a more resistive basement. Thus as was demonstrated with the Devine data the imaging scheme recovers a smoothed version of the well logs. In addition comparing the two

images definitely shows the conductivity changes at a depth of 30m near the source well that are caused by the injection of the conductive salt water . A method to better resolve the extent of this plume will be examined below.

A closer examination of the logs in Appendix D indicates the three dimensional nature of the subsurface. Even the logs for INJ1 and EMNW that are given in Figure 5.21 do not correlate to each other particularly well. The 3-D nature of the subsurface and thus the cross well data manifests itself as artifacts in the 2-D images. Although the contact between the conductive sediment and the resistive basement is shown in the logs to exhibit a slight dip, it is clearly not as severe as the cross well image in Figure 5.21a shows it to be. In addition the image shows a large conductor at a depth of 25m near the receiver well which is not apparent in the well log. Because the well logs correlate so poorly with the images, these results should not be considered to be high resolution images of the subsurface. Rather, the safest conclusion that can be made is that at least a portion of the injected water is migrating in a north-western direction.

The three dimensional effects are also apparent in the residual errors. Figure 5.22 shows a non-random distribution in the errors with respect to the source and receiver depth. As was demonstrated in Section 4.4 this type of behavior suggests that there is a 3-D component in the data. The residuals are especially large when both the source and receiver are in the basement. This implies that the iterative Born scheme is finding it especially hard to fit the basement region with a cylindrical model. In Figure 5.22a large errors exist when the receiver is at 40 m and the source is between 30 and 40m. This corresponds to the previously described contact between the conductive sediments and resistive basement, and further emphasizes that the image of the dipping contact is most likely incorrect. In contrast the post injection residuals show a slightly different character in this region. Figure 5.22b shows substantial residuals for all receiver locations whenever the source is at 30m depth. Realizing that this is the depth of injection and comparing this with the residual plots given in Section 4.4.2 indicates that the plume itself is exhibiting a three dimensional nature which the imaging scheme can not account for. Thus some caution must be must be taken when interpreting the edges of the injected body from the images.

The images of the cross well the data collected between INJ1 and the EMNE well are given in Figure 5.23. These results demonstrate many of the same characteristics as those given in Figure 5.21. The general structure of conductive sediments overlying resistive basement is recovered, and a comparison of the pre- and post- injection images indicates the appearance of a conductive body near the source well after injection. Again this indicates that at least some of the salt water is migrating in this direction. However there

exists a poor correlation between the well logs and the images which again suggests that the imaging scheme is having problems fitting a cylindrical model to the data.

The residual errors plotted in Figure 5.24 do indicate that there is a 3-D nature to the data. Again the largest magnitude errors occur when both the source and receiver are at depth suggesting that the basement is very inhomogenous. This inhomogenous nature is present in the logs for these two wells, with the basement in EMNE being approximately twice as conductive as that in INJ1 (Figure 5.23a). In addition notice that large residuals exist at a source depth of 30m in the pre-injection residuals that are not present in the post-injection plots. This suggests that either the introduction of the salt water imposes more of 2-D geometry on the medium, or that the post-injection data is of better quality. In either case it seems apparent that the post-injection image (Figure 5.23b) may be a more accurate representation of the subsurface between INJ1 and EMNE than the pre-injection image in Figure 5.23a.

In general the images of the cross well data collected in the EMSE and EMSW wells (Figures 5.25 and 5.27, respectively) display the same characteristics as those collected in the wells to the north. A conductive section overlies a more resistive basement and the correlation between the logs and the images is fairly poor. As before the cylindrical symmetry of the imaging scheme has problems imaging the 3-D geometry which is present in the data. In fact Figure 5.26 shows that for the southeast data the maximum residual errors line up along the diagonal. The fact that the iterative Born scheme always experiences problems fitting the data when the source and receiver are at the same depth suggests that the geology between these two wells is extremely complex. Although the residuals for the EMSW images (Figure 5.28) also tend to line up along the diagonal, the tpattern is not nearly as strong as that shown in Figure 5.26.

Although the images of the data collected to the north and south show the same general characteristics, one major difference does exist. The results for the southern wells do not indicate a drastic change between the pre- and post-injection images within the injection zone. In both cases the region of interest is slightly less conductive after injection. These results are similar to those in Figure 4.46b which demonstrates that when a 3-D sheet is offset in the direction away from the receiver well, resistive artifacts are formed in the images. Thus, even though the images in Figures 5.20 through 5.27 probably do not represent the true conductivity distribution between the wells, they do yield valuable information about the injection process. It is apparent that the water is moving a northerly direction which coincides both with the results of Bevc and Morrison (1992) and the data analysis presented earlier in this chapter.

The direction of migration and possibly even the horizontal extent of the plume become more apparent if the difference in conductivity between the post- and pre-injection images are plotted. This is a simple process of subtracting the values in each cell of the pre-injection image from those in the post injection image. Figure 5.29 leaves little doubt that the water is heading primarily in a northern direction. Both of the images of the data collected in the northern wells (Figures 5.29a and 5.29b) show large positive changes in conductivity within the injection zone. In addition notice that the imaged plume for the EMNW data seems to be slightly larger and more conductive than that for EMNE. This tends to agree with the results of Bevc and Morrison (1992) who showed that when the injection occurred in INJ, the plume trended in a northwest rather than northern direction. However, the greater differences in conductivity in one direction may be an artifact of the imaging routine, and this possibility will be discussed in the following sections.

Also present in each of the images given in Figure 5.29 are negative changes in conductivity. Although these could represent resistive water displacing conductive water within the injection zone, they are more likely 3-D artifacts of the 2-D imaging scheme similar to those observed in the images of section 4.4.2. Again the presence of these types of artifacts will be discussed in the next section.

In this section the iterative Born scheme has been applied to the total-vertical- magnetic field data collected at the Richmond Field Station in order to image the subsurface conductivity structure. It has been determined that although the general geologic structure is recovered, the 2-D model employed by the imaging scheme experiences problems in fitting the data to the estimated noise level. This is most likely due to the three dimensional nature of the conductivity structure combined with the relatively low operating frequency. This inability to fit the data accurately results in the creation of artifacts which don't agree with the well logs. However it has also been demonstrated that by observing the changes in conductivity between the pre- and post-injection images, the general migration direction of the plume can be determined. In the next section a method for imaging the location of the plume will be discussed which is not as time and memory intensive.

5.3.2 Imaging the scattered field data

The second method of imaging the injected body involves inverting on the scattered fields that are generated by the plume, i.e. those fields that are given in Figures 5.11, 5.14, 5.17 and 5.20. However, because the geology of the Richmond Field station consists of conductive sediments overlying a resistive basement, it isbe inappropriate to simulate the injection as occurring in a homogenous half space. Rather, a two layer background model can be introduced using the theory outlined in Section 4.4.4. The conductivities of the

layers as well as the depth of the interface were obtained using a least squares inversion technique on the pre-injection data (Deszcz-Pan, 1993, personnel communication). The two layer background models that were employed are listed as a function of the cross well data set in Table 5.6.

Cross Well Pair (See Figure 5.1)	Layer 1 Conductivity (S/m)	Layer 1 Thickness (m)	Layer 2 Conductivity (S/m)
INJ1 - EMNW	0.073	34.0	0.0043
INJ1 - EMNE	0.079	36.0	0.0045
INJ1 - EMSE	0.067	38.0	0.0150
INJ1 - EMSW	0.076	38.0	0.0041

Table 5.6 - Two layer background models employed to image the scattered fields.

The mesh parameters were identical to those used in Section 5.4.1 except for one major difference. Because the body that is generating the scattered fields is confined to the region between the wells, the mesh does not need to be extended as far horizontally or vertically. Thus for the two data sets that were collected between wells 20m apart, the mesh was 10 cells wide and 30 cells deep to cover the 20m by 60m region between. In the two other cases where the bore holes are separated by 25m, the mesh width was 12 cells. Again the cell size was 2m by 2m.

This reduced mesh size combined with the smaller magnitude scattered fields results in a much quicker run time. For the images given in Section 5.4.1, the CPU time needed to calculate the Green's functions and electric fields for each source-receiver-cell combination, and then iterate 10 times to produce an image, was approximately 1000 to 1200 minutes on a Silicon Graphics, Inc. *IRIS INDIGO* workstation. In addition, to produce both pre-injection and post-injection images the iterative sequence was repeated. Therefore the time needed to produce each of the images given in Figure 5.29 was approximately 1600 to 2000 CPU minutes. However when the scattered rather than total magnetic fields are employed a final image of the plume is produced in less than 100 CPU minutes. This time savings is the product of two factors: 1) a lower computing time because fewer cells are present in the mesh and 2) the Born series converges quicker because the magnitude of the scattering body is much smaller. Although this imaging method results in a less accurate description of the overall conductivity distribution, it does produce a fairly accurate description of the plume in a much more time-efficient manner.

The scattered field images that result after five iterations are shown in Figure 5.30. Notice that these results compare very well to the "differenced" images in Figure 5.29. Images of the data collected between INJ1 and the two wells to the north (Figures 5.30a and 5.30b) indicate the presence of large conductors in the zone of interest, while those to the south (Figures 5.30c and 5.30d) show very little response at all. Thus again the conclusion is that the plume is heading in a northerly direction.

There are however significant differences between these images and those given in Figure 5.29. Figures 5.30a and 5.30b show that to the north most of the conductive material is confined within the injection zone. However these images also contain "arms" which extend upwards from the plume. It will be shown in the next section that these are artifacts which can be attributed to 3-D nature of the conductivty distribution. Artifacts are also present in the images of the data collected in the southern wells (Figures 5.30c and 5.30d) but they are less well defined. In fact these show much less response compared to the corresponding difference images given in Figures 5.29c and 5.29d.

A possibly more significant difference between the two set of results is that the scattered field image of the data collected in the EMNE well (Figure 5.30b) shows the plume to be extending out further horizontally than that of the difference image (Figure 5.29b). Unfortunately due to the complexity of the geology it is extremely difficult and time consuming to accurately model the Richmond Fields Station experiment before and after the injection and thus simulate the process that produces the differenced images. Because of this it was not determined which of these two methods of reconstructing the geometry and conductivity of the plume is more accurate.

If the aforementioned artifacts are due to a plume geometry that is three dimensional, then these effects should also be present in plots of the residual errors. Figure 5.31 shows that this is indeed the case, as for each image given in Figure 5.30 relatively large residual errors exist at a source depth of 30m which corresponds to the injection zone. Thus it is obvious that the cylindrically symmetric model can not accurately fit the 3-D data.

In order to determine if better resolution is attainable, the scheme was allowed to iterate ten times on the scattered fields. The resulting images (Figure 5.32) again indicate conductive anomalies within the injection zone for the data collected in EMNW and EMNE. However, before coming to the conclusion that the extra iterations have improved both the accuracy of the images to the north, it must be noted that the mean residual error is approaching data noise level that was estimated in Section 5.3.3 and thus the increased resolution in these images should be interpreted with caution.

In addition to the added resolution, the extra iterations seem to have improved the accuracy of the solutions somewhat. When comparing Figures 5.32a and 5.32b to Figures

5.30a and 5.30b, it appears as though the magnitude of the 3-D artifacts actually decreased. However, this is not the case for the images of the cross well data collected in EMSE (Figure 5.32c) and EMSW (Figure 5.32d) as these phenomenon seem to have increased with the extra iterations. This decrease and increase of the image artifacts is also apparent in the plots of the residuals. It is evident from comparing Figure 5.33 to Figure 5.31 that for the images between INJ1 and the two northern wells, the magnitude of the errors at a source depth of 30m decreases somewhat with the extra iterations. This is not true of the images between INJ1 and the southern wells as the magnitude of these residuals remains approximately the same.

To demonstrate that it is better to employ a layered background model rather than a homogenous half space to image the Richmond data, the iterative Born scheme has again been applied to the scattered fields that were measured in the EMNE well. However in this example a half space with a conductivity of 0.054S/m has been employed. Figure 5.34 shows the results after five and ten iterations. Notice that in both images the artifacts below the injection zone are more pronounced than those above it. In fact Figure 5.34b shows part of the plume diffusing downward as well as outward. Thus although it may seem unnecessary to employ a layered background model, incorporating it into the solution seems to produce more accurate results.

In this section the scattered fields in a layered background model were used to image the location of the injected plume. In terms of determining the direction in which the injected body migrated, this method is much more time efficient than imaging the total field data before and after injection. Unfortunately it has also been demonstrated that the two different methods of recovering the scatterer location can differ in the horizontal extent of the body between the wells. In the next section the iterative Born scheme will be applied to some simple forward models simulating these scattered fields and the resulting images compared to those of the real data to determine the accuracy of the experiment.

5.3.3 Simulation of the injection experiment

To crudely simulate the injection experiment, the thin sheet model that was used in Chapters 3 and 4 was again employed. However the purpose here was not to find the sheet model that best fit the scattered field data. Rather, the objective was to demonstrate that a three dimensional body which is not symmetric about the source borehole can produce the artifacts that were observed in the scattered field images of Section 5.4.2. In addition by observing how the images differ for various sheet positions we can determine the sensitivity of the cross well EM to the location of the plume in the Richmond Field Station experiment.

The models that were employed are shown on a map of the Richmond Field Station in Figure 5.35. The depth of the horizontal sheet is 31.25 m and its conductance is 1S. Originally the dimensions were 10m by 10m as suggested by H.W. Tseng (1993, personnel communication) as he had found that a sheet of this size this provided an adequate fit to the data. However initial attempts with this and other models indicated better results occur when a sheet is used that is 12 m long in the east-west direction and 8.5m wide in the north-south direction.

The scattered magnetic fields were calculated for models A, B and C in Figure 5.36 to simulate a plume which is migrating to the north of the injection point by varying amounts while staying symmetric an east-west direction. Model A in Figure 5.36 simulates a minimum of northerly offset as suggested by Tseng, while model C represents the plume migrating entirely to the north away from the injection well. In addition results have been calculated for model D to simulate additional asymmetry to the west.

Unfortunately there are some serious differences between these simulations and the injected salt water plume that limit how much information can be derived from this study. The first major discrepancy is the shape of the sheet. Here the body of salt water is being simulated as an infinitesimally thin, rectangular sheet of uniform conductivity. However it is known from the borehole logs collected after the injection (Appendix D) that the plume is at least 3m thick. In addition it is most likely not rectangular in shape but rather is some type of smoothly curved, three dimensional body in which the conductivity is greatest near the injection well and diffusively decreases outwards to the edges. A second major difference between these simulations and the measured results is that the forward modeling code does not allow for the two layer background models that were employed in section 5.4.2. Instead a uniform half-space model of 0.05S/m was employed. Finally, because of numerical considerations, the scattered fields could not be calculated with the sources within or in close proximity to the sheet. Thus instead of exactly imitating the data collection process, results were calculated at 18.5 kHz for 23 source and 23 receiver stations separated at 2.5 m intervals from 5m to 60m depth.

The first set of synthetic images simulate those of the cross well EM data measured between INJ1 and EMNW. Figure 5.36 shows the results for models A, B and C after 5 iterations which should be compared to Figure 5.30a, while Figure 5.37 demonstrates the results after 10 iterations which correspond to Figure 5.32a. Making the appropriate comparisons suggests that models A and B offer reasonable approximations to the observations while model C does not. Not only do the images of A and B recover the position of the sheet in a manner that is similar to the EMNW images in Section 5.4.2, but also the resistive artifacts just above the injection zone and the conductive "arms" extending

off the end of the sheet are similar in appearance. The fact that the magnitude of the reconstructed conductivity in these synthetic images is not as great as in those of the real data may be a product of the sheet thickness, the cruder sampling of the synthetic data in source position, and possibly a model conductance which is too low.

To determine the extent of the plume to the south, the results for models A, B and C were calculated to simulate the measurements made between INJ1 and EMSE (Figure 5.35). Figure 5.38 shows the results after 5 iterations which can be contrasted against Figure 5.30c, and in Figure 5.39 the 10 iterations images are given which should be compared to Figure 5.32c. The characteristic that is immediately visible is that the model A does not produce images that resemble those of the observed data at all. This is due to the fact that this model extends far enough to the south so that the cylindrical symmetry at least partially is obeyed. Thus the iterative Born scheme is able to reconstruct an image that rather accurately recovers the horizontal limits of the sheet. Unfortunately as demonstrated in Figures 5.30c and 5.32c this is not the case for the real data.

Synthetic data calculated with Models B and C produce images that more accurately recover those resulting from the scattered field data measured between INJ1 and EMSE. This conclusion has been reached by observing the resistive artifact that is reconstructed within the injection zone . Figures 5.38b and 5.39b show that for model B this artifact is not as well developed as in Figures 5.30c and 5.32c, while in the images of model C it is too strong and close to the injection well (Figures 5.38c and 5.39c). Thus the conclusions are that the best sheet model to fit the data collected between INJ1 and EMSE lies somewhere between models B and C, and as expected, the plume is not migrating much to the south but rather is primarily heading northward.

To verify that the conclusions deduced from the forward modeling experiments presented above hold for all of the data collected in the experiment, models A,B and C were again employed to simulate the two other sets of cross well data. The results for the simulated measurements made between INJ1 and EMNE are given in Figures 5.40 and 5.41, and for those made between INJ1 and EMSW in Figures 5.42 and 5.43. Comparing Figure 5.40 to 5.30b and Figures 5.41 to 5.32b indicate that a model somewhere between A and B seems to offer the best approximation to the data collected in EMNE. Similarly comparing Figure 5.42 to 5.30d and Figure 5.43 to 5.32d suggests that the south sheet model that best fits the images of the EMSW data probably lies somewhere between models B and C. Thus the conclusion is that out of these three models, model B seems to produce the images which generally fits all of the data both to the north and to the south.

One problem that to this point has not been addressed is the fact that the images of the salt water body that are present between INJ1 and EMNW (Figures 5.30a and 5.32a) are

more conductive than those for the body between INJ1 and EMNE (Figures 5.30b and 5.32b, respectively). In the simulations presented above this phenomenon was not present. To determine if this effect could be produced by the plume moving asymmetrically towards the west as well as the north, Model D in Figure 5.35 was employed to simulate the data measured between INJ1 and both EMNW and EMNE.

Figure 5.44 shows the images of this simulation after 10 iterations of the iterative Born scheme. Comparing 5.44a to 5.37b indicates that offsetting the plume in this direction does cause a slight increase in the reconstructed conductivity. However the scheme is also tracking the edge of the plume as the conductive zone in Figure 5.44a is shown to extend further out than in Figure 5.37b. A similar phenomenon is present when Figure 5.44b is compared to 5.41b. Moving the sheet asymmetrically to the west not only results in a reduction in magnitude of the reconstructed conductivity, but also the edge of the sheet is not imaged as far out between the two wells. Thus the greater plume conductivity in that is evident when Figure 5.32a is compared to 5.32b is probably not due to this type of asymmetry. Unfortunately at this point we are unable to determine if this is caused by error in the data or if the conductive water is migrating preferentially to the northwest.

There is a good deal of uncertainty about how much accurate information can be derived from these simulations and how much credence can be given to these results. As previously mentioned, this uncertainty is primarily caused by the fact that 1) the sheet is infinitesimally thin while the plume is approximately 3m thick, 2) the models are rectangular in shape which is not very realistic and 3) the synthetic data were not sampled at the same source-receiver intervals as in the experiment. Because of these problems the sheet model was not used in an exact, inverse sense. However there are some useful and realistic conclusions that can be drawn from the simulations. First of all, the plume is definitely migrating off to the north of the injection well with less than than 2m extension towards the south. In addition the maximum northward extension is probably no greater than 7 m. Finally, the fact that the nature of the images changes so dramatically as the sheet was moved around suggests that the cross well scattered field data contains very high resolution information about the plume location. Thus in order to more accurately recover the true conductivity distribution within the plume, a three-dimensional inversion code such as developed by Newman (1992) which uses all the data from all wells simultaneously should be employed.

5.4 Summary

The 1992 Richmond Field experiment has proven that a salt water injection process can be monitored using cross well electromagnetics. Although the cross well EM system

performed well enough to detect the large changes caused by the salt water, there is definite room for equipment improvement to alleviate problems with drift and system repeatability that were observed. A long term repeatability analysis seems to indicate that at least part of this problem may be due to some type of electrical leakage from the source tool. In addition, if greater data accuracy is required then better methods of data calibration need to be designed.

Even with these problems the data is of sufficient quality not only to detect the presence of the salt water, but also to allow for the application of the iterative Born imaging scheme. Results from this imaging process correlate well with previous experiments which show the injected body to be moving off to the north -northwest rather than spreading symmetrically about the injection well. Unfortunately, though the images of the total field data provide valuable information about the plume location, they do not correlate very well with the available conductivity logs and thus can not be used to accurately interpret the geologic structure at the field station. This poor correlation between the images and the logs is most likely due to the extremely 3-D nature of the conductivity distribution at this site. Although the 3-D nature of the plume is also apparent in the scattered field images, the size of the plume and the fact that the fields generated by it can be isolated make these types of effects much easier to deal with. Finally, simple simulations with a thin, conductive sheet model verify the conclusions of the general location of the plume, although the exact boundaries can not be defined.

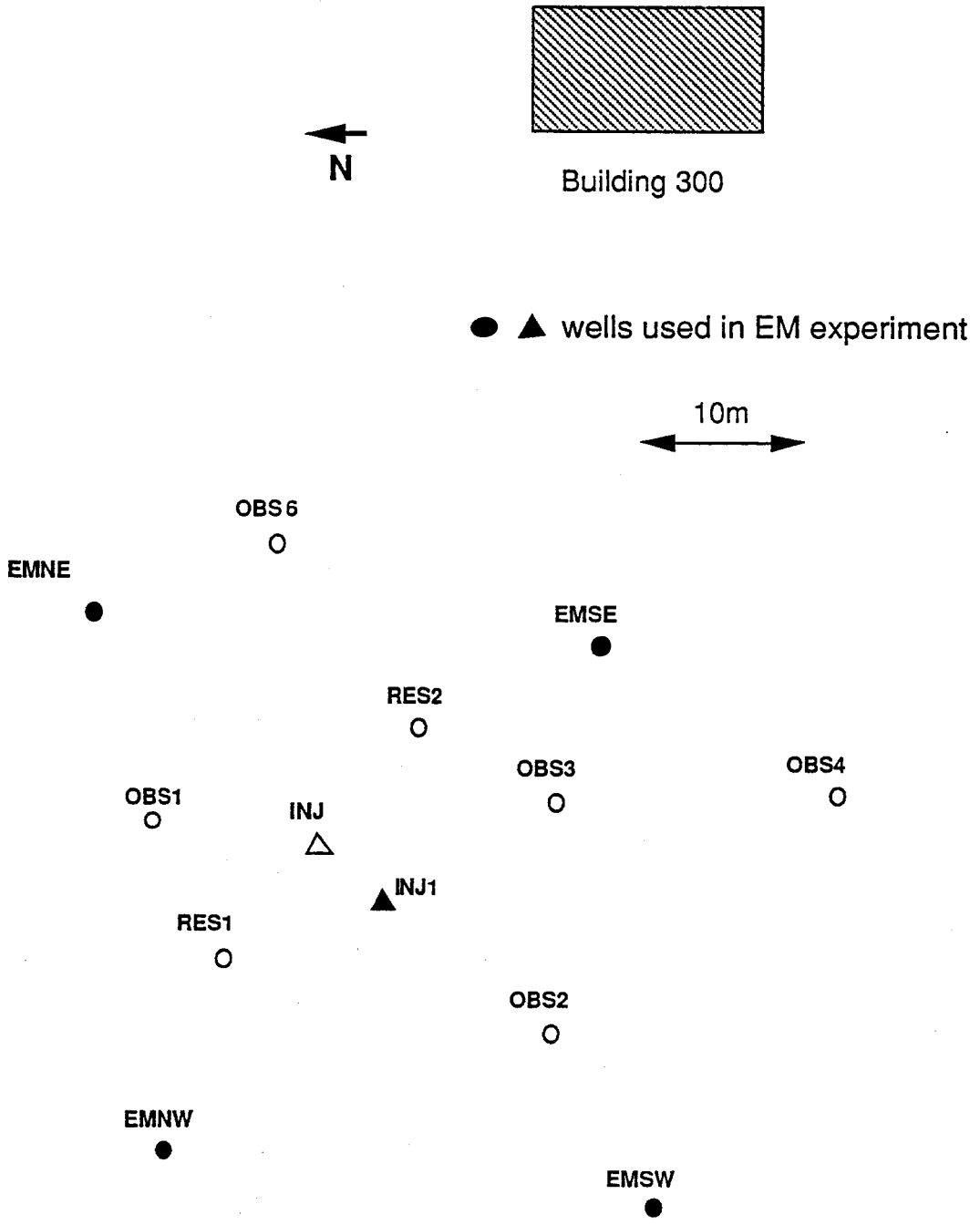

Figure 5.1 - Location map for the building 300 well field at the Richmond Field Station.

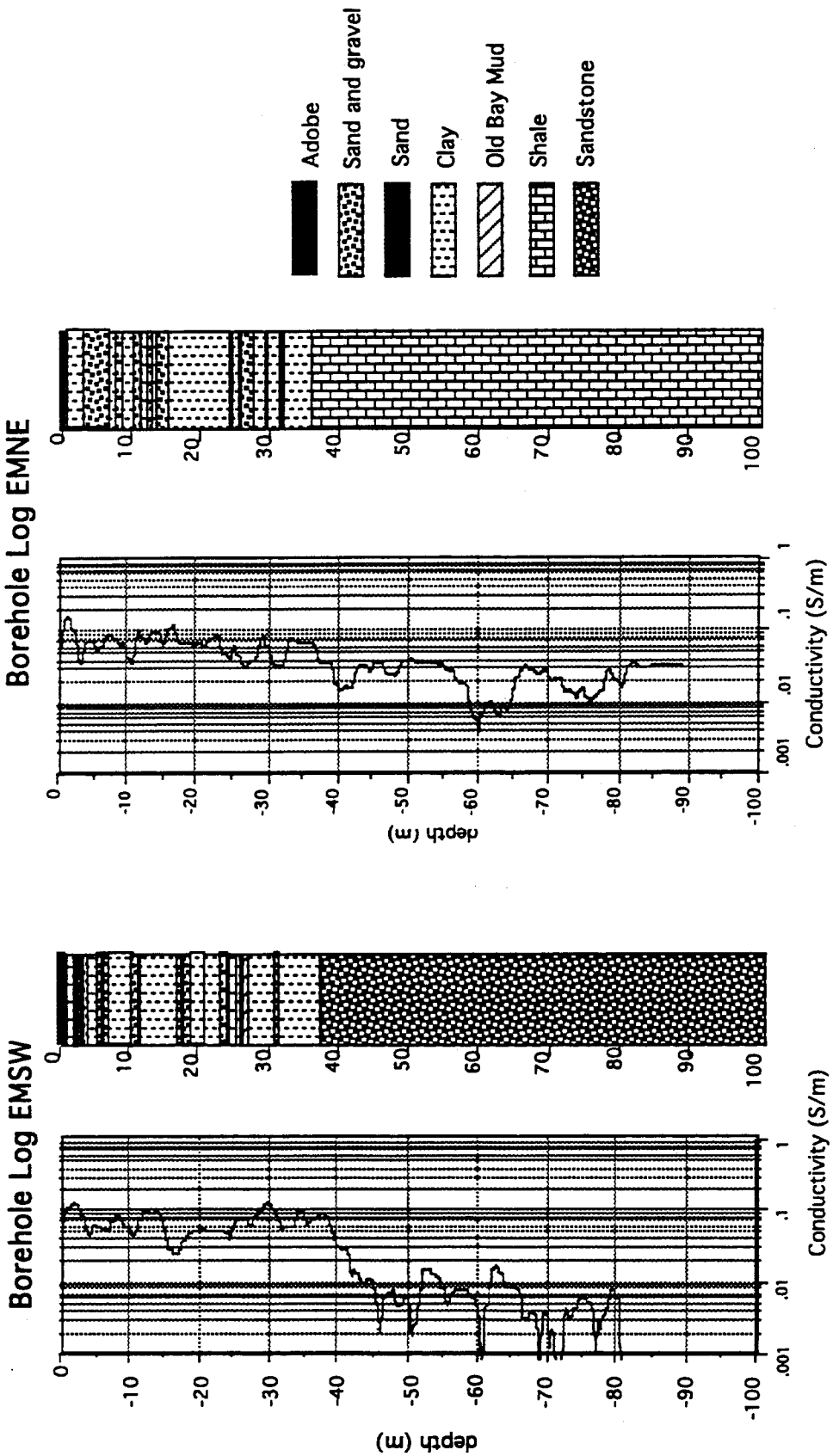

Figure 5.2 - Electrical conductivity and stratigraphic logs for the EMSW and EMNE wells at the Richmond Field Station. The stratagraphic logs were derived from the drill cuttings.

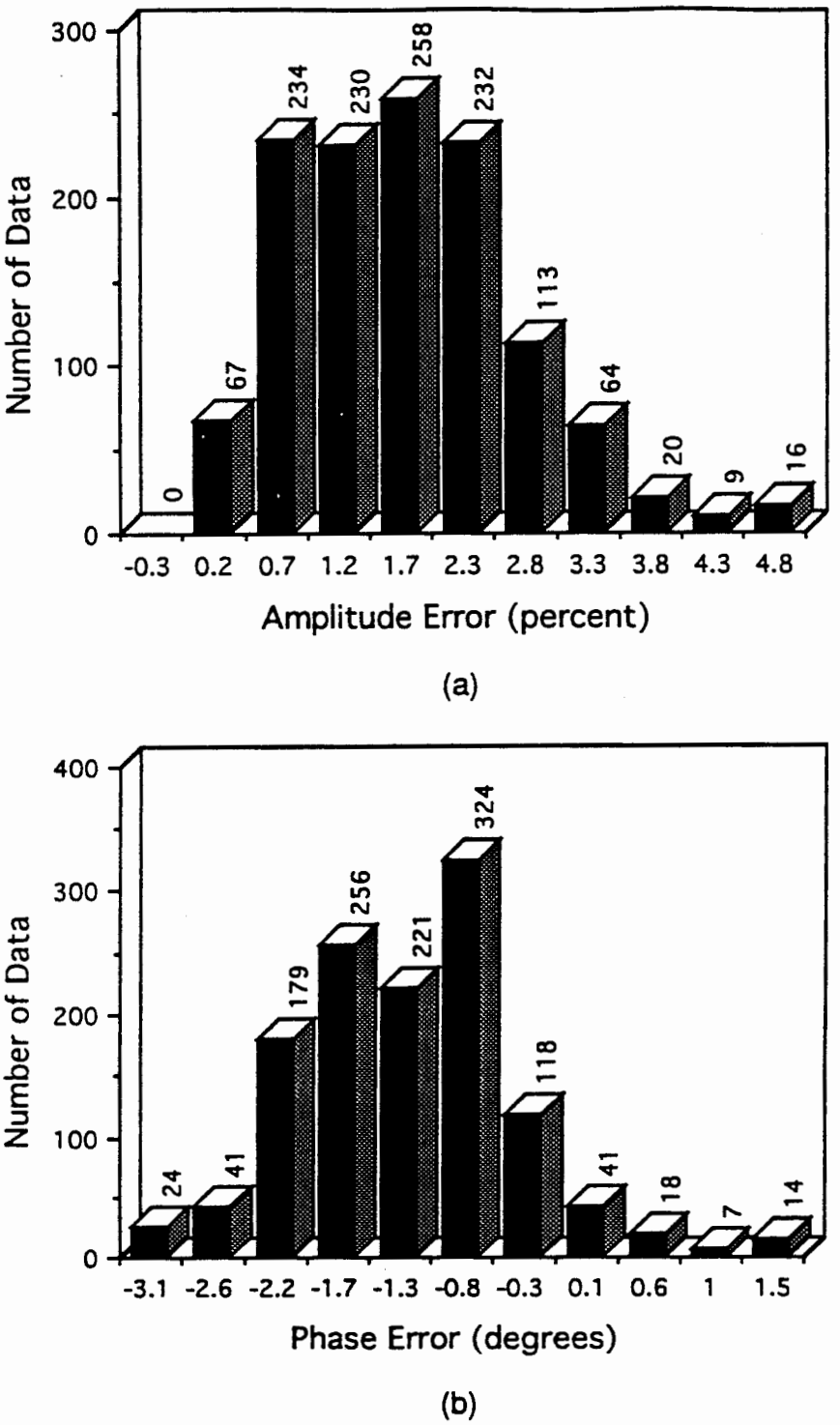

Figure 5.3 - Histogram analysis of repeatbility errors in EMNW data: (a) amplitude , (b) phase.

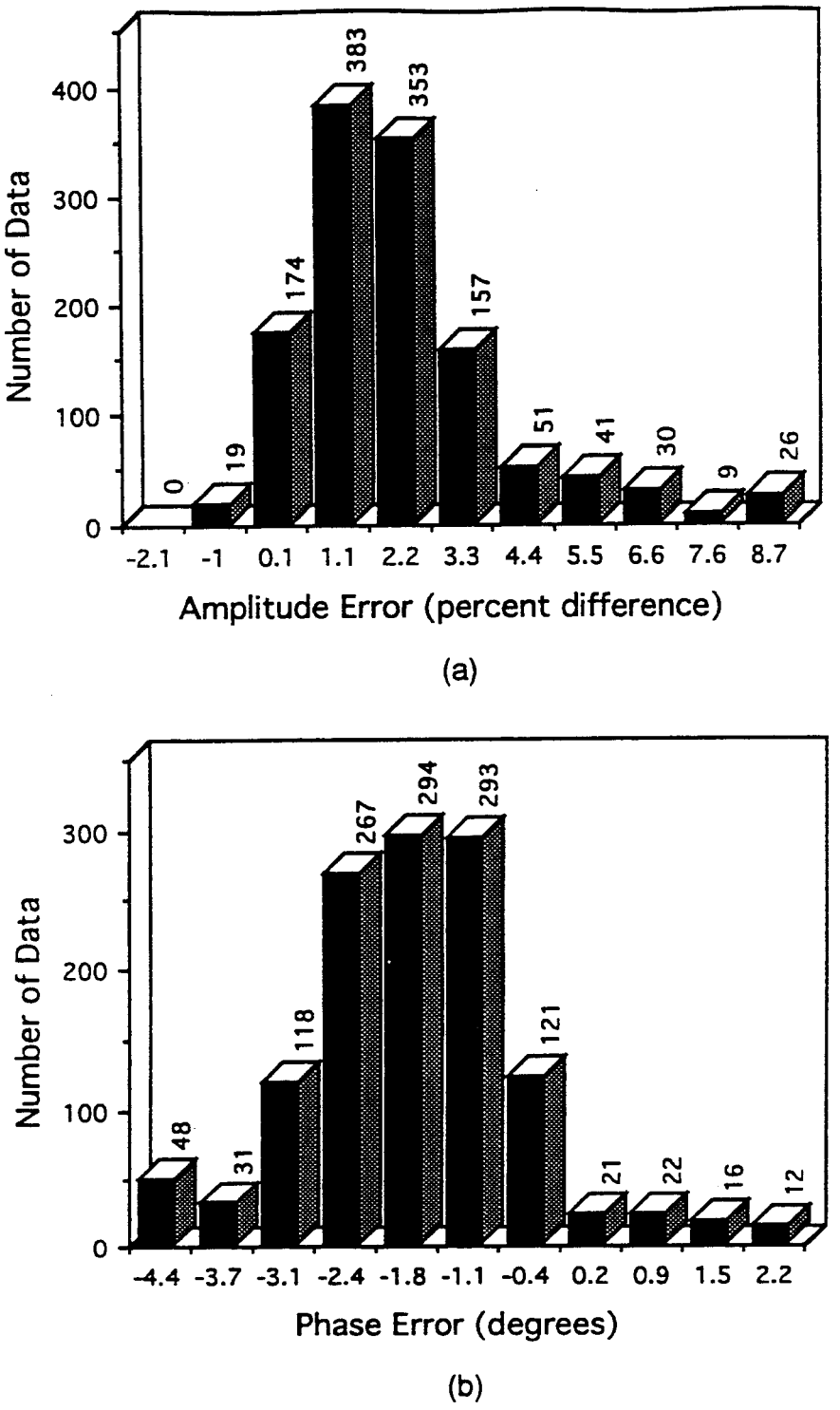

Figure 5.4 - Histogram analysis of repeatability errors for EMSW data: (a) amplitude , (b) phase.

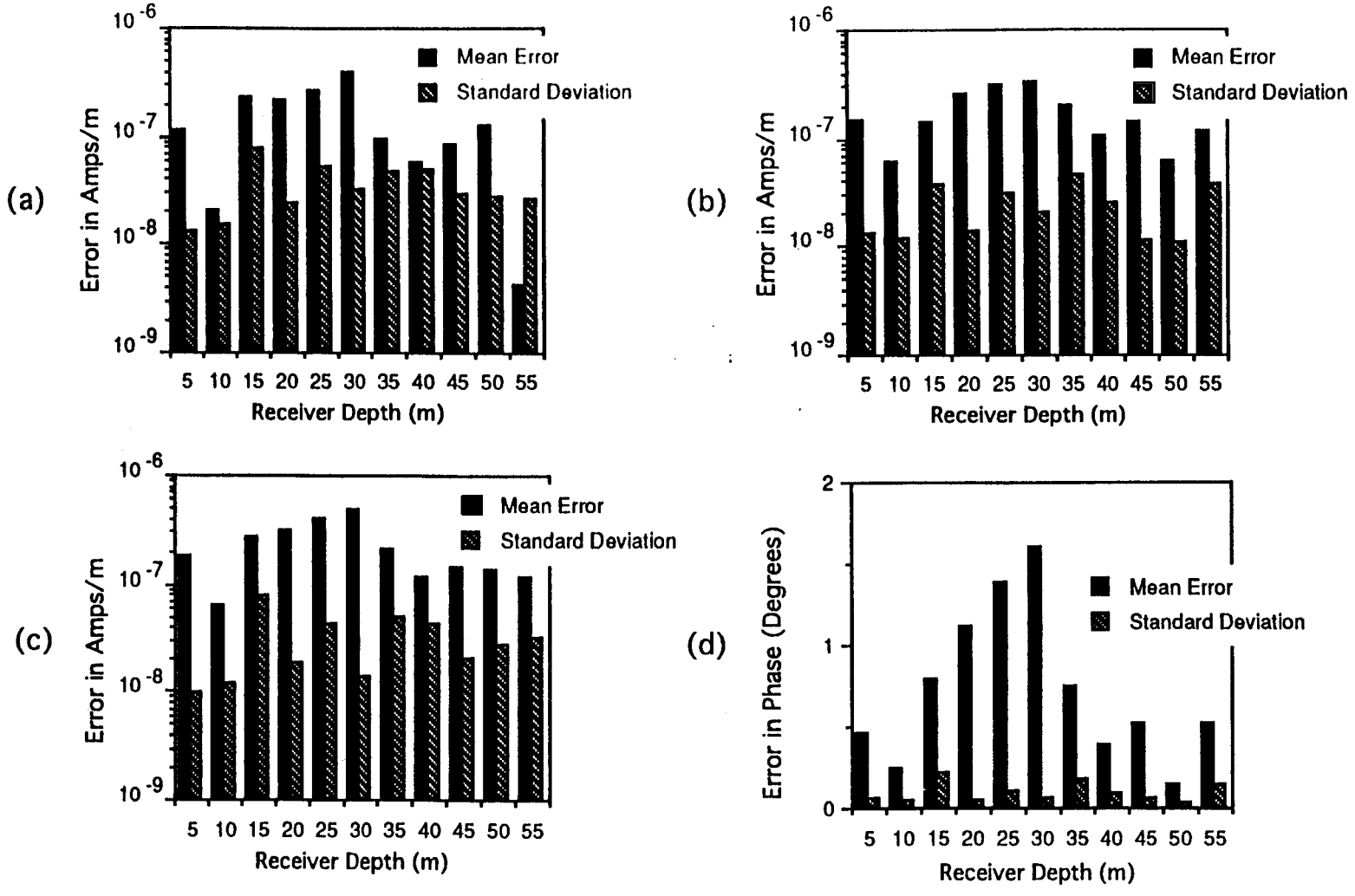

Figure 5.5 - Error analysis for EMNW repeats with the transmitter and receiver at the same level: (a) real component, (b) Imaginary component , (c) amplitude and (d) phase.

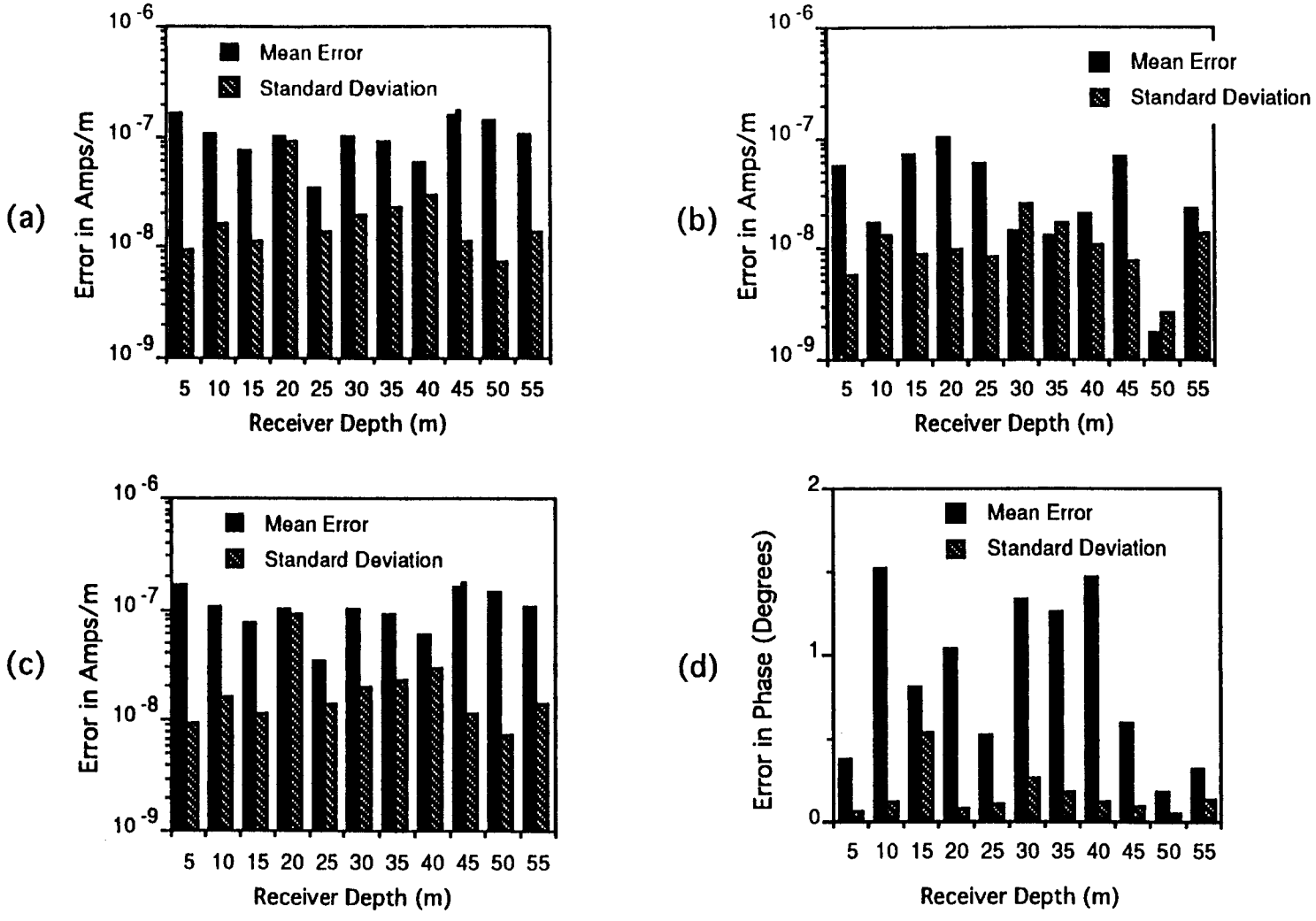

Figure 5.6 - Error analysis for EMSW repeats with the transmitter and receiver at the same level: (a) real component, (b) Imaginary component , (c) amplitude and (d) phase.

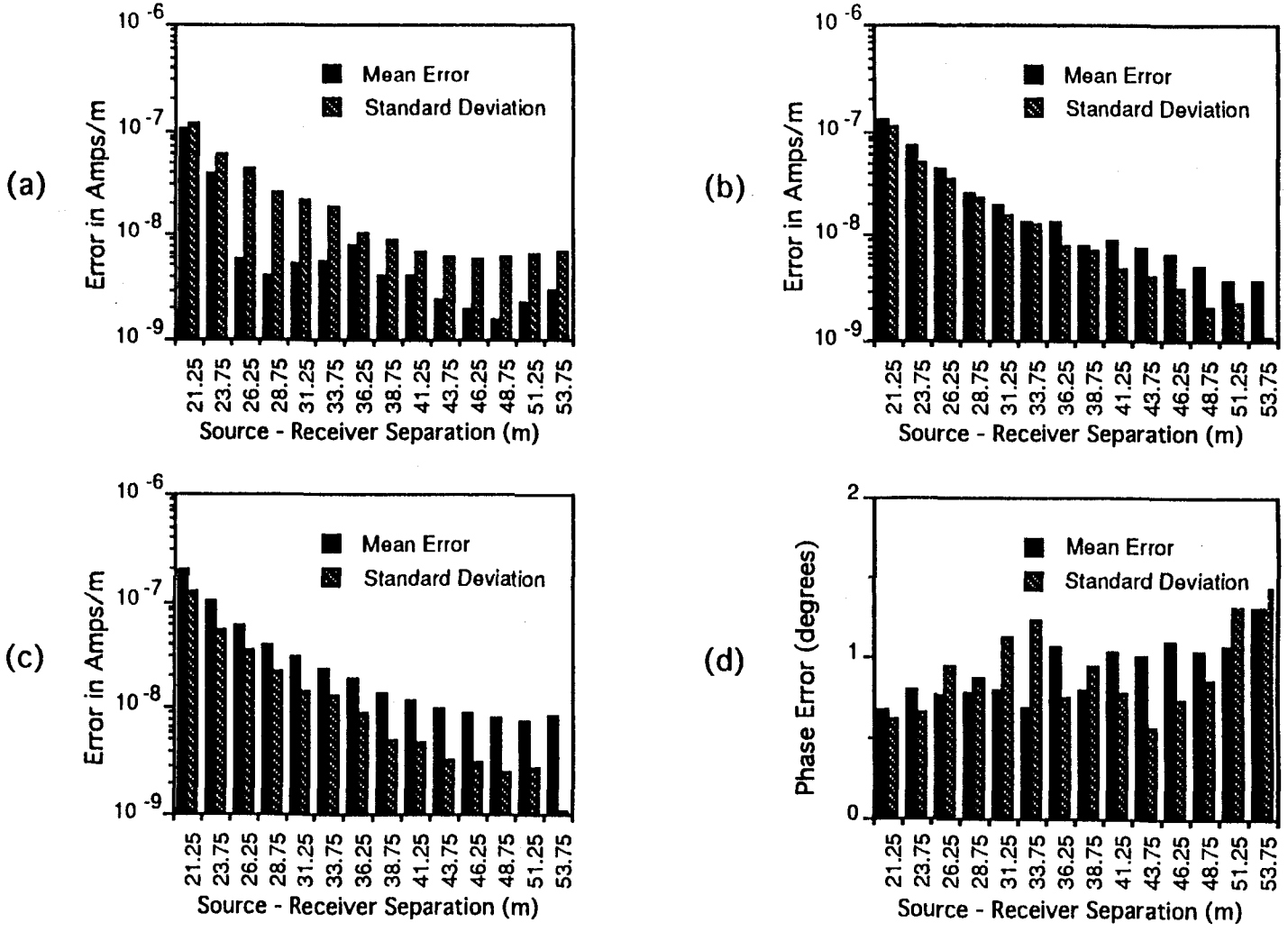

Figure 5.7 - Error analysis for EMNW repeats for different source-receiver separations: (a) real component, (b) Imaginary component , (c) amplitude and (d) phase.

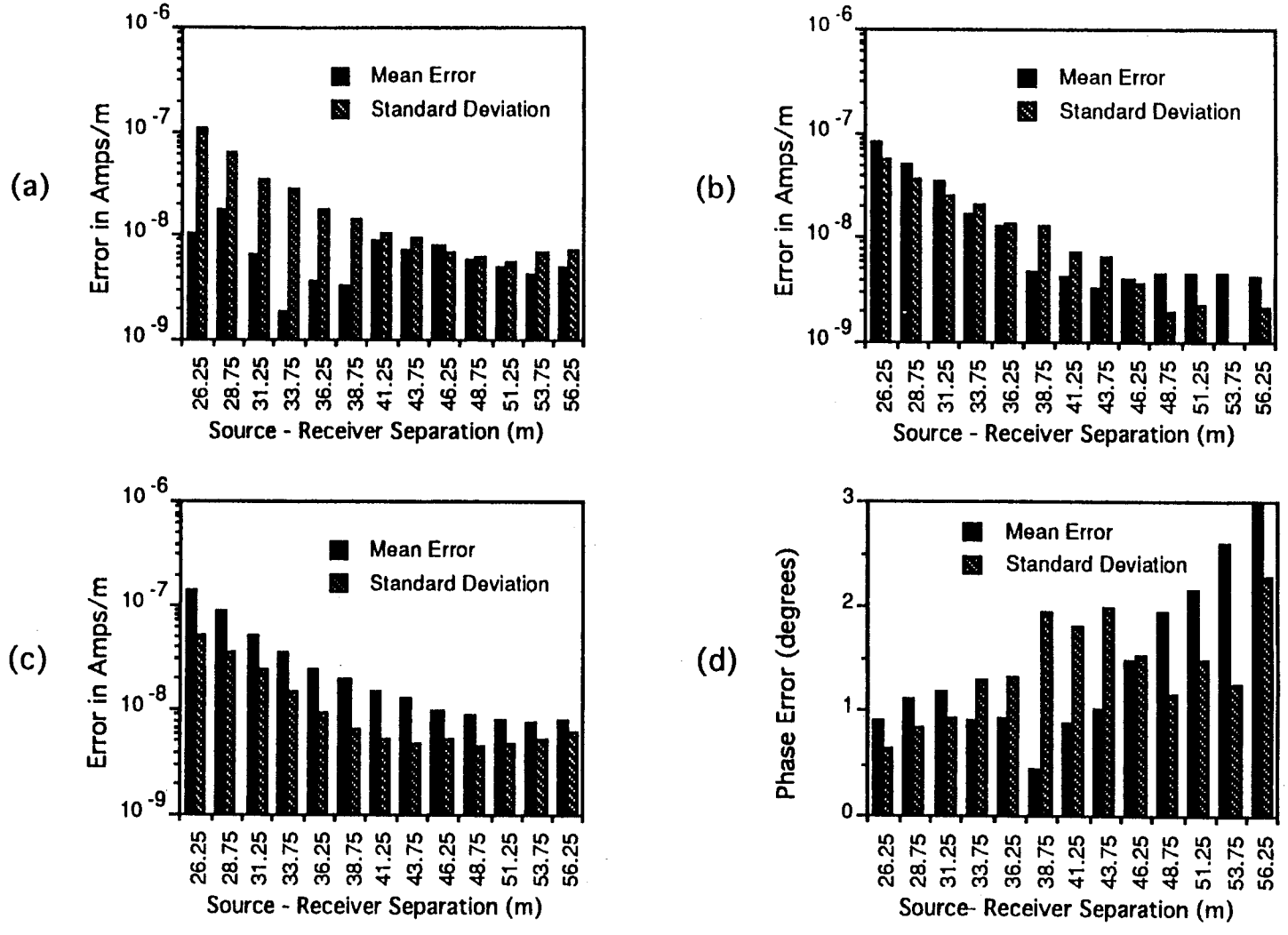

Figure 5.8 - Error analysis for EMSW repeats for different source-receiver separations: (a) real component, (b) Imaginary component , (c) amplitude and (d) phase.

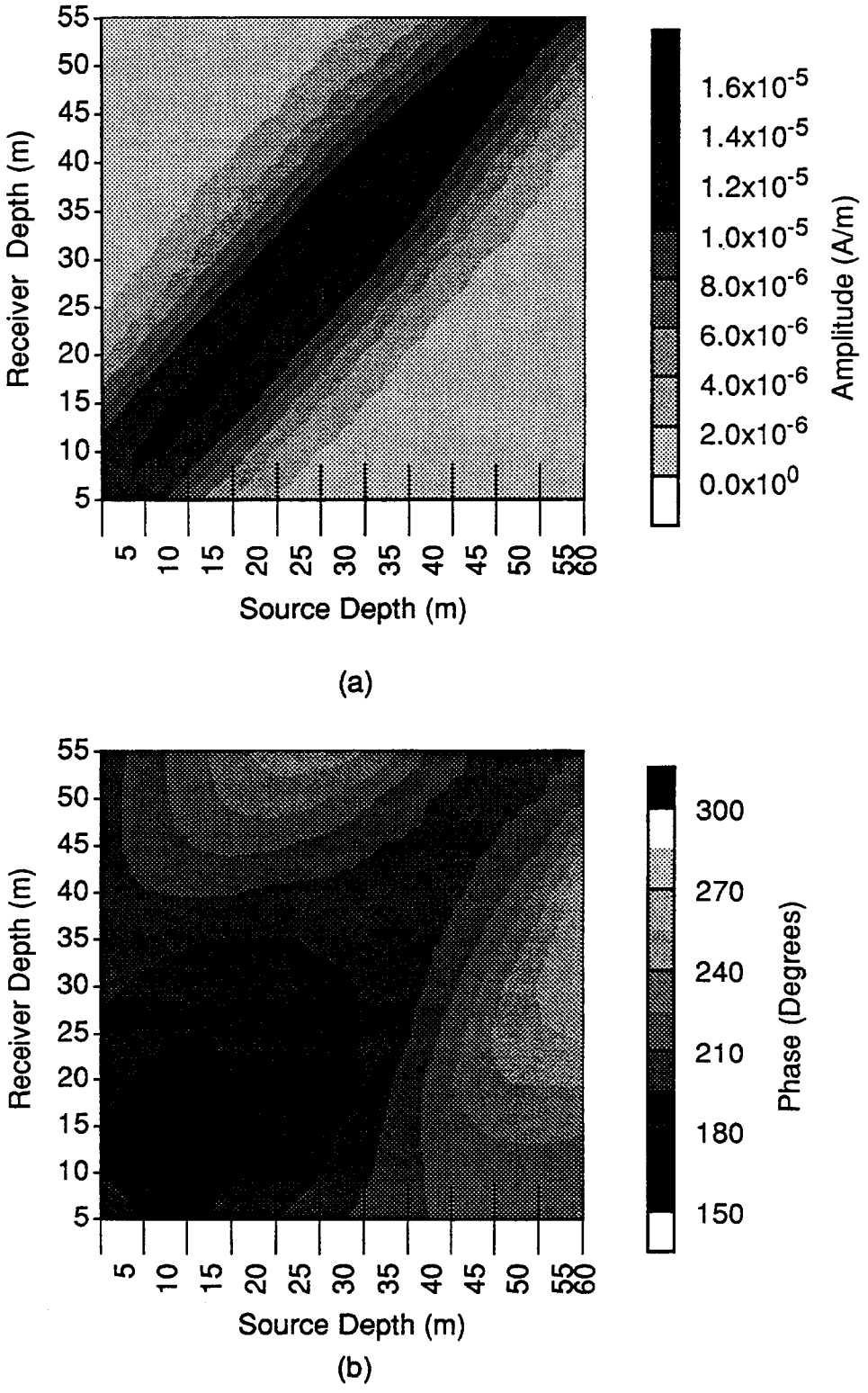

Figure 5.9 - EMNW data prior to injection. Each line on the receiver axis represents an individual profile of continuous data in transmitter depth. (a) Amplitude. (b) Phase.

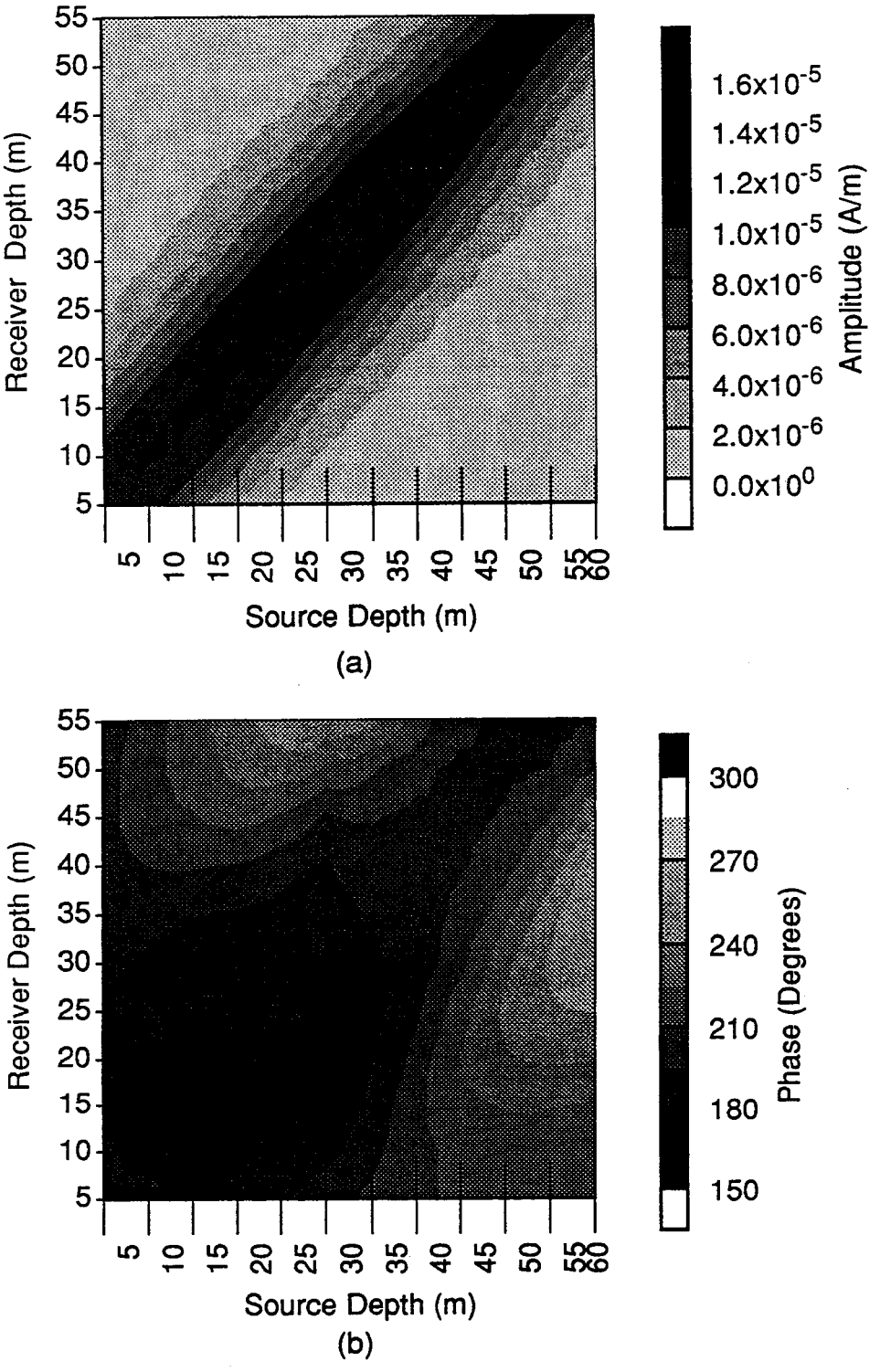

Figure 5.10 - EMNW data after injection. Each line on the receiver axis represents an individual profile of continuous data in transmitter depth. (a) Amplitude. (b) Phase.

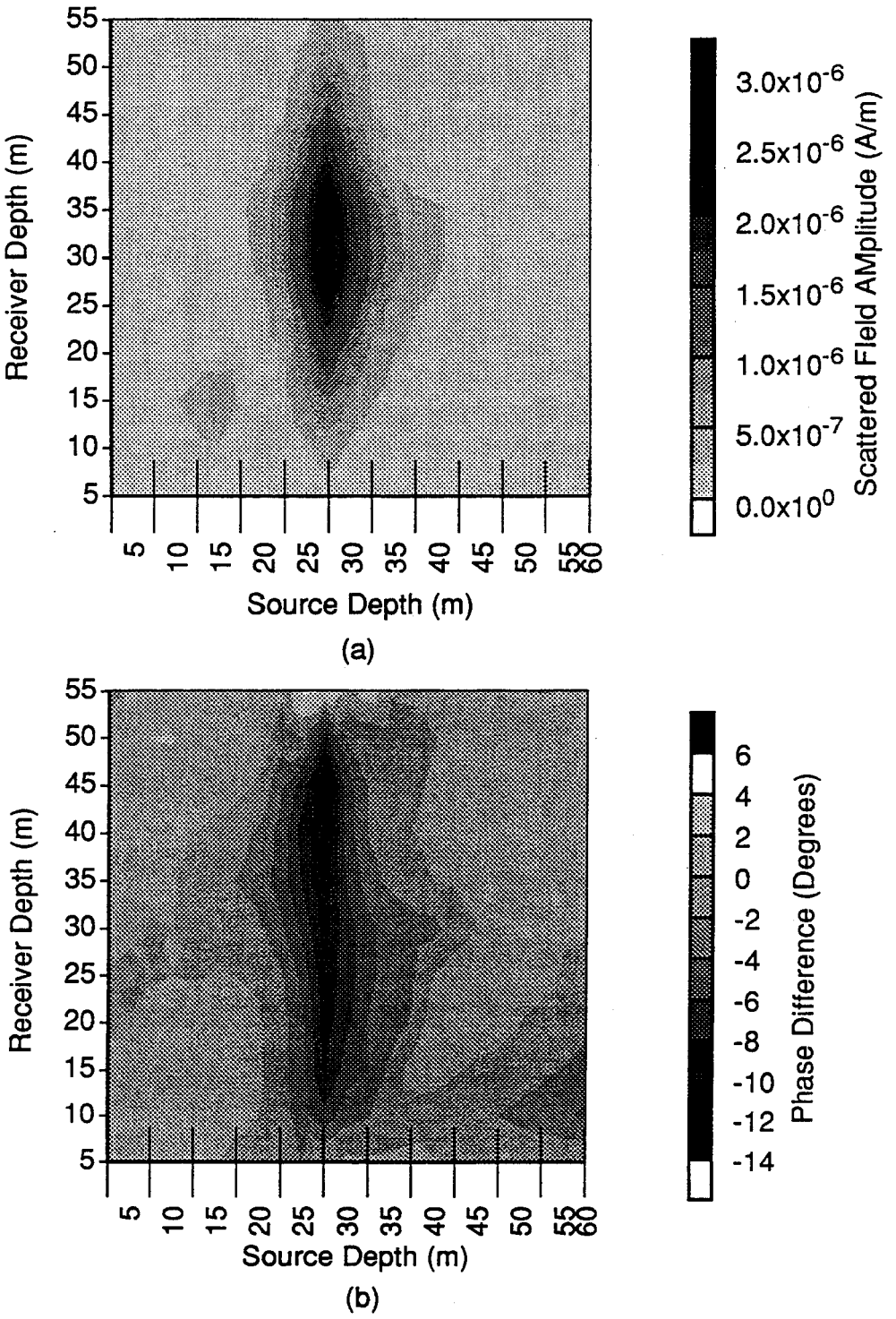

Figure 5.11 - EMNW secondary fields calculated by subtracting the preinjection data from the postinjection data. Each line on the receiver axis represents an indivdual profile of continuous data in transmitter depth. (a) Amplitude of the scattered field. (b) Phase difference between the post and pre injection data.

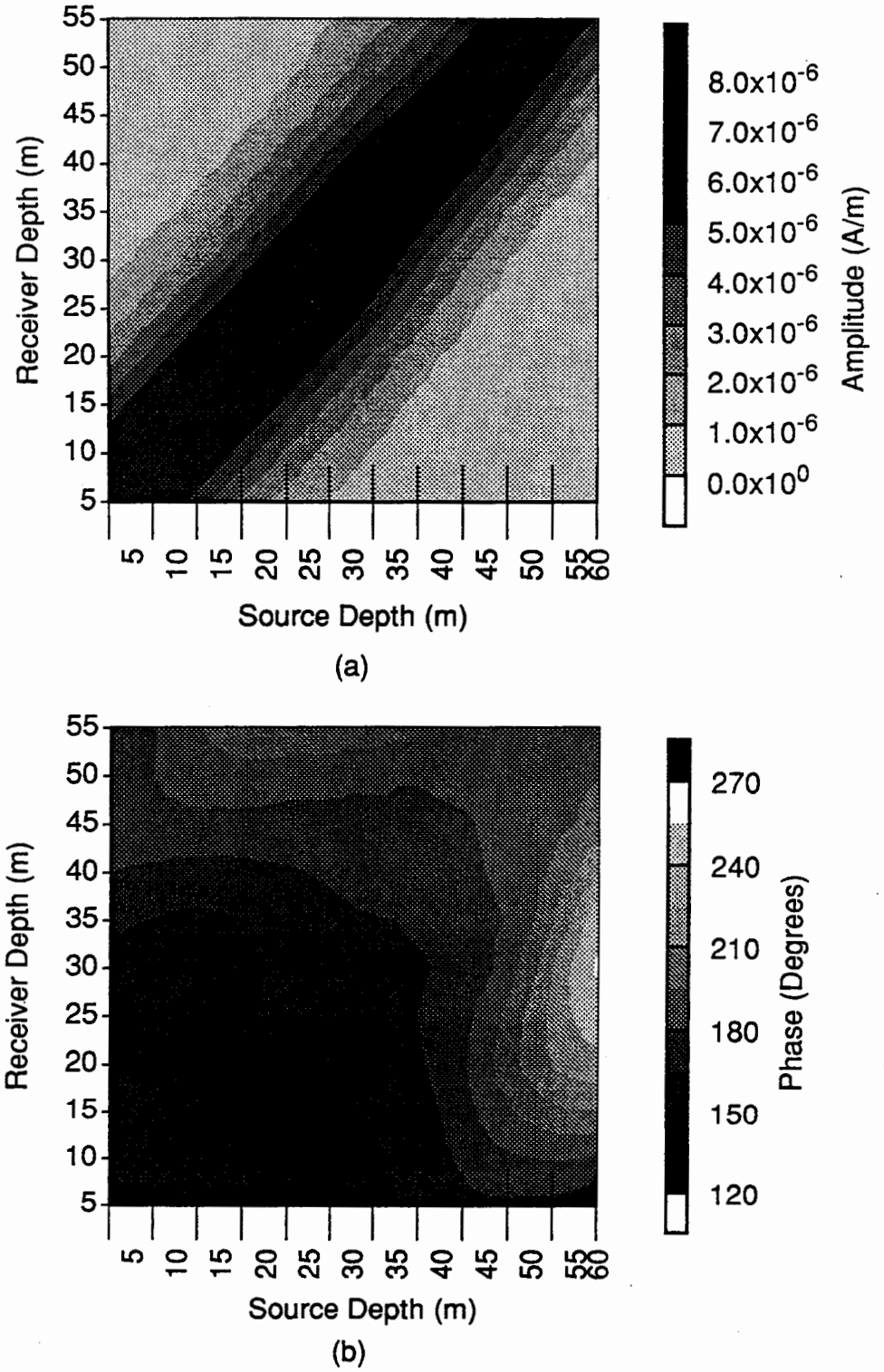

Figure 5.12 - EMNE data prior to injection. Each line on the receiver axis represents an individual profile of continuous data in transmitter depth. (a) Amplitude. (b) Phase.

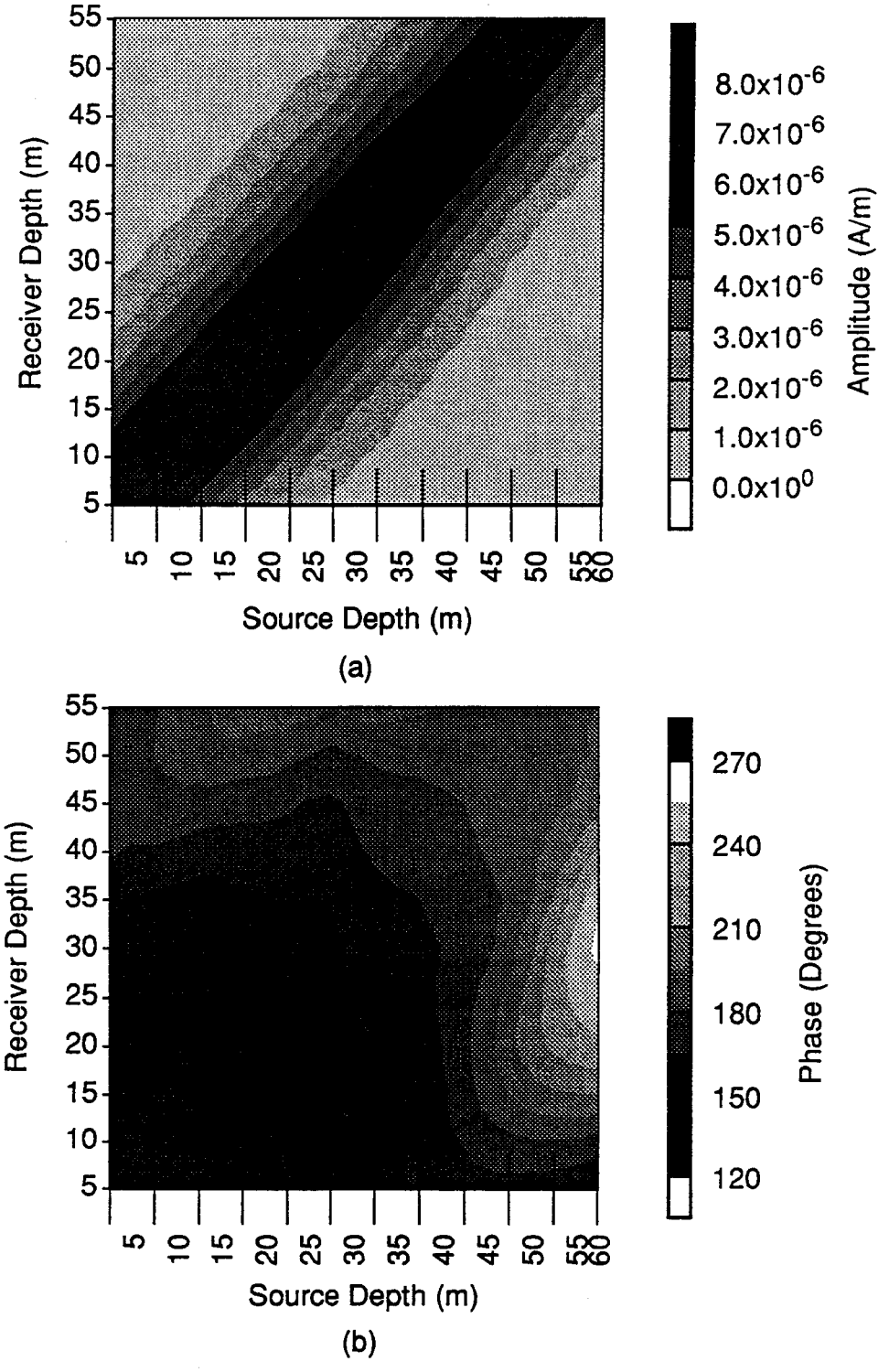

Figure 5.13 - EMNE data after the injection. Each line on the receiver axis represents an individual profile of continuous data in transmitter depth. (a) Amplitude. (b) Phase.

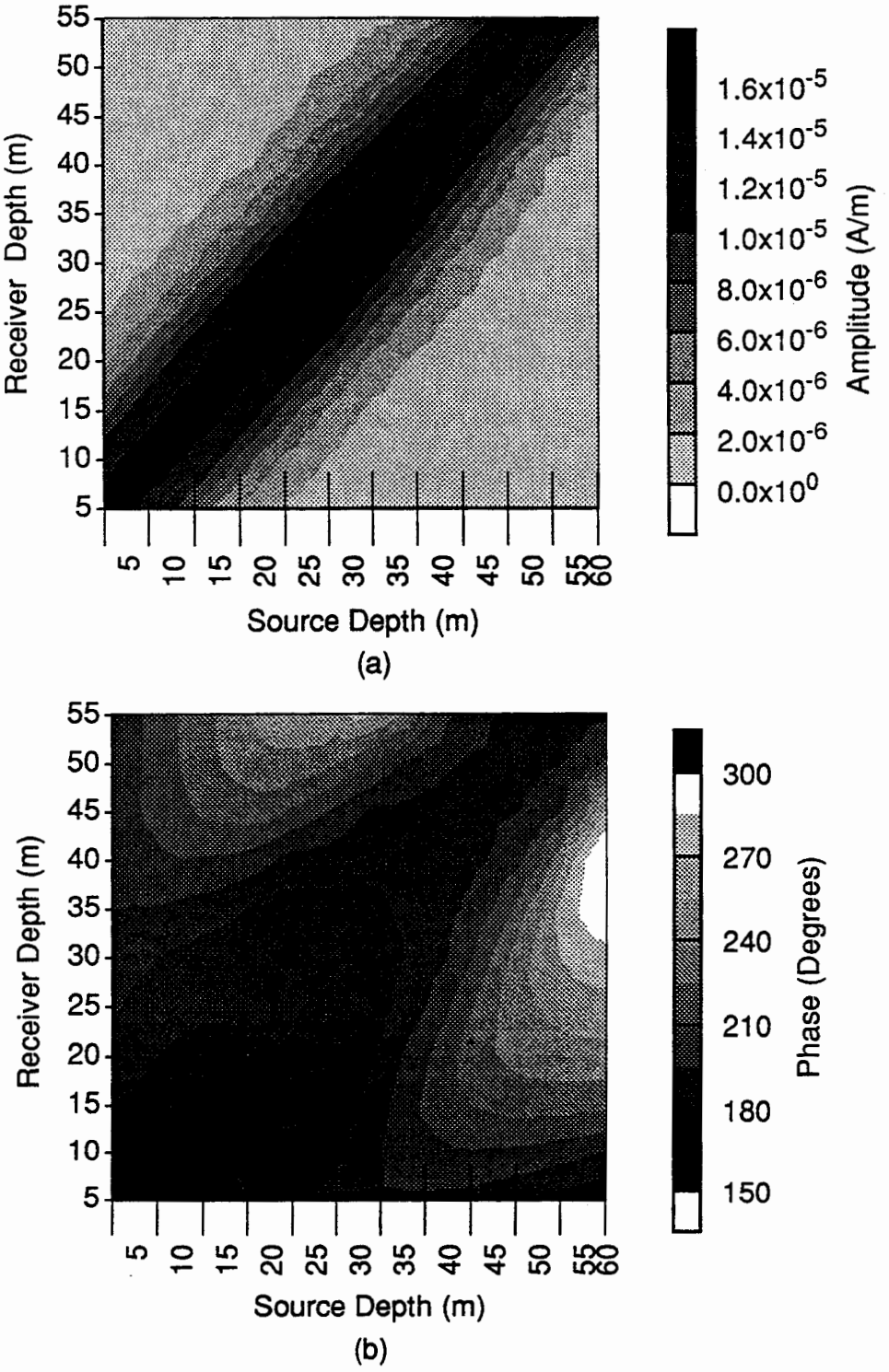

Figure 5.16- EMSE data after the injection. Each line on the receiver axis represents an individual profile of continuous data in transmitter depth. (a) Amplitude. (b) Phase.

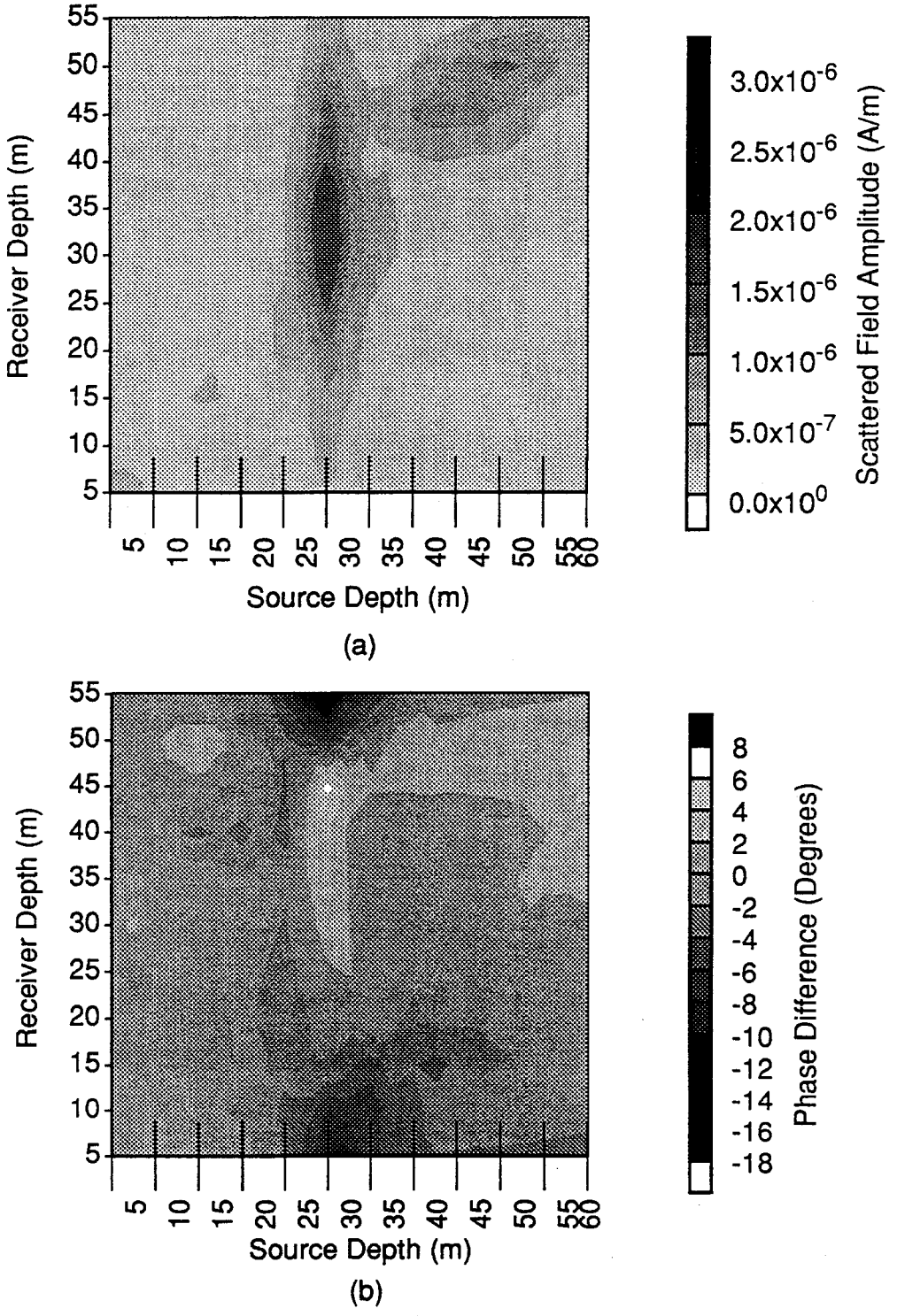

Figure 5.17- EMSE secondary fields calculated by subtracting the preinjection data from the postinjection data. Each line on the receiver axis represents an indivdual profile of continuous data in transmitter depth. (a) Amplitude of the scattered field. (b) Phase difference between the post and pre injection data.

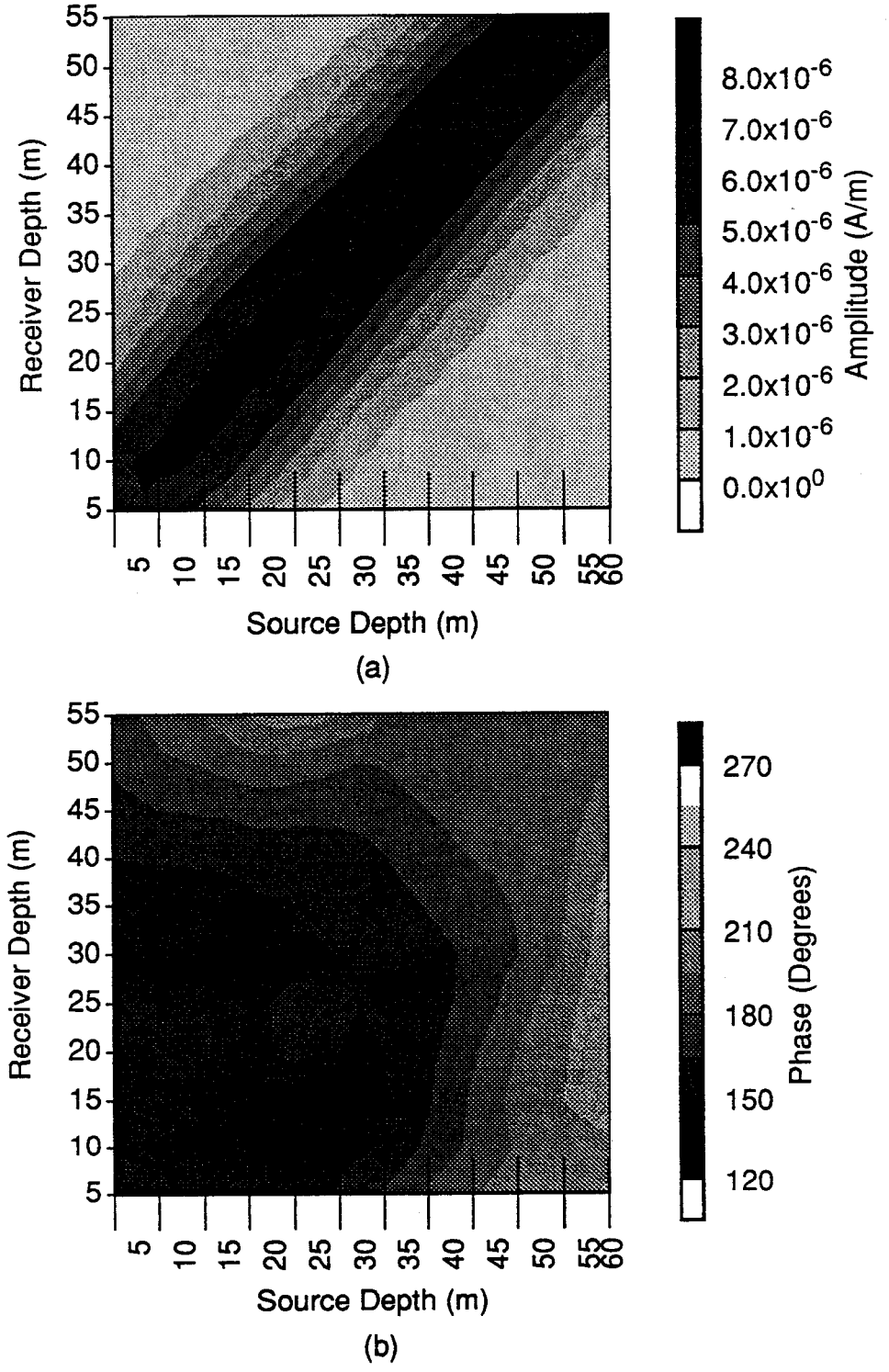

Figure 5.18 - EMSW data prior to injection. Each line on the receiver axis represents an individual profile of continuous data in transmitter depth. (a) Amplitude. (b) Phase.

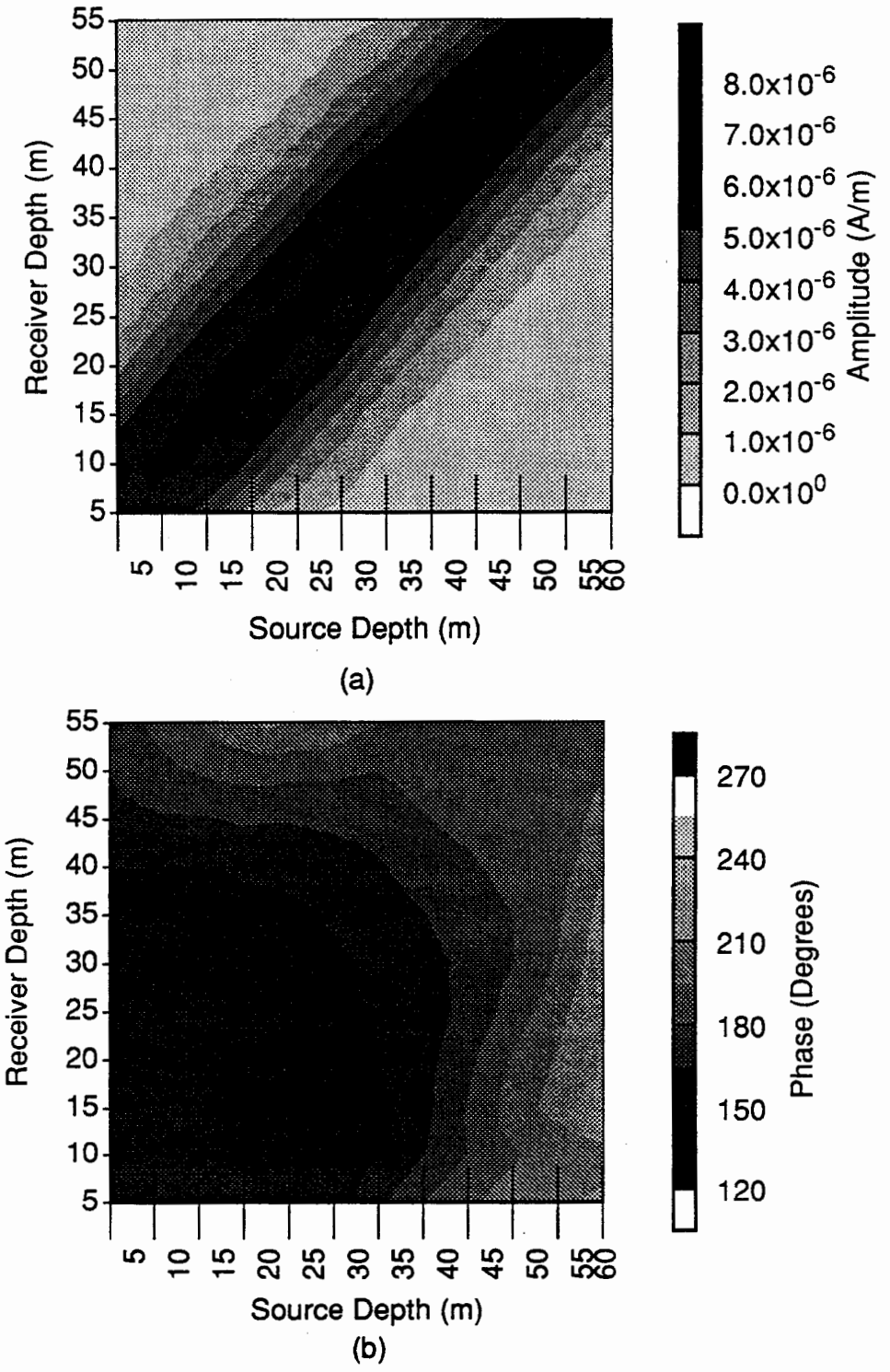

Figure 5.19- EMSW data after the injection. Each line on the receiver axis represents an individual profile of continuous data in transmitter depth. (a) Amplitude. (b) Phase.

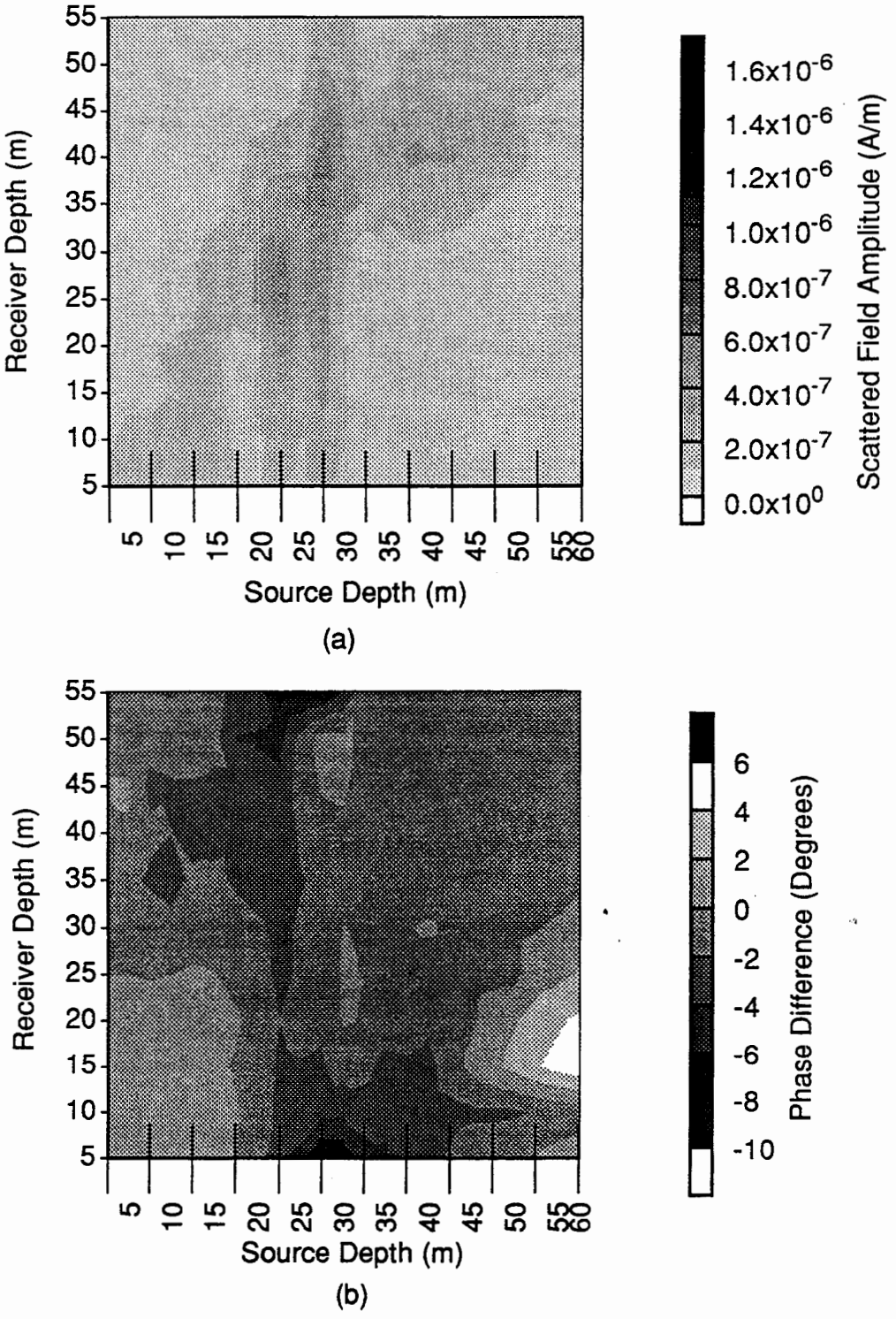

Figure 5.20 - EMSW secondary fields calculated by subtracting the preinjection data from the postinjection data. Each line on the receiver axis represents an indivdual profile of continuous data in transmitter depth. (a) Amplitude of the scattered field. (b) Phase difference between the post and pre injection data.

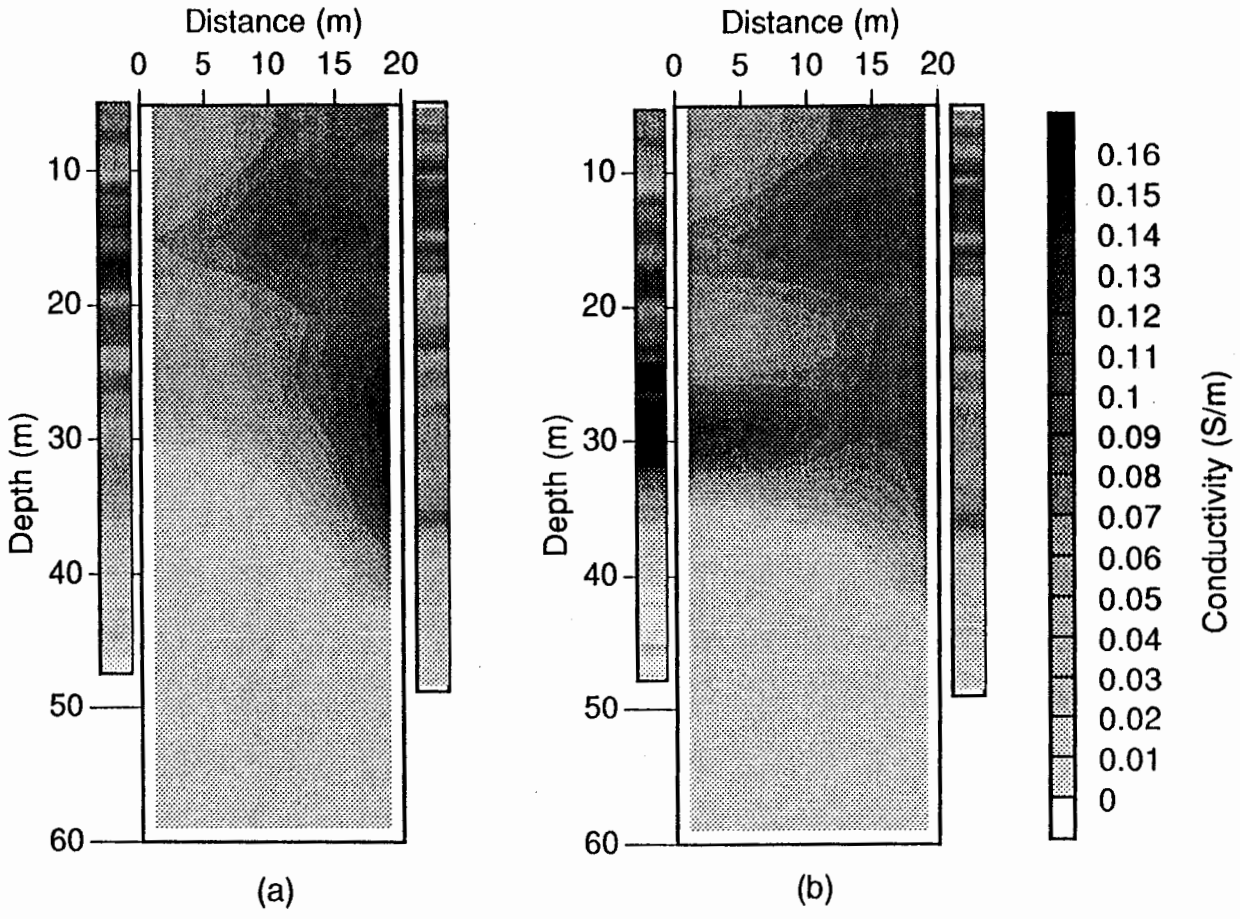

Figure 5.21 - Images of the Richmond cross well data collected between INJ1 and EMNW plotted with the conductivity well logs. The left hand axis (x=0m) represents well INJ1 while the right hand axis (x=20) represents well EMNW. (a) Images of the preinjection data and well logs. Mean residual error after 10 iterations=1.93e-7 A/m. (b) Images of the post injection data and well logs. Mean residual error after 10 iterations=1.82e-7 A/m.

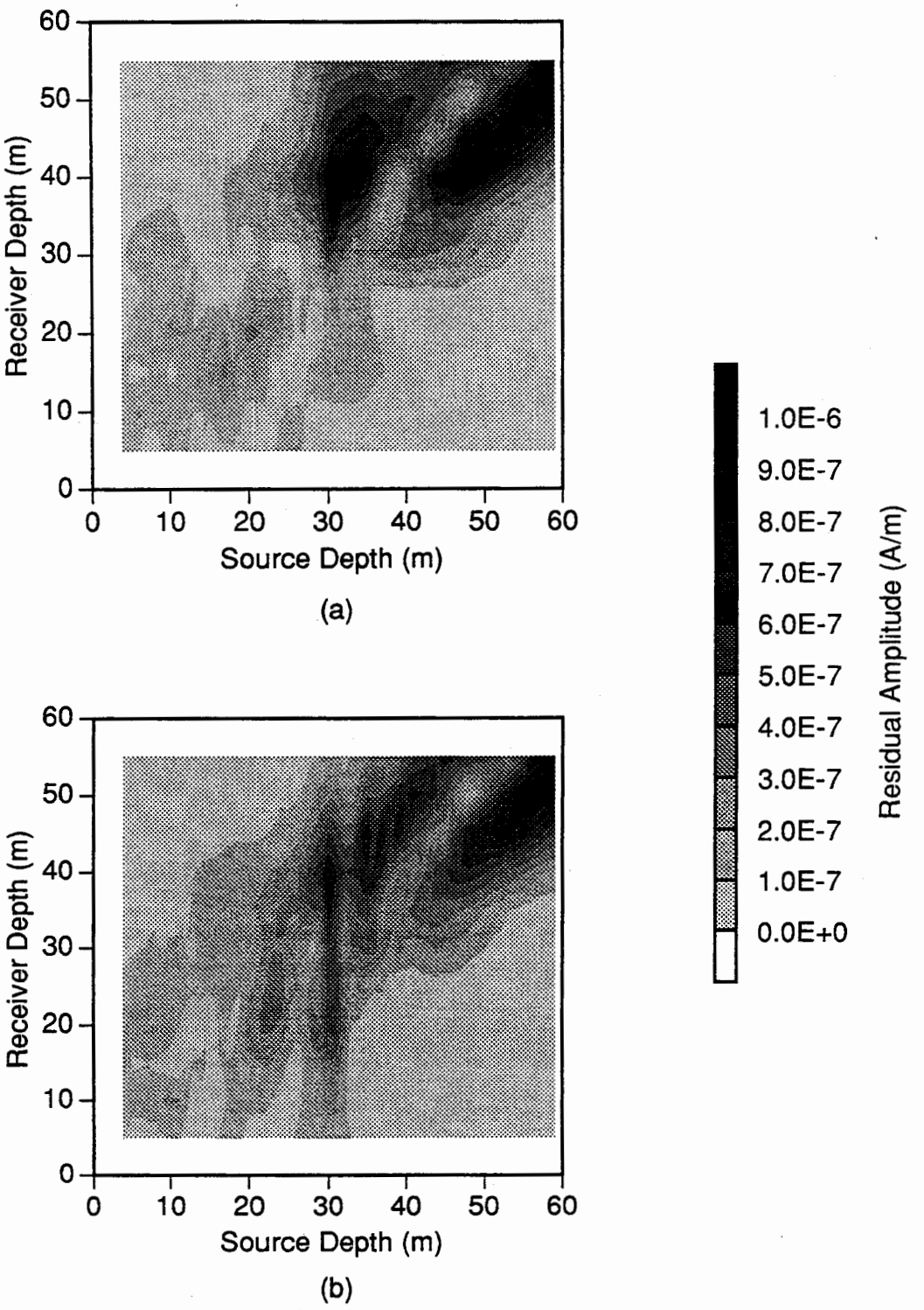

Figure 5.22 - Residual amplitude error between the Richmond cross well data collected between wells INJ1 and EMNW, and the calculated results for the images in Figure 5.21. The errors have been plotted as a function of source and receiver depth. (a) Residuals for the preinjection image given in Figure 5.21a. (b) Residuals for the postinjection image given in Figure 5.21b.

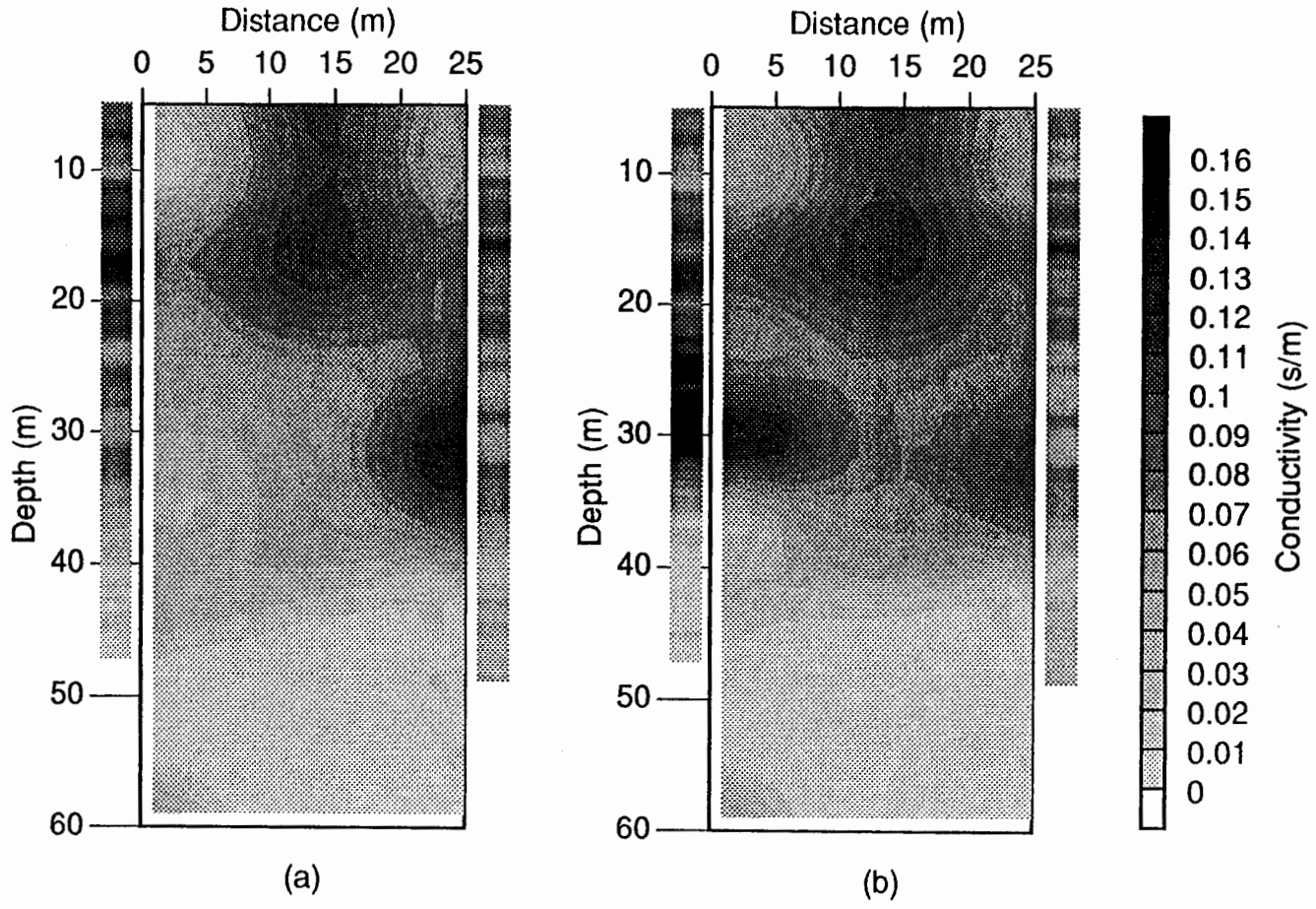

Figure 5.23 - Images of the Richmond cross well data collected between INJ1 and EMNE plotted with the conductivity well logs. The left hand axis (x=0m) represents well INJ1 while the right hand axis (x=20) represents well EMNE. (a) Images of the preinjection data and well logs. Mean residual error after 10 iterations=1.27e-7 A/m. (b) Images of the post injection data and well logs. Mean residual error after 10 iterations=1.19e-7 A/m.

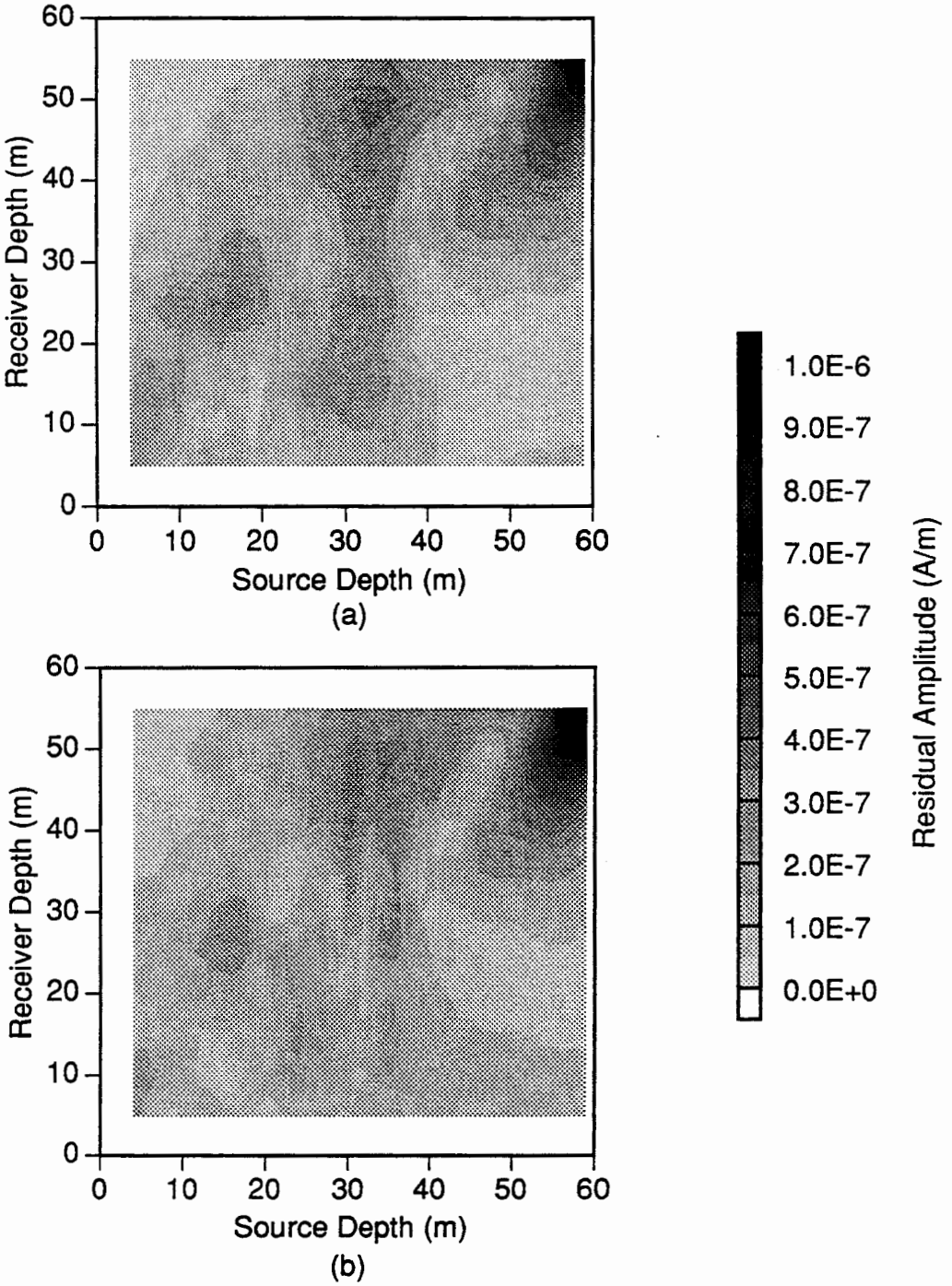

Figure 5.24 - Residual amplitude error between the Richmond cross well data collected between wells INJ1 and EMNE, and the calculated results for the images in Figure 5.23. The errors have been plotted as a function of source and receiver depth. (a) Residuals for the preinjection image given in Figure 5.23a. (b) Residuals for the postinjection image given in Figure 5.23b.

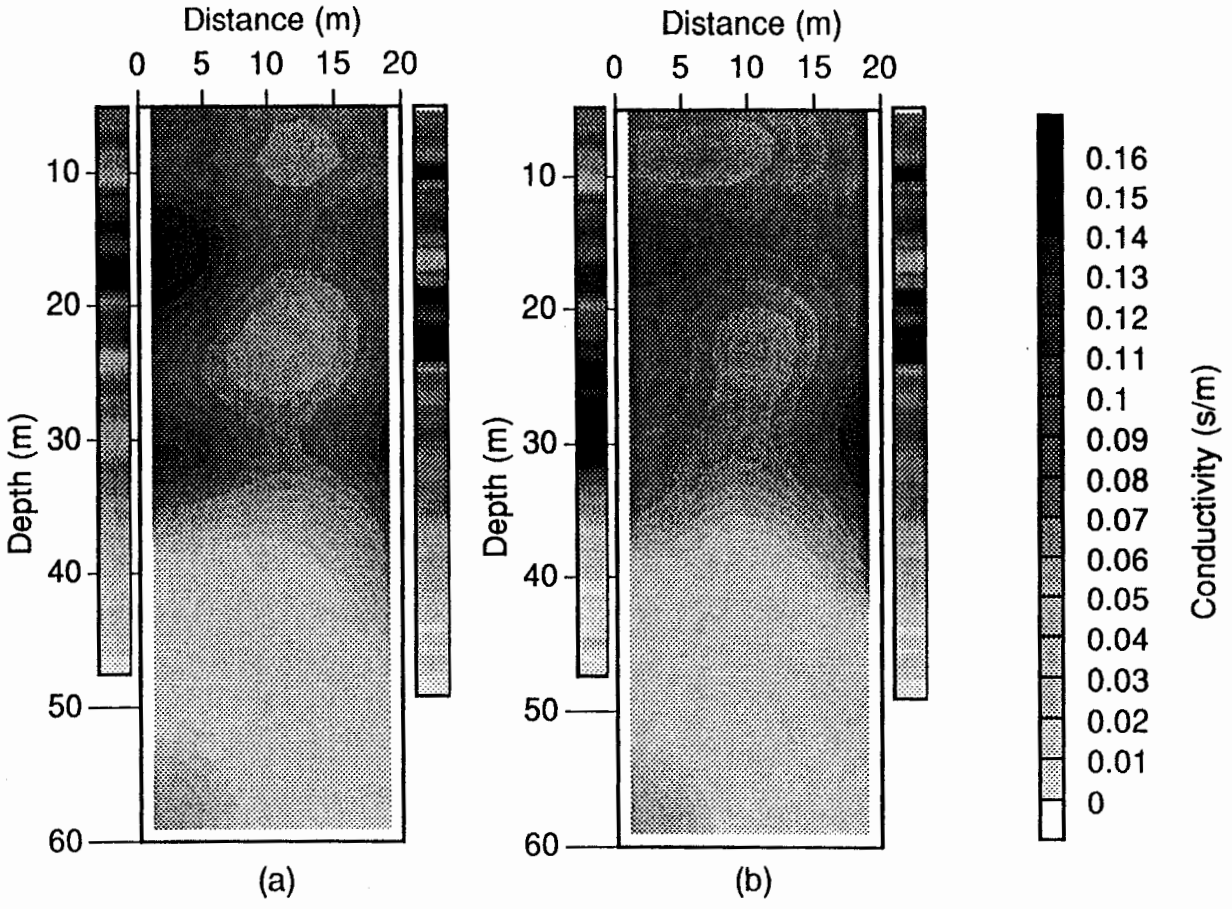

figure 5.25- Images of the Richmond cross well data collected between INJ1 and EMSE plotted with the conductivity well logs. The left hand axis (x=0m) represents well INJ1 while the right hand axis (x=20) represents well EMSE. (a) Imagse of the preinjection data and well logs. Mean residual error after 10 iterations=4.97e-7 A/m. (b) Images of the post injection data and well logs. Mean residual error after 10 iterations=5.04e-7 A/m.

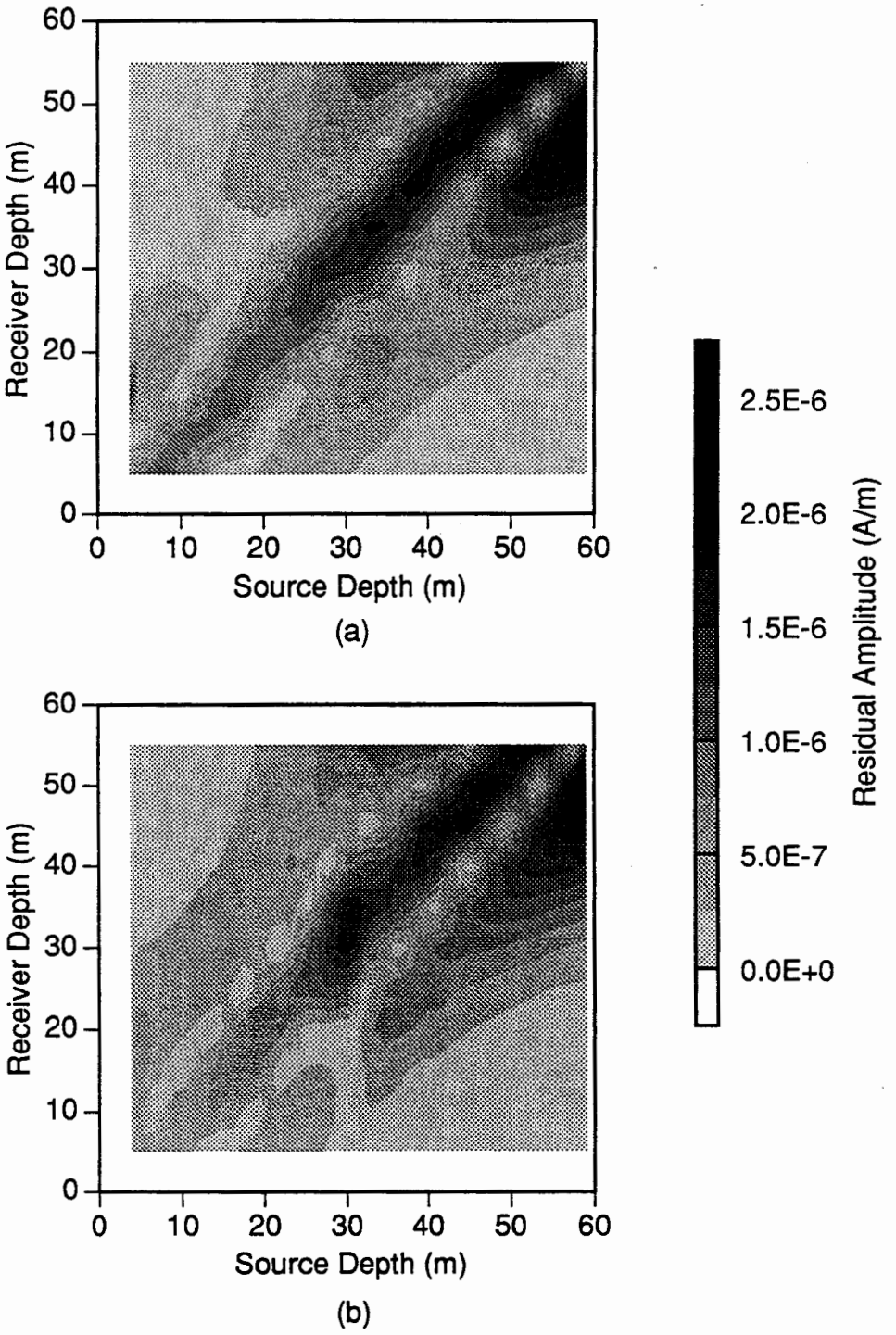

Figure 5.26 - Residual amplitude error between the Richmond cross well data collected between wells INJ1 and EMSE, and the calculated results for the images in Figure 5.25. The errors have been plotted as a function of source and receiver depth. (a) Residuals for the preinjection image given in Figure 5.25a. (b) Residuals for the postinjection image given in Figure 5.25b.

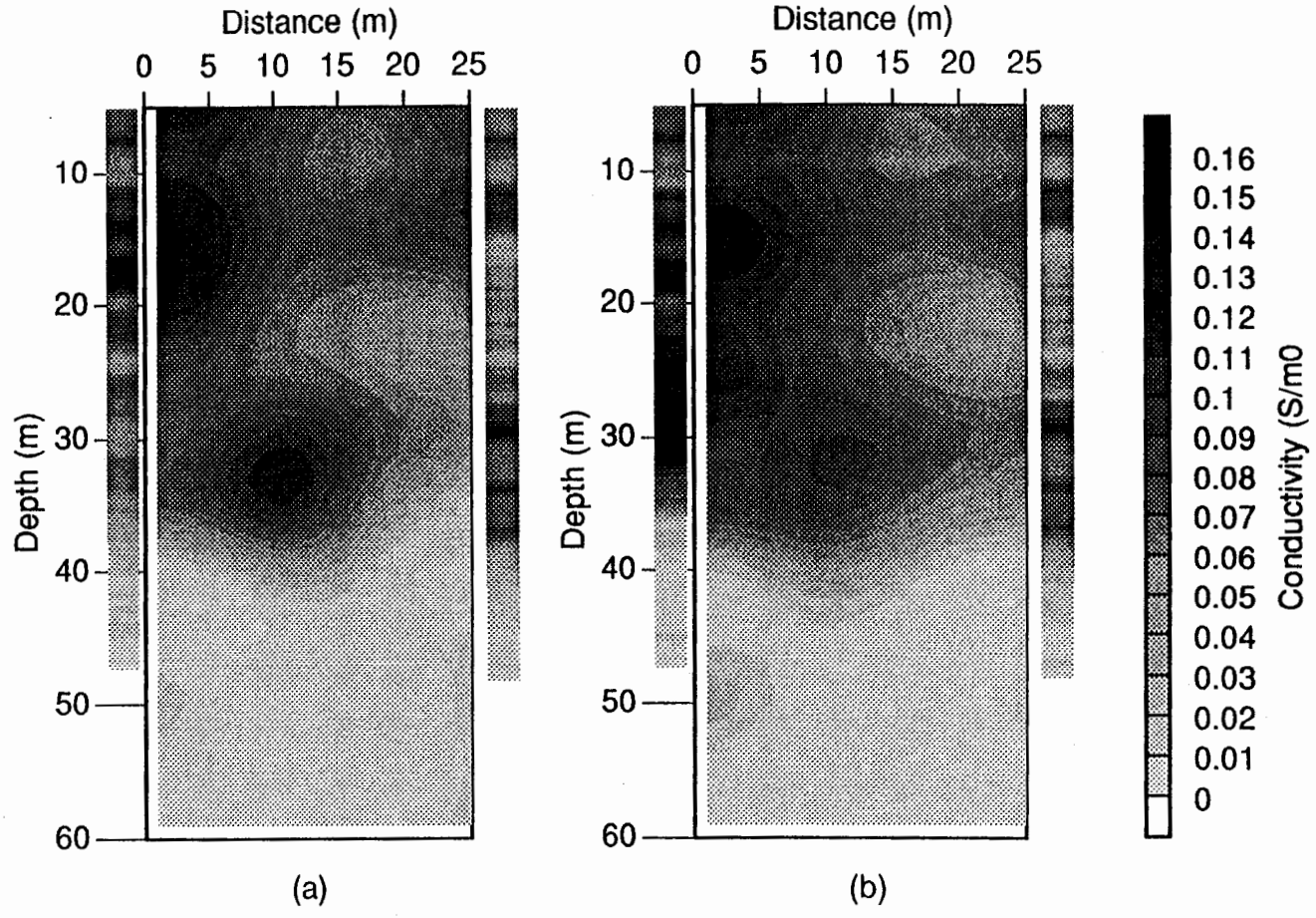

Figure 5.27- Images of the Richmond cross well data collected between INJ1 and EMSW plotted with the conductivity well logs. The left hand axis (x=0m) represents well INJ1 while the right hand axis (x=20) represents well EMSW. (a) Images of the preinjection data and well logs. Mean residual error after 10 iterations=9.39e-8 A/m. (b) Images of the post injection data and well logs. Mean residual error after 10 iterations=8.61e-8 A/m.

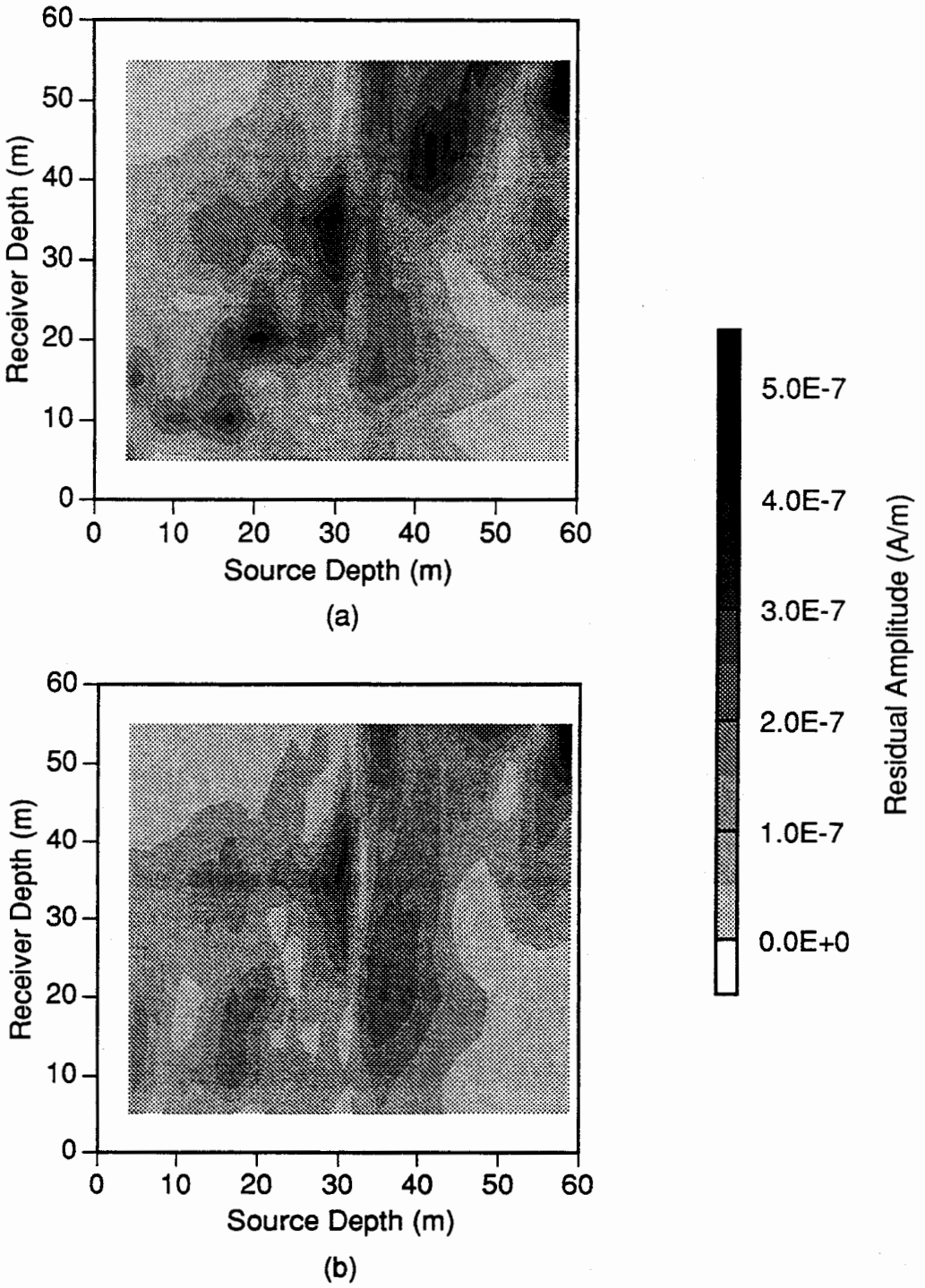

Figure 5.28 - Residual amplitude error between the Richmond cross well data collected between wells INJ1 and EMSW, and the calculated results for the images in Figure 5.27. The errors have been plotted as a function of source and receiver depth. (a) Residuals for the preinjection image given in Figure 5.27a. (b) Residuals for the postinjection image given in Figure 5.27b.

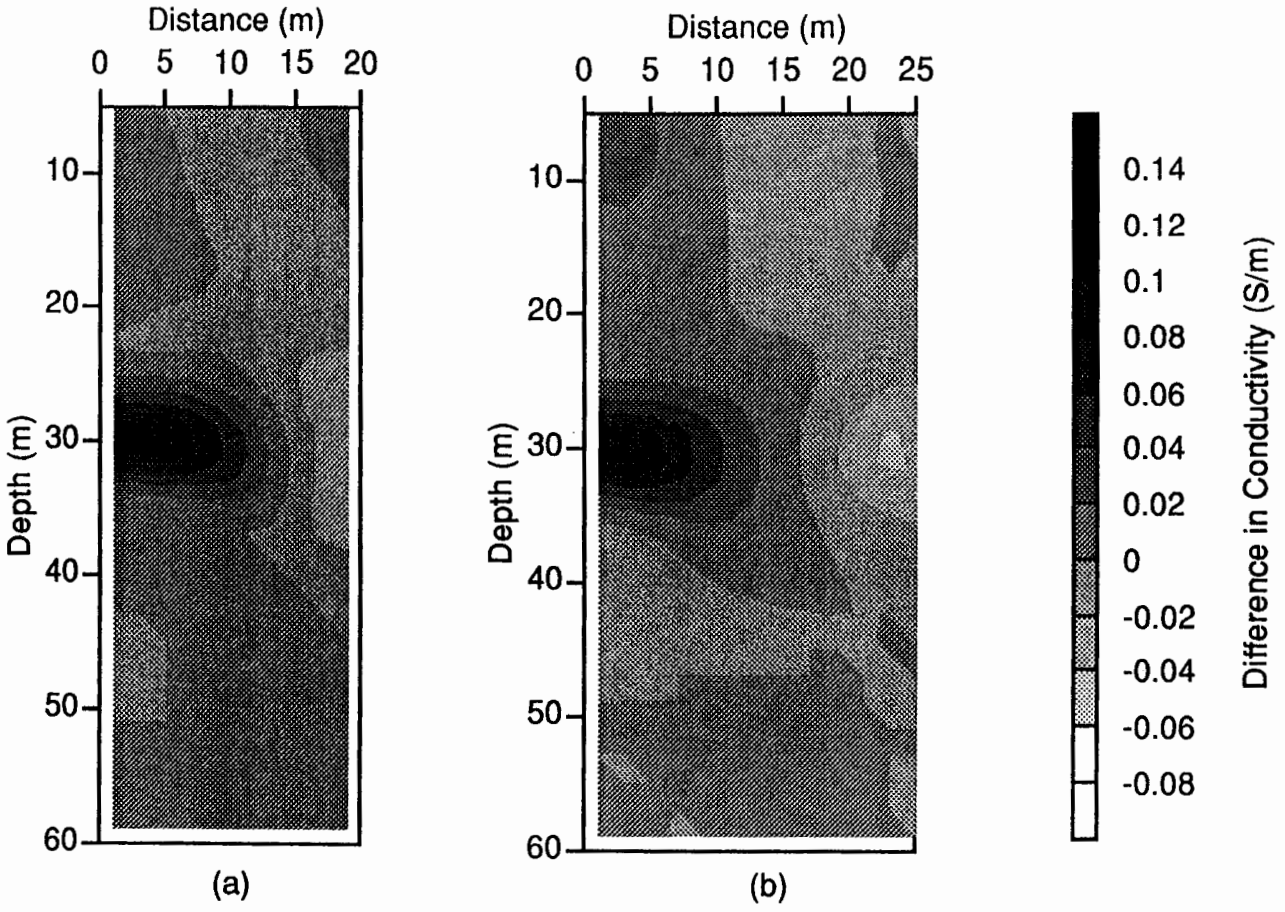

Figure 5.29 - Difference in conductivity between the post- and pre-injection images of the cross well data collected at the Richmond Field station. (a) Changes in the images of data collected between wells INJ1and EMNW. (b) Changes in the images of data collected between wells INJ1and EMNE. (c) Continued on next page.

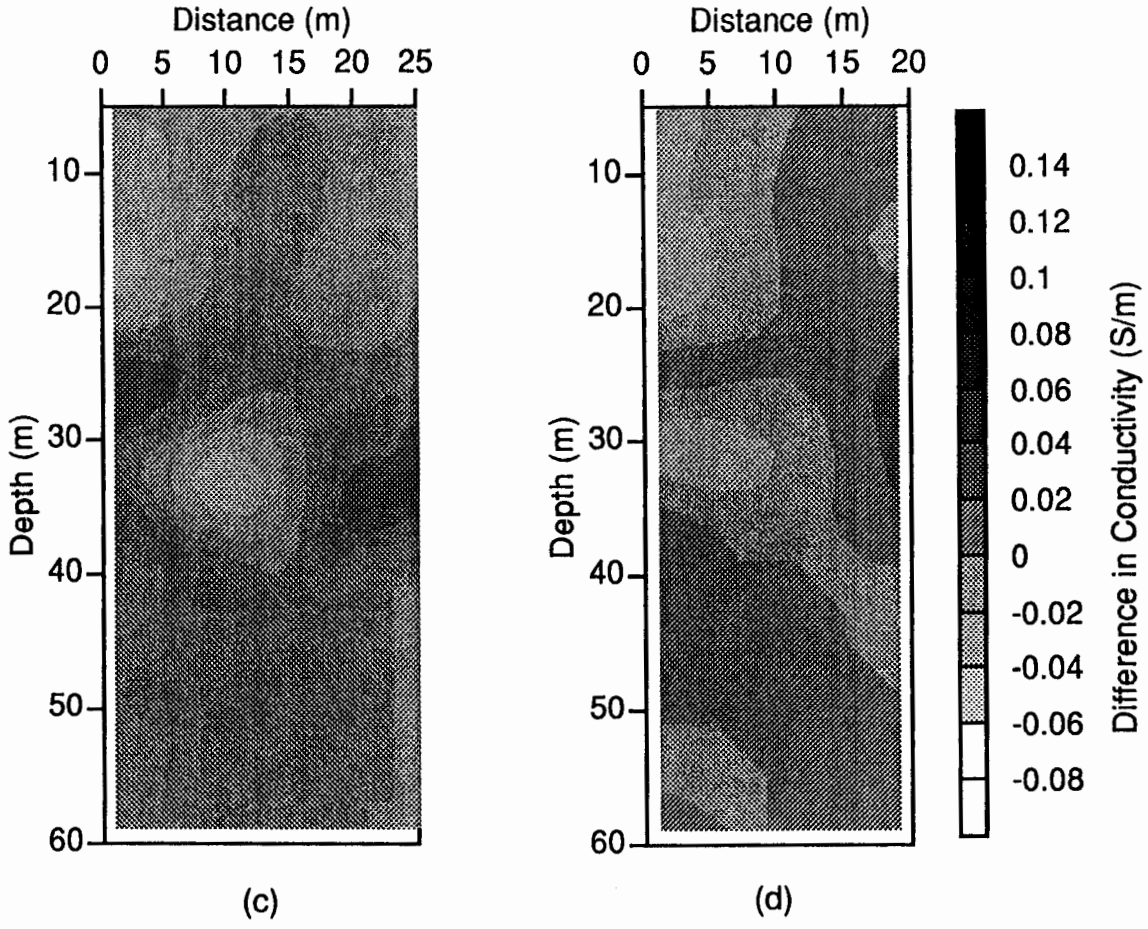

Figure 5.29 (Continued from previous page) - (c) Changes in the images of data collected between wells INJ1 and EMSW. (d) Changes in the images of data collected between wells INJ1and EMSE.

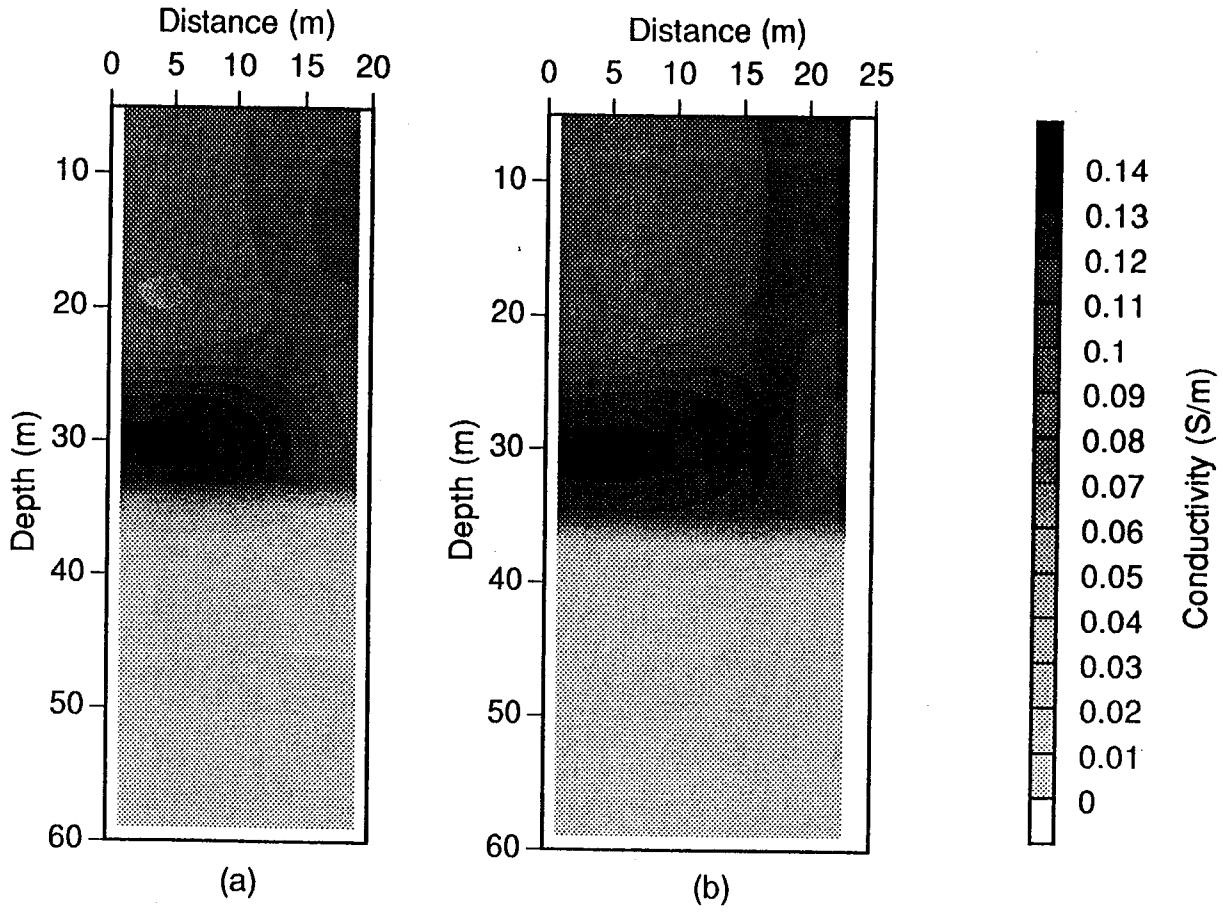

Figure 5.30 - Images of the scattered magnetic field data collected at the Richmond Field Station. The two layer background models that were employed are given in Table 5.6. (a) Image of the data collected betwenn wells INJ1 and EMNW. Mean residual error after 5 iterations=1.44e-7 A/m. (b) Image of the data collected betwenn wells INJ1 and EMNE. Mean residual error after 5 iterations=7.13e-8 A/m. (c) Continued on next page.

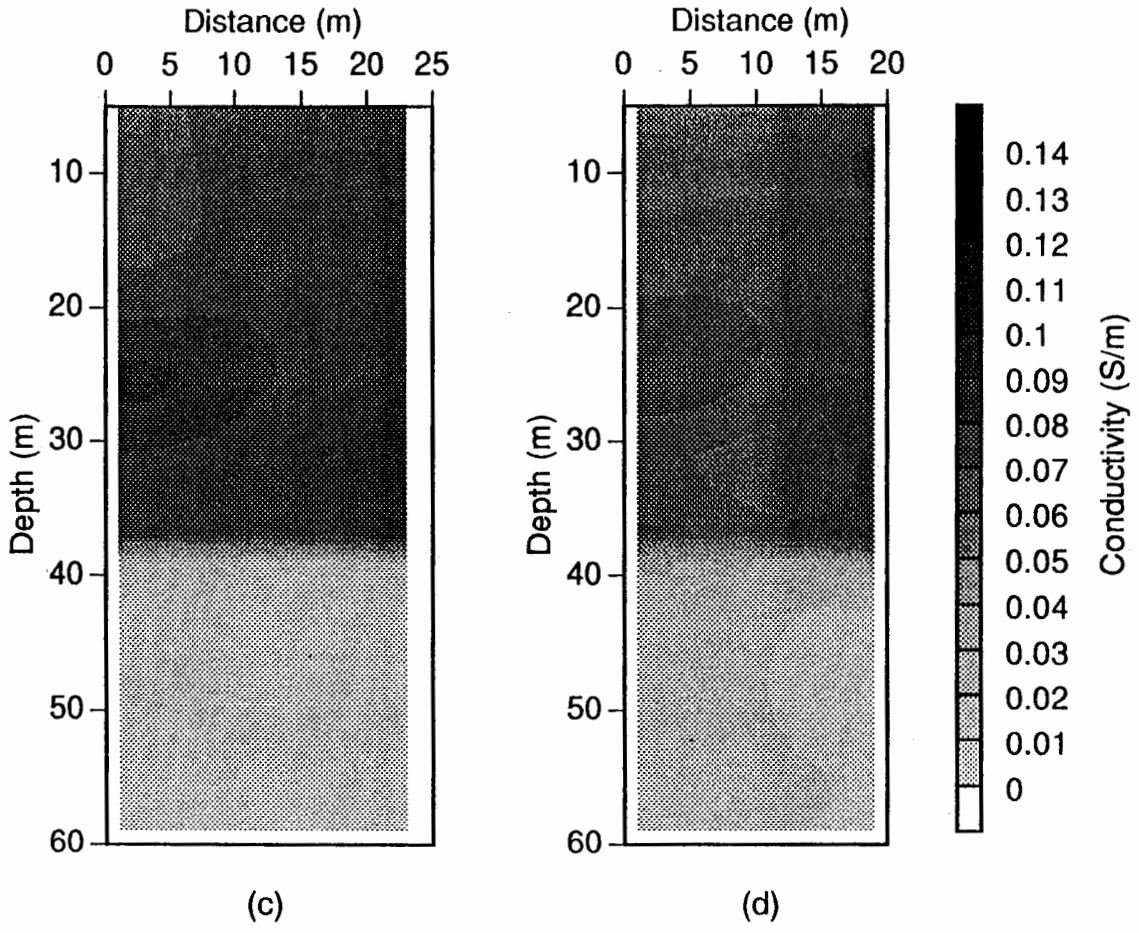

Figure 5.30 (Continued from previous page) - (c) Image of the data collected between wells INJ1 and EMSE. Mean residual error after 5 iterations=6.47e-8 A/m. (d) Image of the data collected between wells INJ1 and EMSW. Mean residual error after 5 iterations=1.38e-7 A/m.

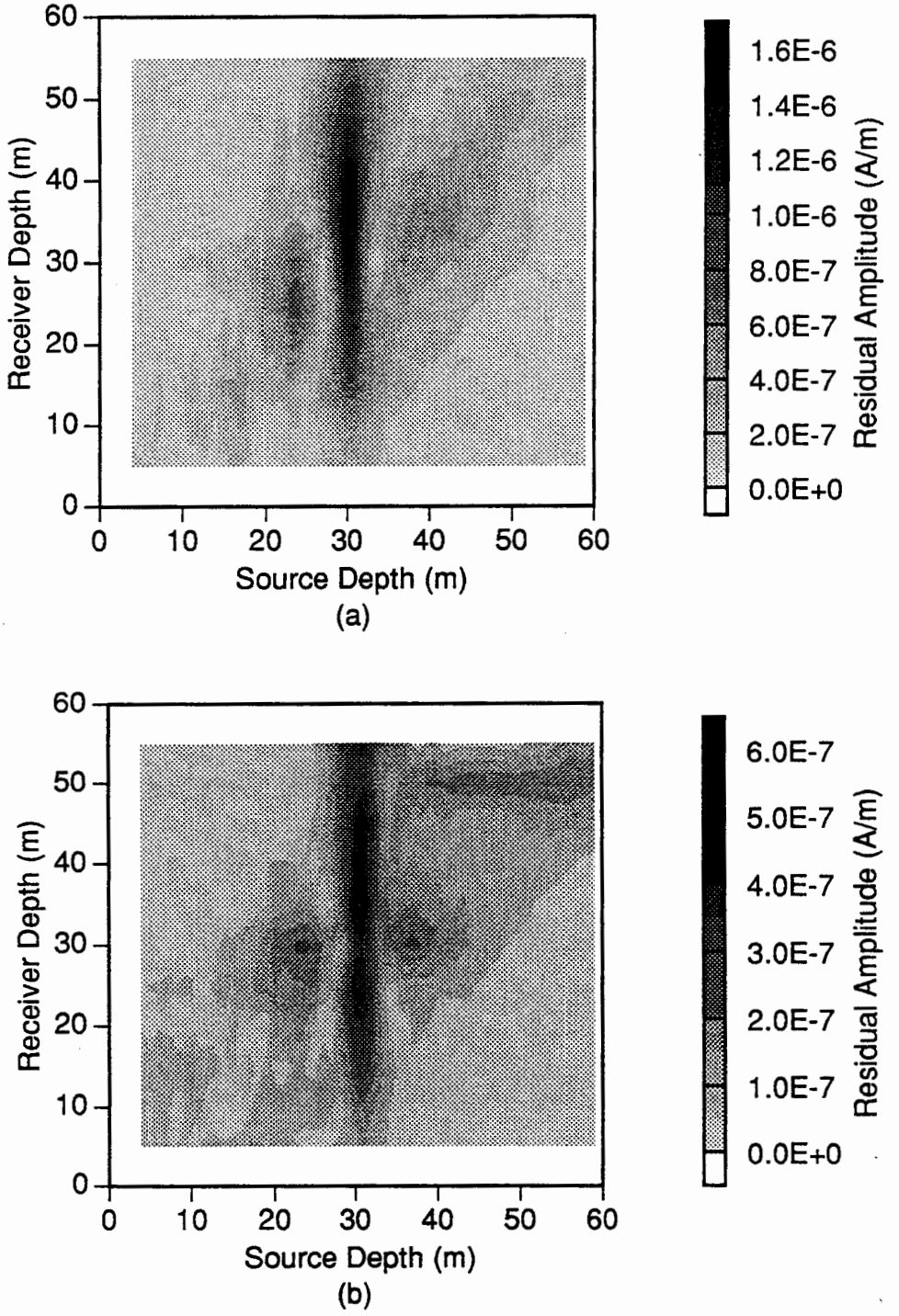

Figure 5.31 - Residual amplitude error between the scattered magnetic field data measured in the Richmond cross well experiment and the calculated results for the images in Figure 5.30. The errors have been plotted as a function of source and receiver depth. (a) Residuals for the image given in Figure 5.30a of data collected between INJ1 and EMNW. (b) Residuals for the image given in Figure 5.30b of data collected between INJ1 and EMNE. (c) Continued on next page.

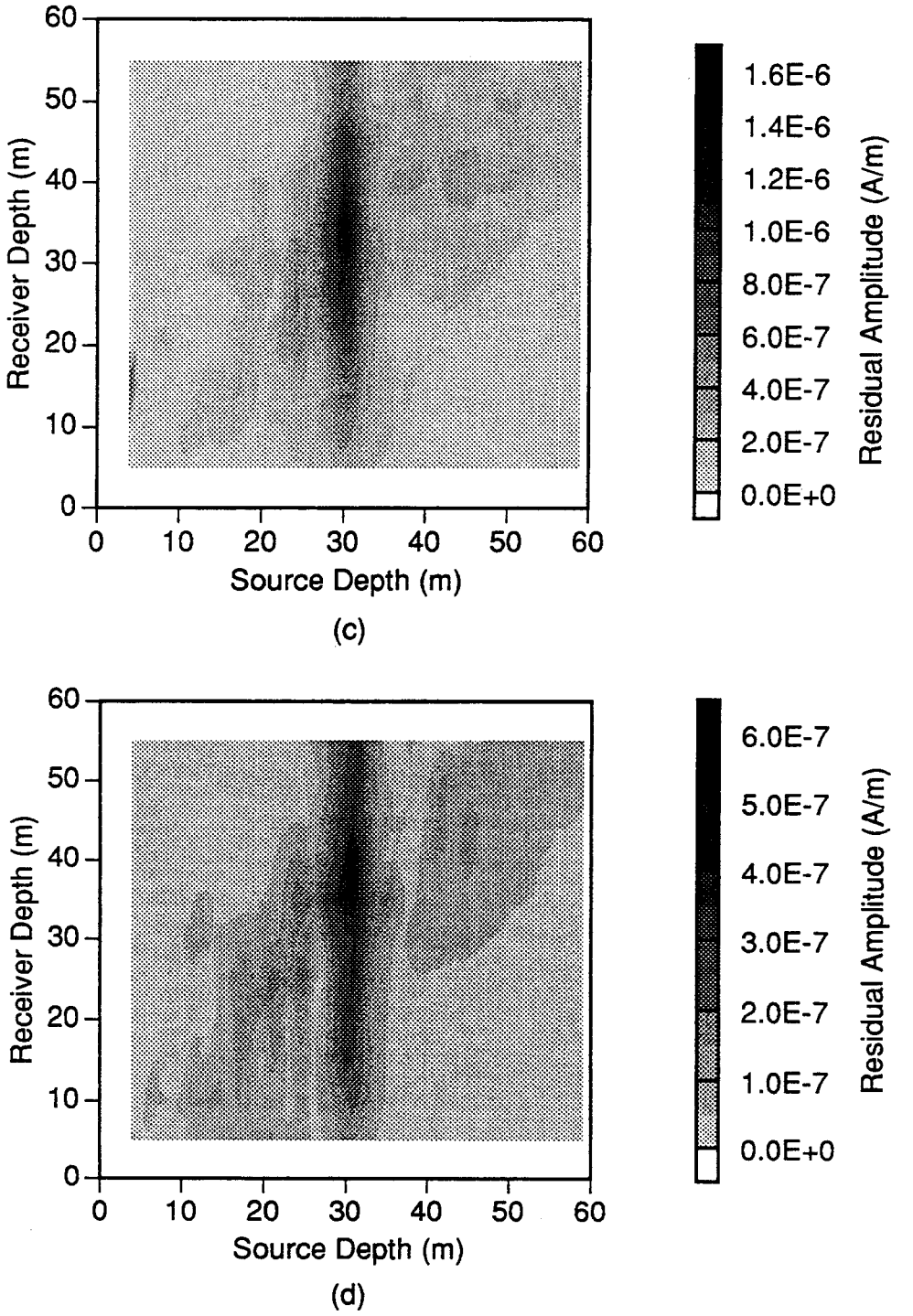

Figure 5.31 (Continued from previous page) - (c) Residuals for the image given in Figure 5.30c of data collected between INJ1 and EMSE. (d) Residuals for the image given in Figure 5.30dof data collected between INJ1 and EMSW.

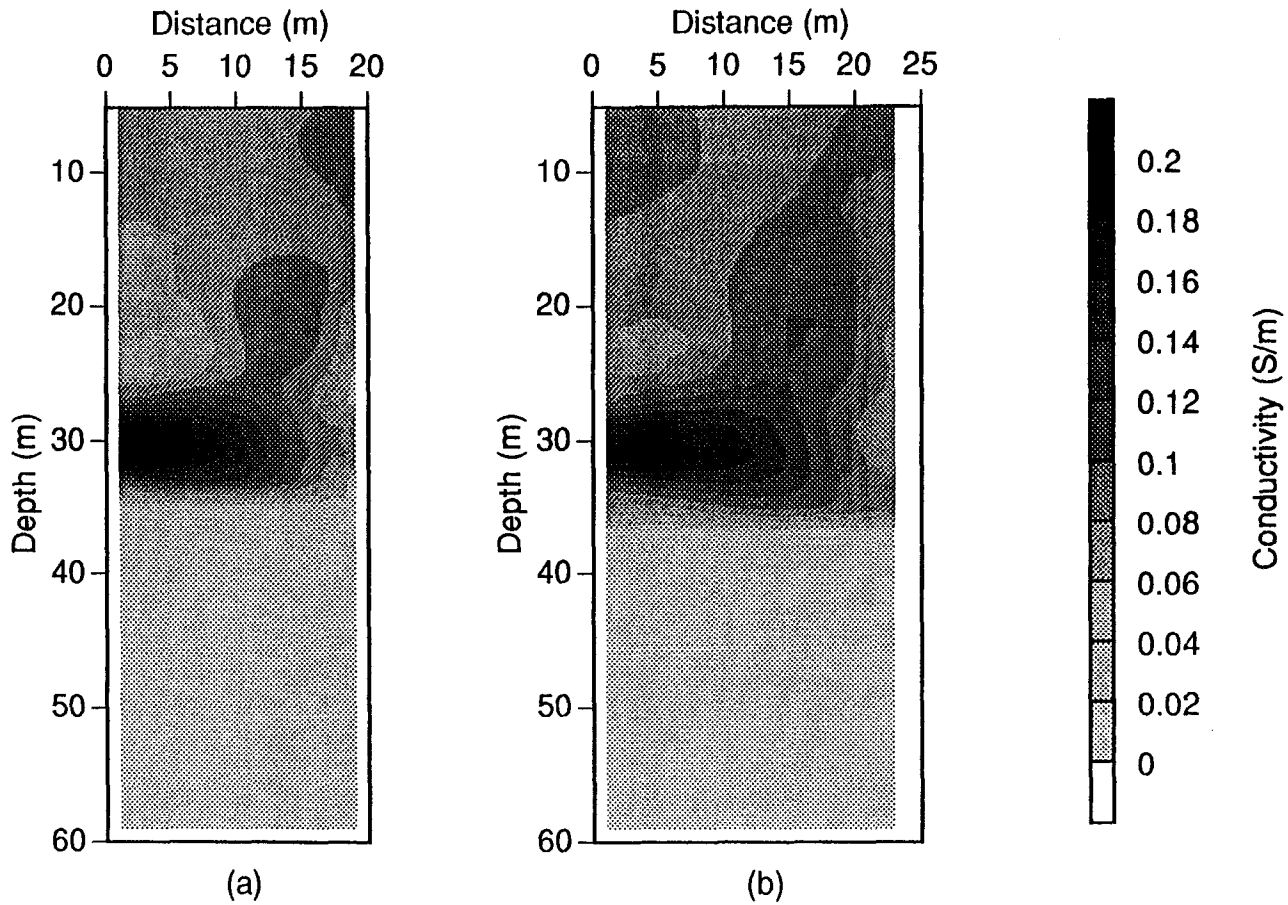

Figure 5.32 - Images of the scattered magnetic field data collected at the Richmond Field Station. The two layer background models that were employed are given in Table 5.6. (a) Image of the data collected betwenn wells INJ1 and EMNW. Mean residual error after 10 iterations=1.03e-7 A/m. (b) Image of the data collected betwenn wells INJ1 and EMNE. Mean residual error after 10 iterations=5.36e-8 A/m. (c) Continued on next page.

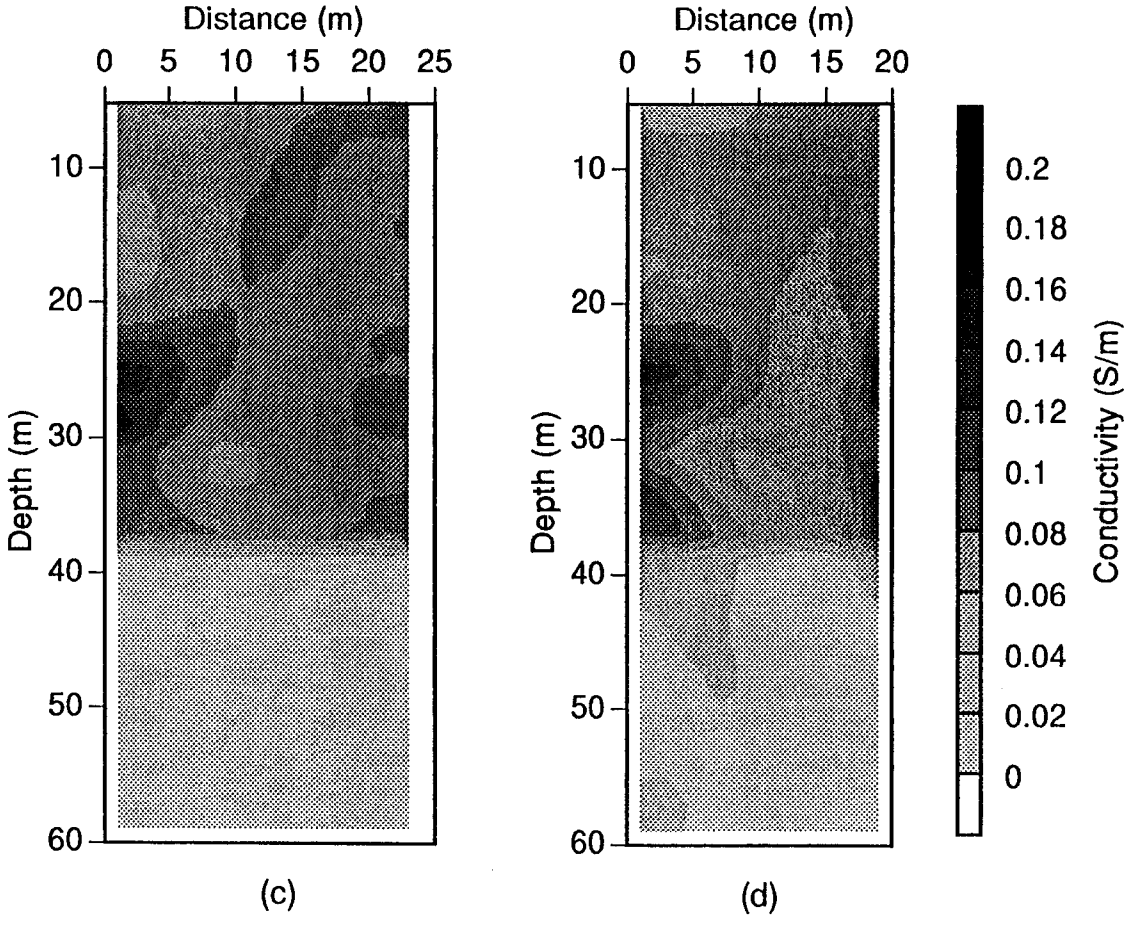

Figure 5.32 (Continued from previous page) - (c) Image of the data collected between wells INJ1 and EMSW. Mean residual error after 5 iterations=6.10e-8 (d) Image of the data collected between wells INJ1 and EMSE. Mean residual error after 5 iterations=1.26e-7.

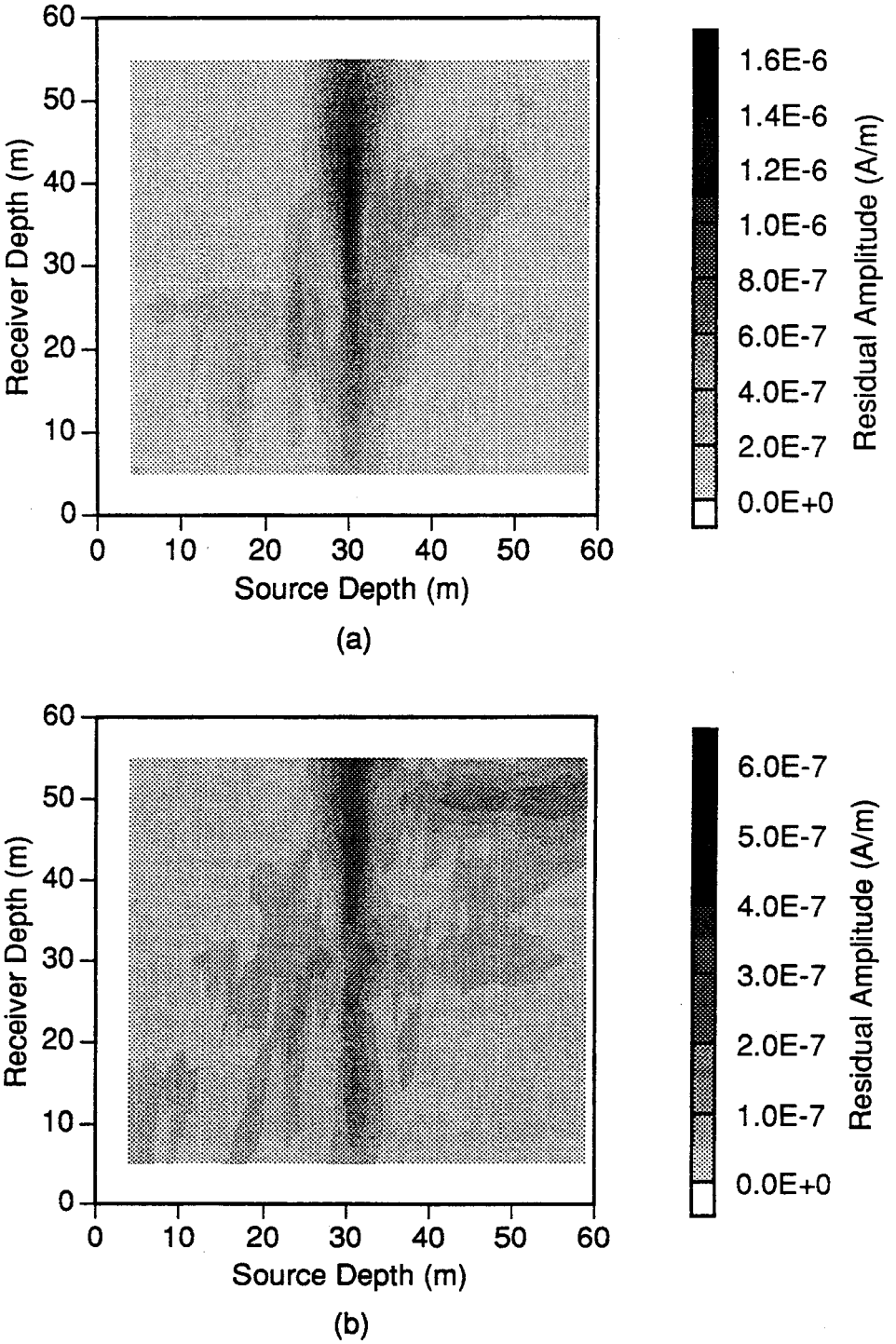

Figure 5.33 - Residual amplitude error between the scattered magnetic field data measured in the Richmond cross well experiment and the calculated results for the images in Figure 5.32. The errors have been plotted as a function of source and receiver depth. (a) Residuals for the image given in Figure 5.32a of data collected between INJ1 and EMNW. (b) Residuals for the image given in Figure 5.32b of data collected between INJ1 and EMNE. (c) Continued on next page.

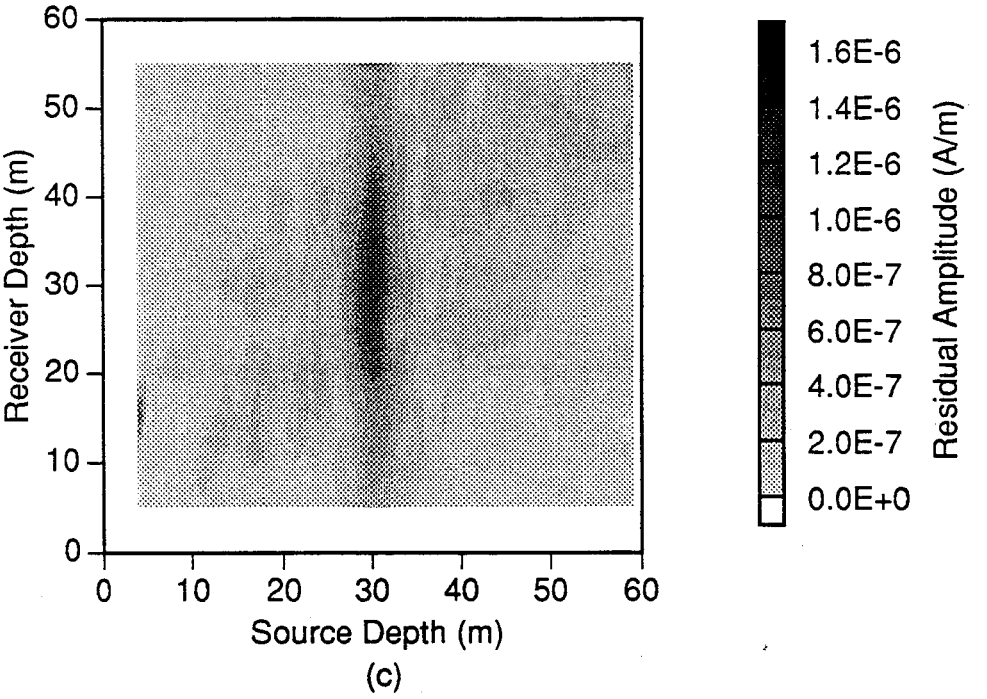

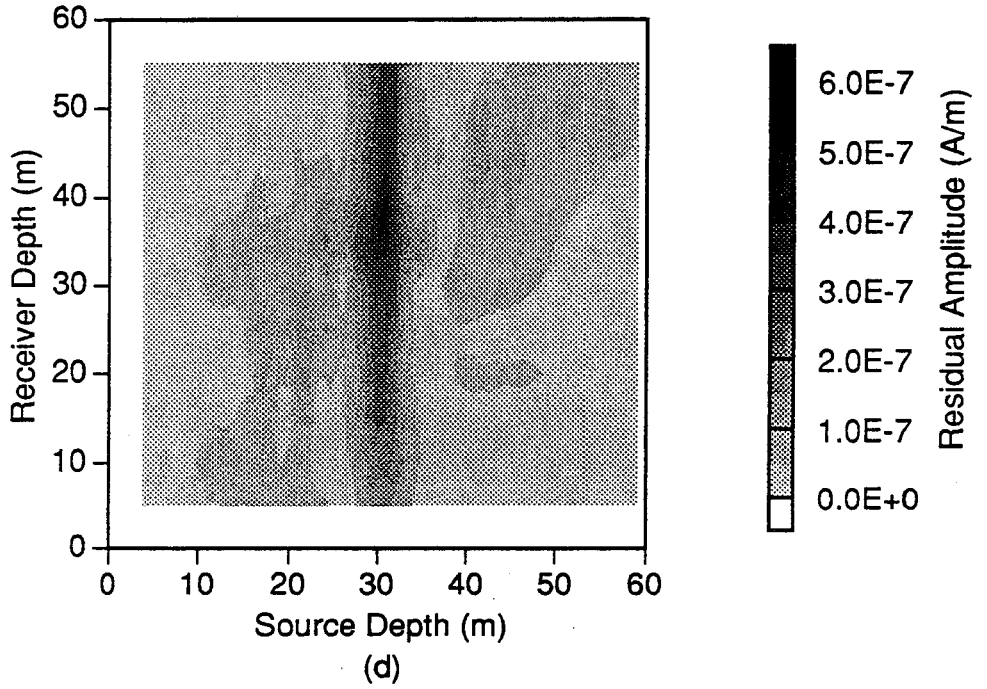

Figure 5.33 (Continued from previous page) - (c) Residuals for the image given in Figure 5.32c of data collected between INJ1 and EMSE. (d) Residuals for the image given in Figure 5.32dof data collected between INJ1 and EMSW.

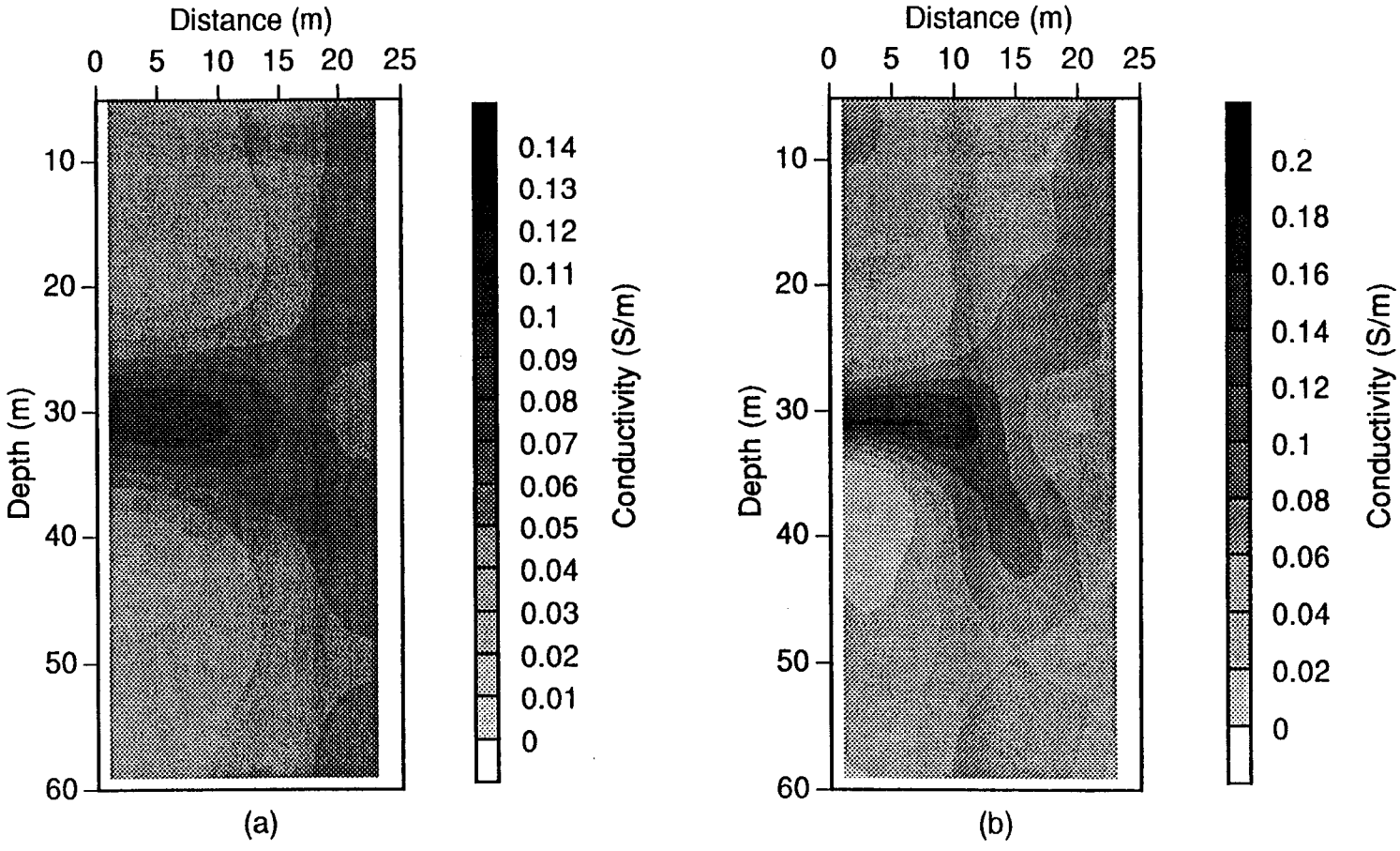

Figure 5.34 - Images of the scattered magnetic field data collected at the betwen wells INJ1 and EMNE at the Richmond Field Station. The background model is a half space with a conductivity of 0.054 S/m.(a) Image after 5 iterations. Mean residual error=7.09e-8 A/m. (b) Image after 10 iterations. Mean residual error =5.62e-8 A/m.

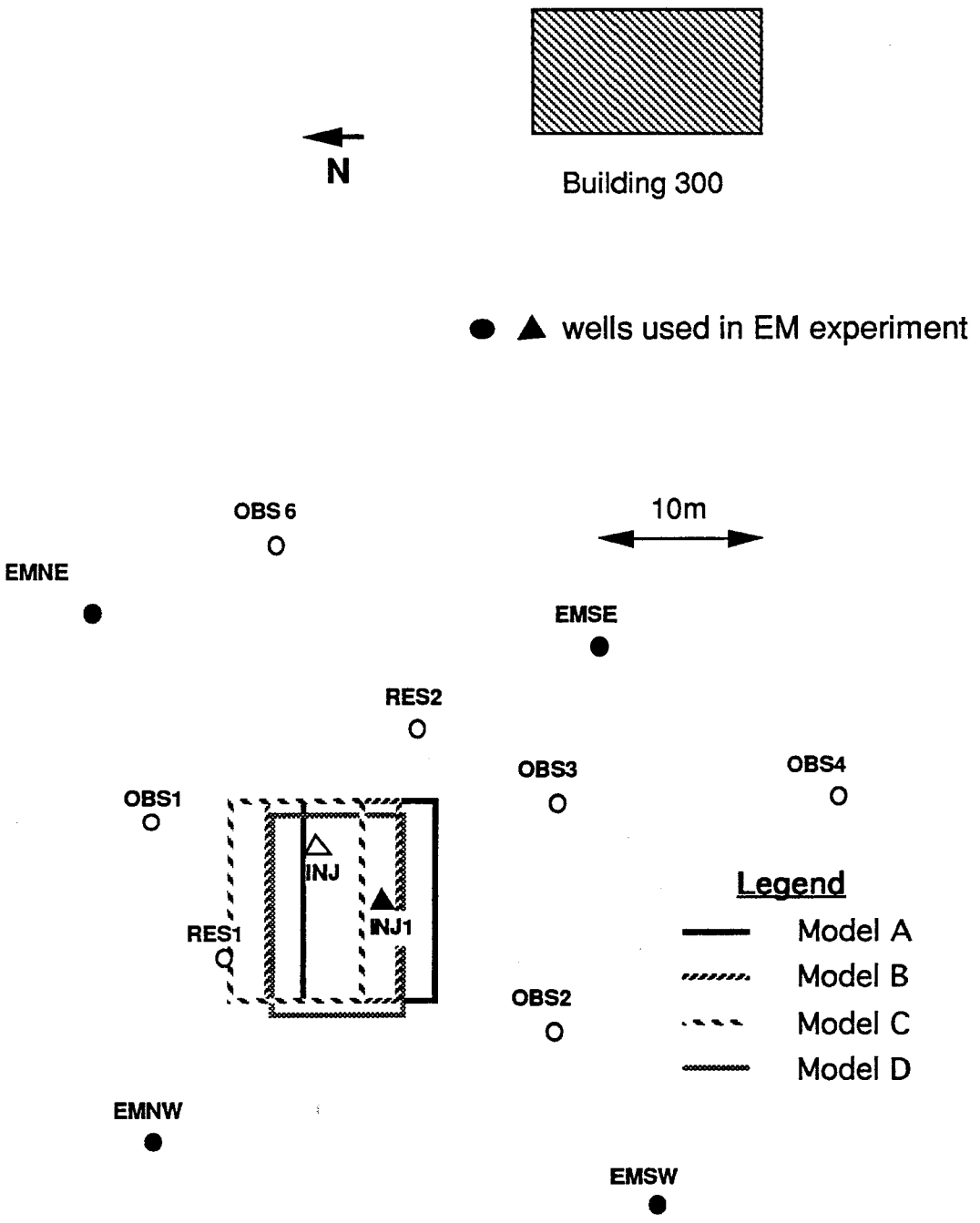

Figure 5.35 - Location map for the building 300 well field at the Richmond Field Station showing the location of the thin sheet models used to simulate the injected plume. The sheet is 12m by 8.5m,. has a conductance of 1.0S and is buried at 30m depth. Models A,B, and C represent different amounts of plume offset to the North. Model D is identical to model B except that it is offset by 1m to the west.

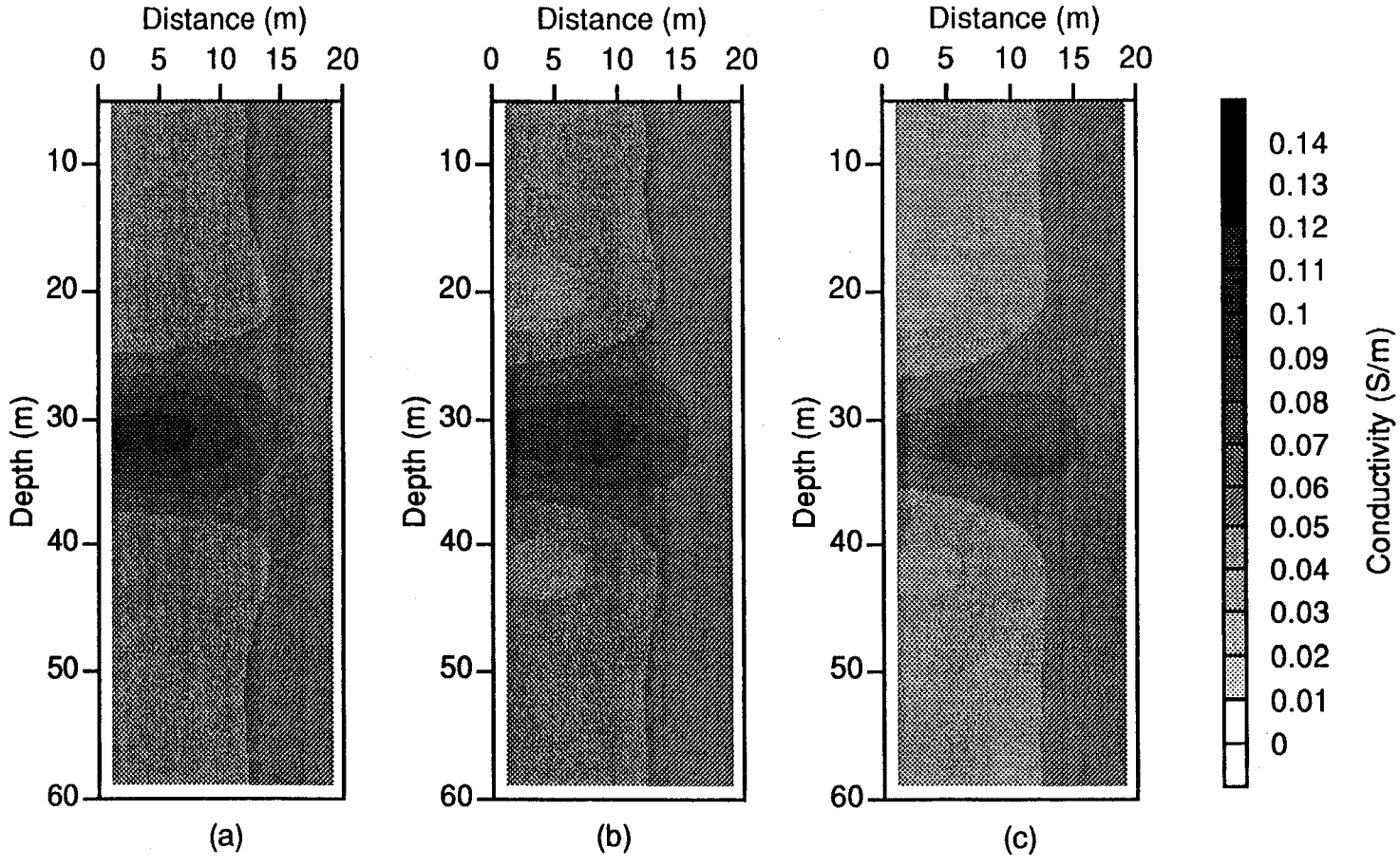

Figure 5.36 - Images of the Richmond Field Station simulation shown in Figure 5.35 for the INJ1-EMNW cross well pair. A background conductivity of 0.05 S/m was employed and the iterative Born scheme was terminated after 5 iterations. (a) Image for model A. (b) Image for model B. (c)Image for model C.

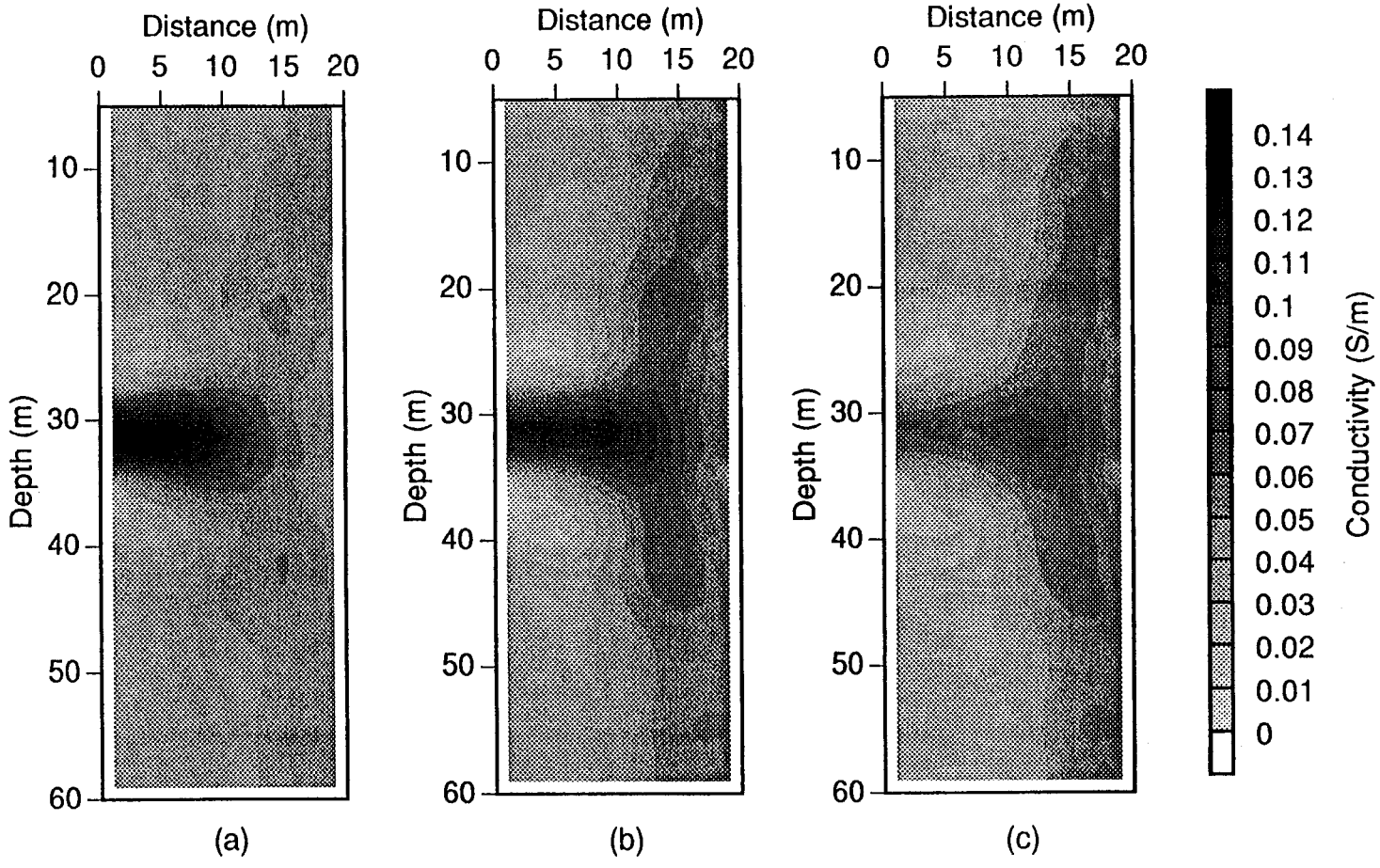

Figure 5.37 - Images of the Richmond Field Station simulation shown in Figure 5.35 for the INJ1-EMNW cross well pair. A background conductivity of 0.05 S/m was employed and the iterative Born scheme was terminated after 10 iterations. (a) Image for model A. (b) Image for model B. (c)Image for model C.

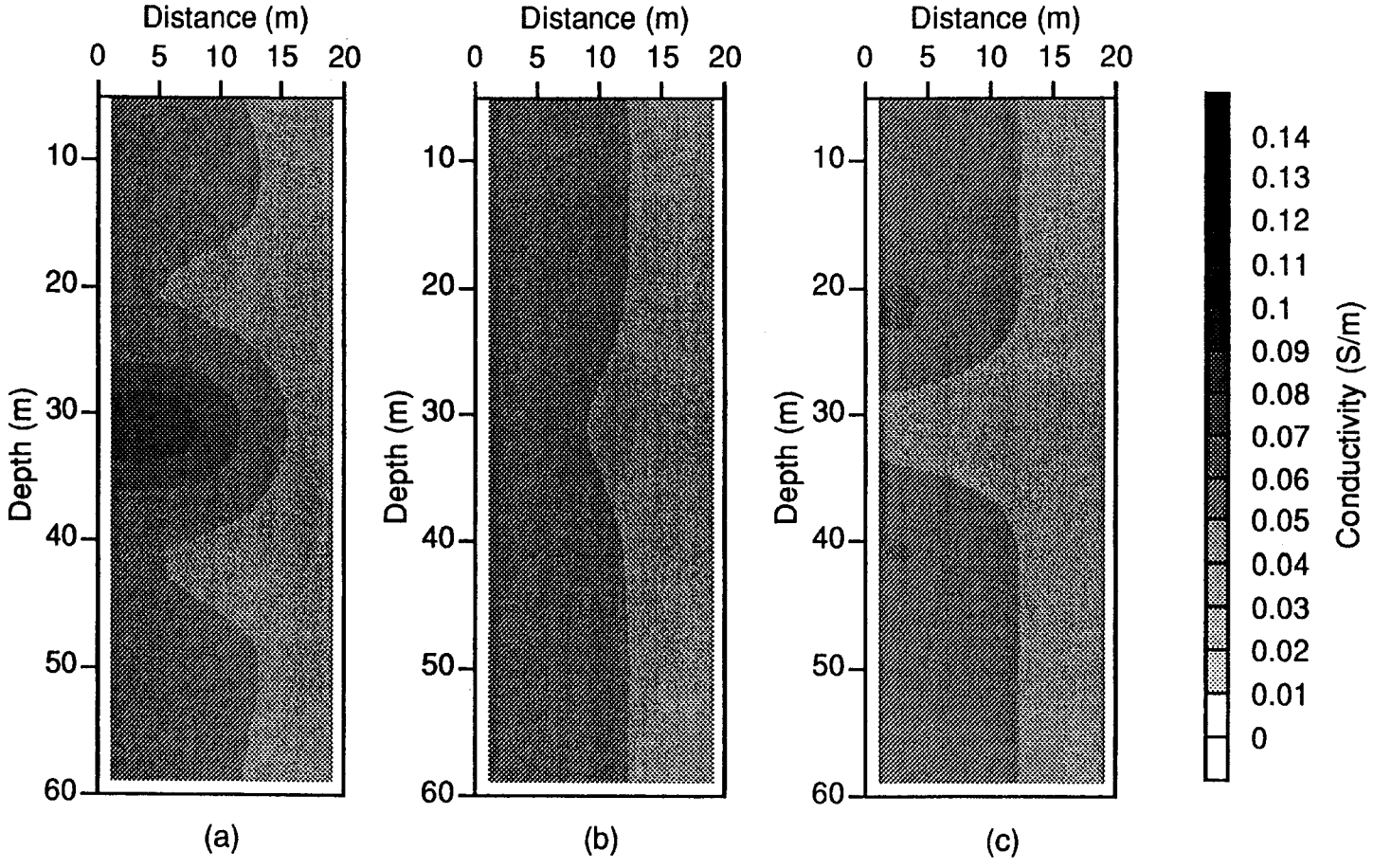

Figure 5.38 - Images of the Richmond Field Station simulation shown in Figure 5.35 for the INJ1-EMSE cross well pair. A background conductivity of 0.05 S/m was employed and the iterative Born scheme was terminated after 5 iterations. (a) Image for model A. (b) Image for model B. (c)Image for model C.

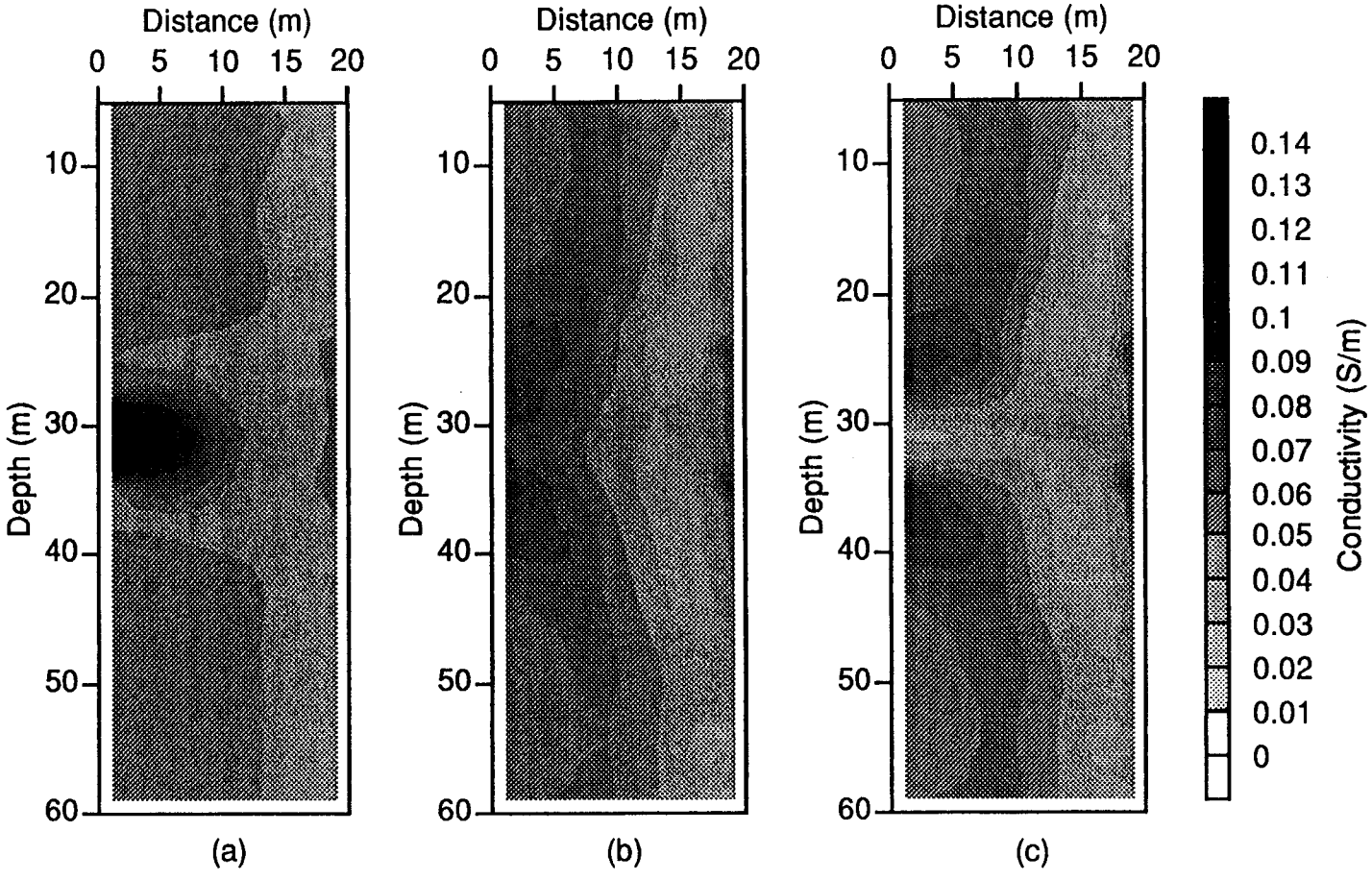

Figure 5.39- Images of the Richmond Field Station simulation shown in Figure 5.35 for the INJ1-EMSE cross well pair. A background conductivity of 0.05 S/m was employed and the iterative Born scheme was terminated after 10 iterations. (a) Image for model A. (b) Image for model B. (c)Image for model C.

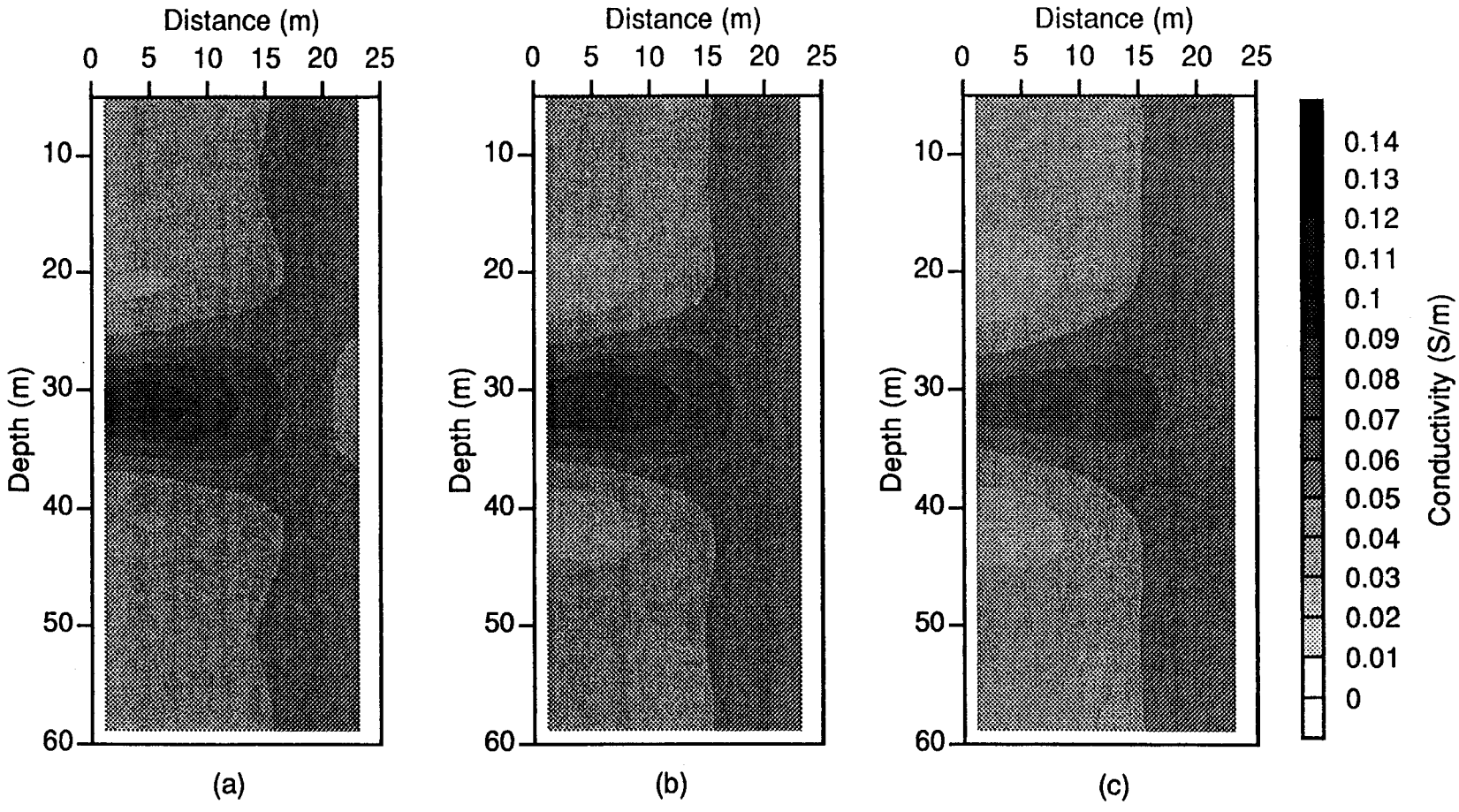

Figure 5.40 - Images of the Richmond Field Station simulation shown in FIgure 5.35 for the INJ1-EMNE cross well pair. A background conductivity of 0.05 S/m was employed and the iterative Born scheme was terminated after 5 iterations. (a) Image for model A. (b) Image for model B. (c)Image for model C.

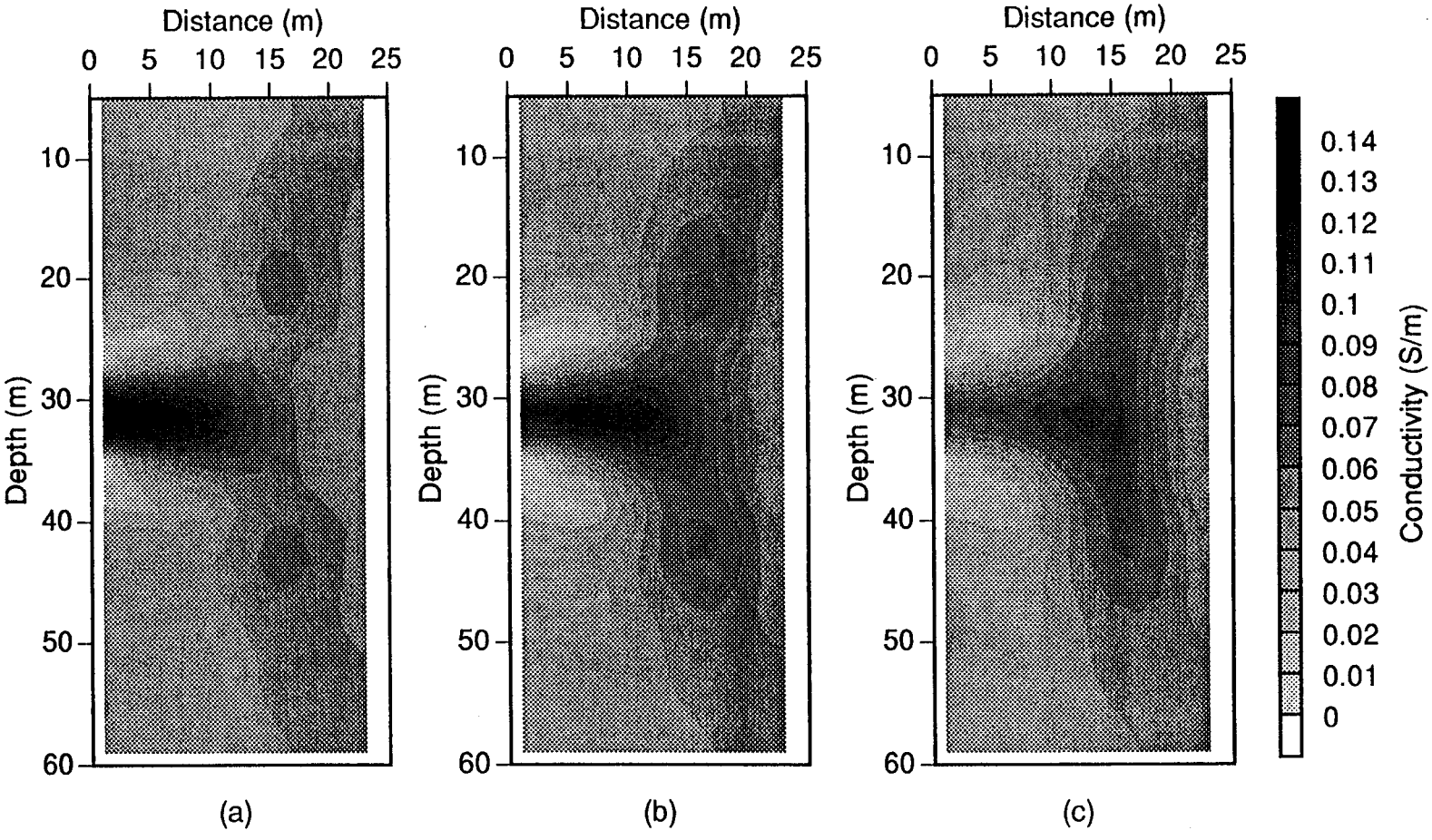

Figure 5.41 - Images of the Richmond Field Station simulation shown in FIgure 5.35 for the INJ1-EMNE cross well pair. A background conductivity of 0.05 S/m was employed and the iterative Born scheme was terminated after 10 iterations. (a) Image for model A. (b) Image for model B. (c)Image for model C.

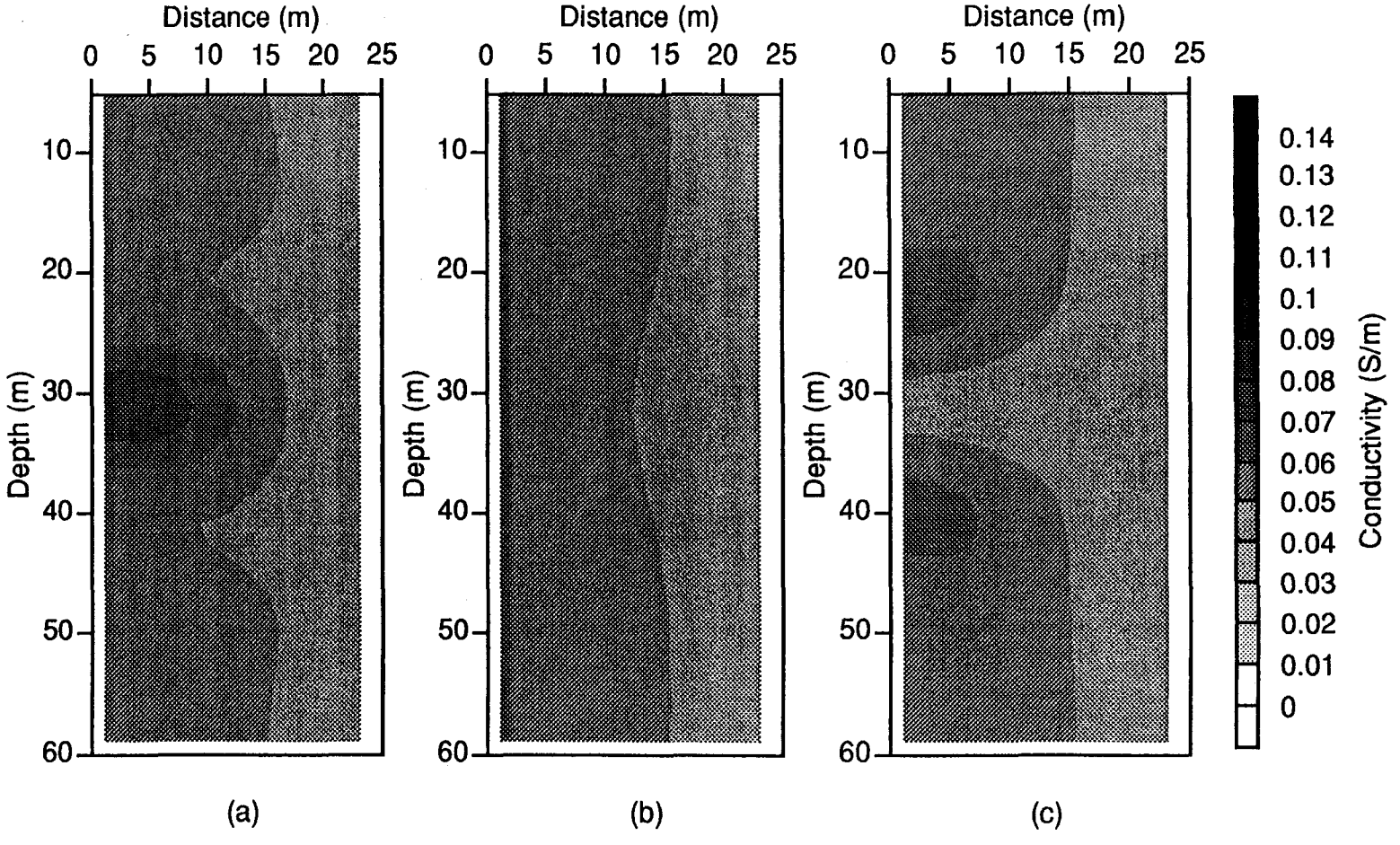

Figure 5.42 - Images of the Richmond Field Station simulation shown in Figure 5.35 for the INJ1-EMSW cross well pair. A background conductivity of 0.05 S/m was employed and the iterative Born scheme was terminated after 5 iterations. (a) Image for model A. (b) Image for model B. (c)Image for model C.

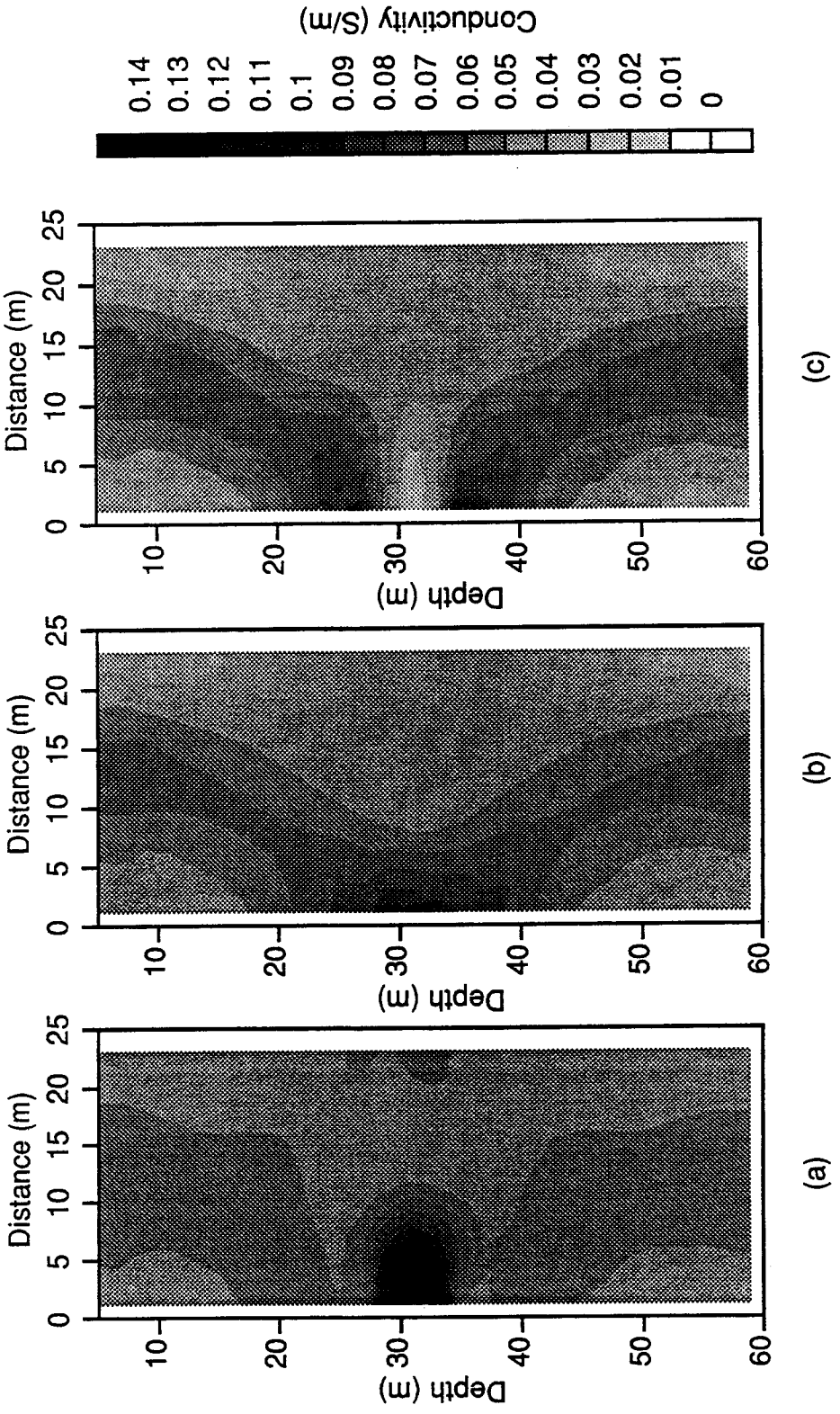

Figure 5.43 - Images of the Richmond Field Station simulation shown in Figure 5.35 for the INJ1-EMSW cross well pair. A background conductivity of 0.05 S/m was employed and the iterative Born scheme was terminated after 10 iterations. (a) Image for model A. (b) Image for model B. (c)Image for model C.

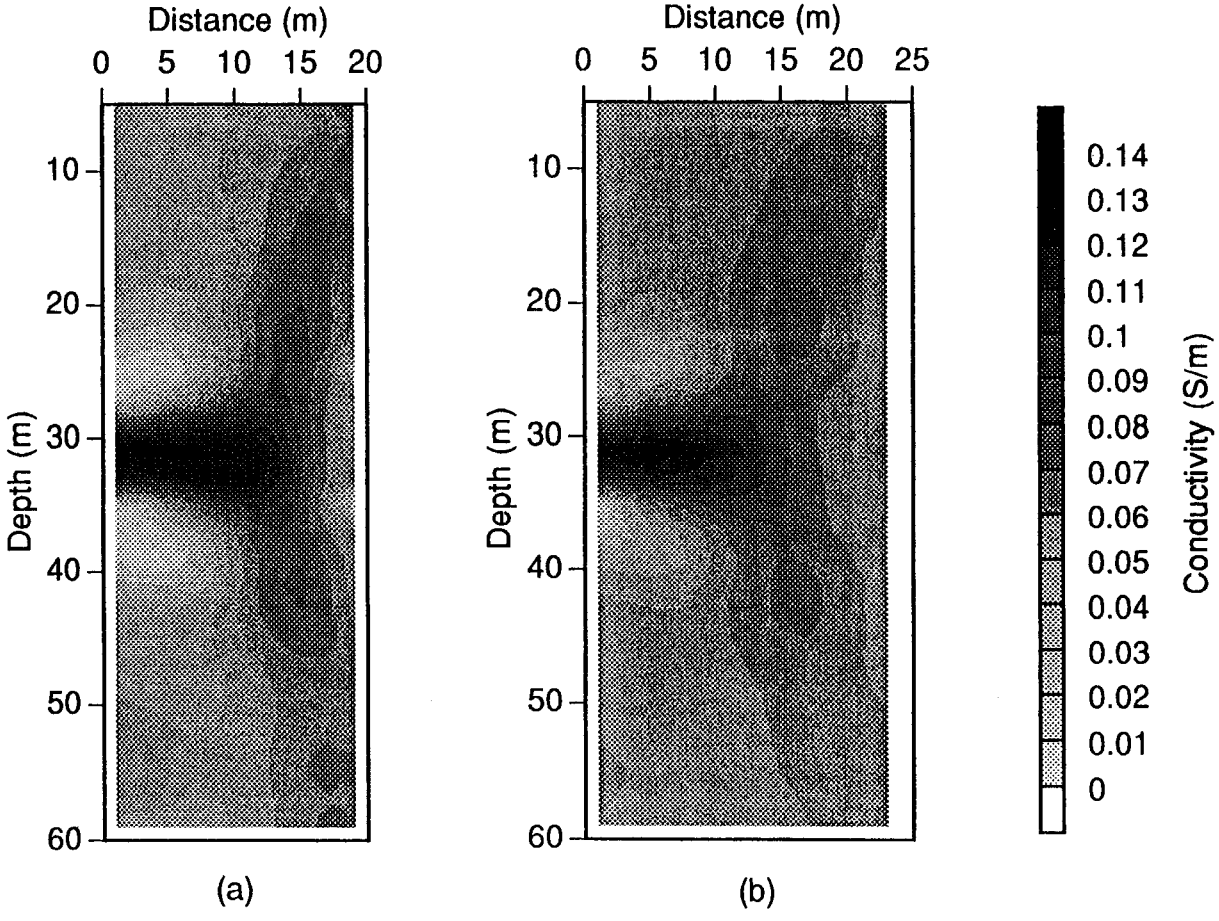

Figure 5.44 - Images of the model D Richmond Field Station simulation shown in Figure 5.35 for the INJ1-EMNW and INJ1-EMNE cross well pairs. A background conductivity of 0.05 S/m was employed and the iterative Born scheme was terminated after 10 iterations. (a) Image for the INJ1-EMNW simulation. (b) mage for the INJ1-EMNE simulation.

Chapter 6
Discussion and Recommendations for Future Research

6.1 Discussion

The use of cross well electromagnetic (EM) probes to image the conductivity structure of the subsurface has been investigated for frequencies less than 1 MHz. This analysis is based on nonlinear integral equations which govern the electromagnetic fields generated by inhomogeneities imbedded in an otherwise homogenous earth. A sinusoidally oscillating, vertically oriented magnetic dipole is employed as a source, and it is assumed that the scattering bodies are azimuthally symmetric about the source dipole axis (Figure 2.1). The use of this model geometry reduces the 3-D vector problem to a more manageable 2-D scalar form.

To further simplify the theoretical formulation, the first order Born approximation which is the first term in the Born series, has been applied to linearize the integral equations. The resulting approximate equations are extremely useful in analyzing different aspects of cross well EM imaging. The kernel of the linearized equations can be employed to study the sensitivity of various source-receiver configurations and operating frequencies to the conductivity structure between and around the boreholes. Fast forward modeling schemes can be developed using the first order Born approximation and/or the more accurate Born series approximation. In addition the linearized equations can be used as a first step in an iterative, nonlinear inversion technique to image the conductivity structure between the boreholes.

The sensitivity analysis has shown that certain characteristics of the cross well EM problem are dependent only upon the configuration of the source-receiver array that is employed (Figures 2.7 through 2.9). Moving both the source and receiver at the same rate downward in the wells such that the tools are always at the same depth results in good vertical resolution but poor horizontal resolution. In order to increase the resolution in the radial direction, various vertical separations or *offsets* between the source and receiver must be employed. Additional horizontal resolution can be obtained by making measurements with both the source and receiver in the same hole (Figure 2.18).

These are the only general characteristics of cross well EM imaging that are independent of the operating frequency and the properties of the medium. However, because of the diffusive nature of the fields in the frequency range that we are working, the majority of the remaining analysis can be accomplished in terms of two dimensionless parameters. The first is the background induction number of the medium which is given as $\sigma\omega\mu l^2$ where σ is the background conductivity, ω is the frequency of operation, μ is

the magnetic permeability of free space and l is the source-receiver separation. Developing the sensitivity analysis in terms of this parameter allows for experimental design and optimization with only a minimal amount of a prior information. For example, if the borehole separation is known and an estimate of the background conductivity is available, the appropriate frequency can be predicted to operate the system such that it is optimal for imaging purposes.

The second dimensionless parameter has been termed the anomalous induction number of the scattering body which is defined as $\Delta\sigma\omega\mu S$ where $\Delta\sigma$ is the conductivity contrast between the background and the body, S is the cross sectional area of the scattering body, and the other terms are defined as above. This parameter is useful in defining the limits of the approximate forward modeling scheme. The first order Born scheme has been found to be accurate for anomalous induction numbers less than 0.02 while the Born series converges for $\Delta\sigma\omega\mu S$ less than 2.0.

For low background induction numbers($\sigma\omega\mu l^2 < 10$), the sensitivity analysis indicates that the secondary fields are small in magnitude when compared to the primary field (Figure 2.3). Because of this, the scattered fields generated by an inhomogeneity will be difficult to measure unless the dimensions of the scattering body are large. The problem is further complicated by the high sensitivity of a given source-receiver pair to regions outside the interwell zone (Figures 2.7 and 2.11). This phenomenon makes data analysis difficult for two reasons. First, the region being considered as a possible source for the anomalous fields must not only include the interwell zone but also a large volume surrounding the wells. The second factor involves the geometry of the inhomogenous region. As demonstrated in Tables 3.7 and 3.8, models with a 2-D cylindrical symmetry, 2 1/2D models and 3-D models yield drastically different results even though their cross-sectional area in the plane containing the wells is identical. Thus even though both the first order Born and Born series approximate modeling schemes work extremely well for these low induction numbers, the proper model geometry must be chosen to even crudely interpret the data.

When combined the low induction number phenomena described above result in low resolution images. For example Figures 4.3b and 4.4b show that not only is the spatial resolution poor but the conductivity is not accurately recovered. In addition if the data are generated by a body which does not obey the cylindrical geometry, artifacts can result in the images which may lead to misinterpretation. The resolution can be improved somewhat if the fields are measured very accurately, and if the horizontal rather than vertical field component of the field is employed (Figure 2.14).

At background induction numbers greater than 50, the problems described above are

dramatically reduced. A given source-receiver pair detects only a "ray path" like region located immediately between the probes and the sensors are much less sensitive to the third dimension outside of the image plane (Figure 2.9). Thus the fields that are generated by an inhomogeneity between the wells will be independent of whether the body exhibits a 2-D cylindrical, a 2 1/2-D, or a 3-D geometry. In addition, the scattered fields are on the same order of magnitude as the primary fields which allows the signals of interest to be more easily detected in the presence of noise (Figure 2.3). When all of these factors combined result in excellent image resolution of the region between the wells (Figures 4.3d and 4.4d).

There are however two major drawbacks at the large induction numbers that limit the usefulness of the imaging scheme developed in this thesis. The first drawback is attenuation at high frequencies. Because the EM fields are attenuated much quicker at high induction numbers than at low induction numbers, the long vertical offset data needed for the horizontal resolution is not measurable within the dynamic range of any system that has been designed to date. The second major factor is that the Born series solution fails easily at these large induction numbers and thus can not be employed for quick forward modeling within the inversion scheme (Figure 3.10).

Between the background induction numbers values of 10 to 50 lies a region in which the problems that are present at lower and higher values are minimized. Not only are the scattered fields within an order of magnitude of the primary fields, but the rate of attenuation is still low enough so that the large vertical offset data are measurable(Figure 2.3). Although the sensitivity functions in this range lack the "ray path" quality that is apparent at higher induction numbers, the sensitivity of a given source-receiver pair is far more focused between the wells than at lower induction numbers (Figure 2.8). The Born series converges rather quickly in this range of induction numbers and thus provides for quick forward modeling. All of these factors result in excellent image resolution in the presence of noise (Figures 4.3c and 4.4c), and thus this seems to be the optimal region in which to employ the iterative Born imaging scheme. The only notable exception to this rule of thumb occurs when the medium is three dimensional in which case the imaging scheme fails to accurately recover the structure because of the appearance artifacts (Figures 4.38 and 4.40).

The use of cross well EM to map the conductivity structure between two wells was verified with two field experiments. The analysis of the data collected at the Devine, Texas geophysical test site showed that the method recovers the general geologic structure (Figure 4.21). In this particular case it was demonstrated that the resulting image reproduces a low pass filtered version of the conductivity well log. Unfortunately

it was also demonstrated that a drift error is present in this data which was not removed in the initial data processing.

The data collected during the injection experiment at the Richmond field station provided a more interesting case. Comparisons of the measurements before and after the injection definitely show the presence of the electrically conductive salt water. Unfortunately noise with a non-Gaussian distribution was again found to be present in the calibrated data, however the nature of this noise suggests that it was caused by some type of electrical leakage from the transmitter tool.

The images that result from the iterative Born inversion of the Richmond data are very useful for interpreting the hydrologic heterogeneity of the aquifer at depth. Unfortunately the three dimensional nature of the geology at Richmond makes high resolution imaging of the background structure with the cylindrical scheme impossible. However, the crude cylindrical symmetry provided by the injected plume allows for the subsurface changes caused by the experiment to be approximately mapped. Although artifacts are present in the results, images resulting from 3-D thin-sheet models have shown these same type of features. By analyzing these how these artifacts change from well to well, the direction of plume migration has been defined to be to the north-northwest with very little extension to the south.

6.2 Recommendations for future research

The analysis in this thesis has concentrated almost exclusively on the cross well method of probing the subsurface. However there are often situations in which only a single well, or possibly no wells, are available for use in a geophysical survey. Thus the first task is to extend the analysis developed here to other source-receiver configurations such as those provided by surface-to-borehole and surface-to-surface arrays. Different sources such as electric dipoles, long lines of current, and large loop sources need to be examined, as do the pros and cons of measuring both the electric and magnetic fields. This analysis should incorporate the coverage diagram concept presented by Zhou (1989) in addition to the sensitivity diagrams and the image resolution tests employed here to examine the different types of array configurations.

It was determined that for background induction numbers greater than approximately 50, the fields resulting from a scattering body become less and less dependent on the third dimension of the body outside of the image plane. Unfortunately it was also determined that the Born series approximation fails to converge at these high induction numbers. Thus to take advantage of the benefits of imaging at these high induction numbers, a more accurate forward modeling scheme must be incorporated into the iterative Born scheme. Although the

imaging code will run considerably slower, the use of the cylindrical geometry should still be much quicker than employing a 2 1/2-D or 3-D geometry.

A second improvement to the 2-D cylindrical imaging code will involve better incorporation of a priori knowledge into the solution. Currently the scheme allows upper and lower bounding constraints and a layered space background model to be applied. Both of these have been shown to improve image accuracy. However valuable information present in borehole conductivity logs and any surface conductivity measurements can currently only be employed in a qualitative manner to interpret the images. The incorporation of these data to constrain the solutions near the boreholes and/or along the surface should significantly improve the accuracy and resolution of the resulting images.

At lower induction numbers where the Born series does converge, the 2-D cylindrically symmetric scheme has been demonstrated to be extremely susceptible to artifacts caused by 3-D geology. This phenomenon is due to the fact that simple model geometry does not allow for electric current flow perpendicular to conductivity boundaries. In order to at least partially account for this phenomenon while still assuming a two dimensional medium, an imaging code that employs the 2 1/2-D geometry will need to be developed. This code and the 2-D cylindrical scheme should then be compared against each other to determine the benefits and limitations of the respective geometries in recovering two dimensional images of 3-D conductivity distributions. Although codes employing this 2 1/2-D geometry have previously been developed (e.g. Torres-Verdin and Habashy, 1993, and Wang and Chew, 1992), for this comparison the same least squares inversion technique should be employed so that the only differences in the resulting images are caused by the model geometry.

Along these same lines, simple 3-D inversion codes should be examined as a final step in the imaging process. It is obvious from the results presented in Chapter 5 that at lower induction numbers there is valuable 3-D information present in the data that the 2-D imaging codes can not handle. However, although the 2-D images contain artifacts, they do provide reasonable results which can be used to constrain a 3-D inversion. Thus simple 3-D inversion codes should be developed which incorporate the 2-D images as starting models and as constraints to provide more accurate estimates of the conductivity distribution.

In Chapter 4 it was demonstrated that multiple frequency data can be employed to produce better image resolution than single frequency results. However it was also demonstrated that the data must be weighted properly in order for these results to be obtained. Because the schemes that were employed here give too great of a weight to the noise present in the large offset data, different weighting schemes must be examined

such that wide band data can be more routinely incorporated. In addition, two dimensional, multiple frequency imaging of data generated by 3-D structures must be examined to determine the benefits and limitations of this approach.

References

Adenekan, A. E., and Patzek, T.W., 1993, Cleaning up gasoline with steam; compositional simulations :Paper SPE 25257 in the Proceedings of the 12th SPE symposium on Reservoir Simulation, New Orleans, LA.

Alumbaugh D.L., and Morrison, H.F., 1992, Tomographic Imaging of Cross well EM Data : Extended abstracts from the Society of Exploration Geophysicists 1992 annual meeting, New Orleans, Louisiana.

Anderson, W. L., 1982, Fast Hankel transforms using related and lagged convolutions: Assn. Comp. Mach. Trans. on Math. Software, **8**, 344-368.

Archie, G.E., 1942, The electrical resistivity log as an aid in determining some reservoir characteristics: Trans. AIME, **146**, 54-62.

Backus, G.E. and Gilbert, J. F., 1968, The resolving power of gross earth data: Geophys. J. Roy. Astr. Soc., **16**, 169-205.

Barber, T., 1992, High-resolution induction logs using a multi-array induction tool: Presented at International Geoscience and Remote Sensing Symposium (IGARSS) '92, Houston, Texas.

Bartel, L.C., 1982, Modeling and analysis of CSAMT geophysical technique results to map oil receovery processes: Soc. Petr. Eng. Paper SPE 11192.

Bartel, L.C., and Ranganayaki, R.P., 1989,Acquisition of controlled-source audiofrequency magnetotelluric (CSAMT) data at an active steam drive site. 59'th Ann. Int. Mtg., Soc. Explor. Geophys., Dallas, Exp. Abstr., 213-218.

Barthes, V. and Vasseur, G., 1978, An inverse problem for electromagnetic prospecting: *in* P. C. Sabatier, ed., Applied Inverse Problems, Lecture Notes in Physics, **85**, 325-329.

Beasley, C.W., and Tripp, A.C., 1991, Application of the cross-borehole direct-current resistivty technique for EOR process monitoring - a feasibility study: Geoexploration, **28**, 313-328.

Bevc, D., Asch, T., Lee, S., and Morrison, H. F., 1989, Mapping and monitoring enhanced oil recovery processes with borehole-to-surface resistivity measurements: Progress report and baseline data presentation. Engineering Geoscience Report, Univ. of Calif. at Berkeley, dated 1-26-89.

Bevc, D and Morrison, H.F., 1991, Borehole-to-surface electrical conductivity monitoring of a salt water injection experiment: Geophysics, **56**, 769-777.

Bregman, N.D., Hurley, P.A., and West, G.F., 1989, Seismic tomography at a fire-flood site: Geophysics, **54**, 1082-1090.

Chang, S.K., and Anderson, B., 1984, Simulation of induction logging by the finite-element method: Geophysics, **49**, 1943-1958.

Chave, A. D., 1985, The Freschet derivitives of electromagnetic induction; J. Geophys. Res., **89**, 3373-3380.

Chew, W. C. and Chuang, S. L., 1984, Profile inversion of a planar medium with a line source or a point source: paper presented at International Geoscience and Remote Sensing Symposium, Inst. of Electr. and Electron. Eng., Strasbourg, France.

Chew, W.C., Nie, Z., Liu, Q.H., and Anderson, B., 1991, An efficient solution for the response of electrical well-logging tools in a complex environment: IEEE trans. geosci. and remote sensing,**29**, 308-313.

Constable, S. C., Parker, R. L., and Constable, C. G., 1987, Occam's inversion; a practical algorithm for generating smooth models from electromagnetic sounding data: geophysics, **52**, 289-300.

Daily, W. and Ramirez, A., 1992, Electrical resistivity tomography of vadose water movement: Water Resources Research, **28**, 1429-1442.

Daily, W, 1984, Underground oil-shale retort monitoring using geotomography: Geophysics, **49**, 1701-1707.

Davis, D.T., Lytle, R.J., and Laine, E.F., 1979, Use of hig frequency electromagnetic waves for mapping an in situ coal gassification burn front: In Situ, **3**, 95-119.

Deszcz-Pan, M., 1993, The crosswell electromagnetic response of layered media: Ph.D. thesis, University of California at Berkeley, In Progress.

Devaney, A. J., 1984, Geophysical diffraction tomography: Trans., Inst. Electr. Electron. Eng., **GE-22**, 3-13.

Dorfman, M.H., Oskay, M.M. and Gaddis, M.P., 1977, Self-potential profiling-a new technique for determination of heat movement in thermal oil recovery flood, Soc. Petrol. Eng. Pap. SPE 6790.

Druskin, V., Fast differential-difference numerical methods in geophysical electrodynamics: Presented at International Geoscience and Remote Sensing Symposium (IGARSS) '92, Houston, Texas.

Gill, P. E., Murray, W. and Wright, M.H., 1981, Practical Optimization: Academic Press, London.

Gomez-Trevino, E., 1987, A simple sensitivity analysis of time domain and frequency domain electromagnetic measurements: Geophysics, **52**, 1418-1424.

Greaves, R.J. and Fulp, T.J., 1987, Three-dimensional seismic monitoring of an enhanced oil receovery process : Geophysics, **52,** 1175-1187.

Habashy, T. M., Chew, W. C. and Chow, E. Y., 1986, Simultaneous reconstruction of permittivity and conductivity profiles in a radially inhomogeneous slab: Radio Science, **21**, 635-645.

Habashy, T. M. and Mittra, R., 1987, On some inverse methods in electromagnetics: Journal of Electromagnetic Waves and Applications, **1**, 25-58.

Habashy, T.M., Groom, R. W., Spies, B.R., 1993, Beyond the Born and Rytov approximations: a nonlinear approach to electromagnetic scattering: J. Geophys. Res., **98**, no. B2, 1759-1775.

Hardage, B.A., 1983, Vertical Seismic Profiling Part A: Principles, Geophysical Press, London.

Hanson, J.C., Tweeton, D.R., Friedel, M.J. and Dahl, L.J., 1991, A field test of electromagnetic methods for the detection of conductive plumes:61'st Ann. Int. Mtg., Soc. Explor. Geophys., Houston, Exp. Abstr., 569-572.

Hohmann, G. W., 1971, Electromagnetic scattering by conductors in the earth near a line source of current: Geophysics, **36**, 101-131.

Hohmann, G. W., 1975, Three-dimensional induced polarization and electromagnetic modeling: Geophysics, **40**, 309-324.

Hohmann, G. W., 1988, Numerical modeling for electromagnetic methods of geophysics,*in* M. N. Nabighian, ed., Electromagnetic Methods in Applied Geophysics-Theory, Vol. 1:Soc. Explor. Geophys., 313-363.

Hohmann, G. W. and Raiche, A. P., 1988, Inversion of controlled-source electromagnetic data, *in* M. N. Nabighian, ed., Electromagnetic Methods in Applied Geophysics-Theory, Vol. 1: Soc. Explor. Geophys., 469-503.

Hopper, M. J., 1979, HARWELL subroutine library - A catalogue of subroutines: AERE, Harwell, Didcot, Oxon, OX11 ORA, England.

Howard, A. Q., Jr., Glass, C.E., Henry, D.B., N'Guessam, D.M., and Siemers, D.M., 1983, Indirect rock mass investigations for optimizing borehole drilling programs. (Wave Diffusion Tomography, Univ. of Arizona report#NUREG/CR-3143,v.4,111pp.

Justice, J.H., Vassiliou, A.A., Singh, S., Logel,J.D., Hansen, P.A., Hall, B.R., Hutt, P.R. and Solanki, J.J., 1989, Acoustic tomography for monitoring enhanced oil recovery, The Leading Edge, **8**, no. 2 , 12-19.

Keller, G.V., 1988, Rock and mineral properties, *in* M. N. Nabighian, ed., Electromagnetic Methods in Applied Geophysics-Theory, Vol. 1: Soc. Explor. Geophys., 13-52.

Luke, Y. L., 1962, Integrals of Bessel's functions: McGraw-Hill Book Co., Inc., New York.

Kong, J. A., 1975, Theory of Electromagnetic Waves, John-Wiley & Sons, New York.

Laine, E.F., 1987, Remote monitoring of the steam-flood enhanced oil recovery process, Geophysics,**52**, 1457-1465.

Lawson, C.L., and Hanson, R.J., 1974, Solving least squares problems: Prentice Hall, Chpt. 23.

Lee, K.H, 1988, EM1D, Fortran code developed at Lawrence Berkeley Labratory.

Lee, K. H., and Xie, G. Q., 1993, A new approach to imaging with low frequency electromagnetic fields; Geophysics, **58**, 780-796.

Mansure, A.J., and Meldau, R.F., 1990, Steam-zone electrical characteristics for geodiagnostic evaluation of steamflood performance, SPE Formations Evaluation, **5**, 241-247.

Menke, W., 1984, Geophysical data analysis-discrete inverse theory: Academic Press, Inc.

Morse, P.W. and Feshbach, H., 1953, Methods of Theoretical Physics: McGraw-Hill Book Co., Inc.

Nekut, A. G., 1992, Crosswell electromagnetic tomography using raytracing:Presented at International Geoscience and Remote Sensing Symposium (IGARSS) '92, Houston, Texas.

Newman, G. A., 1992a, Electromagnetic sensing of 3-D obstacles through steel-cased wells: Presented at International Geoscience and Remote Sensing Symposium (IGARSS) '92, Houston, Texas.

Newman, G.A., 1992b, Three-dimensional electromagnetic inversion of insufficient and inadequate data: 62'nd Ann. Int. Mtg., Soc. Explor. Geophys., New Orleans, Exp. Abstr., 453-456.

Newman, G.A. and Hohmann, G.W., 1988. Transient electromagnetic responses of high-contrast prisms is a layered earth: *Geophysics* **53** 691-706.

Newmark, R.L., and Wilt, M.J., Changes in formation electrical properties during steam floods:62'nd Ann. Int. Mtg., Soc. Explor. Geophys., New Orleans, Exp. Abstr., 488-491.

Pai, D.M., and Huang, M., 1988, A generalized Haskell matrix method for borehole electromagnetics: theory and applications: Geophysics, **53**, 1577-1586.

Palacky, G.J., 1988, Resistivity characteristics of geologic targets, *in* M. N. Nabighian, ed., Electromagnetic Methods in Applied Geophysics-Theory, Vol. 1: Soc. Explor. Geophys., 53- 129.

Park, S. K., and Van, G. P., 1991, Inversion of pole-pole data for 3-D resistivity structure beneath arrays of electrodes: Geophysics, **56**, 951-960.

Parker, R. L., 1977, Understanding inverse theory: Ann. Rev. Earth Planet. Sci., **5**, 35-64.

Paulsson, B.N.P., Smith, M.E., Tucker, K.E., and Fairborn, J.W., 1992, Characterization of a steamed oil reservoir using cross-well seismology:The Leading Edge, **11**, no. 7 , 24-33.

Pouch, G.W., 1987, Hydrogeological Site Assessment of the Engineering Geoscience Well Field at the Richmond Field Station, Contra Costa County, California. Unpublished MS Thesis, Department of Material Sciences and Mineral Engineering, University of California, Berkeley.

Press, W. H., Flannery, B.P., Teukolsky, S.A., and Vetterling, W.T., 1986, Numerical recipes: the art of scientific computing: Cambridge University Press, Cambridge, England.

Ramirez, A.L., Daily, W., LaBrecque, D.J., Owen, E.W. and Chesnut, D.A., 1992, Electrical resistance tomography used to monitor subsurface steam injection:62'nd Ann. Int. Mtg., Soc. Explor. Geophys., New Orleans, Exp. Abstr., 492-494.

Ranganayaki, R.P., Akturk, S.E., and Fryer, S.M.,1992, Formation resitivity variation due to steam flooding: a log study: Geophysics, **57**, 488-494.

Robertson, J.D., 1989, Reservoir management using 3-D seismic data: The Leading Edge, **8**, no. 2 , 25-31.

Romo, S., Whinnery, J. R. , 1953, Fields and waves in modern radio:John Wiley and Sons, Inc.

Ryu, J., Morrison, H.F., and Ward, S. H., 1970, Electromagnetic fields about a loop source of current: Geophysics, **35**, 862-896.

Sasaki, Y., Matsuo, K., and Yokoi, K., 1992, Audio-frequency electromagnetic tomography using vertical magnetic dipole sources - a model study: **********

Schenkel, C.J., 1991, The Electrical Resitivity Method in Cased Boreholes:Ph.D. thesis, University of California at Berkeley.

Sena, A. G. and Toksoz, M., 1990, Simultaneous reconstruction of permittivity and conductivity for cross hole geometries: Geophysics, **55**, 1302-1311.

Sheriff, R.E., and Geldart, L.P.,1982, Exploration seismology vol. 1 : history, theory and data acquisition, Cambridge University Press, Cambridge, England.

Shima, H. and Imamura, S, 1991, Application of high-resolution resitivity tomography to a small oil reservoir: field test at Buckhorn test facility, Illinois: 61'st Ann. Int. Mtg., Soc. Explor. Geophys., Houston, Exp. Abstr., 391-396.

Sill, W.R., and Sjostrom, K.J., 1990, Groundwater flor direction from borehole-to-surface electrical measurements: 60'th Ann. Int. Mtg., Soc. Explor. Geophys., San Francisco, Exp. Abstr., 535-537.

Spies, B.R. and Greaves, R.J., 1991, Numerical modeling of surface-to-borehole electromagnetic surveys for monitoring thermal enhanced oil receovery: Geoexploration, **28**, 293-311.

Spies, B.R., and Habashy, T.M., 1992, Sensitivity analysis of cross-well electromagnetics: Expanded Abstracts from Society of Exploration Geophysicists Annual Meeting, New Orleans Louisiana. 502-505.

Stark, P.B., 1987, Strict bounds and applications: Proceedings of RCP 264 Recontre Interdisciplinaire Problemes Inverses Montpellier, France.

Stoyer, C.H., 1977, Electromagnetic fields of dipoles in stratified media: IEEE Trans. on Ant. and Prop., **AP-25**, 547-552.

Stolarczyk, L. G., Comparison of electrical conductivity measured with logging and crosshole radio tomography methods:Presented at International Geoscience and Remote Sensing Symposium (IGARSS) '92, Houston, Texas.

Swokowski, E.W.,1979, Calculus with analytical geometry :Prindle, Webeber and Schmidt, Boston, Massachusetts.

Tikhonov, A.N., and Arsenin, V.Y., 1977, Solutions of ill-posed problems: John Wiley and Sons, Inc.

Torres-Verdin, C. and Habashy, T.M., 1993, An approach to nonlinear inversion with applications to cross-well EM tomography:to be presented at the 63'rd Ann. Int. Mtg., Soc. Explor. Geophys., Washington, D.C.

Uchida, T., Lee, K.H., and Wilt, M.J., 1991,Effect of a steel casing on crosshole EM measurement: Expanded Abstracts from Society of Exploration Geophysicists Annual Meeting, Houston, Texas, 442-445.

vanPoolen, H.K., and Associates, 1981, Fundamentals of enhanced oil recovery: PennWell Books.

Wait, J.R., 1970,Electomagnetic waves in stratified media: Pergammon Press, New York.

Wait, J.R., and Hill, D.A., 1980, Fields of a horizontal loop of arbitrary shape buried in a two-layer earth: Radio Science, **15**, 903-912.

Wannamaker, P.E., Hohmann, G.W., and San Filipo, W.A., 1984, Electromagnetic modeling of three-dimensional bodies in layered earths using integral equations: Geophysics, **49**, 60-74.

Ward, S.H. , and Fraser, D.C.,1967, Electrical methods: Part B-Conduction of electricity in rocks, *in* Hanson, D.A., Heinrichs, W.E., Holmer, R.C., MacDougall, R.E., Rogers,

G.R., Sumner, J.S. and Ward, S.H., Ass. Ed., Mining Geophysics Volume II - Thoery, Soc. Explor. Geophys., 197-223.

Ward, S.H., and Hohmann, G.W., 1988, Electromagnetic theory for geophysical applications,*in* M. N. Nabighian, ed., Electromagnetic Methods in Applied Geophysics-Theory, Vol. 1: Soc. Explor. Geophys., 131-311.

Waxman, M.H. , and Smits, E.C., 1968, Electrical conductivities in oil-bearing shaley sands: SPEJ transactions AIME, **243**, 107-122.

Waxman, M.H. and E.C. Thomas, 1974, Electrical conductivities in shaly sands-I the relation between hydrocarbon saturation and resistivity index. Journal of Petroleum Technology 213-215; transactions AIME, 257.

Weidelt, P., 1981, Dipole induction on a thin plate with host medium and overburden: Res. project NTS 83, no. 89727, Federal Inst. earth Sci. and Raw Materials, Hannover, West Germany.

Wilt, M.J., and Ranganayaki, R.P., 1990, Surface-to-borehole electromagnetic logging for enhanced oil receovery (EOR) applications:60'th Ann. Int. Mtg., Soc. Explor. Geophys., San Francisco, Exp. Abstr., 532-534.

Wilt, M.J., Morrison, H.F., Becker, A. and Lee, K.H., 1991, Cross-boerhole and surface-to-borehole electromagnetic induction for reservoir characterization: U.S. Dept. of Energy Report DOE/BC/91002253.

Wilt, M.J., and Schenkel, C., 1992, Cross-borehole electromagnetic induction for steam flooding monitoring, 62'nd Ann. Int. Mtg., Soc. Explor. Geophys., New Orleans, Exp. Abstr., 484-487.

Wilt, M.J., Alumbaugh, D.L., Morrison, H.F., Becker, A. and Lee, K.H., and Deszcz-Pan, M., 1993, Crosshole electromagnetic imaging for reservoir definition and monitoring; to be submitted to Geophysics.

Worthington, M. H., 1984, An introduction to geophysical tomography: First Break, **2**, 20-26.

Wu, R. S., and Toksoz, M. N., 1987, Diffraction tomography and multisource holography applied to seismic imaging: Geopysics, **52**, 11-25.

Zhou, Q., 1989, Audio-frequency Electromagnetic Tomography for Reservoir Evaluation: Lawrence Berkeley Laboratory Report LBL-28171.

Zhou, Q., Becker, A., and Morrison, H.F., Audio-frequency electromagnetic tomography in 2-D: Geophysics, **58**, 482-495.

Appendix A
Definition of the Smoothing Matrices

The formulation for the smoothing matrices that are employed to regularize the iterative Born scheme is identical to that given in Zhou (1989). Although described as a smoothest model approach, the method that is employed here actually is a *flattest model* type of regularization. The difference between the two methods is that the flattest approach involves minimizing the *first* derivative between adjacent cells in the model while the smoothest model minimizes the second derivative (Menke, 1984).

Recall from Chapter 4 that the function we wish to minimize is given by

$$s(\mathbf{O}') - 2\mathbf{D}^T\mathbf{D} = \mathbf{O}'^T(\mathbf{K}^T\mathbf{K} + \lambda_h\mathbf{A}_h^T\mathbf{A}_h + \lambda_v\mathbf{A}_v^T\mathbf{A}_v)\mathbf{O}' - 2\mathbf{D}^T\mathbf{K}^T\mathbf{O}'^T \qquad \text{(A-1)}$$

where $\mathbf{O}'$ is the object function that we are solving for, $\mathbf{D}$ is the data vector, $\mathbf{K}$ is the sensitivity matrix, $\mathbf{A}_h$ and $\mathbf{A}_v$ are matrices representing a discretization of the *first* derivative in the horizontal and vertical directions, respectively, and the λ's are the associated Lagrangian multipliers which control the degree of flatness. Thus $\mathbf{A}_h^T\mathbf{A}_h$ represents the square of the first derivative in the horizontal direction which is given in matrix form as

$$\mathbf{A}_h^T\mathbf{A}_h = \begin{bmatrix} \mathbf{H} & 0 & 0 & \cdots & 0 \\ 0 & \mathbf{H} & 0 & \cdots & 0 \\ 0 & 0 & \mathbf{H} & \cdots & 0 \\ \vdots & \vdots & \vdots & \ddots & \vdots \\ 0 & 0 & 0 & \cdots & \mathbf{H} \end{bmatrix}_{LXL} \qquad \text{(A-2)}$$

where $\mathbf{H}$ has the form

$$\mathbf{H} = \begin{bmatrix} 1 & -1 & 0 & \cdots & 0 \\ -1 & 2 & -1 & \cdots & 0 \\ 0 & -1 & 2 & \cdots & 0 \\ \vdots & \vdots & \vdots & \ddots & \vdots \\ 0 & 0 & 0 & \cdots & 1 \end{bmatrix}_{KXK} . \qquad \text{(A-3)}$$

In these equations K is the number of cells, or unknowns in the horizontal direction and L the number in the vertical direction. Similarly the square of the first derivative in the

vertical direction, $\mathbf{A}_v^T\mathbf{A}_v$, has the matrix form

$$\mathbf{A}_v^T\mathbf{A}_v = \begin{bmatrix} \mathbf{I} & -\mathbf{I} & 0 & \cdots & 0 \\ -\mathbf{I} & 2\mathbf{I} & -\mathbf{I} & \cdots & 0 \\ 0 & -\mathbf{I} & 2\mathbf{I} & \cdots & 0 \\ \vdots & \vdots & \vdots & \ddots & \vdots \\ 0 & 0 & 0 & \cdots & \mathbf{I} \end{bmatrix}_{LXL} \tag{A-4}$$

where $\mathbf{I}$ is the identity matrix given by

$$\mathbf{I} = \begin{bmatrix} 1 & 0 & 0 & \cdots & 0 \\ 0 & 1 & 0 & \cdots & 0 \\ 0 & 0 & 1 & \cdots & 0 \\ \vdots & \vdots & \vdots & \ddots & \vdots \\ 0 & 0 & 0 & \cdots & 1 \end{bmatrix}_{KXK} . \tag{A-5}$$

Appendix B
Derivation of the Layered Space Background Model

The method employed here to derive the theoretical formulation for the 1-D layered model containing either a magnetic dipole or large loop source follows that of Stoyer (1977) and Wait and Hill (1980). The reader is referred to Figure 4.26 which shows the geometry of the problem.

The starting point for the derivation is Maxwell's equations as given in equation 2.1;

$$\nabla \times \mathbf{H} = \sigma \mathbf{E} + \mathbf{J}_s \tag{B-1}$$

and

$$\nabla \times \mathbf{E} = -i\omega\mu\mathbf{H} \tag{B-2}$$

where **E** is the electric field, **H** is the magnetic field and $\mathbf{J}_s$ is the applied source distribution. In order to formulate a general solution that can handle both dipole sources as well as the Green's functions which consist of large loops of current, $\mathbf{J}_s$ takes the form

$$\mathbf{J}_s = j_\phi(r)\hat{\phi} = I\delta(r - a)\hat{\phi} \tag{B-3}$$

where I is the current flowing in the loop source, a is the radius of the loop and $\delta(r - a)$is the Dirac delta function. Thus for a magnetic dipole source, a is set equal to zero.

The general solution for the fields can be written in terms of the magnetic Hertz potential , Π_m (Stoyer, 1979). The electric fields are given in terms of this potential as

$$\mathbf{E} = -i\omega\mu\nabla \times \Pi^m \tag{B-4}$$

while the magnetic fields have the form

$$\mathbf{H} = k^2\Pi^m + \nabla(\nabla \cdot \Pi^m) \tag{B-5}$$

where k. is the wave number in the medium given by

$$k^2 = -i\sigma\omega\mu . \tag{B-6}$$

The solutions given in Equations B-4 and B-5 are derived such that the Hertz potential in each layer satisfies the relation

$$(\nabla^2 + k_i^2)\Pi_i^m = \delta(i)\delta(r - a)\delta(z - d)I \qquad \text{(B-7)}$$

where the subscript i refers to the i'th layer. Wait and Hill (1980) show that the problem can be further simplified due to the cylindrical symmetry. If the model obeys this geometry, then Π_m contains only a vertical component and thus Equations B-4 and B-5 become

$$E_\phi = i\omega\mu\frac{\partial\Pi^m}{\partial r}, \qquad \text{(B-8)}$$

$$H_r = \frac{\partial^2\Pi^m}{\partial r\partial z} \qquad \text{(B-9)}$$

and

$$H_z = (\frac{\partial}{\partial z^2} + k_j^2)\Pi_j^m. \qquad \text{(B-10)}$$

In addition this assumption allows for equation B-7 to be expanded and simplified;

$$(\frac{1}{r}\frac{\partial}{\partial r}r\frac{\partial}{\partial r} + \frac{\partial^2}{\partial z^2} + k_j^2)\Pi_j^m = \delta(i)\delta(r - a)\delta(z - d)I. \qquad \text{(B-11)}$$

Wait (1970) has shown that the solution to equation B-11 is a zero order inverse Hankel transform which is given by

$$\Pi_j^m = -\frac{Ia}{2}\int_0^\infty\left[\delta(i)e^{-\gamma_i|z+d|}U_i(\lambda)e^{\gamma_i z\alpha} + D_i(\lambda)e^{-\gamma_i z\alpha}\right]\frac{J_1(\lambda a)}{\gamma_i}J_0\ (\lambda r)d\lambda \qquad \text{(B-12)}$$

where $J_0(\lambda r)$ and $J_1(\lambda a)$ are the zero-th and first order Bessel's functions of the first kinds, respectively, and $U_i(\lambda)$ and $D_i(\lambda)$ represent the reflected upgoing and downgoing components of the EM wavefield in the i'th layer. Notice that if we consider the case of the magnetic dipole source of unit moment we can use a small argument approximation to let $2J_1(\lambda a)/\lambda a = 1$ and thus expression B-12 becomes

$$\Pi_i^m = -\frac{1}{4\pi}\int_0^\infty\left[\delta(i)e^{-\gamma_i|z+d|} + U_i(\lambda)e^{\gamma_i z} + D_i(\lambda)e^{-\gamma_i z}\right]\frac{\lambda}{\gamma_i}J_0\ (\lambda r)d\lambda. \qquad \text{(B-13)}$$

Equation B-9 can also be integrated in r and z over a cell of dimensions Δ^2 to yield equations for the integrated Green's function. The resulting expressions have the form

$$\Pi_i^m = -\frac{\pi}{2}\int_0^\infty \Big[\delta(i)\big[1-e^{-\gamma_i\Delta/2}\big]+U_i(\lambda)\big[e^{\gamma_i(z_k+\Delta/2)}-e^{\gamma_i(z_k-\Delta/2)}\big] \qquad \text{(B-14)}$$

$$+D_i(\lambda)\big[e^{-\gamma_i(z_k+\Delta/2)}-e^{-\gamma_i(z_k-\Delta/2)}\big]\Big]\nu(\lambda,r_k+\Delta/2,r_k-\Delta/2)\frac{J_0(\lambda r)}{\lambda\gamma_i}d\lambda$$

if $z_k = z$, i.e. if the cell is singular, and

$$\Pi_i^m = -\frac{\pi}{4}\text{sign}(z_k+\Delta/2-z)\int_0^\infty \Big[\delta(i)\big[e^{-\gamma_i|z_k+\Delta/2+dl}-e^{\gamma_i|z_k-\Delta/2+dl}\big]+ \qquad \text{(B-15)}$$

$$U_i(\lambda)\big[e^{\gamma_i(z_k+\Delta/2)}-e^{\gamma_i(z_k-\Delta/2)}\big]+D_i(\lambda)\big[e^{-\gamma_i(z_k+\Delta/2)}-e^{-\gamma_i(z_k-\Delta/2)}\big]\Big]\cdot$$

$$\nu(\lambda,r_k+\Delta/2,r_k-\Delta/2)\frac{J_0(\lambda r)}{\lambda\gamma_i}d\lambda$$

for the non-singular cell where the subscript k indicates the cell across which the current is being integrated, and $\nu(\lambda,r_k+\Delta/2,r_k-\Delta/2)$ is calculated using expression (3.9). These three expressions combined with equations B-8 through B-10 account for any source field and/or Green's function that will be encountered in a medium that obeys the cylindrical symmetry.

The solutions for $U_i(\lambda)$ and $D_i(\lambda)$ come from solving the boundary conditions of tangential **E** and **H** at each of the layer interfaces. Assuming that the magnetic permeability in each layer is equal to that of free space, the tangential electric field boundary condition is given by

$$\Pi_i^m(z_i) = \Pi_{i+1}^m(z_i) \qquad \text{(B-16)}$$

where z_i designates the depth of the interface between the two layers. Similarly the tangential magnetic field boundary condition is given as

$$\frac{\partial}{\partial z}\Pi_i^m(z_i) = \frac{\partial}{\partial z}\Pi_{i+1}^m(z_i). \qquad \text{(B-17)}$$

Notice that although expressions B-8 and B-9 both contain partial derivatives with respect to r, these types of derivatives are not present in Equations B-13 and B-14. This

is due to the fact that the derivative with respect to r involves only the zero'th order Bessel's function , the solution of which is given as $dJ_0(x)/dx = -J_1(x)$. Taking this derivative on each side of equations B-16 and B-17 yields identical results in r, and thus they cancel each other out.

The last step in the derivation is to define conditions at infinity. In the lower half space there can be no upgoing component and thus $U_n(\lambda) = 0$. Similarly in the upper half space there can be no down going component which yields $D_{-m}(\lambda)=0$. Thus the boundary conditions given in expressions B-16 and B-17 are solved from the layer containing the source to the point of interest with these conditions imposed upon the problem to yield the expressions given in Section 4.3.4.

Appendix C
The LLNL/LBL Cross Well EM System

The contents of this appendix are condensed from a paper submitted for publication by Wilt et al. (1993). The measurement system consists of two modules. The transmitter section includes a transmitter solenoid, a current source to drive it, and a winch and cable system to allow for a downhole deployment of the source. The receiver module consists of a commercial sensor attached to an armored cable, one stage of surface amplification and filtering and a commercial synchronous detector. Data is logged using a desktop computer. The modules are connected only via electrically isolated cables. A requirement of the instrumentation from each module is that it be locally grounded, have its own power supply and be electrically isolated from the other module. Such grounding and isolation is vital for the elimination of stray currents and ground loops that degrade data quality.

C1 Transmitter section

A schematic diagram of the cross hole transmitter system is given in Figure C-1. Although a down hole oscillator is preferred, simplicity of assembly dictated that the initial prototypes of the transmitter be powered from the surface. The source used in the Richmond experiment was built around a ferrite core. This is the preferred material for induction coils at frequencies greater than 5 kHz because it is essentially nonconductive thereby eliminating eddy current losses. Making use of readily available material, a tubular core was constructed from of a large number of stacked 1.27 cm thick ferrite (Cornell type XYZ) toroids. The resulting tube has an outside diameter of 4.4 cm and a length of 197 cm. The diameter of the inner void space is 1.91 cm. The core was wound with 125 turns to maximize the output at 18 kHz and has an inductance of about 2 mH. In order to attain the required moment of about 100 A-m^2 a current of 3.5 A was used. The effective relative magnetic permeability for this core is about 150. This minimizes inductive losses in the core such that only about 125 watts of power are needed to drive the resonant transmitter circuit. These power requirements can be easily met by using an ordinary laboratory signal generator coupled to a Crown model 610 power amplifier.

To move the source within the boreholes a lightweight portable electrical winch that holds 200 m of cable was employed. This lightweight winch and coil may be easily moved by two people and are convenient to use in shallow applications such as those encountered at Richmond. The transmitter depth and rate of movement are monitored with a wheel-driven encoder/counter. In addition to providing depth information, this

encoder pulse also serves as a data acquisition trigger at the receiver.

The transmitter current is monitored with an inductive-type current meter connected to the source output. This analog record of the current is sent to the receiver via an isolated line where it is used as a phase reference. Note that the current is only roughly proportional to the source moment due to the non linearity of the core material. Therefore calibration corrections such as those derived in Section 5.3.2 are relied upon to determine the source moment from the transmitter current measurement.

C2 Receiver section

Signals are detected at the receiver using a vertical-axis custom-designed borehole coil (Electromagnetic Instruments, BH-8). This receiver coil is an ultrasensitive device (maximum sensitivity of 10^{-13} Teslas), operable in the frequency range from 1-100,000 Hz. The tool is housed in a pressure vessel designed for depths up to 2 km. Detected signals are amplified within the coil then transmitted to the surface up a logging cable. At the surface they are further amplified and filtered before input to the receiver van (Figure C-2). In the van all instruments are controlled from a desktop computer via the GPIB interface. The computer can adjust instrument gains and sensitivities as well as select sample and averaging rates for the logging system.

Data logging in the computer is triggered by the depth-encoder pulses originating at the transmitter winch. The computer counts the incoming pulses until one corresponding to a pre-selected measurement depth is received. When this occurs the computer reads the transmitter current data from a digital voltmeter connected to the inductive current probe, and magnetic field data from the lock-in detector. The lock-in detector uses the transmitter current wave form as a reference signal and detects receiver signals in-phase and out-of-phase. It is a very effective device for accurately discriminating low level signals in a noisy background. The spectrum analyzer depicted in Figure C-2 is used as a debugging tool as well as to calibrate system components.

C3 Cross-Borehole Logging

A particular borehole segment is logged by moving the transmitter coil upwards at a fixed rate while the receiver remains stationary in another borehole. Although equivalent information could be collected by moving the receiver coil while the transmitter is fixed, doing so results in very noisy data due to the motion of the sensitive detector in the earth's magnetic field. The source coil is typically moved at a rate of 3-5 m /minute. This allows sufficient time for signal averaging but is still a reasonable rate for data collection. Data is collected at approximately 1.5 cm intervals within a logging

span. However the data are stored by the computer only at 0.5m intervals with these values consisting of seven readings that are averaged as the transmitter moves past. Typically the source well is logged over a depth interval that is 1.5-2.0 times the separation between boreholes as this is a minimum interval required for tomographic reconstruction (Zhou, 1989). Due to time considerations only 10-15 receiver stations are employed to cover the depth interval traversed by the transmitter.

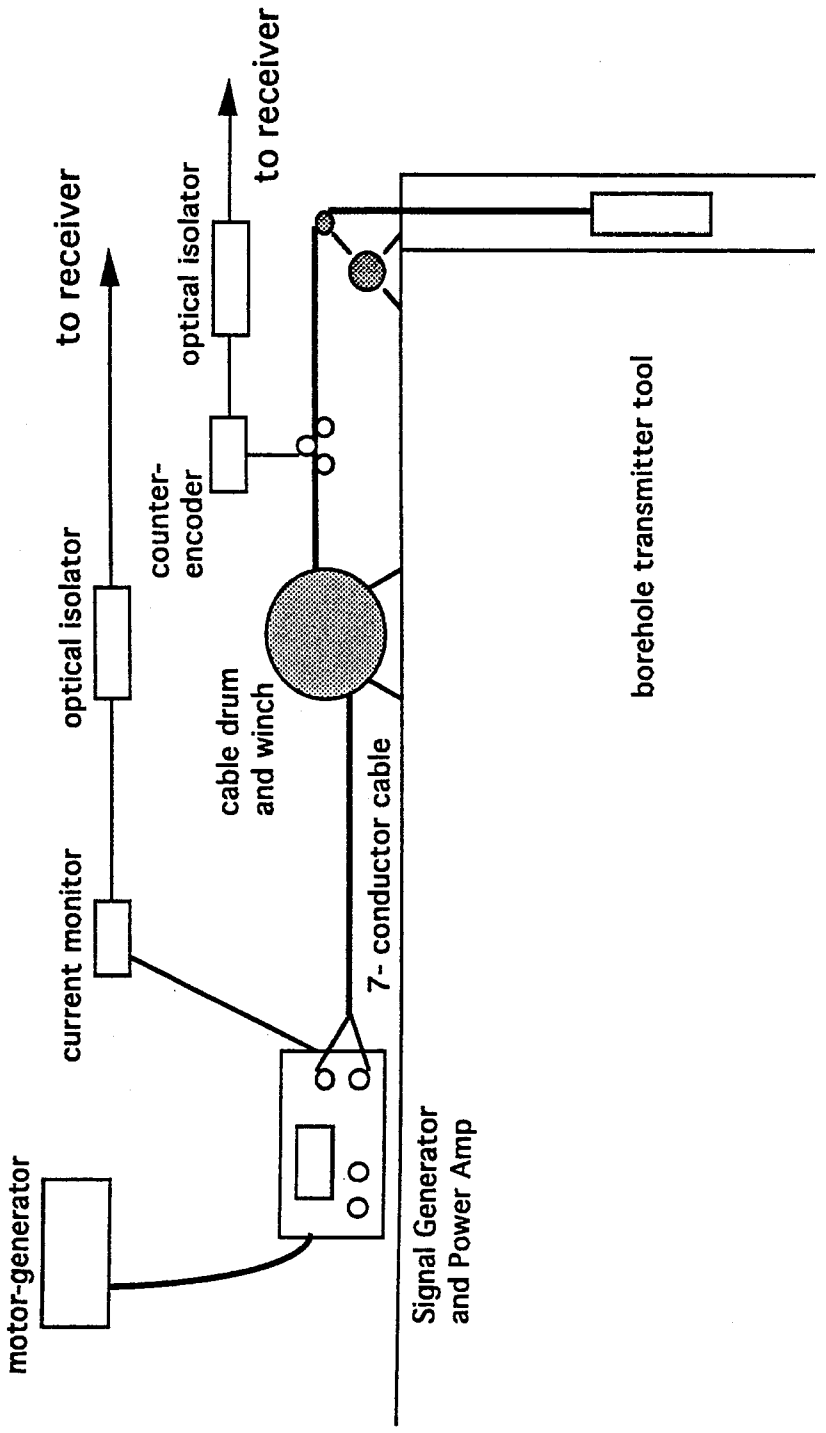

Figure C-1 : Schematic of the bore hole transmitter system.

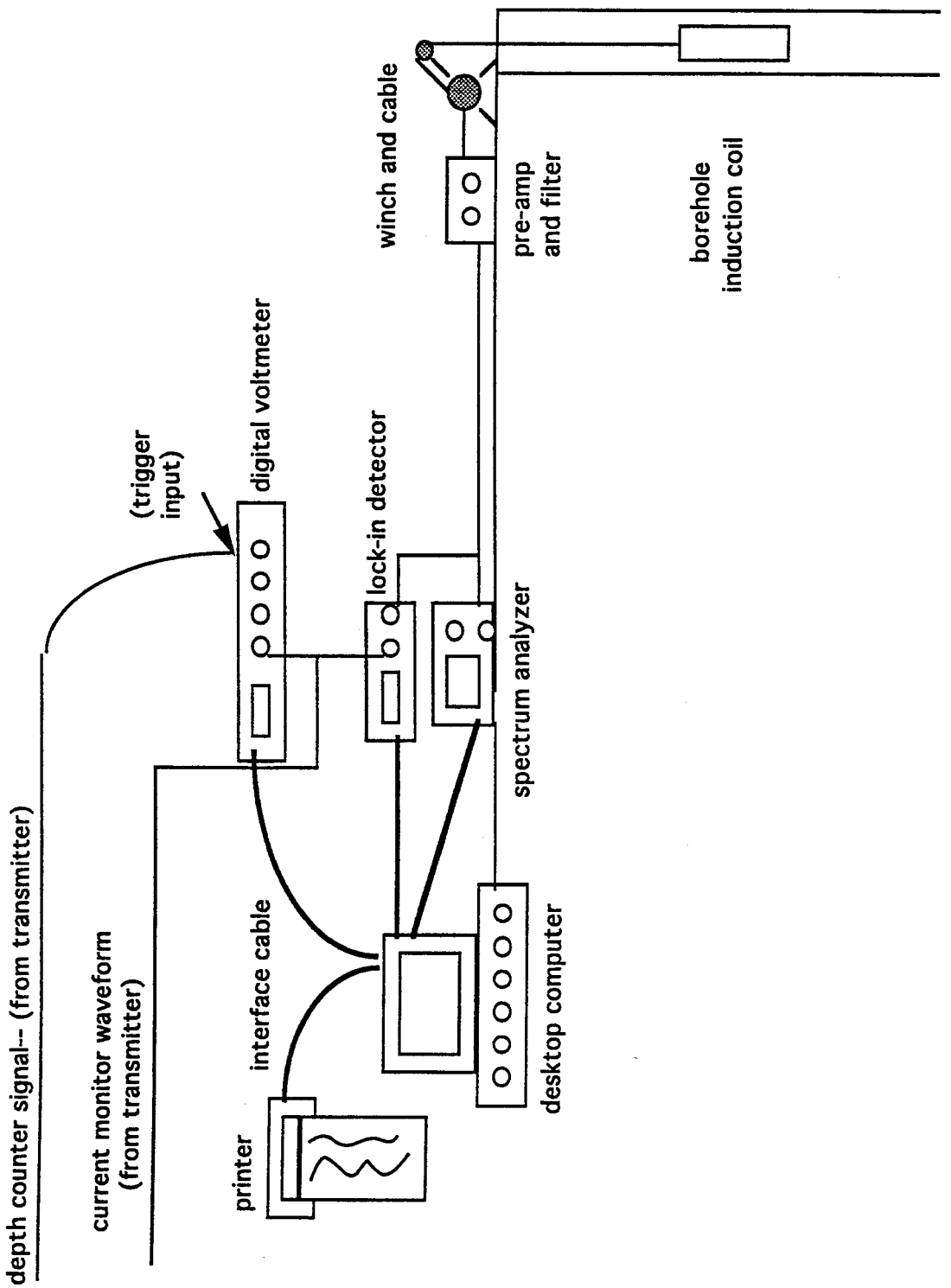

Figure C-2 : Schematic of the borehole receiver system

Appendix D
The Richmond Well Field and Borehole Logs

This appendix summarizes the well logging information that was obtained during the 1992 Richmond field station experiment. Table A1 provides information on the well field at Richmond Field Station which is shown in Figure 5.1. Through February, 1992 14 wells have been drilled in the 10 acre field west of building 300. These wells were drilled in four separate episodes beginning in 1986.

The first nine wells were drilled in 1986 for a borehole-to-surface resistivity experiment (Bevc and Morrison, 1991). Wells INJ and EXT (not shown in Figure 5.1) are opened through steel-screening to a gravel aquifer at 26-30 m. This screened interval is also used an electrode. There are also two other steel electrodes in each well located 10 m above and below the screened interval. Wells OBS1-6 are plastic-cased observation wells opened only at the bottom of the 30 m casing. These wells were designed for water level measurements although they have also been used as geophysical observation wells.

Wells EMNE and EMSW, which straddle the injection well INJ, were added in 1989 in order to make crosshole EM measurements. These wells are separated by 52 m and penetrate to a depth of 90 m making them the deepest wells in the field. They are sealed at the bottom and are not open to the formation at any point.

In 1990 wells CAS1 and CAS2 were drilled at the southern end of the field (not shown in Figure 5.1) and cased with steel. These wells are designed for experiments involving measurements through steel casing. At this same time two 30m deep wells (RES1 and RES2) were drilled and a series of downhole electrodes grouted in place for the purpose of making crosshole resistivity and MMR measurements. Eight resistivity electrodes, spaced at 3 m intervals, are emplaced in each of these wells beginning at a depth of 9 m.

The most recent set of boreholes (INJ1, EMNW and EMSE) were added in 1992 for the present salt water monitoring experiment. Each of these wells are 70m deep, capped at the bottom and are open to the aquifer at 30m depth.

Borehole	Depth(m)	Year Drilled	Casing	Open Interval (m)	Remarks
OBS1	30	1986	4" PVC	at bottom	depth=20m
OBS2	30	1986	4" PVC	at bottom	
OBS3	30	1986	4" PVC	at bottom	
OBS4	30	1986	4" PVC	at bottom	
OBS5	30	1986	4" PVC	at bottom	
OBS6	30	1986	4" PVC	at bottom	
INJ	40	1986	6" PVC	26-30	
EXT	40	1986	6" PVC	26-30	
EMNE	90	1990	6" PVC	no open int	
EMSW	90	1990	6" PVC	no open int	
RES1	30	1990	-	no open int	grouted
RES2	30	1990	-	no open int	grouted
CAS1	30	1990	4" steel	at bottom	steel-cased
CAS2	30	1990	4"steel	at bottom	steel-cased
EMNW	70	1992	6"PVC	26-30	
EMSE	70	1992	6"PVC	26-30	
INJ1	70	1992	6"PVC	26-30	

Table D1 - Richmond Field Station well field.

D1 Borehole induction logs

Baseline borehole induction resistivity logs were recorded in most of the boreholes at Richmond during April 1992 using a Geonics model EM-39 logging instrument. The induction logs that were collected are listed as a function of the well location in table D-2 and are plotted in Figure D-1. Measurements were made at 0.05 m increments as the tool was moving upwards in the borehole. Although five of the wells are drilled to depths of 70 m or more, the induction logs were limited to a depth of 50 m by the length of the available logging cable. Several logs were done twice and typically these repeated to within 5 percent.

A second set of logging data was collected in June, 1992 after the salt water was injected. The only significant difference that was observed was in well INJ1 which is the salt water injection well. Figure D-2 shows both the pre- and post-injection logs that were measured in this well. The difference between the two logs indicates a change in resistivity due to the salt water in the vicinity of the injection well. The largest decrease is observed in a 4 m thick sandy-gravel aquifer at a depth of 26-30 m, where the well is perforated. In this zone the rock has decreased in resistivity from 15 ohm-m to 3.5 ohm-m. A second, thinner zone where the resistivity is different is present from 23 to 25 m depth. These two zones of low resistivity zone around well INJ1 are surprisingly large and suggests that the unconsolidated silts and sands have a fairly high permeability.

borehole	Ind logs	Water conduct
OBS1	yes	yes
OBS2	yes	yes
OBS3	yes	yes
OBS4	yes	yes
OBS5	yes	yes
OBS6	yes	yes
INJ	yes	yes
EXT	no	no
EMNE	yes	no
EMSW	yes	no
RES1	no	no
RES2	no	no
CAS1	no	no
CAS2	no	no
EMNW	yes	yes
EMSE	yes	yes
INJ1	yes	yes

Table D2 - List of the logging data collected during the 1992 Richmond experiment.

Except for well INJ1 we observed no significant changes in well log resistivity due to salt water injection. This includes well INJ, which is located only 5 m northeast of well INJ1. However there were variations noticed in the borehole fluid conductivity at depths from 26-30 m (see next section) which suggest that any perturbations in the resistivity of the open interval (26-30 m) in this well were most likely obscured by the presence of steel screening. Notice that no significant changes in resistivity were observed from 23 m to 25 m depth as had been in borehole INJ1.

D2 Borehole fluid conductivity logs

In addition to the induction logs we also measured the conductivity of the borehole water before and after salt water injection. These measurements are designed to improve the tracking of the salt water and also to provide knowledge of the in-situ groundwater conductivity.

In Figure D-14 the borehole water conductivity profiles measured after the injection are plotted for seven of the wells. Of these seven, high conductivity water ($\approx$1 S/m) was found in only two of the wells, INJ1 and INJ. Both these profiles show the water

conductivity increasing towards the bottom of the well with values that approach the conductivity of the injected fluid. Because salt water is more dense than fresh water, this sort of stratification was expected with the salt water occupying the basal layer. (Note: the higher conductivity in INJ when compared to INJ1 is due to INJ1 being flushed out with fresh water after the injection was completed.) In all other wells the groundwater conductivity was the same before and after injection ($\approx$ 0.08S/m).

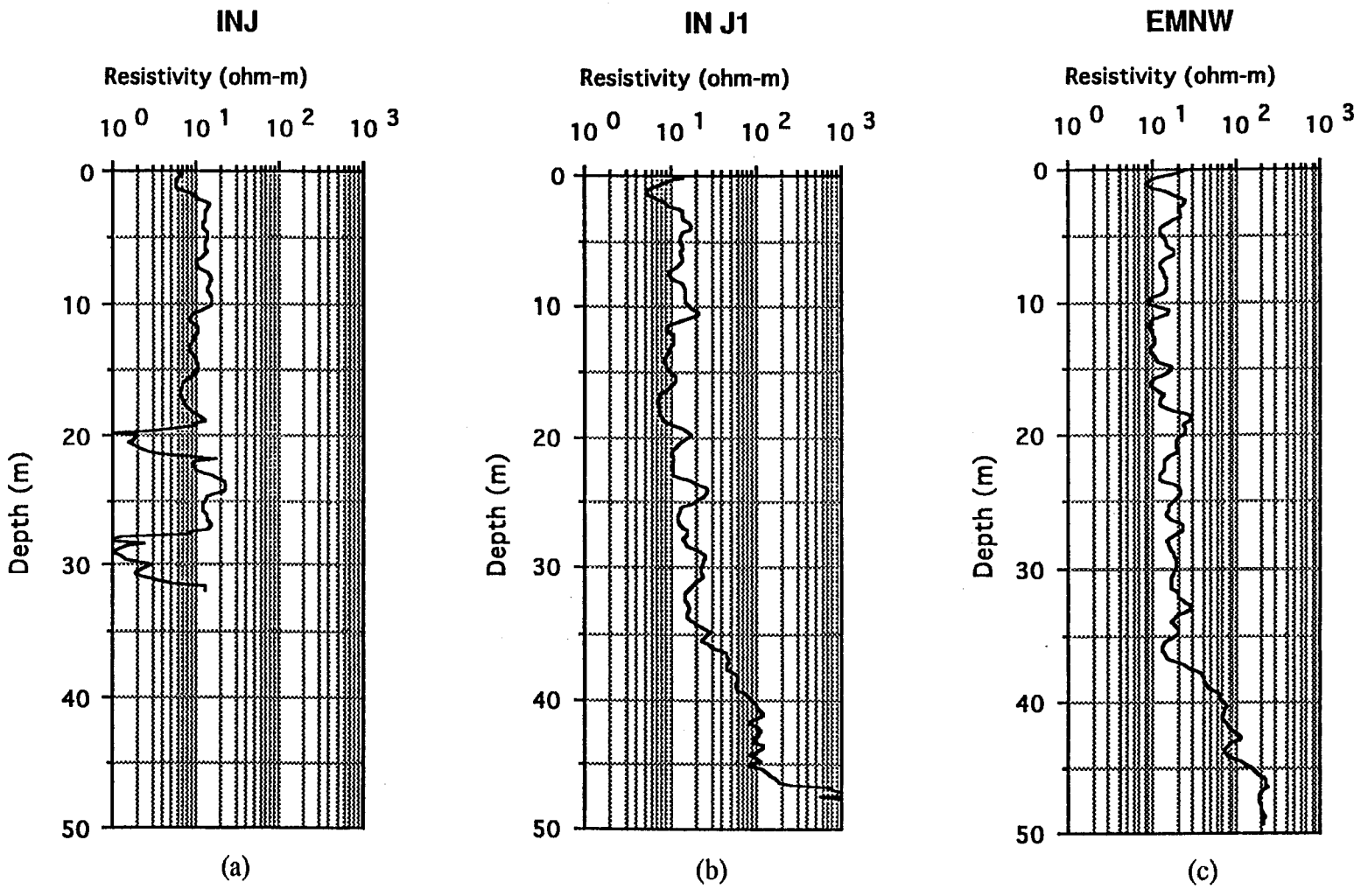

Figure D1 - Borehole resistivity logs for the wells at the Richmond Field Station that were measured on April 2, 1993. (a) Log of well INJ. (b) Log of well INJ1. (c) Log of well EMNW. (d) Continued on next page.

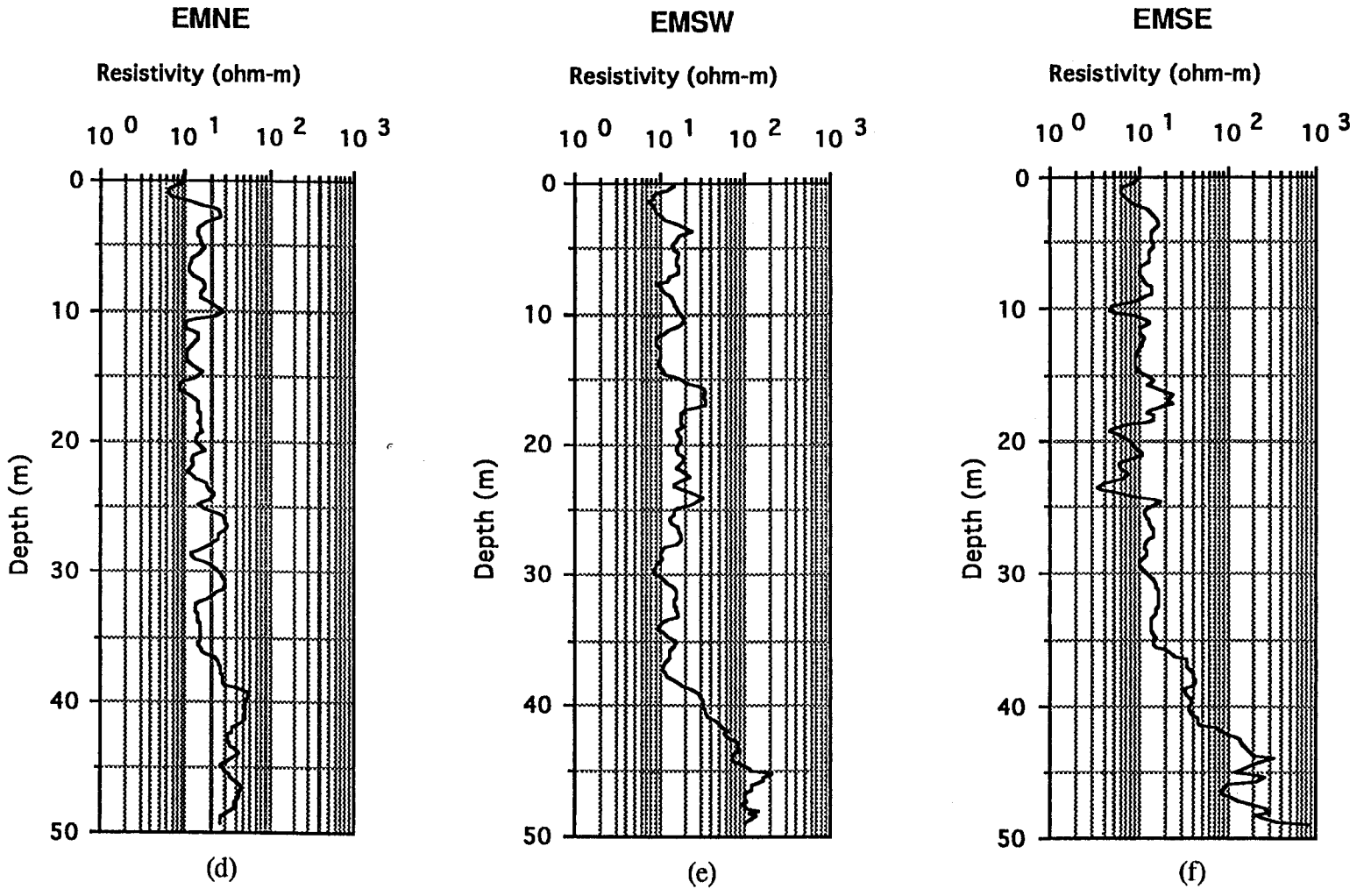

Figure D1 - (Continued from previous page) (d) Log of well EMNE. (e) Log of well EMSW. (f) Log of well EMSE. (g) Continued on next page.

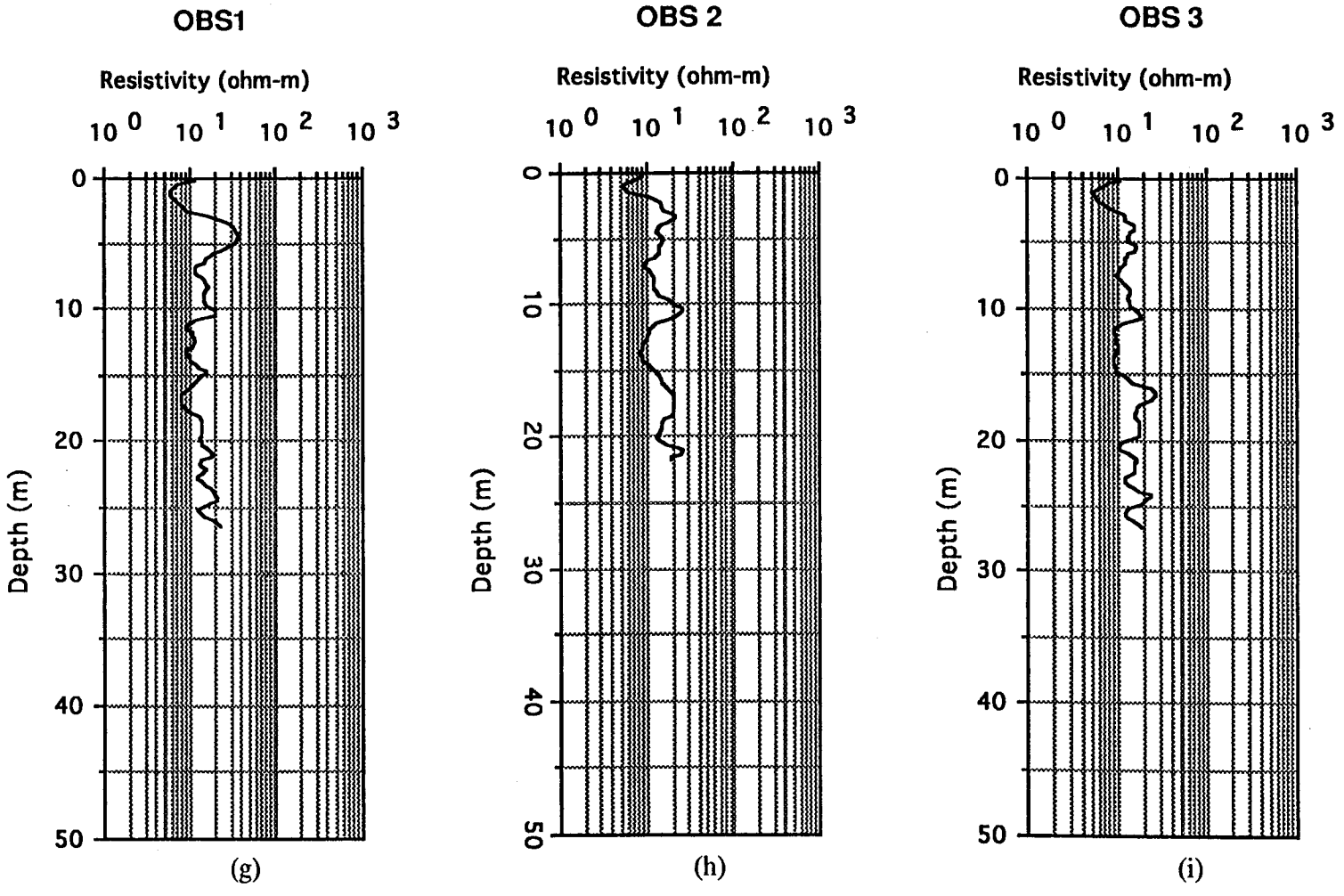

Figure D1 - (Continued from previous page) (g) Log of well ObS 1. (h) Log of well OBS 2. (i) Log of well obs 3. (j) Continued on next page.

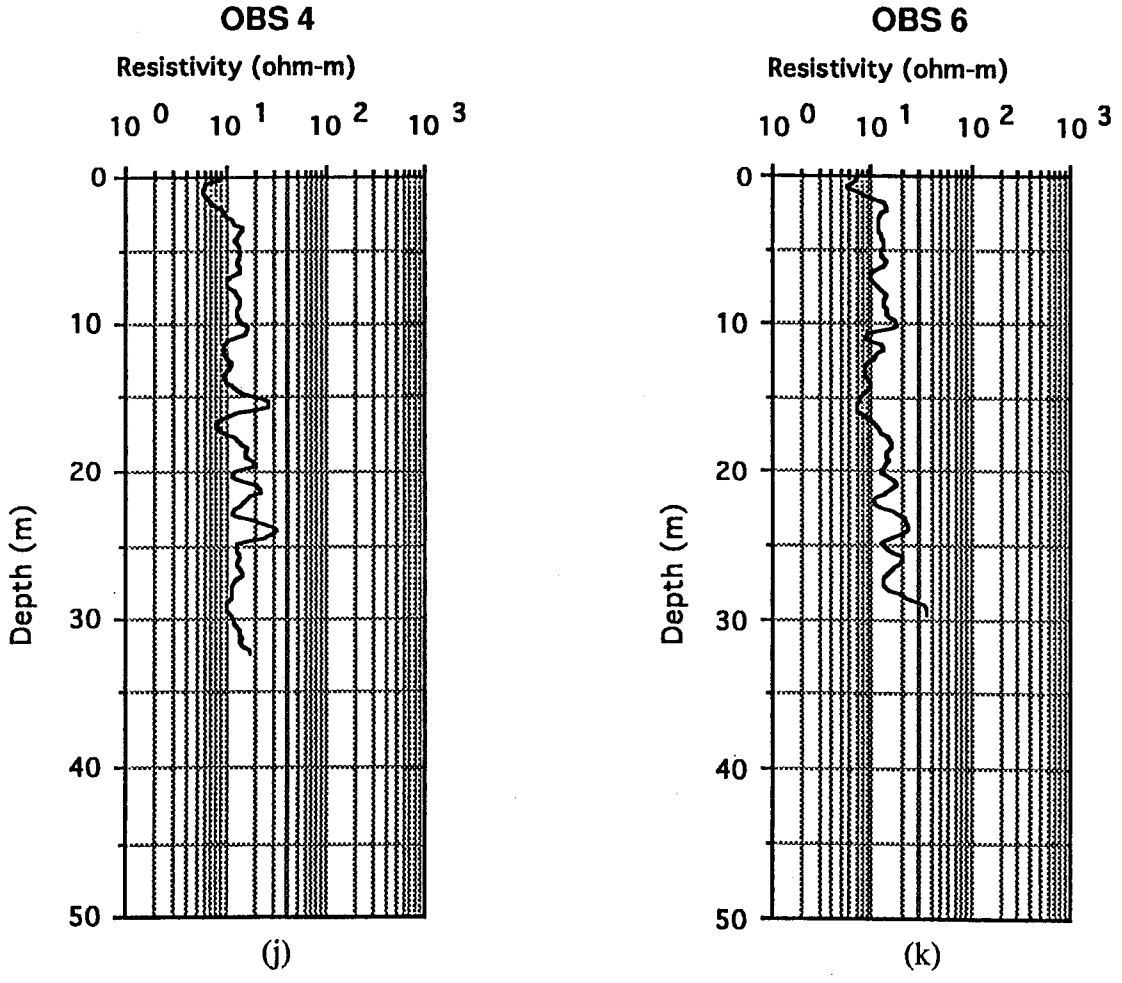

Figure D1 - (Continued from previous page) (j) Log of well ObS 4. (k) Log of well OBS 6.

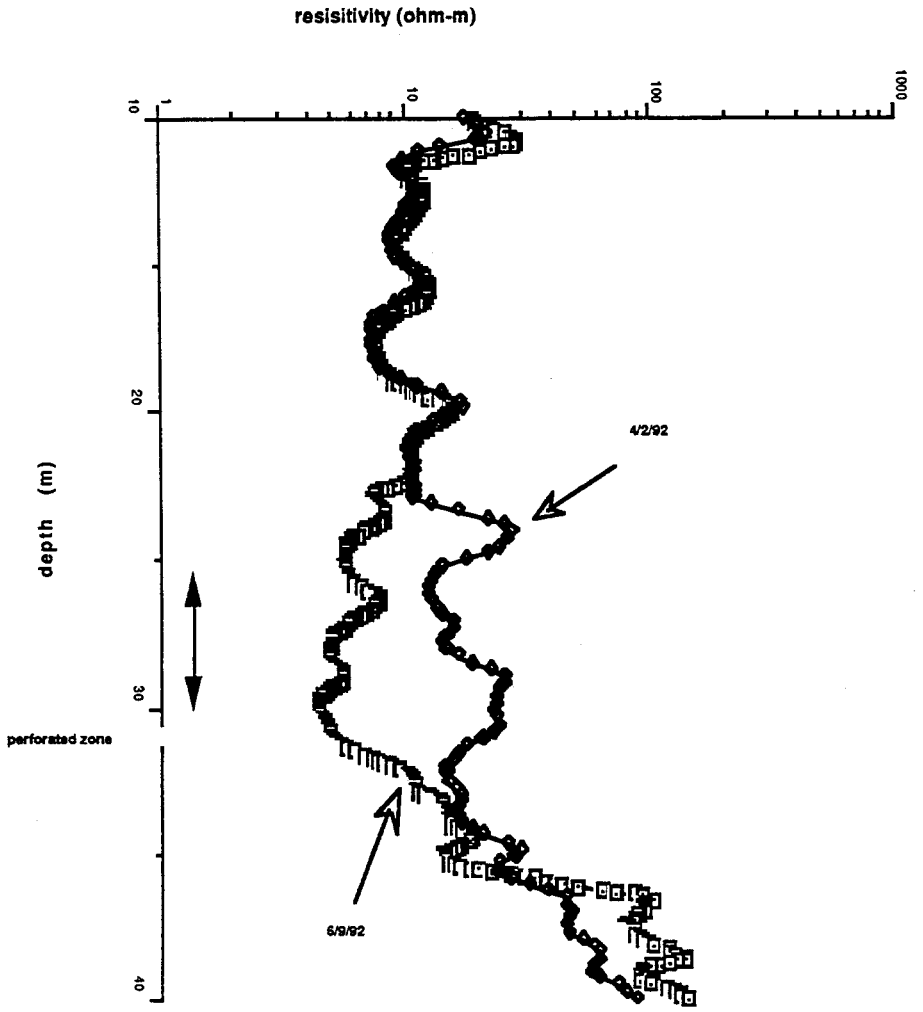

Figure D2 - Pre- and post-injection resistivity well logs collected in well INJ1.

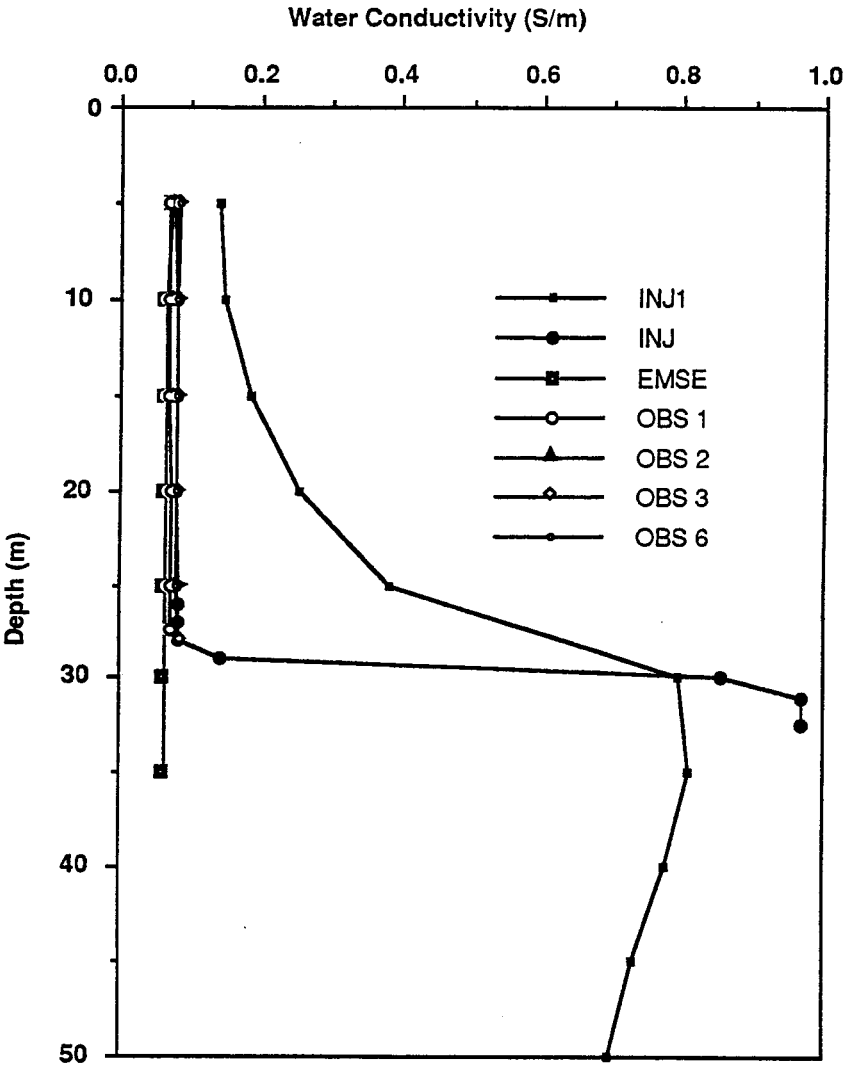

Figure D3 - Water conductivity measured on June 10, 1993 in seven of the boreholes at the Richmond Field Station.

Appendix E
Well Drawdown Data

To withdraw the 50,000 gallons of salt water that were injected in May, water was pumped out of INJ1 starting at 11:00 am on July 6, 1992 and continuing until 1:15 PM on July 28, 1992. During the withdrawal approximately 318,000 gallons was removed with the pump fixed in the well at 40 m depth and the pumping rate held at 10 gallons per minute. Water level measurements were made in eight of the boreholes open to the aquifer by Hung Wen Tseng and Peter Persoff starting immediately after the pumping began and continuing throughout the salt water extraction. These measurements were made to determine the hydrologic characteristics of the site and are plotted as a function of time in Figure B1.

To ensure that the salt water had been completely withdrawn, the electrical conductivity of the water pumped out of INJ1 was monitored with a conductance meter. The conductivity as a function of time is plotted in Figure B2 with the drawdown data from the INJ borehole. At the conclusion of the pumping the conductivity of the extracted water approached 0.076 S/m. Water conductivities measured in borehole OBS4 ranged from 0.068 S/m at the water table to 0.072 S/m at the bottom of the well. Because this well is 36 m from INJ1 and did not experience a large drawdown, it was determined that the conductances measured here are representative of the original values. Therefore we concluded that all of the injected salt water had been extracted.

Two conclusion were made from this pumping test. The first is that drawdowns in the boreholes to the south of INJ1 were much smaller than those to the north. This suggests that the aquifer is more conductive to the north and thus the injected plume moved in a northerly direction. The second conclusion is that EMNW and OBS6 have the largest drawdowns compared to the other boreholes except INJ. This indicates that EMNW and OBS6 have better hydrologic connection with INJ1 than the other wells that are open to the aquifer.

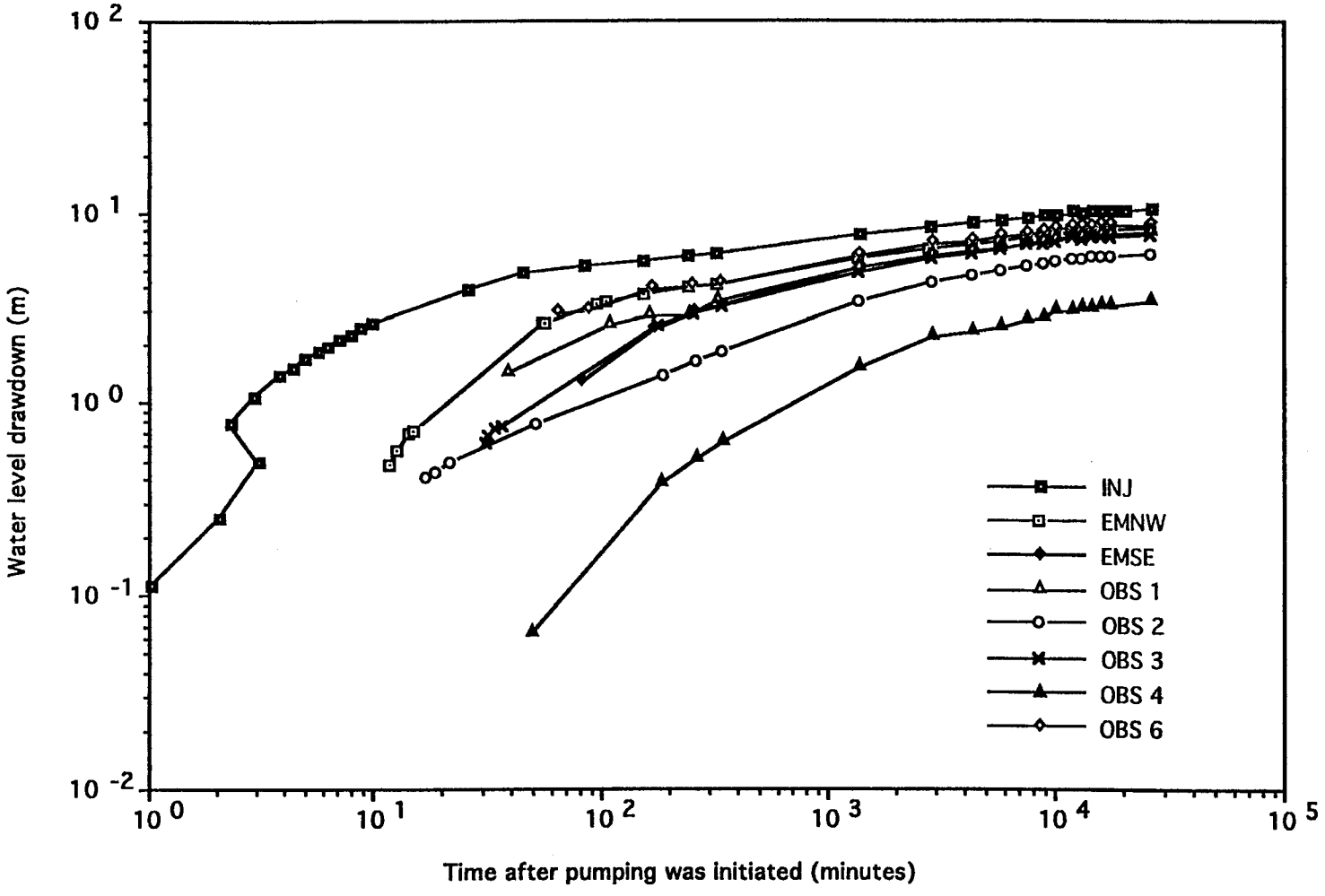

Figure E1 - Drawdown in the eight boreholes open to the aquifer during the saltwater extraction that was conducted from July 6 to July 26, 1992. The water was being pumped from well INJ1.

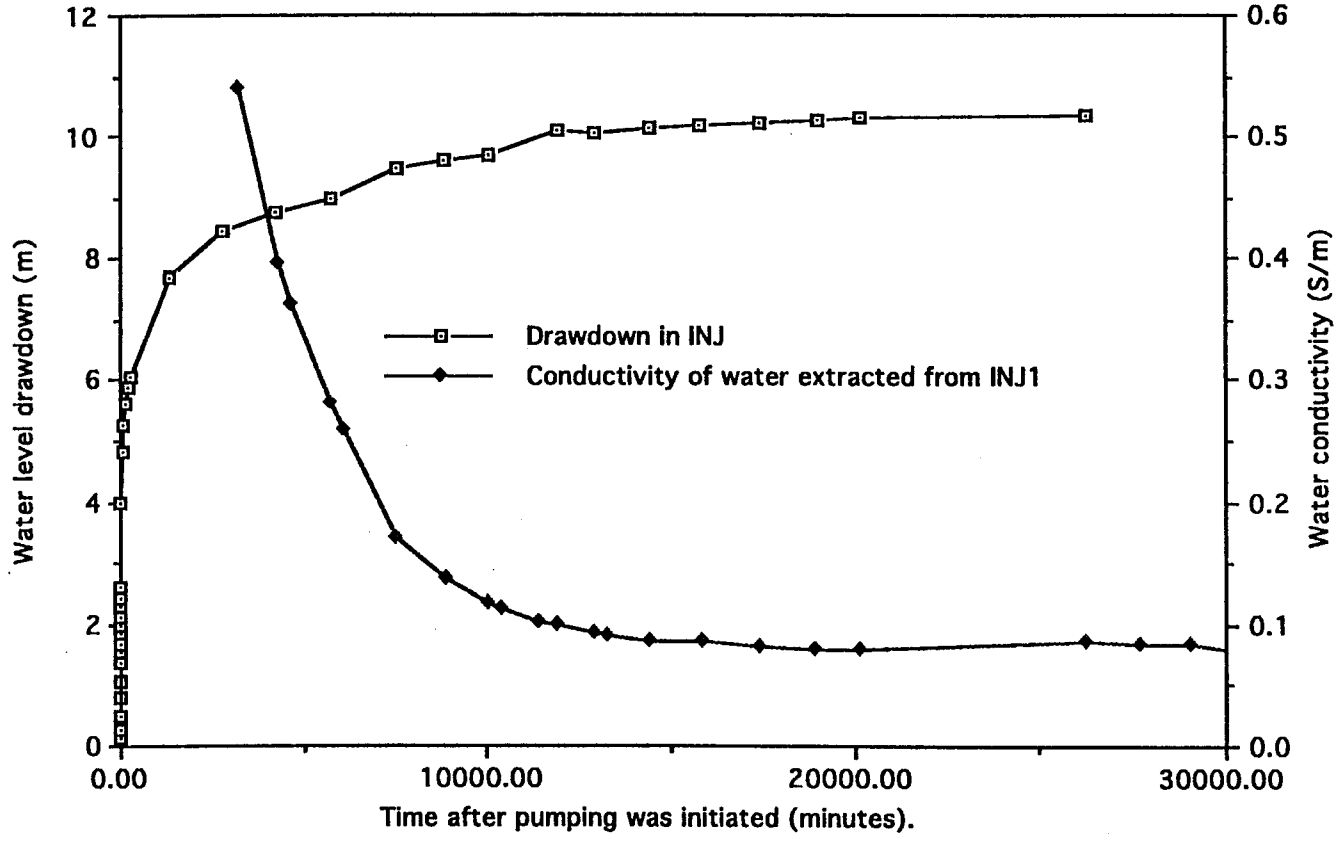

Figure E2 - Electrical conductivity of the water extracted from INJ1 and drawdown in INJ as a function of time.

LAWRENCE BERKELEY LABORATORY
UNIVERSITY OF CALIFORNIA
TECHNICAL INFORMATION DEPARTMENT
BERKELEY, CALIFORNIA 94720